A Nearby Galaxy Perspective on Interstellar Dust Properties and their Evolution

Frédéric Galliano

université
PARIS-SACLAY

Habilitation à diriger des recherches

A Nearby Galaxy Perspective on Interstellar Dust Properties and their Evolution

Habilitation à diriger des recherches de l'Université Paris-Saclay

Habilitation présentée et soutenue à Gif-sur-Yvette, le vendredi 14 janvier 2022, par

Frédéric GALLIANO
Département d'Astrophysique, CEA Paris-Saclay

Composition du jury:

Véronique BUAT Professeure, Laboratoire d'Astrophysique de Marseille	Rapportrice
Stéphane CHARLOT Directeur de recherche, Institut d'Astrophysique de Paris	Examinateur
Vassilis CHARMANDARIS Professeur, Université de Crète, Grèce	Rapporteur
François-Xavier DÉSERT Astronome, Institut de Planétologie et d'Astrophysique de Grenoble	Examinateur
Thomas HENNING Professeur, Institut Max Planck d'Astronomie, Heidelberg, Allemagne	Rapporteur
Laurent VERSTRAETE Professeur, Institut d'Astrophysique Spatiale, Orsay	Président

Contents

Contents iii

List of Figures ix

List of Tables xiv

Abstract xvii

Introduction xix
Interstellar Dust: A Key To Understanding Galaxy Evolution . . . xix
The Relevance of Nearby Galaxies . . . xx
Scope of the Manuscript . . . xxi

I Propaedeutics in Dust Physics 1
I.1 The Make-Up of Solids . . . 3
I.1.1 Atomic Structure . . . 3
I.1.1.1 The Hydrogen Atom . . . 3
I.1.1.2 Polyelectronic Atoms . . . 3
I.1.1.3 The Valence Shell . . . 4
I.1.1.4 Orbital Hybridisation . . . 7
I.1.2 Molecular Bonding . . . 7
I.1.2.1 Covalent Bonds . . . 7
I.1.2.2 Ionic Bonds . . . 9
I.1.2.3 Metallic Bonds . . . 10
I.1.2.4 Intermolecular Attraction . . . 10
I.1.3 The Solid State . . . 10
I.1.3.1 The Different Types of Solids . . . 10
I.1.3.2 The Band Structure of Solids . . . 10
I.1.3.3 The Fermi Level . . . 11
I.1.4 Interstellar Dust Candidates . . . 12
I.1.4.1 Silicates . . . 12
I.1.4.2 Hydrogenated Amorphous Carbon . . . 13
I.1.4.3 Graphite . . . 15
I.1.4.4 Polycyclic Aromatic Hydrocarbons (PAH) . . . 15
I.2 The Interaction of Light with Solids . . . 15
I.2.1 Bonds as Harmonic Oscillators . . . 17
I.2.1.1 The Harmonic Oscillator Amplitude . . . 17
I.2.1.2 The Plasma Frequency . . . 17
I.2.1.3 The Dielectric Function . . . 18
I.2.1.4 Harmonic Oscillator Cross-Section . . . 19
I.2.1.5 Optical Constants of Conductors . . . 21
I.2.1.6 The Kramers-Kronig Relations . . . 22
I.2.2 Grain Optical Properties . . . 23

I.2.2.1 Why Are Most Dust Features in the MIR? . . . 23
I.2.2.2 Dielectric Functions of Realistic Materials . . . 23
I.2.2.3 Computing Grain Cross-Sections . . . 24
I.2.2.4 Beyond Homogeneous Spheres . . . 30
I.2.2.5 Polarization . . . 32
I.2.3 Heat Capacities . . . 34
I.2.3.1 Distribution of Harmonic Oscillators . . . 34
I.2.3.2 Debye's Model . . . 36
I.2.3.3 Heat Capacities of Realistic Materials . . . 37
I.2.4 Heating and Cooling . . . 37
I.2.4.1 Kirchhoff's Law . . . 37
I.2.4.2 Equilibrium Heating . . . 40
I.2.4.3 Stochastic Heating . . . 42
I.2.4.4 Collisionnal Heating . . . 48

II Dust Observables and Models **51**
II.1 A Brief History of Interstellar Dust Studies . . . 53
II.1.1 The Challenges of Observing Interstellar Regions . . . 55
II.1.1.1 Limitations Due to the Atmosphere . . . 55
II.1.1.2 Historical Ground-Based Observatories . . . 55
II.1.1.3 Airborne Observatories . . . 56
II.1.1.4 Space Telescopes . . . 57
II.1.1.5 Grain-Collecting Spacecrafts . . . 61
II.1.2 Chronology of the Main Breakthroughs . . . 62
II.1.2.1 Obscuration and Dimming of Starlight . . . 62
II.1.2.2 The Dust Continuum . . . 63
II.1.2.3 Identification of Dust Features . . . 64
II.1.2.4 Dusty Epiphenomena . . . 66
II.1.2.5 Dust Models . . . 66
II.2 The Current Empirical Constraints . . . 68
II.2.1 Extinction . . . 68
II.2.1.1 UV-to-NIR Extinction . . . 70
II.2.1.2 MIR Extinction . . . 72
II.2.1.3 X-Rays . . . 73
II.2.1.4 Dichroic Extinction . . . 75
II.2.1.5 Diffuse Interstellar Bands . . . 75
II.2.2 Emission . . . 76
II.2.2.1 Infrared Continuum and Features . . . 76
II.2.2.2 Polarized Emission . . . 77
II.2.2.3 Non-Thermal Emission . . . 77
II.2.3 Elemental Abundances in Grains . . . 78
II.2.3.1 Measuring ISM Abundances . . . 78
II.2.3.2 Depletions . . . 79
II.2.4 Direct Measures . . . 81
II.2.4.1 Meteorite Inclusions . . . 82
II.2.4.2 Interplanetary Dust . . . 83
II.2.4.3 Laboratory Measurements . . . 83
II.3 State-of-the-Art Dust Models . . . 85
II.3.1 Composition and Size Distributions of Different Models . . . 85
II.3.1.1 Diversity in Composition . . . 85

II.3.1.2 Difference in Size Distributions . . . 86
II.3.2 The Model Properties . . . 87
II.3.2.1 Extinction and Emission . . . 88
II.3.2.2 The Fitted Constraints . . . 89
II.3.3 Some Useful Quantities . . . 89
II.3.3.1 Grain Sizes, Areas and Masses . . . 89
II.3.3.2 Opacity and Emissivity . . . 93

III The Grain Properties of Nearby Galaxies 97
III.1 Spectral Energy Distribution Modeling . . . 100
III.1.1 Radiative Transfer . . . 100
III.1.1.1 Definition of the Main Radiative Transfer Quantities . . . 100
III.1.1.2 The Radiative Transfer Equation . . . 103
III.1.1.3 Approximations for Clumpy Media . . . 108
III.1.1.4 Rigorous Solutions . . . 109
III.1.2 Approximate Treatments of the Mixing of Physical Conditions . . . 116
III.1.2.1 The Historical Model: the MBB . . . 116
III.1.2.2 A Phenomenological, Composite Approach . . . 117
III.1.2.3 Panchromatic Empirical SED Models . . . 122
III.1.2.4 The Matryoshka Effect . . . 128
III.1.3 Application to Nearby Galaxies . . . 128
III.1.3.1 The Different Types of Galaxies . . . 128
III.1.3.2 Large-Scale Dust Distribution in Galaxies . . . 131
III.1.3.3 Constraining the Grain Opacity . . . 135
III.1.3.4 Constraining the Size Distribution . . . 138
III.2 Studies Focussing on Specific Spectral Domains . . . 141
III.2.1 Scrutinizing Mid-IR Spectra . . . 141
III.2.1.1 The Aromatic Feature Spectrum . . . 142
III.2.1.2 Spectral Decomposition Methods . . . 144
III.2.1.3 PAH Band Ratio Studies . . . 151
III.2.1.4 Variations of the Aromatic Feature Strength . . . 157
III.2.2 Long-Wavelength Properties . . . 159
III.2.2.1 The Elusive Submillimeter Excess . . . 160
III.2.2.2 The Anomalous Microwave Emission . . . 162
III.3 Dust in Relation with the Gaseous and Stellar Contents . . . 165
III.3.1 The Phases of the ISM . . . 165
III.3.1.1 The Neutral Atomic Gas . . . 166
III.3.1.2 The Ionized Gas . . . 168
III.3.1.3 The Molecular Gas . . . 170
III.3.2 Dust as a Diagnostic Tool . . . 171
III.3.2.1 Dust to Study Star Formation . . . 171
III.3.2.2 Photodissociation Regions . . . 173
III.3.2.3 The Molecular Gas and its Dark Layer . . . 174

IV Modeling Cosmic Dust Evolution 177
IV.1 Stellar Evolution . . . 180
IV.1.1 The Fate of Stars of Different Masses . . . 180
IV.1.1.1 Nucleosynthesis . . . 180
IV.1.1.2 Brief Outline of Stellar Evolution . . . 181
IV.1.1.3 Parametrizing Star Formation . . . 183

IV.1.2 Elemental and Dust Yields . . . 185
IV.1.2.1 Injection of Heavy Elements in the ISM . . . 186
IV.1.2.2 Production of Stardust . . . 188
IV.2 Dust Evolution Processes in the ISM . . . 189
IV.2.1 Grain Formation and Transformation . . . 189
IV.2.1.1 Evidence of Grain Growth and Coagulation in the ISM . 190
IV.2.1.2 Studies of the Magellanic Clouds . . . 190
IV.2.1.3 Quantifying Grain Growth . . . 192
IV.2.2 Grain Destruction . . . 195
IV.2.2.1 Photodestruction of Small Grains . . . 195
IV.2.2.2 Thermal Sputtering . . . 196
IV.2.2.3 Destruction by SN Blast Waves . . . 199
IV.3 Cosmic Dust Evolution . . . 201
IV.3.1 Constraining the Dust Build-Up in Galaxies . . . 201
IV.3.1.1 Cosmic Dust Evolution Models . . . 202
IV.3.1.2 Empirical Inference of Dust Evolution Timescales . . . 206
IV.3.2 Evolution of the Aromatic Feature Carriers . . . 212
IV.3.2.1 The Different Evolution Scenarios . . . 213
IV.3.2.2 The Observed Trends . . . 214

V Methodological Effort and Epistemological Reflection 217
V.1 Understanding the Opposition between Bayesians and Frequentists . . 219
V.1.1 Two Conceptions of Probability and Uncertainty . . . 220
V.1.1.1 The Concept of Conditional Probability . . . 220
V.1.1.2 The Bayesian and Frequentist Assumptions . . . 221
V.1.2 Comparison of the Two Approaches on Simple Cases . . . 223
V.1.2.1 Simple Case: When the Two Approaches Agree . . . 223
V.1.2.2 Benefits of Using an Informative Prior . . . 225
V.1.2.3 Case Where the Two Approaches Differ: Non Gaussianity and Few Data . . . 227
V.1.3 Numerical Methods to Solve Bayesian Problems . . . 229
V.1.3.1 Sampling the Posterior Distribution . . . 229
V.1.3.2 Post-Processing MCMCs . . . 232
V.1.4 Decision Making and Limitations of the Frequentist Approach . 238
V.1.4.1 Hypothesis Testing . . . 238
V.1.4.2 Pros and Cons of the two Approaches . . . 241
V.2 Bayesianism, an Alternative to Popper's Scientific Method . . . 243
V.2.1 Bayes Formula Throughout History . . . 243
V.2.1.1 The Origins . . . 243
V.2.1.2 The Frequentist Winter . . . 245
V.2.1.3 The Bayesian Renaissance . . . 246
V.2.2 Bayesian and Popperian Epistemologies . . . 248
V.2.2.1 The Epistemological Debate at the Beginning of the XXth Century . . . 248
V.2.2.2 Popper's Logic of Scientific Discovery . . . 249
V.2.2.3 Verifiability, Holisticity and Parsimony: the Bayesian Alternative . . . 250
V.3 Relevance for Interstellar Dust Studies . . . 253
V.3.1 The Particularities of Interstellar Dust Studies . . . 254
V.3.1.1 Complexity of the Physics . . . 254

V.3.1.2 Entanglement of the Observations . . . 254
V.3.2 The Principles of Hierarchical Bayesian Inference . . . 255
V.3.2.1 Non-Hierarchical Bayesian Formalism for SED Modeling 255
V.3.2.2 The Introduction of Nuisance Variables . . . 256
V.3.2.3 The Role of the Hyperparameters . . . 257
V.3.3 Hierarchical Bayesian Models for ISD Studies . . . 258
V.3.3.1 Efficiency and Comparison to Other Methods . . . 258
V.3.3.2 The Role of the Prior . . . 262
V.3.3.3 Other Developments . . . 264

VI Conclusion and Prospective **267**
VI.1 What Have We Learned About ISD in the Past Decade? . . . 268
VI.1.1 About Dust Properties . . . 268
VI.1.2 About Dust Evolution . . . 269
VI.2 What Are the Open Questions for the Next Decade? . . . 270
VI.2.1 Extragalactic Dust . . . 270
VI.2.2 Dust Evolution Modeling . . . 271
VI.2.3 Dusty Epiphenomena . . . 271
VI.2.4 The Need for a New FIR Observatory . . . 272
VI.2.5 The Public Image of Interstellar Dust . . . 272
VI.3 Current Future Projects . . . 272
VI.3.1 The *Modelosaur* Approach . . . 272
VI.3.2 Out-of-the-Box Idea Bin . . . 273

A List of Acronyms **275**
A.1 General Acronyms . . . 275
A.2 Telescope and Instrument Acronyms . . . 277
A.3 Model and Project Acronyms . . . 278
A.4 Denomination of the Main Spectral Windows . . . 279

B Astronomers and Units **281**
B.1 Brief History of Unit Systems . . . 281
B.2 Working with Units . . . 282

C Useful Formulae **289**
C.1 3D Quantities and Volume Integrals . . . 290
C.1.1 Differential Operators . . . 290
C.1.1.1 Gradient . . . 290
C.1.1.2 Laplacian . . . 291
C.1.1.3 Divergence . . . 291
C.1.1.4 Curl . . . 291
C.1.2 Vectorial Analysis . . . 291
C.1.3 Integral Theorems . . . 292
C.1.4 Dust Heating and Cooling: Two Ways of Slicing the Pis . . . 292
C.1.4.1 Solution 1 . . . 293
C.1.4.2 Solution 2 . . . 293
C.2 Statistics . . . 293
C.2.1 General Formulae . . . 293
C.2.1.1 Moments of a PDF . . . 293
C.2.1.2 Marginalization . . . 294
C.2.1.3 Variable Change . . . 294

C.2.1.4 Combining Uncertainties . . . 294
C.2.2 Useful Probability Distributions . . . 295
C.2.2.1 Binomial Distribution . . . 295
C.2.2.2 Poisson Distribution . . . 295
C.2.2.3 Gaussian Distribution . . . 295
C.2.2.4 Student's t Distribution . . . 296
C.2.2.5 Split-Normal Distribution . . . 296
C.2.2.6 Lorentzian Distribution . . . 296
C.2.3 Drawing random variables from an arbitrary distribution . . . 296
C.2.3.1 The Rejection Method . . . 296
C.2.3.2 Inverting the CDF . . . 297
C.3 Trigonometry . . . 297
C.3.1 Transformations . . . 298
C.3.1.1 Rotations . . . 298
C.3.1.2 Relations Between Functions . . . 298
C.3.2 Addition . . . 298
C.3.2.1 Summing Angles . . . 298
C.3.2.2 Inverse Relations . . . 298
C.3.3 Linearization . . . 298
C.3.3.1 Squares and Cubes . . . 298
C.3.3.2 Inverse Relations . . . 299

Acknowledgements **301**

Bibliography **303**

List of Figures

I Propaedeutics in Dust Physics **1**

I.1 Shape of s, p, d, f electron orbitals . . . 5
I.2 Periodic table of elements . . . 5
I.3 First ionization potentials and electron affinities . . . 6
I.4 Hybrid orbitals of carbon . . . 8
I.5 Different types of molecular bonds . . . 8
I.6 An example of σ and π bonds . . . 9
I.7 Origin of the band structure of a solid . . . 11
I.8 The Fermi level and the different types of solid . . . 12
I.9 Structure of interstellar dust candidates . . . 14
I.10 Appearance of various minerals . . . 14
I.11 Absorption, scattering and emission . . . 16
I.12 Effect of an electromagnetic wave on a dielectric . . . 16
I.13 Amplitude of a forced harmonic oscillator . . . 18
I.14 Idealized optical constants . . . 20
I.15 Molecular transitions . . . 23
I.16 Dielectric functions of different materials . . . 25
I.17 Illustration of the extinction paradox . . . 27
I.18 Mie, Rayleigh and geometric optics regime . . . 28
I.19 Cross-sections of silicate and graphite grains . . . 29
I.20 Oblate and prolate spheroids . . . 31
I.21 Absorption cross-sections of grain aggregates computed with DDA . . . 32
I.22 Stokes parameters . . . 33
I.23 The three types of grain-induced polarization of light . . . 35
I.24 Phonon modes . . . 37
I.25 Heat capacities. . . . 38
I.26 Emissivity of grains at thermal equilibrium with the radiation field . . . 39
I.27 Planck averages of graphite and silicates . . . 41
I.28 Diffuse Galactic ISRF . . . 41
I.29 Grain equilibrium temperatures . . . 42
I.30 Temperature fluctuations of grains with different radii . . . 44
I.31 Temperature fluctuations of grains with different starlight intensities 45
I.32 Stochastically heated grains . . . 47
I.33 Transition radius for stochastically heated grains . . . 48
I.34 Photon and electron energy densities . . . 50
I.35 Collisional heating rate . . . 50

II Dust Observables and Models **51**

II.1 Early ISM and IR astronomy . . . 54
II.2 Absorbance of Earth's atmosphere . . . 56

II.3 Airborne observatories . . . 57
II.4 All sky maps . . . 60
II.5 Analysis of the Stardust mission . . . 61
II.6 First evidences of interstellar dust . . . 63
II.7 The pioneers . . . 64
II.8 First detection of UIBs . . . 65
II.9 Désert et al. (1990) dust model . . . 67
II.10 Panchromatic dust observables . . . 70
II.11 Galactic extinction curves . . . 72
II.12 MIR extinction . . . 73
II.13 X-ray edges . . . 74
II.14 Polarized extinction and DIBs . . . 75
II.15 Galactic diffuse ISM SED . . . 76
II.16 Solar abundances . . . 79
II.17 Depletion variations within the MW . . . 80
II.18 MW dust composition inferred from depletions . . . 81
II.19 Presolar grains in meteorites . . . 82
II.20 Micrometeorite collection in Antarctica . . . 83
II.21 NASA Ames PAH experiment . . . 84
II.22 Laboratory measurement of silicate opacities . . . 84
II.23 Size distribution of several dust models . . . 87
II.24 Model opacity and emissivity . . . 90
II.25 THEMIS fit of the Galactic constraints . . . 91
II.26 IR approximation of the opacity . . . 93
II.27 Effect of U on the SED . . . 95

III The Grain Properties of Nearby Galaxies **97**
III.1 Moments of the specific intensity . . . 102
III.2 The radiative transfer equation . . . 104
III.3 Solution to the radiative transfer equation for an isothermal cloud, without scattering . . . 105
III.4 Escaping radiation from a spherical cloud . . . 107
III.5 Escaping SED from clumpy spherical clouds . . . 110
III.6 Principle of Monte-Carlo radiative transfer . . . 112
III.7 Drawing photons in a Monte-Carlo radiative transfer model . . . 113
III.8 Drawing scattering angles in a Monte-Carlo radiative transfer model . . . 113
III.9 Spatial distributions of the clumpy radiative transfer model . . . 114
III.10 Random photon path within a clumpy medium . . . 115
III.11 Total SED from the clumpy radiative transfer model . . . 115
III.12 MBB fitting . . . 117
III.13 Phenomenological mixing of physical conditions . . . 119
III.14 Effect of the ISRF hardness on the SED . . . 120
III.15 Degeneracy of the grain size and ISRF distributions . . . 121
III.16 SED fit with the Draine & Li (2007) starlight intensity distribution . . . 122
III.17 Comparison of different SED models . . . 123
III.18 Stellar isochrones . . . 125
III.19 Evolution of stellar SEDs as a function of time . . . 126
III.20 Multiphase SEDs of galaxies . . . 127
III.21 Matryoshka effect demonstrated on the LMC . . . 129

III.22 Hubble-de-Vaucouleurs galaxy morphology diagram . . . 130
III.23 Visible-range image of three nearby galaxies . . . 132
III.24 Principal sources of contaminations encountered when modeling SEDs 134
III.25 Radiative transfer modeling of NGC 4565 . . . 136
III.26 Dust mass discrepancy in the LMC . . . 137
III.27 Effect of a blast wave on the grain size distribution . . . 139
III.28 Grain size distribution in four dwarf galaxies . . . 140
III.29 Extinction curves of low-metallicity environments . . . 141
III.30 MIR spectra of galaxies . . . 143
III.31 Vibrational modes of PAHs . . . 144
III.32 Laboratory and theoretical PAH spectra . . . 145
III.33 Empirical calibration of UIB profiles . . . 148
III.34 MIR spectral fitting methods . . . 149
III.35 PAH and small grain templates . . . 151
III.36 Diversity of MIR spectra among and within galaxies . . . 152
III.37 PAH band ratio correlations inside and among galaxies . . . 153
III.38 Theoretical MIR band ratio variations . . . 154
III.39 Calibration of PAH ratio diagnostics . . . 156
III.40 PAH band ratio as diagnostics of the physical conditions . . . 157
III.41 Effect of ISRF hardness on PAH strength . . . 158
III.42 Effect of metallicity on the PAH strength . . . 159
III.43 Submillimeter excess in NGC 1569 . . . 160
III.44 Spatially-resolved submm excess in the LMC . . . 162
III.45 AKARI 9 μm map of λ-Orionis . . . 164
III.46 AME correlation with ionized PAHs in λ-Orionis . . . 165
III.47 Cooling function of the ISM at Solar metallicity . . . 167
III.48 Photoelectric heating in PDRs . . . 168
III.49 Neutral ISM phase diagram . . . 169
III.50 H_2 formation on grain surface . . . 170
III.51 Structure of a PDR . . . 172
III.52 Comparison of visual extinctions in 30 Doradus . . . 174
III.53 Metallicity effect on the CO-dark gas . . . 175
III.54 Molecular gas pressure in the center of M 83 . . . 176

IV Modeling Cosmic Dust Evolution **177**
IV.1 The interstellar dust lifecycle . . . 179
IV.2 Average nuclear binding energies per nucleon . . . 181
IV.3 Schematic representation of stellar evolution . . . 184
IV.4 Initial mass functions . . . 185
IV.5 Parametric star formation histories . . . 186
IV.6 Nucleosynthesis origin of the main elements . . . 187
IV.7 Solar metallicity elemental stellar yields . . . 187
IV.8 Spatially-resolved SED fits in N 44 and N 66 . . . 191
IV.9 Dust-to-gas mass surface density relation in N 44 and N 66 . . . 192
IV.10 Grain growth timescales . . . 194
IV.11 Lifetimes of small grains in a radiation field . . . 197
IV.12 Carving out of PAHs by UV photons in N 11 . . . 197
IV.13 Thermal and kinetic sputtering times of silicates and carbon grains . . . 198
IV.14 Evidence of thermal sputtering in elliptical galaxies . . . 199

IV.15 Effects of dust evolution on the SEDs of galaxies. 201
IV.16 Dust evolution tracks for a MW-like galaxy 205
IV.17 Effects of SFH-related parameters on dust evolution 207
IV.18 Effects of tuning parameters on dust evolution 208
IV.19 Dustiness-metallicity relation fitted with a dust evolution model . . . 209
IV.20 Empirical estimates of dust evolution timescales as a function of metallicity 211
IV.21 Evolution of the mass fraction of small a-C(:H) grains with metallicity and starlight intensity 214
IV.22 The potential of quiescent very-low-metallicity galaxies to understand the origin of small a-C(:H) grains 215

V Methodological Effort and Epistemological Reflection 217
V.1 Venn diagram to demonstrate Bayes' rule 221
V.2 Simulation of the measure of a stellar flux to compare Bayesian and frequentist methods 223
V.3 Bayesian and frequentist solutions to the problem of Fig. V.2 225
V.4 The benefits of using an informative prior 226
V.5 Flux measures with a non-linear detector 228
V.6 Markov Chain Monte-Carlo algorithms 231
V.7 Importance of the choice of the Metropolis-Hastings proposal distribution 234
V.8 Post-processing of the MCMC of a sample of sources 235
V.9 MCMC statistics of a sample of sources 236
V.10 Demonstration of the use of posterior predictive p-values 237
V.11 Bayesian and frequentist hypothesis testing 239
V.12 The probability pioneers 244
V.13 The frequentist promoters 246
V.14 The Bayesian resistance 247
V.15 Three figures of modern epistemology 248
V.16 Bayes factors and parsimony 252
V.17 Example of hierarchical Bayesian SED fits 259
V.18 Posterior distributions with standard and hierarchical Bayesian methods 260
V.19 Comparison of least-squares, standard Bayesian and HB methods . . 261
V.20 Solving the emissivity-index-temperature degeneracy of MBBs with a HB model 262
V.21 Demonstration of the effect of the prior in a HB model 263
V.22 The holistic approach: inclusion of external parameters into the prior 264

VI Conclusion and Prospective 267

A List of Acronyms 275
A.1 Spectral domains represented over the SED of a nearby galaxy 279

B Astronomers and Units 281

C Useful Formulae 289

C.1 Most common coordinate systems 290
C.2 Two ways of slicing the πs 292
C.3 Methods for drawing random numbers from arbitrary distributions . 297

D.1 Nerdy allegory of my collaboration network 301

List of Tables

I Propaedeutics in Dust Physics **1**
I.1 Atomic quantum numbers . . . 3
I.2 Atomic shell structure . . . 4
I.3 General properties of interstellar dust candidates . . . 15

II Dust Observables and Models **51**
II.1 Chronology of the main ISD breakthroughs . . . 69
II.2 Comparison between different dust models . . . 86
II.3 Moments of the THEMIS size distribution . . . 92
II.4 Dustiness and other ratios for the THEMIS model . . . 92
II.5 Optical properties of the THEMIS model . . . 94
II.6 Transition wavelengths between small and large grain emission . . . 94
II.7 Emissivity of the THEMIS model . . . 95

III The Grain Properties of Nearby Galaxies **97**
III.1 Mean free path as a function of wavelength and density . . . 103
III.2 Basic properties of the main stellar classes . . . 124
III.3 Free emissivity index MBB fits of nearby galaxies by the *Planck* collaboration . . . 136
III.4 UIB profile parameters . . . 147
III.5 Most prominent MIR gas lines . . . 150
III.6 Phases of the ISM . . . 166

IV Modeling Cosmic Dust Evolution **177**
IV.1 IMF properties . . . 184
IV.2 Summary of the observational evidence about interstellar dust origin at normal metallicity . . . 212

V Methodological Effort and Epistemological Reflection **217**
V.1 Jeffreys strength of evidence scale . . . 240
V.2 Pros and cons of the Bayesian and frequentist methods . . . 242
V.3 Comparison of Bayesian and Popperian epistemologies . . . 253
V.4 Inferred statistical properties of the HB model in Fig. V.19.c . . . 261

VI Conclusion and Prospective **267**

A List of Acronyms **275**

A.1 List of acronyms used throughout the manuscript 277
A.2 List of instrumental acronyms used throughout the manuscript 278
A.3 List of model acronyms used throughout the manuscript 278
A.4 Denomination of the main spectral windows 280

B Astronomers and Units **281**
B.1 Unit conversion 283
B.2 Fundamental constants 284
B.3 Astronomical constants 285
B.4 Classical electrodynamics 286
B.5 The magnitude system 287

C Useful Formulae **289**

Abstract

The truth is the whole.

(George Wilhelm Friedrich HEGEL; Hegel, 1807)

Interstellar dust is a key physical ingredient of galaxies, obscuring star formation, regulating the heating and cooling of the gas, and building-up chemical complexity. In this manuscript, I give a wide review of interstellar dust properties and some of the modern techniques used to study it. I start with a general introduction presenting the main concepts, in molecular and solid-state physics, required to understand the contemporary literature on the subject. I then review the empirical evidence we currently use to constrain state-of-the-art dust models. Follows a long discussion about our current understanding of the grain properties of nearby galaxies, with an emphasis on the results from spectral energy distribution modeling. The following chapter presents dust evolution at all scales. I review the different microphysical evolution processes, and the way they are accounted for in cosmic dust evolution models. I give my take on the origin of interstellar dust in galaxies of different metallicities. The last chapter focusses on methodology. I give an introduction to the Bayesian method and compare it to frequentist techniques. I discuss the epistemological consequences of the two approaches, and show why the field of interstellar dust requires a probabilistic viewpoint. I end the manuscript with a summary of the major breakthroughs achieved in the past decade, and delineate a few prospectives for the next decade.

Introduction

The unity of all science consists alone in its method, not in its material.

(Karl PEARSON; Pearson, 1892)

Interstellar Dust: A Key To Understanding Galaxy Evolution

Understanding galaxy evolution is one of the main objectives of observational cosmology, as it allows mapping the history of the Universe, from the dark ages to the present times (*e.g.* Madau & Dickinson, 2014; Buat, 2015). At the center of this evolution lies the *InterStellar Medium* (ISM). This complex intertwining of ionized, atomic and molecular gas phases mixed with dust grains, fills the volume of a galaxy, ultimately leading to star formation (SF), by gravitational collapse (*e.g.* Klessen & Glover, 2016). Although accounting for only $\simeq 1\,\%$ of its mass, dust is an essential component of the ISM. It consists of solid particles ($0.3\ \text{nm} \lesssim \text{radius} \lesssim 0.3\ \mu\text{m}$) made out of the available heavy elements, predominantly arranged in silicate and carbonaceous compounds (*e.g.* Draine, 2003a). These grains, absorbing and scattering starlight, have a radical impact on a galaxy.

- They have a nefarious role of obscuring our direct view of star formation. They normally re-radiate $\simeq 25\,\%$ of the stellar power in the *InfraRed* (IR; *cf.* Table A.4), and up to $\simeq 99\,\%$ in ultraluminous IR galaxies (*e.g.* Bianchi et al., 2018; Clements et al., 1996).
- Dust is an essential ingredient of star formation, as it contributes to (*e.g.* Li & Greenberg, 2003):
  - radiatively evacuating the gravitational energy of collapsing molecular clouds;
  - shielding the molecules from starlight, which protect them from destruction and reduces their ionization fraction, allowing the formation of protostellar cores.
- In addition, grains are responsible for the heating of the gas in *PhotoDissociation Regions* (PDR), by the photoelectric effect (Draine, 1978; Kimura, 2016).
- They are also catalysts of numerous chemical reactions, including the formation of the most abundant molecule in the Universe, H_2 (Gould & Salpeter, 1963; Bron et al., 2014).
- Elongated grains tend to align with the magnetic field. Polarized extinction (in the visible) and emission (in the IR) by grains are therefore one of the most popular tools to study the magnetic field in the ISM (*e.g.* Planck Collaboration et al., 2016b,d; Guillet et al., 2018).

  ☞ A detailed knowledge of the dust properties and their evolution is therefore imperative in order to both interpret observations of galaxies and model their ISM.

Dust physics is characterized by the great complexity of its make-up, as the number of ways to combine elements to build interstellar solids is virtually limitless. Most of the progress in this field thus relies on empirical constraints: observations and laboratory experiments on cosmic dust analogs. Our current knowledge of *interstellar dust* (ISD) properties is however hampered by several factors (Galliano et al., 2018, for a review). First, observations of interstellar regions are always the superimposition, along the line of sight and within the telescope beam, of a range of physical conditions: *(i)* intensity and hardness of the *InterStellar Radiation Field* (ISRF); *(ii)* gas density; and

(iii) presence of shocks. Consequently, since we can never accurately recover the *3-Dimensional* (3D) structure of a region, several degeneracies between the grain constitution and their excitation prevent a unique solution. Second, the grain constitution [1] is known to evolve under the effects of ISRF and gas density (*e.g.* Draine, 2009; Jones et al., 2013; Ysard et al., 2015). It is thus likely that, in addition to variations of excitation conditions, ISD observables are coming from a combination of altered grain mixtures. Finally, the derivation of precise dust properties, even from observations towards a uniform, uncontaminated region, is limited by an incomplete spectral coverage and by instrumental uncertainties.

> ☞ It follows that a rigorous attempt at quantifying grain parameters and their evolution must account for these factors in both the choices of astrophysical targets and modeling approach.

The Relevance of Nearby Galaxies

Due to their proximity, ISM regions of our own galaxy, the *Milky Way* (MW), can be observed with the finest linear resolution. MW studies have consequently laid the ground for the development of physical dust models (Draine, 2003a, for a review). They are however limited by the small range of environmental conditions they span.

- There are no really massive star-forming regions in the MW. The only *Super Star Cluster* (SSC; $M_\star \gtrsim 10^5\ M_\odot$; *e.g.* Johnson, 2001; Dowell et al., 2008) is Westerlund 2 in RCW 49 (Moffat et al., 1991).
- As in most spiral galaxies, there is a radial gradient of metallicity (the mass fraction of elements heavier than He, noted Z; *e.g.* Asplund et al., 2009). It however ranges narrowly ($0.7\ Z_\odot \lesssim Z \lesssim 2\ Z_\odot$; Henry & Worthey, 1999).
- The massive central black hole, Sgr A* of the Galactic center is relatively passive (Mezger et al., 1996) compared to *Active Galactic Nuclei* (AGN), such as NGC 1068 (*e.g.* Le Floc'h et al., 2001).

MW studies are also limited by the confusion along the sightline, as we are seeing the projected material of the entire disk. Finally, distances of interstellar clouds can be difficult to estimate for the same reason, although 3D maps of the MW are becoming more precise (*e.g.* Lallement et al., 2018).

In contrast, nearby galaxies (closer than $\simeq 100$ Mpc; Galliano et al., 2018) represent an undertapped population with several potentials. First, they harbor a wider range of environmental parameters, allowing us, in particular, to probe dust in extreme conditions.

- Nearby galaxies, especially *Blue Compact Dwarfs* (BCD), contain numerous SSCs (*e.g.* O'Connell et al., 1994; Johnson et al., 2000; Martín-Hernández et al., 2005). They are ideal laboratories to understand the impact of massive star formation on the ISM.
- Extremely low-metallicity objects, such as I Zw 18 ($Z \simeq 1/35\ Z_\odot$; Izotov et al., 1999), allow us to study dust in environments where the chemical enrichment resembles primordial galaxies.
- AGNs have a radical impact on the ISM of their host galaxies, heavily processing the grains (*e.g.* their crystalline fraction; Spoon et al., 2006). In addition, bright AGNs can be used to study grains in absorption (*e.g.* Spoon et al., 2002; Mason et al., 2007).

Second, face-on galaxies, observed at high Galactic latitude, provide clearer sightlines than in the MW. Finally, the lower linear resolution we can reach in nearby objects ($\simeq 100$ pc to 1 kpc in the IR) is the ideal length scale to adopt a statistical description of the distribution of clouds and stars [2], whereas detailed, parsec-scale MW studies are left to the nearly impossible task of inferring the precise geometry of each single cloud and the position in space of the surrounding stars.

1. Stoichiometry, chemical composition, solid-state structure, size distribution and abundance relative to the gas.
2. The average distance between stars is $\simeq 1$ pc, and the typical size of molecular clouds ranges from $\simeq 1$ to $\simeq 100$ pc (*e.g.* Solomon et al., 1987).

Scope of the Manuscript

Most of my career until now has been devoted to studying the dust properties and their evolution in nearby galaxies. I have chosen to focus the present manuscript on the following directions.

- It is primarily a synthesis of my achievements in this field. The goal is not to repeat the content of my publications, but to put them in perspective with other studies. For that reason, the presentation of my results occupy only a small fraction of the manuscript.
- It also provides a review of our current understanding of ISD, and outlines the most promising directions this field should explore during the next decade.
- Finally, I have tried to compile introductory material, concepts and figures that could be useful to students starting in this field, but that are otherwise scattered across the literature. Unless otherwise noted in the caption, the figures presented here are original and are licensed under CC BY-SA 4.0 [3].

It is divided as follows.

Chap. I provides a reminder of the main concepts at the foundation of ISD physics.

Chap. II gives a general introduction about the most reliable observational evidences we have about ISD, and the current models attempting at synthesizing them.

Chap. III reviews dust properties in the MW and nearby galaxies, and the way they are constrained.

Chap. IV reviews evidences of dust evolution and models accounting for their formation and destruction at the scale of a galaxy.

Chap. V is a more original take on my methodological approach, motivated by some epistemological concepts.

Chap. VI is a summary of what we have learned about ISD in the past decade and what we should do during the next one.

3. This means you can freely reproduce or modify a figure without my permission, as long as you credit my name, by citing this HDR, and give the link to the license.

Chapter I

Propaedeutics in Dust Physics

As soon as we thought something, look in what sense the opposite is true.

(Simone WEIL; Weil, 1947)

Contents

I.1 The Make-Up of Solids . . . 3
I.1.1 Atomic Structure . . . 3
I.1.1.1 The Hydrogen Atom . . . 3
I.1.1.2 Polyelectronic Atoms . . . 3
I.1.1.3 The Valence Shell . . . 4
Ionization potential. . . . 4
Electron affinity. . . . 4
Electronegativity. . . . 4
I.1.1.4 Orbital Hybridisation . . . 7
I.1.2 Molecular Bonding . . . 7
I.1.2.1 Covalent Bonds . . . 7
I.1.2.2 Ionic Bonds . . . 9
I.1.2.3 Metallic Bonds . . . 10
I.1.2.4 Intermolecular Attraction . . . 10
I.1.3 The Solid State . . . 10
I.1.3.1 The Different Types of Solids . . . 10
I.1.3.2 The Band Structure of Solids . . . 10
I.1.3.3 The Fermi Level . . . 11
I.1.4 Interstellar Dust Candidates . . . 12
I.1.4.1 Silicates . . . 12
Olivine. . . . 13
Pyroxene. . . . 13
I.1.4.2 Hydrogenated Amorphous Carbon . . . 13
I.1.4.3 Graphite . . . 15
I.1.4.4 Polycyclic Aromatic Hydrocarbons (PAH) . . . 15
I.2 The Interaction of Light with Solids . . . 15
I.2.1 Bonds as Harmonic Oscillators . . . 17
I.2.1.1 The Harmonic Oscillator Amplitude . . . 17
I.2.1.2 The Plasma Frequency . . . 17
I.2.1.3 The Dielectric Function . . . 18
I.2.1.4 Harmonic Oscillator Cross-Section . . . 19

I.2.1.5 Optical Constants of Conductors . . . 21
I.2.1.6 The Kramers-Kronig Relations . . . 22
Implications. . . . 22
Interpretation. . . . 22
Constraint on the Cross-Section. . . . 22
I.2.2 Grain Optical Properties . . . 23
I.2.2.1 Why Are Most Dust Features in the MIR? . . . 23
I.2.2.2 Dielectric Functions of Realistic Materials . . . 23
I.2.2.3 Computing Grain Cross-Sections . . . 24
Geometrical optics. . . . 26
The Mie regime. . . . 26
The Rayleigh regime. . . . 27
I.2.2.4 Beyond Homogeneous Spheres . . . 30
Effective medium theory (EMT). . . . 30
Ellipsoids in the Rayleigh regime. . . . 31
Discrete Dipole Approximation (DDA). . . . 31
I.2.2.5 Polarization . . . 32
The Stokes parameters. . . . 32
Grain alignment. . . . 33
Polarization by scattering. . . . 33
Dichroic extinction. . . . 34
Polarized emission. . . . 34
I.2.3 Heat Capacities . . . 34
I.2.3.1 Distribution of Harmonic Oscillators . . . 34
I.2.3.2 Debye's Model . . . 36
I.2.3.3 Heat Capacities of Realistic Materials . . . 37
I.2.4 Heating and Cooling . . . 37
I.2.4.1 Kirchhoff's Law . . . 37
Opacity. . . . 38
Emissivity. . . . 38
Modified Black Body (MBB). . . . 39
I.2.4.2 Equilibrium Heating . . . 40
Planck average. . . . 40
ISRF-averaged efficiency. . . . 40
The diffuse ISRF. . . . 40
Equilibrium temperatures. . . . 42
I.2.4.3 Stochastic Heating . . . 42
Absorption and cooling times. . . . 42
The temperature fluctuations. . . . 43
Out-of-equilibrium emission. . . . 43
Numerical methods. . . . 46
Equilibrium criterion. . . . 46
I.2.4.4 Collisionnal Heating . . . 48
Electronic heating rate. . . . 48
Cases where collisions dominate the heating. . . . 49

Most reviews about ISD (*e.g.* Draine, 2003a; Whittet, 2003; Tielens, 2005; Draine, 2011; Jones, 2016a,b,c; Galliano et al., 2018) assume that the reader has a good knowledge of solid-state physics [1]. It is however not always the case, especially among students. The present chapter is intended to synthesize

1. The book by Krügel (2003) is a notable exception. It starts from elementary electrodynamics and atomic physics.

the basic knowledge necessary to understand contemporary publications in the field. We have opted for a simple presentation of the most important concepts, accompanied with a few original figures. We present the most important formulae and refer the reader to reliable textbooks for their proofs. We have tried to answer everything students always wanted to know about dust, but were afraid to ask.

I.1 The Make-Up of Solids

Atoms can be combined to form molecules or solids. The properties of these compounds depend greatly on the way their constitutive atoms are bonded together, by their electrons. Electrons being fermions (their spin is 1/2), the *Pauli exclusion principle* implies that each of them must occupy a different state in a system, characterized by its wave function (*e.g.* Tome II, Chapter XIV of Cohen-Tannoudji et al., 1996). The electronic shells of atoms, the bonds of molecules and the band structure of solids all follow from this principle.

I.1.1 Atomic Structure

I.1.1.1 The Hydrogen Atom

The electrons of an atom each have a distinct wave function, Ψ, called *orbital*. The probability density function of presence of the electron is proportional to $|\Psi|^2$. These orbitals are solutions to the Schrödinger equation, in the electrostatic well created by the nucleus, assumed to be infinitely heavy[2]. These solutions are relatively simple in the case of the hydrogen atom (*cf. e.g.* Chap. 3 of Bransden & Joachain, 1983). Its single electron can occupy different shells, characterized by their *principal quantum number*, n. This quantum number determines the energy level of the orbitals ($\mathrm{E} \propto 1/n^2$) as well as their size (*cf.* Table I.1). Each individual shell is divided into subshells, characterized by the *azimuthal number*, l, quantifying the angular momentum of the electron ($\mathrm{L} \propto \sqrt{l(l+1)}$), which can be 0, for s subshells (*cf.* Table I.2). The orbitals in each subshell are combinations of spherical harmonic functions. These functions are anisotropic. The *magnetic quantum number*, m_l, quantifies their orientation in space, as displayed in Fig. I.1. Finally, the *spin quantum number*, m_s, quantifies the direction of the electronic spin (up or down).

Name	Symbol	Values	Signification
Principal	n	$1, 2, \ldots, \infty$	Energy ($\mathrm{E} \propto 1/n^2$ for H) or size of the shell
Azimuthal	l	$0, 1, \ldots, n-1$	Angular momentum ($\mathrm{L} \propto \sqrt{l(l+1)}$)
Magnetic	m_l	$l, l-1, \ldots, -l$	Orientation (spherical harmonic combination)
Spin	m_s	$+1/2, -1/2$	Magnetic moment (spin direction)

TABLE I.1 – *Atomic quantum numbers.* Adapted from Table 7.2 of Atkins (1992).

I.1.1.2 Polyelectronic Atoms

The different energy levels of an atom can be populated by excitation (collision or photon absorption). In the fundamental state of the H atom, the electron occupies the $n = 1$ level. The electrons of a polyelectronic atom in its fundamental state occupy the lowest energy orbitals available. Each electron must have a unique set of the four quantum numbers (Table I.1). The nucleus charge, Z, is higher, which causes the inner shells to be closer to the nucleus. The electric field seen by the outer shells is thus partially screened by the inner shells. A fundamental difference between polyelectronic

2. The electron-to-proton mass ratio is $m_e/m_p \simeq 5 \times 10^{-4}$ (*cf.* Table B.2).

Principal quantum number	Bohr shells	Azimuthal quantum number				Subshell letter Number of electrons per subshell
		s 2	p 6	d 10	f 14	
$n=1$	K	$l=0$				
$n=2$	L	$l=0$	$l=1$			
$n=3$	M	$l=0$	$l=1$	$l=2$		
$n=4$	N	$l=0$	$l=1$	$l=2$	$l=3$	

TABLE I.2 – *Atomic shell structure.* We have highlighted the correspondence with the shells of Bohr's pre-quantum atomic model. The letters s, p, d, f are used to label orbitals with different values of l.

atoms and hydrogen is however the mutual repulsion of the electrons (*cf. e.g.* Chap. 7 of Bransden & Joachain, 1983). The different subshells (s, p, d, f) of a given shell having different geometries, the mutual repulsion depends on l. The subshells of a given n thus have different energies. The electronic configuration of atoms in their fundamental state results from the ranking in energy of these levels. The possible number of electrons per subshell is given in Table I.2. We have represented the electronic configuration of atoms in the periodic table (Fig. I.2).

I.1.1.3 The Valence Shell

The outer shell is called the *valence* shell. It contains the electrons responsible for molecular bonds (*cf.* Sect. I.1.2) and shaping the optical properties of solids (*cf.* Sect. I.2). We will see that the nature of the chemical bond depends on the tendency of its atoms: *(i)* to share electrons; *(ii)* to form *cations*, by losing one or several electrons; or *(iii)* to form *anions*, by gaining one or several electrons.

Ionization potential. Panel *(a)* of Fig. I.3 shows the *first ionization potential*, I_1, of the elements in Fig. I.2. Atoms with a low I_1 tend to form stable cations. Noble gases have the largest I_1 of their row, because their last shell is full. More generally, Fig. I.3 shows that I_1 increases from the left to the right of the periodic table (Fig. I.2), as the valence shell gets fuller. This is because, at a given n, moving to the right of the table increases the effective nucleus charge $Z - Z_{subshells}$, making the valence shell more tightly bound. It also decreases from the top to the bottom, as the energy level of the outer shell decreases with n as $1/n^2$.

☞ Metals tend to form stable cations.

Electron affinity. Panel *(b)* of Fig. I.3 shows the *first electron affinity*, A_1, of the elements in Fig. I.2. Atoms with a high electron affinity tend to form stable anions. A_1 follows roughly the same trend as I_1, with some exceptions. Noble gases have their last shell full, they therefore tend to remain neutral and have a negative A_1. Alkaline earth metals also have negative A_1, because of the energy difference between their full ns and empty np shells.

☞ Non metals tend to form stable anions.

Electronegativity. The balance between I_1 and A_1 gives an idea of the tendency of an atom to attract electrons in a bond. Mulliken's *electronegativity*, χ, is defined as (*e.g.* Huheey et al., 1993):

$$\chi = 0.187 \times \left(\frac{I_1}{1\ \mathrm{eV}} + \frac{A_1}{1\ \mathrm{eV}} \right) + 0.17. \tag{I.1}$$

If we except noble gases, we see that χ will be higher to the right of the periodic table, and will decrease from the top to the bottom.

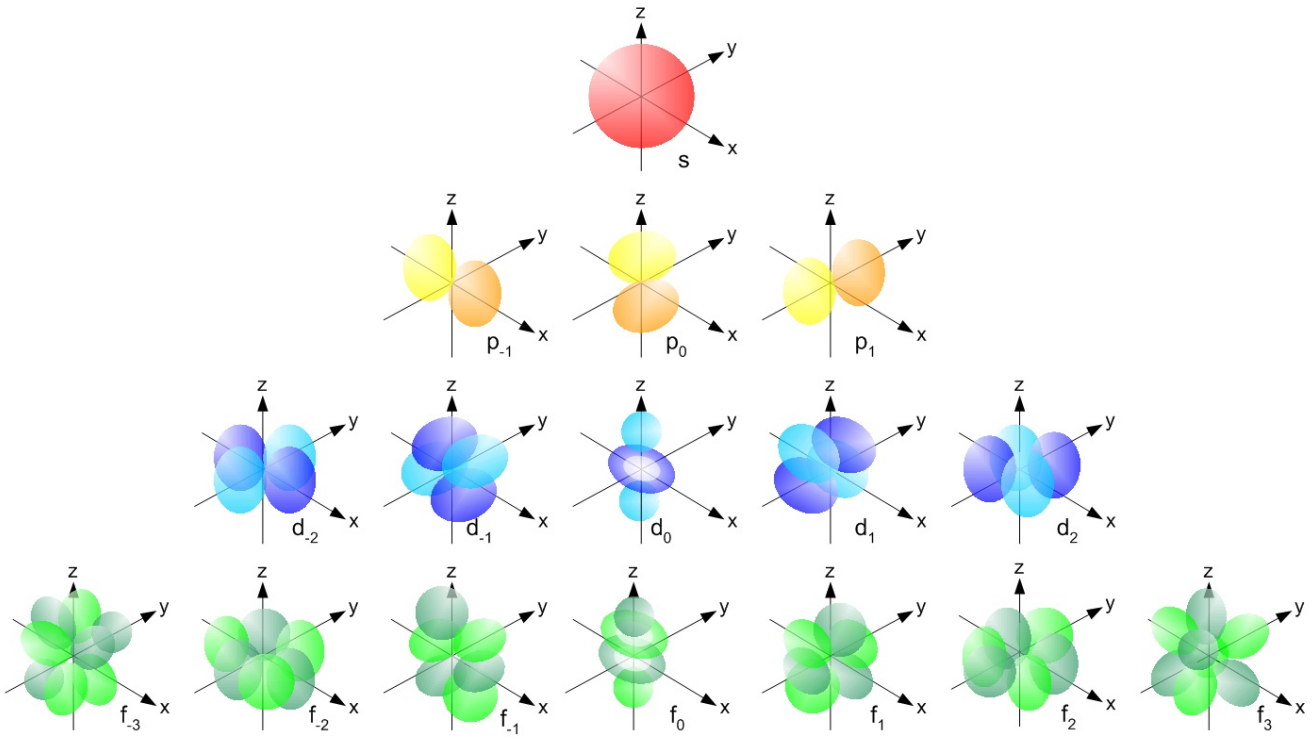

FIGURE I.1 – *Shape of s, p, d, f electron orbitals.* These shapes represent the surfaces encompassing the region where the electron has a 90 % probability of presence. The orbitals are identified by the letter corresponding to the value of l (*cf.* Table I.2), with the value of m_l as an index. Credit: UCDavis Chemwiki, licensed under CC BY-NC-SA 3.0 US.

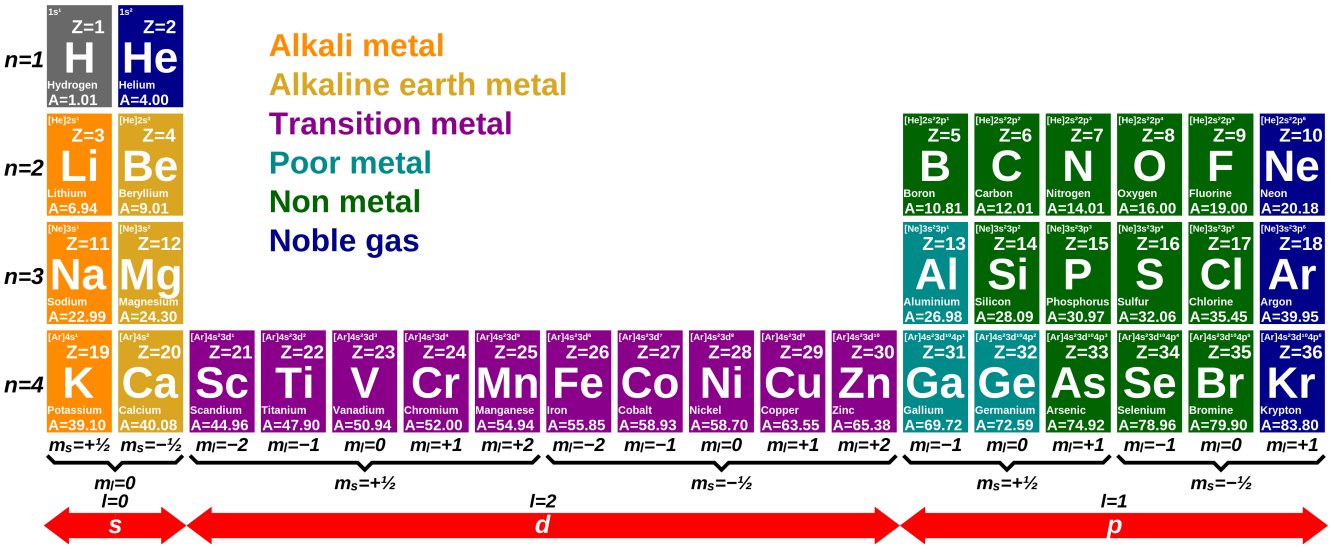

FIGURE I.2 – *Periodic table of elements.* We show only the first four rows, as they contain all the elements relevant to ISM physics. Z is the charge and A, the atomic weight. In each cell, we show the electronic configuration in the fundamental state. We do not repeat the part of the configuration corresponding to the noble gas of the previous row ([He], [Ne], [Ar]). We have annotated the table with the four quantum numbers of the last electron. Licensed under CC BY-SA 4.0.

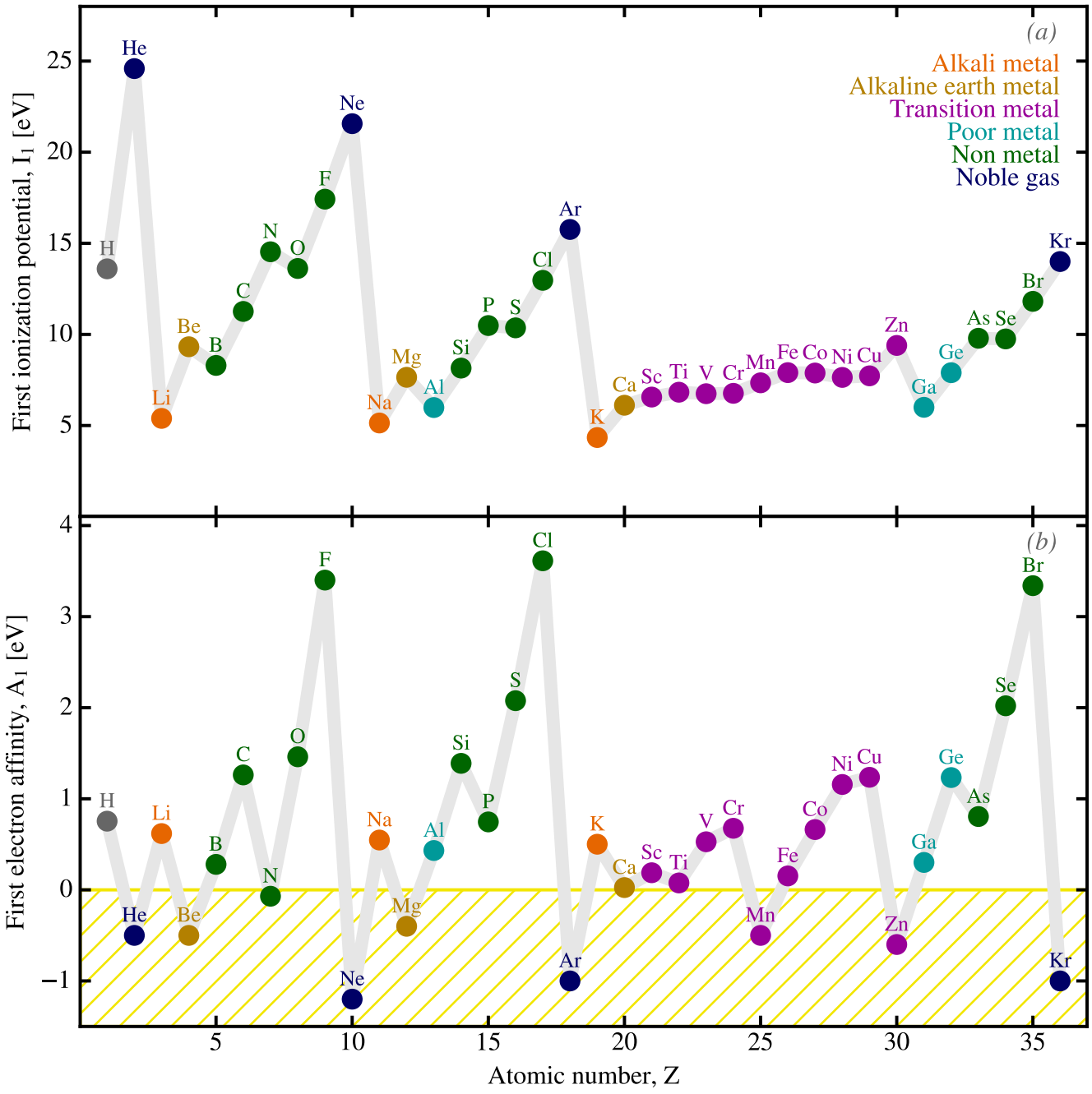

FIGURE I.3 – *First ionization potentials and electron affinities.* In panel *(a)*, we display the first ionization potential. It is the minimum energy required to expel the most loosely bound electron, in the fundamental state. It is the energy lost during the gas phase reaction: $X \longrightarrow X^+ + e^-$. In panel *(b)*, we display the first electron affinity, which is the energy gained by adding an electron to the atom. It is the energy released during the gas phase reaction: $X + e^- \longrightarrow X^-$. Elements with a negative electron affinity (yellow hatched area) do not form stable anions. We display the different groups with the same color code as in Fig. I.2. Licensed under CC BY-SA 4.0.

I.1.1.4 Orbital Hybridisation

To explain the shape of molecules, the concept of *hybrid orbitals* was introduced in the 1930's by Linus PAULING. The principle is that orbitals with similar energies can be linearly combined together to form new orbitals with different shapes [3]. The most relevant example to ISD is the hybridisation of carbon. A 2s electron can be promoted to 2p, resulting in the following configuration.

The carbon is now in an excited state, noted C*. The promotion requires 4.2 eV. From this new state, the following combinations of orbitals are possible.

sp^3 hybrids are 1/4 s and 3/4 p. This hybridisation results in four sp^3 orbitals arranged in a tetrahedron, shown in Fig. I.4.a. For instance, C in methane (CH_4) is sp^3 hybridized. The electronic configuration of the $n = 2$ shell becomes the following.

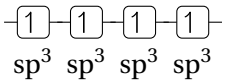

sp^2 hybrids are 1/3 s and 2/3 p. This hybridisation results in one standard p orbital and three sp^2 orbitals trigonally-arranged, shown in Fig. I.4.b. For instance, C in benzene (C_6H_6) is sp^2 hybridized. The electronic configuration of the $n = 2$ shell becomes the following.

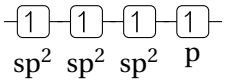

sp hybrid is 1/2 s and 1/2 p. This hybridisation results in two standard p orbitals and two sp orbitals linearly-arranged, shown in Fig. I.4.c. For instance, C in acetylene (C_2H_2) is sp hybridized. The electronic configuration of the $n = 2$ shell becomes the following.

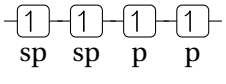

I.1.2 Molecular Bonding

Chemical bonds are the result of the overlap between the outer orbitals of two atoms whose valence shell is not full (*cf. e.g.* Chap. 8 of Atkins, 1992). Despite their mutual repulsion, sharing electrons leads to a lower energy state, in which a stable bonded molecule is formed. Covalent, ionic and metallic bonds, that we will define below, typically have dissociation energies of a few eV. The atomic spacing in a molecule or a solid is of the order of a few Å.

I.1.2.1 Covalent Bonds

A *covalent bond* is formed when a pair of electrons with anti-parallel spin is shared between two atoms of similar electronegativity. The more the orbitals overlap, the stronger the bond is. The electron density is the highest between the two atoms, resulting in a directional bond. For instance, the H_2 (Fig. I.5.a) and CO molecule bonds, as well as the C-C and C-H bonds in hydrocarbons, are all covalent. Covalent bonds are weakly polar. Symmetric molecules such as H_2 are non-polar, whereas asymmetric molecules, such as CO are polar, because of the difference in electronegativity of C and O.

3. The Schrödinger equation is linear. Any combination of solutions is a solution.

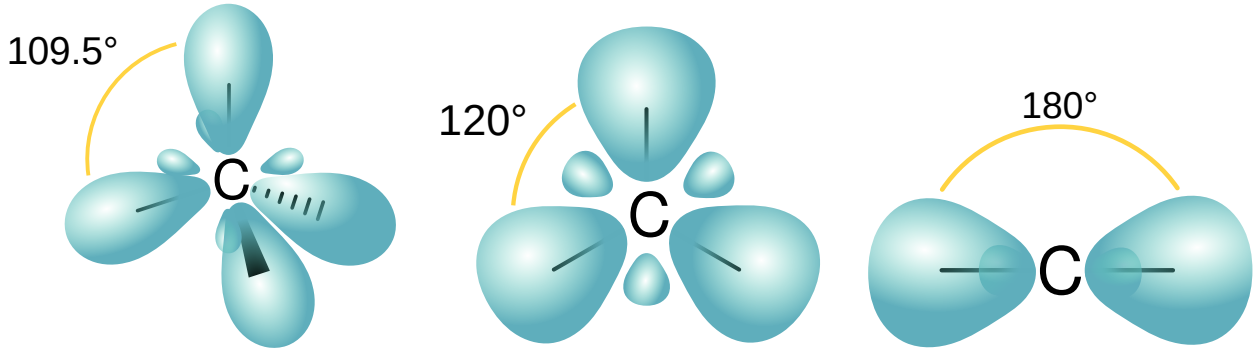

(a) sp^3 hybrid (b) sp^2 hybrid (c) sp hybrid

FIGURE I.4 – *Hybrid orbitals of carbon.* The left image shows the shape of the four sp^3 orbitals of a C atom. They are arranged in a tetrahedral geometry. The center image shows the shape of the three sp^2 orbitals of a C atom. They are arranged in a trigonal geometry. We have not displayed the remaining p orbital of this C atom. The right image shows the shape of the two sp orbitals of a C atom. They are arranged along a line. We have not displayed the remaining two p orbitals of this C atom. Each bond is represented with a black line indicating its direction: *(i)* thin solid lines show bonds within the plane of the image; *(ii)* the thick solid line shows a bond pointing toward the reader; *(iii)* the dashed line shows a bond pointing in the opposite direction. Credit: adapted from Wikipedia's Orbital hybridisation article (changed the central letter), licensed under CC BY-SA 3.0.

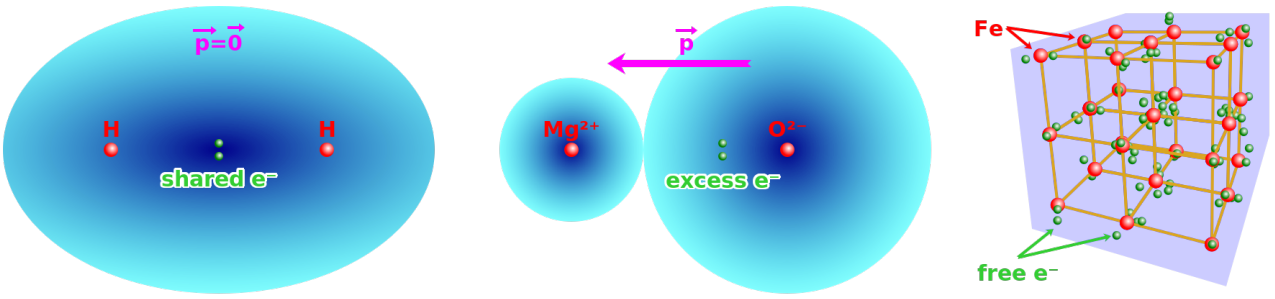

(a) Covalent bond: H_2 (b) Ionic bond: Mg-O in silicates (c) Metallic bond: Fe

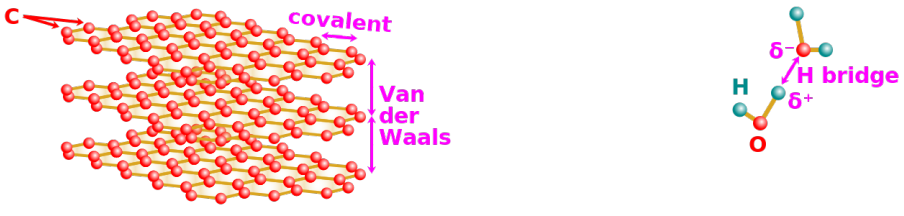

(d) Van der Waals force: graphite (e) Hydrogen bridge: H_2O ice

FIGURE I.5 – *Different types of molecular bonds.* We have noted $\vec{p}$, the dipole moment created by the bond. In general, $\vec{p} = \iiint_V \vec{r}.\rho(\vec{r})\,dV$, where $\rho(\vec{r})$ is the charge number density. In the case of MgO, it reduces to $e.\overrightarrow{O.Mg}$, where $\overrightarrow{O.Mg}$ is the distance vector between the two ions. The electrons are noted e^-, and δ^+ and δ^- are the excess dipolar charges of both signs. Licensed under CC BY-SA 4.0.

☞ Covalent bonds are preferentially formed between non metals.

Covalent bonds are of one of the two following types.

σ bonds result from the frontal overlap of two s, p or sp^n ($n = 1,2,3$) orbitals. These bonds have a rotational symmetry around their axis (Fig. I.6.a). The electron density is maximum between the two atoms. It is the strongest covalent bond. The C–C bond of ethane (C_2H_6) is a σ bond.

π bonds result from the side-by-side overlap of the two lobes of two p orbitals (Fig. I.6.b). The electron density is maximum above and below the plane of the molecule and zero between them. These bonds are weaker than σ bonds. In the double C=C bond of ethylene (C_2H_4), there are one σ and one π bonds (Fig. I.6). In the triple C≡C bond of acetylene (C_2H_2), there are one σ bond and two π bonds.

Finally, some transitions in interstellar solids involve *antibonding* orbitals. When a bond forms, both a bonding and an antibonding molecular orbitals with different energy levels become available. This is demonstrated for the H_2^+ molecule, with the Schödinger equation, in Chap. 9 of Bransden & Joachain (1983). Bonding orbitals have a lower energy level than the dissociated atoms, thus favoring a stable molecule. On the contrary, the population of an antibonding orbital makes the molecule unstable. For instance, the splitting of molecular orbitals for both σ and π bonds of ethylene (Fig. I.6) are the following.

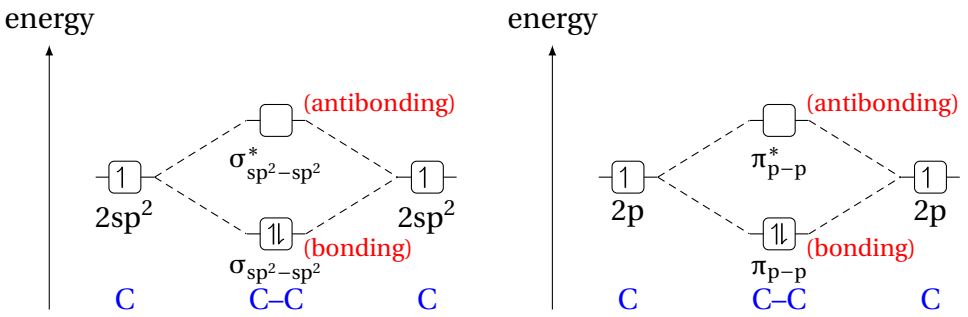

We emphasize those are electronic levels of molecules. Molecules also have rotational and vibrational modes that will be discussed in Sect. I.2.2.1.

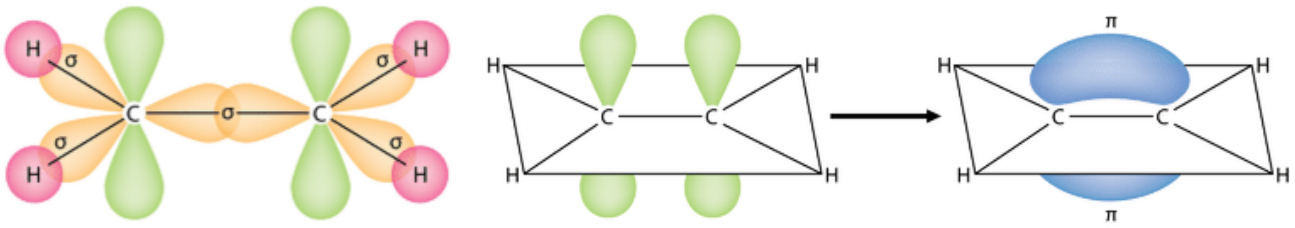

(a) σ bonds *(b)* overlap of two p orbitals to form one π bond

FIGURE I.6 – *An example of* σ *and* π *bonds.* We demonstrate the two types of bonds on ethylene (C_2H_4). On the left image: the s orbital of each H atom is shown in red; the p orbital of each C atom is shown in green; and the three sp^2 hybridized orbitals of each C atom are in orange. The frontal overlap of the sp^2 hybridized orbitals of two C atoms, as well as the overlap of one sp^2 hybridized C orbital with the s orbital of an H atom, both form a σ bond. On the middle image, we show the plane of the molecule with the p orbital of each C atom in green. The right image shows the overlap of these two p orbitals to form one single π bond, in blue, on both sides of the plane. Credit: adapted from the Chemistry Library, licensed under CC BY-NC 4.0.

I.1.2.2 Ionic Bonds

An *ionic bond* is formed between two atoms of significantly different electronegativities. The electron is transferred from the cation to the anion, resulting in a polar bond. The adhesion is due to

long-range Coulomb forces ($\propto 1/r^2$) between the two ions. Ionic bonding is non-directional as the electron cloud stays centered around the atoms. The most relevant example to ISD is the O^{2-}–Mg^{2+} bond in silicates (Fig. I.5.b).

☞ Ionic bonds are preferentially formed between a metal and a non metal.

Covalent and ionic bonds are two extreme cases. Most bonds involving at least one non metal are intermediate between both.

I.1.2.3 Metallic Bonds

Metals can easily be ionized. Bonding several metal atoms therefore results in a lattice of cations bathed in a sea of free valence electrons. The electrons are not attached to a particular atom and can be found anywhere in the solid. This explains the electric and thermal conductivities of metals. Fig. I.5.c represents solid iron.

☞ Metallic bonds are formed between a large number of metal atoms.

I.1.2.4 Intermolecular Attraction

Weaker forms of attraction between molecules exist. Their dissociation energy is typically of the order of $\simeq 0.1$ eV. They are relevant to ISD studies.

Van der Waals bonds are due to the induced dipole attraction of neutral atoms and molecules. Their potential energy drops as $1/r^6$. They are in particular responsible for binding graphene sheets together in graphite (Fig. I.5.d).

Hydrogen bridges are formed when the induced dipole of the H atom of a molecule is attracted by the induced dipole of a strongly electronegative atom in another molecule. For instance, hydrogen bridges tie the H_2O molecules together in water ice (Fig. I.5.e).

I.1.3 The Solid State

I.1.3.1 The Different Types of Solids

There are two main types of solids: *insulators* and *conductors*. Their properties are radically different. Their difference originates in the type of chemical bond making up their crystal lattice.

Insulators, also called *dielectrics*, are solids, whose atoms are tied together with covalent or ionic bonds. The valence electrons are therefore located around their specific atoms and can not move freely through the lattice. Consequently, when an electric field is applied, it induces a polarization of the bonds, distorting them, but no current is flowing. For instance, silicates are dielectric materials.

Conductors are solids, whose atoms are tied together with metallic bonds. Their valence electrons are therefore free to move through the solid. Consequently, when an electric field is applied, a current is flowing. For instance, iron is a metallic conductor. There are a few non-metal conductors, such as graphite, which is classified as a *semimetal*. This peculiar property is due to the delocalized electrons within the aromatic cycles constituting graphite (*cf.* Sect. I.1.4).

There is a third, intermediate type of solids, called *semiconductors*. Semiconductors are insulators at T = 0 K and conductors at ambient temperatures. Several cosmic dust candidates belong to this category. We will define it more precisely in Sect. I.1.3.3.

I.1.3.2 The Band Structure of Solids

A solid can be idealized as a periodic lattice of atoms bonded to each other. The permitted energy levels of a single valence electron, in the periodic electrostatic potential created by this lattice, are

a series of continuous functions, also called *bands* (*e.g.* Chap. 8 of Ashcroft & Mermin, 1976, for a derivation from the Schrödinger equation). This can be viewed as a generalization of the molecular level splitting (Fig. I.7). The spacing between a large number of levels is so small that it appears continuous. At T = 0 K, the lowest energy bands are filled in priority. Two of these bands are particularly important.

The valence band is the highest energy band populated by valence electrons, at T = 0 K.

The conduction band is the lowest energy band where electrons can move freely through the solid. It is the band immediately superior to the valence band.

The energy difference between the top of the valence band and the bottom of the conduction band is called the *band gap*, noted E_g (Fig. I.7).

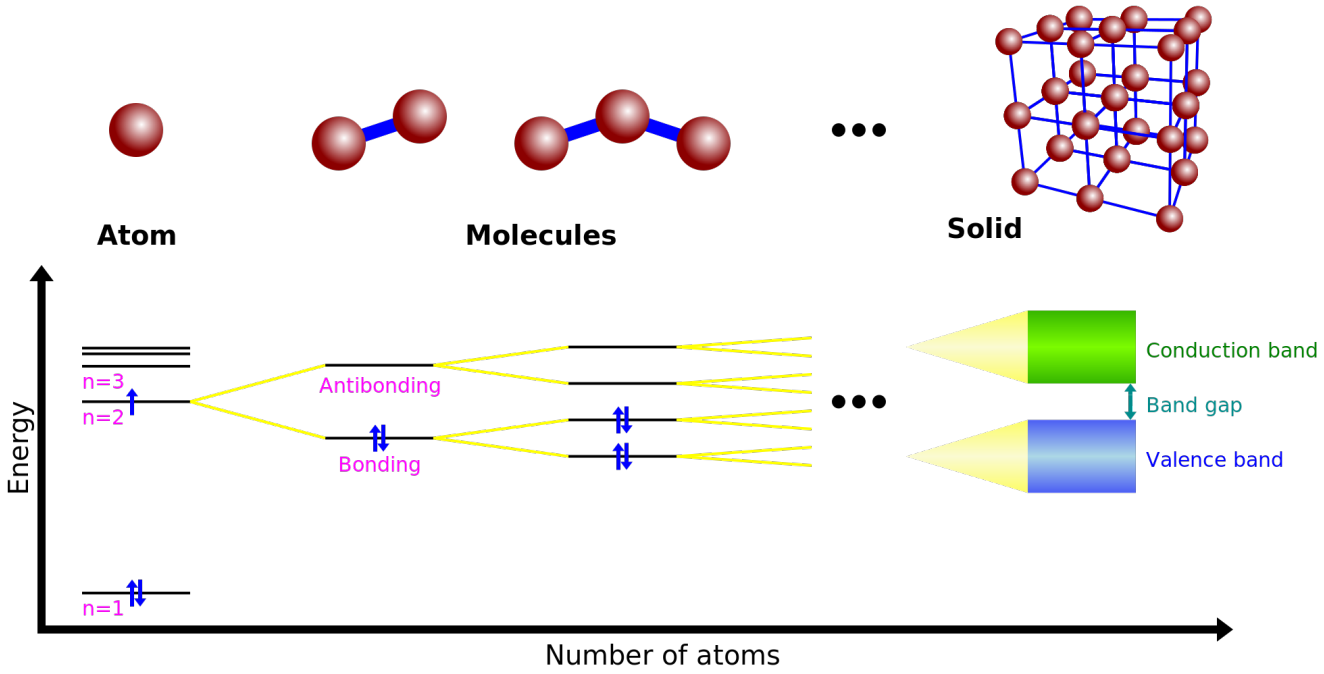

FIGURE I.7 – *Origin of the band structure of a solid.* From the left to the right, we represent: *(i)* typical discrete atomic levels, *(ii)* the successive splitting of molecular orbitals, *(iii)* resulting in the quasi continuous distribution of levels in bands. Electrons are represented with a vertical blue arrow (up or down), corresponding to their spin. Licensed under CC BY-SA 4.0.

I.1.3.3 The Fermi Level

The probability distribution of identical fermions, such as electrons in a solid, over the energy states of a system at temperature T, is given by the *Fermi-Dirac distribution*:

$$f(\mathrm{E}) = \frac{1}{\exp\left(\dfrac{\mathrm{E}-\mathrm{E_F}}{k\mathrm{T}}\right)+1}, \tag{I.2}$$

where k is the *Boltzmann constant* (*cf.* Table B.2), E denotes the different energy levels and $\mathrm{E_F}$ is the *Fermi level*[4]. This distribution is displayed in Fig. I.8.a. The Fermi level is an intrinsic quantity characterizing a solid. It is the energy required to add an electron to the system. It also corresponds to the maximum energy an electron can have at T = 0 K. The latter interpretation of $\mathrm{E_F}$ can be seen in Fig. I.8.a. The blue curve shows Eq. (I.2) at T = 0 K: *(i)* it gives equal probability to electrons to occupy

4. In the general Fermi-Dirac distribution, the Fermi level, which is proper to solids, is replaced by the *chemical potential* of the system, μ. In our case, the Fermi level is the chemical potential of an electron.

energy levels $E \leq E_F$; *(ii)* it gives zero probability to energy levels $E > E_F$. The actual number density of electrons, n_e, is:

$$n_e = \int_{-\infty}^{\infty} g(E)\, f(E)\, dE, \tag{I.3}$$

where $g(E)$ is the density of states per infinitesimal energy bin. This density of states corresponds to the band structure. It is 0 between the bands. We emphasize that E_F can fall between two bands. It does not necessarily correspond to an actual allowed level. This is demonstrated in Fig. I.8.

Insulators have their valence and conduction bands widely spread apart (Fig. I.8.b). At ambient temperature, no electron will populate the conduction band. It is another way to see that their valence electrons are localized around their cations.

Semiconductors have their valence and conduction bands close to each other (Fig. I.8.c). They are insulators at T = 0 K, but their conduction band can be populated at ambient temperature (E_g gets closer to kT).

Conductors are solids for which the valence and the conduction bands are the same (Fig. I.8.d). The Fermi level is within the band. It is another way to see that the valence electrons are free to move through the lattice at any temperature.

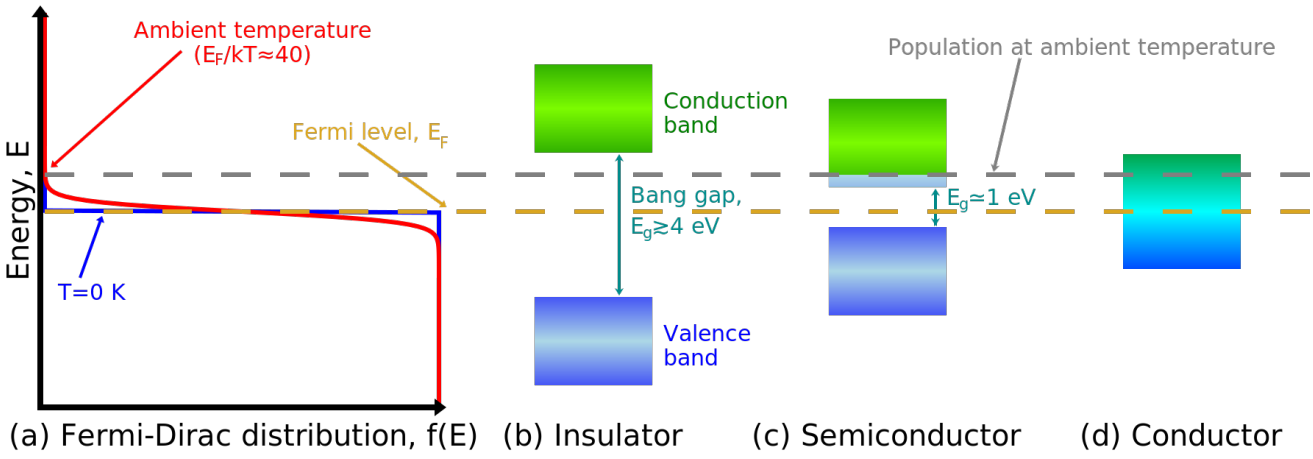

FIGURE I.8 – *The Fermi level and the different types of solid.* The left plot shows the rotated Fermi-Dirac distribution (Eq. I.2), for two values of the temperature, T = 0 K and T ≃ 300 K. The three diagrams on the right show the valence and conduction bands relative to the Fermi level, E_F, for insulators, semiconductors and conductors. For conductors, the valence band is also the conduction band. Licensed under CC BY-SA 4.0.

I.1.4 Interstellar Dust Candidates

We briefly review here the constitution of the most likely ISD grain candidates. Some general properties are given in Table I.3. Their optical properties are extensively discussed in Sect. I.2.2.

I.1.4.1 Silicates

The different types of silicates are built around silica tetrahedra (SiO_4^{4-}), paired with various cations to produce a neutral compound (*cf. e.g.* Henning, 2010, for a review). The silica tetrahedra have a central Si^{4+} cation tied to four O^{2-} anions with covalent/ionic bonds. In the ISM, the most widely available divalent cations that can be paired with silica tetrahedra are Mg^{2+} and Fe^{2+} (*cf.* Sect. II.2.3). Silicates have two strong features at 9.7 µm (Si–O stretching) and 18 µm (O–Si–O bending). They are ubiquitous: *(i)* they are the main constituent of Earth's crust; *(ii)* they are also found in Solar system and *CircumStellar Dust* (CSD); *(iii)* they account for probably 2/3 of interstellar grain mass

(*e.g.* Draine, 2003a); *(iv)* their features are observed in distant galaxies, in absorption (*e.g.* Marcillac et al., 2006) and in emission (*e.g.* Hony et al., 2011). Interstellar silicates are widely amorphous (*e.g.* Kemper et al., 2004). Crystalline silicates have additional distinctive narrow features, due to SiO_4 as well as (Fe,Mg)–O vibrations, in the 9.0–12.5 µm and 14-22 µm ranges, with a few bands above 33 µm. The following two types of silicates are the most relevant to ISD (*cf.* Table I.3).

Olivine. Olivine have the general formula $(Mg,Fe)_2SiO_4$, with different proportions of Mg and Fe. Its crystalline structure is represented on Fig. I.9.b. The two following compounds are the extreme cases of the Fe-to-Mg ratio.

Forsterite is the Mg-end of the series, with formula Mg_2SiO_4.

Fayalite is the Fe-end of the series, with formula Fe_2SiO_4.

Olivine have an olive green color (Fig. I.10.a).

Pyroxene. Pyroxene have the general formula $(Mg,Fe)SiO_3$, with different proportions of Mg and Fe. They are constituted of silica tetrahedron chains, sharing one O atom (Fig. I.9.c), which explains their stoichiometry. The two following compounds are the extreme cases of the Fe-to-Mg ratio.

Enstatite is the Mg-end of the series, with formula $MgSiO_3$.

Ferrosilite is the Fe-end of the series, with formula $FeSiO_3$.

Pyroxene can be darker than olivine (Fig. I.10.b).

☞ In general, silicates are translucent minerals. They are gemstones, used in jewelry.

I.1.4.2 Hydrogenated Amorphous Carbon

This is a broad class of solids, noted a-C(:H) (a notation introduced by Jones, 2012b). Carbon atoms can be paired in the following ways (Fig. I.9.d).

Aromatic cycles are hexagonal rings made of six sp^2 hybridized C atoms. Two of the three available sp^2 orbitals of each C atom make σ bonds, tying the cycle together. The last sp^2 orbital can be used to make a σ bond with another C atom, extending the compound, or with an H atom, ending the solid in this direction. The six remaining p orbitals of the cycle make a sort of ring-shaped π bond. The electrons of these bonds are delocalized, they do not belong to a specific C atom, but they are confined to the cycle. This is why compounds with aromatic cycles have some properties of metals: electric conductivity and shiny appearance.

Aliphatic groups are centered around a sp^3 hybridized C atom. Its four sp^3 orbitals can be paired to other C atoms or to H atoms, forming σ bonds.

Olefinic bonds are alkene-type double bonds between two sp^2 hybridized C atoms (Fig. I.6). There is one σ bond bridging two sp^2 orbitals, and one π bond linking the p orbital of each C atom.

The hydrogenation of a-C(:H) influences directly their band gap (Jones, 2012b). Generally, H-poor a-C(:H), which can be noted a-C, are sp^2 dominated (aromatic/olefinic), and have a low band gap ($E_g \simeq 0.4-0.7$ eV). On the contrary, H-rich a-C(:H), which can be noted a-C:H, are mostly aliphatic (sp^3), and have a larger band gap ($E_g \simeq 1.2-2.5$ eV). The aromatic domains are responsible for bright features at 3.3, 6.2, 7.7, 8.6 and 11.3 µm, that will be extensively discussed in Sect. III.2.1.1, whereas the main aliphatic feature is at 3.4 µm. An important feature at 2175 Å (Sect. II.2.1) is thought to originate in the transition between the π and π^* bands of sp^2 domains (*e.g.* Draine & Li, 2001).

☞ a-C(:H) tend to be more opaque than silicates (Fig. I.10.c).

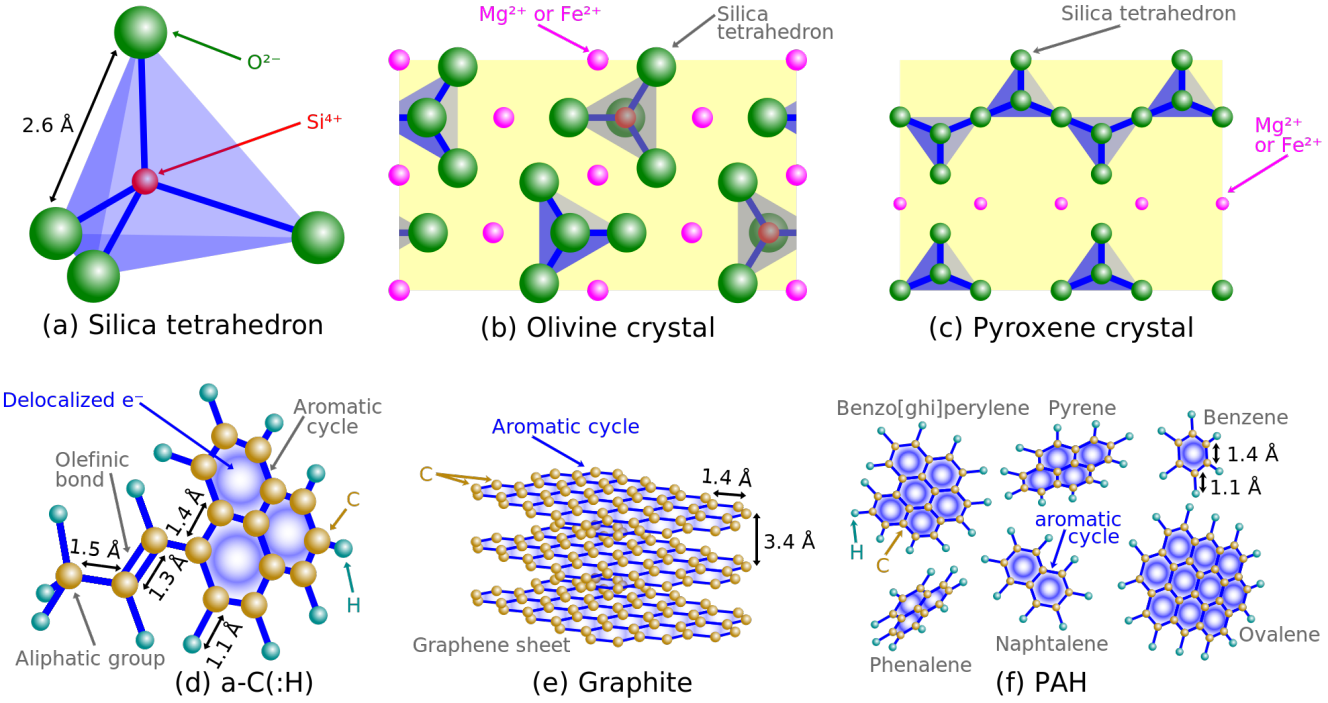

FIGURE I.9 – *Structure of interstellar dust candidates.* The (a) image shows the silica tetrahedron, which is the building block of silicates. The (b) image shows the structure of crystalline olivine. Some silica tetrahedra are pointing toward the reader above the yellow plane, and some are pointing backward. The latter appear dimmer and the Si atom are visible in red. The (c) image shows the structure of crystalline pyroxene. Its most important feature is the chain of alternate silica tetrahedra. They share one O atom, explaining why the stoichiometry of pyroxene is different from olivine. The (d) image shows the diversity of carbon pairing in an a-C(:H). Every C atom is sp^2 hybridized, except the aliphatic C, which is sp^3 hybridized. Every bond is a σ bond except: *(i)* the 6 delocalized electrons within each aromatic cycles are π bond pairing of p orbitals; *(ii)* one of the olefinic bonds is a π bond. The example we have shown corresponds to a very small grain. In a larger a-C(:H), most of these bonds would be linked into the rest of a contiguous 3D network (*e.g.* Micelotta et al., 2012, for more realistic structures). The (e) image shows that graphite is the stack of graphene sheets. Each graphene sheet is made exclusively of aromatic cycles. The (f) image displays a few different PAHs. Licensed under CC BY-SA 4.0.

(a) Forsterite *(b)* Enstatite *(c)* Soot ≃ a-C(:H) *(d)* Graphite *(e)* PAHs

FIGURE I.10 – *Appearance of various minerals.* The *(a)* and *(b)* images show crystalline silicates. The soot powder *(c)* is an approximate analog of a-C(:H), on the a-C end, except that soot can contain radicals with O, N, *etc.* These images are useful to visualize the differences in optical properties of these compounds. They however show macroscopic samples. Even the powder in image *(c)* is made of particles much larger than 1 µm, which is the maximum size of interstellar grains. Credit: *(a)* forsterite from Rob LAVINSKY, licensed under CC BY-SA 3.0; *(b)* enstatite from Rob LAVINSKY, licensed under CC BY-SA 3.0; *(c)* soot from Wikipedia, not licensed; *(d)* graphite from Rob LAVINSKY, licensed under CC BY-SA 3.0; *(e)* PAHs from the Astrochemistry Lab, NASA Ames Research Center, with permission from Lou ALLAMANDOLA.

I.1.4.3 Graphite

Graphite is a mineral made of the stacking of graphene sheets, bonded by Van Der Waals interactions (Sect. I.1.2). Graphene sheets are planar compounds exclusively constituted of aromatic cycles (Fig. I.9.e). Pure graphite is solely made of sp^2 carbon. Its aromaticity explains its shiny silver metallic appearance (Fig. I.10.d). It has a strong $\pi \rightarrow \pi^*$ transition around 2175 Å. The exact central wavelength however depends on the size and shape of the particles, and pure graphite seems too wide to account for the interstellar feature (*e.g.* Draine & Malhotra, 1993; Voshchinnikov, 2004; Papoular & Papoular, 2009). Graphite also has a broad band at 30 µm, seen parallel to the sheets, which corresponds to the oscillation frequency of the delocalized π electrons (*e.g.* Venghaus, 1977; Draine & Li, 2007).

I.1.4.4 Polycyclic Aromatic Hydrocarbons (PAH)

PAHs are a class of molecules made of aromatic cycles, with peripheral H atoms (Fig. I.9.f). They have the aromatic features of a-C, as well as the $\pi \rightarrow \pi^*$ transition around 2175 Å (*e.g.* Joblin et al., 1992). Similarly to graphite, the exact central wavelength depends on the particle size and shape (*e.g.* Duley & Seahra, 1998). They can be colorful (*cf.* Fig. I.10.e). They are highly flammable and carcinogenic.

Name	Stoichiometry	Density	Melting	Main spectroscopic features
SILICATES				
Forsterite	Mg_2SiO_4	3.3 g/cm^3	2200 K	9.7, 18 µm
Fayalite	Fe_2SiO_4	4.4 g/cm^3	1500 K	9.7, 18 µm
Enstatite	$MgSiO_3$	3.2 g/cm^3	2100 K	9.7, 18 µm
Ferrosilite	$FeSiO_3$	4.0 g/cm^3	1200 K	9.7, 18 µm
CARBONACEOUS				
a-C(:H)	C_nH_m	1.8–2.1 g/cm^3	N/A	2175 Å, 3.3, 3.4, 6.2, 7.7, 8.6, 11.3 µm
Graphite	C_n	2.3 g/cm^3	3600 K	2175 Å, 30 µm
PAH	C_nH_m	2.2 g/cm^3	N/A	2175 Å, 3.3, 6.2, 7.7, 8.6, 11.3 µm

TABLE I.3 – *General properties of interstellar dust candidates.* The values of the density and melting temperature are approximate. They vary between samples and experimental conditions.

I.2 The Interaction of Light with Solids

The interaction of an electromagnetic wave with dust grains results in the three following phenomena (*cf.* Fig. I.11).

Absorption: a fraction of the electromagnetic energy is stored into the grain;

Scattering: the wave vector of the fraction that is not absorbed changes direction, its field polarization changes, but its frequency is not affected;

Emission: the energy stored in the grain is ulteriorly re-emitted in the IR.

The sum of absorption and scattering is called *extinction*. These three phenomena can be modeled, assuming valence electrons are harmonic oscillators. This way, the response to an electromagnetic wave of bonds in a dielectric or free electrons in a metal can be quantified. This is illustrated in Fig. I.12. Throughout this manuscript, we use λ, $\nu = c/\lambda$ and $\omega = 2\pi\nu$ to respectively denote the *wavelength*, *frequency* and *angular frequency* of an electromagnetic wave, c being the *speed of light* (*cf.* Table B.2).

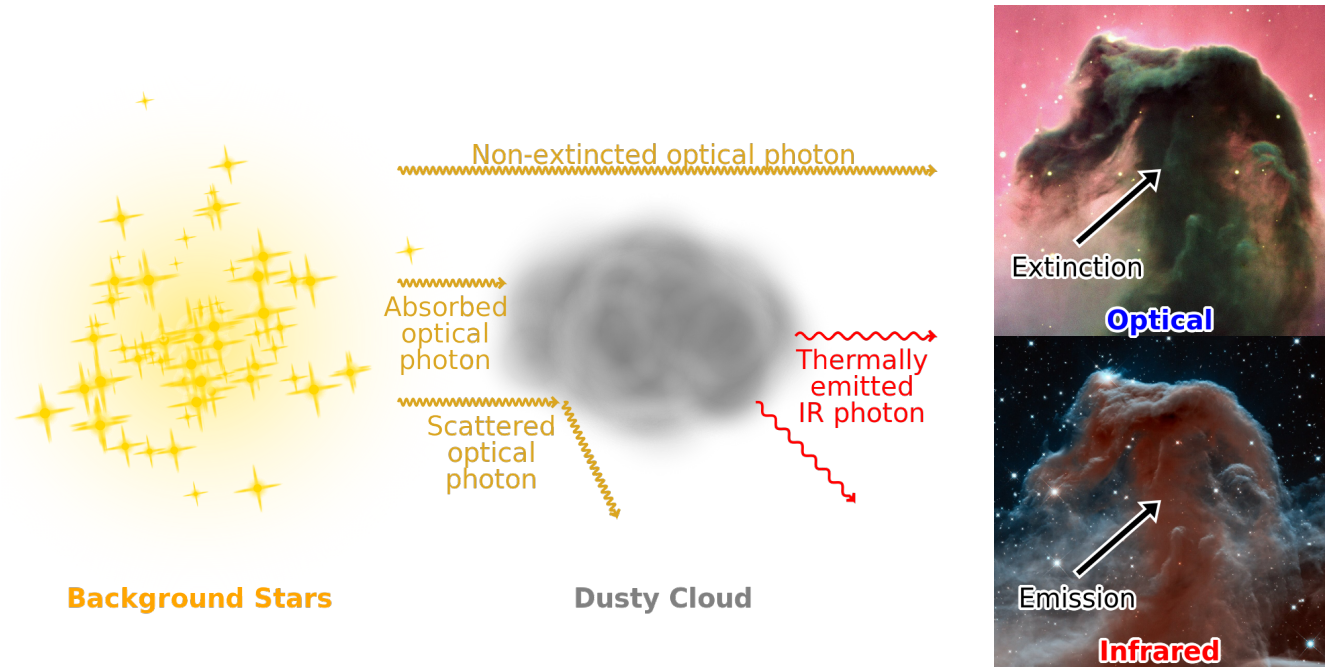

FIGURE I.11 – *Absorption, scattering and emission.* The images on the right are the Horsehead nebula. Licensed under CC BY-SA 4.0. Credit: Horsehead nebula images from NASA, ESA, and the Hubble Heritage Team (AURA/STScI); ESO, licensed under CC BY 4.0.

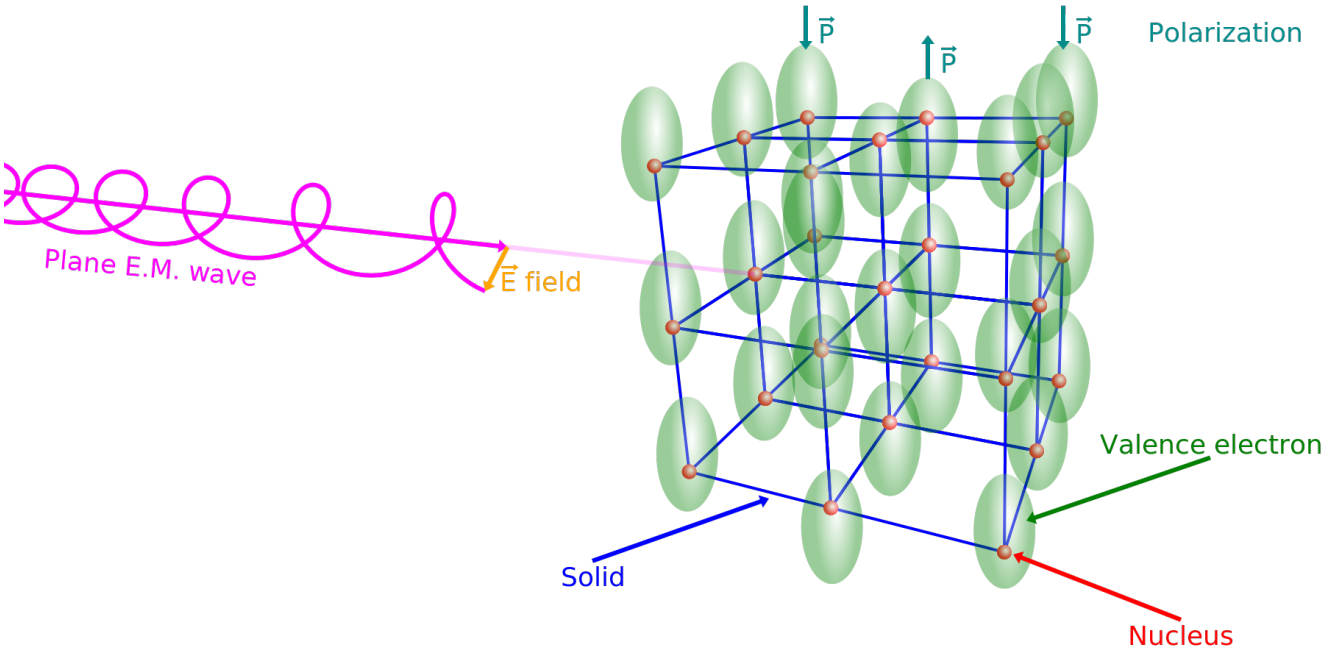

FIGURE I.12 – *Effect of an electromagnetic wave on a dielectric.* An incoming, circularly polarized, electromagnetic wave is figured in magenta. The cube on the right represents a solid. The nuclei, assumed to be fixed, are the red spheres. The valence electrons are the green ellipsoids. They are displaced out of their equilibrium positions by the electromagnetic wave, inducing a time-dependent polarization. Licensed under CC BY-SA 4.0.

I.2.1 Bonds as Harmonic Oscillators

The harmonic oscillator model is particularly useful to describe the way bonds react to electromagnetic waves.

I.2.1.1 The Harmonic Oscillator Amplitude

The position along the x-axis of a unidimensional harmonic oscillator of mass, m, as a function of time, t, follows the equation:

$$\underbrace{m\frac{\mathrm{d}^2x(t)}{\mathrm{d}t^2}}_{\text{inertia}}+\underbrace{b\frac{\mathrm{d}x(t)}{\mathrm{d}t}}_{\text{friction}}+\underbrace{k_e x(t)}_{\text{restoring force}}=\underbrace{\mathrm{F}(t)}_{\text{external force}}, \tag{I.4}$$

where F is the external force applied to the oscillator, k_e is the strength of the restoring force, and b is a dissipation constant. This equation is simply the Newton law ($\mathbb{F}=m\ddot{x}$), where the force, $\mathbb{F}$, has three components: *(i)* the external force, F, displacing the oscillator out of its equilibrium position ($x=0$); *(ii)* the restoring force, $-k_e x$, which is proportional to the distance, meaning it is stronger when the oscillator is farther away from its equilibrium position; *(iii)* the friction force, $-b\dot{x}$, proportional to the velocity, having the effect of slowing down the oscillator.

In the case of the motion of an electron, excited by the Lorentz force of a complex, harmonic plane electromagnetic wave with angular frequency ω, $\mathrm{F}(t)=e\mathrm{E}_0\exp(-i\omega t)$, Eq. (I.4) can be rewritten:

$$\frac{\mathrm{d}^2x(t)}{\mathrm{d}t^2}+\gamma\frac{\mathrm{d}x(t)}{\mathrm{d}t}+\omega_0^2x(t)=\frac{e\mathrm{E}_0\exp(-i\omega t)}{m_e}, \tag{I.5}$$

where m_e is the electron mass. We have also introduced the *natural frequency*, ω_0, and the *damping constant*, γ:

$$\omega_0\equiv\sqrt{\frac{k_e}{m_e}}\quad\text{and}\quad\gamma\equiv\frac{b}{m_e}. \tag{I.6}$$

In this case, the restoring force is created by the atom's electrostatic potential well, and the friction can be interpreted as collisions of the electron with the lattice. The solution to Eq. (I.5) has the form $x(t)=x_0\exp(-i\omega t)$, with complex amplitude (*e.g.* Levi, 2016):

$$x_0=\frac{e\mathrm{E}_0}{m_e(\omega_0^2-\omega^2-i\omega\gamma)}. \tag{I.7}$$

It is important to consider both $\vec{x}$ and $\vec{\mathrm{E}}$ as complex quantities, since there is a phase shift induced by the dissipation term. The module of x_0, giving the physical value of the amplitude, is:

$$|x_0|=\frac{e|\mathrm{E}_0|}{m_e\sqrt{\left(\omega^2-\omega_0^2\right)^2+\gamma^2\omega^2}}. \tag{I.8}$$

This is the classic harmonic oscillator solution. It is represented in Fig. I.13. The amplitude is maximum at the *resonant frequency*, $\omega_r=\sqrt{\omega_0^2-\gamma^2/2}$. If there is no dissipation ($\gamma=0$), the amplitude becomes infinite, and the electron escapes.

I.2.1.2 The Plasma Frequency

Free electrons oscillate around heavy cations at the *plasma frequency*, ω_p. Its formula is (*cf. e.g.* Chap. 1 of Krügel, 2003, for a simple proof):

$$\omega_p\equiv\sqrt{\frac{n_e e^2}{m_e\epsilon_0}}, \tag{I.9}$$

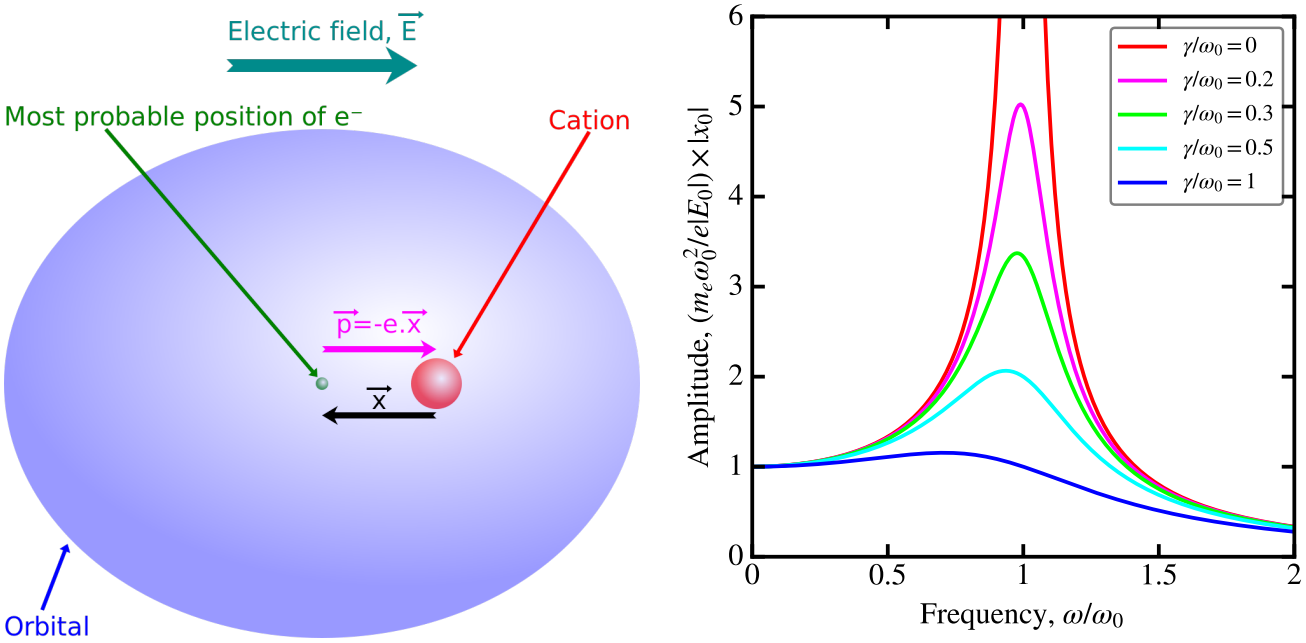

FIGURE I.13 – *Amplitude of a forced harmonic oscillator.* The left image represents the effect of an electromagnetic field, $\vec{E}$, on an orbital. The displacement between the nucleus and the most probable position of the electron induces a permanent dipole, $\vec{p} = -e.\vec{x}$. In this simple picture, the nucleus (cation) is assumed fixed and the electron oscillates around it. The right panel shows the amplitude of the motion of the electron (Eq. I.8) as a function of frequency, for different values of the friction, γ. We have normalized both axes in order to display dimensionless quantities. Licensed under CC BY-SA 4.0.

where n_e is the number density of free electrons. It applies to metals, as well as actual gaseous plasmas. These media absorb and scatter electromagnetic waves with frequencies lower than ω_p. For instance, in the case of the Earth's ionosphere, $n_e \simeq 10^{12}$ m^{-3}, thus $\omega_p \simeq 60$ MHz. This explains why amateur radio operators communicate over long distances at frequencies lower than this value, to benefit from the reflection of their transmission on the ionosphere (*e.g.* Perry et al., 2018). In the case of a metal, with density $n_e \simeq 10^{29}$ m^{-3}, $\omega_p \simeq 20$ PHz, corresponding to a wavelength $\lambda_p \simeq 0.1$ µm, in the *UltraViolet* (UV; *cf.* Table A.4). This explains the shiny appearance of metals, as they are able to reflect the visible light, which has a lower frequency than UV photons. It happens that the expression of ω_p also appears in the optical properties of dielectrics, and we will use it extensively.

I.2.1.3 The Dielectric Function

In a dielectric, an electromagnetic wave polarizes the bonds. If we consider each bond as a dipole with moment $\vec{p}$, the *polarization density* is defined as:

$$\vec{P} = n_e \vec{p}, \tag{I.10}$$

where n_e is the number density of valence electrons. The induced polarization density is directly related to the electric field:

$$\vec{P} = \epsilon_0 \chi \vec{E}, \tag{I.11}$$

where χ is the *electric susceptibility*. The *electric displacement field*, $\vec{D}$, which accounts for the charge displacement induced by an electric field $\vec{E}$ is defined as:

$$\vec{D} = \epsilon \vec{E}, \tag{I.12}$$

where ϵ is the *electric permittivity* of the medium. The *relative electric permittivity*, ϵ_r is defined such that: $\epsilon = \epsilon_r \epsilon_0$. It is a macroscopic quantity, as no medium is truly continuous. At atomic scales, Eq.

(I.12) can be broken into two terms:

$$\vec{D} = \underbrace{\epsilon_0 \vec{E}}_{\text{vacuum between atoms}} + \underbrace{\vec{P}}_{\text{induced dipoles}} = \epsilon_0 \underbrace{(1+\chi)}_{\epsilon_r} \vec{E}. \tag{I.13}$$

The second equality derives from Eq. (I.11). It also implies that $\epsilon_r = 1+\chi$. The induced polarization is, using Eq. (I.7) and Eq. (I.10):

$$\vec{P} = n_e e \vec{x} = \underbrace{\frac{n_e e^2}{m_e} \frac{1}{\omega_0^2 - \omega^2 - i\omega\gamma}}_{\epsilon_0 \chi} \vec{E}. \tag{I.14}$$

Finally, a bit of algebra and introducing the plasma frequency (Eq. I.9), gives:

$$\epsilon_r(\omega) = \underbrace{1 + \frac{\omega_p^2(\omega_0^2 - \omega^2)}{(\omega_0^2 - \omega^2)^2 + \gamma^2\omega^2}}_{\epsilon_1(\omega)} + i \underbrace{\frac{\omega_p^2 \gamma \omega}{(\omega_0^2 - \omega^2)^2 + \gamma^2\omega^2}}_{\epsilon_2(\omega)}. \tag{I.15}$$

This dispersion relation is called the *dielectric function*. It is displayed in Fig. I.14.a. It can be related to the refractive index of the material, m. Indeed, plane electromagnetic waves propagating in a dielectric have a phase velocity $v_{\text{ph}} = 1/\sqrt{\epsilon\mu}$, where μ is the *magnetic susceptibility* (*cf. e.g.* Chap. 7 of Jackson, 1999, for a derivation from Maxwell's equations). This phase velocity can also be expressed as a function of the speed of light, c: $v_{\text{ph}} = c/m$, where m is the refractive index. Since we can decompose $\mu = \mu_r \mu_0$, and because $\epsilon_0 \mu_0 = 1/c^2$, we have:

$$m(\omega) \equiv \sqrt{\epsilon_r(\omega)\mu_r(\omega)} = n(\omega) + ik(\omega). \tag{I.16}$$

The refractive index is sometimes referred to as the *optical constants*, or simply the *"n and k"*. In a nonmagnetic medium, $\mu_r = 1$, thus:

$$\begin{cases} \epsilon_1(\omega) &= n^2(\omega) - k^2(\omega) \\ \epsilon_2(\omega) &= 2n(\omega)k(\omega). \end{cases} \tag{I.17}$$

The two complex quantities $\epsilon(\omega)$ and $m(\omega)$ contain the same information. Eq. (I.15) corresponds to one single type of harmonic oscillator, that is to one mode of one type of bond. An actual dielectric is usually the linear combination of several resonances, such as Eq. (I.15), with different sets of ω_p, ω_0, and γ.

I.2.1.4 Harmonic Oscillator Cross-Section

The flux carried by a plane electromagnetic wave is given by the time average of the *Poynting vector*:

$$\langle|\vec{\mathscr{P}}|\rangle = \frac{\epsilon_0 c}{2}|\vec{E_0}|^2. \tag{I.18}$$

The power radiated by a dipole, harmonically oscillating, is (*cf. e.g.* Chap. 9 of Jackson, 1999):

$$W_{\text{rad}} = \frac{2}{3}\frac{\langle|\ddot{\vec{p}}|^2\rangle}{4\pi\epsilon_0 c^3} = \frac{\omega^4 e^2 |x_0|^2}{12\pi\epsilon_0 c^3}. \tag{I.19}$$

This power is the radiation in response to the excitation by the incident wave. This is the scattering contribution. The *scattering cross-section* of this harmonic oscillator is thus simply: $C_{\text{sca}} = W_{\text{rad}}/\langle|\vec{\mathscr{P}}|\rangle$. Replacing $|x_0|$ by Eq. (I.8), we obtain:

$$C_{\text{sca}}(\omega) = C_T \frac{\omega^4}{(\omega^2 - \omega_0^2)^2 + \gamma^2\omega^2}, \tag{I.20}$$

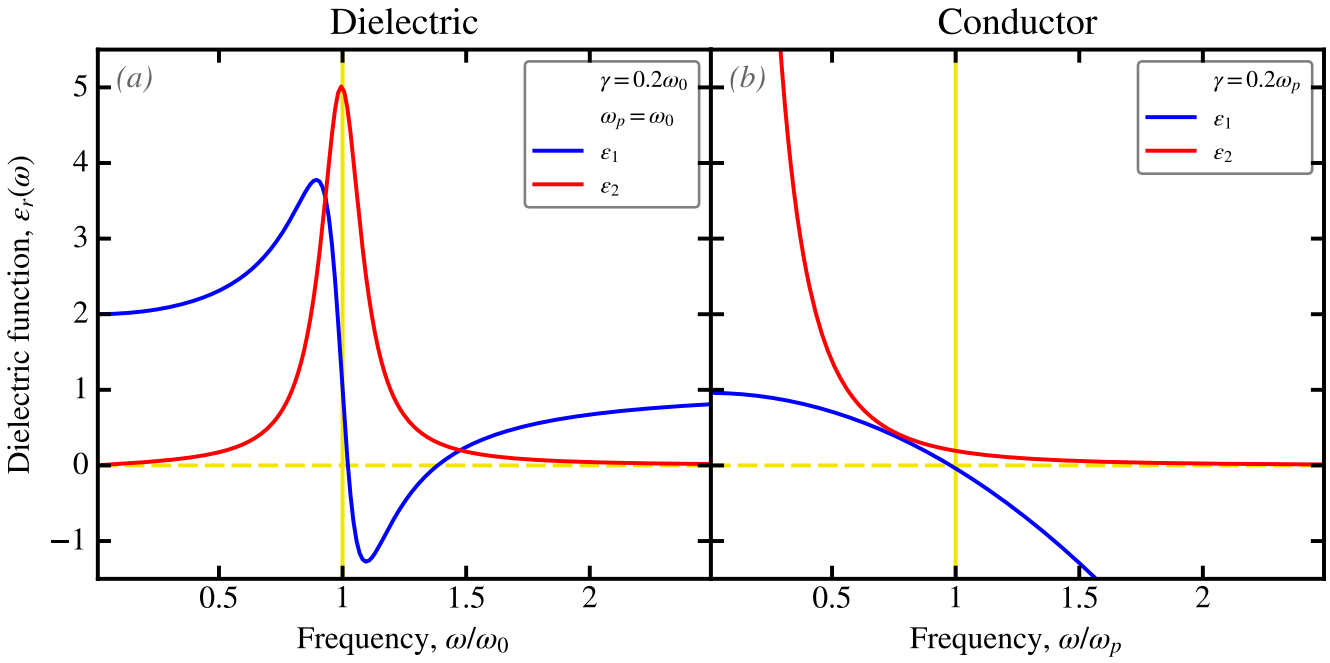

FIGURE I.14 – *Idealized optical constants.* Both panels show dielectric functions where the bonds (in the dielectric case) or the free electrons (in the case of a conductor) are treated as harmonic oscillators. Panel *(a)* displays Eq. (I.15). We see that the imaginary part, ϵ_2, which corresponds to the absorption, peaks around the resonant frequency and drops rapidly to zero on both sides. Panel *(b)* displays Eq. (I.28). We see that the absorption by a conductor rises rapidly below the plasma frequency. It is another way to witness the fact that metals can absorb any light below ω_p. At high frequency, $\epsilon_2 \to 0$. Licensed under CC BY-SA 4.0.

where we have introduced the *Thomson cross-section*:

$$C_T \equiv \frac{8\pi}{3}\left(\frac{e^2}{4\pi\epsilon_0 m_e c^2}\right)^2 \simeq 6.66 \times 10^{-29}\ \mathrm{m}^2. \tag{I.21}$$

Now, the absorbed power comes from the dissipation into the solid. The dissipation force in Eq. (I.5) is $\vec{F}_{dis} = -m_e\gamma\dot{\vec{x}}$. The dissipated power is thus the work of this force:

$$W_{dis} = m_e\gamma|\dot{\vec{x}}|^2 = \frac{1}{2}m_e\gamma\omega^2|x_0|^2. \tag{I.22}$$

The absorption cross-section of the harmonic oscillator is therefore: $C_{abs} = W_{dis}/\langle|\vec{\mathscr{P}}|\rangle$. Using Eq. (I.8) and Eq. (I.21), we obtain:

$$C_{abs}(\omega) = \frac{e^2}{m_e\epsilon_0 c}\frac{\gamma\omega^2}{(\omega^2+\omega_0^2)^2+\gamma^2\omega^2} \tag{I.23}$$

It is interesting to look at the limiting behavior of both C_{sca} and C_{abs} (see also Chap. 1 of Krügel, 2003).

At high frequency ($\omega \gg \omega_0$; short wavelength), we have:

$$\begin{cases} C_{sca}(\omega) &\simeq C_T \\ C_{abs}(\omega) &\simeq \dfrac{e^2}{4m_e\epsilon_0 c}\dfrac{\gamma}{\omega^2}. \end{cases} \tag{I.24}$$

Around the resonant frequency ($\omega \simeq \omega_0$), we have:

$$\begin{cases} C_{sca}(\omega) &\simeq \dfrac{C_T}{4}\dfrac{\omega_0^2}{(\omega-\omega_0)^2+(\gamma/2)^2} \\ C_{abs}(\omega) &\simeq \dfrac{e^2}{4m_e\epsilon_0 c}\dfrac{\gamma}{(\omega-\omega_0)^2+(\gamma/2)^2}. \end{cases} \tag{I.25}$$

It shows that around the resonant frequency, both C_{sca} and C_{abs} have *Lorentz profiles* centered at ω_0, with *Full Width at Half Maximum* (FWHM), γ.

At short frequency ($\omega \ll \omega_0$; long wavelength):

$$\begin{cases} C_{sca}(\omega) & \simeq & C_T \left(\dfrac{\omega}{\omega_0}\right)^4 \\ C_{abs}(\omega) & \simeq & \dfrac{e^2\gamma}{m_e \epsilon_0 c \omega_0^2} \left(\dfrac{\omega}{\omega_0}\right)^2 . \end{cases} \tag{I.26}$$

Those approximations are particularly useful.

☞ For dielectrics, $C_{sca} \propto 1/\lambda^4$ and $C_{abs} \propto 1/\lambda^2$ at long wavelength.

I.2.1.5 Optical Constants of Conductors

Eq. (I.15) is valid for a dielectric, as it assumes the medium is only constituted of dipoles. This is not the case in a conductor where there are also free charges. An electromagnetic wave induces a current, $\vec{j}$, related to the electric field, $\vec{E}$, by the *conductivity*, σ:

$$\vec{j} = \sigma \vec{E} = n_e e \vec{v}, \tag{I.27}$$

where the second equality relates the current to its microscopic origin, the velocity of free electrons, $\vec{v}$. Maxwell's equations for plane waves give (*e.g.* Chap. 7 of Jackson, 1999):

$$\epsilon_r(\omega) = \underbrace{\epsilon_d(\omega)}_{\text{bound electrons}} + \underbrace{i\frac{\sigma(\omega)}{\epsilon_0 \omega}}_{\text{free electrons}}, \tag{I.28}$$

where $\epsilon_d(\omega)$ is the leftover dielectric term. We can apply the harmonic oscillator model again to these free electrons. The difference is that there is no restoring force, $\omega_0 = 0$. From Eq. (I.7), the velocity of free electrons becomes:

$$|\vec{v}| = \frac{e|\vec{E}|}{m_e(\gamma - i\omega)}. \tag{I.29}$$

Injecting this quantity in Eq. (I.27), we obtain:

$$\sigma(\omega) = \epsilon_0 \omega_p^2 \frac{\gamma}{\gamma^2 + \omega^2} + i\epsilon_0 \omega_p^2 \frac{\omega}{\gamma^2 + \omega^2}. \tag{I.30}$$

Focussing on the free electron term in Eq. (I.28), *i.e.* assuming $\epsilon_d = 0$, we get:

$$\epsilon_r(\omega) = \underbrace{1 - \frac{\omega_p^2}{\gamma^2 + \omega^2}}_{\epsilon_1(\omega)} + i \underbrace{\frac{\gamma}{\omega} \frac{\omega_p^2}{\gamma^2 + \omega^2}}_{\epsilon_2(\omega)}. \tag{I.31}$$

It is also known as the *Drude model*. This equation is displayed in Fig. I.15.b. Interestingly enough, the cross-sections of Eq. (I.20) and Eq. (I.23) apply also to conductors, with $\omega_0 = 0$. We can easily derive their limiting behavior.

☞ Conductors have the same behavior than dielectrics at long wavelength: $C_{sca} \propto 1/\lambda^4$ and $C_{abs} \propto 1/\lambda^2$.

I.2.1.6 The Kramers-Kronig Relations

The residue theorem implies that, if $f(x)$ is a complex function of the complex variable x, analytical over $\Im(x) \geq 0$, and dropping faster than $1/|x|$, we have the relation:

$$f(\omega) = \frac{1}{i\pi} \mathrm{P} \int_{-\infty}^{\infty} \frac{f(x)}{x-\omega} \mathrm{d}x, \tag{I.32}$$

with ω real and positive. We have used the *Cauchy principal value*:

$$\mathrm{P} \int_{-\infty}^{\infty} \frac{f(x)}{x-\omega} \mathrm{d}x = \lim_{\delta \to 0} \left(\int_{-\infty}^{\omega-\delta} \frac{f(x)}{x-\omega} \mathrm{d}x + \int_{\omega+\delta}^{\infty} \frac{f(x)}{x-\omega} \mathrm{d}x \right), \tag{I.33}$$

which is simply an integral avoiding the singularity in $x = \omega$. Decomposing $f(x) = f_1(x) + i f_2(x)$, we obtain cross-relations between $f_1(x)$ and $f_2(x)$. These general mathematical relations are usually applied to the susceptibility, from which we derive the dielectric function (*e.g.* Chap. 21 of Draine, 2011):

$$\left\{ \begin{array}{rcl} \epsilon_1(\omega) - 1 & = & \frac{2}{\pi} \mathrm{P} \int_0^{\infty} \frac{x \epsilon_2(x)}{x^2 - \omega^2} \mathrm{d}x \\ \epsilon_2(\omega) & = & -\frac{2}{\pi} \omega \mathrm{P} \int_0^{\infty} \frac{\epsilon_1(x) - 1}{x^2 - \omega^2} \mathrm{d}x. \end{array} \right. \tag{I.34}$$

These relations are known as the *Kramers-Kronig relations*.

Implications. We only need to specify ϵ_1 or ϵ_2 at all frequencies, and can use Eq. (I.34) to derive the other one. These relations are used to check laboratory data consistency (*e.g.* Zubko et al., 1996).

Interpretation. They are a consequence of the causality requirement for a linear system (here, we have $\vec{\mathrm{P}} = \epsilon_0 \chi \vec{\mathrm{E}}$). In our case, they impose that the response of the polarization does not precede the effect of the electric field. Sect. 62 of Landau & Lifshtiz (1960), Chap. 21 of Draine (2011), and Chap. 2 of Krügel (2003) discuss these relations more extensively.

Constraint on the Cross-Section. They give some constraints on the long wavelength behavior of the dielectric function. Let's assume that $\epsilon_2(\omega) \propto \omega^{\beta-1}$ for $\omega < \delta$, for an arbitrary δ. The first relation tells us that:

$$\epsilon_1(0) = 1 + \frac{2}{\pi} \int_0^{\delta} x^{\beta-2} \mathrm{d}x + \int_{\delta}^{\infty} \frac{\epsilon_2(x)}{x} \mathrm{d}x. \tag{I.35}$$

The second integral is finite by requirement. For the first integral to be finite, we need to have $\beta > 1$. At long wavelength, Eq. (I.15) tells us that, for a dielectric:

$$\left\{ \begin{array}{lcll} \epsilon_1(\omega) & \underset{\omega \to 0}{\to} & 1 + \left(\frac{\omega_p}{\omega_0} \right)^2 & = \quad \mathrm{const} \\ \epsilon_2(\omega) & \underset{\omega \to 0}{\to} & \frac{\omega_p^2 \Upsilon}{\omega_0^4} \omega & \ll \quad \epsilon_1(\omega). \end{array} \right. \tag{I.36}$$

We will see in Eq. (I.46) that, at long wavelength, $\mathrm{C_{abs}} \propto \epsilon_2 / [(\epsilon_1 + 2)^2 + \epsilon_2^2] / \lambda$. Using Eq. (I.36), we get $\mathrm{C_{abs}}(\lambda) \propto \epsilon_2(\lambda)/\lambda \propto \lambda^{-\beta}$. We will see in Sect. III.1.2 that this β parameter is sometimes referred to as the *emissivity index*.

☞ Assuming that $\mathrm{C_{abs}}(\lambda) \propto \lambda^{-\beta}$ at long wavelengths, we need to have $\beta > 1$.

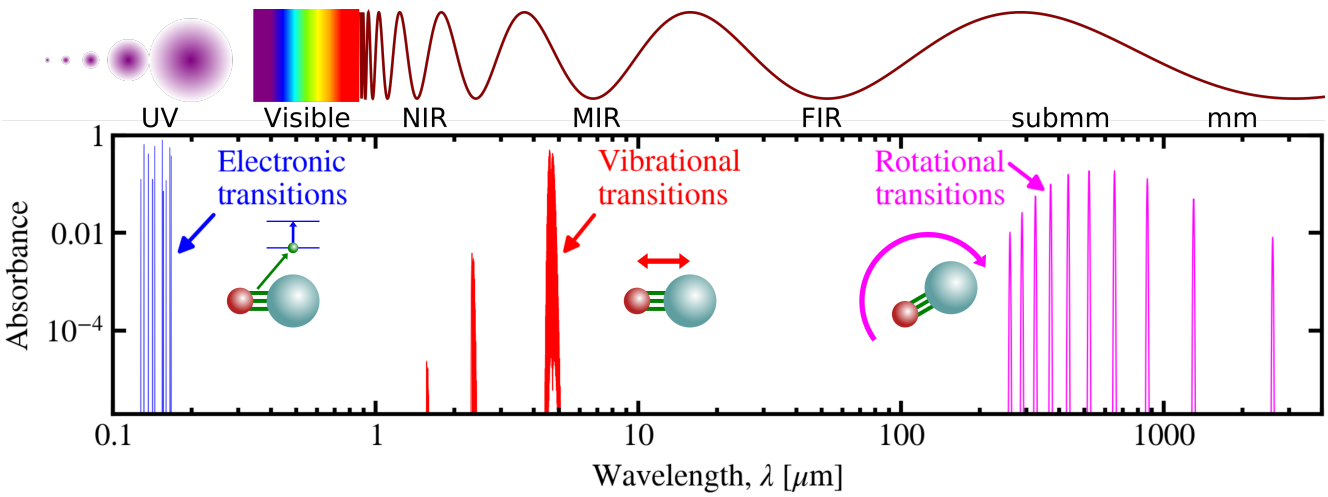

FIGURE I.15 – *Molecular transitions.* The different types of transitions are illustrated with the CO molecule. Licensed under CC BY-SA 4.0.

I.2.2 Grain Optical Properties

I.2.2.1 Why Are Most Dust Features in the MIR?

All but one spectral features of the interstellar grain candidates we have listed in Table I.3 are in the MIR. This is a general trend (*e.g.* Table 1 of van der Tak et al., 2018a). It can be understood by making an analogy with the different types of molecular transitions (*cf. e.g.* Chap. 2 of Tielens, 2005, for a review). Those are illustrated in Fig. I.15.

Electronic transitions are transitions between the quantum harmonic oscillator levels of the bonding electron. In the case of solids, they are transitions between bands, such as the $\pi \rightarrow \pi^\star$ transition of aromatic carbon, at 2175 Å (*cf.* Sect. I.1.4). The natural frequency of these resonances is given by Eq. (I.6): $\omega_0 = \sqrt{k_e/m_e}$. The energy of these resonances is comparable to the binding energy, or the band gap. They typically range between $\simeq 4$ and $\simeq 20$ eV. They are thus in the UV domain ($\lambda \simeq 0.06 - 0.30$ μm).

Vibrational transitions are associated with the stretching or bending of a bond. These modes involve the motion of the nuclei, which are much heavier than the electrons. Their frequency is $\omega_v = \sqrt{k_v/\mu_{1,2}}$, where $\mu_{1,2} = m_1 m_2/(m_1 + m_2)$ is the reduced mass of the two atoms, m_1 and m_2. Typically, $\mu_{1,2} = 0.9, 6, 10 \times m_p$ for C–H, C–C and Si–O bonds, respectively (m_p is the proton mass; *cf.* Table B.2). At first order, the new force constant is similar to previously, $k_e \simeq k_v$. The frequency is now reduced by a factor $\simeq \sqrt{m_e/\mu_{1,2}} \simeq 0.007 - 0.02$. These transitions are thus in the MIR ($\lambda \simeq 2 - 40$ μm). They are the most relevant transitions for ISD.

Rotational transitions are associated with the rotation of the molecule. Their energy depends on the centrifugal force, which reduces the frequency by a factor $\simeq m_e/m_p$. These transitions are thus in the millimeter regime. Most dust grains do not have detectable rotational transitions, because of their inertia. Only the smallest, charged grains have a non-negligible rotational emission that will be discussed in Sect. II.2.2.3.

I.2.2.2 Dielectric Functions of Realistic Materials

The dielectric functions of Eq. (I.15) and Eq. (I.28) correspond to simple cases where there is only one type of oscillator. Realistic materials have more complex structures, with several modes per bond. Deriving dielectric functions of potential interstellar grain analogs is the subject of a rich literature. There are three types of approaches to determine the dispersion relation of a medium.

The theoretical knowledge of the microscopic structure of the crystal can be used to determine the different resonances that we have demonstrated in Sect. I.2.1. The resonant or plasma fre-

quency, as well as the collisional rates (γ) have to be known. The Kramers-Kronig relations (Sect. I.2.1.6) can be used to obtain complementary constraints.

Laboratory data about the spectral profile of some features, or the density of the material, or any relevant characteristics can also be used. The ISM community is active in this field, as our results largely depend on the accurate values of atomic and molecular data. Several teams focus their research effort on laboratory measures of dust analogs.

Astronomical observations can be used to constrain some features. The most famous example is the use of observations of the 9.7 and 18 µm band profiles to build the optical properties of *astronomical silicates*, by Draine & Lee (1984). Indeed, we have seen in Sect. I.1.4 that there is a diversity of silicate composition, and we do not know which one is relevant to ISD (it is likely a mixture).

These approaches are not exclusive and are usually combined as observations and laboratory data are always partial. The work by Draine & Lee (1984) was the first study to use these principles to derive the UV-to-mm dielectric functions of graphite and astronomical silicates. We now have a better knowledge of the dispersion relations of several important materials: *(i)* silicates (*e.g.* Laor & Draine, 1993; Weingartner & Draine, 2001a; Draine, 2003b,c); *(ii)* amorphous carbon (*e.g.* Rouleau & Martin, 1991; Zubko et al., 1996; Jones, 2012a,b,c); *(iii)* graphite (*e.g.* Laor & Draine, 1993; Draine, 2003b,c, 2016); *(iv)* PAHs (*e.g.* Li & Draine, 2001; Draine & Li, 2007); and *(v)* composite grains (*e.g.* Köhler et al., 2014, 2015). Fig. I.16 shows a few examples.

I.2.2.3 Computing Grain Cross-Sections

The dielectric functions are intensive quantities characterizing the bulk optical properties of solids, but independent of their size and shape. To compute usable absorption and scattering cross-sections, there is one last step to do. Let's assume our grains are spheres of radius a.

- The extinction cross-section of the grain can be written:

$$C_{ext}(\lambda, a) = \underbrace{\pi a^2}_{\text{geometric cross-section}} \times \underbrace{Q_{ext}(\lambda, a)}_{\text{efficiency}}. \tag{I.37}$$

  This expression is simply the geometric cross-section, πa^2, times an *extinction efficiency*, Q_{ext}, which is a dimensionless quantity. We can express the scattering and absorption cross-section the same way:

$$C_{sca}(\lambda, a) = \pi a^2 Q_{sca}(\lambda, a) \tag{I.38}$$
$$C_{abs}(\lambda, a) = \pi a^2 Q_{abs}(\lambda, a). \tag{I.39}$$

  Out of these three efficiencies, only two are independent, as we have $Q_{ext} = Q_{sca} + Q_{abs}$.

- Another useful quantity that can be derived from the efficiencies is the *albedo*, quantifying the fraction of the incident light that is scattered by the grain:

$$\tilde{\omega}(\lambda, a) \equiv \frac{C_{sca}(\lambda, a)}{C_{ext}(\lambda, a)} = \frac{Q_{sca}(\lambda, a)}{Q_{ext}(\lambda, a)}. \tag{I.40}$$

- Let's call θ the angle between the directions of the incident and scattered light. The probability distribution of scattering angles is called the *scattering phase function*:

$$\Phi(\cos\theta, \lambda, a) \equiv \frac{1}{C_{sca}(\lambda, a)} \frac{d\mathscr{C}_{sca}(\cos\theta, \lambda, a)}{d\Omega}, \tag{I.41}$$

  where $\mathscr{C}_{sca}(\cos\theta, \lambda, a)$ is the *differential scattering cross-section* (*i.e.* the cross-section for scattering in a given direction), and $d\Omega = d\cos\theta\, d\phi$ is the solid angle element. It is normalized over all directions, such that:

$$\iint_\Omega \Phi(\cos\theta, \lambda, a)\, d\Omega = 2\pi \int_{-1}^{1} \Phi(\cos\theta, \lambda, a)\, d\cos\theta = 1. \tag{I.42}$$

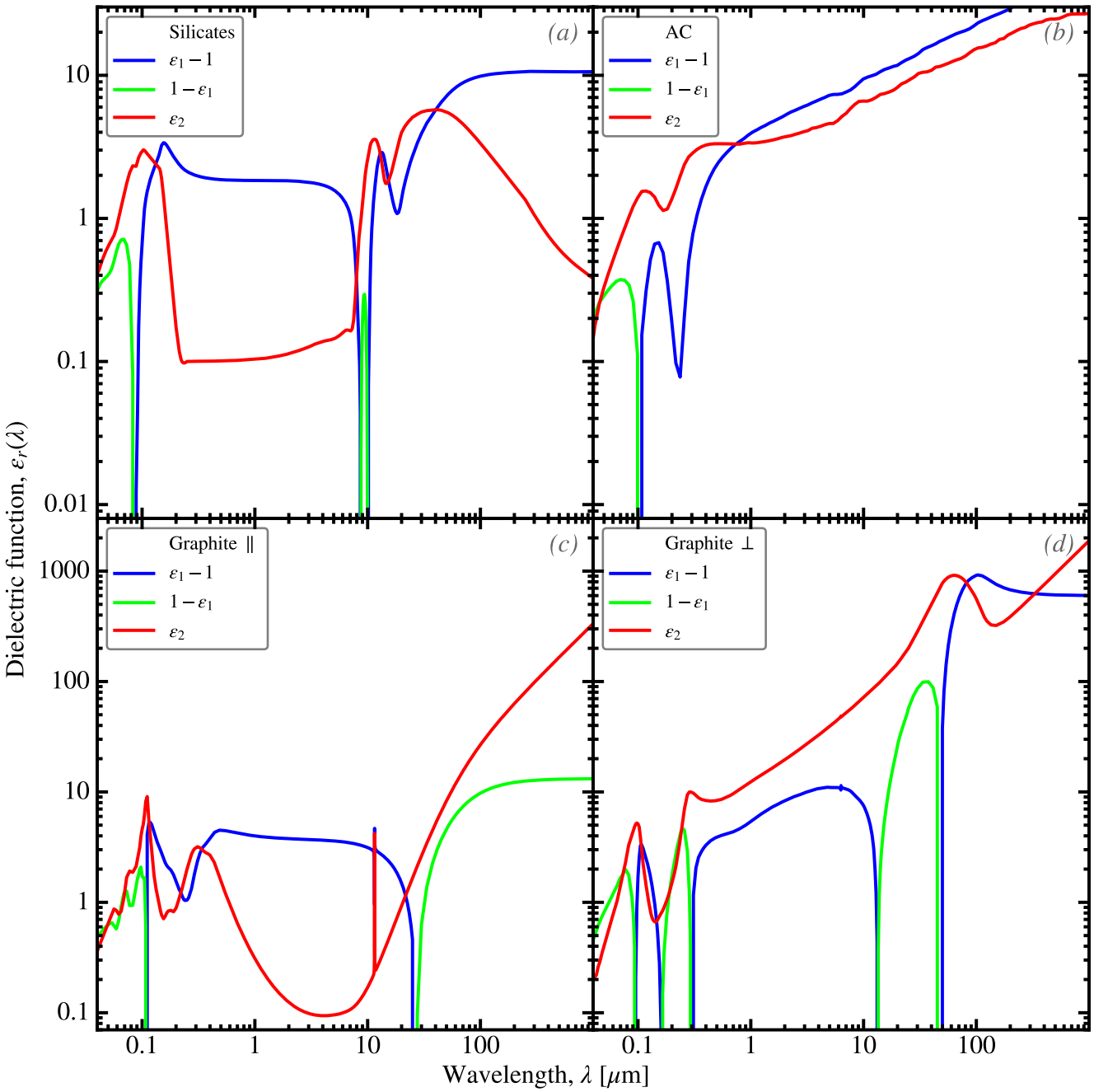

FIGURE I.16 – *Dielectric functions of different materials.* In each panel, we show the real part of the dielectric function as $\epsilon_1 - 1$ (blue) and $1 - \epsilon_1$ (green), as this quantity can be negative. The imaginary part, ϵ_2, is in red. Panel *(a)* shows the astronomical silicates by Draine (2003b,c). Panel *(b)* shows the ACAR type of amorphous carbon by Zubko et al. (1996). These are produced by arc discharges between amorphous carbon electrodes in a 10 mbar Ar atmosphere. Panel *(c)* and *(d)* show the graphite by Draine (2003b,c). Graphite is anisotropic, as we have seen in Fig. I.9.e. It is usually approximated by mixing 2/3 of the optical properties parallel to the graphene sheets *(c)*, and 1/3 perpendicular *(d)*.

For isotropic scattering, we have $\Phi(\cos\theta, \lambda, a) = 1/4\pi$. The first moment of this distribution is called the *asymmetry parameter*, defined as:

$$g(\lambda, a) = \langle\cos\theta\rangle = 2\pi \int_{-1}^{1} \Phi(\cos\theta, \lambda, a) \cos\theta \, \mathrm{d}\cos\theta. \tag{I.43}$$

This parameter is a direct product of Mie theory. Forward and backward scattering correspond to $\langle\cos\theta\rangle \simeq 1$ and $\langle\cos\theta\rangle \simeq -1$, respectively, whereas isotropic scatterers have $\langle\cos\theta\rangle \simeq 0$. There are approximate analytical phase functions. The most famous is from Henyey & Greenstein (1941):

$$\Phi(\cos\theta, \lambda, a) = \frac{1}{4\pi} \frac{1 - g^2(\lambda, a)}{(1 + g^2(\lambda, a) - 2g(\lambda, a)\cos\theta)^{3/2}}. \tag{I.44}$$

Other distributions have been proposed (*e.g.* Draine, 2003b).

The treatment to compute Q_{sca}, Q_{abs} and g depends on the value of the *size parameter*:

$$x = \frac{2\pi a}{\lambda}. \tag{I.45}$$

As long as we do not zoom in scales where the hypothesis of a continuous medium breaks down, that is scales of a few Å (*i.e.* grains made of a few atoms, or hard X-ray photons), the estimation of the efficiencies of a grain only depends on x and m. The *Mie theory* (*cf. e.g.* Chap. 4 of Bohren & Huffman, 1983) [5] is the central tool to compute grain cross-sections. It is a numerical method, exactly solving Maxwell's equations for the scattering of a plane electromagnetic wave by a homogeneous sphere of known refractive index, $m(\lambda)$. Several regimes can be identified, depending on the value of the size parameter. They are illustrated in Fig. I.18. In Fig. I.19, we show the actual cross-sections of silicate and graphite grains of different sizes.

Geometrical optics. It is the regime for which $x \gg 1$ (*cf. e.g.* Chap. 7 of Bohren & Huffman, 1983). For interstellar grains, which have submicronic sizes, it corresponds to UV wavelengths and shorter. This regime is more relevant to circumstellar dust, where grains can be significantly larger. In geometrical optics, the undulatory nature of light is put aside. Instead, light is modeled as rays, using the formalism of Fresnel. Mie theory is valid in this regime, but numerical problems start arising.

- The important feature of this regime is that, $Q_{sca} \simeq Q_{abs} \simeq 1$ (*cf.* Fig. I.18.b). This can also be seen in panels *(a)* to *(d)* of Fig. I.19. When the size of the grain increases, the range where both Q_{sca} and Q_{abs} are flat extends to shorter wavelengths. The cross-sections are independent of wavelength, as the grains are effectively behaving as opaque circular screens. It also means that the cross-section is proportional to the area of the grain, but independent of its volume.
- $Q_{sca} \simeq Q_{abs} \simeq 1$ implies that $Q_{ext} \simeq 2$, meaning that the extinction cross-section is twice the geometric cross-section. This counter-intuitive result is called the *extinction paradox* (Chap. 4 of Bohren & Huffman, 1983, for an extensive discussion). It is a real diffraction effect, that is not actually predicted by the methods of geometrical optics, for which $Q_{ext} \simeq 1$. Its resolution lies in accounting for the diffraction around the grain. It is illustrated in Fig. I.17. The exact interpretation of this paradox is still debated nowadays (*e.g.* Berg et al., 2011).
- Another feature of this regime is that grains are efficient forward scatterers ($\langle\cos\theta\rangle \simeq 1$; Fig. I.18.c).

The Mie regime. It corresponds to grain sizes comparable to the wavelength of the incident light ($x \simeq 1$). Mie theory is valid outside this regime, but this is the regime where none of the other approximations are valid.

5. See also B. Draine's public code, bhmie.f, implementing the algorithm in Appendix A of Bohren & Huffman (1983).

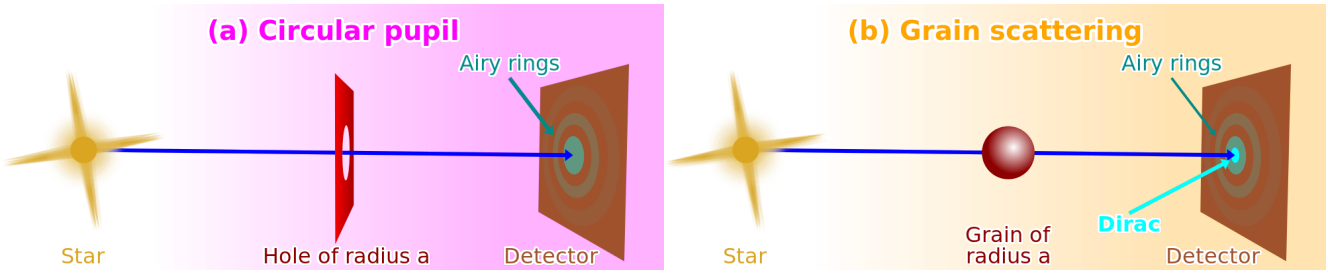

FIGURE I.17 – *Illustration of the extinction paradox.* We have represented two situations. In panel *(a)*, we show the radiation from a distant star passing through a circular pupil of radius a, and projected onto the plane of a detector. We assume that: *(i)* the star is very distant, so that the incident wave can be considered planar; *(ii)* the detector is at a distant from the pupil much larger than a. The observed pattern is a series of Airy rings. In panel *(b)*, we show the same stellar radiation absorbed and scattered by a dust grain of the same radius a as the pupil, at the same distance from a detector. The observed pattern is made of the same Airy rings, but there is a bright spot in the center. This property is a result of *Babinet's theorem*. This theorem is based on the fact that the wave function of a plane wave, $\psi(x,y)$, diffracted by a pupil of transmission $T(x,y)$, is proportional to the Fourier transform of the pupil, $\mathscr{F}(T)$. Here, the direction represented by the blue arrow is the z axis. The x and y axes are the coordinates in the plane of the pupil and of the detector, both being parallel. If we have two pupils, $T_{(a)}$ and $T_{(b)}$, that are complementary, that is $T_{(a)}(x,y)+T_{(b)}(x,y)=1$, $\forall(x,y)$, we have, by linearity of the Fourier transform $\psi_{(a)}(x,y)+\psi_{(b)}(x,y) \propto \mathscr{F}(T_{(a)})+\mathscr{F}(T_{(b)})=\delta(x,y)$, where δ is the Dirac distribution centered in the middle of the screen. In our case, the two complementary pupils are the circular hole in panel *(a)*, and the grain, appearing as a circular screen to the stellar radiation, in panel *(b)*. The intensity is the squared module of the wave function, $I(x,y)=|\psi(x,y)|^2$. We see that $\psi_{(b)}(x,y)=\psi_0\delta(x,y)-\psi_{(a)}(x,y)$, thus $I_{(b)}(x,y)=I_{spot}\delta(x,y)+I_{(a)}(x,y)$, confirming that the pattern in panel *(b)* is the pattern in panel *(a)* plus a bright spot. In panel *(b)*, the bright spot is just the incident wave (rays parallel to the z axis). We note that $I_{(a)}(x,y)=I_{(b)}(x,y)$, except in $(0,0)$. The incident light of intensity I_0 on the grain surface (πa^2) is absorbed. Thus, the absorbed power is $P_{abs}=\pi a^2 I_0$. Now, the Airy pattern is the fraction diffracted by the grain contour, that is the scattered light. Babinet's theorem tells us that it is identical in both cases we have represented. We clearly see in panel *(a)* that the scattered power is also $P_{sca}=\pi a^2 I_0$. The grain thus extinct a power $P_{ext}=2\pi a^2 I_0$. This is the extinction paradox: *(i)* the flux incident on the grain surface is fully absorbed; *(ii)* the contour of the grain scatters the same power at small angles, corresponding to the Airy rings in both panels.

- The optical properties have non-trivial features, depending on x and on the actual resonances of m. For instance, panels *(a)* and *(c)* of Fig. I.19 show the 9.7 and 18 μm features of silicates. These features disappear only for radii $a \gtrsim 10$ μm, as the geometrical optics regime extends in the mid-IR (MIR; *cf.* Table A.4), in this case.
- The scattering pattern is non-trivial, $\langle\cos\theta\rangle$ varying between 0 and 1. It is schematically represented in the central cartoon at the top of Fig. I.18, using the Eq. (I.44). It shows that backward scattering is likely, although forward scattering is more probable.
- Finally, we notice small oscillations in the visible and near-IR (NIR; *cf.* Table A.4) ranges, mostly visible in the Q_{abs} of micronic size grains (panels *(c)* and *(d)* of Fig. I.19). These patterns are called *interference structure*. They are due to the interference between the incident and scattered waves. They are more prominent for weakly absorbent material, such as silicate, which is more transparent than graphite (*cf.* Sect. I.1.4).

The Rayleigh regime. It corresponds to grain sizes significantly smaller than the wavelength of the incident light, $x \ll 1$ (*cf. e.g.* Chap. 5 of Bohren & Huffman, 1983). In the case of interstellar grains,

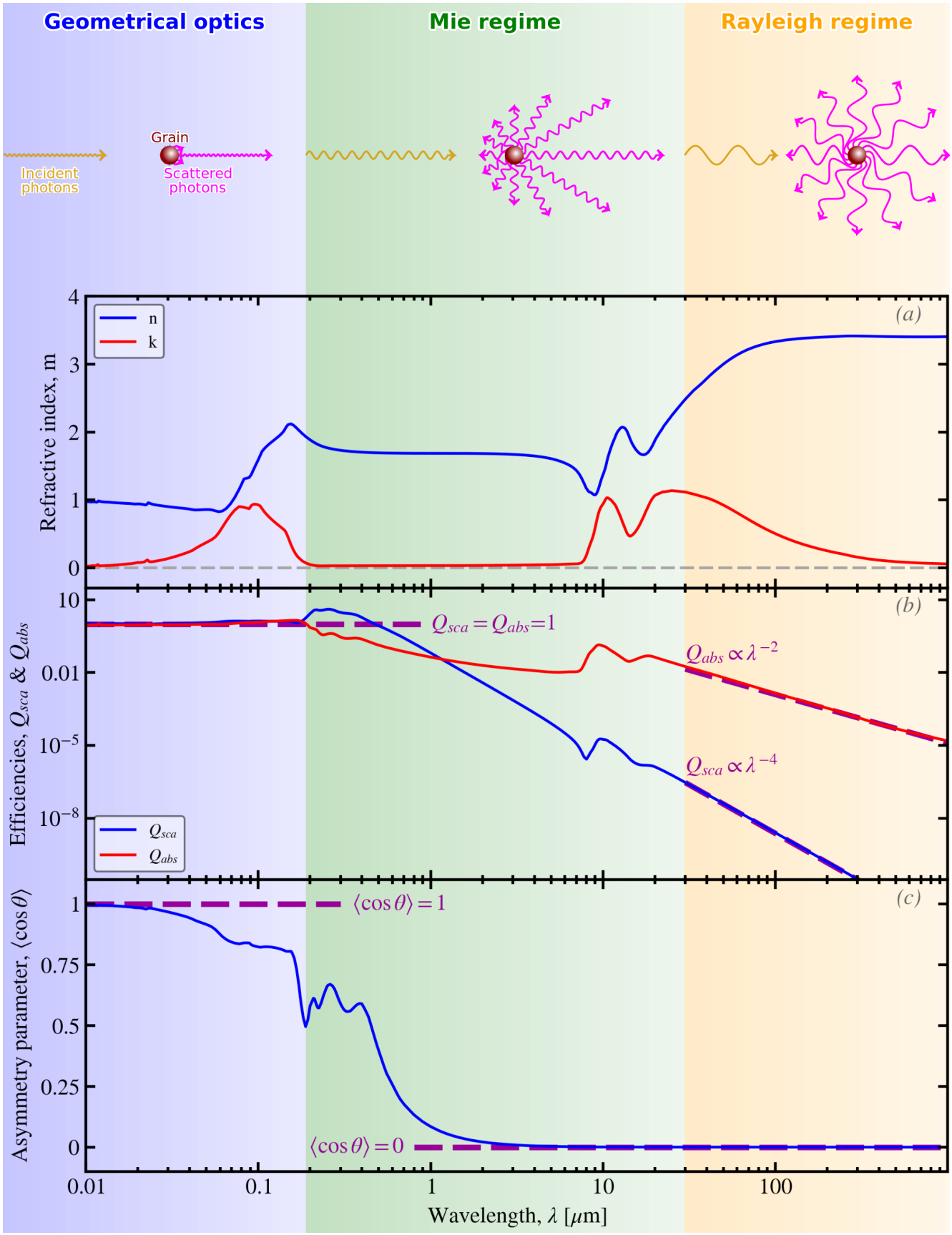

FIGURE I.18 – *Mie, Rayleigh and geometric optics regime.* The top pictures represent the scattering pattern (in magenta) of a spherical grain (red sphere), in the three regimes. The direction of the incident photon is shown in yellow. The scattering pattern has been calculated using the Henyey & Greenstein (1941) phase function. The length of each wiggly arrow is proportional to its scattering probability. The three panels plot below show the optical properties of a $a = 0.1$ µm radius silicate, by Draine (2003b,c). Licensed under CC BY-SA 4.0.

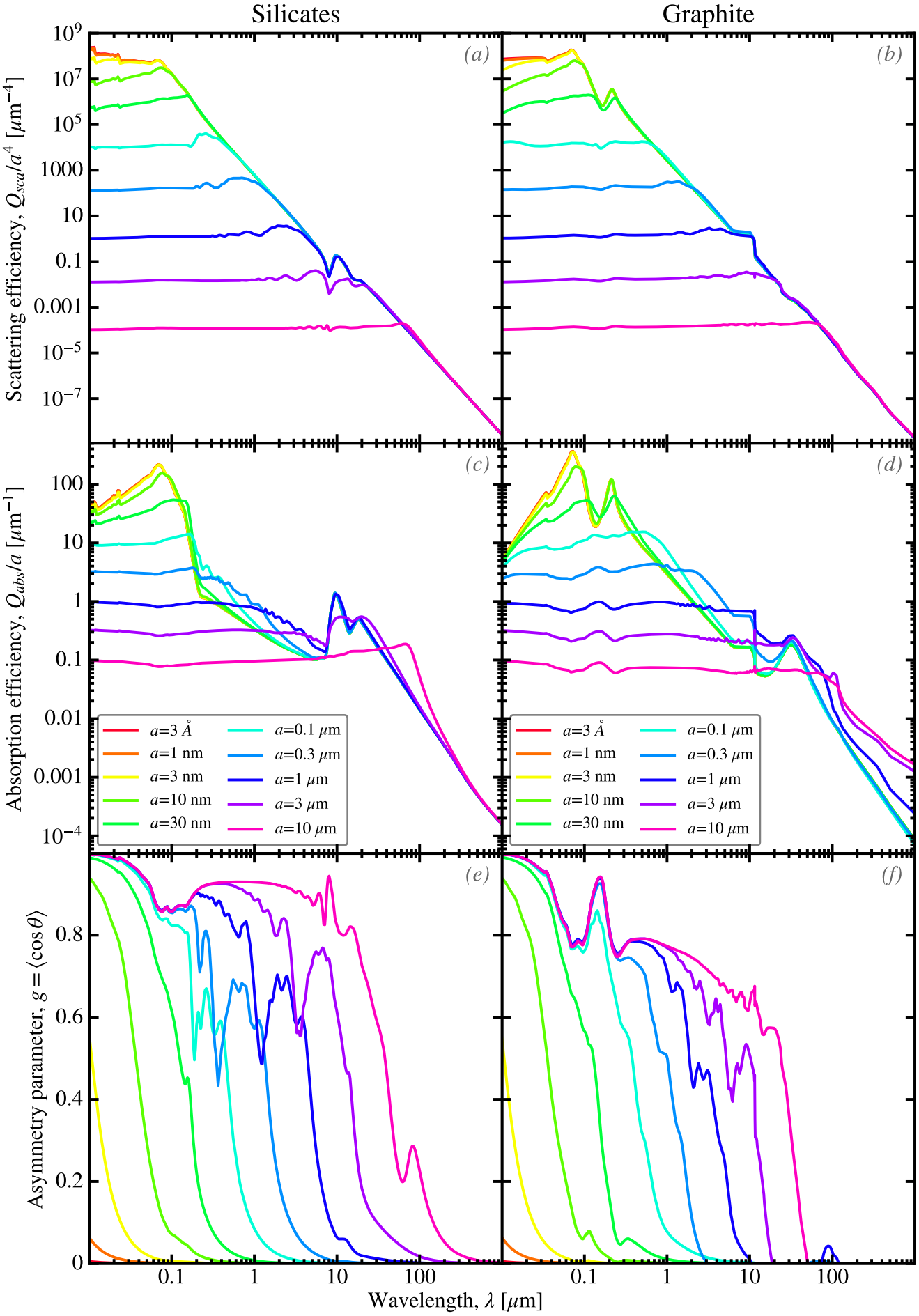

FIGURE I.19 – *Cross-sections of silicate and graphite grains.* The color lines show the optical properties of grains with different radius, a, from Draine (2003b,c). Licensed under CC BY-SA 4.0.

it applies essentially to the NIR regime and longward. The refraction index needs to be small, too: $|m|x \ll 1$. The solutions are analytic (*e.g.* Li, 2008):

$$\begin{cases} C_{sca}(\lambda, a) &= \dfrac{128\pi^5}{3}\left|\dfrac{\epsilon_r(\lambda)-1}{\epsilon_r(\lambda)+2}\right|^2 \dfrac{a^6}{\lambda^4} \\ C_{abs}(\lambda, a) &= 24\pi^2 \dfrac{\epsilon_2(\lambda)}{(\epsilon_1(\lambda)+2)^2+\epsilon_2^2(\lambda)} \dfrac{a^3}{\lambda}. \end{cases} \tag{I.46}$$

- Eq. (I.46) and panels *(a)* to *(d)* of Fig. I.19 show that Q_{sca}/a^4 and Q_{abs}/a are independent of radius in this regime. This explains why small grains have a negligible albedo, whereas large grains are efficient scatterers.
- The fact that Q_{abs}/a is independent of radius implies that the absorption cross-section is proportional to the grain volume: $C_{abs} \propto a^3$. The dust mass can thus be probed by measures in absorption or in emission. An interpretation of this property is that, the wavelength being comparable to the size of the grain, each bond can interact with the electromagnetic field, independently of its location within the solid. The interaction of the incident light with the grain is thus proportional to the total number of oscillators, which is proportional to the mass.
- It explains why scattering appears negligible in this regime: $(C_{sca} \propto a^6) \ll (C_{abs} \propto a^3)$. Finally, we can see that scattering is isotropic ($\langle\cos\theta\rangle \simeq 0$).

  ☞ The absorption cross-section of most interstellar grains, in the NIR-to-mm window, is proportional to their volume. The dust mass can thus be probed by absorption or emission measures.

I.2.2.4 Beyond Homogeneous Spheres

Mie theory is restricted to homogeneous spheres. However, there are several observational indications that this hypothesis is not fully accurate (*cf.* Sect. IV.2.1.1).

- Grains are rapidly formed and destroyed in the ISM, implying that they likely are composites of several materials with different dielectric functions, and voids.
- The polarization of starlight and of ISM emission in the far-IR (FIR; *cf.* Table A.4) indicates that at least some of the grains are elongated.

There are several methods to estimate cross-sections of grains beyond the hypothesis of homogeneous spheres.

Effective medium theory (EMT). EMT is a class of methods to replace the individual dielectric functions of a composite material by an average, $\epsilon_{av}(\lambda)$. Cross-sections can then be estimated using Mie theory or any other approximation. EMT assumes that the different domains are smaller than the wavelength and well-mixed in the grain. There are different *mixing rules* (*cf. e.g.* Chap. 8 of Bohren & Huffman, 1983). It seems that their accuracy depends on the type of sample they are applied to, as independent studies find better agreements with one or the other (*e.g.* Abeles & Gittleman, 1976; Perrin & Lamy, 1990).

Maxwell Garnett's rule assumes that the medium is constituted of a matrix with dielectric function $\epsilon_m(\lambda)$, and some inclusions. The inclusions can be of N different types, with dielectric functions $\epsilon_i(\lambda)$ ($i = 1 \ldots N$), and volume filling factors, ϕ_i. It is implicit that $\phi_i \ll 1$.

$$\epsilon_{av}(\lambda) = \frac{\epsilon_m(\lambda) + \sum_{i=1}^{N} \phi_i c_i \epsilon_i(\lambda)}{1 + \sum_{i=1}^{N} \phi_i c_i}, \tag{I.47}$$

with:

$$c_i = \frac{3\epsilon_m(\lambda)}{\epsilon_i(\lambda) + 2\epsilon_m(\lambda)}. \tag{I.48}$$

Bruggeman's rule does not put a hierarchy between a predominant matrix and a few inclusions. The dielectric function is the solution of:

$$\sum_{i=1}^{N} \phi_i \frac{\epsilon_i(\lambda) - \epsilon_{av}(\lambda)}{\epsilon_i(\lambda) + 2\epsilon_{av}(\lambda)} = 0. \tag{I.49}$$

Ellipsoids in the Rayleigh regime. They have general analytical solutions (*e.g.* Chap. 5 of Bohren & Huffman, 1983). When the three axes of the ellipsoid are aligned on the coordinates x, y, z and if the the electric field is along x, we have:

$$\begin{cases} C_{sca}(\lambda, a) &= \dfrac{128\pi^5}{27} \left| \dfrac{\epsilon_r(\lambda) - 1}{1 + (\epsilon_r(\lambda) - 1)L_x} \right|^2 \dfrac{a^6}{\lambda^4} \\ C_{abs}(\lambda, a) &= \dfrac{8\pi^2}{3} \Im\left[\dfrac{\epsilon_r(\lambda) - 1}{1 + (\epsilon_r(\lambda) - 1)L_x} \right] \dfrac{a^3}{\lambda}, \end{cases} \tag{I.50}$$

where L_x is the *shape factor*. Noting $l_a > l_b$ the two lengths, oblate spheroids have dimensions along the three axes (l_a, l_a, l_b), whereas prolate spheroids have dimensions (l_a, l_b, l_b) (*cf.* Fig. I.20). With these notations, the shape factor is (*e.g.* Chap. 22 of Draine, 2011):

$$\begin{cases} L_x &= \dfrac{1+\xi^2}{\xi^2} \left[1 - \dfrac{\arctan \xi}{\xi} \right] & \text{for oblate spheroids} \\ L_x &= \dfrac{1-\xi^2}{\xi^2} \left[\dfrac{1}{2\xi} \ln\left(\dfrac{1+\xi}{1-\xi} \right) - 1 \right] & \text{for prolate spheroids,} \end{cases} \tag{I.51}$$

with $\xi^2 = |1 - (l_b/l_a)^2|$. In case of randomly oriented ellipsoids, we simply need to take the arithmetic mean of the cross-sections along the three axes.

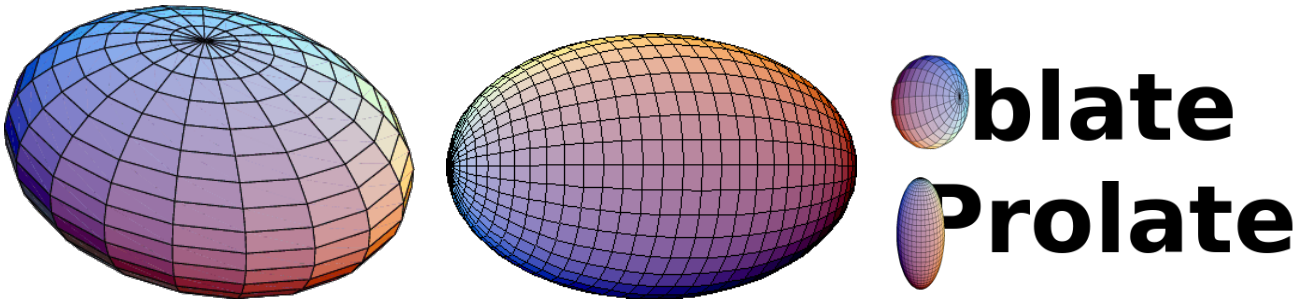

(a) Oblate *(b)* Prolate *(c)* Mnemotechnics

FIGURE I.20 – *Oblate and prolate spheroids.* Credit: volumes produced with Mathematica.

Discrete Dipole Approximation (DDA). DDA (Purcell & Pennypacker, 1973) [6] allows the user to model complex composite grains as arbitrary arrays of independent domains. These domains are approximated by a series of discrete dipoles, which must be much smaller than the incoming wavelength. This method is computer intensive, but very flexible (*cf. e.g.* the results of Köhler et al., 2015; Ysard et al., 2018). We show some of the results of Köhler et al. (2015) in Fig. I.21. This figure exhibits an important result we will discuss later:

> ☞ the addition of mantles and the aggregation of grains tend to increase the absorptivity per unit mass in the FIR window.

6. See the public code DDSCAT by Draine & Flatau (1994).

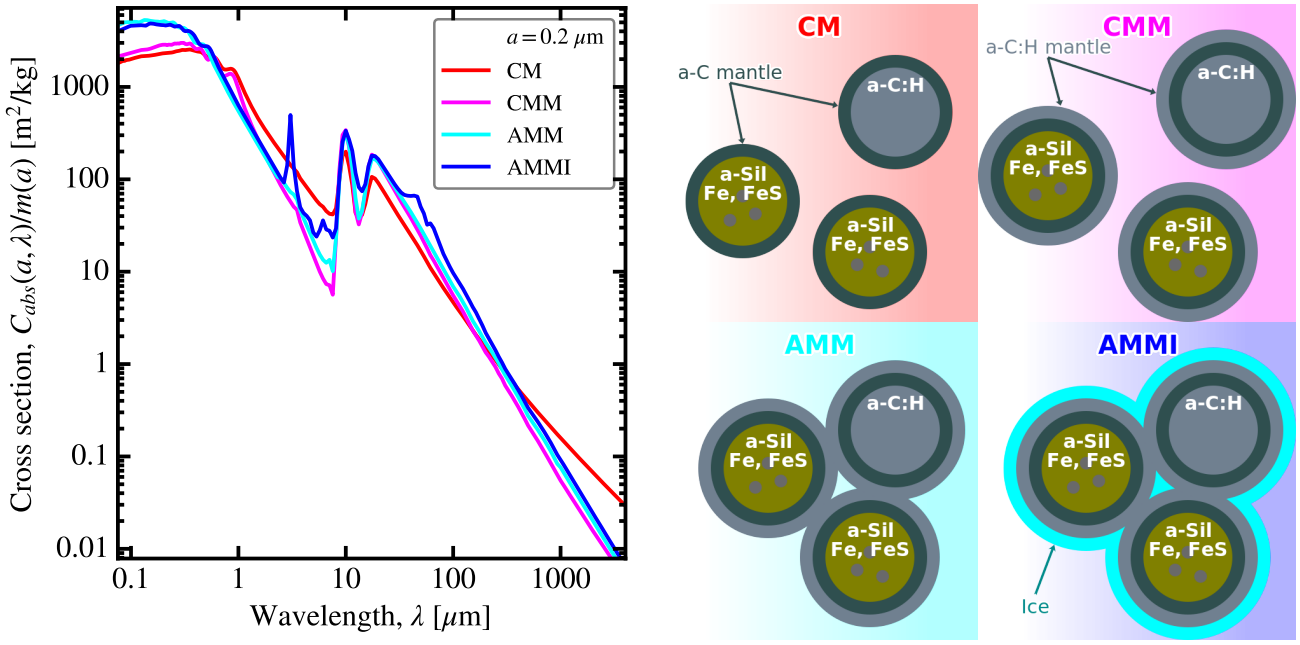

FIGURE I.21 – *Absorption cross-sections of grain aggregates computed with DDA.* The curves in the left panel are the absorption cross-sections of grains of radius $a = 0.2$ µm: $C_{abs}(a,\lambda)/m(a) = 3/(4\rho) \times Q_{abs}(a,\lambda)/a$, where ρ is the density. The four curves correspond to the four main mixtures of the THEMIS model (Jones et al., 2013, 2017), represented in the right panel: *(i)* the *Core-Mantle* (CM) mixture is made amorphous Forsterite and Enstatite with Fe and FeS (troilite) inclusions, and aliphatic amorphous carbon (a-C:H); both grains are coated with an aromatic mantle (a-C); *(ii)* the *Core-Mantle-Mantle* (CMM) is the CM mixture with additional coating by aliphatic material; *(iii)* the *Aggregate-Mantle-Mantle* (AMM) mixture is constituted of aggregated CMM grains; *(iv)* the *Aggregate-Mantle-Mantle-Ice* (AMMI) mixture is the AMM aggregates coated with water ice. The CM optical properties are from Jones et al. (2013). The CMM, AMM and AMMI optical properties have estimated by Köhler et al. (2015) using DDA. Notice the apparition of the 3 µm water ice band (Fig. II.12) in the AMMI model. Licensed under CC BY-SA 4.0.

I.2.2.5 Polarization

The real part of the electric field of a monochromatic, plane electromagnetic wave, propagating along the z-axis, can be written at time t and at $z = 0$:

$$\Re(\vec{E}) = \vec{E_1}\cos\omega t + \vec{E_2}\sin\omega t, \tag{I.52}$$

where $\vec{E_1} \perp \vec{E_2}$ (*cf. e.g.* Chap. 2 of Bohren & Huffman, 1983). This is the parametric equation of an ellipse in the (x, y) plane (*cf.* Fig. I.22.a). It is the most general case, called *elliptical polarization*. It is fully characterized by the modules of $\vec{E_1}$ and $\vec{E_2}$, the angle φ and the rotation direction $\eta = \pm 1$ (-1: clockwise; +1:counterclockwise). Particular cases are: *(i) linear polarization*, if $|\vec{E_1}| = 0$ or $|\vec{E_2}| = 0$; and *(ii) circular polarization*, if $|\vec{E_1}| = |\vec{E_2}|$.

The Stokes parameters. They constitute a four element vector easier to observationally measure than the ellipse parameters. They are noted $(I, Q, U, V) = \vec{S}$. I is the total intensity of the beam, that can be partially polarized. The three others can be expressed as:

$$\begin{cases} Q &= \left(|\vec{E_1}|^2 - |\vec{E_2}|^2\right)\cos(2\varphi) \\ U &= \left(|\vec{E_1}|^2 - |\vec{E_2}|^2\right)\sin(2\varphi) \\ V &= 2\eta|\vec{E_1}||\vec{E_2}|. \end{cases} \tag{I.53}$$

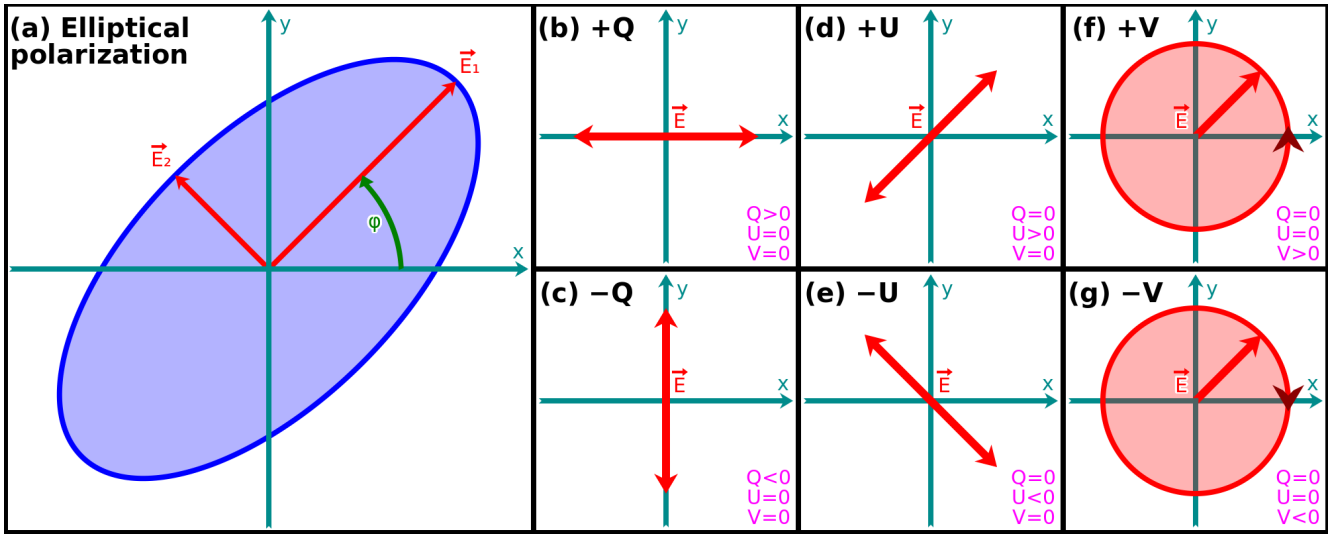

FIGURE I.22 – *Stokes parameters.* Panel *(a)* displays the notations we have used to parametrize the elliptical polarization. Panels *(b)* to *(g)* demonstrate the type of polarization each parameter represents (linear or circular, in different directions), when the rest is zero. Licensed under CC BY-SA 4.0.

The interpretation of these parameters is illustrated in Fig. I.22. They allow us to decompose the light into its linear and circular polarization components. The intensity of the polarized light is $I_p = \sqrt{Q^2+U^2+V^2} \leq I$. It is also frequent to quote the *linearly polarized intensity*:

$$P \equiv \sqrt{Q^2+U^2}, \tag{I.54}$$

and the *linear polarization fraction*, P/I.

Grain alignment. Asymmetric grains tend to be aligned with the magnetic field. If we consider the simple case of spheroidal grains (*cf.* Fig. I.20): *(i)* the rotation axis of oblate grains is along their symmetry axis; *(ii)* the rotation axis of prolate grains is perpendicular to their long axis, their cross-section thus needs to be integrated over their spinning dynamics (*e.g.* Guillet et al., 2018). The rotation axis of the grains tends to align with the magnetic field, $\vec{B}$. This is represented in panels *(b)* and *(c)* of Fig. I.23. Several mechanisms have been proposed to explain this alignment (*cf.* Andersson et al., 2015, for a review). Nowadays, *Radiative Alignment Torques* (RAT; Dolginov & Mitrofanov, 1976) are favored, because they provide the best account of the observational constraints. This complex scenario is based on the fact that irregular grains have different cross-sections for clockwise and counterclockwise circularly polarized light. Light scattering on such grains therefore provides a torque that increases the angular momentum of the grains. If these grains have paramagnetic inclusions (such as iron), the grain rotation precesses and aligns with $\vec{B}$. Although the alignment is caused by the radiation field, it is independent of its direction. This mechanism becomes inefficient at high optical depth, which is consistent with observations.

Polarization by scattering. It is represented on Fig. I.23.a. When an incident beam is scattered by a grain (this grain does not have to be asymmetric), the electric field component in the scattering plane is diminished, inducing a polarization perpendicular to the plane. The larger the scattering angle is, the larger the polarization. The polarization of an incident Stokes vector, $\vec{S_i}$, resulting in a scattered beam, $\vec{S_s}$, is described as: $\vec{S_s} = \overleftrightarrow{M}\vec{S_i}$, where $\overleftrightarrow{M}$ is the 4×4 *Müller matrix* (*cf.* Chap. 3 of Bohren & Huffman, 1983, for different examples of Müller matrices). This polarization process is not related to grain alignment with the magnetic field, but it depends on the distribution of stars and dust clouds (*e.g.* Wood, 1997).

Dichroic extinction. It is the selective extinction of the electric field oscillating along the major axis of an elongated grains. It is represented in Fig. I.23.b. Since grains in the diffuse ISM tend to align their rotation axis with the magnetic field, they polarize starlight parallel to $\vec{B}$. For this reason, the polarization of starlight has historically been used to map the magnetic field of the MW (Mathewson & Ford, 1970).

Polarized emission. The polarization of the emission by elongated grains has been predicted by Stein (1966). Such grains emit IR light preferentially polarized along the direction of their major axis. Since their major axis is perpendicular to the magnetic field, their IR emission is perpendicular to $\vec{B}$. It is represented in Fig. I.23.c. The FIR polarized emission has been extensively used to map the magnetic field in the MW, with the *Planck* satellite (*e.g.* Planck Collaboration et al., 2016d).

☞ Grain polarization is parallel to the magnetic field in the visible and perpendicular in the IR: $\vec{P_{vis}} \parallel \vec{B}$ and $\vec{P_{IR}} \perp \vec{B}$.

I.2.3 Heat Capacities

In Sect. I.2.1, presenting the harmonic oscillations of valence electrons, we argued that the energy dissipation was due to collisions with the lattice. The energy absorbed by the grain is thus redistributed throughout the lattice and stored in the harmonic oscillations of its atoms.

I.2.3.1 Distribution of Harmonic Oscillators

The energy levels of a one-dimensional quantum harmonic oscillator, of natural frequency ν, are (*e.g.* Chap. 2 of Atkins & Friedman, 2005):

$$\mathrm{E}_n = h\nu\left(n+\frac{1}{2}\right) \quad \text{with} \quad n=0,1,\ldots, \tag{I.55}$$

where h is the *Planck constant* (*cf.* Table B.2). At thermal equilibrium, the probability distribution of a large ensemble of such harmonic oscillators, at temperature T, is the *Boltzmann distribution*:

$$p_n(\mathrm{T}) = \frac{\exp\left(\frac{-\mathrm{E}_n}{k\mathrm{T}}\right)}{\mathrm{Z}(\mathrm{T})}, \tag{I.56}$$

where we have introduced the *partition function*:

$$\mathrm{Z}(\mathrm{T}) = \sum_{n=0}^{\infty} \exp\left(-\frac{\mathrm{E}_n}{k\mathrm{T}}\right) = \frac{\exp\left(-\frac{h\nu}{k\mathrm{T}}\right)}{1-\exp\left(-\frac{h\nu}{k\mathrm{T}}\right)}. \tag{I.57}$$

The second equality comes from injecting Eq. (I.55) into the first equality. The mean energy of this ensemble of oscillators is the first moment of the distribution in Eq. (I.56):

$$\langle \mathrm{E} \rangle = \frac{h\nu}{2} + \frac{h\nu}{\exp\left(\frac{h\nu}{k\mathrm{T}}\right)-1}. \tag{I.58}$$

Since each one of the N atoms of the lattice has three degrees of freedom (along the three Cartesian axes x, y, z), the number of oscillators is 3N[7]. The *internal energy* of the grain, which is the energy

7. This is for $\mathrm{N} \gg 1$. The actual number of degrees of freedom is 3N-6, subtracting the three translatory and three rotational possible motions of the grain as a whole.

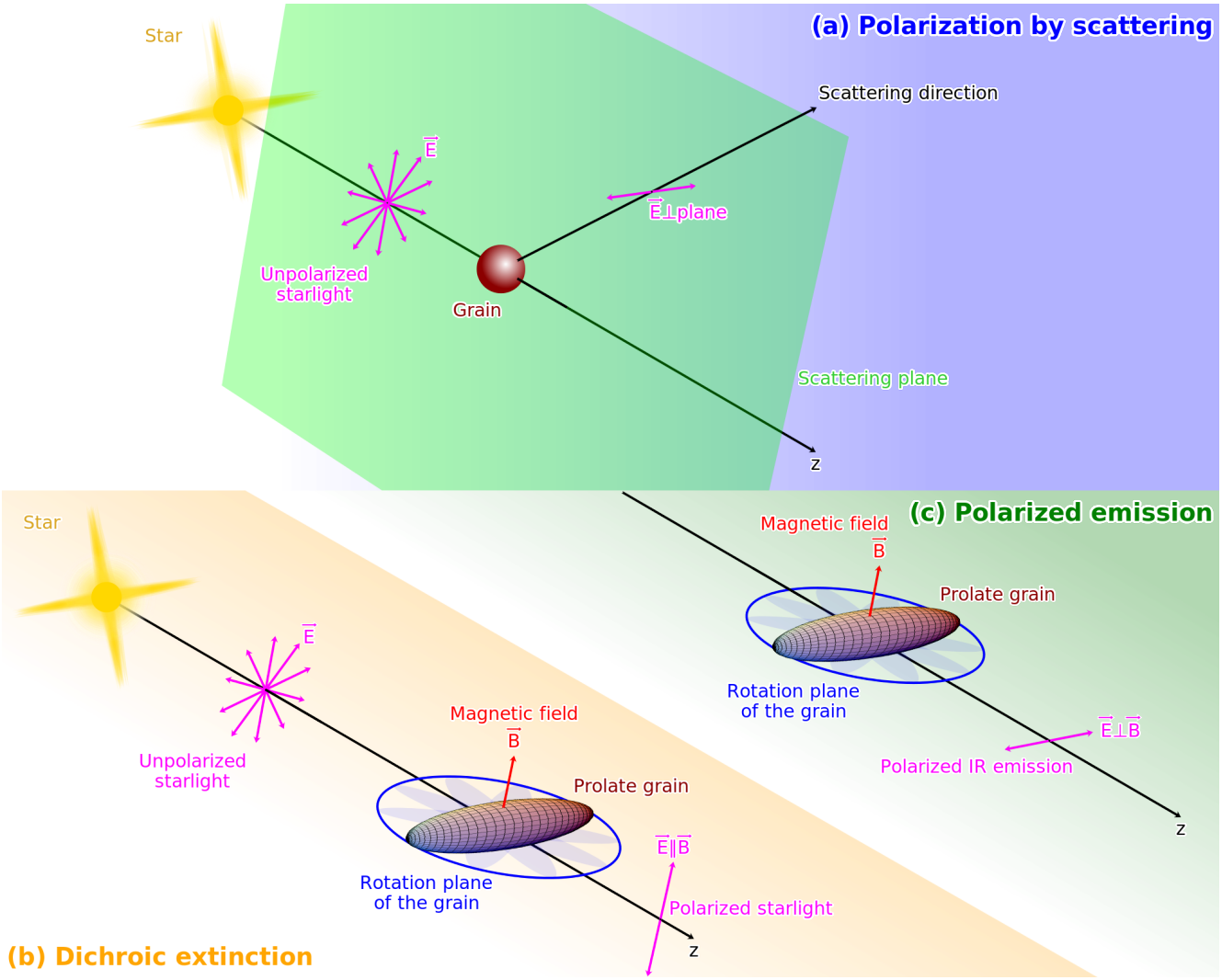

FIGURE I.23 – *The three types of grain-induced polarization of light.* Panel *(a)* represents the unpolarized starlight radiation being scattered by a grain. The electric field of the scattered light oscillates predominantly perpendicularly to the scattering plane. The larger the scattering angle is, the higher the linear polarization fraction is. Panels *(b)* and *(c)* represent a single prolate grain whose rotation axis is aligned with the magnetic field, $\vec{B}$. The case of oblate grains is more trivial as their rotation axis is their symmetry axis. Panel *(b)* illustrates dichroic extinction of starlight in the visible/near-IR. The grain extinct preferentially the component of the electric field oscillating in its rotation plane. The extincted starlight is thus polarized parallel to $\vec{B}$. Panel *(c)* shows the IR emission of the same prolate grain is polarized along its major axis, perpendicular to $\vec{B}$. In both panels *(b)* and *(c)*, we have represented the optimal case, when the magnetic field is perpendicular to the sightline. In the more general case, the polarization will be relative to the projection of $\vec{B}$ on the plane of the sky. Licensed under CC BY-SA 4.0.

stored in all its oscillators, is thus:

$$U(T) = 3N\langle E\rangle = 3Nh\nu\left(\frac{1}{2} + \frac{1}{\exp\left(\frac{h\nu}{kT}\right) - 1}\right). \tag{I.59}$$

I.2.3.2 Debye's Model

Eq. (I.59) considers that each atom oscillates independently of its neighbors. In reality, there are collective vibrational modes in a crystal lattice. These modes actually are sound waves, propagating at the sound speed of the material, c_s. Because the size of a grain is finite, the number of these possible modes is quantified. Indeed, if L is the size of the grain along one dimension, the wavelength of the modes along this dimension is $\lambda_n = 2\mathrm{L}/n$, with $n = 1, 2, \ldots$ (*cf.* Fig. I.24). The shortest possible wavelength corresponds to oscillations of adjacent atoms in opposition of phase: $\lambda_\mathrm{D} = 2d_\mathrm{at}$, where d_at is the interatomic distance. These quantified modes can be treated as quasi-particles, called *phonons*. These phonons have energies hc_s/λ_n, thus:

$$\mathrm{E}_n = \frac{nhc_s}{2\mathrm{L}} \quad \text{for} \quad n = 1, \ldots, n_\mathrm{D}. \tag{I.60}$$

We now need to integrate Eq. (I.58) over the different modes:

$$\mathrm{U(T)} = \mathrm{U}_0 + \int_0^{\nu_\mathrm{D}} \frac{h\nu}{\exp\left(\dfrac{h\nu}{k\mathrm{T}}\right) - 1} g(\nu)\,\mathrm{d}\nu, \tag{I.61}$$

where $g(\nu)$ is the density of modes with frequency ν, and U_0 is a constant coming from the $1/2$ term in Eq. (I.58). It can be shown that (*cf.* Chap. III.E of Diu et al., 1997):

$$g(\nu) = \frac{9\mathrm{N}\nu^2}{\nu_\mathrm{D}^3}, \tag{I.62}$$

where the Debye frequency can be explicited as a function of the density of atoms, n_at:

$$\nu_\mathrm{D} = c_s \sqrt[3]{\frac{9n_\mathrm{at}}{4\pi}}. \tag{I.63}$$

From ν_D, we can also define the *Debye temperature*, $\mathrm{T}_\mathrm{D} \equiv h\nu_\mathrm{D}/k$. Eq. (I.61) thus becomes:

$$\mathrm{U(T)} = \mathrm{U}_0 + \frac{9\mathrm{N}}{\nu_\mathrm{D}^3} \int_0^{\nu_\mathrm{D}} \frac{h\nu^3}{\exp\left(\dfrac{h\nu}{k\mathrm{T}}\right) - 1} \mathrm{d}\nu, \tag{I.64}$$

and the *Debye heat capacity* can be derived:

$$\mathrm{C(T)} = \frac{\partial \mathrm{U}}{\partial \mathrm{T}} = 9k\mathrm{N}\left(\frac{\mathrm{T}}{\mathrm{T}_\mathrm{D}}\right)^3 \int_0^{\mathrm{T}_\mathrm{D}/\mathrm{T}} \frac{x^4 e^x}{(e^x - 1)^2}\,\mathrm{d}x. \tag{I.65}$$

It is represented in Fig. I.25.a.

The Dulong-Petit regime is the limiting behavior of Eq. (I.65) at high temperature, namely:

$$\mathrm{C(T)} \simeq 3\mathrm{N}k \quad \text{for} \quad \mathrm{T} \gg \mathrm{T}_\mathrm{D}. \tag{I.66}$$

It is the classical expression of heat capacity. It is constant becomes it assumes that energy can be indifferently stored in oscillators, ignoring their limited number.

The Debye regime is the low-temperature limit of Eq. (I.65), namely:

$$\mathrm{C(T)} \simeq \frac{12\pi^4}{5}\mathrm{N}k\left(\frac{\mathrm{T}}{\mathrm{T}_\mathrm{D}}\right)^3 \quad \text{for} \quad \mathrm{T} \ll \mathrm{T}_\mathrm{D}. \tag{I.67}$$

It accounts for the quantification of the modes. It provides a correct agreement with laboratory measurements.

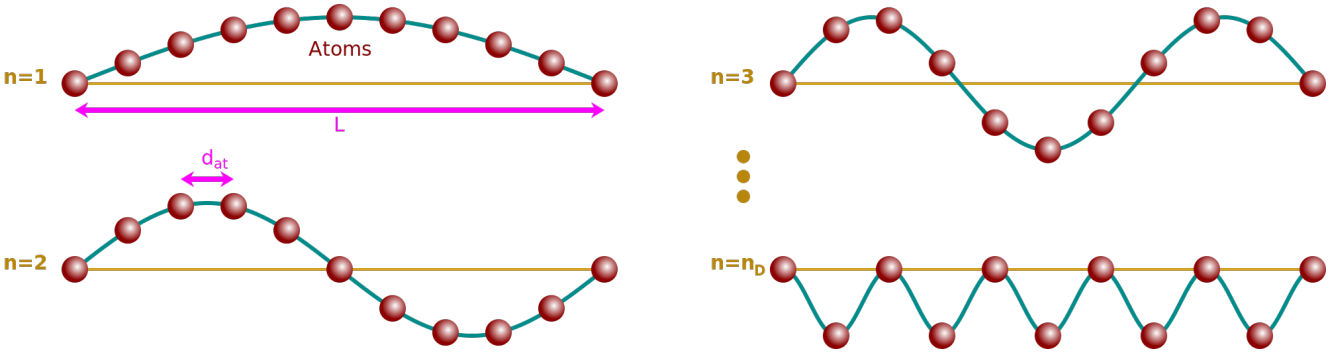

FIGURE I.24 – *Phonon modes.* We represent the simplest case of a string of atoms (red spheres). The total length of the solid is materialized by the yellow horizontal line. The two atoms at each end of this line are fixed. The modes are thus quantified. The shortest possible wavelength is $2d_{\rm at}$, corresponding to the $n = n_{\rm D}$ mode. Licensed under CC BY-SA 4.0.

I.2.3.3 Heat Capacities of Realistic Materials

The Debye model is an idealization providing a good approximation. It has however several limitations.

Conduction electrons contribute to the heat capacity of metals, and dominate at low temperatures. Their contribution to the heat capacity is (*cf. e.g.* Chap. 2 of Ashcroft & Mermin, 1976):

$$\mathrm{C_{cond}(T)} = \frac{\pi^2 \mathrm{N}k}{2}\frac{\mathrm{T}}{\mathrm{T_F}}, \tag{I.68}$$

where $\mathrm{T_F} = \mathrm{E_F}/k$ is the Fermi temperature (Eq. I.2).

Laboratory data can be used to determine the Debye and Fermi temperatures of the compound. If the structure of the grain is too complex, the heat capacity can be fitted on experimental measurements (*e.g.* Draine & Li, 2001). We show the heat capacity of various interstellar grain candidates in Fig. I.25.b.

I.2.4 Heating and Cooling

I.2.4.1 Kirchhoff's Law

Let's consider a grain at thermal equilibrium with a radiation source, such as the light from a star. The *specific intensity* received by the grain, $\mathrm{I_\nu}(\lambda, \Omega)$, is the electromagnetic power per unit frequency, area (A) and solid angle (Ω) [8]: $\mathrm{dE_\star} = \mathrm{I_\nu}\,\mathrm{d}t\,\mathrm{d}\nu\,\mathrm{dA}\,\mathrm{d}\Omega$ (we discuss this quantity in more details in Sect. III.1.1). The *absorption coefficient* of this grain, $\alpha(\lambda)$, is the fraction of this specific intensity it absorbs per unit length, l: $\mathrm{dI_\nu} = -\alpha \mathrm{I_\nu}\,\mathrm{d}l$. The *emission coefficient* of this grain, $j_\nu(\lambda)$, is the power it emits per unit frequency, volume (V) and solid angle (it is isotropic): $\mathrm{dE_{em}} = j_\nu\,\mathrm{d}t\,\mathrm{d}\nu\,\mathrm{dV}\,\mathrm{d}\Omega$. Kirchhoff (1860)'s law states that the ratio $j_\nu(\lambda)/\alpha(\lambda) = f_\nu(\mathrm{T}, \lambda)$ is a universal function depending only on T and λ (*e.g.* Robitaille, 2009, for a review). Planck (1900) later gave an analytical expression of this empirical function, assuming the energy levels were discrete, providing a quantum formulation of the *black body* radiation. It became the *Planck function*, $f_\nu(\mathrm{T}, \lambda) = \mathrm{B_\nu(T}, \lambda)$, where:

$$\mathrm{B_\nu(T}, \lambda) = \frac{2hc}{\lambda^3}\frac{1}{\exp\left(\dfrac{hc}{\lambda k \mathrm{T}}\right) - 1}. \tag{I.69}$$

8. Throughout this manuscript, we use the subscript ν to exclusively denote *spectral densities*, that is quantities per unit frequency, f_ν. Such a quantity can also be expressed per unit wavelength: $f_\lambda = f_\nu\,\mathrm{d}\nu/\mathrm{d}\lambda = f_\nu c/\lambda^2$. Quantities depending on the frequency, but not per unit frequency, should not be written with subscript ν: ~~κ_ν~~ $\longrightarrow \kappa(\nu)$.

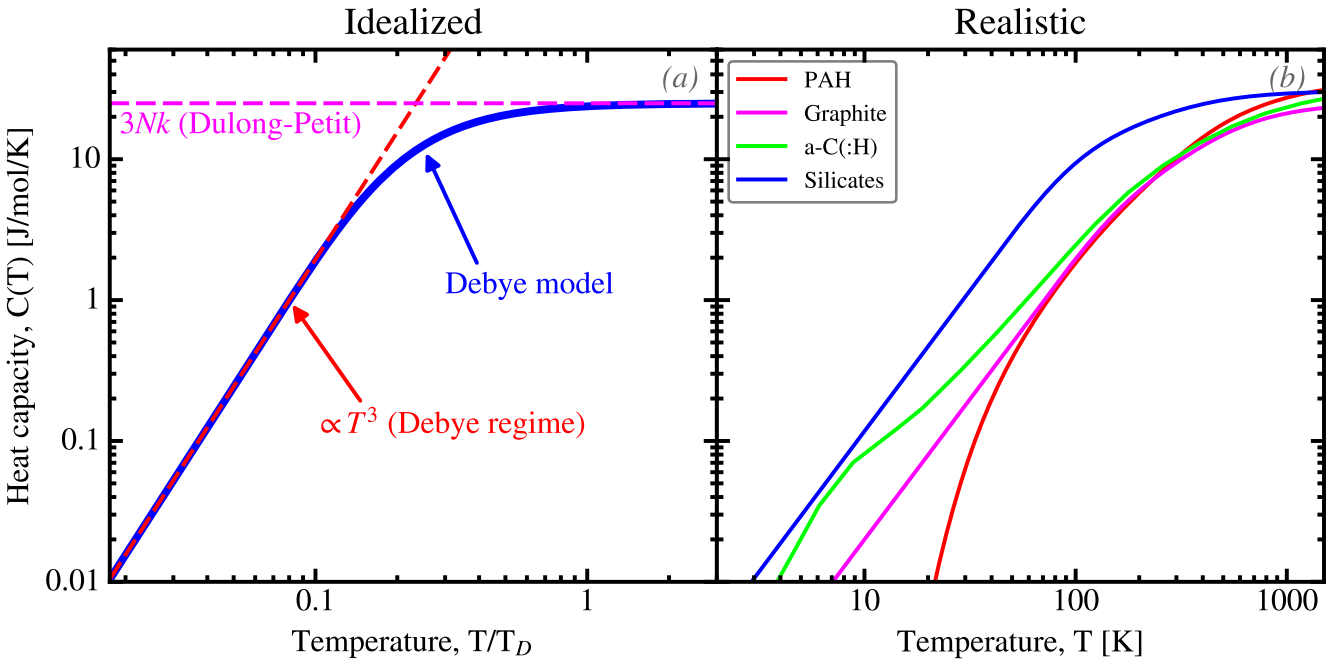

FIGURE I.25 – *Heat capacities.*. Panel *(a)* shows the Debye model (Eq. (I.65); blue), with the two limiting regimes: *(i)* the classical Dulong-Petit regime (magenta dashed line); and *(ii)* the quantum Debye regime (red dashed line). Panel *(b)* shows the heat capacities of realistic materials: PAH, graphite and silicate from Draine & Li (2001) and a-C(:H) from Jones et al. (2013). Licensed under CC BY-SA 4.0.

Opacity. The *mass absorption coefficient* of a grain, $\kappa_{abs}(\lambda)$, is its absorption cross-section per unit mass: $\kappa_{abs}(\lambda) = \alpha(\lambda)/\rho$. For a single spherical grain, it is, using Eq. (I.39):

$$\kappa_{abs}(a,\lambda) = \frac{\overbrace{C_{abs}(a,\lambda)}^{\text{cross-section}}}{\underbrace{\frac{4\pi}{3}a^3\rho}_{\text{mass}}} = \frac{3}{4\rho}\frac{Q_{abs}(a,\lambda)}{a}. \tag{I.70}$$

This quantity is often referred to as the *opacity*. In this manuscript, we however extend this term to its scattering component, too. We will therefore call $\kappa \equiv \kappa_{ext} = \kappa_{sca} + \kappa_{abs}$, the *opacity*, κ_{abs} and κ_{sca} being called the *absorption* and *scattering opacities*, respectively. We have seen in Sect. I.2.2 that Q_{abs}/a is practically independent of radius for most interstellar grains in the NIR regime and longward, thus:

> ☞ the NIR-to-mm opacity of interstellar grains having the same homogeneous composition is independent of their radius.

Emissivity. The *emissivity* of a grain, $\epsilon_\nu(\lambda)$, is the power it emits per unit frequency and mass ($dm = \rho dV$): $dE_{em} = \epsilon_\nu(\lambda)\rho\, dt\, d\nu\, dV\, d\Omega/4\pi$. The last differential element simply denotes an average over solid angles. We thus see that $\epsilon_\nu = 4\pi j_\nu/\rho$. Kirchhoff's law then becomes:

$$\epsilon_\nu(\lambda) = 4\pi\kappa_{abs}(\lambda) \times B_\nu(T,\lambda). \tag{I.71}$$

Eq. (I.71) is the emission spectrum of grains at thermal equilibrium with the radiation field. We show a few examples in Fig. I.26. The limiting behavior of Eq. (I.71) when $\lambda \gg hc/kT$ is given by the *Rayleigh-Jeans law*:

$$\epsilon_\nu(\lambda) \simeq 8\pi kT\frac{\kappa_{abs}(\lambda)}{\lambda^2}. \tag{I.72}$$

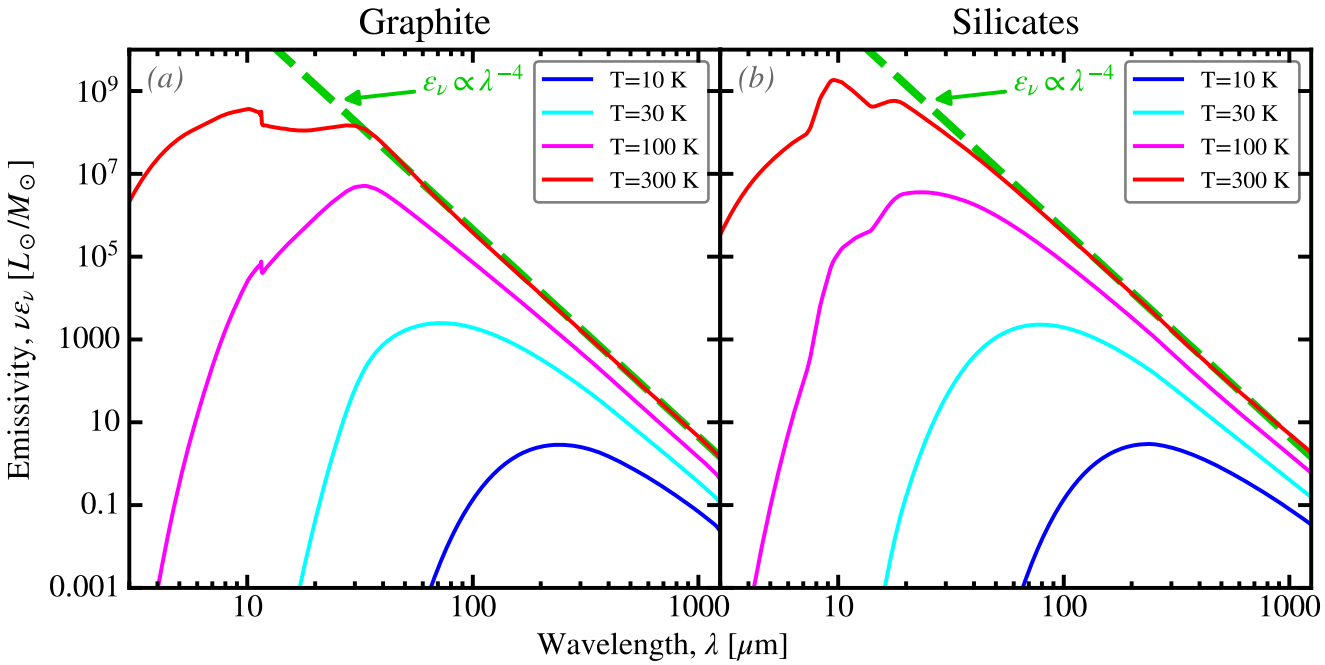

FIGURE I.26 – *Emissivity of grains at thermal equilibrium with the radiation field.* We show the emission spectrum of spherical graphite *(a)* and silicates *(b)* from Draine (2003b,c), at different equilibrium temperatures (Eq. I.71). We have overlaid in green the Rayleigh-Jeans approximation ($\beta = 2$ for both compounds). Licensed under CC BY-SA 4.0.

Modified Black Body (MBB). A MBB is an idealized body, at thermal equilibrium with the radiation field, that does not perfectly absorb all frequencies. In other words, it has a non zero albedo. It is an imperfect black body, sometimes also called *grey body*. Eq. (I.71) is a MBB. In the ISM literature, MBB usually refers to the case where we approximate the opacity as a power-law:

$$\kappa_{abs}(\lambda) \simeq \kappa_0 \left(\frac{\lambda_0}{\lambda}\right)^\beta, \tag{I.73}$$

where λ_0 is a reference wavelength, and κ_0, the opacity at λ_0. This approximation was popularized by Hildebrand (1983). We have seen in Sect. I.2.1 that $\beta \simeq 2$ for typical grains, and that we must have $\beta > 1$ in order to satisfy the Kramers-Kronig relations (*cf.* Sect. I.2.1.6). Eq. (I.72) implies that $\epsilon_\nu(\lambda) \propto \lambda^{2+\beta}$, in the Rayleigh-Jeans regime. We have shown this relation in Fig. I.26.

The net flux radiated by a black body is:

$$F_{BB}(T) = \int_0^\infty \pi B_\nu(T,\nu)\,d\nu = \sigma T^4, \tag{I.74}$$

where σ is the *Stefan-Boltzmann constant* (*cf.* Table B.2). In the case of a MBB, the emitted power per unit mass is:

$$\frac{P_{MBB}(\beta,T)}{M_{MBB}} = \int_0^\infty 4\pi\kappa_0 \left(\frac{\lambda_0}{\lambda}\right)^\beta B_\lambda(T,\lambda)\,d\lambda = \frac{8\pi\kappa_0\lambda_0^\beta (kT)^{4+\beta}}{c^{2+\beta}h^{3+\beta}}\Gamma(4+\beta)\zeta(4+\beta), \tag{I.75}$$

where Γ is the *gamma function*, and ζ is the *Riemann zeta function*.

Wien's law states that the emission peak of $B_\nu(T,\lambda)$ is located at $\lambda_{max}(T) = 5.0996 \times 10^3/T$ µm. For a MBB, the wavelength peak of $\nu\epsilon_\nu(\beta,T,\lambda)$ [9] is located at:

$$\lambda_{max}(\beta,T) = \frac{hc}{kT}\frac{1}{(4+\beta)+W\left(-(4+\beta)\exp\left[-(4+\beta)\right]\right)}, \tag{I.76}$$

where W is the *Lambert W function*.

9. In general, we prefer displaying νf_ν quantities than simply f_ν or f_λ, as it represents better the energy balance.

I.2.4.2 Equilibrium Heating

Eq. (I.71) expresses the general emissivity of a grain at thermal equilibrium with the radiation field. To use this formula, we need to determine the equilibrium or *steady-state* temperature of the grain. This is simply performed by equating the absorbed and emitted powers. It is convenient to define the *mean intensity* of the ISRF:

$$J_\nu(\lambda) = \frac{1}{4\pi} \iint_{\text{sphere}} I_\nu(\lambda, \Omega)\, d\Omega, \tag{I.77}$$

which is simply the specific intensity from the stars, averaged over solid angle. The power absorbed by the grain is:

$$P_{\text{abs}}(a) = \iint_{\text{sphere}} \int_0^\infty J_\nu(\nu) \times \pi a^2 Q_{\text{abs}}(a,\nu)\, d\nu\, d\Omega = \int_0^\infty 4\pi J_\nu(\nu) \times \pi a^2 Q_{\text{abs}}(a,\nu)\, d\nu. \tag{I.78}$$

Similarly, the emitted power is:

$$P_{\text{em}}(a,T) = \iint_{\text{sphere}} \int_0^\infty B_\nu(T,\nu) \times \pi a^2 Q_{\text{abs}}(a,\nu)\, d\nu\, d\Omega = \int_0^\infty 4\pi B_\nu(T,\nu) \times \pi a^2 Q_{\text{abs}}(a,\nu)\, d\nu. \tag{I.79}$$

The *equilibrium temperature*, T_{eq}, is then simply the numerical solution to $P_{\text{abs}}(a) = P_{\text{em}}(a, T_{\text{eq}})$. Several quantities can be precomputed to simplify this task.

Planck average. The *Planck average* of a grain is defined as:

$$\langle Q \rangle_P(a,T) \equiv \frac{\pi}{\sigma T^4} \int_0^\infty Q_{\text{abs}}(a,\nu) B_\nu(T,\nu)\, d\nu. \tag{I.80}$$

This quantity needs to be computed only once for a range of temperatures. Eq. (I.79) then simplifies: $P_{\text{em}}(a,T) = 4\pi a^2 \sigma T^4 \langle Q \rangle_P(a,T)$. Since interstellar grains emit predominantly in the IR, where the approximation of Eq. (I.73) is valid, we can derive an analytical expression of Eq. (I.80), knowing that $\sigma \equiv 2\pi^5 k^4 / 15 h^3 c^2$:

$$\langle Q \rangle_P(a,T) = \frac{15}{\pi^4} Q_{\text{abs}}(a,\lambda_0) \Gamma(4+\beta) \zeta(4+\beta) \left(\frac{\lambda_0 kT}{hc} \right)^\beta. \tag{I.81}$$

We show the Planck average of typical grains in Fig. I.27. We can see that $\langle Q \rangle_P$ is almost independent of radius for grains smaller than 0.1 μm.

ISRF-averaged efficiency. The ISRF-averaged efficiency is the equivalent of the Planck average for the absorbed power:

$$\langle Q \rangle_\star(a) \equiv \frac{\pi}{J_\star} \int_0^\infty Q_{\text{abs}}(a,\nu) J_\nu(\nu)\, d\nu, \tag{I.82}$$

where $J_\star = \pi \int_0^\infty J_\nu(\nu)\, d\nu$. This quantity is less general than Eq. (I.81) as it needs to be evaluated for each particular shape of the ISRF. Eq. (I.78) then simplifies: $P_{\text{abs}}(a) = 4\pi a^2 J_\star \langle Q \rangle_\star(a)$. The equilibrium temperature is thus the solution to: $\sigma T^4 \langle Q \rangle_P(a,T) = J_\star \langle Q \rangle_\star(a)$.

The diffuse ISRF. The diffuse ISRF of the MW has been modeled by Mathis et al. (1983). It is represented in Fig. I.28. This ISRF is commonly used to describe grain heating (*i.e.* how much power a grain absorbs) in the MW, and also in nearby galaxies. Most of the heating is provided by the stellar component, as the integrand in Eq. (I.78) is $J_\nu Q_{\text{abs}} \propto J_\nu / \lambda^2$. The long wavelengths have a negligible weight. This stellar ISRF can be scaled by a dimensionless factor U, to account for variations of the stellar density. This scaling factor is not totally realistic, as regions with high radiation densities ($U \gtrsim 10^3$) usually are star-forming regions, containing young star associations. The UV bump of the stellar ISRF, corresponding to these young stars in Fig. I.28, would be dominating the emission, while the NIR bump, corresponding to older stellar populations, would be, at first order constant. This is however not very important for grains at thermal equilibrium, as their spectrum depends only on the total absorbed power, given by $\langle Q \rangle_\star$.

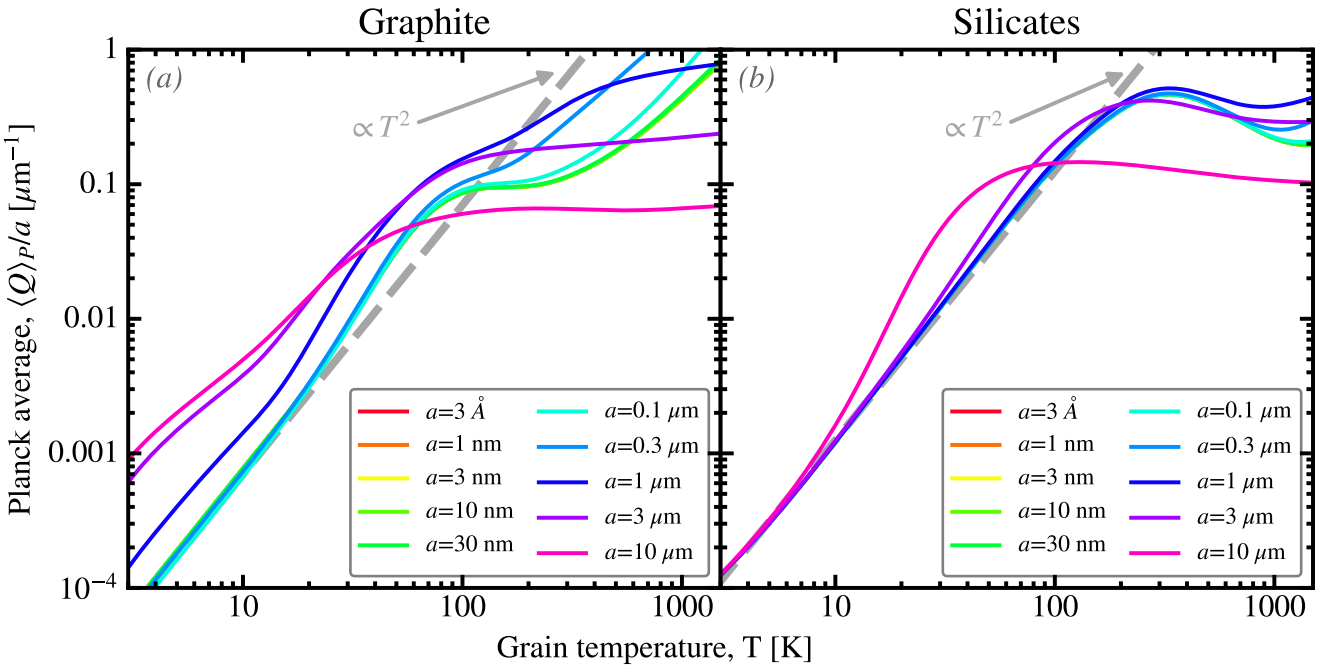

FIGURE I.27 – *Planck averages of graphite and silicates.* We show the result of Eq. (I.80) applied to the graphite *(a)* and silicates *(b)* of Draine (2003b,c), for several radii, a. We overplot the approximation of Eq. (I.81) in grey. Licensed under CC BY-SA 4.0.

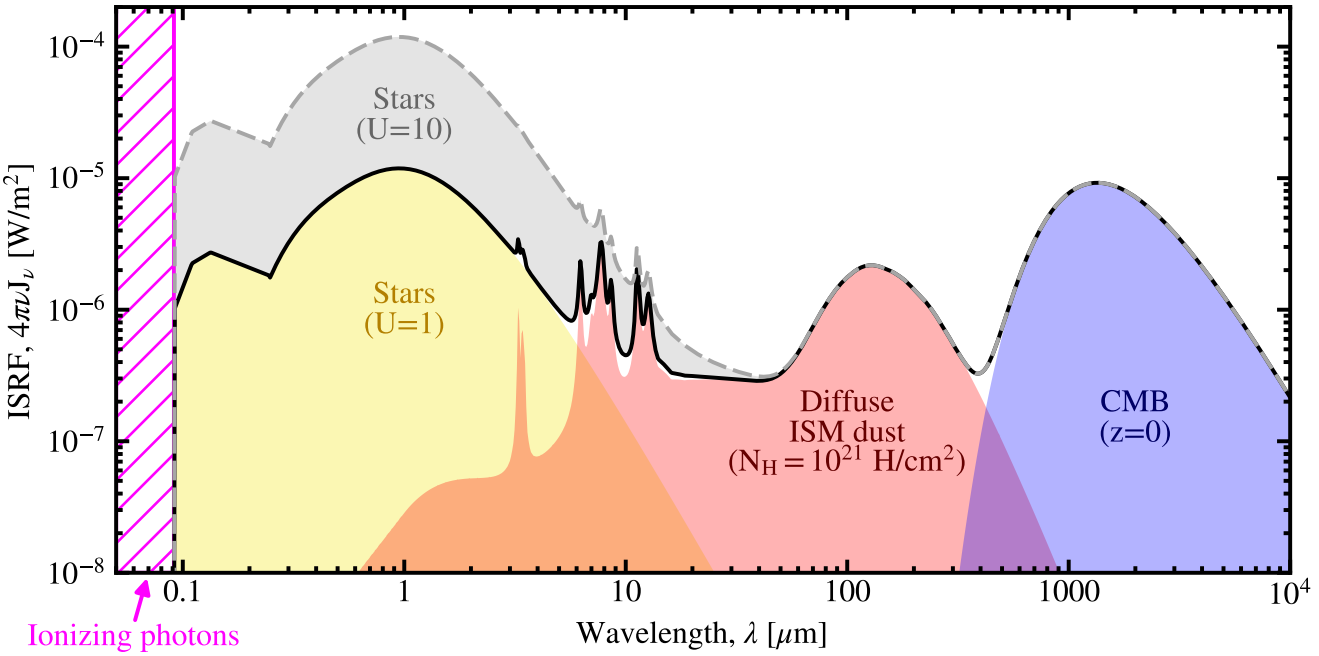

FIGURE I.28 – *Diffuse Galactic ISRF.* This black line represents the average ISRF experienced in the diffuse ISM of the MW. The stellar component (yellow) has been modeled by Mathis et al. (1983). The UV and NIR bumps are the contributions by young and old stars, respectively. This ISRF represents the neutral ISM, there is therefore no emission shortward the Lyman break (λ_{Lyc} = 0.0912 μm). This stellar ISRF can be scaled by the factor U. We have represented the U = 10 case in grey. The diffuse dust emission is shown in red. The original Mathis et al. (1983) work did not have the constraints we have today on this component. The emission represented here is the Jones et al. (2017) model, for a typical hydrogen column density $N_H = 10^{21}$ cm^{-2}. The blue component is the *Cosmic Microwave Background* (CMB), which is a perfect black body at $T_{CMB}(z = 0) = 2.73$ K (Mather et al., 1994). At higher redshift, z, the temperature of this component is $T_{CMB}(z) = (1+z) \times 2.73$ K. The *Cosmic Infrared Background* (CIB; *e.g.* Dole et al., 2006) is not represented here as its *Spectral Energy Distribution* (SED) is similar to the dust emission, and is slightly lower. Licensed under CC BY-SA 4.0.

Equilibrium temperatures. The equilibrium temperature of typical grains is shown in Fig. I.29, as a function of U. Assuming the heating is solely provided by the stellar component in Fig. I.28, $J_\star(U) = U \times J_\star(1)$ and $\langle Q\rangle_\star(U,a) = \langle Q\rangle_\star(1,a)$. In this case, the integrated mean intensity is:

$$\int_0^\infty 4\pi J_\nu(U=1,\nu)\,d\nu = 4 \times J_\star(1) = 2.2\times10^{-5}\,\mathrm{W/m^2}. \tag{I.83}$$

The equilibrium temperature is thus:

$$T_{eq}(U,a) = \underbrace{\left(\frac{\pi^4 J_\star(1)\langle Q\rangle_\star(a)}{\sigma Q_{abs}(a,\lambda_0)\Gamma(4+\beta)\zeta(4+\beta)}\right)^{1/(4+\beta)}}_{\text{weakly dependent on } a} \left(\frac{hc}{k\lambda_0}\right)^{\beta/(4+\beta)} U^{1/(4+\beta)}. \tag{I.84}$$

For grains smaller than $a \simeq 0.1$ µm, we thus have $T_{eq}(U) \propto U^{1/(4+\beta)}$. We show the equilibrium temperature of graphite and silicates, varying U in Fig. I.29. We see that:

- for graphite, $T_{eq}^{gra}(U) \simeq U^{1/6} \times 20$ K;
- for silicates, $T_{eq}^{sil}(U) \simeq U^{1/6} \times 17.5$ K.

☞ Interstellar grains of a given homogeneous composition, at thermal equilibrium with the radiation field, mostly have the same temperature.

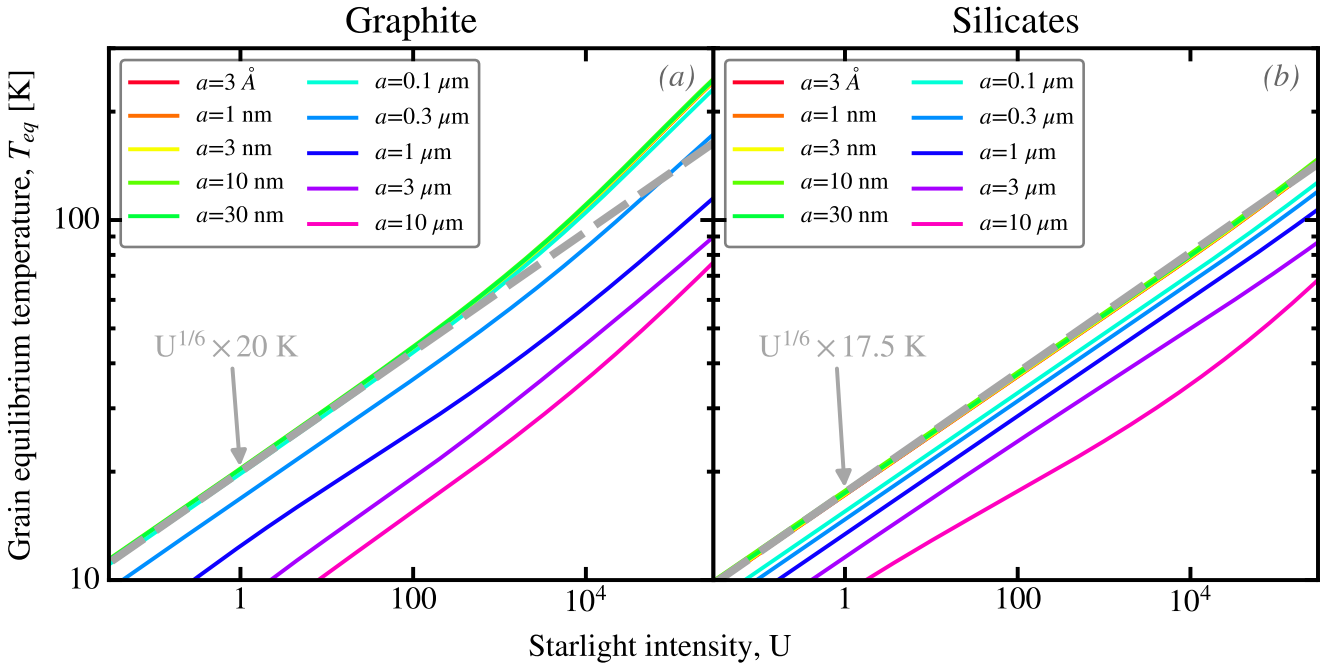

FIGURE I.29 – *Grain equilibrium temperatures.* We show the equilibrium temperatures derived by equating Eq. (I.78) and Eq. (I.79) for the graphite of Laor & Draine (1993) and the silicates of Draine (2003b,c). For grains smaller than ≃ 20 nm, this temperature does not have reality, as these grains are out of equilibrium with the ISRF. The grains are heated by the stellar ISRF of Mathis et al. (1983), scaled by the factor U. We see that grains smaller than ≃ 0.1 µm roughly have the same temperature. This is because these grains are essentially in the Rayleigh regime over most of the visible-to-NIR range. In this regime, the dashed grey line is a good approximation. Licensed under CC BY-SA 4.0.

I.2.4.3 Stochastic Heating

Absorption and cooling times. Not all grains are at thermal equilibrium with the ISRF. To determine if this is the case, we need to estimate the *photon absorption rate* of the grain:

$$\frac{1}{\tau_{abs}(U,a)} = \int_0^\infty \pi a^2 Q_{abs}(a,\nu)\frac{4\pi J_\nu(\nu)}{h\nu}\,d\nu \propto a^3 U, \tag{I.85}$$

where the proportionality has been derived using Eq. (I.46). The grain absorption timescale, τ_{abs}, gives the average time between two photon absorptions. We also need to estimate the *cooling rate* of the grain:

$$\frac{1}{\tau_{cool}(a,T)} = \frac{P_{em}(a,T)}{H(T)} \propto T^{3-n+\beta}, \tag{I.86}$$

where H(T) is the *enthalpy* of the grain at temperature T:

$$H(T) = \int_0^T C(T')\,dT'. \tag{I.87}$$

It is the vibrational energy content of the grain. The proportionality of Eq. (I.86) has been derived from Eq. (I.81) for P_{em}, and from the low-temperature behaviour of $H(a,T) \propto a^3 T^{n+1}$ (Eq. I.67; $n = 3$ corresponding to the three-dimensional Debye model). The cooling time, τ_{cool}, is independent of the grain size.

The temperature fluctuations. If $\tau_{abs} \gtrsim \tau_{cool}$, the grain has the time to significantly cool down between two photon absorptions. Its temperature is thus changing with time. This is represented on the simulation in Fig. I.30.a, as follows.

1. A grain, with $a = 2$ nm, starts at $T = T_{CMB}$.
2. It then receives a photon after $\simeq 6$ h, which causes its temperature to spike to $T_s \simeq 100$ K. The value of T_s is such that $H(T_s) - H(T_{CMB}) = h\nu_s$, where $h\nu_s$ is the energy of the incident photon. It is the only photon it receives within the 50 h displayed here. Its absorption time is indeed $\tau_{abs} \simeq 140$ h.
3. The grain then cools down by radiating. The heat capacity we have used here (Draine & Li, 2001) has $n \simeq 2$. The cooling time is thus $\tau_{cool} \propto T^{-3}$. The cooling time is short when the grain is hot, but decreases with the temperature. Such a grain spends most of its time at low temperatures.

In practice, we do not see the emission of the grain varying with time, as observations encompass a statistical number of grains, with different time histories. What we observe is an *ergodic*[10] average: small grains appear to have a temperature distribution, represented in Fig. I.30.b for $a = 2$ nm. When the radius of the grain increases, the absorption time decreases as $\tau_{abs} \propto a^{-3}$, as shown in the remaining panels of Fig. I.30. The number of temperature spikes increases, as the grain being larger, it intercepts more photons. The temperature of the spikes also decreases with a, as the grain stores the energy of a single photon in a larger number of phonon modes. For large enough grains (Fig. I.30.g), the temperature fluctuations become negligible. The grain appears to have a single temperature; its temperature distribution tends toward a Dirac distribution (Fig. I.30.h): it has reached thermal equilibrium. Fig. I.31 shows the same type of simulations, fixing the radius of the grain, and varying the starlight intensity. In this case, the heating rate increases linearly with U (downward in Fig. I.31).

Out-of-equilibrium emission. At each time, in the simulations of Figs. I.30 – I.31, the emission of the grain is: $\epsilon_\nu(a,\nu,t) = 3\pi/\rho \times Q_{abs}(a,\nu)/a \times B_\nu(T(t),\nu)$. To average over time, we simply need to integrate over the temperature distribution:

$$\epsilon_\nu(a,\nu) = \frac{3\pi}{\rho}\frac{Q_{abs}(a,\nu)}{a}\int_0^\infty B_\nu(T,\nu)\frac{dP(T,a)}{dT}\,dT. \tag{I.88}$$

The left panels of Fig. I.32 show the temperature distributions of PAHs, graphite and silicates of different sizes. The corresponding emission spectra, computed using Eq. (I.88), are shown in the right panels. We see that the smallest grains fluctuate to the highest temperatures. Their emission is thus the broadest, and extends to the shortest wavelengths. An important difference between equilibrium

10. The ergodicity is a principle stating that the steady-state statistical distribution of the properties of a large number of identical particles is the average of their properties over time.

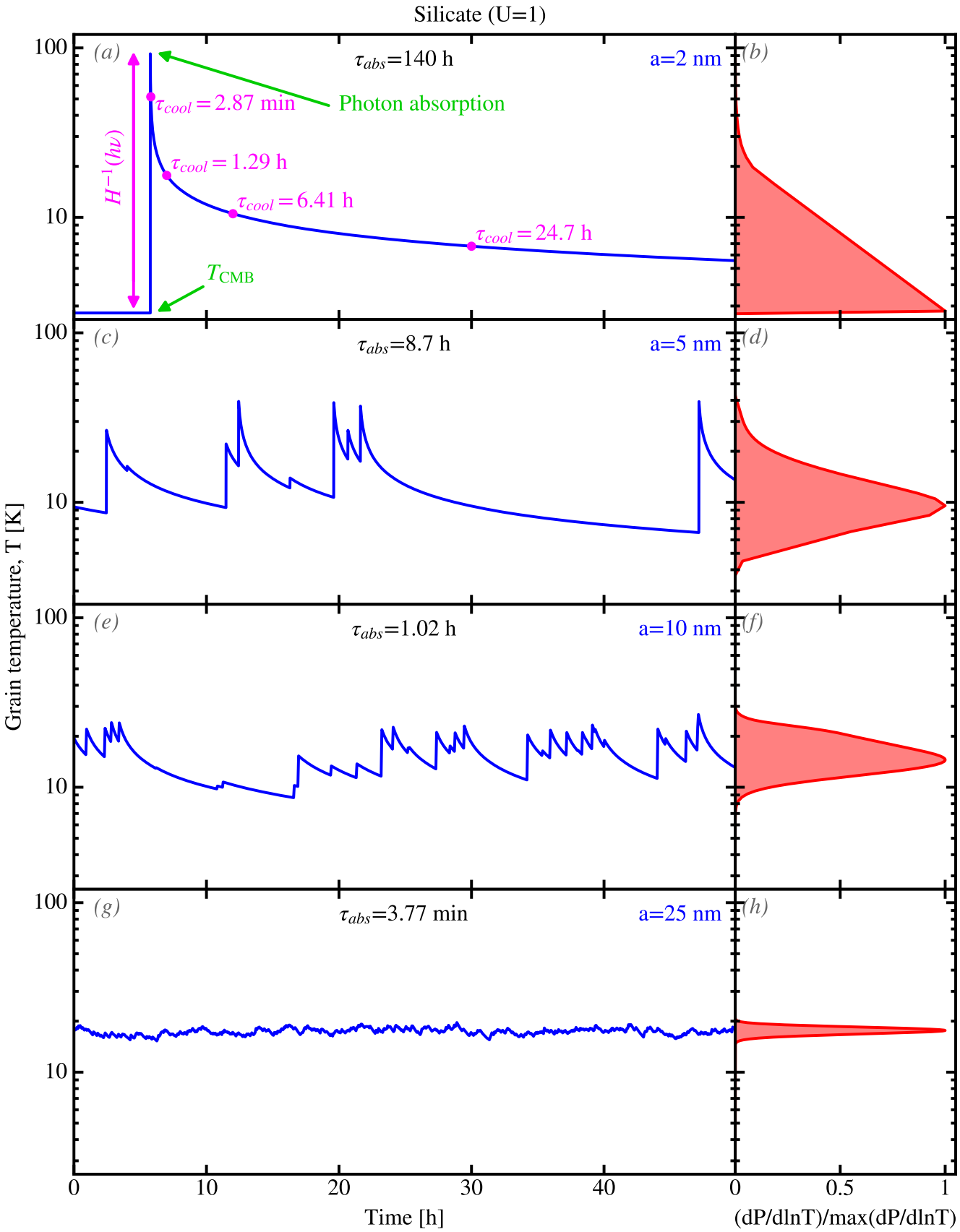

FIGURE I.30 – *Temperature fluctuations of grains with different radii.* The left panels show the time variation of the temperature of silicate grains (Draine, 2003b,c), exposed to the Mathis et al. (1983) ISRF with U = 1. The radius of the grain, *a*, increases downward. The right panels show the corresponding probability distribution of the temperature. These simulations were performed using the Draine & Anderson (1985) Monte-Carlo method. See Draine (2003a) for a similar simulation with graphite.

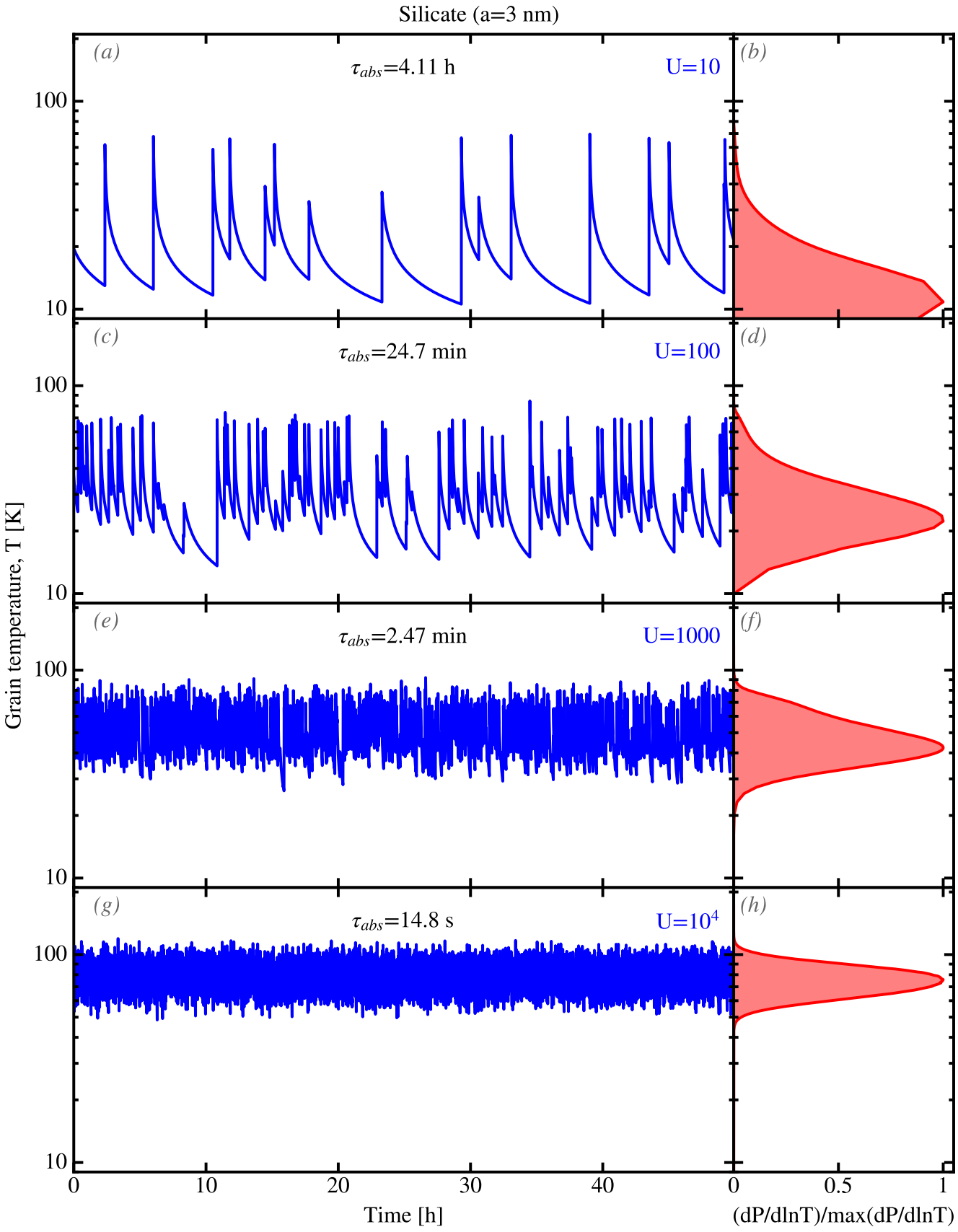

FIGURE I.31 – *Temperature fluctuations of grains with different starlight intensities.* This is a variation on Fig. I.30. The grain radius is constant (a = 3 nm), and the starlight intensity, U, increases downward. Licensed under CC BY-SA 4.0.

and stochastic heating is that the emission spectrum of small grains depends not only on the intensity of the ISRF, but also on its hardness. The latter can be quantified with the mean energy of stellar photons:

$$\langle h\nu \rangle \equiv \frac{\int_0^\infty \mathrm{J}_\nu(\nu)\,\mathrm{d}\nu}{\int_0^\infty \frac{\mathrm{J}_\nu(\nu)}{h\nu}\,\mathrm{d}\nu}. \tag{I.89}$$

This parameter determines the average temperature spikes. This is the reason why stochastic heating is sometimes referred to as *single photon heating*, *transient heating* or *quantum heating*. The ISRF intensity roughly scales with the emissivity, but does not affect its spectral shape.

Numerical methods. To compute the emission spectrum of an out-of-equilibrium grain, we need to calculate its temperature distribution, dP/dT (Eq. I.88). This is done numerically. Several methods can be found in the literature.

The Monte-Carlo method (Draine & Anderson, 1985) consists in simulating the temporal evolution of the grain, by drawing random stellar photons. This is the method we have used in Figs. I.30 – I.31. This method is easy to implement, but it is not the most numerically efficient.

Solving the integral equation governing dP/dT (Desert et al., 1986). This method is efficient and is used by the `DustEM` code (Compiègne et al., 2011).

The transition matrix method (Guhathakurta & Draine, 1989) consists in building a squared matrix whose elements are the probability per unit time that a grain will transit from a state to another. The row and columns of this matrix correspond to the final and initial energy bins. This matrix can then be diagonalized to compute dP/dT. This is the method we have implemented in our code. It has been used in Fig. I.32. We have implemented an adaptative grid in energy, represented by the dots in the left panels of Fig. I.32. The grid is refined to ensure the accuracy of the emission spectrum. We can see that more points are needed at high temperatures.

ISRF moment approximations (Natale et al., 2015) consists in interpolating a precomputed grid, characterizing the ISRF by its first two moments: its intensity, U, and the mean energy of the photons, $\langle h\nu \rangle$. This method is not exact, but it is fast enough to be implemented in radiative transfer simulations.

Equilibrium criterion. A simple criterion to determine if a grain is at thermal equilibrium with the ISRF consists in comparing its equilibrium enthalpy with the average energy of a stellar photon. Fig. I.33 compares these two quantities for graphite and silicates, varying a and U.

☞ A grain is at thermal equilibrium if $\mathrm{H}(a, \mathrm{T_{eq}}) \gg \langle h\nu \rangle$.

The transition radius between stochastically heated and equilibrium grains can therefore be estimated as the radius for which $\mathrm{H}(a_t, \mathrm{T_{eq}}) \simeq 20 \times \langle h\nu \rangle$. This value is indicative as the transition to equilibrium is a smooth, continuous process. These transition radii are the vertical dashed lines in Fig. I.33. The mean stellar photon energy of the Mathis et al. (1983) ISRF is a constant: $\langle h\nu \rangle \simeq 1.05$ eV. The equilibrium enthalpy behaves as $\mathrm{H}(a_t, \mathrm{T_{eq}}) \propto a_t^3 \mathrm{T_{eq}}^{n+1}$. Since $\mathrm{T_{eq}} \propto \mathrm{U}^{1/(4+\beta)}$, we have $a_t \propto \mathrm{U}^{-(n+1)/3(4+\beta)} \simeq \mathrm{U}^{-1/6}$ ($n = 2$ and $\beta = 2$ for the grains in Fig. I.33). The following approximations provide good fits:

- for graphite, $a_t^{\mathrm{gra}}(\mathrm{U}) \simeq 22\,\mathrm{nm} \times \mathrm{U}^{-1/6}$;
- for silicates, $a_t^{\mathrm{sil}}(\mathrm{U}) \simeq 15\,\mathrm{nm} \times \mathrm{U}^{-1/6}$.

Role of the CMB: note that, contrary to a common misconception, the smallest grains are not in thermal equilibrium with the CMB. For instance, a 3 Å silicate has an enthalpy at 2.7 K of $\mathrm{H}(\mathrm{T_{CMB}}) \simeq 0.5$ μeV, while the average photon energy received from the CMB is $\langle h\nu_{\mathrm{CMB}} \rangle \simeq 1$ meV.

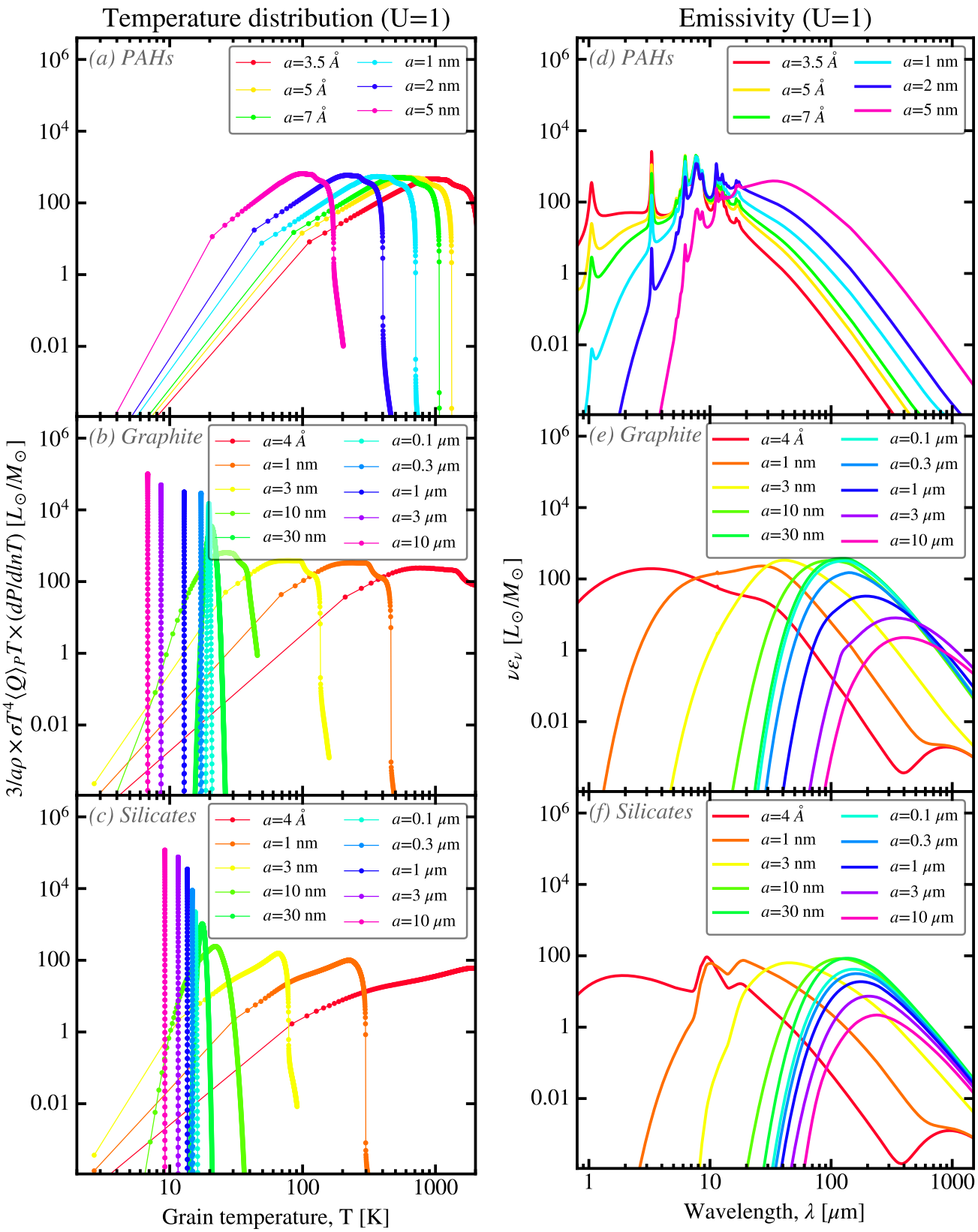

FIGURE I.32 – *Stochastically heated grains.* The left panels show the temperature distribution of grains with different radii. The dots represent the sampling of our adaptative energy grid. The PAHs are a mixture of neutral (50%) and ionized (50%) molecules (Draine & Li, 2007), the graphite and silicates are from Draine (2003b,c). The right panels show the corresponding emissivities.

The effect of considering photons with $\lambda > 1000$ µm as a source of *continuous heating* (following Guhathakurta & Draine, 1989), creates an artificial minimum temperature close to the actual CMB temperature. This is the bump peaking at $\lambda \simeq 1$ mm for the smallest grains in panels *(e)* and *(f)* of Fig. I.32. This is an artefact due to this approximation. Fortunately, this artefact does not affect the emitted spectrum, integrated over the size distribution, in any detectable way.

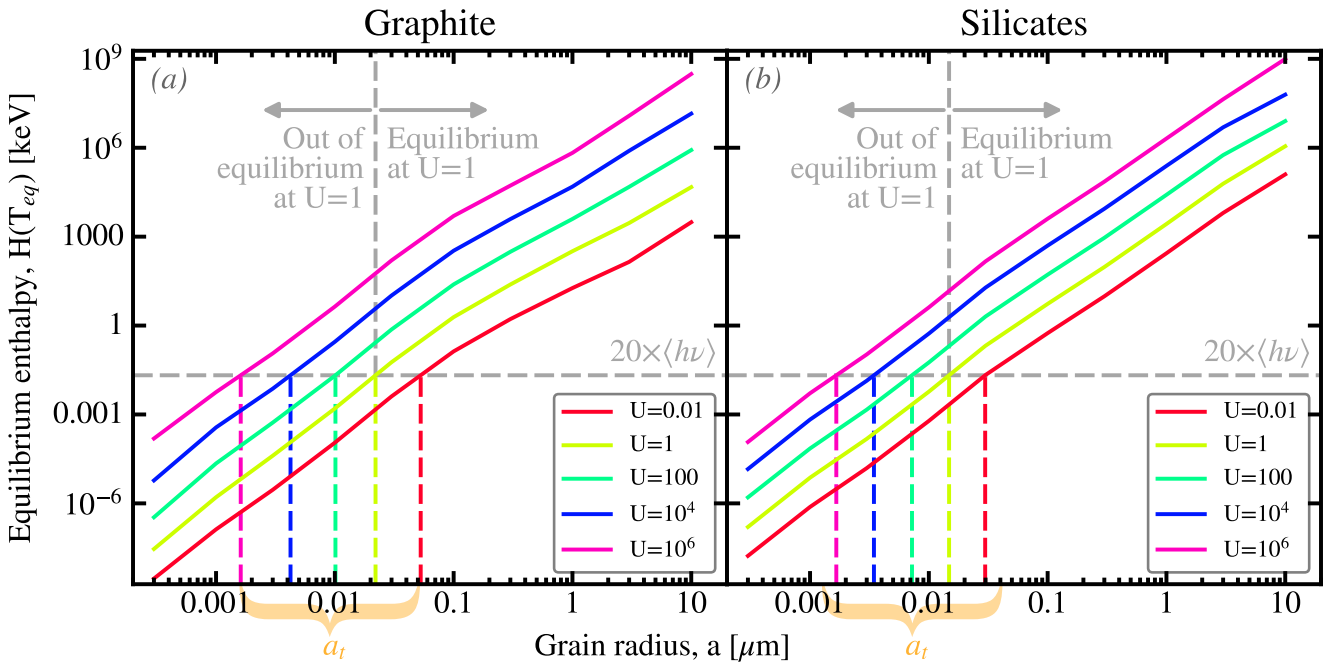

FIGURE I.33 – *Transition radius for stochastically heated grains.* These two panels show the enthalpy at the hypothetical equilibrium temperature, for the graphite of Laor & Draine (1993) and the silicates of Draine (2003b,c). The horizontal dashed grey line represents the $20 \times \langle h\nu \rangle$ level, for the Mathis et al. (1983) ISRF. The enthalpies above this line correspond to $H(T_{eq}) \gg \langle h\nu \rangle$, that is to equilibrium grains. The vertical dashed color lines, show the transition radius for each U. Left of this line, grains are stochastically heated. Licensed under CC BY-SA 4.0.

I.2.4.4 Collisionnal Heating

In addition to photon absorption, collisions with gas particles can, in specific conditions, contribute to dust heating. Obviously, this will happen when the temperature of the gas is the hottest, such as in a plasma. The collision rate of gas particles, following a Maxwell-Boltzmann distribution, with a dust grain is:

$$\frac{1}{\tau_{\rm coll}} \simeq \underbrace{\sqrt{\frac{8kT}{\pi m}}}_{\text{mean velocity}} \underbrace{\frac{1}{n\pi a^2}}_{\text{mean free path}} , \tag{I.90}$$

where n is the density of the gas, and m, the mass of the particles. Assuming that the protons and the electrons are thermalized, the ratio of their collision rates is $\tau_{\rm coll}(e^-)/\tau_{\rm coll}(H^+) = \sqrt{m_e/m_p} \simeq 0.02$ (*cf.* Table B.2). The collisions with the protons can thus be neglected.

Electronic heating rate. The Maxwell-Boltzmann distribution of the electrons of energy, E, can be written:

$$f(E,T) = \frac{2}{\sqrt{\pi}} \sqrt{\frac{E}{(kT)^3}} \exp\left(-\frac{E}{kT}\right). \tag{I.91}$$

This distribution is normalized: $\int_0^\infty f(\mathrm{E},\mathrm{T})\,\mathrm{dE} = 1$. It is displayed in Fig. I.34 and compared to the stellar radiation field. The collisional cross-section is very poorly constrained. At low energies, it should be close to the geometric cross-section, πa^2. However, at high energies, electrons can pass thought the grain. Dwek (1986) proposed the following cross-section:

$$\sigma_{\mathrm{coll}}(a,\mathrm{E}) = \pi a^2 \times \begin{cases} 1 & \text{for } \mathrm{E} < \mathrm{E}_\star(a) \\ 1 - \left[1 - \left(\dfrac{\mathrm{E}_\star(a)}{\mathrm{E}}\right)^{3/2}\right]^{2/3} & \text{for } \mathrm{E} \geq \mathrm{E}_\star(a), \end{cases} \tag{I.92}$$

where $\mathrm{E}_\star(a)$ is the threshold energy. According to the fit of experimental data shown in Fig. 1 of Dwek (1987), this threshold energy is (*cf.* the discussion in Bocchio et al., 2013):

$$\begin{cases} \mathrm{E}_\star^{\mathrm{car}}(a) & \simeq & 10\,\mathrm{keV} \times \left(\dfrac{a}{1\,\mu\mathrm{m}}\right)^{2/3} & \text{for carbonaceous} \\ \mathrm{E}_\star^{\mathrm{sil}}(a) & \simeq & 14\,\mathrm{keV} \times \left(\dfrac{a}{1\,\mu\mathrm{m}}\right)^{2/3} & \text{for silicates.} \end{cases} \tag{I.93}$$

Assuming the grains are at rest, the collision rate for a given energy, E, is now:

$$\frac{1}{\tau_{\mathrm{coll}}(a,\mathrm{E})} = n \times \sigma_{\mathrm{coll}}(a,\mathrm{E}) \times v(\mathrm{E}), \tag{I.94}$$

where the velocity of an electron with energy E is:

$$v(\mathrm{E}) = \sqrt{\frac{2\mathrm{E}}{m}}. \tag{I.95}$$

The collisional power received by the grain is finally the integral of the energy deposit per unit time, $\mathrm{E}/\tau_{\mathrm{coll}}$, over the whole Maxwell-Boltzmann distribution:

$$\mathrm{P}_{\mathrm{coll}}(a,n,\mathrm{T}) = \int_0^\infty \frac{\mathrm{E}}{\tau_{\mathrm{coll}}(a,\mathrm{E})} f(\mathrm{E},\mathrm{T})\,\mathrm{dE}. \tag{I.96}$$

Cases where collisions dominate the heating. Coronal plasmas, that can be found in the *Hot Ionized Medium* (HIM; *cf.* Table III.6) of the MW or the halo of elliptical galaxies, have typical temperatures of $\mathrm{T} \simeq 10^6 - 10^7$ K. This gas has been heated by successive *SuperNova* (SN) blast waves. It has a low density ($n \simeq 10^{-3} - 10^{-2}$ cm^{-3}), but can have a large filling factor (it fills 50 % of the volume of the MW). At these temperatures, it is responsible for a diffuse X-ray emission. When dust grains are present in such a gas, collisions can dominate the heating, depending on the balance between the photon and electron energy densities (*cf.* Fig. I.34).

The collisional heating rate is displayed as a function of the grain radius in Fig. I.35. This figure basically shows that, if a grain is in a coronal plasma, collisional heating dominates for $\mathrm{U} < 0.01$, and photon heating dominates if $\mathrm{U} > 10$. In between, both can play a role, depending on n and T.

The transition radius between stochastically-heated and equilibrium grains can be computed similarly to Eq. (I.33), using the heating rate of Fig. I.35. This time, the single heating events are due to electron collisions, with average energies: $\langle \mathrm{E} \rangle = 3/2 k\mathrm{T} \simeq 0.13\,\mathrm{keV} \times \mathrm{T}/10^6$ K. They are much higher than the typical ISRF photon energy, $\langle h\nu \rangle \simeq 1$ eV. The stochastic heating will be the most efficient for the lowest densities and highest temperatures. For the extreme case, $n = 10^{-3}$ cm^{-3} and $\mathrm{T} = 10^7$ K, the transition radii are: $a_t^{\mathrm{gra}} \simeq 58$ nm and $a_t^{\mathrm{sil}} \simeq 35$ nm.

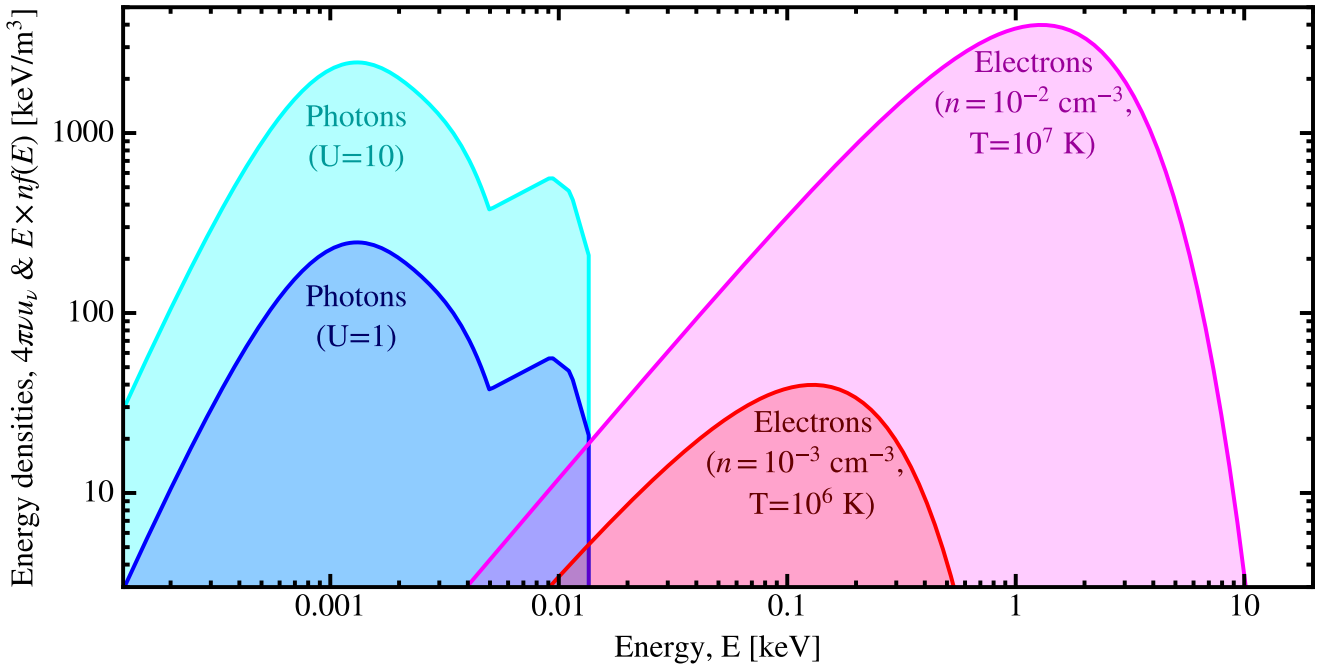

FIGURE I.34 – *Photon and electron energy densities.* The blue and cyan curves show the energy per unit volume ($u_\nu = 4\pi c J_\nu$) of the stellar photons, for U = 1 and U = 10. The electron energy density is the Maxwell-Boltzmann distribution (Eq. I.91): $n \times f$(E). We have plotted it for densities and temperatures typical of coronal plasmas: $n = 10^{-3} - 10^{-2}$ cm^{-3} and T = $10^6 - 10^7$ K. Licensed under CC BY-SA 4.0.

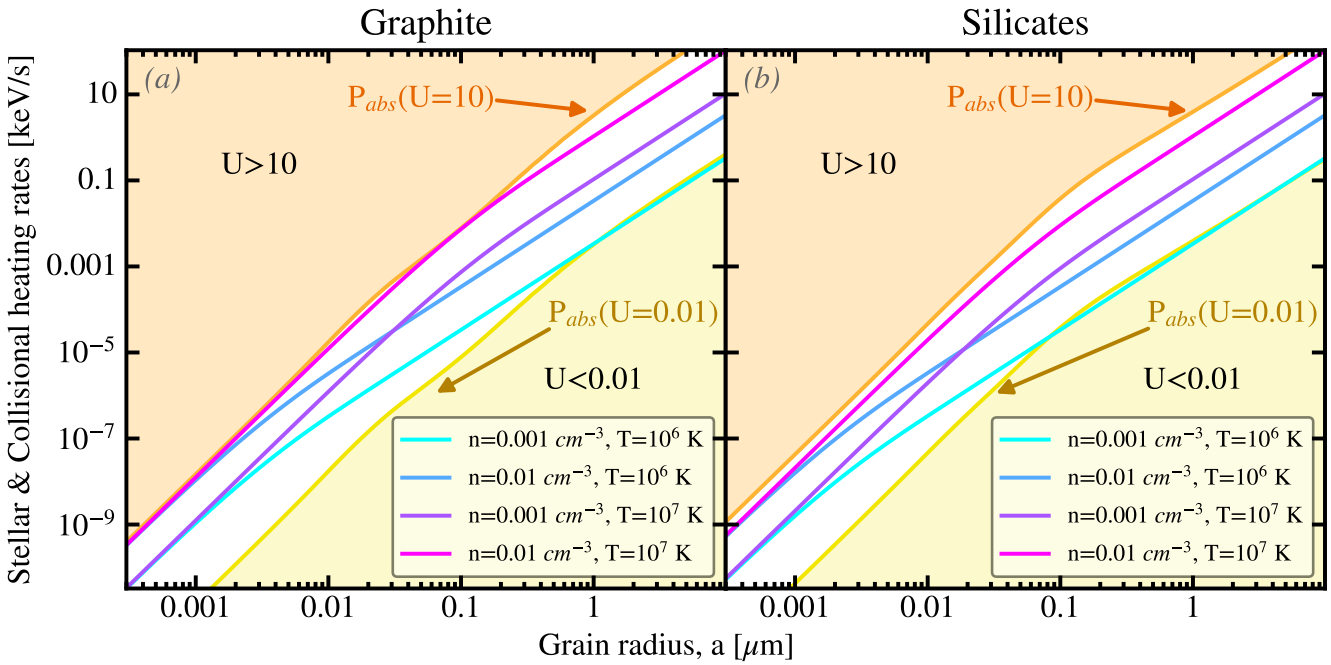

FIGURE I.35 – *Collisional heating rate.* In each panel, the cyan, blue, purple and magenta lines show the collisional heating rates from Eq. (I.96), for different values of n and T. We compare the stellar photon heating rate in yellow (U = 0.01) and orange (U = 10). The area colored in yellow corresponds to U < 0.01, where photon heating is negligible. The area colored in orange corresponds to U > 10, where photon heating dominates. Licensed under CC BY-SA 4.0.

Chapter II

Dust Observables and Models

All models are wrong, but some are useful.

(George E. P. Box; Box, 1979)

Contents

II.1 A Brief History of Interstellar Dust Studies . . . 53
II.1.1 The Challenges of Observing Interstellar Regions . . . 55
II.1.1.1 Limitations Due to the Atmosphere . . . 55
II.1.1.2 Historical Ground-Based Observatories . . . 55
The meter-class visible telescopes. . . . 55
The first MIR telescopes. . . . 55
The submillimeter observatories. . . . 55
II.1.1.3 Airborne Observatories . . . 56
Balloons. . . . 56
Airplanes. . . . 57
II.1.1.4 Space Telescopes . . . 57
IRAS. . . . 57
COBE. . . . 57
ISO. . . . 58
Spitzer. . . . 58
AKARI. . . . 58
WISE. . . . 59
Herschel. . . . 59
Planck. . . . 59
The JWST. . . . 59
UV and X-ray Satellites. . . . 61
II.1.1.5 Grain-Collecting Spacecrafts . . . 61
II.1.2 Chronology of the Main Breakthroughs . . . 62
II.1.2.1 Obscuration and Dimming of Starlight . . . 62
The discovery of dark nebulae. . . . 62
The reddening of starlight. . . . 62
II.1.2.2 The Dust Continuum . . . 63
The Shape of the extinction curve. . . . 63
Polarization by dichroic extinction. . . . 64
Dust emission. . . . 64
II.1.2.3 Identification of Dust Features . . . 64
Silicates. . . . 65

Carbonaceous grains. . . . 65
Ices. . . . 65
X-ray edges. . . . 65
II.1.2.4 Dusty Epiphenomena 66
Diffuse Interstellar Bands. . . . 66
Extended Red Emission. . . . 66
Spinning Grains. . . . 66
II.1.2.5 Dust Models 66
First models. . . . 66
Calculation of the optical properties. . . . 67
Elemental depletions. . . . 67
Modern panchromatic models. . . . 67
II.2 The Current Empirical Constraints 68
II.2.1 Extinction 68
II.2.1.1 UV-to-NIR Extinction 70
The extinction magnitude. . . . 70
The selective extinction. . . . 71
Measuring extinction. . . . 71
UV-visible scattering. . . . 71
II.2.1.2 MIR Extinction 72
The MIR continuum. . . . 72
Silicate features. . . . 73
Ices. . . . 73
II.2.1.3 X-Rays 73
X-ray halos. . . . 73
X-ray absorption edges. . . . 74
II.2.1.4 Dichroic Extinction 75
II.2.1.5 Diffuse Interstellar Bands 75
II.2.2 Emission 76
II.2.2.1 Infrared Continuum and Features 76
Observations of the diffuse ISM. . . . 76
MIR features. . . . 76
II.2.2.2 Polarized Emission 77
II.2.2.3 Non-Thermal Emission 77
Spinning Grains. . . . 77
Photoluminescence. . . . 77
II.2.3 Elemental Abundances in Grains 78
II.2.3.1 Measuring ISM Abundances 78
Solar abundances. . . . 78
Present-day Solar abundances. . . . 78
II.2.3.2 Depletions 79
The depletion strength. . . . 79
Volatile and refractory elements. . . . 80
Inferred dust composition. . . . 80
II.2.4 Direct Measures 81
II.2.4.1 Meteorite Inclusions 82
Grain identification. . . . 82
Limitations. . . . 82
II.2.4.2 Interplanetary Dust 83
ISD flux and cometary dust. . . . 83

Micrometeorites. . . . 83
II.2.4.3 Laboratory Measurements . . . 83
Spectroscopic characterization. . . . 83
Grain reactivity and evolution. . . . 84
II.3 State-of-the-Art Dust Models . . . 85
II.3.1 Composition and Size Distributions of Different Models . . . 85
II.3.1.1 Diversity in Composition . . . 85
Inherent degeneracies of dust models. . . . 85
Common compositional choices. . . . 85
II.3.1.2 Difference in Size Distributions . . . 86
Origin of the Size Distribution. . . . 86
Comparison Between Different Models. . . . 87
II.3.2 The Model Properties . . . 87
II.3.2.1 Extinction and Emission . . . 88
The opacity. . . . 88
The SED. . . . 88
II.3.2.2 The Fitted Constraints . . . 89
The THEMIS model. . . . 89
Discussion of the fit. . . . 89
II.3.3 Some Useful Quantities . . . 89
II.3.3.1 Grain Sizes, Areas and Masses . . . 89
For the MRN size distribution. . . . 89
The case of the THEMIS model. . . . 92
Mass fraction of small grains. . . . 92
Dustiness and other ratios. . . . 92
II.3.3.2 Opacity and Emissivity . . . 93
Optical properties. . . . 93
Heating regimes. . . . 93
Emissivity. . . . 93

The present chapter is intended to provide a comprehensive overview of the current state of the field. It discusses both the observables that can be used to constrain dust properties, and the current state-of-the-art models. It bridges the basic physical knowledge of Chap. I with their current application.

II.1 A Brief History of Interstellar Dust Studies

The History of our progressive understanding of ISD is driven by the successive technological innovations that allowed us to shed light on its nature.

Telescopes allowed *deep-sky* observations already through the XVIIIth century (*e.g.* Wilson, 2007). Charles MESSIER's catalog of "*nebulae*" was first established in 1774. The quality and size of mirrors increased through the XIXth century, and at the beginning of the XXth century, the first meter-class telescopes, with silvered-glass mirrors [1], were built. The Mount Wilson Observatory was founded in 1904, and its 1.5-m Hale telescope was commissioned in 1908.

Photographic plates turned astronomical observations into a reproducible empirical science. They required long exposures and reliable tracking of the sky's apparent rotation. Photography was invented by Nicéphore NIÉPCE in the 1820's. His associate, Louis DAGUERRE, perfected the

1. Before that, telescope mirrors were made of the lower optical quality speculum metal alloy. The process of silvering glass mirrors was invented by Léon FOUCAULT in the 1860's.

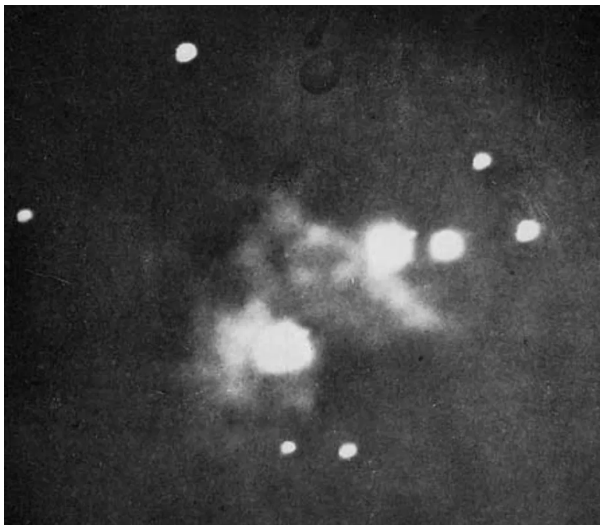

(a) First photograph of Orion (1880)

(b) Sir William HERSCHEL

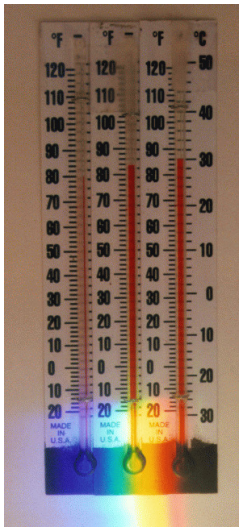

(c) Reenactment

FIGURE II.1 – *Early ISM and IR astronomy.* Panel *(a)* shows the 1880 picture of the Orion nebula taken at the Lick observatory, by Henry DRAPER. Panel *(b)* represents Sir William HERSCHEL measuring the SED of the Sun. We can see in the background his 1.2 m speculum mirror telescope. Panel *(c)* shows a simple recreation of his experiment with commercial thermometers. We see that the temperature is the highest on the last thermometer, after the red. Credit: *(a)* Henry DRAPER, public domain; *(b)* El Sofista, not licensed; *(c)* courtesy of NASA/JPL-Caltech.

technique and commercialized the first *daguerreotype*[2] in 1839. The first attempts to capture images of the sky (the Moon and the Sun), were performed using this invention, in the 1840's. Emulsion plates were substituted to daguerreotypes, and the first deep-sky picture (the Orion nebula; Fig. II.1.a) was taken by Henry DRAPER in 1880 (Barker, 1888).

Solid-state physics was given a strong impulse, after World War II, by the prospective development of electronics (Martin, 2013). The transistor was invented in 1947, at Bell laboratories in New Jersey. This impulse led to the development of technical and conceptual tools for the optical and electronic properties of solids that our field would benefit from.

The introduction of computers revolutionized all scientific fields. The principle of the computer was laid out in Alan TURING's seminal 1937 article (Turing, 1937). The first computers were developed during World War II to break the German encryption codes (*e.g.* McGrayne, 2011). They started to be used in astrophysics during the 1950's, to compute stellar structures. Before that, some calculations were impossible. For instance, the first dust model of the 1930's was made of small iron particles (*e.g.* Schoenberg & Jung, 1937; Greenstein, 1938), in part because Mie computations for small metal spheres were easier on paper than for large dielectrics (van de Hulst, 1986). The first dust radiative transfer numerical computations were performed in the early 1970's, using iterative methods (Mathis, 1970) and Monte-Carlo methods (Mattila, 1970).

The development of modern detectors solved the issues of photography: *(i)* non-linear response; *(ii)* restricted dynamic range; *(iii)* low detection efficiency; *(iv)* reciprocity failure; and *(v)* adjacency effects (Boksenberg, 1982). The first *Charge-Coupled Device* (CCD) was invented in 1969 at Bell laboratories (Amelio et al., 1970). In the IR, photomultipliers and bolometers were developed in the 1930's, and found important military applications during World War II and later: night vision and guiding rockets (Rogalski, 2012, for an extensive review). The first IR thermal detector had in fact been built 150 years earlier by Sir William HERSCHEL, in 1800. He used a prism to split the Sun light over several thermometers (*cf.* Fig. II.1.b; Rogalski, 2012). He found

2. A daguerreotype is the capture of an image directly on a chemically-treated metal plate, without the recourse to a negative.

that the highest temperature was beyond the red, that is in the infrared[3] (Fig. II.1.c).

The possibility to send airborne and space observatories opened the spectral windows where the atmosphere is opaque (*cf.* Sect. II.1.1.1). The interest to send telescopes in space was first advocated for by Lyman SPITZER Jr., in 1946 (Spitzer, 1946). The first successful space telescope was launched in 1968. It was the *Orbiting Astronomical Observatory* (OAO), operating in the UV (Code et al., 1970). The first airborne observatory was the balloon experiment *Stratoscope I*, operating in the IR, in 1958.

The next technological innovation that will revolutionize our field is difficult to predict. We can however note that quantum computers should permit *ab initio* calculations of the properties and evolution of complex molecules and solids, in the near future. If this is true, it should allow us to precisely characterize the dust composition in different environments.

II.1.1 The Challenges of Observing Interstellar Regions

II.1.1.1 Limitations Due to the Atmosphere

The atmosphere of Earth is transparent in only a few spectral windows. The bottom panel of Fig. II.2 shows its absorbance as a function of wavelength. We see in particular that the UV and FIR ranges are completely opaque, and thus inaccessible from the ground. This is the reason why the first evidences for ISD came from the extinction of starlight in the visible range. The last forty years have seen the development of space and airborne observatories in the UV and IR windows, providing us with a panchromatic view of ISD properties (top panel of Fig. II.2).

II.1.1.2 Historical Ground-Based Observatories

The meter-class visible telescopes. The first discoveries about ISD were performed in the visible domain, by understanding the extinction toward stars. Robert TRUMPLER's seminal paper (Trumpler, 1930) was based on observations made at the Lick observatory, near San Jose, as well as Edward BARNARD's most famous observations (Barnard, 1899, 1919). Such telescopes, all across the world, were the main source of empirical constraints on dust, until the end of the 1970's.

The first MIR telescopes. Ground-based observations, at high altitude, in dry regions of the globe such as the Mauna Kea, are possible in the MIR (*cf.* Fig. II.2). IR astronomy really started in the 1960's (*cf.* Walker, 2000, for an historical review). The first IR surveys of the northern and southern skies were performed by Neugebauer & Leighton (1968) and Price (1968), at 2 µm. A generation of 2-to-3-m MIR telescopes were commissioned at the end of the 1970's, such as the *Wyoming InfraRed Observatory* (WIRO; 1977; ⌀ = 2.3 m), the *United Kingdom InfraRed Telescope* (UKIRT; 1978; ⌀ = 3.8 m) and the *InfraRed Telescope Facility* (IRTF; 1979; ⌀ = 3 m). Current large telescopes such as Subaru (Mauna Kea; ⌀ = 8.2 m) or the *Very Large Telescope* (VLT; Paranal; ⌀ = 8.2 m) operate in the visible-to-MIR range.

The submillimeter observatories. On the other side of the FIR atmospheric absorption, the submillimeter domain can be observed from the ground in dry conditions. The first ground-based submillimeter observatories appeared in 1990's. Among them are: the *Caltech Submilleter Observatory* (CSO; Mauna Kea; ⌀ = 10 m; 1986-2015), the *James Clerk Maxwell Telescope* (JCMT; Mauna Kea; ⌀ = 15 m; 1987), the *Atacama Pathfinder Experiment* (APEX; Atacama desert; ⌀ = 12 m; 2004) and the *Atacama Large Millimeter/submillimeter Array* (ALMA; Atacama desert; interferometer; 2011).

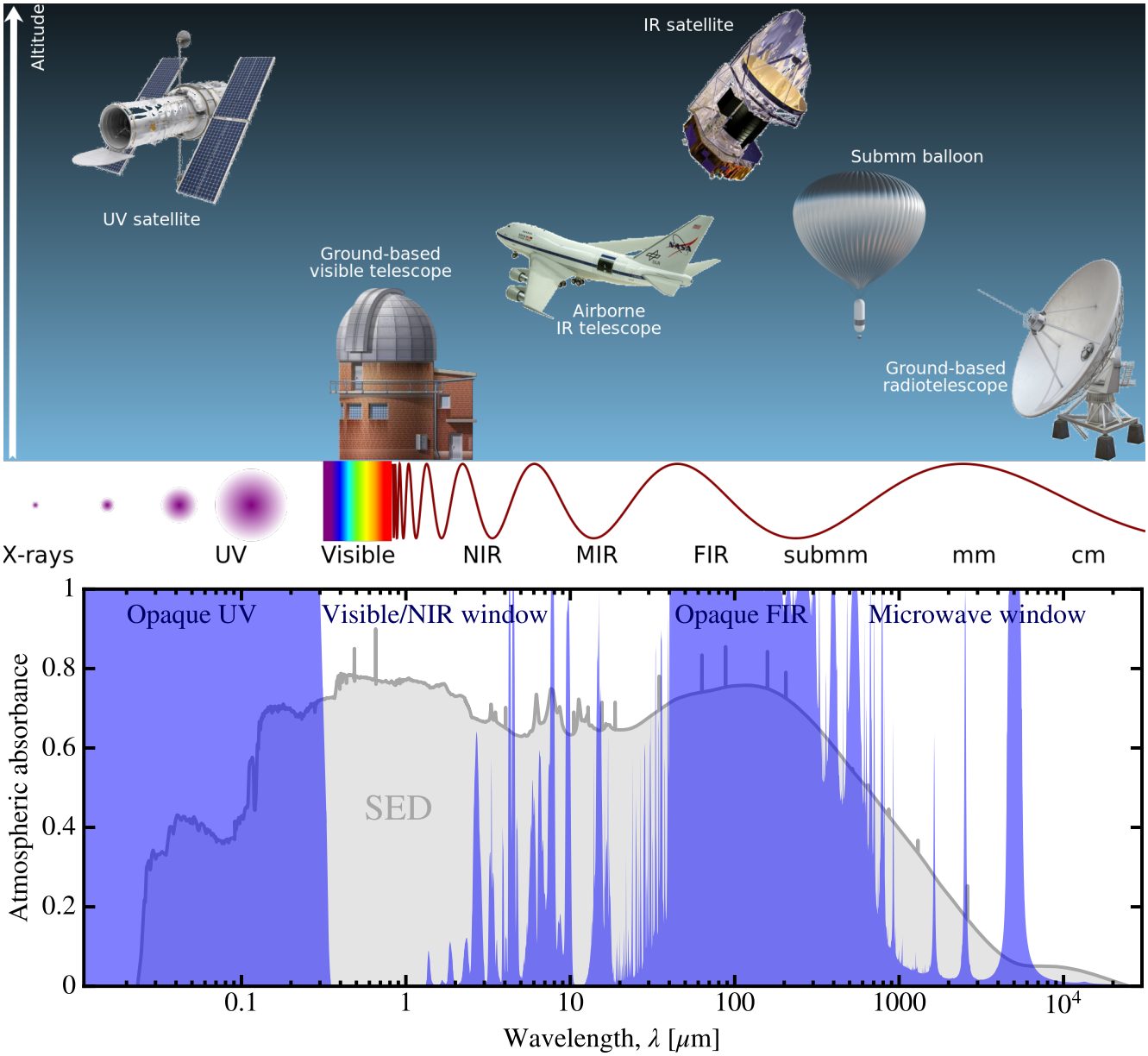

FIGURE II.2 – *Absorbance of Earth's atmosphere.* The bottom panel shows the absorbance of the atmosphere, in blue. Most of the absorption is due to H_2O, with some contribution by N_2, O_2, O_3, N_2O, CH_4 and CO_2. We have displayed in grey, in the background, the typical SED of a galaxy, for reference. We see that the UV and FIR windows are totally opaque from the ground (*cf.* Table A.4 for the denomination of the different spectral windows). Consequently, observations in these spectral windows can only be achieved from space, or above the troposphere (stratospheric airplane or balloon). Licensed under CC BY-SA 4.0.

II.1.1.3 Airborne Observatories

Balloons. Stratospheric balloons can reach altitudes of ≃ 40 km, well above most water vapor absorption. They can observe for several days continuously, but landing is hazardous (Fig. II.3.a). The first IR balloon was launched from Johns Hopkins in 1959, and a balloon sent by the Goddard Institute of Space Sciences mapped the sky at 100 µm in 1966 (Walker, 2000). During the past two decades, several balloons provided observations of the dust continuum intensity and polarization in different regions of the sky, including: the *Balloon-borne Large Aperture Submillimeter Telescope* (BLAST;

3. The photosphere of the Sun is indeed a T ≃ 5800 K black body, peaking at $\lambda_{max} \simeq 0.88$ µm. This is the first SED in history.

(a) Balloon crash

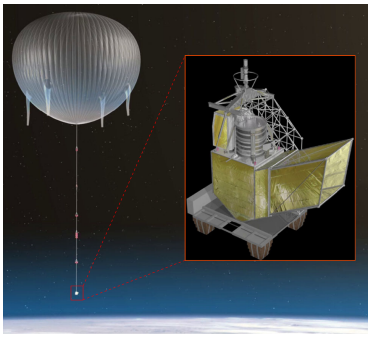

(b) PILOT

(c) SOFIA

FIGURE II.3 – *Airborne observatories.* Panel *(a)* shows the 2010 crash site of the *Nuclear Compton Telescope* (NCT) in order to illustrate the challenges of such observation campaigns. Panel *(b)* shows an artist rendering of the PILOT balloon with a zoom on the gondola where the telescope is (Bernard et al., 2016). Panel *(c)* shows a picture of SOFIA in flight, with the telescope door open. Credit: *(a)* courtesy of NASA; *(b)* Bernard et al. (2016), with permission from Jean-Philippe BERNARD; *(c)* courtesy of NASA.

1997-2010; ⌀ = 2 m; Pascale et al., 2008); the *PROjet National pour l'Observation Submillimétrique* (PRONAOS; 1994-1999; ⌀ = 2 m; Serra et al., 2002); the *Polarized Instrument for the Long-wavelength Observation of the Tenuous ISM* (PILOT; 2015-2017; ⌀ = 0.73 m; Bernard et al., 2016, Fig. II.3.b).

Airplanes. Airplanes can fly up to ≃ 15 km altitude and operate during ≃ 10 h. Numerous flights can be scheduled, contrary to balloons, which usually do only a few flights in their whole lifetime. The telescope motion being limited by its orientation perpendicular to the plane (Fig. II.3.c), the flight path has to be adapted to the observed source. The *Kuiper Airborne Observatory* (KAO; 1974-1995; ⌀ = 0.9 m; Erickson & Meyer, 2013) was a transport jet plane converted into an observatory. The *Stratospheric Observatory for Infrared Astronomy* (SOFIA; 2010-; ⌀ = 2.5 m; Young et al., 2012, Fig. II.3.c) is its current successor. It is a retired Boeing 747, modified to host the telescope.

II.1.1.4 Space Telescopes

IRAS. The *InfraRed Astronomical Satellite* (IRAS; 1983; ⌀ = 0.57 m; Neugebauer et al., 1984) was the first observatory to perform an all-sky survey at IR wavelengths. It mapped the sky in four broadbands centered at $\lambda = 12$, 25, 60 and 100 µm, with angular resolutions of $0.5' - 2'$. It opened the IR window, which was largely unexplored at the time. It discovered more than 300 000 point sources, many of them being starburst galaxies. These new objects, with deeply embedded star formation at the scale of the whole galaxy, emitting more than 95 % of their luminosity in the IR, were unexpected (*e.g.* Soifer et al., 1987, for a review). The new categories of *Luminous InfraRed Galaxies* (LIRG) and *UltraLuminous InfraRed Galaxies* (ULIRG) were created to describe what had been observed. Dusty disks around stars were also discovered (Beichman, 1987). By accessing the cold grain emission, the first reliable dust masses of galaxies and Galactic clouds could be estimated. The IR emission provided a new constraint that shaped modern dust models (Désert et al., 1990). IRAS data are still used nowadays (*e.g.* Galliano et al., 2021, , hereafter G21).

COBE. The *COsmic Background Explorer* (COBE; 1989-1993; ⌀ = 0.2 m; Boggess et al., 1992) was aimed at mapping the CMB, as its name indicates. However, two of its three instruments were used to map the whole sky in the MIR and FIR, providing the main constraints on the emission of dust models until the *Planck* mission (Sodroski et al., 1994; Dwek et al., 1997). The third instrument, covering the microwave range was also instrumental in providing the first evidence of spinning grains.

DIRBE (*Diffuse Infrared Background Experiment*) was an instrument observing through ten broadbands at: $\lambda = 1.25, 2.2, 3.5, 4.9, 12, 25, 60, 100, 140$ and 240 µm (Hauser et al., 1998).

FIRAS (*Far-InfraRed Absolute Spectrophotometer*) was a low spectral resolution spectro-imager, observing between $\lambda = 100$ µm and 10 mm (Mather et al., 1999). At long wavelengths, the angular resolution was only 7°.

DMR (*Differential Microwave Radiometer*) was mapping the sky in three broadbands centered at $\lambda = 3.3, 5.6$ and 9.5 cm (Smoot et al., 1994).

ISO. The *Infrared Space Observatory* (ISO; 1995-1998; $\varnothing = 0.6$ m; Kessler et al., 1996) was the first mission to extensively perform spectroscopy over the whole IR range. For that reason, it provided a wealth of data about all spectral features: silicates (Molster & Kemper, 2005), PAHs (Abergel et al., 2005; Sauvage et al., 2005), ices (Dartois et al., 2005). Studies of IR gas lines also took off: molecular (Habart et al., 2005) and ionized (Peeters et al., 2005). Finally, it refined our knowledge, through dust tracers, of star formation at all scales (Nisini et al., 2005; Verma et al., 2005; Elbaz et al., 2005). There were four instruments onboard.

ISOCAM (Cesarsky et al., 1996a) was a low spectral resolution MIR spectro-imaging camera, in the $\lambda = 2.5 - 17$ µm range. It also had twenty broad and narrow bands in the same range.

SWS (de Graauw et al., 1996) was a medium to high spectral resolution ($R \equiv \lambda/\Delta\lambda = 1\,000 - 35\,000$) MIR spectrometer in the $\lambda = 2.4 - 45$ µm range.

LWS (Clegg et al., 1996) was a low to medium spectral resolution ($R \simeq 150 - 9700$) FIR spectrometer, in the $\lambda = 43 - 198$ µm range. Combined together, SWS and LWS provided several continuous spectra over the whole IR range ($\lambda = 2.4 - 198$ µm; *e.g.* Peeters et al., 2002b), that have never been equaled.

ISOPHOT (Lemke et al., 1996) was a photometer observing through several broad and narrow band filters, in the $\lambda = 2.5 - 240$ µm.

Spitzer. The *Spitzer space telescope* (cryogenic operation: 2003-2009; $\varnothing = 0.85$ m; Werner et al., 2004) was the successor of ISO. Its larger mirror size and more modern detectors allowed it to refine our understanding of what ISO discovered, and observe a significantly larger number of targets. Its angular resolution was $40''$ at 160 µm. It had three instruments onboard.

IRAC (*InfraRed Array Camera*; Fazio et al., 2004) was performing photometry through four broadbands, centered at $\lambda = 3.6, 4.5, 5.8$ and 8.0 µm.

IRS (*InfraRed Spectrograph*; Houck et al., 2004) was a medium and high spectral resolution ($R = 90 - 600$) spectro-imager, observing in the $\lambda = 5.3 - 38$ µm range.

MIPS (*Multiband Imaging Photometer for Spitzer*; Rieke et al., 2004) was a photometer observing through three broadbands centered at $\lambda = 24, 70$ and 160 µm.

AKARI. The *AKARI space telescope* (cryogenic phase: 2006-2008; $\varnothing = 0.69$ m; Murakami et al., 2007) was comparable to *Spitzer*. One of its advantages was its ability to record spectra down to 2 µm, while *Spitzer*/IRS was limited to 5 µm. AKARI performed an all-sky survey in several MIR to FIR bands. It had two instruments onboard.

IRC (*InfraRed Camera*; Onaka et al., 2007) was a MIR camera with numerous broad and narrow bands, as well as a low/mid-spectral resolution spectrometer, observing in the $\lambda = 1.8 - 26.5$ µm range.

FIS (*Far-Infrared Surveyor*; Kawada et al., 2007) was a FIR photometer observing through four broadbands centered at $\lambda = 65, 90, 140$ and 160 µm. It also had a *Fourier Transform Spectrometer* (FTS) over the same range.

WISE. The *Wide-field Infrared Survey Explorer* (WISE; 2009-2011; ⌀ = 0.4 m; Wright et al., 2010) was a MIR all sky surveyor. It mapped the sky through four broad photometric bands centered at λ = 3.4, 4.6, 12 and 22 μm.

Herschel. The *Herschel space observatory* (2009-2013; ⌀ = 3.5 m; Pilbratt et al., 2010) was a FIR-submm mission. Its large mirror allowed it to reach subarcminute angular resolution at long wavelength (36″ at λ = 500 μm). Combined with *Spitzer* data at shorter wavelengths, it gives access to the full dust emission and provides the most reliable dust property estimates of galaxies and Galactic regions. *Herschel* data allowed us to build large databases of galaxy dust properties (*e.g.* Davies et al., 2017). It also allowed us to better constrain the submillimeter grain opacity (Meixner et al., 2010; Galliano et al., 2011). Among its discoveries, it demonstrated the filamentary nature of star-forming regions (André et al., 2010). It had three instruments onboard.

PACS (*Photodetector Array Camera and Spectrometer*; Poglitsch et al., 2010) was an imager observing through three broadbands centered at λ = 70, 100 and 160 μm. It also had a spectrometer that could target specific FIR lines.

SPIRE (*Spectral and Photometric Imaging REceiver*; Griffin et al., 2010) was a photometer observing through three broadbands centered at λ = 250, 350 and 500 μm. It also had a FTS providing a continuous, medium spectral resolution spectrum over the λ = 194 – 671 μm spectral range.

HIFI (*Heterodyne Instrument for the Far-Infrared*; de Graauw et al., 2010) was a very high spectral resolution (R ≃ 10^7) spectrometer covering the λ = 157 – 625 μm spectral range. It was designed to accurately measure gas line intensities.

Planck. The *Planck space observatory* (2009-2013; ⌀ = 1.5 m; Tauber et al., 2010) was a FIR-to-microwave satellite designed to study the cosmological background. It is a successor to COBE. It was launched in the same rocket as *Herschel*. It performed an all sky survey in all its bands (Fig. II.4). *Planck* had a larger beam than *Herschel* (5′ at λ = 1 mm), but had an accurate absolute calibration. Its measure of the emission of the diffuse ISM of the MW is now the main constraint on dust models (*e.g.* Compiègne et al., 2011). *Planck* could also measure the linear polarization in all its bands. It thus provided unique constraints on the grain properties (*e.g.* Guillet et al., 2018) and maps of the Galactic magnetic field (*e.g.* Planck Collaboration et al., 2016b). It had two instruments onboard.

HFI (*High Frequency Instrument*; Lamarre et al., 2010) was a photometer/polarizer observing through six broadbands centered at λ = 350, 550, 850, 1380, 2096 and 2997 μm.

LFI (*Low Frequency Instrument*; Mandolesi et al., 2010) was a photometer/polarizer observing through three broadbands centered at λ = 4.3, 6.8 and 10 cm.

The JWST. The *James Webb Space Telescope* (JWST; 2021-; ⌀ = 6.5 m; McElwain et al., 2020) should be launched a few months after the time this manuscript is being written. Its large segmented mirror, that will unfold in space, will allow us to access sub-arcsec resolution in the MIR. It will have four instruments onboard.

MIRI (*Mid-InfraRed Instrument*; λ = 5 – 27 μm; Rieke et al., 2015) contains an camera and an imaging spectrometer. It will be the most relevant instrument to ISD studies.

NIRspec (*Near-InfraRed Spectrograph*; λ = 0.6 – 5 μm; Birkmann et al., 2016) is a NIR spectrometer.

NIRcam (*Near-InfraRed Camera*; λ = 0.6 – 5 μm; Beichman et al., 2012) is a NIR camera.

NIRISS (*Near-InfraRed Imager and Slitless Spectrograph*; λ = 0.8 – 5μm; Doyon et al., 2012) will perform NIR imaging and spectroscopy.

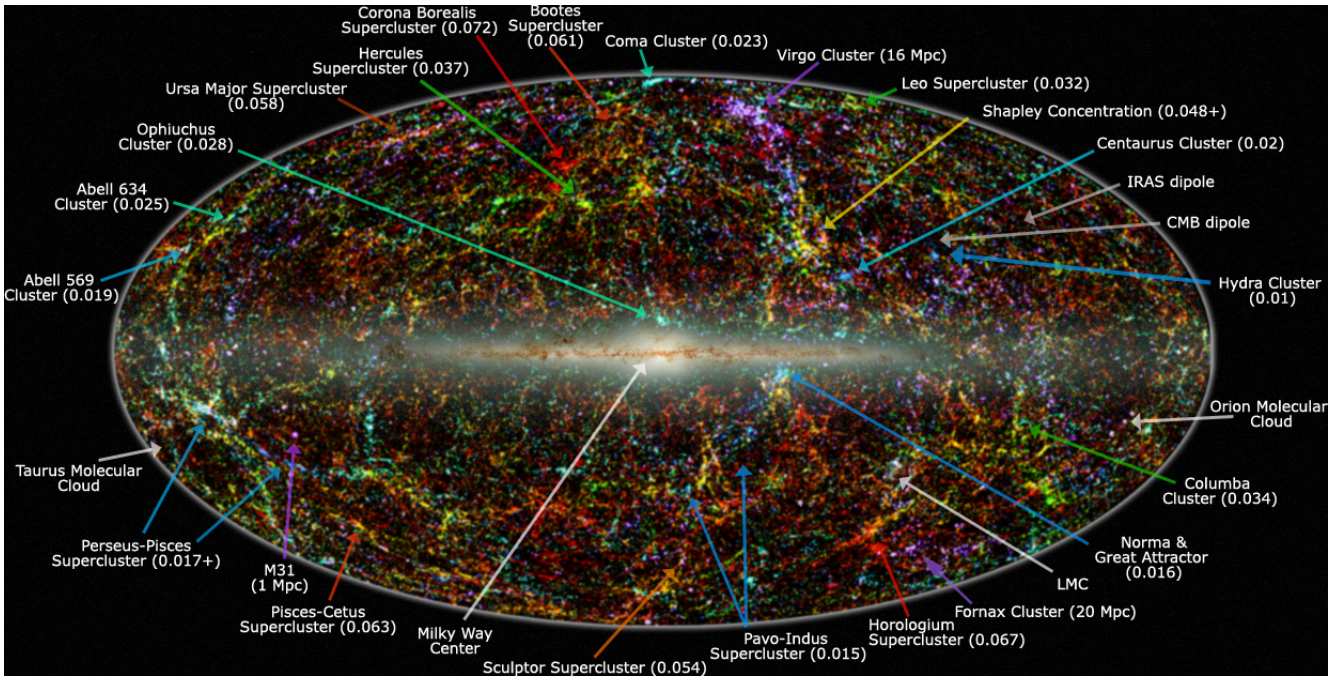

(a) Uranography of all sky map projections

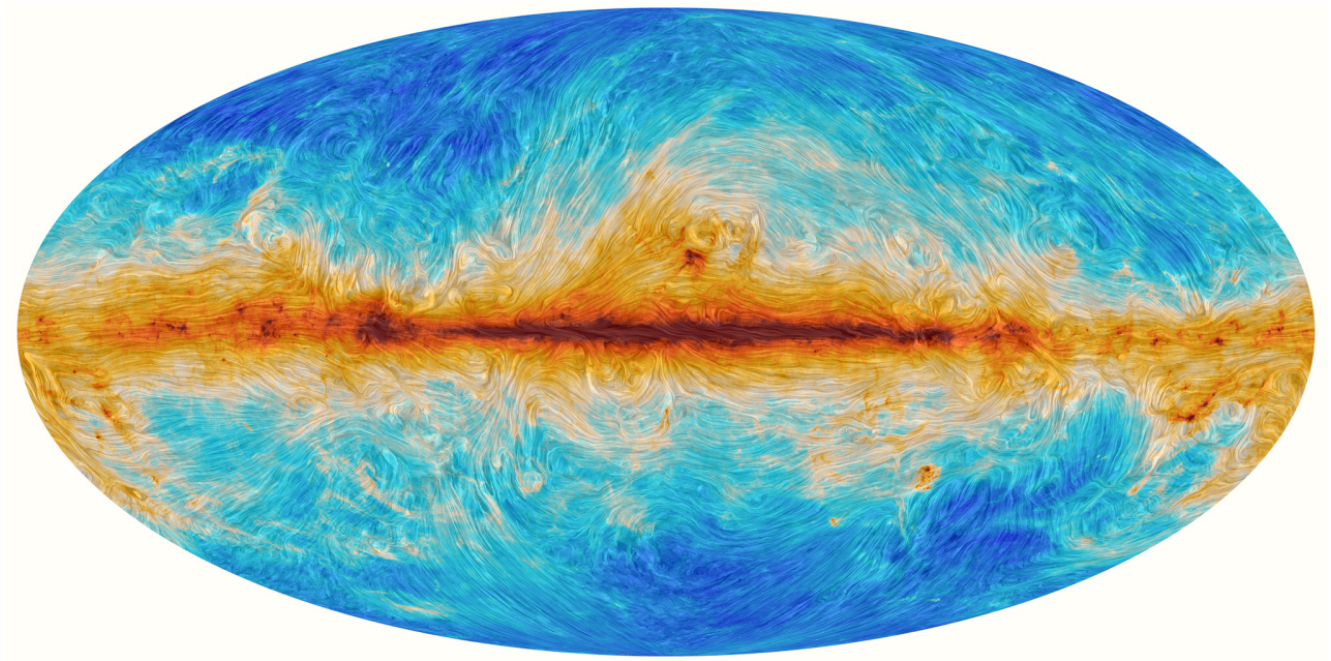

(b) *Planck* all sky map of the dust polarized emission

FIGURE II.4 – *All sky maps.* Panel *(a)* describes the main features of the usual all sky projections. It shows both Galactic and extragalactic structures. Panel *(b)* shows the all sky map of the dust polarized emission. It is a *Van Gogh representation*, where the brush lines show the orientation of the projected magnetic field. Credit: *(a)* Jarrett (2004), with permission from Tom JARRETT; *(b)* copyright ESA/*Planck* collaboration, credit Marc-Antoine MIVILLE-DESCHÊNES, with his permission.

UV and X-ray Satellites. The UV spectral shape of the extinction curve is an important constraint on dust models. UV satellite have one advantage over IR instruments: they do not need to be cooled down. IR instruments indeed need a cryostat to limit their proper emission. The lifetime of IR missions is thus the lifetime of their helium supply, typically only a few years, whereas UV telescopes can operate during several decades. The most important UV missions are the following.

IUE (*International Ultraviolet Explorer*; 1978-1996; $\varnothing = 0.45$ m; Boggess et al., 1978) was the first important UV mission, expanding our view on dust extinction at $\lambda = 115 - 320$ nm.

HST (*Hubble Space Telescope*; 1990-; $\varnothing = 2.4$ m; Burrows et al., 1991) can take spectra in the near-UV range.

FUSE (*Far Ultraviolet Spectroscopic Explorer*; 1999-2007; $\varnothing = 1.5$ m; Moos et al., 2000) extended the spectral coverage of IUE at $\lambda = 90.5 - 110.5$ nm.

As we will see in Sect. II.2.1.3, the X-ray regime can provide interesting constraints on the dust properties. The most important missions are: ROSAT (1990-1999; $\varnothing = 0.84$ m; $\lambda = 0.06 - 30$ nm; Aschenbach, 1991), XMM-Newton (1999-; $\varnothing = 0.7$ m; $\lambda = 0.1 - 12$ nm; Jansen et al., 2001) and Chandra (1999-; $\varnothing = 1.2$ m; $\lambda = 0.1 - 12$ nm; Weisskopf et al., 2002). The *Advanced Telescope for High ENergy Astrophysics* (ATHENA; $\simeq$ 2030; Wilms et al., 2014) will revolutionize the field.

II.1.1.5 Grain-Collecting Spacecrafts

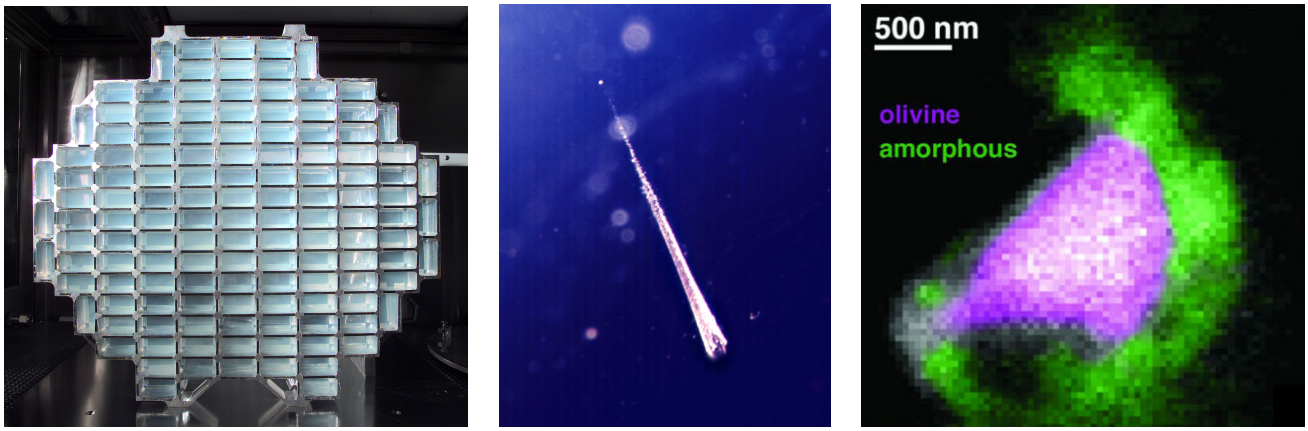

(a) Aerogel honeycomb matrix *(b)* Aerogel dust track *(c)* X-ray image of a grain

FIGURE II.5 – *Analysis of the Stardust mission.* Panel *(a)* shows the honeycomb matrix of Stardust. Each array is filled with an ultralight silica aerogel. It is $\simeq$ 1000 times less dense than glass. Dust grains arriving at several km/s are slowed down without being pulverized. Panel *(b)* shows the cone-shaped track of one of the grains captured in the aerogel. Panel *(c)* shows the X-ray image of one of the grains. The magenta part corresponds to olivine crystals, surrounded by non-crystalline magnesium silicate in green. Credit: *(a)* courtesy of NASA/JPL; *(b)* courtesy of NASA/JPL; *(c)* Anna Butterworth/UC Berkeley from STXM data, courtesy of Berkeley Lab.

Electromagnetic waves are not the only vectors of information about ISD we can get. The motion of the heliosphere relative to the local interstellar cloud creates an inflow of ISD through the Solar system (at 26 km/s; *e.g.* Krüger et al., 2019, for a review). Contrary to interplanetary grains, this interstellar flow is important at high ecliptic latitude, allowing us to discriminate grains from extrasolar origins. Several spacecrafts have collected actual interstellar grains, and analyzed them *in situ* or returned them to Earth.

Ulysses (1990-2009; Bame et al., 1992) was a spacecraft designed to analyze the Solar wind. It was the first mission to capture dust grains from interstellar origin.

Galileo (1989-2003; Johnson et al., 1992) was a spacecraft sent to study Jupiter and its satellites. It detected interstellar grains on its way.

Cassini (1997-2017; Matson et al., 2002) was a spacecraft sent to study Saturn and its satellites. It embarked an instrument called the *Cosmic Dust Analyzer* (CDA), recording the size, speed, direction and chemical composition of interstellar grains. It identified thirty six of them, smaller than 200 nm (Altobelli et al., 2016). They appeared to be essentially Mg-rich silicates with iron inclusions.

Stardust (1999-2006; Brownlee et al., 2003) was a spacecraft that captured grains in a low-density aerogel, and returned them to Earth for laboratory analysis (Fig. II.5). It identified seven interstellar grains (Westphal et al., 2014). Those were Mg-rich silicates, with sizes $\gtrsim 1$ µm. Two of them had crystalline structures.

II.1.2 Chronology of the Main Breakthroughs

In what follows, we present the main discoveries about ISD. We order the discussion by themes. Table II.1 puts all these breakthroughs in chronological order. This is a partial and incomplete review. We refer the reader to van de Hulst (1986), Dorschner (2003), Whittet (2003), Li & Greenberg (2003) and Li (2005), for more complete historical reviews.

II.1.2.1 Obscuration and Dimming of Starlight

The discovery of dark nebulae. The first evidence of ISD came through the obscuration of visible starlight. There was a debate during the whole XIX$^{\text{th}}$ century about the reality of this obscuration.

- Sir William HERSCHEL, in his treaty on *The Construction of the Heavens* (Herschel, 1785), reported"*an opening or a hole*" in the Scorpius constellation. This hole was later identified as the *Ink Spot* nebula, B86 (Fig. II.6.a; *cf.* Steinicke, 2016, for the historical branching out of this discovery).
- Edward BARNARD's photographs of Ophiucus showed dark lanes through the nebula (Barnard, 1899). They were at the time interpreted by Agnes CLERKE, as "*glades and clearing*" in the stellar distribution (Clerke, 1903).
- Twenty years later, Edward BARNARD (Fig. II.7.a) realized these black patches were actually "*real, obscuring masses, most probably dark nebulae*" (Barnard, 1919).

The reddening of starlight. The selective extinction of starlight provided the first consensual evidence of ISD. This was realized at the beginning of the 1930's.

- Already in the middle of the XIX$^{\text{th}}$ century, Friedrich Georg Wilhelm STRUVE found that the stellar volume density is decreasing with distance from the Sun (Struve, 1847). This decrease could be explained by a $\simeq 1$ mag/kpc absorption by interstellar material. This is a factor of $\simeq 2$ from the actual value, which is wavelength-dependent.
- Dark nebulae and the extinction of starlight were both understood by Henry N. RUSSELL (Russell, 1922). In advance on his time, he noticed that "*in certain instances stars embedded in dense luminous nebulosity are abnormally red*". He finally deduced that this "*obscuration of light in space, therefore, whether general or selective with respect to wave-length, will be produced mainly by dust particles a few millionths of an inch in diameter*" (*i.e.* $\simeq 0.03-0.1$ µm).
- The seminal study of Robert J. TRUMPLER (Fig. II.7.b; Trumpler, 1930) provided the first solid evidence of ISD. His study was based on the observation, at the Lick observatory, of 100 open clusters. He found that the *diameter distances* (assuming all clusters have the same diameter) are always smaller than the *photometric distances* (based on the stellar spectral types), and this discrepancy increases with distance (Fig. II.6.b). This allowed him to interpret stellar color excesses as selective extinction by fine dust particles. He inferred particles of average mass

10^{-19} g or larger[4]. At the same time, Schalén (1929, 1931) independently arrived at a similar conclusions, at the Uppsala observatory.

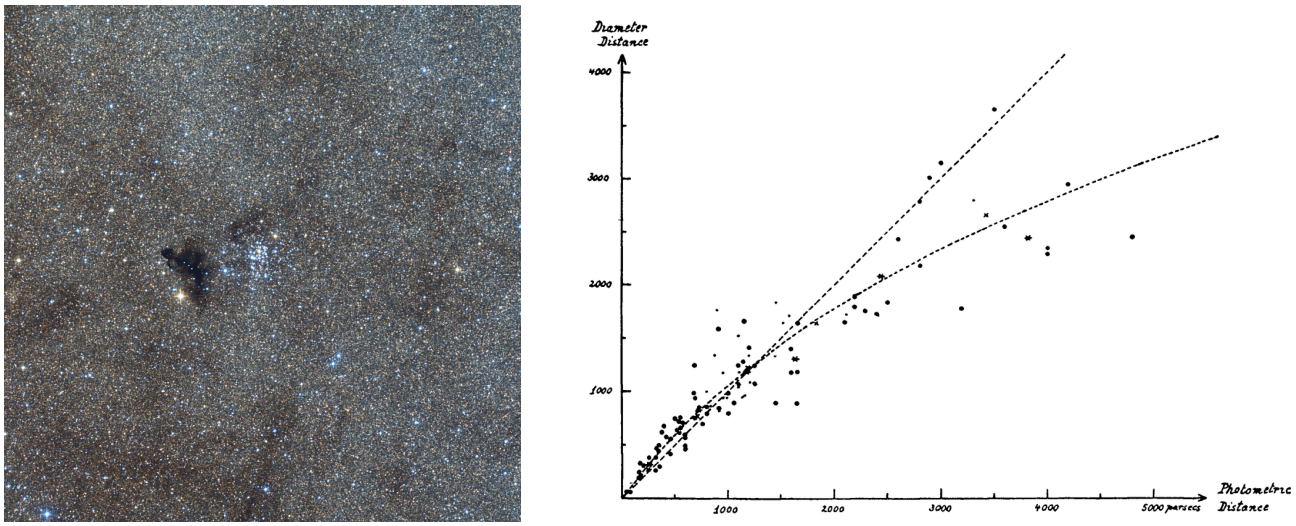

(a) The Ink Spot nebula *(b)* Trumpler (1930)'s relation

FIGURE II.6 – *First evidences of interstellar dust.* Panel *(a)* shows the *Ink spot* nebula (B 86), that was originally mistaken by Herschel as a "*hole in the heavens*". Panel *(b)* shows the relation between the photometric and diameter distances of 100 open clusters (Fig. 1 of Trumpler, 1930). The non-linearity of this relation provided the first unambiguous evidence for ISD. Notice the absence of error bars: this plot is from a long gone epoch, when major scientific discoveries could be accompanied by a feeling of airiness and eyeball statistics. Credit: *(a)* Gábor Tóth Astrophotography, licensed under CC BY-NC-ND; *(b)* Trumpler (1930).

II.1.2.2 The Dust Continuum

The Shape of the extinction curve. The investigation of the spectral shape of the extinction curve started right after Trumpler's study.

- A series of papers (Rudnick, 1936; Hall, 1937; Greenstein, 1938; Stebbins et al., 1939) concluded that $\kappa(\lambda)$ was roughly proportional to $1/\lambda$ in the $\lambda = 0.3-1$ µm range. By the end of the 1930's, it was thus clear that the grains responsible for the visible light extinction were not in the Rayleigh regime ($\kappa_{sca}(\lambda) \propto 1/\lambda^4$; Sect. I.2.2.3).
- Stebbins & Whitford (1943) extended the study of extinction curves to the $0.35\ \mu m < \lambda < 1.03\ \mu m$ range, and found deviations to the $1/\lambda$ behavior, due to the now well-known far-UV rise and NIR knee (Sect. II.2.1).
- During the 1950's and 1960's followed a discussion on the universality of the shape of the extinction curves (*cf.* references in Li, 2005).
- Starting in the 1960's, the first airborne and space observatories opened the UV window, up to the Lyman break (York et al., 1973). The 2175 Å bump was discovered by Stecher (1965, *cf.* Sect. II.1.2.3).
- The first UV extinction curves in the *Large Magellanic Cloud* (LMC) were measured by Borgman et al. (1975), and by Koornneef (1978) in 30 Doradus. In the *Small Magellanic Cloud* (SMC), it was first measured by Rocca-Volmerange et al. (1981). In both cases, the steepness of the curve and the weakness of the bump were noted.

4. Assuming $\rho \simeq 3$ g/cm^3, the radius of these particles would be $a \simeq 2$ nm or larger.

- Cardelli, Clayton, & Mathis (1989) performed a mathematical fit to a collection of extinction curves toward different sightlines in the MW. They found that, over the 0.125 µm < λ < 3.5 µm range, the shape is universal and controlled by a single parameter, R(V) = A(V)/(A(B) − A(V)) (where A(λ) is the magnitude extinction; *cf.* Sect. II.2.1).
- ISO observations of the Galactic center exhibited a flatter MIR curve (Lutz et al., 1996), confirmed by Indebetouw et al. (2005) with *Spitzer* data.

Polarization by dichroic extinction. Hall (1949) and Hiltner (1949) found that starlight was linearly polarized.

- Davis & Greenstein (1951) proposed that this polarization is due to dichroic extinction by non-spherical particles aligned on the magnetic field (*cf.* Sect. I.2.2.5).
- Serkowski (1973) determined the wavelength dependence of the polarization fraction, known as the *Serkowski curve* (*cf.* Sect. II.2.1.4).

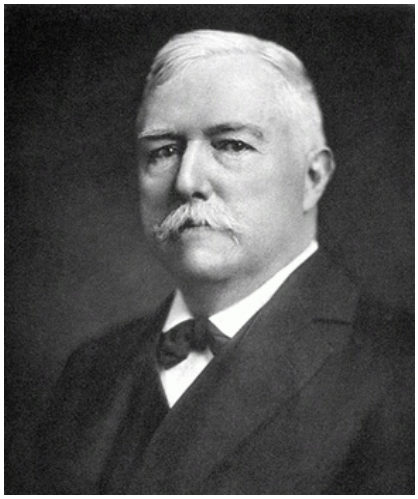

(a) Edward E. BARNARD (1857–1923)

(b) Robert J. TRUMPLER (1886–1956)

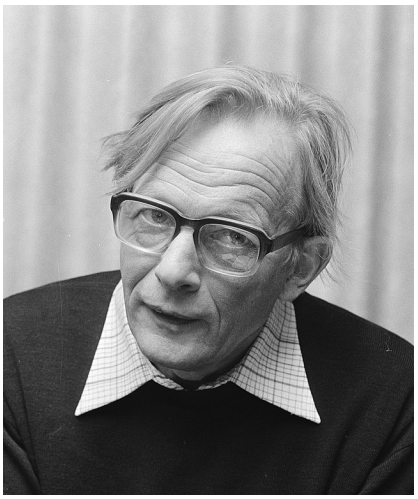

(c) Hendrik C. VAN DE HULST (1918–2000)

FIGURE II.7 – *The pioneers.* Credit: *(a)* Wikipedia, public domain; *(b)* Weaver & Weaver (1957); *(c)* Rob BOGAERTS, licensed under CC BY-SA 3.0 NL.

Dust emission. The thermal emission of heated grains started to be observed in the 1960's. The presence of very small grains or large molecules with $a \lesssim 1$ nm was speculated by Platt (1956, they are known as *Platt particles*).

- Greenberg (1968) first realized that small grains must be stochastically heated.
- Andriesse (1978) reported the first observational evidence of such transiently heated Platt particles in M 17. The spectral shape of the MIR spectrum was indeed constant over the region, and much wider than a single grey body emission, consistent with temperatures up to 150 K.
- Similarly, the NIR continuum and 3.3 µm feature emission of several reflection nebulae was shown by Sellgren et al. (1983) to be consistent with small grains fluctuating up to 1000 K.
- The presence of small grains in the diffuse ISM was clearly evidenced by the 12 and 25 µm IRAS emission (Boulanger & Perault, 1988). It was observed by numerous studies afterward in all types of interstellar regions and galaxies.

II.1.2.3 Identification of Dust Features

The confirmation of the presence of various solid-state and molecular features was important to better constrain the dust composition.

Silicates. The first identification of silicates was reported by Woolf & Ney (1969), in absorption toward M giant and supergiant stars. Kemper et al. (2004) provided a 2 % upper limit on the crystalline silicate fraction, based on ISO observations toward the Galactic center. The MIR features, proper to crystalline silicates were indeed not detected.

Carbonaceous grains. MIR aromatic emission features were first detected in the *Planetary Nebula* (PN) NGC 7027 by Gillett et al. (1973, *cf.* Fig. II.8.a). They were called at the time *Unidentified Infrared Bands* (UIBs). They were attributed to the bending and stretching modes of PAHs ten years later (Duley & Williams, 1981; Léger & Puget, 1984; Allamandola et al., 1985, *cf.* Fig. II.8.b). The 3.4 µm aliphatic feature in absorption was first detected toward the Galactic center by Willner et al. (1979).

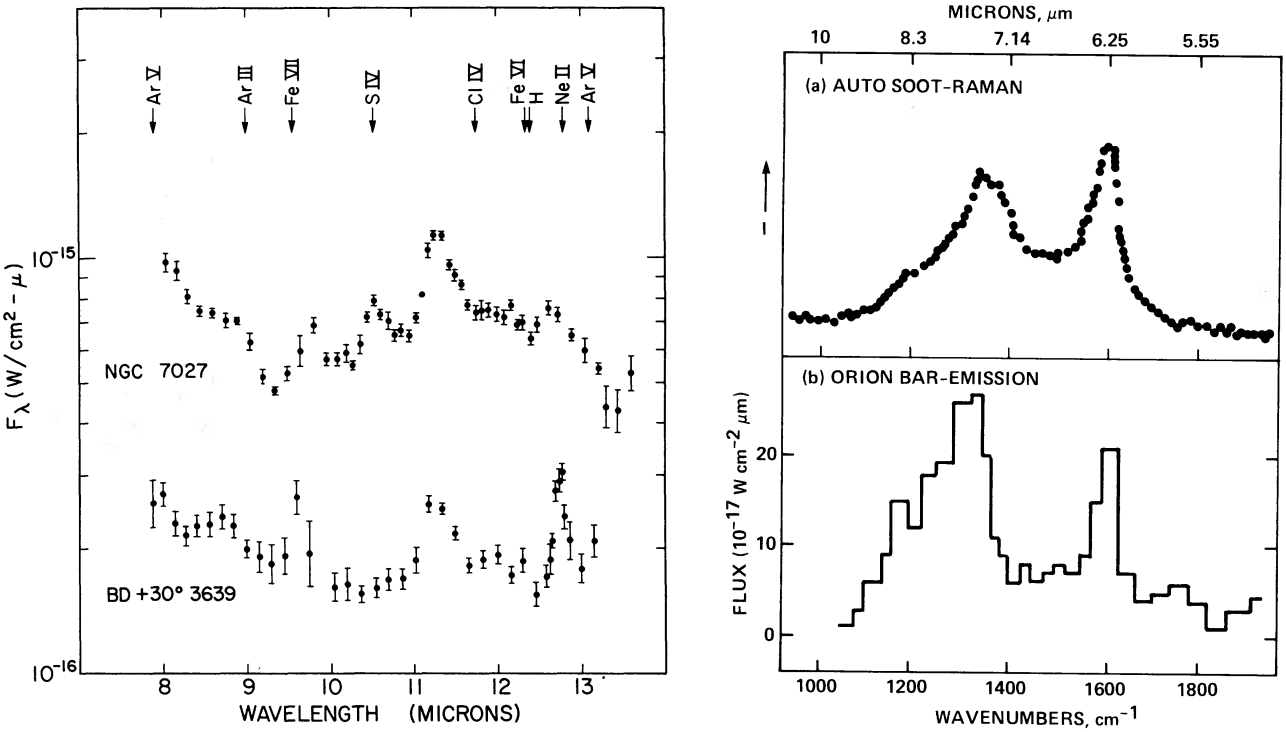

(a) First detection of UIBs *(b)* Attribution of UIBs to PAHs

FIGURE II.8 – *First detection of UIBs.* Panel *(a)* shows the first detection of the 8.6 and 11.3 µm aromatic features by Gillett et al. (1973), in the planetary nebulae NGC 7027 and BD+30°3639. The red wing of the 7.7 µm is also visible. Panel *(b)* shows the qualitative comparison between a laboratory spectrum of soot and the UIBs in the Orion bar, by Allamandola et al. (1985). Credit: *(a)* Fig. 1 of Gillett et al. (1973); *(b)* Fig. 1 of Allamandola et al. (1985).

Ices. Ice absorption features have been searched for since the 1940's and the *dirty ice model* (*cf.* Sect. II.1.2.5).

- The 3.1 µm H_2O ice band was finally detected by Gillett & Forrest (1973).
- Lacy et al. (1984) provided the first observational identification of CO ice absorption.
- CO_2 ice absorption was discovered in ISO/SWS spectra (de Graauw et al., 1996; D'Hendecourt et al., 1996; Guertler et al., 1996).

X-ray edges. The absorption of X-ray photons by inner electronic shells can provide information on the crystalline configuration of solids (*e.g.* Forrey et al., 1998; Draine, 2003c, for the theoretical predictions). The first X-ray absorption edges were detected in Chandra and XMM-Newton data (Paerels

et al., 2001), but their interpretation remained problematic. More recent studies have been able to constrain grain structures using these features (*e.g.* Lee et al., 2009b).

II.1.2.4 Dusty Epiphenomena

Diffuse Interstellar Bands. There are unidentified, ubiquitous absorption features in the $\lambda \simeq 0.4 - 2$ µm range, called *Diffuse Interstellar Bands* (DIBs; *cf.* Sect. II.2.1.5).

- They were first reported by Heger (1922a,b).
- It was only Merrill (1934) who showed their interstellar nature.
- More than 400 of them have been identified toward a diversity of sightlines, even in external galaxies (Hobbs et al., 2009). They remain largely unidentified, although four of them have been attributed to C_{60}^+ (Campbell et al., 2015; Walker et al., 2015).

Extended Red Emission. The *Extended Red Emission* (ERE) is a broad emission band, found in the $\lambda \simeq 0.6 - 0.9$ µm range of a diversity of Galactic environments. It is attributed to dust photoluminescence (*e.g.* Witt & Vijh, 2004), but the nature of its carriers is still debated. Photoluminescence is a non-thermal emission process in which, subsequently to the absorption of a UV photon, a grain is brought to an excited electronic state. After partial internal relaxation, a redder photon is emitted, bringing the electron back to its fundamental state. The ERE was first reported in the *Red Rectangle* reflection nebula (Schmidt et al., 1980).

Spinning Grains. The radio emission of fastly spinning dust grains was predicted by several authors (Erickson, 1957; Hoyle & Wickramasinghe, 1970; Ferrara & Dettmar, 1994).

- Kogut et al. (1996) detected an *Anomalous Microwave Emission* (AME) in the COBE/DMR data. This excess could not be explained by thermal dust, free-free and synchrotron emissions.
- Draine & Lazarian (1998a,b) showed the AME could be explained by the rotational emission of small, charged, fastly rotating grains.

II.1.2.5 Dust Models

First models. The first dust models of the 1930's, following Trumpler's study, were mainly speculative.

- The first assumptions about the dust composition were made by analogy with micrometeorites. Schalén (1936) and Greenstein (1938) assumed grains were made of $a = 0.01$ µm iron particles. Lindblad (1935) had assumed dust could form by condensation in space.
- The *dirty ice model* (Oort & van de Hulst, 1946; van de Hulst, 1949) was the first attempt to base the dust composition on the abundant atoms: H, C, N, O. These atoms would form various ices (H_2O, CH_4, NH_3) nucleating on grain seeds. The predicted dust temperature of this model was $\simeq 15$ K, close to the actual value ($\simeq 18$ K).
- Several studies hypothesized that graphite could be a major dust constituent, explaining the polarization of starlight, because of its anisotropic crystalline structure (Cayrel & Schatzman, 1954; Hoyle & Wickramasinghe, 1962). Graphite was supported by the discovery of the 2175 Å bump (Stecher, 1965; Stecher & Donn, 1965).
- Donn (1968) hypothesized that PAHs could be responsible for the 2175 Å bump, which was supported by the laboratory measurements of Joblin et al. (1992).
- The *MRN model* (Mathis, Rumpl, & Nordsieck, 1977) was the first attempt at fitting the average extinction curve of the MW with a mixture of graphite and silicate grains, with a power-law size distribution:

$$f(a) \equiv \frac{\mathrm{d}N}{\mathrm{d}a} \propto a^{-3.5} \quad \text{for} \quad a_- < a < a_+, \tag{II.1}$$

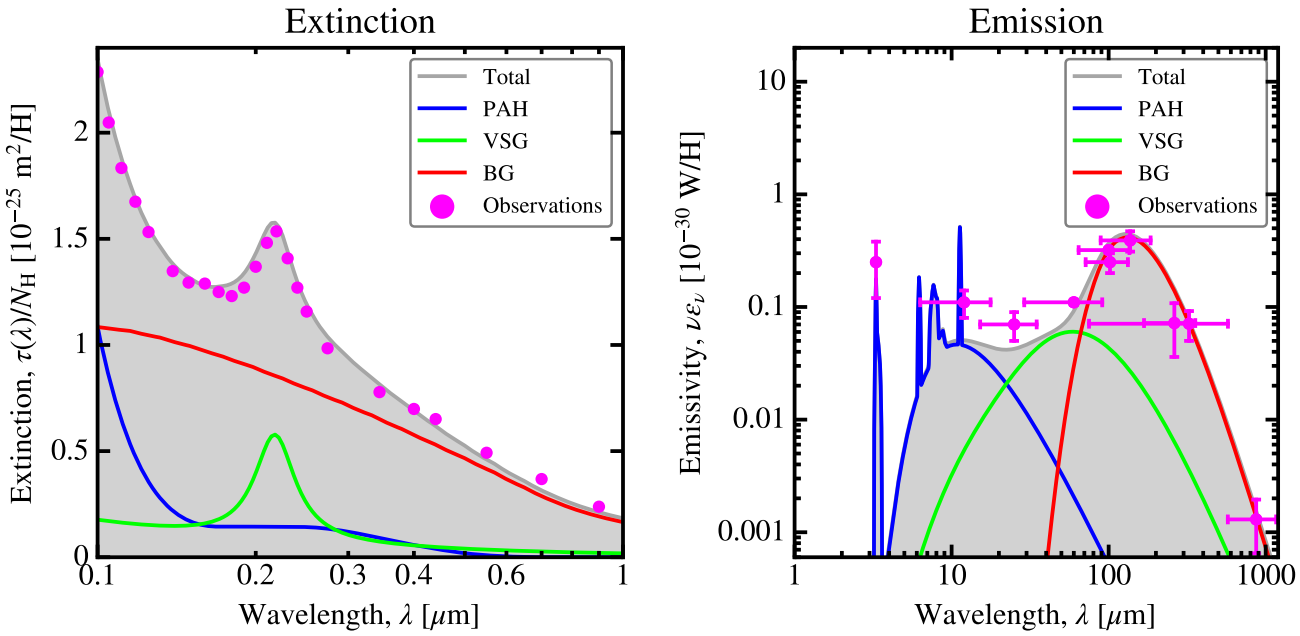

FIGURE II.9 – *Désert et al. (1990) dust model.* These two panels show the DBP90 model extinction and emission, and how it fits the observations of the diffuse Galactic ISM. We have shown its three components: PAH, VSG and BG. Notice the vintage-looking square shaped PAH features of this pre-ISO model. Licensed under CC BY-SA 4.0.

where $[a_-, a_+] = [0.005, 1]$ µm for graphite and $[a_-, a_+] = [0.025, 0.25]$ µm for silicates.

Calculation of the optical properties. Dust models rely on the computation of optical properties. The techniques have improved with time. The laboratory measurements on the most relevant compounds also expanded.

- Mie theory (*cf.* Sect. I.2.2.3) was independently developed by Gustav MIE and Peter DEBYE (Mie, 1908; Debye, 1909).
- The DDA method (*cf.* Sect. I.2.2.4) was developed by Purcell & Pennypacker (1973).
- Draine & Lee (1984) presented the first UV-to-mm optical properties of astronomical silicate and graphite. These properties have been refined by numerous studies afterward.
- Similarly, synthetic optical properties of a mixture of astronomical PAHs were presented by Li & Draine (2001) and updated by Draine & Li (2007).
- The properties of various amorphous carbon compounds were inferred from laboratory data by Rouleau & Martin (1991) and Zubko et al. (1996). Jones (2012a,b,c) presented a physical parametrization of the optical properties of a-C(:H).

Elemental depletions. Elemental depletions (*cf.* Sect. II.2.3) are an important set of constraints on the dust mass and on the stoichiometry of the dominant grain compounds. Greenberg (1974) laid the ground for such studies. Savage & Bohlin (1979) showed that the depletion strength correlates well with the average density of the gas. Several studies have refined this approach. Jenkins (2009) presented a unified view, showing depletions were controlled by a single parameter, correlated with the column density.

Modern panchromatic models. With the COBE and IRAS data, dust models started to have the possibility to be constrained by both the emission and the extinction. These simultaneous constraints are important to break the degeneracy between the composition and the size distribution.

- The Désert, Boulanger, & Puget (1990) model (hereafter DBP90) was the first silicate-carbon-PAH model, fitting the extinction and emission of the Galactic diffuse ISM (Fig. II.9). This model had three components: the PAHs, the *Very Small Grains* (VSG; small carbon grains) and the *Big Grains* (BG; large carbon-coated silicates).
- Dwek et al. (1997) built the first model constrained by the fine spectral sampling of the COBE data (DIRBE broadbands and FIRAS spectrum).
- Zubko, Dwek, & Arendt (2004) added the elemental depletions to the emission and extinction, to constrain more accurately the grain composition.
- Jones et al. (2013, 2017) developed the *The Heterogeneous Evolution Model for Interstellar Solids* (THEMIS). This model is physically parametrized to account for the known evolution of the dust mixture as a function of the physical conditions.
- Guillet et al. (2018) presented a dust model accounting for the polarized emission observed by *Planck*.

II.2 The Current Empirical Constraints

We now review the current empirical constraints that are used to build dust models. These models are calibrated on observations of the diffuse Galactic ISM. This medium indeed presents several advantages.

- It is optically thin. No radiative transfer is thus needed.
- It appears to be rather uniformly illuminated. The mixing of heterogeneous physical conditions along the sightline is probably limited.
- Dust properties of the diffuse ISM appear rather uniform.
- It benefits from a wealth of observations.

Observations of the diffuse Galactic ISM are thus the most important ones. Extragalactic constraints are the focus of Chap. III. It is currently impossible to gather the same type of data set, at the same level of accuracy, in external galaxies.

Several reviews discuss the available dust observables (*e.g.* Draine, 2003a; Dwek, 2005; Draine, 2009; Galliano et al., 2018; Hensley & Draine, 2021). We have represented on Fig. II.10 most of these observables on top of the typical SED of a gas-rich galaxy.

☞ A fundamental local quantity of the ISM is the *dust-to-gas mass ratio* or *dustiness*[5]:

$$Z_{dust} \equiv \frac{M_{dust}}{M_{gas}}. \tag{II.2}$$

II.2.1 Extinction

Dust extincts light from the X-rays to the MIR. The effect of dust extinction on a background source is sometimes referred to as *reddening*. It is indeed more important on the blue side of the visible window.

5. We are trying to promote the term *dustiness*, introduced by G21, as it is much more concise than *dust-to-gas mass ratio*.

	THE PREHISTORY
1785	Herschel's *Construction of Heavens*
1800	Herschel's discovery of infrared radiation
1847	Struve's dimming of starlight
1880	First deep-sky photograph by Henry DRAPER
1900	Planck's black body radiation
1908	Mie theory
1919	Barnard's obscuration
1922	Heger's first observation of DIBs
	THE CLASSICAL ERA
1930	Trumpler's color excess study
1934	Interstellar nature of DIBs
1936	Small metallic particle model
1949	Dirty ice model
1949	Polarization of starlight
1965	Discovery of the 2175 Å bump
1969	First observation of silicate features
1970	First dust radiative transfer models
1973	First detection of the UIBs
1973	Serkowski curve
1977	MRN model
1978	First evidence of small, stochastically heated grains
1979	First detection of the 3.4 µm feature
1980	First detection of ERE
1983	ISRF of Mathis, Mezger & Panagia
	THE SPACE AGE
1983	Launch of IRAS
1984	Draine & Lee optical properties
1984	PAHs proposed to explain the UIBs
1989	Launch of COBE
1989	Parametrization of the Galactic extinction curve by Cardelli, Clayton & Mathis
1990	Désert, Boulanger & Puget model
1995	Launch of ISO
1996	First detection of AME
2003	Launch of *Spitzer*
2004	Zubko, Dwek & Arendt model
2009	Launch of *Herschel* & *Planck*
2011	Revision of dust opacities
2013	THEMIS model
2015	Whole-sky maps of the polarized dust emission
2015	Identification of two DIBs
2018	Polarized dust emission model
2021	Launch of JWST?
	...
	THE QUANTUM AGE?

TABLE II.1 – *Chronology of the main ISD breakthroughs.* If this chronology happens to be representative in any way, it shows that the recent progress relies more on conceptual breakthroughs and space missions, whereas the progress in the early days was mainly observational.

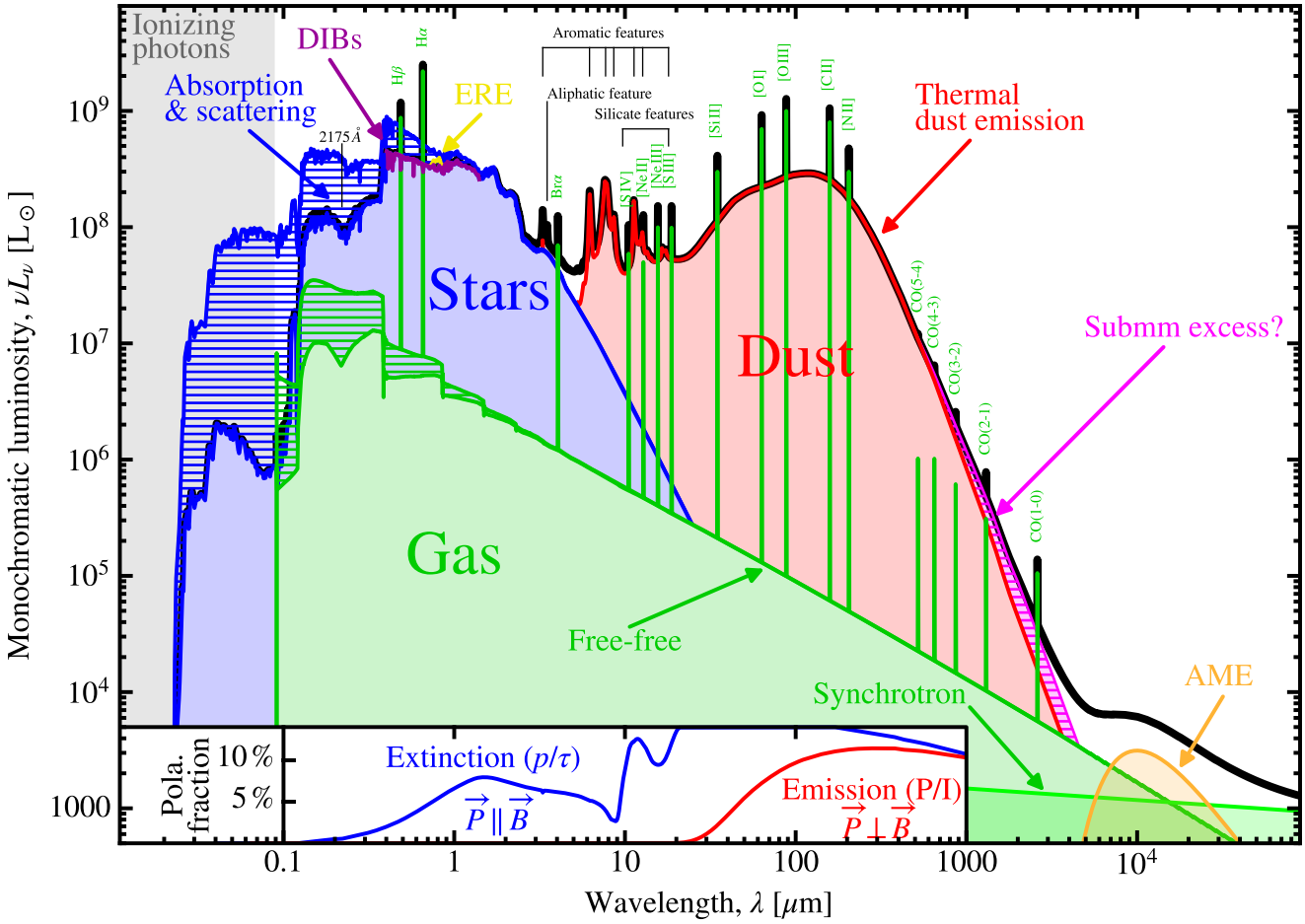

FIGURE II.10 – *Panchromatic dust observables.* Spectral energy distribution of a typical late-type galaxy (Galliano et al., 2018). The blue hatched area shows the power absorbed by dust. Typical DIB, ERE and AME spectra are shown, together with the most relevant gas lines. The free–free continuum is emitted by the deceleration of free electrons scattering off ions in ionized regions. The synchrotron continuum is emitted by electrons spiraling through the magnetic field. Here, L_ν is the electromagnetic power emitted per unit frequency. Inset: Model D of Guillet et al. (2018), with $G_0 = 100$; τ is the optical depth, p is the starlight polarization degree, P is the polarization intensity, I is the total intensity, $\vec{P}$ is the light polarization vector, and $\vec{B}$ is the magnetic field vector. Licensed under CC BY-SA 4.0.

II.2.1.1 UV-to-NIR Extinction

The extinction magnitude. We saw in Sect. II.1.2.1 that the first dust studies were performed in extinction, in the visible range. Consequently, extinction properties were characterized by quantities depending on the magnitude system. The magnitude, $m(\lambda_0)$, of a star of flux $F_\nu(\lambda_0)$, observed through a photometric filter centered at wavelength λ_0, is:

$$m(\lambda_0) \equiv -2.5 \log\left(\frac{F_\nu(\lambda_0)}{F^0_\nu(\lambda_0)}\right), \tag{II.3}$$

where $F^0_\nu(\lambda_0)$ is the reference flux or *zero-point* of the photometric filter. The zero-point is a calibration quantity, independent of the observed source. Two important bands for characterizing extinction are the B and V bands, centered respectively at $\lambda_B = 0.44$ µm and $\lambda_V = 0.55$ µm (Table B.5). The *total extinction* or *extinction in magnitude* is defined as:

$$A(\lambda_0) \equiv m_{obs}(\lambda_0) - m_{int}(\lambda_0) = 2.5 \log\left(\frac{F^{int}_\nu(\lambda_0)}{F^{obs}_\nu(\lambda_0)}\right), \tag{II.4}$$

where the index "*obs*" refers to the *observed* quantity, and "*int*" refers to the *intrinsic* quantity, that is the quantity not affected by dust extinction. In the MW, the average V-band extinction over the distance to the star, d, is $A(V)/d \simeq 1.8\,\mathrm{kpc}^{-1}$ (*e.g.* Whittet, 2003). $A(\lambda_0)$ can be linked to a more physical quantity, the *optical depth*:

$$\tau(\lambda) = \underbrace{\kappa(\lambda)}_{\text{dust opacity}} \times \underbrace{\rho}_{\text{ISM density}} \times \underbrace{L}_{\text{length of the sightline}} = \kappa(\lambda) \times \underbrace{\frac{Z_{\mathrm{dust}}}{1-Y_\odot-Z_\odot}}_{\text{H mass fraction}} \times \underbrace{m_{\mathrm{H}}}_{\text{H atom mass}} \times \underbrace{N_{\mathrm{H}}}_{\text{column density}} . \tag{II.5}$$

The expression above has been derived assuming homogeneous properties along the sightline (*cf.* Sect. III.1.1 for a more rigorous definition of τ). The observed flux can conveniently be expressed as a function of the optical depth:

$$F_\nu^{\mathrm{obs}}(\lambda) = F_\nu^{\mathrm{int}}(\lambda) \times \exp\left[-\tau(\lambda)\right]. \tag{II.6}$$

☞ Eq. (II.4) therefore implies that: $A(\lambda) = 1.086 \times \tau(\lambda)$.

The selective extinction. The spectral shape of the extinction curve varies among sightlines. It can be quantified by the *selective extinction*, $E(\lambda-\lambda_0) \equiv A(\lambda) - A(\lambda_0)$. In the MW, Cardelli, Clayton, & Mathis (1989) showed that the UV-to-NIR extinction curves follow a universal law, parametrized by the sole visual-to-selective extinction ratio:

$$R(V) \equiv \frac{A(V)}{A(B)-A(V)}. \tag{II.7}$$

This parametrization is demonstrated in Fig. II.11.a. We see that $A(V)$ is a scaling parameter quantifying the amount of extinction along the sightline. According to Eq. (II.5), $A(V) \propto Z_{\mathrm{dust}} \times N_{\mathrm{H}}$. In the MW, there are no drastic dustiness variations, thus $A(V) \propto N_{\mathrm{H}}$. On the other hand, $R(V)$ is a shape parameter. It typically varies between $R(V) \simeq 2$ and $R(V) \simeq 5$. On average, $R(V) \simeq 3.1$ in the MW. Curves with $R(V) \gtrsim 3.1$ tend to be flatter.

☞ The amount of extinction in the MW is $N_{\mathrm{H}}/E(B-V) \simeq 8.8 \times 10^{25}\,\mathrm{m}^{-2}\,\mathrm{mag}^{-1}$ (Lenz et al., 2017), or, for $R(V) = 3.1$, $N_{\mathrm{H}}/A(V) \simeq 2.8 \times 10^{25}\,\mathrm{m}^{-2}\,\mathrm{mag}^{-1}$.

The most notable features of the UV-to-NIR extinction curves are the following (*cf.* Fig. II.11.a).

The Far-UV (FUV) rise is mainly due to the absorption by small grains, in the Rayleigh regime ($A(\lambda) \propto 1/\lambda$; *cf.* Sect. I.2.2.3).

The 2175 Å bump is attributed to small sp^2-hybridized C bonds (*cf.* Sect. I.1.4).

The optical knee is mainly due to scattering by larger grains.

The NIR extinction can be approximated by a power-law: $A(\lambda) \propto \lambda^{-\alpha}$, with $\alpha \simeq 2.27$ (Maíz Apellániz et al., 2020).

Measuring extinction. The original method to measure the wavelength dependence of the extinction curve is the *pair method* (Stecher, 1965): two stars of the same spectral type are observed, one with a low, and one with a high foreground extinction. The extinction curve is directly derived from the differential SED or spectrum, assuming the dust properties are uniform along both sightlines. An alternative to this method consists in replacing the reference star by a synthetic spectrum, knowing the precise spectral type of the star (*e.g.* Fitzpatrick & Massa, 2005). This is demonstrated in Fig. II.11.b.

UV-visible scattering. Observations of starlight scattering by ISD can constrain the average albedo, $\tilde{\omega}$, and asymmetry parameter, $\langle\cos\theta\rangle$, of the grains (*cf.* Sect. I.2.2.3). Two types of observations are usually favored to that purpose.

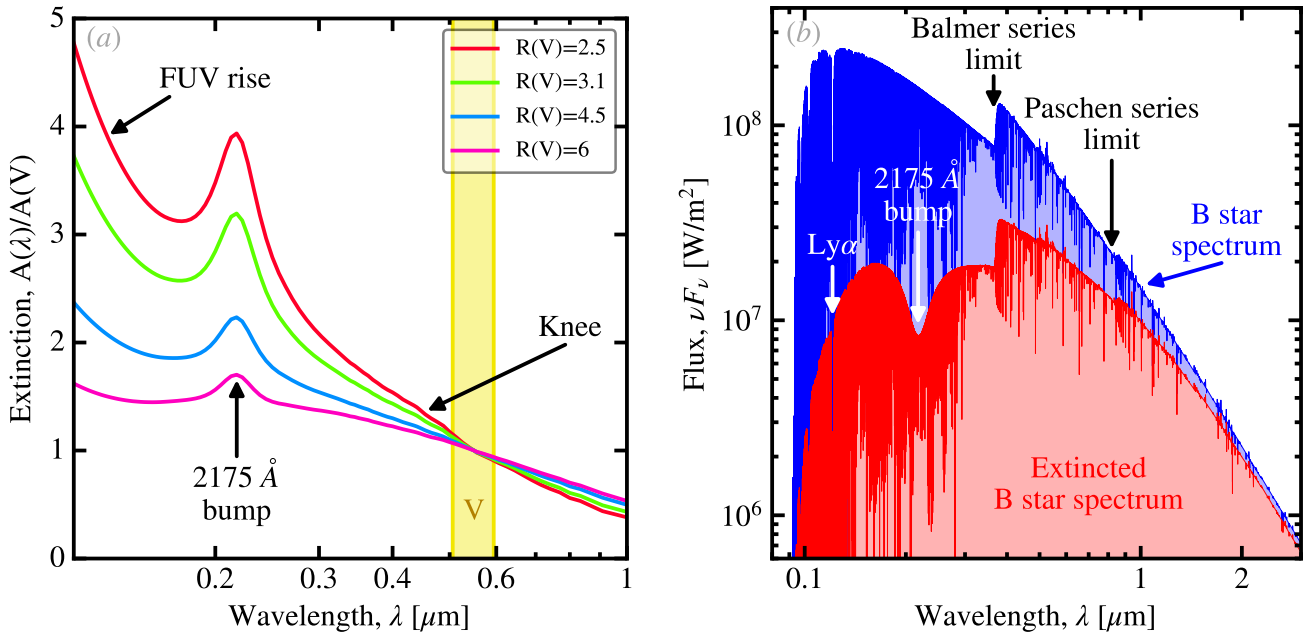

FIGURE II.11 – *Galactic extinction curves.* Panel *(a)* represents the average extinction curves from the spectroscopic sample of Fitzpatrick et al. (2019), for different values of R(V). Panel *(b)*: the blue line represents the synthetic, intrinsic UV-visible SED of a B star from the Lanz & Hubeny (2007) library; the red line is the extincted SED with A(V) = 1 and R(V) = 3.1. Licensed under CC BY-SA 4.0.

The *Diffuse Galactic Light* (DGL) is the scattering of the general ISRF by dust. It is the diffuse visible light seen in ISM regions without associated stars. The DGL was first detected by Elvey & Roach (1937). Henyey & Greenstein (1941) built their scattering phase function (*cf.* Sect. I.2.2.3) to explain this phenomenon.

Reflection nebulae are obvious objects to measure $\tilde{\omega}$ and $\langle\cos\theta\rangle$, as the visible light comes from a nearby star or cluster, and is scattered on the surface of a cloud facing us.

Both methods converge toward qualitatively consistent results:

☞ ISD has a UV-visible albedo around $\tilde{\omega} \simeq 0.5$, and is rather forward scattering ($\langle\cos\theta\rangle \gtrsim 0.5$), meaning grains are not in the Rayleigh regime (*cf.* Sect. I.2.2.3).

II.2.1.2 MIR Extinction

The MIR continuum. The spectral shape of the MIR extinction is harder to constrain than its UV-visible counterpart. The MIR range is indeed the domain where the stellar and dust SEDs intersect (*cf.* Fig. II.10). It is therefore difficult to precisely model the background sources toward which the extinction is measured.

- The Rayleigh-Jeans continuum of old stars, peaking in the NIR, such as G and K-type stars, can be used (*e.g.* Xue et al., 2016).
- Otherwise, H recombination lines (*e.g.* Lutz et al., 1996) or H_2 rovibrational lines (*e.g.* Bertoldi et al., 1999) provide an alternative. The ratio of a series of these lines can indeed be reasonably well modeled. Differences between the theoretical and observed ratios result from the extinction.

In the ISO days, there was a controversy about the 4-to-8 μm continuum, which seemed to be following the extrapolation of the NIR power-law trend (*e.g.* Bertoldi et al., 1999). However, Lutz et al. (1996) showed this continuum toward the Galactic center was relatively flat (*cf.* Fig. II.12.a). This has been confirmed by ulterior observations with *Spitzer*, WISE and AKARI (*e.g.* Indebetouw et al., 2005; Xue et al., 2016; Gordon et al., 2021). It seems to be a general feature of a wide variety of sightlines. The new synthetic extinction of Hensley & Draine (2021) reproduces this flat continuum (*cf.* Fig. II.12.a).

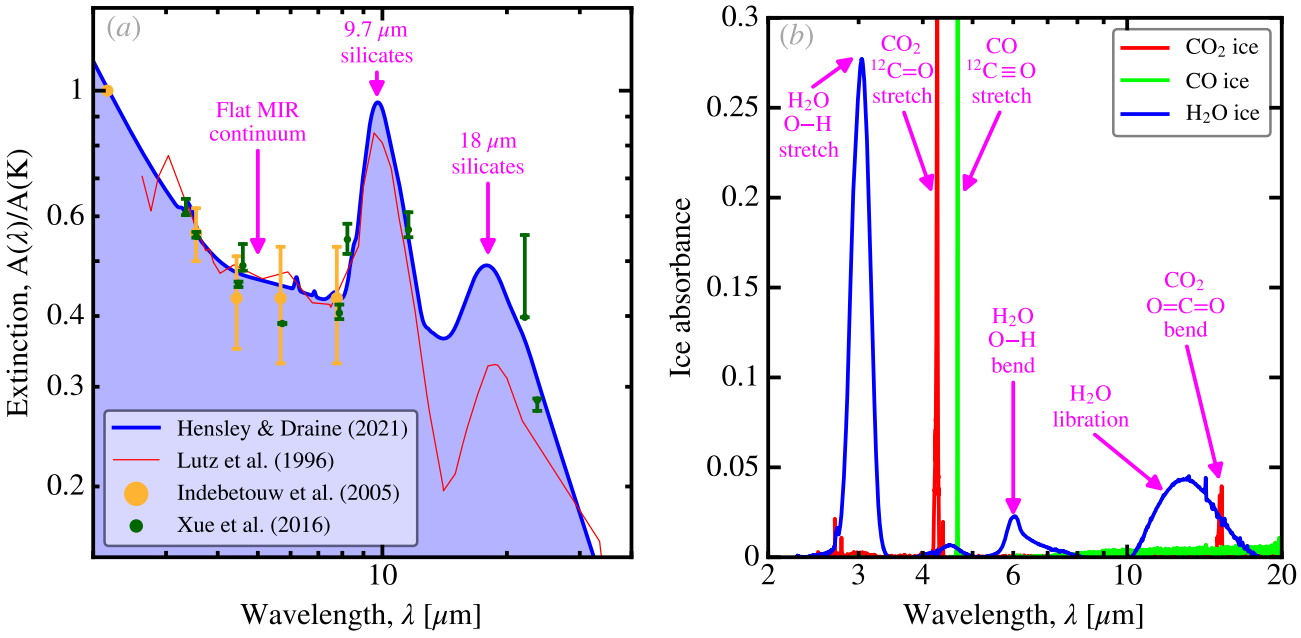

FIGURE II.12 – *MIR extinction.* Panel *(a)* shows the synthetic MIR extinction curve of Hensley & Draine (2021) (in blue). The ISO observations of the Galactic center by Lutz et al. (1996) are overlaid in red. We also show the *Spitzer*, WISE and AKARI observations (Indebetouw et al., 2005; Xue et al., 2016). Panel *(b)* shows the absorbance of the most abundant ices, taken from the *Leiden Database for Ice*. Water ice data are from Öberg et al. (2007), CO, from Fraser & van Dishoeck (2004), and CO_2, from Bisschop et al. (2007). All ices have been measured at 15 K. Licensed under CC BY-SA 4.0.

Silicate features. The observed profiles of the Si–O stretching and O–Si–O bending silicate features, at 9.7 and 18 μm (*cf.* Sect. I.1.4), are not perfectly matching those of olivine and pyroxene. This is the reason of the introduction of the concept of *astrosilicates* by Draine & Lee (1984).

- Interstellar silicates are indeed a mixture of different varieties of compounds, with different stoichiometry, and probably metallic inclusions.
- Interstellar silicates are predominantly amorphous. The interstellar crystalline silicate fraction seems to be $\lesssim 2\%$ (Demyk et al., 1999; Kemper et al., 2004; Do-Duy et al., 2020).

There are uncertainties about the profile of the features and its potential variations between sightlines.

The 9.7 μm feature has on average a FWHM of $\simeq 2.2$ μm. $A(V)/\tau(9.7) \simeq 9 \pm 1$ toward the GC (Kemper et al., 2004), but is higher when averaged over sightlines: $A(V)/\tau(9.7) \simeq 19$ (Roche & Aitken, 1984; Mathis, 1998). The synthetic extinction of Hensley & Draine (2021) has $A(V)/\tau(9.7) = 20$.

The 18 μm feature is weaker than the 9.7 μm, making its characterization more uncertain. The depth ratio of the two features is $\tau(9.7)/\tau(18) \simeq 2$ (Chiar & Tielens, 2006).

Ices. In regions shielded from the stellar radiation, some molecules can freeze out to form icy mantles onto grains (*cf. e.g.* Boogert et al., 2015, for a review). The dominant species are H_2O, CO and CO_2. They are responsible for several MIR absorption bands, shown in Fig. II.12.b. These ice features are not observed in the diffuse ISM. They start appearing at higher values of A(V), different compositions having different melting points. They are observed in dense regions, toward molecular clouds, *Young Stellar Objects* (YSO) or AGNs.

II.2.1.3 X-Rays

X-ray halos. Although the opacity of typical interstellar grains peaks in the UV (*cf. e.g.* Fig. I.19), grains extinct significantly X-rays. In this regime, photons have wavelengths approaching the size of

the atoms in the grain. Dust grains, when present along the sightline of an X-ray point source (such as a low-mass X-ray binary), scatter the radiation at small angles, creating an *X-ray halo* (Overbeck, 1965; Smith & Dwek, 1998). The properties of this halo are complex, as they depend on the grain properties: composition, porosity and maximum size (*e.g.* Smith, 2008). Such studies are limited by the uncertainty on the distance of the intervening dust and the background source. They however confirm the low abundance of grains larger than ≃ 0.1 µm (*e.g.* Valencic & Smith, 2015).

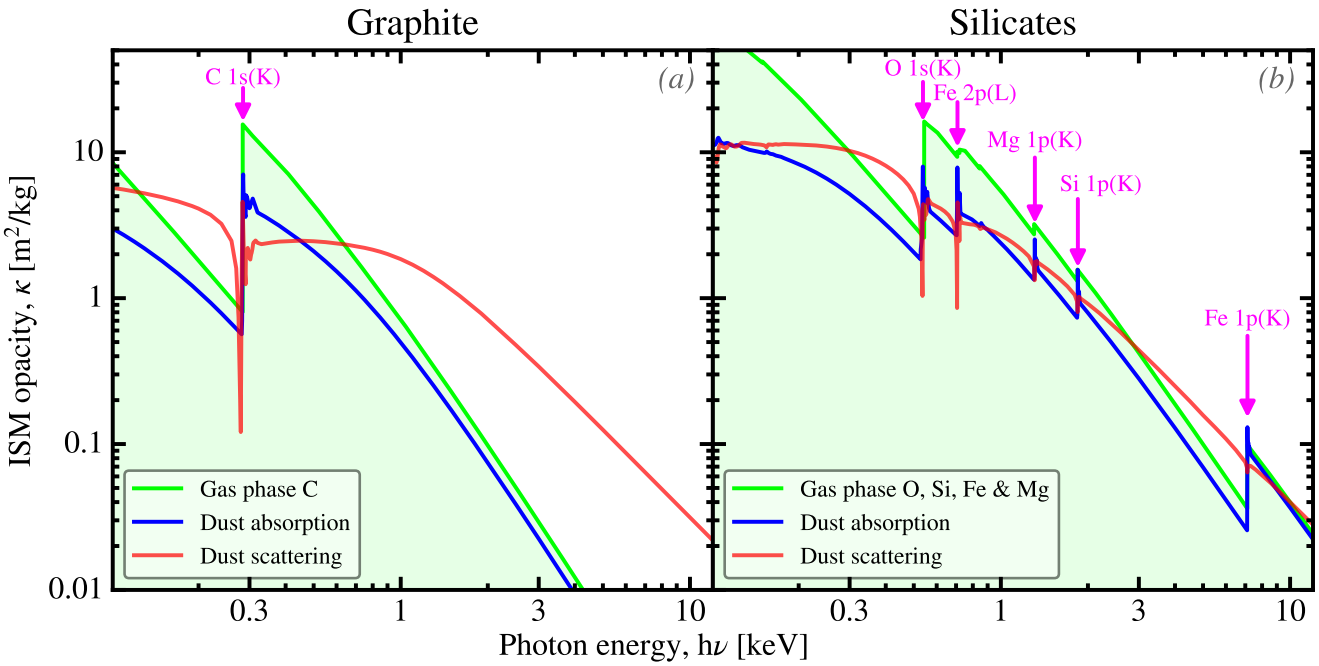

FIGURE II.13 – *X-ray edges.* The two panels show the absorption and scattering dust opacities (blue and red), and the gas opacity (green). The opacities are expressed per unit ISM mass. The gas opacity includes only the elements of the grains they are compared to (*i.e.* C for graphite, and O, Si, Fe and Mg for silicates). The dust cross-sections are from Draine (2003c). We have assumed an MRN size distribution and a Galactic dustiness. The gas cross-section has been computed with the `python` interface of `X-ray DB`. We have assumed the Solar abundances of Asplund et al. (2009). Licensed under CC BY-SA 4.0.

X-ray absorption edges. Atoms, whether in the gas phase, or locked-up in grains, exhibit X-ray absorption features at specific wavelengths, called *X-ray photoelectric edges* (*cf.* Fig. II.13). These edges correspond to the binding energies of the inner electrons, the letter (K or L in our case) corresponding to Bohr's orbitals (*cf.* Table I.2). The important point is that the energy and the spectral shape of these edges depend on the way the atom is paired (*e.g.* Draine, 2003c). It is thus possible, using X-ray spectroscopy, to differentiate atoms in the gas and dust phase, but also the crystalline structure of the grains (*e.g.* Lee et al., 2009a). For instance, Zeegers et al. (2017) studied the Si K edge along the line of sight of a Galactic X-ray binary. They were able to constrain the column density and the chemical composition of the silicate grains. This method was used to show that interstellar silicates are essentially Mg-rich, whereas the iron content is in metallic form (Costantini et al., 2012; Rogantini et al., 2019; Westphal et al., 2019). Finally, the crystalline fraction of silicates has been estimated to be in the range ≃ 11 – 15 %, using X-ray spectra (Rogantini et al., 2019, 2020). This is significantly higher than the ≃ 2 % upper limit derived from MIR spectroscopy (*cf.* Sect. II.2.1.2). This discrepancy might originate in the challenges of X-ray spectroscopy, which requires both high spectral resolution and high signal-to-noise ratios.

II.2.1.4 Dichroic Extinction

The light from a background source seen through a cloud containing elongated grains, with their rotation axis aligned along the magnetic field, is partially polarized (*cf.* Sect. I.2.2.5). In the MW, the wavelength-dependent polarization fraction follows the empirical law of Serkowski (1973), shown in Fig. II.14.a. It runs from the near-UV (NUV) to the NIR, peaking around $\lambda \simeq 0.55$ µm. It is well reproduced by models with elongated grains (*cf.* Fig. II.14.a and Guillet et al., 2018). The *polarized extinction fraction*, $p(\lambda)$, is often quoted: $p(\lambda) \equiv C_{pol}(\lambda)/C_{ext}(\lambda)$, where C_{pol} and C_{ext} are the polarized and total cross-sections.

☞ The interstellar polarized extinction peaks around $\lambda_{max} \simeq 0.55$ µm, and its fraction is $p(\lambda)/A(V) \lesssim 3\,\%/\mathrm{mag}$ (Andersson et al., 2015).

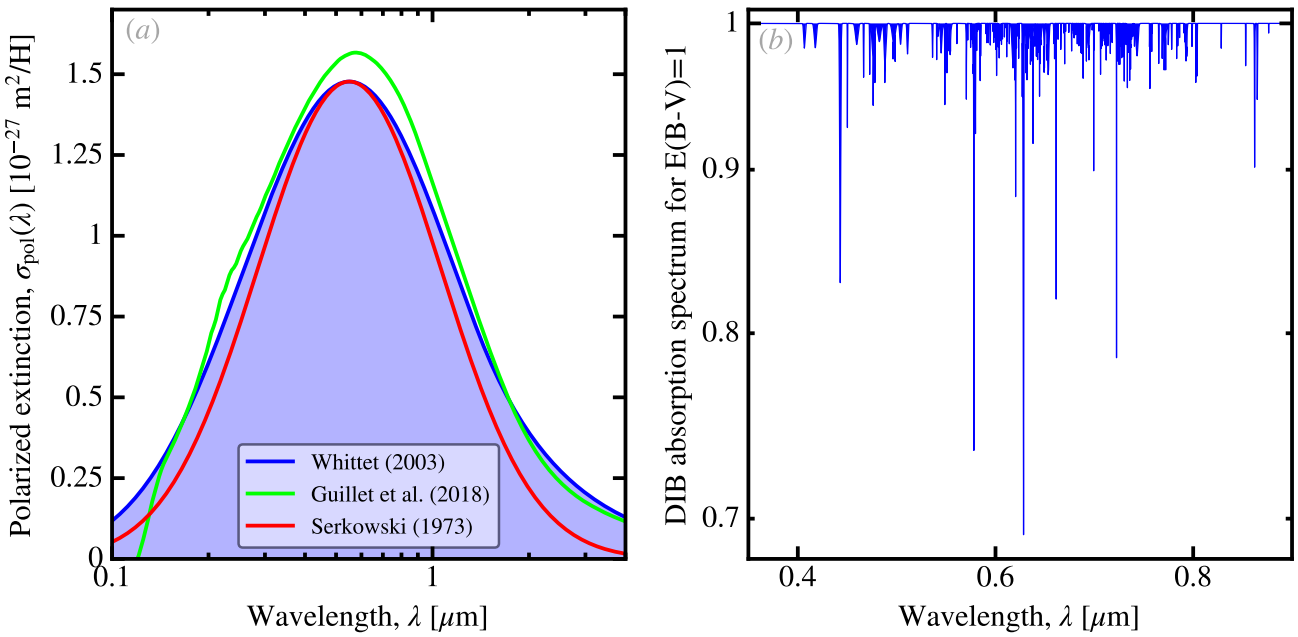

FIGURE II.14 – *Polarized extinction and DIBs.* Panel *(a)* shows the wavelength-dependent polarized extinction. The plotted quantity is the ratio between the polarized optical depth and the H column density, $\sigma_{pol}(\lambda) \equiv \tau_{pol}(\lambda)/N_H$ The blue curve represents the synthetic, compromise fit of Whittet (2003). The red curve is the original Serkowski (1973) profile. Both have been normalized so that $p(V)/E(B-V) = 0.13$ (Hensley & Draine, 2021). The green curve shows the model E of Guillet et al. (2018). Panel *(b)* shows the average absorption spectrum of DIBs from the study of Jenniskens & Desert (1994). It is for given for a typical $E(B-V) = 1$. Licensed under CC BY-SA 4.0.

II.2.1.5 Diffuse Interstellar Bands

DIBs are ubiquitous absorption features in the $\simeq 0.4-2$ µm range (*cf.* Fig. II.14.b). They are too broad to originate in atoms or simple molecules. They have to come from large molecules and/or small grains. Over 500 of them have been detected in the ISM (Fan et al., 2019). They are empirically associated with dust, as their strength correlates with $E(B-V)$ at low values, but they disappear in denser sightlines (*e.g.* Lan et al., 2015). To first order, DIBs correlate with each other, but there are some notable differences, suggesting that they have different carriers (Herbig, 1995). For instance, the so-called C_2 DIBs (Thorburn et al., 2003) appear to be found preferentially in diffuse molecular clouds. They remain largely unidentified, although four of them have been attributed to the ionized buckminsterfullerene, C_{60}^+, a football-shaped carbon molecule (Campbell et al., 2015; Walker et al., 2015). The MIR transitions of this molecule, as well as C_{70}, had been detected in the ISM, a few years before (Cami et al., 2010).

II.2.2 Emission

As we have discussed in Sect. I.2.4, dust emits thermally in the IR. This thermal emission is also partially polarized. We will see in this section that there are also non-thermal emission components.

II.2.2.1 Infrared Continuum and Features

Observations of the diffuse ISM. Fig. II.15 represents the NIR-to-cm SED of the diffuse Galactic ISM. Those are the observations used to constrain the dust models we will discuss in Sect. II.3. The challenge of building such a data set is ensuring that these fluxes correspond to the emission of the most diffuse regions of the MW, characterized by its H column density ($N_H \simeq 10^{24}$ m^{-2}). The disk of the MW contains the densest regions (*cf.* Fig. II.4.b). It is also important to ensure avoiding denser regions, as grain properties evolve, probably due to the accretion of mantles (*e.g.* Ysard et al., 2015). These observations therefore focus at high Galactic latitude, b, and low N_H. For instance, Compiègne et al. (2011) used data at $|b| > 6°$ and $N_H < 5.5 \times 10^{24}$ m^{-2}. Hensley & Draine (2021) gives a more a complete discussion about the homogenization of the different datasets. At these emission levels, there are several contaminations that need to be subtracted.

The zodiacal foreground is the MIR emission from the interplanetary dust in the Solar system disk.

The CIB that we have already discussed in Fig. I.28 is the accumulated emission of background galaxies. Its SED is very similar to the emission of the MW, and thus difficult to subtract.

The CMB is the mm emission shown in Fig. I.28.

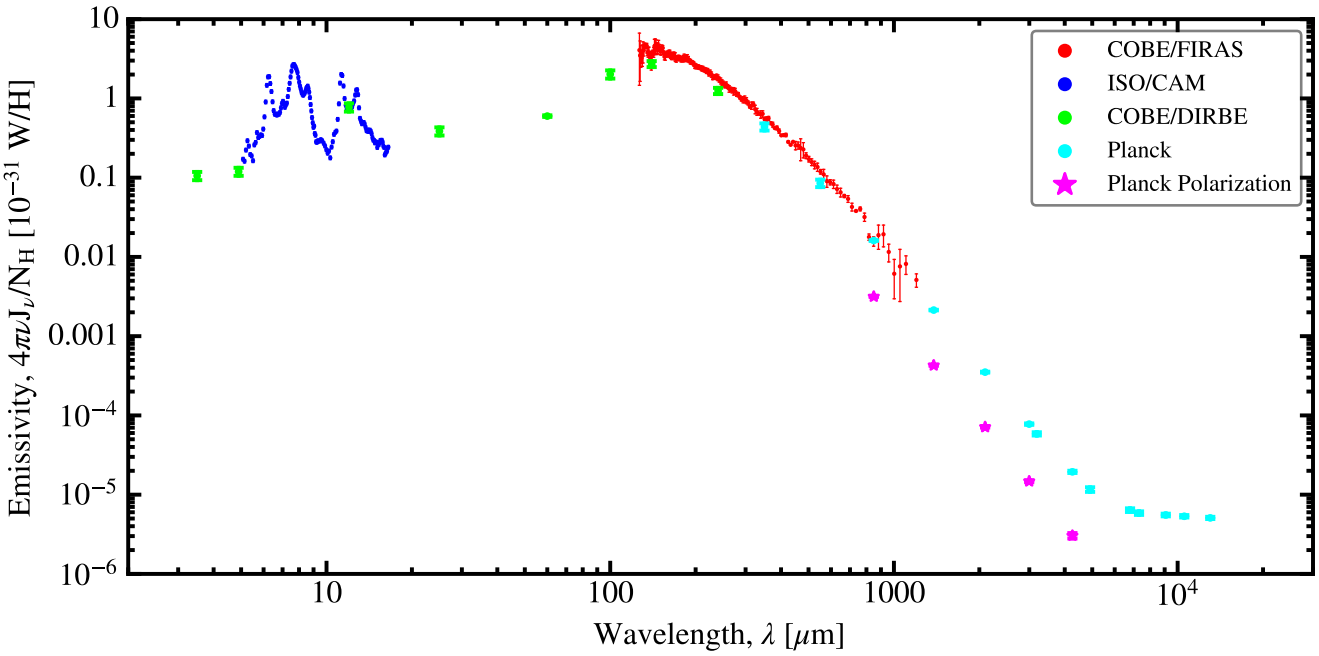

FIGURE II.15 – *Galactic diffuse ISM SED.* These observations are the typical constraints on the emission of dust models. The DIRBE data are from Dwek et al. (1997); the ISOCAM spectrum is from Flagey et al. (2006); the FIRAS spectrum has been reprocessed by Compiègne et al. (2011); and the *Planck* data are from Planck Collaboration et al. (2014b, 2015b). The polarized emission is from Planck Collaboration et al. (2015b): it is the linearly polarized intensity (Eq. I.54), $4\pi\nu P_\nu/N_H$. Licensed under CC BY-SA 4.0.

MIR features. The average MIR spectrum of the diffuse Galactic ISM is represented in Fig. II.15 (in blue). This particular spectrum corresponds to a smaller patch of the sky, and is scaled on the DIRBE

12 µm photometry (Flagey et al., 2006; Compiègne et al., 2011). There are indeed no MIR spectroscopic all sky surveys. The MIR constraints of dust models prior to Compiègne et al. (2011) were only the DIRBE broadbands. This difference in MIR coverage has consequences on the derived abundances and profiles of the aromatic feature carriers that we will discuss on Sect. II.3. The profiles and relative intensities of the main aromatic features can alternatively be constrained by a combination of laboratory data and the emission of nearby gas-rich galaxies (*e.g.* Draine & Li, 2007; Hensley & Draine, 2021).

II.2.2.2 Polarized Emission

We have seen in Sect. I.2.2.5 that elongated grains emit polarized IR radiation. Although the polarized submm emission of the ISM had been measured from various balloon-borne observatories (Benoît et al., 2004; Bennett et al., 2013), the *Planck* satellite provided the first all sky survey in several bands (Planck Collaboration et al., 2015b). These observations point toward one major result: large ISM grains have homogeneous properties. In other words, the IR emission can not originate in the mixing of several heterogeneous grain populations. Small grains have a negligible polarization effect. The models of Guillet et al. (2018), which account both for total intensity and polarization, indeed provide the best fit for a single population of large composite astrosilicates with a-C mantles. In parallel, Planck Collaboration et al. (2020b) showed that the polarized SED was consistent with a single MBB with $\beta \simeq 1.5$ and $T \simeq 20$ K.

> ☞ The maximum polarization fraction at 850 µm is ≃ 20 % (Planck Collaboration et al., 2020a).

II.2.2.3 Non-Thermal Emission

Spinning Grains. The AME is a centimeter continuum excess that can not be accounted for by the extrapolation of dust models, free-free, synchrotron and molecular line emission (Fig. II.10). It was first detected in the MW (Kogut et al., 1996). Draine & Lazarian (1998a) promptly proposed that it was arising from the dipole emission of fastly rotating ultrasmall grains. The candidate carriers were thought to be PAHs. The *Wilkinson Microwave Anisotropy Probe* (WMAP; $\lambda \simeq 3.2 - 13$ mm; 2001-2010) and *Planck* data of the Galaxy were successfully fitted with spinning dust models, including PAHs (Miville-Deschênes et al., 2008; Ysard & Verstraete, 2010; Planck Collaboration et al., 2011b). The cm SED in Fig. II.15 is dominated by spinning grain emission. In the MW, the AME correlates with all tracers of dust emission (*e.g.* Hensley et al., 2016). However, the AME intensity increases with the ISRF intensity, while PAHs are destroyed in high ISRFs. Hensley et al. (2016) thus proposed that the carriers of the AME could be nano-silicates, rather than PAHs. Refining the modeling of the MIR SED, Bell et al. (2019) showed that AME correlates better with the emission from charged PAHs, in the Galactic region λ-Orionis. This will be discussed in more details in Sect. III.2.2.2.

Photoluminescence. We have seen in Sect. II.1.2.4 that the ERE excess emission was thought to originate in the photoluminescence of dust grains. In reflection nebulae, ERE appears to be excited by FUV photons ($11 \text{ eV} \lesssim h\nu \lesssim 13.6$ eV; *e.g.* Lai et al., 2017). It disappears if the exciting star has an effective temperature $T_{\rm eff} \lesssim 10^4$ K. The conversion efficiency, that is the rate of photoluminescent photons per absorbed UV photon, seems to be around ≃ 1 %. ERE being seen in reflection nebulae, it is expected to be a general property of interstellar grains. There is however a debate about the detection of ERE toward cirrus clouds and its conversion efficiency (*cf.* the discussion in Hensley & Draine, 2021). ERE is observed in C-rich PNe (containing predominantly carbonaceous grains) and not in O-rich PNe (containing predominantly silicates grains; Witt & Vijh, 2004). The carriers should thus be carbon grains, such as PAHs.

II.2.3 Elemental Abundances in Grains

The logarithmic abundance of an element E, relative to H, is often noted:

$$\epsilon(\mathrm{E}) \equiv 12 + \log\left(\frac{\mathrm{N_E}}{\mathrm{N_H}}\right), \tag{II.8}$$

$\mathrm{N_E}$ being its column density. The number abundance ratio can also be noted E/H instead of $\mathrm{N_E}/\mathrm{N_H}$, when it is not directly derived from the measure of a column density. An element in the ISM belongs either to the gas or to the dust phase. If we know the total or *reference* abundance of an element E in the ISM, we can thus infer its abundance locked in dust grains, by measuring its abundance in the gas phase. This difference is the *depletion*. The *logarithmic depletion* of an element E is defined as (Jenkins, 2009):

$$\delta(\mathrm{E}) \equiv \epsilon(\mathrm{E_{gas}}) - \epsilon(\mathrm{E_{ref}}), \tag{II.9}$$

The observable δ(E) is a measure of the ratio between the abundance of an element E observed in the gas phase to its total assumed abundance. The abundance of element E, locked in grains, is thus:

$$\left(\frac{\mathrm{E_{dust}}}{\mathrm{H}}\right) = \left(\frac{\mathrm{E_{ref}}}{\mathrm{H}}\right)\left(1 - 10^{\delta(\mathrm{E})}\right). \tag{II.10}$$

Note that, in Eq. (II.10), we do not differentiate the origin of H, as H is predominantly in the gas phase: $\mathrm{H_{ref}} \simeq \mathrm{H_{gas}} \gg \mathrm{H_{dust}}$.

II.2.3.1 Measuring ISM Abundances

Solar abundances. The abundance of elements and their isotopes are the most accurately known in the Solar system (*e.g.* Asplund et al., 2009, for a review). Those are thus used as a reference in the ISM. The abundances of the protosolar nebula, at the time the Sun formed, 4.56 Gyr ago, can be determined the two following ways.

Meteorites, analyzed with mass spectroscopy, provide the most precise abundances. The most primitive meteorites are the carbonaceous (CI) chondrites. The issue with meteorites is that the most volatile elements (*i.e.* the lightest ones and the noble gases) have been depleted due to high-temperature processes within the Solar nebula (*e.g.* Hellmann et al., 2020).

Solar photosphere absorption spectroscopy is less precise, as it requires some modeling. It however provides more reliable abundances of the volatile elements.

These abundances are compared in Fig. II.16. We see that both tracers are in very good agreement, except for the volatile elements. It is common to define the mass fractions of H, He, and elements heavier than He ($\mathrm{M_{ISM}}$ being the total ISM mass):

$$\mathrm{X} \equiv \frac{\mathrm{M_H}}{\mathrm{M_{ISM}}}, \quad \mathrm{Y} \equiv \frac{\mathrm{M_{He}}}{\mathrm{M_{ISM}}}, \quad \mathrm{Z} \equiv \frac{\mathrm{M_{>He}}}{\mathrm{M_{ISM}}}, \quad \text{with } \mathrm{X+Y+Z} = 1. \tag{II.11}$$

In the literature, the ratio Z is unanimously called *metallicity*. Some even call the elements heavier than He, *metals*, which is even worse, knowing what we have learned in Sect. I.1.3.1. This is one of the worst choices of terminology in the whole history of sciences. It is however difficult to avoid using the term *metallicity*. We will thus reluctantly use it in the rest of this manuscript.

Present-day Solar abundances. The abundances displayed in Fig. II.16 are present-day photospheric values. They are however not perfectly representative of the present-day abundances of the Solar neighborhood ISM. To go from the former to the latter, a factor +0.03 dex has to be added to the heavy element abundances of Fig. II.16 to account for diffusion in the Sun (Turcotte & Wimmer-Schweingruber, 2002). This provides protosolar abundances. Present-day abundances can then be inferred by modeling the chemical evolution of the MW during the last 4.56 Gyr (*e.g.* Chiappini et al.,

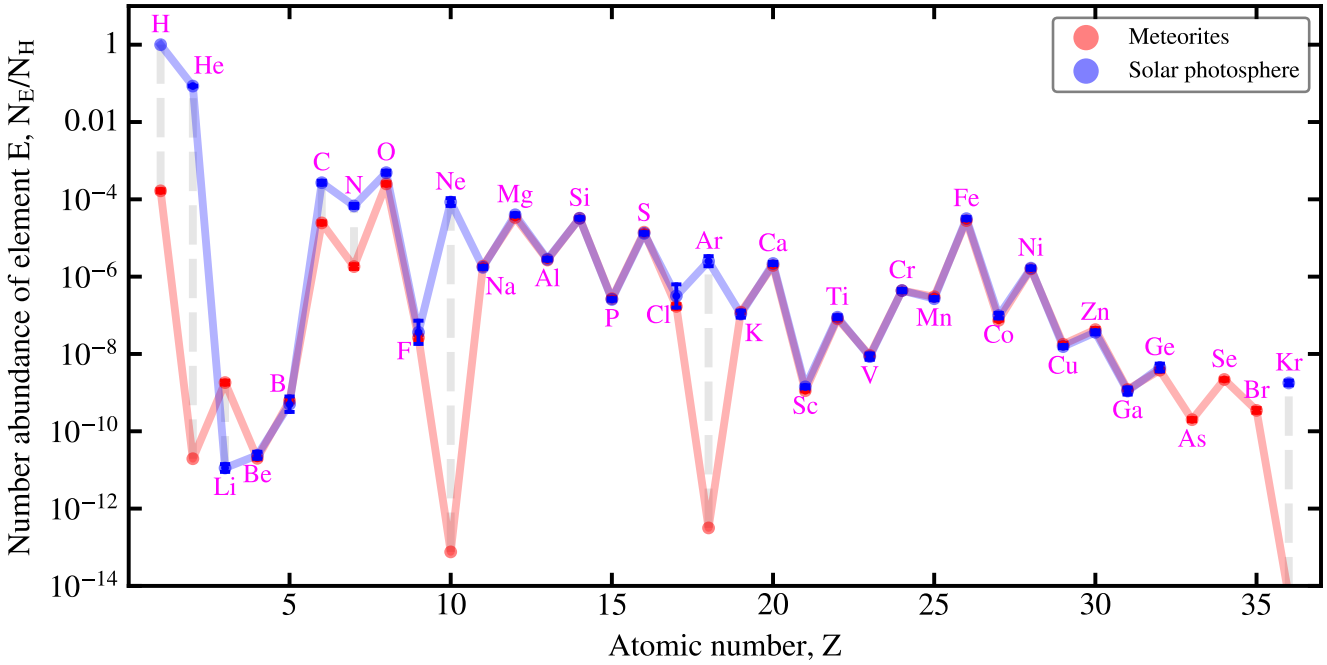

FIGURE II.16 – *Solar abundances.* The two lines show the elemental abundances relative to H of the Solar system, as a function of the atomic number, from Asplund et al. (2009). The red line and circles correspond to meteorites, and the blue line and circles correspond to the Solar photosphere. Licensed under CC BY-SA 4.0.

2003; Bedell et al., 2018). This leads to correcting each element with a different factor, up to ≃ 0.2 dex (*cf. e.g.* Hensley & Draine, 2021, for the correction of the major dust constituents). The present-day Solar photospheric abundances are (Asplund et al., 2009):

$$X_\odot = 0.7381, \quad Y_\odot = 0.2485, \quad Z_\odot = 0.0134. \tag{II.12}$$

To put it in words, three quarters of the gas mass is made of H, one quarter is made of He, and only 1.3 % is made of heavy elements, in the MW. Besides H and He, the most abundant species in the ISM are O and C ($M_O/M_{ISM} \simeq 8.0 \times 10^{-3}$ and $M_C/M_{ISM} \simeq 2.8 \times 10^{-3}$). These abundances can be used as references in Eq. (II.9). Alternatively, B stars or young F and G stars can provide a more direct estimate of the abundances in nowadays ISM. These abundances are however more difficult to estimate accurately.

II.2.3.2 Depletions

The depletion strength. The abundances in the gas phase are most reliably measured by absorption spectroscopy toward stars. Gas atoms in the neutral ISM are essentially in their ground state. Most of the corresponding transitions are in the UV ($\lambda = 0.0912 - 0.3$ µm). Jenkins (2009) compiled and homogenized the abundances of 17 elements measured along 243 sightlines, throughout the literature, to propose a unified representation of the depletions in the MW. Jenkins (2009) showed that the logarithmic depletions of each element are all linearly related, and controlled by a single parameter, $F_\star$, called the *depletion strength factor*:

$$\delta(E) \simeq A_E \times F_\star + B_E. \tag{II.13}$$

The factors A_E and B_E are empirically determined for each element. The depletion factor accounts for the fact that depletions are different along different sightlines. They however vary according to Eq. (II.13). This effect is due to dust growth in the ISM. It is supported by the good correlation between $F_\star$ and the average density of the ISM, demonstrated on Fig. II.17.a. When the density of the ISM

increases, the collisional rate of a grain with heavy elements increases. A fraction of these elements stick on the grain surface and grow mantles.

- When $F_\star \simeq 0$, we are in the most diffuse ISM, the depletion is $\delta(E) \simeq B_E$.
- When $F_\star \simeq 1$, such as toward ζ Oph, we are sampling the dense ISM. The amplitude of the depletion, A_E, reflects the composition of the grain mantles.

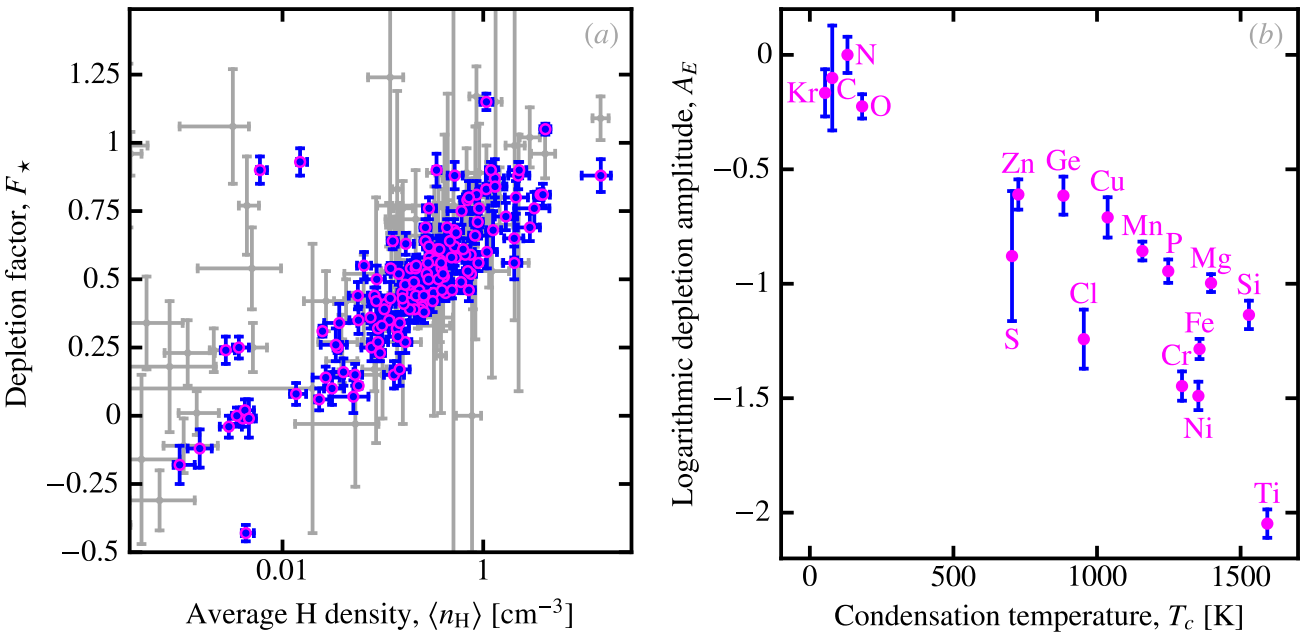

FIGURE II.17 – *Depletion variations within the MW.* Panel *(a)*: depletion factor (Eq. II.13) as a function of the average density, $\langle n_H \rangle \equiv (N_{H_I} + N_{H_2})/d$, where d is the distance to the star (Jenkins, 2009). The points represented in grey are those for which the uncertainty on $F_\star$ is greater than 0.07. Panel *(b)*: depletion amplitude (from Eq. II.13) as a function of condensation temperature (Lodders, 2003; Jenkins, 2009). Licensed under CC BY-SA 4.0.

Volatile and refractory elements. Not all the most abundant elements in the ISM enter the dust composition. Some elements such as N or the noble gases are not significantly depleted. Fig. II.17.b shows a general relation between the depletion amplitude and the condensation temperature of the most abundant heavy elements. The most depleted elements are those which have a high condensation temperature. For that reason, elements are often classified in the two following categories.

Volatile elements are the elements with low condensation temperatures (C, N, O, noble gases). A moderate temperature is sufficient to remove them from the grains. These elements thus exist mainly in the gas phase.

Refractory elements are the elements with high condensation temperatures (those are essentially the metals). They can be present in grains up to high temperatures. Their abundance in the gas phase therefore exhibits large variations as a function of environment.

We note that, although C and O are two of the main dust constituents, these elements are classified as volatile. These elements are indeed mainly in the gas phase, as their depletion is moderate (*cf.* Fig. II.18.a). However, this modest depletion is sufficient to account for a large fraction of the dust mass.

Inferred dust composition. Since the individual depletion of each element can be inferred, it provides the unique prospect of constraining the average composition of dust grains. This composition changes with density, as mantles grow. Following Hensley & Draine (2021), we quote depletions for

$F_\star = 0.5$ as they correspond to $\langle n_H \rangle \simeq 0.3$ cm^{-3}, which is appropriate for the diffuse ISM. From this vantage point, the dustiness of the diffuse Galactic ISM is:

$$Z_{dust} \equiv \frac{M_{dust}}{M_{gas}} \simeq \frac{1}{126 \pm 20} \simeq 0.0079 \pm 0.0012. \tag{II.14}$$

The dust-to-metal mass ratio is thus:

$$DM \equiv \frac{Z_{dust}}{Z} \simeq \frac{1}{2 \pm 0.26} \simeq 0.592 \pm 0.093. \tag{II.15}$$

The results of Jenkins (2009) indicate that the dustiness is $\simeq 2.7$ times higher at $F_\star = 1$ than at $F_\star = 0$. The number and mass abundance in grains is represented in Fig. II.18. The carbonaceous-to-silicate mass ratio is:

$$\frac{M_{C\text{-}dust}}{M_{Sil.}} \simeq 0.177 \pm 0.085. \tag{II.16}$$

Finally, we can have an idea of what the stoichiometry of silicates should be:

$$SiO_{6.6\pm2.5}Mg_{1.21\pm0.16}Fe_{1.13\pm0.14}. \tag{II.17}$$

We note it results in a higher Si:O ratio than in olivine (1:4) and pyroxene (1:3) (*cf.* Sect. I.1.4). It is currently difficult to understand where all the depleted oxygen is, even if it also forms various oxides, such as Fe_2O_3, Al_2O_3, *etc.*

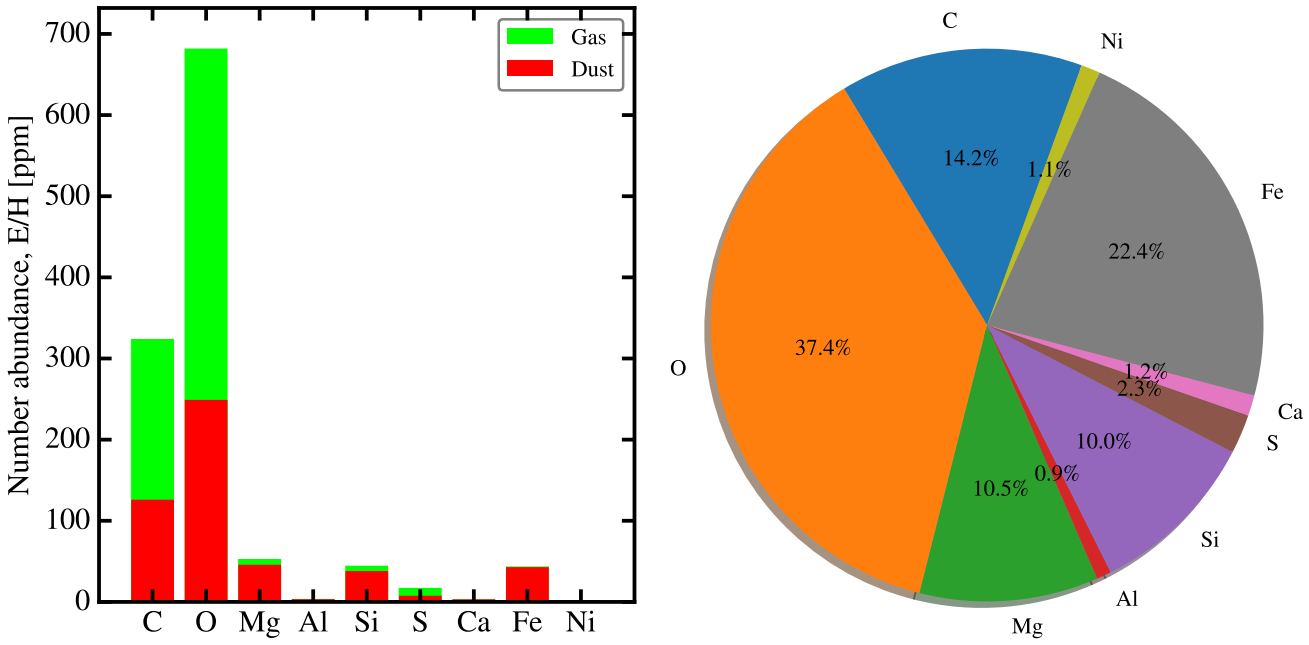

(a) Number abundance, relative to H

(b) Grain composition, in mass

FIGURE II.18 – *MW dust composition inferred from depletions.* Panel *(a)*: number abundances of the main depleted elements, relative to H, in *part per million* (ppm), into dust (red) and gas (green). These values correspond to the MW, for $F_\star = 0.5$ (Table 2 of Hensley & Draine, 2021). The top of each histogram represent the total ISM abundance. Panel *(b)*: mass fraction of the different elements locked in grains, in the MW, for $F_\star = 0.5$. Licensed under CC BY-SA 4.0.

II.2.4 Direct Measures

Direct characterization of interstellar grains is possible in a few particular situations: *(i)* presolar grain inclusions in meteorites; *(ii)* interstellar grains entering the heliosphere; or *(iii)* study of dust analogs in the laboratory.

II.2.4.1 Meteorite Inclusions

Grain identification. Primitive meteorites contain presolar grains, that is grains that formed in the ISM before being incorporated in the early Solar nebula (*e.g.* Hoppe & Zinner, 2000). They are believed to have remained relatively unaltered since the formation of the Solar system. They can be identified by their isotopic anomalies (*cf.* Fig. II.19.a). Carbonaceous chondrites that we have mentioned in Sect. II.2.3.1 are of particular interest (*e.g.* Nittler et al., 2019). Interstellar grains identified in meteorites can have one of the following compositions (*cf.* Fig. II.19.b):

- Silicon carbide (SiC);
- Graphite (C sp^2);
- Silicates (SiO_{3-4});
- Nanodiamonds (C sp^3);
- Silicon nitride (Si_3N_4);
- Corundum (Al_2O_3);
- Spinel ($MgAl_2O_4$); and
- Titanium oxide (TiO_2).

The size of these grains ranges from a few tenths of nanometers to a few microns. Their isotopic ratios are consistent with condensation in the ejecta of SNe or *Asymptotic Giant Branch* (AGB) stars (*cf.* Fig. II.19.a).

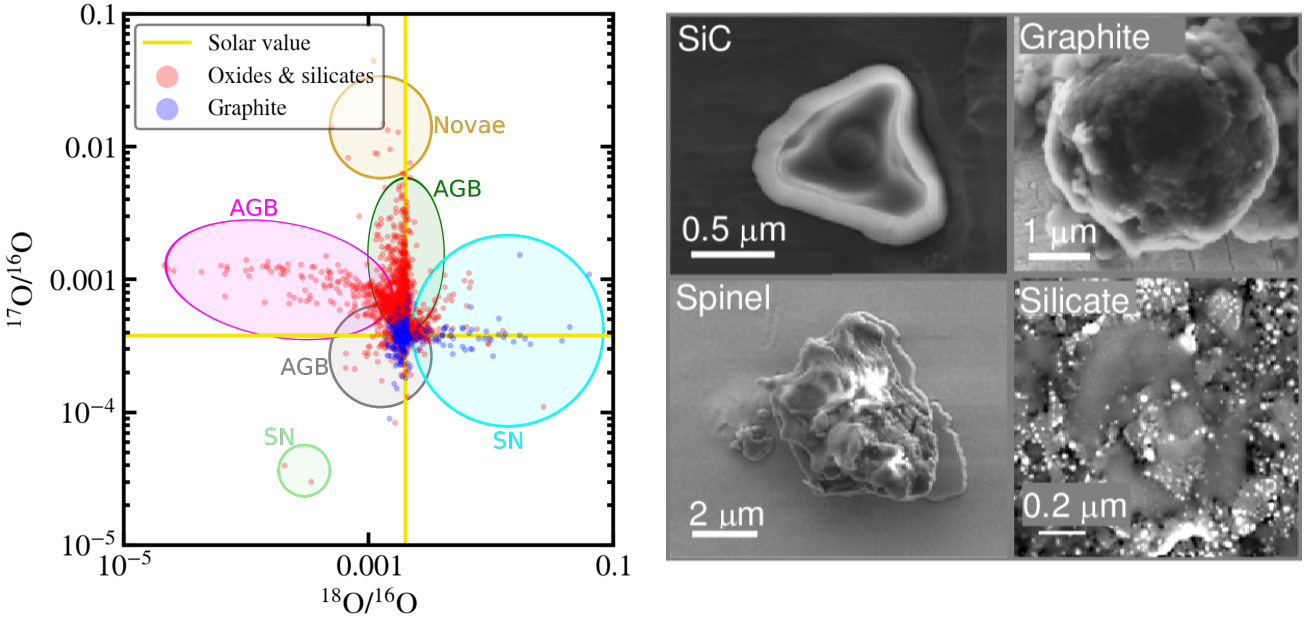

(a) Isotopic abundances

(b) Presolar grains

FIGURE II.19 – *Presolar grains in meteorites.* Panel *(a)* shows the oxygen isotopic ratios of meteoritic presolar grains, from the Presolar Grain Database of Washington University (Hynes & Gyngard, 2009; Stephan et al., 2020). Panel *(b)* shows pictures of presolar grains from primitive meteorites (Hoppe, 2010). The SiC grain is from a SN, the graphite from an AGB star or a SN, and the spinel and silicate grains are from AGB stars. Credit: *(a)* licensed under CC BY-SA 4.0; *(b)* courtesy of the Max Planck Institute for Chemistry, with permission from Peter HOPPE.

Limitations. Overall, the current analysis of presolar grains in meteorites suffers from several biases. The search for presolar grains in meteorites uses chemical treatments dissolving the silicate matrix (Draine, 2003a). It is the likely reason why: *(i)* most grains are crystalline stardust, *(ii)* why so few silicate grains are found, and *(iii)* why the smallest grains are not detected.

II.2.4.2 Interplanetary Dust

ISD flux and cometary dust. We have seen in Sect. II.1.1.5 that several spacecrafts have collected *Interplanetary Dust Particles* (IDP) *in situ*. Among these IDPs, several grains have been shown to be of interstellar origins, because of the direction and speed of their flow. Cometary dust also provides important clues, as comets formed during the early epoch of the Solar system. They should contain pristine material. A class of IDPs called *Glass with Embedded Metals and Sulfides* (GEMS; Bradley, 1994; Keller & Messenger, 2008), are presolar. They have sizes ranging from ≃ 0.1 to 0.5 µm.

FIGURE II.20 – *Micrometeorite collection in Antarctica.* Collecting micrometeorites in the central Antarctic regions, at Dome C, in 2002. Credit: Jean Duprat, Cécile Engrand, courtesy of CNRS Photothèque.

Micrometeorites. In addition to grain collection in space, IDPs entering the atmosphere become micrometeorites. These can be collected on Earth and analyzed in the laboratory. Antarctica is particularly interesting to that purpose, because of the absence of pollution and the possibility to sample the snow (*cf.* Fig. II.19; Rojas et al., 2021, for a review).

II.2.4.3 Laboratory Measurements

Dust analogs, that is solids we think are making up ISD, can be extensively studied in the laboratory (*e.g.* Henning, 2010, for a review). We can distinguish at least two general types of experiments: *(i)* spectroscopic characterization; and *(ii)* reactivity and processing.

Spectroscopic characterization. Two general steps are required to perform such measures: *(i)* synthesizing the target compound; *(ii)* measuring its optical properties, usually in a rather narrow spectral regime. The details of these steps depend a lot on the nature of the compound, and on the spectral range explored. Fig. II.21 shows an example of a particular experimental device to measure PAH

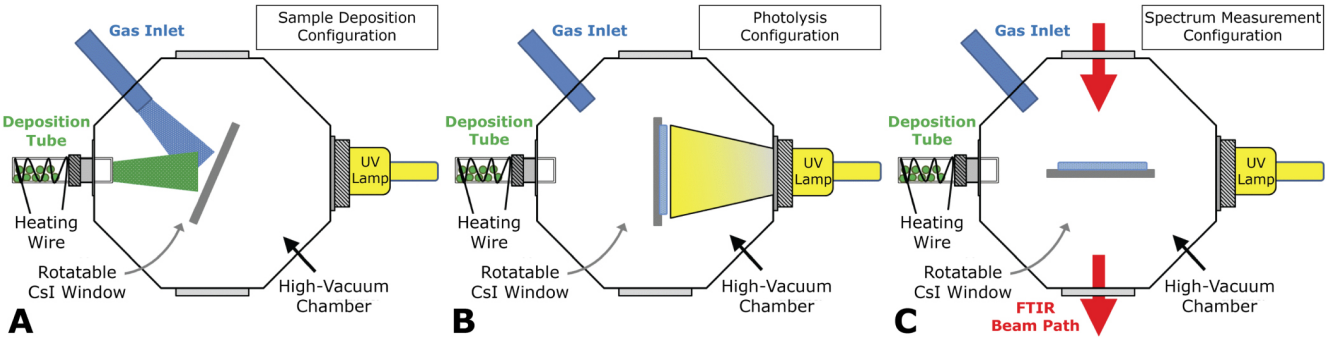

FIGURE II.21 – *NASA Ames PAH experiment.* A typical setup for a matrix-isolation experiment: (A) sample deposition configuration, (B) UV photolysis configuration, and (C) configuration for collecting the IR spectrum. Credit: Mattioda et al. (2020), with permission from Andy MATTIODA.

properties in the IR, at NASA Ames. Different groups across the world specialize in such measures on PAHs (*e.g.* Useli-Bacchitta et al., 2010; Bauschlicher et al., 2018), carbon grains (*e.g.* Mennella et al., 1998; Dartois et al., 2016), silicates (*e.g.* Dorschner et al., 1995; Demyk et al., 2017a) and ices (*e.g.* White et al., 2009), among others. Fig. II.22 shows some of the results of the silicate study of Demyk et al. (2017a,b).

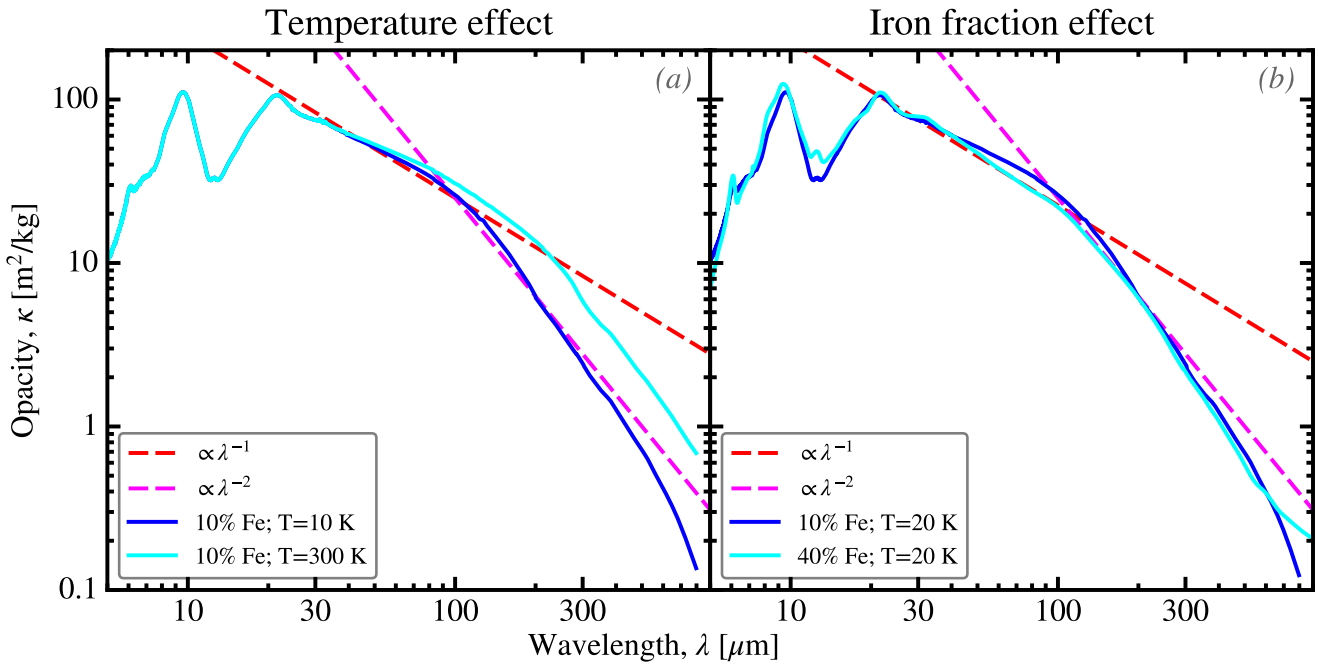

FIGURE II.22 – *Laboratory measurement of silicate opacities.* These data are from the amorphous silicate samples of Demyk et al. (2017a). Among other parameters, this study samples the effects of: *(a)* temperature; and *(b)* iron fraction. Licensed under CC BY-SA 4.0.

Grain reactivity and evolution. Other experiments tackle the reactivity on grain surface (*e.g.* water formation; Dulieu et al., 2010). Grain evolution in the ISM is also studied. For instance, the photoproduction of a-C(:H) (Dartois et al., 2005), the ion absorption on carbon grains (Mennella et al., 2003), the processing under high energy (to mimic cosmic rays, *e.g.* Dartois et al., 2013). Some laboratory samples can even be exposed to space conditions (Kebukawa et al., 2019), onboard the *International Space Station* (ISS).

II.3 State-of-the-Art Dust Models

A dust model is defined by the abundance and size distribution of several grain components, characterized by their composition (PAH, graphite, silicates, *etc.*). We now review how the Galactic observables we have presented in Sect. II.2 are used to constrain modern dust models. These models are therefore specific to the Galactic diffuse ISM. When using such a model to interpret other observations, we can vary the intensity and spectral shape of the ISRF, to account for local variations. In principle, we can also vary the abundance of each component, and some parameters of the size distribution to fit observations of other systems. A dust model is a parametric framework that we can use to interpret any dust observable. There are however some limitations that we will discuss in Chap. III.

II.3.1 Composition and Size Distributions of Different Models

There has been a large number of dust models in the past. We discuss here only some of the most recent ones (Zubko et al., 2004; Draine & Li, 2007; Compiègne et al., 2011; Siebenmorgen et al., 2014; Jones et al., 2017; Guillet et al., 2018).

II.3.1.1 Diversity in Composition

Inherent degeneracies of dust models. Different models make different choices in terms of composition. This is because, even with all the constraints we have listed in Sect. II.2, there are still numerous degeneracies. Several dust mixtures can fit the same observables. This has been best demonstrated by Zubko et al. (2004, hereafter ZDA04). ZDA04 fitted the UV-to-NIR extinction, IR emission and elemental depletions with different compositions, including: PAHs, graphite, different types of amorphous carbons, silicates, and composite grains. They also varied the reference abundances used to estimate elemental depletions. In the end, they showed 15 different dust mixtures providing satisfying fits to the Galactic diffuse ISM observables.

Common compositional choices. A dust model accounting for at least the UV-to-MIR extinction and the IR emission must have the following features.

PAHs or small a-C(:H) are necessary to account for the aromatic features. Among the models we discuss here, only THEMIS also accounts for the 3.4 µm aliphatic feature. In addition, PAHs or small a-C(:H) account for a large fraction of the 2175 Å extinction bump.

Silicate grains are necessary to account for the 9.7 and 18 µm silicate features. In addition, even if depletions are not actually fitted, they indicate that about 2/3 of dust mass must reside in some form of silicate grains (*cf.* Sect. II.2.3).

Large carbon grains are necessary to account for the bulk of the FIR emission with a reasonable dustiness. Large, uncoated silicate grains are indeed not emissive enough to explain the FIR SED without requiring more heavy elements locked up in grains than what is available in the ISM. Graphite and, even more, a-C(:H) will increase the overall emissivity of the large grain mixture to the desirable level, using the second most abundant dust specie available.

In addition to these choices, grain mantles and/or inclusions can also enter the composition. Some have been explored by ZDA04. These are an essential part of the THEMIS model, which is designed as an evolution model (*cf.* Sect. II.3.2.2). The mantle thickness is indeed one of the parameters quantifying grain evolution through the ISM. Another important parameter is the shape of the grains. Elongated grains are necessary to account for the polarization in extinction and emission (*cf.* Sect. I.2.2.5). Siebenmorgen et al. (2014) designed a model accounting for the polarized extinction. The model of Guillet et al. (2018) is currently the only one also accounting for the polarized emission measured by *Planck*. Table II.2 summarizes the differences between the most recent dust models.

	Zubko et al. (2004, BARE-GR-S)	Draine & Li (2007)	Compiègne et al. (2011)	Siebenmorgen et al. (2014)	Jones et al. (2017)	Guillet et al. (2018)
Observational constraints accounted for						
UV-to-NIR extinction	✓	✓	✓	✓	✓	✓
Polarized extinction				✓		✓
MIR extinction			✓		✓	✓
Albedo			✓		✓	✓
NIR-to-mm emission	✓	✓	✓	✓	✓	✓
Polarized emission						✓
Elemental depletions	✓		✓	✓	✓	✓
Composition of the dust mixture						
PAHs	✓	✓	✓	✓		
Small a-C(:H) grains			✓	✓	✓	✓
Large a-C(:H) grains			✓	✓	✓	✓
Small graphite grains	✓	✓		✓		
Large graphite grains	✓	✓		✓		
Small silicate grains	✓			✓		
Large silicate grains	✓	✓	✓	✓	✓	✓
Grain mantles					✓	✓
Grain inclusions					✓	✓

TABLE II.2 – *Comparison between different dust models.* The goal of this table is to illustrate the diversity of observational constraints and the possible choices of dust mixtures. In the first part of the table, some checkmarks are questionable. A given model may indeed not actually use a particular constraint, but end up being consistent with it, whereas another one may use it but provide an imperfect fit. In the second part, the difference between "small" and "large" grains is around a radius of $a \simeq 10$ nm corresponding to the typical transition radius for stochastically heated grains (*cf.* Sect. I.2.4.3).

II.3.1.2 Difference in Size Distributions

Origin of the Size Distribution. The size distribution of interstellar grains is a complex balance between the formation and destruction processes that we will discuss in Chap. IV. Two of these processes explain quite naturally two widely-used functional forms.

Collisional fragmentation of an initial distribution of large grains leads to a power-law size distribution with an index close to $\simeq -3.5$, similar to the MRN size distribution (Eq. II.1; $f(a) \propto a^{-3.5}$). This result was demonstrated for asteroids by Hellyer (1970, with a different index, in his case). Dorschner (1982) explained the interstellar size distribution as a result of collisions in the circumstellar envelopes where grains are produced. A simplified demonstration of this process is given in Chap. 7 of Krügel (2003).

Turbulent grain growth results in a log-normal dust size distribution (Mattsson, 2020).

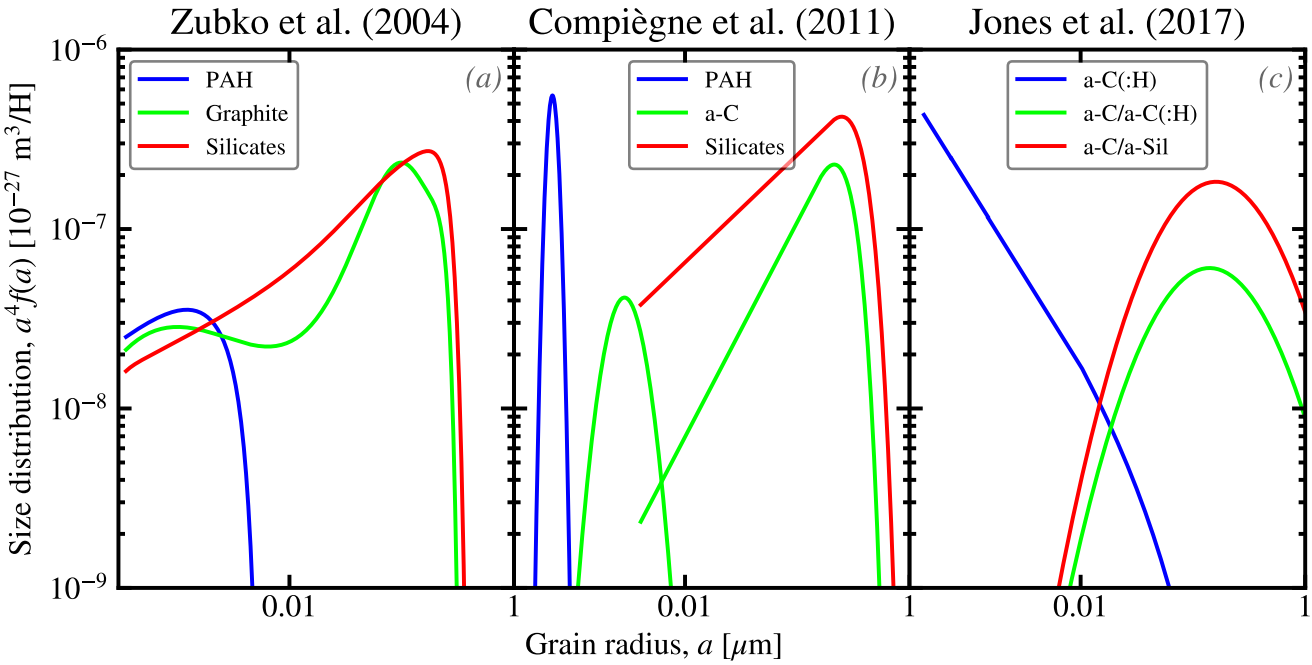

FIGURE II.23 – *Size distribution of several dust models.* This figure shows the size distribution of the Zubko et al. (2004, BARE-GR-S), Compiègne et al. (2011) and THEMIS models. Licensed under CC BY-SA 4.0.

Comparison Between Different Models. Fig. II.23 compares the size distributions of three of the models we are discussing in this section. The displayed size distributions, $a \times f(a)$, are multiplied by a^3 so that they are mass-weighted. Although they manage to fit the same observables, these size distributions are quite different. ZDA04 adopt complex functional forms (Fig. II.23.a). Compiègne et al. (2011) use log-normal size distributions for PAHs and small a-C, and power-law with an exponential cut-off for large grains (Fig. II.23.b). It is the opposite for THEMIS, which uses log-normals for large grains and a power-law with an exponential cut-off for small a-C(:H) (Fig. II.23.c). Despite these differences, we notice the common features that we have listed in Sect. II.3.1.1.

- In the three panels of Fig. II.23, the aromatic feature carrying grains (in blue) are the smallest carbon grains. Their size distribution needs to peak around $3\,\text{Å} \lesssim a \lesssim 50\,\text{Å}$, for these grains to fluctuate to high enough temperatures. Current observables are not accurate enough to distinguish differences in the shape of $f(a)$ in this range.
- Intermediate-size grains ($5\,\text{nm} \lesssim a \lesssim 20\,\text{nm}$) are necessary to account for the MIR continuum. ZDA04 use both graphite and silicate grains, resulting in the presence of the 9.7 and 18 µm features in emission. Compiègne et al. (2011) use a separate a-C log-normal component (in green). For the THEMIS model, the MIR continuum is accounted for by the tail of the small a-C(:H) (in blue).
- The large grain distributions (in blue and red) all peak around $a \simeq 0.1$ µm. They need to drop sharply above this value, as larger grains tend to have lower equilibrium temperatures (*cf.* Sect. I.2.4.2) that would broaden the FIR emission peak of the SED.

II.3.2 The Model Properties

Each model computes the panchromatic opacity, albedo and emissivity of its grain mixture. There are slight differences between different models, because they use different data sets and because the coverage of these data sets is not complete. The properties of the dust mixture of a model are simply the properties of its individual grains, integrated over the size distribution. For a given function X(a),

we note:

$$\langle \mathrm{X} \rangle_a \equiv \int_{a_-}^{a_+} \mathrm{X}(a) f(a) \, \mathrm{d}a. \tag{II.18}$$

The general properties defined in Sect. I.2.2.3 and Sect. I.2.4.3 can therefore be generalized as:

$$\langle m_{\mathrm{dust}} \rangle_a = \left\langle \frac{4}{3} \pi a^3 \rho \right\rangle_a \tag{II.19}$$

$$\kappa_{\mathrm{abs/sca}}(\lambda) = \frac{\left\langle \pi a^2 \mathrm{Q}_{\mathrm{abs/sca}}(a,\lambda) \right\rangle_a}{\langle m_{\mathrm{dust}} \rangle_a} \tag{II.20}$$

$$g(\lambda) = \frac{\left\langle g(a,\lambda) \pi a^2 \mathrm{Q}_{\mathrm{sca}}(a,\lambda) \right\rangle_a}{\left\langle \pi a^2 \mathrm{Q}_{\mathrm{sca}}(a,\lambda) \right\rangle_a} \tag{II.21}$$

$$\epsilon_{\mathrm{v}}(\lambda) = \frac{\left\langle 4\pi \mathrm{Q}_{\mathrm{abs}}(a,\lambda) \pi \int_0^{\infty} \frac{\mathrm{dP}(\mathrm{T},a)}{\mathrm{dT}} \mathrm{B}_{\mathrm{v}}(\lambda,\mathrm{T}) \, \mathrm{dT} \right\rangle_a}{\langle m_{\mathrm{dust}} \rangle_a}. \tag{II.22}$$

II.3.2.1 Extinction and Emission

The opacity. Fig. II.24.a compares the panchromatic opacity of different models. At first order, the four models are in good agreement.

- The discrepancies in the UV-to-NIR range are due to the different compositions. For instance, the THEMIS model tends to have more opaque material. The observations of the Galaxy being expressed per H atom, this model therefore requires a slightly lower dustiness.
- The Hensley & Draine (2021) model has a much flatter MIR continuum, to account for Galactic-center-type extinction curves (*cf.* Sect. II.2.1.2).
- At wavelengths longer than 100 µm, the THEMIS and Hensley & Draine (2021) models have a flatter opacity than the other ones. *Planck* constraints are indeed higher in this regime than the extrapolation of the COBE/FIRAS spectrum.

The bottom left panels of Fig. II.24 show the decomposition of the opacity of the THEMIS model.

Scattering and absorption are shown in Fig. II.24.b. We can see that scattering is dominant only in the NIR range. This scattering component mainly originates in large grains (*cf.* Sect. I.2.2.3).

Carbonaceous and silicates are shown in Fig. II.24.c. We can see that carbon grains dominate the UV and submm opacity. In the particular case we have displayed (the THEMIS model), silicate grains are coated with a-C(:H) mantles. The carbon component of a model made of bare grains would be sensibly higher.

The SED. Fig. II.24.d compares the SED of the same four models as previously. The shapes of these SEDs are relatively similar.

- The differences in the peak of the FIR SED is due to the difference in composition, mirroring the difference in opacity previously discussed.
- The difference in the level of the MIR continuum is due to the paucity of observational constraints in this regime.
- The difference in the level of the aromatic feature emission is due to: *(i)* the different dustiness; and *(ii)* the different sets of MIR constraints (*cf.* Sect. 3.1.1 of G21, for a discussion of this discrepancy).

The bottom right panels of Fig. II.24 show the decomposition of the THEMIS model in sizes and composition.

Small and large grains are shown in Fig. II.24.e. We can see that the small grains are responsible from the MIR emission, as they are stochastically heated (*cf.* Sect. I.2.4.3).

Carbonaceous and silicates are shown in Fig. II.24.f. Carbon grains are responsible for the entire MIR emission and for a small fraction of the FIR peak. Amorphous-carbon-coated-silicates are responsible for most of the FIR emission peak.

II.3.2.2 The Fitted Constraints

We now demonstrate the fit of the observational constraints by one the models, THEMIS. We start by presenting this model in more depth.

The THEMIS model. It is a laboratory-data-based model. As we have previously discussed, it uses two populations of grains: *(i)* a-C(:H) grains with the optical properties of Jones (2012a,b,c); and *(ii)* a-Silicates with Fe and FeS inclusions and a-C(:H) mantles, whose optical properties have been computed by Köhler et al. (2015). The largest a-C(:H) are coated with a-C. A first version was presented by Jones et al. (2013) and updated by Jones et al. (2017). At the time this manuscript is being written, a new version is in preparation including the laboratory optical properties of silicates measured by Demyk et al. (2017a,b). It is an evolution model. The hydrogenation of a-C(:H), their size distribution, as well as the mantle thickness of the large grains are parameters evolving with the ISRF intensity and the density of the ISM.

Discussion of the fit. Fig. II.25 shows the fit of the diffuse Galactic ISM constraints by the THEMIS model.

The extinction curve is well fitted except in the 10 µm range (Fig. II.25.a). This region is the most problematic because of: *(i)* the uncertainty about the profiles of the astrophysical silicate mixture features, which is common to every model; and *(ii)* the uncertainty about the shape of the continuum in this range (*cf.* Sect. II.2.1.2). The synthetic observed extinction curve used to constrain this model is provided by Mathis (1990) without error bars.

The elemental depletions are relatively well fitted except for Fe (Fig. II.25.b). This is a common problem of contemporary dust models (*cf.* Sect. II.2.3).

The albedo is relatively well fitted (Fig. II.25.c). The problem is that the observational constraints themselves are rather scattered. Some constraints in the UV range are inconsistent. This is because albedo measurements come from a diversity of regions (DGL, reflection nebulae; *cf.* Sect. II.2.1.1), which are difficult to homogenize. In addition, the asymmetry parameter derived from these observations is rather high. The albedo is thus measured at the tail of the scattering phase function, which adds another layer of uncertainties.

The emissivity is well fitted (Fig. II.25.d). There are no problem with this component. This is important because this model is used to analyze the IR emission of galaxies and Galactic regions.

II.3.3 Some Useful Quantities

We finish this chapter by listing a few quantities and formulae, useful to make simple estimates and approximations. Unless otherwise noted, these quantities are computed using the THEMIS dust model, and might slightly differ if another model is considered.

II.3.3.1 Grain Sizes, Areas and Masses

For the MRN size distribution. The grain surface is important for chemical reactions and for the photoelectric effect. For a MRN size distribution (Eq. II.1), the average grain surface is:

$$\langle \mathrm{S}_{\mathrm{dust}} \rangle_a = \pi \int_{a_-}^{a_+} \underbrace{f(a)}_{\propto a^{-3.5}} a^2 \, \mathrm{d}a \propto \frac{1}{\sqrt{a_+}} - \frac{1}{\sqrt{a_-}} \simeq \frac{1}{\sqrt{a_-}}. \tag{II.23}$$

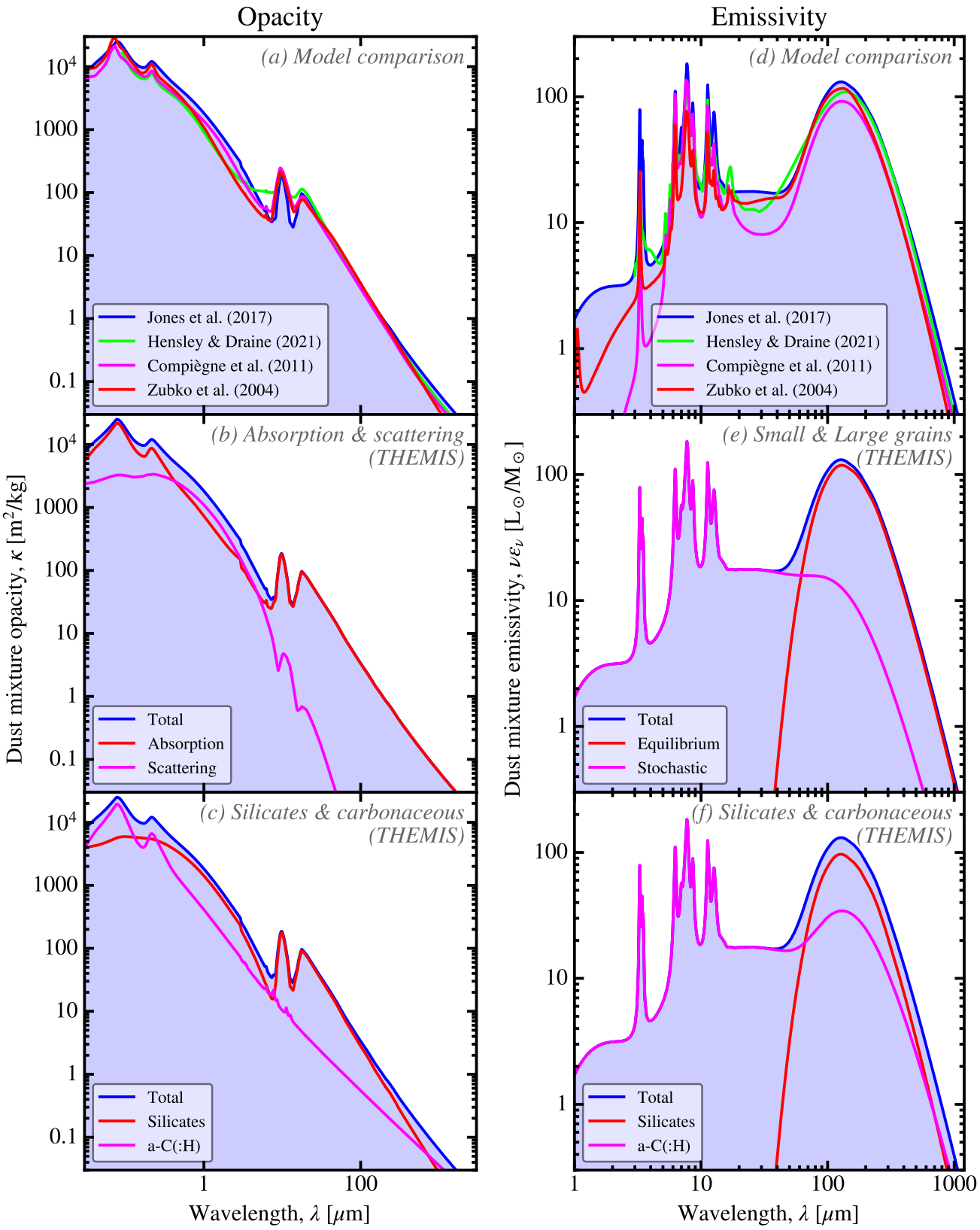

FIGURE II.24 – *Model opacity and emissivity.* Panel *(a)* compares the total opacities of: the BARE-GR-S mixture of Zubko et al. (2004); the Compiègne et al. (2011) model; the THEMIS model (Jones et al., 2017) and the synthetic observations of Hensley & Draine (2021). Panel *(b)* shows the decomposition of the opacity into absorption and scattering (for THEMIS). Panel *(c)* shows the decomposition of the opacity into silicates and carbonaceous grains (for THEMIS). Panel *(d)* compares the emissivity of the different dust models. Panel *(e)* shows the decomposition of the emissivity into large and small grains (for THEMIS). Panel *(f)* shows the decomposition of the emissivity into silicates and carbonaceous grains (for THEMIS).

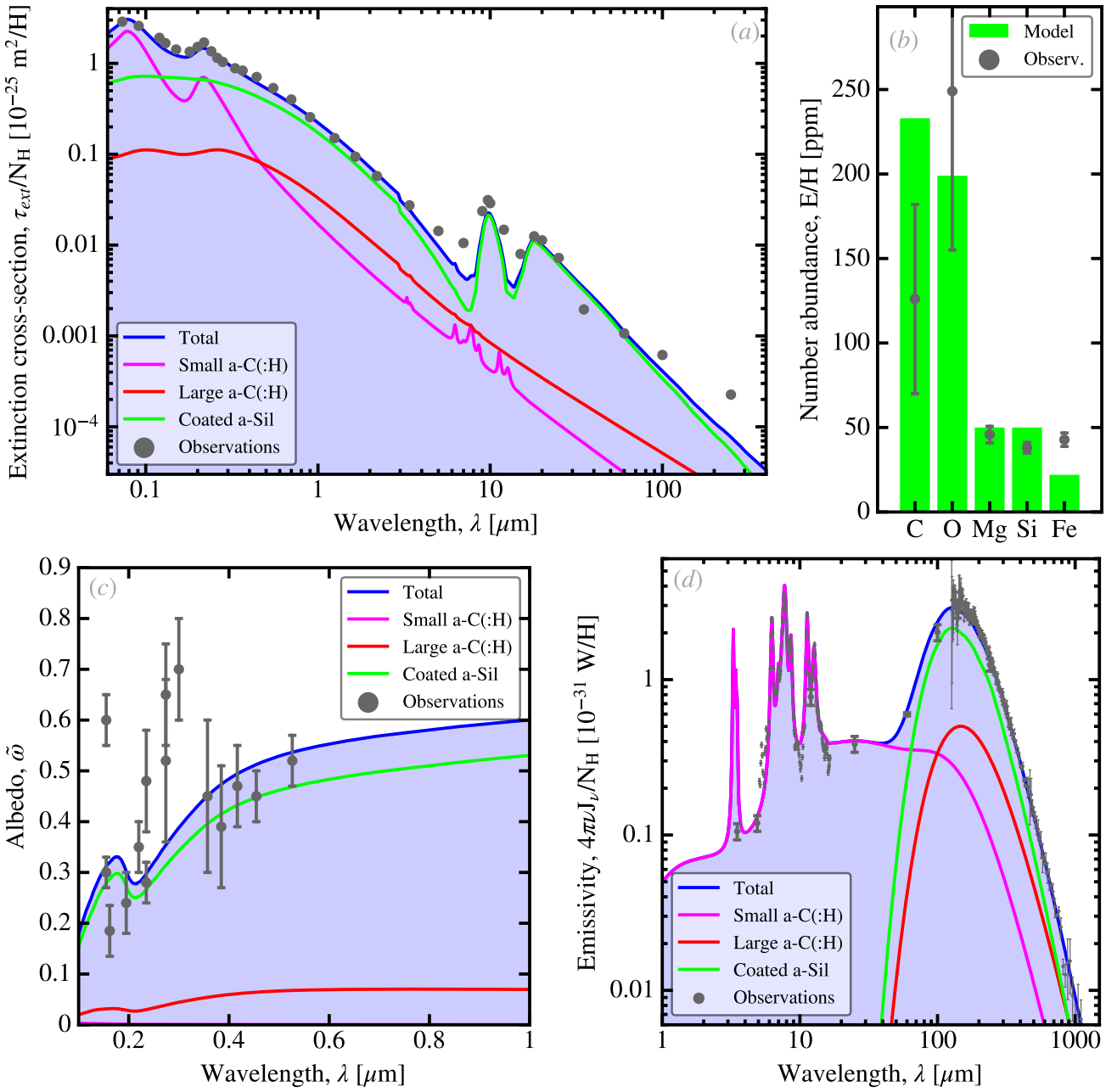

FIGURE II.25 – THEMIS *fit of the Galactic constraints.* Panel *(a)*: fit of the diffuse Galactic ISM extinction curve with the THEMIS model by Jones et al. (2013). The observations (black dots) are from Mathis (1990) and are not provided with uncertainties. Panel *(b)*: albedo fit with the Jones et al. (2013) model. The observations are from: Lillie & Witt (1976); Morgan et al. (1976); Morgan (1980); Chlewicki & Laureijs (1988); Hurwitz et al. (1991); Witt et al. (1997). Panel *(c)*: emissivity fit with the Jones et al. (2013) model. The observations are those of Fig. II.15. Licensed under CC BY-SA 4.0.

where a is the grain radius, $f(a)$, the size distribution from Eq. (II.1), and a_- and a_+, the minimum and maximum sizes ($a_+ \gg a_-$).

☞ The grain surface is thus dominated by small grains.

The average grain volume is:

$$\langle V_{dust}\rangle_a = \frac{4\pi}{3}\int_{a_-}^{a_+} \underbrace{f(a)}_{\propto a^{-3.5}}\, a^3\,da \propto \sqrt{a_+} - \sqrt{a_-} \simeq \sqrt{a_+}, \tag{II.24}$$

For a given grain species, the volume is proportional to the mass, thus the average grain mass is $\langle m_{dust}\rangle_a \propto \sqrt{a_+}$, too.

☞ The grain mass is dominated by large grains.

The case of the THEMIS model. The size distribution of the THEMIS model (Fig. II.23.c) can be split into three components: *(i)* small a-C(:H); *(ii)* big a-C(:H); and *(iii)* silicates. Table II.3 gives the first moments of the size distribution of these three components as well as of the total. The first line indicates that most grains are small grains. This is also reflected in the last column of each line: the value of each parameter is very close to its value for small a-C(:H).

	Small a-C(:H)	Large a-C(:H)	a-Silicates	Total
Grain number fraction, $\langle 1 \rangle_a$	10^9 ppb	36 ppb	80 ppb	10^9 ppb
Average radius, $\langle a \rangle_a$	0.54 nm	12 nm	13 nm	0.54 nm
Average area, $\pi \langle a^2 \rangle_a$	1.02 nm^2	1140 nm^2	1510 nm^2	1.03 nm^2
Average mass, $4/3\pi\rho\langle a^3 \rangle_a$	1040 amu	1.2×10^8 amu	2.5×10^8 amu	2890 amu
Mass fraction	23 %	8.1 %	69 %	100 %

TABLE II.3 – *Moments of the* THEMIS *size distribution.* The number fractions are expressed in *part per billion* (ppb) and the masses in *atomic mass unit* (amu; Table B.2).

Mass fraction of small grains. The mass fraction of aromatic feature emitting grains (*i.e.* a-C(:H) smaller than $a \simeq 1.5$ nm; *cf.* Fig. 1 of G21) is $q_{\rm AF} \simeq 17\,\%$. Other models, using PAHs instead of small a-C(:H), use different values, because PAHs have more aromatic bonds per C atom than a-C(:H). A smaller PAH mass is thus required to account for the same aromatic band strength. The mass fraction of PAHs is $q_{\rm PAH} \simeq 4.6\,\%$ for the Zubko et al. (2004) and Draine & Li (2007) models, and $q_{\rm PAH} \simeq 7.7\,\%$ for the Compiègne et al. (2011) model. The difference between the two latter values is due to the different sets of MIR constraints they use (*cf.* Sect. II.2.2.1; see also Sect. 3.1.1 of G21, for a discussion). For the THEMIS model, the mass fraction of the grains responsible for the MIR continuum (*i.e.* small a-C(:H) with radii $a \gtrsim 1.5$ nm) is $q_{\rm MIRcont} \simeq 6\,\%$.

Dustiness and other ratios. Table II.4 gives various number and mass ratios for the THEMIS model. The dustiness and the dust-to-H mass ratios are equivalent quantities, there is just a factor $(1 - Y_\odot - Z_\odot)$ difference. The third line tells us that there are about 2 dust grains per million H atoms in the ISM. The last line indicates that about 40 % of the mass of heavy elements in the diffuse Galactic ISM is locked-up in dust grains.

	Small a-C(:H)	Large a-C(:H)	a-Silicates	Total
Dustiness, $Z_{\rm dust} \equiv M_{\rm dust}/M_{\rm gas}$	1/800 $\simeq 1.3 \times 10^{-3}$	1/2260 $\simeq 4.4 \times 10^{-4}$	1/270 $\simeq 3.8 \times 10^{-3}$	1/183 $\simeq 5.5 \times 10^{-3}$
Dust-to-H mass ratio, $Y_{\rm dust} \equiv M_{\rm dust}/M_{\rm H}$	1/600 $\simeq 1.7 \times 10^{-3}$	1/1700 $\simeq 5.9 \times 10^{-4}$	1/200 $\simeq 5.0 \times 10^{-3}$	1/138 $\simeq 7.3 \times 10^{-3}$
Dust-to-H number ratio, $N_{\rm dust}/N_{\rm H}$	5300 ppb	0.05 ppb	0.02 ppb	1905 ppb
Dust-to-metal mass ratio, $Z_{\rm dust}/Z$	1/11 ≃ 9 %	1/30 ≃ 3 %	28 %	41 %

TABLE II.4 – *Dustiness and other ratios for the* THEMIS *model.* For the second to fourth columns, the dust mass ($M_{\rm dust}$) or number ($N_{\rm dust}$) are those of the sole component. Therefore, the sum of the second to fourth columns is equal to the fifth column.

II.3.3.2 Opacity and Emissivity

Optical properties. Table II.5 gives the opacity, κ, τ/N_H, and the albedo, $\tilde{\omega}$, at the central wavelengths of the photometric filters displayed in Fig. II.26. The opacity, κ is expressed per mass of dust, whereas τ/N_H is expressed per H atom in the gas phase. The two quantities are related by:

$$\frac{\tau(\lambda)}{N_H} \equiv \kappa(\lambda) \times Z_{dust} \times \frac{m_H}{1 - Y_\odot - Z_\odot}, \tag{II.25}$$

where m_H is the mass an H atom (Table B.2). Fig. II.26 displays a useful approximation, valid for $20\ \mu m \lesssim \lambda \lesssim 1\ mm$:

$$\kappa(\lambda) \simeq 0.64\ m^2/kg \times \left(\frac{250\ \mu m}{\lambda}\right)^{1.79}. \tag{II.26}$$

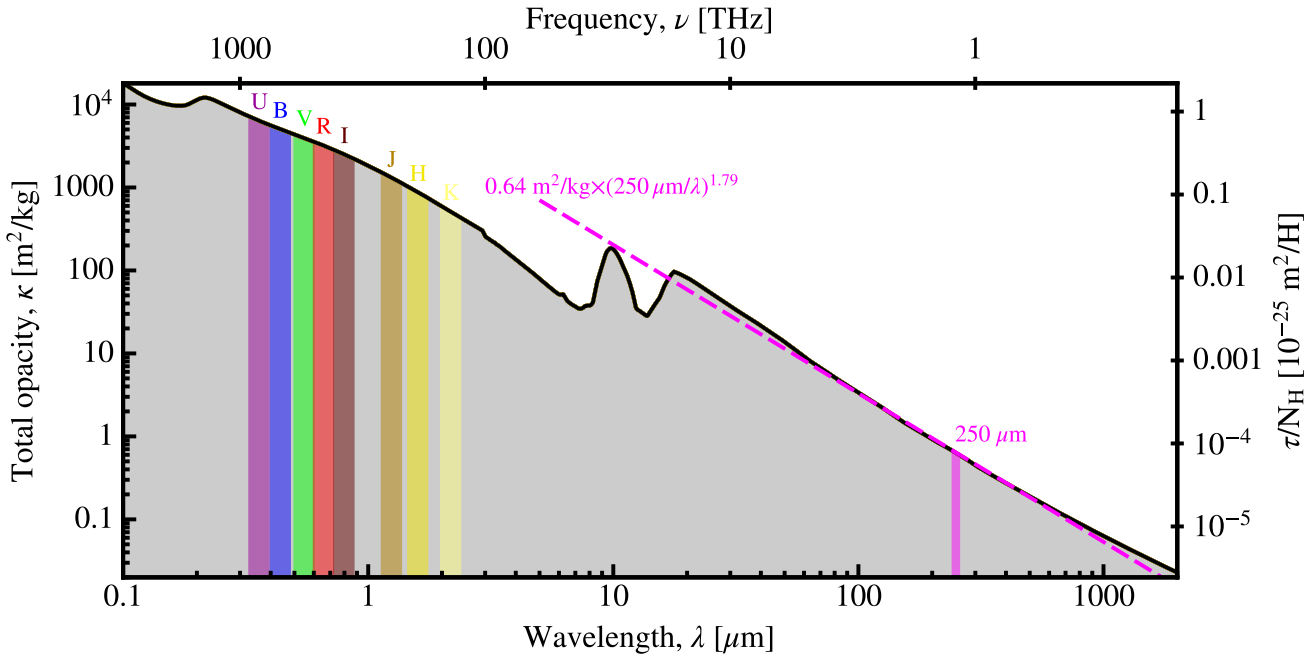

FIGURE II.26 – *IR approximation of the opacity.* This figure shows the extinction opacity of the THEMIS model. We have highlighted the different photometric bands we quote in Table II.5. We also show the power-law approximation of the IR opacity (in magenta; Eq. II.26). Licensed under CC BY-SA 4.0.

Heating regimes. It is important to understand which regime is dominated by large grains at equilibrium with the ISRF (Sect. I.2.4.2), and which one is dominated by small, stochastically heated grains (Sect. I.2.4.3). Fig. II.27.a shows the variation of the SED as a function of the ISRF intensity, U (Sect. I.2.4.2). We can see that when the intensity increases, the emission by large grains shifts to shorter wavelengths, as their equilibrium temperature increases. On the contrary, the emission by small, out-of-equilibrium grains stays constant, as these grains are heated by single photon events. Only their total intensity increases, which is hidden in Fig. II.27.a by the normalization of the intensity. We can estimate the transition wavelength, $\lambda_{trans}(U)$, as the wavelength where the intensity of the small and large grains are equal. This is demonstrated in Fig. II.27.b. The values of $\lambda_{trans}(U)$ for the grid of U displayed in Fig. II.27.a is given in Table II.6.

Emissivity. Table II.7 gives the emissivity of the THEMIS model. The emissivity is proportional to U. We give only the value for U = 1. We quote the following two values.

		Small a-C(:H)	Large a-C(:H)	a-Silicates	Total
U band (0.36 µm)	κ	5934 m^2/kg	9980 m^2/kg	6107 m^2/kg	6381 m^2/kg
	τ/N_H	1.7×10^{-26} m^2/H	9.8×10^{-27} m^2/H	5.1×10^{-26} m^2/H	7.8×10^{-26} m^2/H
	$\tilde{\omega}$	3.4×10^{-3}	0.43	0.60	0.45
	g	0.19	0.57	0.56	0.56
B band (0.44 µm)	κ	3245 m^2/kg	8549 m^2/kg	5180 m^2/kg	5008 m^2/kg
	τ/N_H	9.1×10^{-27} m^2/H	8.4×10^{-27} m^2/H	4.3×10^{-26} m^2/H	6.1×10^{-26} m^2/H
	$\tilde{\omega}$	3.4×10^{-3}	0.46	0.62	0.51
	g	0.18	0.55	0.54	0.54
V band (0.55 µm)	κ	2023 m^2/kg	7027 m^2/kg	4272 m^2/kg	3979 m^2/kg
	τ/N_H	5.7×10^{-27} m^2/H	6.9×10^{-27} m^2/H	3.6×10^{-26} m^2/H	4.8×10^{-26} m^2/H
	$\tilde{\omega}$	2.8×10^{-3}	0.48	0.64	0.54
	g	0.16	0.54	0.53	0.53
R band (0.66 µm)	κ	1395 m^2/kg	5789 m^2/kg	3543 m^2/kg	3231 m^2/kg
	τ/N_H	3.9×10^{-27} m^2/H	5.7×10^{-27} m^2/H	3.0×10^{-26} m^2/H	3.9×10^{-26} m^2/H
	$\tilde{\omega}$	2.3×10^{-3}	0.48	0.65	0.56
	g	0.14	0.53	0.51	0.52
I band (0.80 µm)	κ	920 m^2/kg	4487 m^2/kg	2762 m^2/kg	2479 m^2/kg
	τ/N_H	2.6×10^{-27} m^2/H	4.4×10^{-27} m^2/H	2.3×10^{-26} m^2/H	3.0×10^{-26} m^2/H
	$\tilde{\omega}$	1.7×10^{-3}	0.48	0.66	0.58
	g	0.12	0.52	0.50	0.50
J band (1.25 µm)	κ	398 m^2/kg	2380 m^2/kg	1453 m^2/kg	1286 m^2/kg
	τ/N_H	1.1×10^{-27} m^2/H	2.4×10^{-27} m^2/H	1.2×10^{-26} m^2/H	1.6×10^{-26} m^2/H
	$\tilde{\omega}$	7.5×10^{-4}	0.45	0.70	0.61
	g	0.07	0.49	0.46	0.47
H band (1.60 µm)	κ	260 m^2/kg	1636 m^2/kg	982 m^2/kg	869 m^2/kg
	τ/N_H	7.3×10^{-28} m^2/H	1.6×10^{-27} m^2/H	8.2×10^{-27} m^2/H	1.1×10^{-26} m^2/H
	$\tilde{\omega}$	4.6×10^{-4}	0.42	0.71	0.61
	g	0.05	0.48	0.44	0.45
K band (2.18 µm)	κ	156 m^2/kg	1005 m^2/kg	573 m^2/kg	512 m^2/kg
	τ/N_H	4.4×10^{-28} m^2/H	9.9×10^{-28} m^2/H	4.8×10^{-27} m^2/H	6.2×10^{-27} m^2/H
	$\tilde{\omega}$	2.5×10^{-4}	0.37	0.68	0.58
	g	0.03	0.45	0.42	0.43

TABLE II.5 – *Optical properties of the* THEMIS *model.* This table gives several optical properties at each of the center of the photometric bands displayed in Fig. II.26. The opacity, κ, is the cross-section per mass of the dust component, whereas τ/N_H is the cross-section per H atom in the gas phase. The albedo is $\tilde{\omega} \equiv \kappa_{sca}/\kappa$ (Eq. I.40), and g is the asymmetry parameter (Eq. I.43).

	U=0.1	U=1	U=10	U=100	U=1000	U=10^4
$\lambda_{trans}(U)$	88 µm	62 µm	43 µm	31 µm	22 µm	17 µm

TABLE II.6 – *Transition wavelengths between small and large grain emission.*

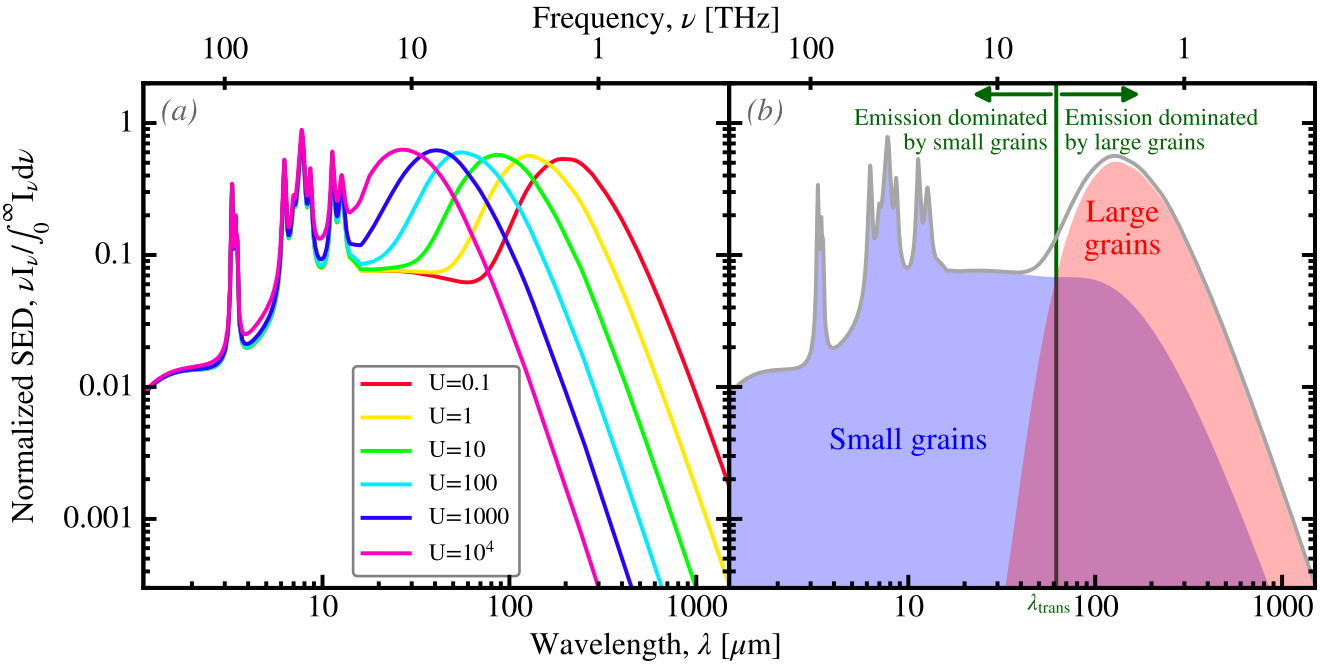

FIGURE II.27 – *Effect of U on the SED.* Panel *(a)* shows the SED of the THEMIS model for different ISRF intensities, U. Panel *(b)* shows the intensity of the THEMIS model for U = 1 (Sect. I.2.4.2). We have decomposed the emission into large (a-Silicates and big a-C(:H)) and small (small a-C(:H)) grains. We show the transition wavelength between the two heating regimes, $\lambda_{trans}(U)$. In both panels, the *y*-axis is the intensity normalized by its bolometric integral. Each displayed SED therefore emits the same total intensity. Licensed under CC BY-SA 4.0.

The emissivity, *per se*, integrated over the wavelengths, is the emitted power per unit dust mass:

$$\epsilon \equiv \int_0^\infty \epsilon_\nu(\nu)\,\mathrm{d}\nu. \tag{II.27}$$

The emitted power per H atom, also integrated over the wavelengths, is expressed per H atom in the gas phase:

$$\frac{4\pi I}{N_H} = \int_0^\infty \frac{4\pi I_\nu(\nu)}{N_H}\,\mathrm{d}\nu. \tag{II.28}$$

These two quantities are related by:

$$\frac{4\pi I}{N_H} = \epsilon \times Z_{dust} \times \frac{m_H}{1 - Y_\odot - Z_\odot}. \tag{II.29}$$

	Small a-C(:H)	Large a-C(:H)	a-Silicates	Total
ϵ	$98 \times U\ L_\odot / M_\odot$	$25 \times U\ L_\odot / M_\odot$	$97 \times U\ L_\odot / M_\odot$	$221 \times U\ L_\odot / M_\odot$
$4\pi I/N_H$	$2.3 \times 10^{-31} \times U\,W/H$	$6.0 \times 10^{-32} \times U\,W/H$	$2.3 \times 10^{-31} \times U\,W/H$	$5.2 \times 10^{-31} \times U\,W/H$

TABLE II.7 – *Emissivity of the* THEMIS *model.* These emissivities are proportional to U.

Chapter III

The Grain Properties of Nearby Galaxies

Without data, you're just another person with an opinion.

(Attributed to W. Edwards DEMING)

Contents

III.1 Spectral Energy Distribution Modeling . . . 100
III.1.1 Radiative Transfer . . . 100
III.1.1.1 Definition of the Main Radiative Transfer Quantities . . . 100
The moments of the specific intensity. . . . 100
Specific energy density. . . . 101
Emission coefficient and emissivity. . . . 101
Extinction coefficient and opacity. . . . 102
Mean free path. . . . 102
III.1.1.2 The Radiative Transfer Equation . . . 103
Propagation in vacuum. . . . 104
Emission only. . . . 104
Absorption only. . . . 104
Emission and absorption. . . . 105
Scattering and absorption with central illumination. . . . 105
Scattering and absorption with uniform illumination. . . . 106
Scattering and absorption with external illumination. . . . 108
III.1.1.3 Approximations for Clumpy Media . . . 108
Effective optical depth of a clumpy medium. . . . 108
The mega-grains approximation. . . . 109
Escape fractions for a clumpy medium. . . . 109
III.1.1.4 Rigorous Solutions . . . 109
Setting the model. . . . 109
The principle of Monte-Carlo radiative transfer. . . . 111
Numerical method to randomly draw photons. . . . 111
Example of a clumpy medium. . . . 112
III.1.2 Approximate Treatments of the Mixing of Physical Conditions . . . 116
III.1.2.1 The Historical Model: the MBB . . . 116
III.1.2.2 A Phenomenological, Composite Approach . . . 117
The average starlight intensity. . . . 118
Constraining the dust properties. . . . 119
Limitations of the composite approach. . . . 120
An alternative distribution. . . . 120

III.1.2.3 Panchromatic Empirical SED Models . . . 122
Stellar SEDs. . . . 122
Putting everything together. . . . 124
Limitations of empirical panchromatic models. . . . 126
III.1.2.4 The Matryoshka Effect . . . 128
Demonstration on the LMC. . . . 128
Generalization. . . . 128
III.1.3 Application to Nearby Galaxies . . . 128
III.1.3.1 The Different Types of Galaxies . . . 128
The outdated galaxy morphological classification. . . . 128
Galactic properties that matter to ISM studies. . . . 130
III.1.3.2 Large-Scale Dust Distribution in Galaxies . . . 131
Homogeneous multi-wavelength data sets. . . . 131
Properties of individual galaxies. . . . 134
Identifying dust heating sources. . . . 134
Large-scale radiative transfer models of galaxies. . . . 135
III.1.3.3 Constraining the Grain Opacity . . . 135
Studies of the emissivity index. . . . 135
Grain opacity in the LMC. . . . 136
Confirmation in other systems. . . . 137
The opacity in nearby galaxies. . . . 138
III.1.3.4 Constraining the Size Distribution . . . 138
Grain processing by shock waves. . . . 138
The modeling strategy. . . . 138
The grain size distribution in four dwarf galaxies. . . . 139
Consequence on the extinction curves. . . . 140
III.2 Studies Focussing on Specific Spectral Domains . . . 141
III.2.1 Scrutinizing Mid-IR Spectra . . . 141
III.2.1.1 The Aromatic Feature Spectrum . . . 142
MIR spectra of galaxies. . . . 142
Laboratory and theoretical PAH physics. . . . 142
III.2.1.2 Spectral Decomposition Methods . . . 144
Calibrating feature properties. . . . 145
Fitting every feature at once. . . . 146
Alternative methods. . . . 146
III.2.1.3 PAH Band Ratio Studies . . . 151
Observed band ratios in galaxies. . . . 152
Effects of ionization and size. . . . 152
The particular case of low-metallicity environments. . . . 154
UIBs as diagnostics of the physical conditions. . . . 155
Other properties. . . . 156
III.2.1.4 Variations of the Aromatic Feature Strength . . . 157
Effect of ISRF hardness. . . . 158
Effect of metallicity. . . . 158
The absence of metallicity threshold. . . . 159
III.2.2 Long-Wavelength Properties . . . 159
III.2.2.1 The Elusive Submillimeter Excess . . . 160
Possible explanations. . . . 160
Empirical properties of the excess. . . . 161
Reality of the phenomenon. . . . 161

III.2.2.2 The Anomalous Microwave Emission . . . 162
The AME in extragalactic environments. . . . 163
Controversy about the carriers of the AME. . . . 163
Correlation with charged PAHs. . . . 163
III.3 Dust in Relation with the Gaseous and Stellar Contents . . . 165
III.3.1 The Phases of the ISM . . . 165
The cooling function. . . . 165
III.3.1.1 The Neutral Atomic Gas . . . 166
The photoelectric heating. . . . 166
The two stable neutral atomic phases. . . . 166
III.3.1.2 The Ionized Gas . . . 168
The Hot Ionized Medium (HIM). . . . 168
H II regions. . . . 168
The Warm Ionized Medium (WIM). . . . 170
III.3.1.3 The Molecular Gas . . . 170
Molecular hydrogen formation. . . . 170
The diffuse molecular gas. . . . 170
Photodissociation regions. . . . 170
Dense molecular clouds. . . . 171
III.3.2 Dust as a Diagnostic Tool . . . 171
III.3.2.1 Dust to Study Star Formation . . . 171
Star formation rates. . . . 171
Resolving star formation. . . . 173
III.3.2.2 Photodissociation Regions . . . 173
PDR Properties. . . . 173
Photoelectric heating. . . . 173
III.3.2.3 The Molecular Gas and its Dark Layer . . . 174
The dark gas. . . . 174
Pressure and radiation field. . . . 175

In this chapter, we review how the models presented in Sect. II.3 are used to derive the grain properties of nearby galaxies. The term "*dust properties*" is vague. In the literature, it often indistinctively encompasses the three following categories (Galliano, Galametz, & Jones, 2018).

The dust mixture constitution is characterized by:

- the chemical composition of the bulk material and its stoichiometry (Sect. I.1.4);
- the structure of the grains (crystalline, amorphous, porous, aggregated, *etc.*; Sect. I.2.2.4);
- the presence of heterogeneous inclusions (Sect. I.2.2.4);
- the presence of organic and/or icy mantles (Sect. I.2.2.4);
- the shape of the grains (Sect. I.2.2.5);
- their size distribution (Sect. II.3.2);
- their abundance relative to the gas (Sect. II.2.3).

The dust physical conditions are the state a grain enters, when exposed to a particular environment:

- thermal excitation due to *(i)* radiative heating (equilibrium or stochastic; Sects. I.2.4.2 – I.2.4.3); and/or *(ii)* collisional heating in a hot plasma (Sect. I.2.4.4);
- grain charging by exchange of electrons with the gas (Sect. III.3.1.1);
- alignment of elongated grains with the magnetic field (Sect. I.2.2.5);
- grain rotation (Sect. I.2.2.5; Sect. II.2.2.3).

The dust observables arise from a grain mixture experiencing a particular set of physical conditions.

Emission of partially polarized components (Sect. II.2.2.2): *(i)* a thermal continuum (IR to mm; Sect. II.2.2.1); *(ii)* molecular and solid-state features (MIR; Sect. II.2.2.1); *(iii)* a possible microwave emission (cm; Sect. II.2.2.3); *(iv)* a possible luminescence (visible; Sect. II.2.2.3).

Absorption of the light from a background source by (Sect. II.2.1): *(i)* a continuum (X-ray to MIR; Sect. II.2.1.1); *(ii)* atomic, molecular and solid-state features (X-rays, UV and MIR; Sect. II.2.1.2), including DIBs (visible; Sect. II.2.1.5) and ices (MIR; Sect. II.2.1.2). The escaping light can be partially polarized as a result (Sect. II.2.1.4).

Scattering of the light from a bright source in our direction, and its polarization (X-rays to NIR; Sect. II.2.1).

Depletion patterns seen through the gas-phase elemental abundances (Sect. II.2.3).

III.1 Spectral Energy Distribution Modeling

SED modeling is one of the main methods to empirically derive the dust properties of a region or a galaxy (*cf. e.g.* Galliano et al., 2018, for a review). The inherent complexity of astrophysical sources requires to account for the diversity of physical conditions within the studied region. The treatment of radiative transfer, even in an extremely approximated fashion, is thus necessary.

III.1.1 Radiative Transfer

Radiative transfer is the method solving the propagation of multiple rays of light, emitted by one or several sources, through a macroscopic heterogeneous medium. It accounts for the scattering, absorption and emission, at each point and along each direction, in the studied region.

III.1.1.1 Definition of the Main Radiative Transfer Quantities

Radiative transfer deals with several quantities that are often improperly defined or mixed together in the literature: intensity, flux, emissivity, brightness, *etc.* We have already seen some of these quantities in Sect. I.2.4. We now define them and explicit their differences (*cf.* Chap. 1 of Rybicky & Lightman, 1979, for a complete review). In what follows, we assume stationary systems. The time variable, t, is used only to denote constant rates.

The moments of the specific intensity. The primary radiative transfer quantity is the *specific intensity* or *brightness* (*cf.* Fig. III.1.a):

$$I_\nu(\nu, \vec{r}, \theta, \phi) \equiv \frac{dE}{dt\,dA\,d\Omega\,d\nu}. \tag{III.1}$$

The specific intensity is the electromagnetic energy, E, per unit time, t, area, A, solid angle, Ω, and frequency, ν. It therefore quantifies the infinitesimal power carried by a monochromatic light ray. This quantity depends on the position in the region, $\vec{r}$, and on the direction of propagation, (θ, ϕ). We adopt the spherical coordinate conventions used in *physics* (Fig. III.1; *cf.* Appendix C.1):

- the *polar angle*, $0 \leq \theta < \pi$, is the angle with the z axis;
- the *azimuthal angle*, $0 \leq \phi < 2\pi$, is the rotation angle in the (x, y) plane;
- the solid angle element is $d\Omega \equiv d\cos\theta d\phi = \sin\theta d\theta d\phi$, with:

$$\iint_{\text{sphere}} d\Omega = \int_0^{2\pi} d\phi \int_{-1}^{1} d\cos\theta = 4\pi. \tag{III.2}$$

The first moments of the specific intensity, relative to its angular distribution, are physically meaningful.

The mean intensity is the zeroth order moment of Eq. (III.1):

$$J_\nu(\nu, \vec{r}) \equiv \frac{1}{4\pi} \iint_{\text{sphere}} I_\nu(\nu, \vec{r}, \theta, \phi)\, d\Omega. \tag{III.3}$$

It is the specific intensity averaged over all directions. It is often used to quantify the ISRF, $4\pi J_\nu$ accounting for rays coming from all directions. In the *isotropic* case, we have $I_\nu(\nu, \vec{r}, \theta, \phi) = J_\nu(\nu, \vec{r})$, $\forall(\theta, \phi)$.

The net flux (*cf.* Fig. III.1.b) is the first order moment of Eq. (III.1):

$$F_\nu(\nu, \vec{r}) \equiv \iint_{\text{sphere}} I_\nu(\nu, \vec{r}, \theta, \phi) \cos\theta\, d\Omega. \tag{III.4}$$

It represents the monochromatic power per unit area passing through a surface element perpendicular to $\hat{z}$. The $\cos\theta$ factor is there to account for the reduction of the density of rays that are not perpendicular to the surface. In the isotropic case, $F_\nu = J_\nu 2\pi \int_{-1}^{1} \cos\theta\, d\cos\theta = 0$, because there is the same amount of flux passing through the area in both directions.

The radiation pressure (*cf.* Fig. III.1.c) is the second order moment of Eq. (III.1):

$$p_\nu(\nu, \vec{r}) \equiv \frac{1}{c} \iint_{\text{sphere}} I_\nu(\nu, \vec{r}, \theta, \phi) \cos^2\theta\, d\Omega \tag{III.5}$$

It is the *momentum flux* carried by the photons, as $p = h\nu/c$ is the momentum of a single photon. The $\cos^2\theta$ term comes from two sources: *(i)* one $\cos\theta$ comes from the reduced fraction of inclined rays, similar to the flux; *(ii)* the second $\cos\theta$ factor comes from the fact the pressure is the momentum vector component that is perpendicular to the surface.

Specific energy density. The radiative energy within a volume element at a given time is the *specific energy density*:

$$u_\nu(\nu, \vec{r}, \theta, \phi) \equiv \frac{dE}{dV d\Omega d\nu} = \frac{dE}{c\, dt\, dA d\Omega d\nu}. \tag{III.6}$$

The second equality comes from the fact that $dV = c\,dt\,dA$, dV being a volume element (*cf.* Fig. III.1.d). The specific intensity is a power per unit area, whereas the energy density is an energy per unit volume. Both quantities are linked, combining Eq. (III.1) and Eq. (III.6):

$$u_\nu(\nu, \vec{r}, \theta, \phi) = \frac{I_\nu(\nu, \vec{r}, \theta, \phi)}{c}. \tag{III.7}$$

If we integrate Eq. (III.6) over all directions, we get, using Eq. (III.3):

$$U_\nu(\nu, \vec{r}) = \iint_{\text{sphere}} u_\nu(\nu, \vec{r}, \theta, \phi)\, d\Omega = \frac{4\pi}{c} J_\nu(\nu, \vec{r}). \tag{III.8}$$

Emission coefficient and emissivity. The monochromatic *emission coefficient* is the power radiated in a given direction, per unit volume and frequency:

$$j_\nu(\nu, \vec{r}, \theta, \phi) \equiv \frac{dE_{\text{em}}}{dt dV d\Omega d\nu}. \tag{III.9}$$

We have also seen, in Sect. I.2.4, the *emissivity*:

$$\epsilon_\nu(\nu, \vec{r}, \theta, \phi) \equiv 4\pi \frac{dE_{\text{em}}}{dt\, dm\, d\Omega d\nu} = 4\pi \frac{dE_{\text{em}}}{dt\, \rho dV d\Omega d\nu}, \tag{III.10}$$

where ρ is the mass density of the ISM, and $dm = \rho dV$, its mass element. The factor 4π, in Eq. (III.10), makes ϵ_ν the solid angle fraction of monochromatic power emitted in a given direction, per unit mass. In Sect. I.2.4, we were considering the volume and mass of a grain, whereas, here, we are considering the volume and mass of the ISM. Combining Eq. (III.9) and Eq. (III.10), we get:

$$j_\nu(\nu, \vec{r}, \theta, \phi) = \frac{\rho(\vec{r})}{4\pi} \epsilon_\nu(\nu, \vec{r}, \theta, \phi). \tag{III.11}$$

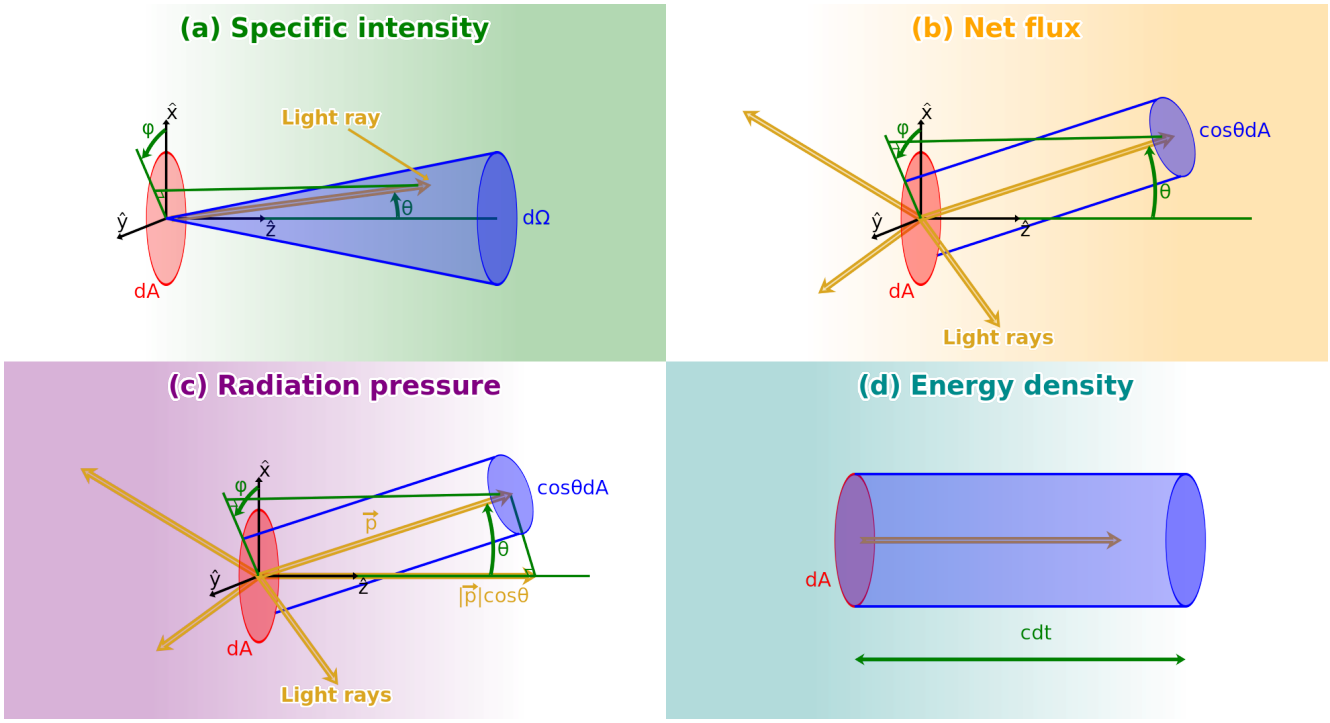

FIGURE III.1 – *Moments of the specific intensity.* Panel *(a)* represents the specific intensity (Eq. III.1). It is the monochromatic power of light rays per area, dA, and within the solid angle dΩ. Panel *(b)* demonstrates the calculation of the flux (Eq. III.4). We have represented several rays, with different directions and intensities. The effective area perpendicular to rays going through dA, but that are inclined at an angle θ, is only $\cos\theta\,\mathrm{dA}$. Panel *(c)* represents the radiation pressure (Eq. III.5). It is similar to panel *(b)*, except that we have shown the component of the momentum vector, $\vec{p}$, perpendicular to the surface, $|\vec{p}|\cos\theta$. Only this component contributes to the pressure on dA. Panel *(d)* represents the energy density (Eq. III.6). Between times t and $t+\mathrm{d}t$, photons going through dA are encompassed within the cylinder of volume $c\,\mathrm{d}t\,\mathrm{dA}$. Licensed under CC BY-SA 4.0.

Extinction coefficient and opacity. The amount of specific intensity absorbed and scattered along an infinitesimal path length, $\mathrm{d}l$, in the direction (θ,ϕ), is the *extinction coefficient*, $\alpha \geq 0$, defined such that:

$$\frac{\mathrm{dI}_\nu(\nu,\vec{r},\theta,\phi)}{\mathrm{d}l} = -\alpha(\nu,\vec{r})\,\mathrm{I}_\nu(\nu,\vec{r},\theta,\phi). \tag{III.12}$$

Similarly to the convention we have adopted for κ in Sect. I.2.4, we pose $\alpha \equiv \alpha_{\mathrm{ext}} = \alpha_{\mathrm{abs}} + \alpha_{\mathrm{sca}}$ to distinguish absorption and scattering.. Eq. (III.12) can be expressed with microscopic quantities, assuming the absorbers and scatterers have a cross-section $\mathrm{C}_{\mathrm{ext}}(\nu,\vec{r})$ and a density $n(\vec{r})$:

$$\alpha(\nu,\vec{r}) = n(\vec{r})\,\mathrm{C}_{\mathrm{ext}}(\nu,\vec{r}). \tag{III.13}$$

If the composition of the ISM is homogeneous, then $\mathrm{C}_{\mathrm{ext}}(\nu,\vec{r}) = \mathrm{C}_{\mathrm{ext}}(\nu)$. The *opacity*, that we have seen in Sect. I.2.4, is related to α by:

$$\alpha(\nu,\vec{r}) = \rho(\vec{r})\,\kappa(\nu,\vec{r}). \tag{III.14}$$

Mean free path. The *mean free path* of a photon with frequency, ν, at position $\vec{r}$ can be defined as:

$$l_{\mathrm{mean}}(\nu,\vec{r}) \equiv \frac{1}{\alpha(\nu,\vec{r})} = \frac{1}{\rho(\vec{r})\kappa(\nu,\vec{r})}. \tag{III.15}$$

It is the average length a photon will be able to travel before being absorbed or scattered. We can make the same remark as for the emissivity: in Sect. I.2.4, we were considering the cross-section of

dust particles per mass of grain, whereas Eq. (III.14) gives the cross-section of the whole ISM per mass of ISM. Table III.1 gives typical values of $l_{\rm mean}$ in a homogeneous medium, assuming the dust constitution of the THEMIS model (*cf.* Sect. II.3.2.2).

☞ In the diffuse ISM (WNM; $n_{\rm H} \simeq 0.3$ cm^{-3}; Table III.6), the mean free path of a photon in the visible range is of the order of a kiloparsec.

	HIM $n_{\rm H} = 0.003$ cm^{-3}	WNM $n_{\rm H} = 0.3$ cm^{-3}	CNM $n_{\rm H} = 30$ cm^{-3}	Molecular clouds $n_{\rm H} = 10^4$ cm^{-3}	Molecular clouds $n_{\rm H} = 10^6$ cm^{-3}
$l_{\rm mean}$(U)	139 kpc	1.39 kpc	13.9 pc	0.0417 pc	86.1 a.u.
$l_{\rm mean}$(B)	177 kpc	1.77 kpc	17.7 pc	0.0532 pc	110 a.u.
$l_{\rm mean}$(V)	223 kpc	2.23 kpc	22.3 pc	0.0669 pc	138 a.u.
$l_{\rm mean}$(R)	275 kpc	2.75 kpc	27.5 pc	0.0824 pc	170 a.u.
$l_{\rm mean}$(I)	358 pc	3.58 kpc	35.8 pc	0.107 pc	222 a.u.
$l_{\rm mean}$(J)	691 kpc	6.91 kpc	69.1 pc	0.207 pc	427 a.u.
$l_{\rm mean}$(H)	1021 kpc	10.2 kpc	102 pc	0.306 pc	632 a.u.
$l_{\rm mean}$(K)	1734 kpc	17.3 kpc	173 pc	0.52 pc	1073 a.u.

TABLE III.1 – *Mean free path as a function of wavelength and density.* These quantities were computed by rewriting Eq. (III.15) as $1/l_{\rm mean}(\lambda) = n_{\rm H} m_{\rm H} {\rm Y}_{\rm dust} \kappa(\lambda)$, taking ${\rm Y}_{\rm dust} \equiv {\rm M}_{\rm dust}/{\rm M}_{\rm H}$ from Table II.4 and κ values from Table II.5. We quote $l_{\rm mean}$ at the same photometric bands as in Table II.5. These values correspond to Solar metallicity, $Z = Z_\odot$. At first order, for metallicities $Z \gtrsim 0.2\,Z_\odot$, we can assume linearity: $l_{\rm mean}(Z) \simeq l_{\rm mean}(Z_\odot) \times Z_\odot/Z$ (*cf.* Chap. IV). The different ISM phases quoted here (HIM, WNM, CNM) will be defined in detail in Sect. III.3.1.

III.1.1.2 The Radiative Transfer Equation

The radiative transfer equation accounts for the variation of the specific intensity under the effects of absorption, scattering and emission (*cf.* Steinacker et al., 2013, for a review in the case of a dusty medium). It is schematically represented in Fig. III.2. This equation can be written:

$$\begin{aligned}\frac{{\rm d}I_\nu(\nu,\vec{r},\theta,\phi)}{{\rm d}l} = & \underbrace{-\alpha_{\rm abs}(\nu,\vec{r})I_\nu(\nu,\vec{r},\theta,\phi)}_{\text{absorption}} \underbrace{-\alpha_{\rm sca}(\nu,\vec{r})I_\nu(\nu,\vec{r},\theta,\phi)}_{\text{scattering out of the sightline}} \\ & \underbrace{+\alpha_{\rm sca}(\nu,\vec{r})2\pi\int_{-1}^{1}\Phi(\cos\theta',\nu)I_\nu(\nu,\vec{r},\theta(\theta'),\phi(\theta'))\,{\rm d}\cos\theta'}_{\text{scattering in the sightline}} \\ & + \underbrace{j_\nu^{\rm dust}(\nu,\vec{r})}_{\text{dust emission}} + \underbrace{j_\nu^{\star}(\nu,\vec{r})}_{\text{stellar emission}} .\end{aligned} \tag{III.16}$$

Scattering in the sightline: this term is the integral of $\alpha_{\rm sca}I_\nu$ (*i.e.* the scattered intensity) over the phase function, Φ (Eq. I.41). This expression depends on the relative angle, θ', between the incident rays and the scattered direction (θ,ϕ). This is the term that makes this equation an *integro-differential equation*, coupling all the directions together. This is why, numerical methods are required to solve Eq. (III.16). If we assume isotropic scattering (*i.e.* $\langle\cos\theta\rangle = 0$, corresponding to the Rayleigh regime; *cf.* Sect. I.2.2.3), this term simplifies and becomes: $\alpha_{\rm sca}(\nu,\vec{r})J_\nu(\nu,\vec{r})$.

Emission: we have assumed that the dust and stellar emissions are both isotropic, (*i.e.* independent of θ and ϕ). This is a reasonable assumption in the ISM. If we also assume that there is only one grain species, and that this species is at equilibrium with the radiation field, we can explicit: $j_\nu^{\rm dust}(\nu) = \alpha(\nu)B_\nu(\nu,T_{\rm eq})$. This simplification still contains the problem that to determine the equilibrium temperature, $T_{\rm eq}$, we need to integrate $\alpha_{\rm abs}I_\nu$ over all directions, and all frequencies.

Eq. (III.16) can be rewritten, using the optical depth, τ, defined such that $d\tau(\nu) = \alpha(\nu, l)\,dl$, or:

$$\tau(\nu, l) = \int_0^l \rho(l')\kappa(\nu, l')\,dl'. \tag{III.17}$$

Eq. (III.15) implies that $\tau(l_{\rm mean}) = 1$. At a given wavelength, a medium is: *(i) optically thin* or *transparent*, if $\tau \ll 1$; and *(ii) optically thick* or *opaque*, if $\tau \gg 1$. Replacing dl by $d\tau/\alpha$ in Eq. (III.16), we obtain:

$$\frac{dI_\nu(\nu, \vec{r}, \theta, \phi)}{d\tau} = -I_\nu(\nu, \vec{r}, \theta, \phi) + S_\nu(\nu \vec{r}, \theta, \phi), \tag{III.18}$$

where the *source function*, S_ν, includes all the terms added to the specific intensity:

$$S_\nu(\nu, \vec{r}, \theta, \phi) = \tilde{\omega}(\nu, \vec{r}) 2\pi \int_{-1}^{1} \Phi(\cos\theta', \nu) I_\nu(\nu, \vec{r}, \theta(\theta'), \phi(\theta'))\,d\cos\theta' + \frac{j_\nu^{\rm dust}(\nu, \vec{r}) + j_\nu^\star(\nu, \vec{r})}{\alpha(\nu, \vec{r})}. \tag{III.19}$$

We will discuss exact numerical solutions to this equation in Sect. III.1.1.4. For now, we discuss trivial solutions, when some processes are assumed negligible.

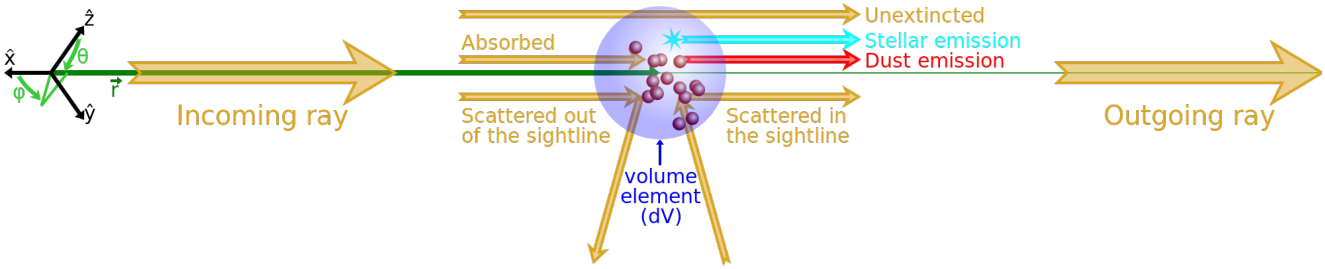

FIGURE III.2 – *The radiative transfer equation.* This figure represents only the different processes contributing to the variation of the specific intensity at one location, $\vec{r}$, in one direction, (θ, ϕ). The blue sphere represents a volume element. The red spheres within represent dust grain and the cyan star represents an actual star that would be present in the volume element. Licensed under CC BY-SA 4.0.

Propagation in vacuum. Let's assume we have a star of radius, R, and surface temperature, $T_\star$, located at $\vec{r} = \vec{0}$. The flux at $r = R$ has to be integrated only over the hemisphere where a surface element of the star emits: $F_\nu(R) = 2\pi \int_0^1 B_\nu(T_\star) \cos\theta\, d\cos\theta = \pi B_\nu(T_\star)$. If there is no ISM around the star, Eq. (III.16) simply becomes $dI_\nu/dl = 0$. The solution is thus $I_\nu = B_\nu(T_\star)$ along the directions coming from the star and 0 in all other directions. At an arbitrary distance, r, from the star, the solid angle it occupies is $\Omega_\star = R^2/r^2$. The flux is thus $F_\nu(r) = \pi B_\nu(T_\star) R^2/r^2$, which is the classic $1/r^2$ dilution of the flux.

Emission only. Let's assume we are observing, at submm wavelengths, a molecular cloud constituted of equilibrium grains at $T \simeq 10$ K, with opacity κ. At these wavelengths, the extinction is negligible. Eq. (III.16) is therefore simply $dI_\nu/dl = \rho\kappa B_\nu(T)$ within the cloud. The solution is thus $I_\nu(l) = \kappa B_\nu(T) \int_{l_0}^{l} \rho(l)\,dl$, where l_0 is the position of the edge of the cloud along the direction of the sightline. If the density is constant, we get $I_\nu(l) = \rho\kappa B_\nu(T) \times (l - l_0)$, which can be simplified as $I_\nu(l) = \tau(l) B_\nu(T)$. This expression of the brightness is often used in radio-astronomy.

Absorption only. Let's assume we are observing a background star through a cold molecular cloud, in the MIR. At these wavelengths, the albedo is close to 0 (Sect. I.2.2.3). If we make the assumption that the background star is much brighter than the thermal emission of the cloud, Eq. (III.16) simply becomes $dI_\nu/dl = -\alpha I_\nu$. The solution is therefore $I_\nu(l) = I_\nu^\star \exp[-\tau(l)]$ along the direction coming from the star and 0 in all other directions.

Emission and absorption. We can merge the two previous cases. It could correspond to a hot molecular cloud, observed at MIR wavelengths. Its thermal emission is absorbed by the cloud itself. The solution of Eq. (III.18), in this case, is:

$$I_\nu(\tau) = I_\nu^\star \exp(-\tau) + \int_0^\tau \exp\left(\tau' - \tau\right) S_\nu(\tau')\, d\tau'. \tag{III.20}$$

If the cloud contains a single grain species at temperature T, the solution becomes:

$$I_\nu(\tau) = B_\nu(T) + \left[I_\nu^\star - B_\nu(T)\right] \times \exp(-\tau). \tag{III.21}$$

If we look in a direction away from the background star, we get the classical self-absorption formula:

$$I_\nu(\tau) = B_\nu(T) \times \left[1 - \exp(-\tau)\right]. \tag{III.22}$$

This solution is displayed in Fig. III.3. Eq. (III.22) has the following two limit regimes.

Optically thin: if $\tau \ll 1$, $I_\nu \simeq \tau B_\nu(T)$, which is the "*emission only*" solution. The emission from the cloud is a grey body (Sect. I.2.4).

Optically thick: if $\tau \gg 1$, $I_\nu \simeq B_\nu(T)$, which means the cloud is not anymore a *grey* body, but a *perfect* one.

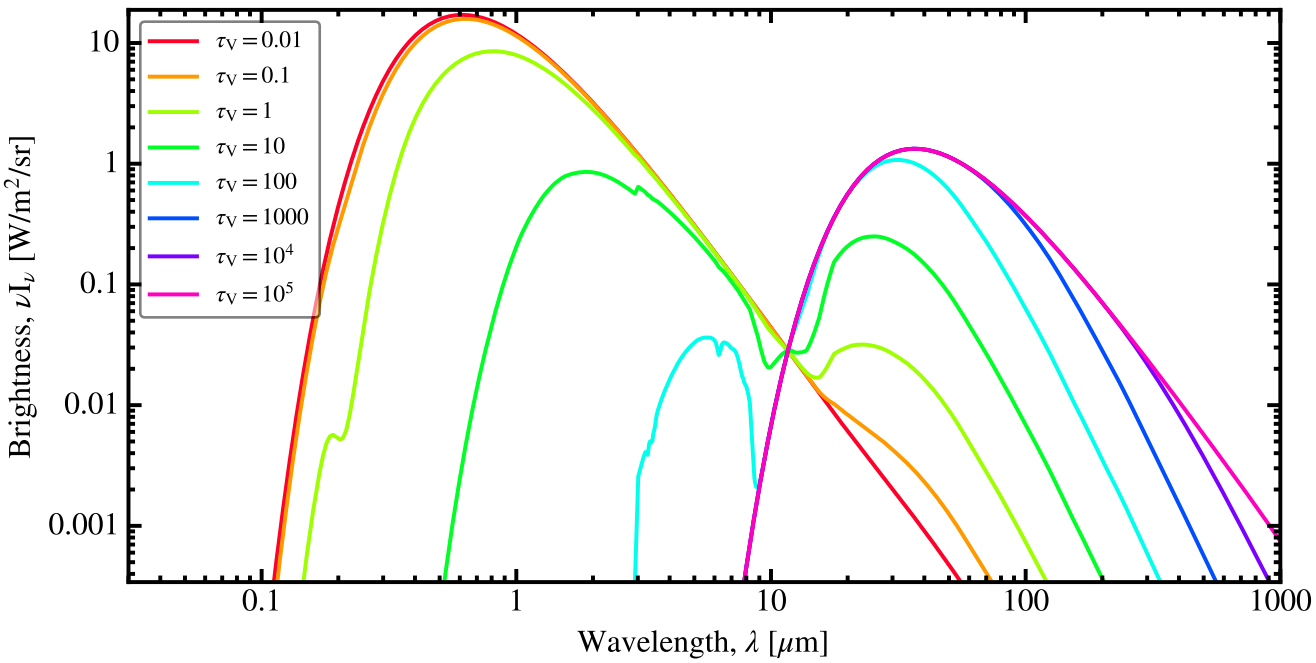

FIGURE III.3 – *Solution to the radiative transfer equation for an isothermal cloud, without scattering.* We have assumed that we are looking at a background star ($T_\star$ = 6000 K), through an homogeneous cloud of grains at equilibrium temperature, T = 100 K, with the THEMIS opacity. We have diluted the stellar emission by a factor 10^{-6}, which could correspond to a situation where the actual angular area of the star is 10^{-6} times the beam of the telescope. We show the SED according to Eq. (III.22), varying the optical depth in the V band, τ_V. We have included very large τ_V, up to 10^5, in order to demonstrate the asymptotic behavior of the dust emission tending toward a perfect black body. In typical ISM studies, it is however rare to find τ_V values higher than $\simeq 100$. Licensed under CC BY-SA 4.0.

Scattering and absorption with central illumination. Let's assume that we have a homogeneous spherical cloud, of radius R_{cl}, and a central isotropically illuminating source, with monochromatic

luminosity, $L_\nu^\star(\lambda)$. If $L_\nu^{esc}(\lambda)$ is the monochromatic luminosity escaping the cloud, the *escape fraction* can be defined as:

$$P_\nu^{esc}(\lambda) \equiv \frac{L_\nu^{esc}(\lambda)}{L_\nu^\star(\lambda)} = \exp\left[-\tau_{eff}(\lambda)\right]. \tag{III.23}$$

The second equality defines τ_{eff} as the *effective optical depth* of the medium.

Optically thick: In the case of pure isotropic scattering ($g = \langle\cos\theta\rangle \simeq 0$), it can be shown that the *net displacement* of a photon after N_{sca} interactions is: $l_{eff} = \sqrt{N_{sca}} l_{mean}$ (*cf.* Chap. 1 of Rybicky & Lightman, 1979). The probability a photon will be absorbed, at the end of a free path, is $1-\tilde{\omega}$. The mean number of free paths can thus be estimated by $N_{sca}(1-\tilde{\omega}) = 1$, or: $N_{sca} = 1/(1-\tilde{\omega})$. The optical depth of the cloud is $\tau \simeq R_{cl}/l_{mean}$ (Eq. III.15 and Eq. III.17). The same way, the effective optical depth can be written $\tau_{eff} \simeq R_{cl}/l_{eff}$. We thus get:

$$\tau_{eff} \simeq \sqrt{1-\tilde{\omega}}\tau. \tag{III.24}$$

Optically thin: in this case, there is a low probability of interaction. Eq. (III.23) tells us that τ_{eff} accounts only for photons that have been absorbed. We therefore simply have (*cf.* Chap. 1 of Rybicky & Lightman, 1979):

$$\tau_{eff} = (1-\tilde{\omega})\tau. \tag{III.25}$$

This formula simply subtracts among the few photons that may have interacted with the grains those which have been scattered. Contrary to Eq. (III.24), it is valid for any value of g.

Városi & Dwek (1999, hereafter VD99) have proposed an empirical approximation to interpolate the two regimes of Eq. (III.24) and Eq. (III.25), resulting in the following escape fraction:

$$P_{esc}^{cen}(\lambda) \simeq \exp\left[-(1-\tilde{\omega}(\lambda))^{\chi(\lambda)}\tau(\lambda)\right], \tag{III.26}$$

with:

$$\chi(\lambda) \equiv 1 - \frac{1}{2}\left[1-\exp\left(-\frac{\tau(\lambda)}{2}\right)\right]\sqrt{1-g(\lambda)}. \tag{III.27}$$

They have benchmarked this approximation with a Monte-Carlo radiative transfer model (*cf.* Sect. III.1.1.4). Both are in very good agreement in most of the astrophysically relevant parameter space. This solution is displayed in Fig. III.4.a.

Scattering and absorption with uniform illumination. VD99 have also proposed an approximation in the case where the internal illumination of the cloud is uniform. They start from the escape probability of a homogeneous sphere with uniform illumination, without scattering, given by Osterbrock (1989):

$$P_{esc}^{nosca} = \frac{3}{4\tau}\left[1 - \frac{1}{2\tau^2} + \left(\frac{1}{\tau} + \frac{1}{2\tau^2}\right)\exp\left(-2\tau\right)\right]. \tag{III.28}$$

A demonstration of this formula is given in Appendix C of VD99. VD99 find, with a recursive argument, that the following expression is in relatively good agreement with a Monte-Carlo radiative transfer model:

$$P_{esc}^{uni}(\lambda) \simeq \frac{P_{esc}^{nosca}(\lambda)}{1-\tilde{\omega}(\lambda)\left[1-P_{esc}^{nosca}(\lambda)\right]}. \tag{III.29}$$

VD99 show that Eq. (III.29) perfectly agrees with the exact solution for a particular value of $g(\tau)$. The largest discrepancies, of about 20 %, are found at high optical depth, for g close to 0. Eq. (III.29) is demonstrated in Fig. III.4.b. We can see that, at a given τ_V, this geometry has an overall larger escape fraction than central illumination.

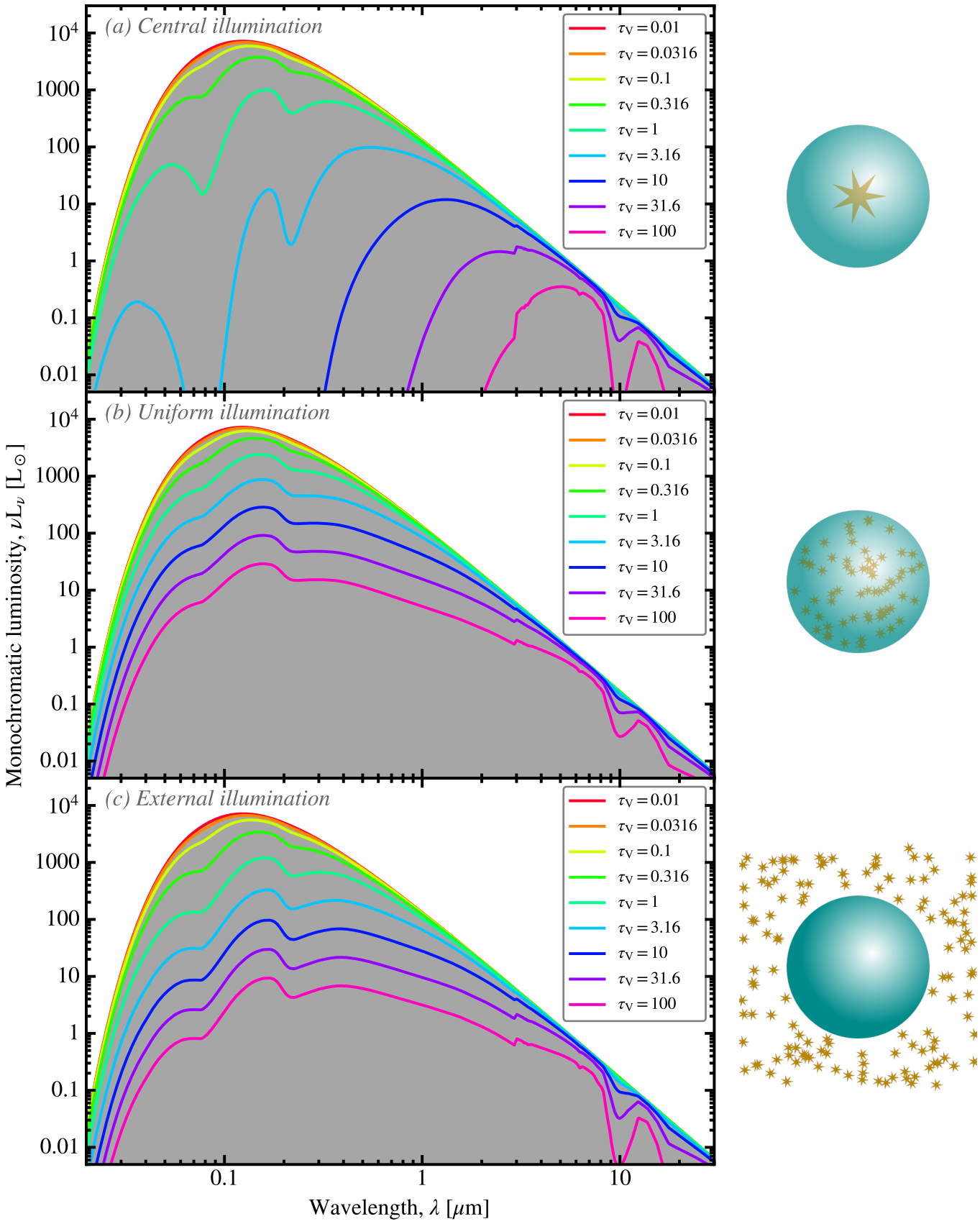

FIGURE III.4 – *Escaping radiation from a spherical cloud.* In the three panels, we show the escaping SED of a homogeneous spherical cloud, made of THEMIS grains. We vary the V-band optical depth, τ_V. The illuminating source is a star ($T_\star = 3 \times 10^4$ K), with a bolometric luminosity $L_\star = 10^4\ L_\odot$. In panel *(a)*, we show the case of central illumination. All the power is in the central source. Panel *(b)* shows the case of uniform illumination. The total power of the sources within the cloud is $L_\star$. Panel *(c)* shows external illumination. In this case, the flux at the surface of the cloud is $L_\star / 4\pi R_{cl}^2$.

Scattering and absorption with external illumination. There are also expressions in the case of a homogeneous spherical cloud, externally illuminated by an isotropic radiation field. VD99 derive the following approximation for the *absorbed fraction*:

$$\mathrm{P}_{\mathrm{abs}}^{\mathrm{ext}}(\lambda) \equiv 1 - \mathrm{P}_{\mathrm{esc}}^{\mathrm{ext}}(\lambda) \simeq \frac{4\tau(\lambda)\,[1-\tilde{\omega}(\lambda)]}{3}\mathrm{P}_{\mathrm{esc}}^{\mathrm{uni}}(\lambda). \tag{III.30}$$

The absorbed fraction is indeed more relevant in the case of external illumination, as it would be difficult to observationally separate the escaping radiation from the cloud and the ambient ISRF. On the contrary the absorbed fraction is meaningful if one wants to evaluate the heating of the cloud. This approximation is demonstrated in Fig. III.4.c.

The three formulae for spherical clouds, given in Eq. (III.26), Eq. (III.29) and Eq. (III.30), do not allow us to model the internal heating of the cloud. These expressions are indeed global escape and absorbed fractions, but they do not account for the gradient of illumination within the cloud that would lead to a gradient of heating rate.

III.1.1.3 Approximations for Clumpy Media

The ISM is a highly heterogeneous medium, with contrast densities of several orders of magnitude. A useful approximation is the *clumpy medium*, composed of: *(i)* a diffuse, uniform *InterClump Medium* (ICM), characterized by its density, n_{ICM}; and *(ii)* dense, spherical clumps, with density, n_{C}, radius, r_{C}, and volume filling factor, f_{V}.

Effective optical depth of a clumpy medium. Let's assume that we are looking at a background star through a cloud, and that the albedo of the grains is negligible. Along a given sightline, we have seen in Sect. III.1.1.2 that the brightness in the direction of the star is $\mathrm{I}_\nu = \mathrm{I}_\nu^\star \times \exp(-\tau)$. If the clumpy structure of the cloud is unresolved, the brightness measured in the telescope beam can be written as the sum of N sightlines, some passing through the ICM, others through the clumps:

$$\mathrm{I}_\nu^{\mathrm{clumpy}} = \frac{\mathrm{I}_\nu^\star}{\mathrm{N}} \sum_{i=1}^{\mathrm{N}} \exp(-\tau_i)\,. \tag{III.31}$$

This is the general expression. In the case of an homogeneous medium, Eq. (III.31) simplifies: $\mathrm{I}_\nu = \mathrm{I}_\nu^\star \exp(-\tau_{\mathrm{hom}})$, where τ_{hom} is the optical depth of the homogeneous medium. In order to have the same dust mass and opacity as in the clumpy medium, we need to have:

$$\tau_{\mathrm{hom}} \equiv \frac{1}{\mathrm{N}} \sum_{i=1}^{\mathrm{N}} \tau_i. \tag{III.32}$$

In the homogeneous medium, $\rho \times \mathrm{L}$ is indeed the mass surface density of a cloud of depth L. If there is a statistical distribution of clumps in the beam, it must be identical in the clumpy medium. Thus, the brightness of the homogeneous medium is:

$$\mathrm{I}_\nu^{\mathrm{hom}} = \exp\left(-\frac{1}{\mathrm{N}}\sum_{i=1}^{\mathrm{N}}\tau_i\right) = \left[\prod_{i=1}^{\mathrm{N}}\exp(-\tau_i)\right]^{1/\mathrm{N}}. \tag{III.33}$$

Invoking the *arithmetic-mean/geometric-mean inequality*[1] (*e.g.* page 456 of Cauchy, 1821), we conclude that: $\mathrm{I}_\nu^{\mathrm{clumpy}} \geq \mathrm{I}_\nu^{\mathrm{hom}}$. An important consequence of this result is that, from an observational point of view, we can miss a large mass of dust hidden in clumps. VD99 discuss this result in more detail.

> ☞ The effective optical depth of a clumpy medium is always lower than that of a homogeneous medium with the same dust constitution and dust mass.

1. Stating that $\sum_{i=1}^{\mathrm{N}} a_i/\mathrm{N} \geq \prod_{i=1}^{\mathrm{N}} a_i^{1/\mathrm{N}}$, provided that $a_i \geq 0$, $\forall i$.

The mega-grains approximation. Neufeld (1991) proposed a simple approach to explain the leakage of Ly-α photons by galaxies. He treated dusty gas clumps, in an empty ICM, as large grains with their own albedo and asymmetry parameter. This idea was then further developed by Hobson & Padman (1993), in cases where the ICM is non empty. They named it the *mega-grains approximation*, as clumps are treated as grains, although they have macroscopic sizes. They applied this approach to a clumpy infinite slab, externally illuminated on one side, and compared the results to a Monte-Carlo radiative transfer model. VD99 then refined some of the expressions of Hobson & Padman (1993) and applied them to the case of a spherical clumpy cloud, with the three types of illuminations we have discussed in Sect. III.1.1.2: *(i)* central; *(ii)* uniform; and *(iii)* external. VD99 systematically benchmarked their results with a Monte-Carlo radiative transfer code. We briefly review their results in the rest of this section.

Escape fractions for a clumpy medium. VD99 derived a series of expressions, based on Eq. (III.26), Eq. (III.29) and Eq. (III.30), but replacing grain properties by effective mega-grains properties. These analytical approximations are all summarized in Sect. 5 of VD99. We demonstrate these analytical expressions for the three types of illuminations in Fig. III.5. Overall, they provide a good agreement with Monte-Carlo radiative transfer calculations. They are also very easy to compute. The weakest point concerns the treatment of the grain heating. The mega-grains formalism allows us to separate the absorbed fractions in the clumps and in the ICM. It thus provides different heating rates in the two phases. In Fig. III.5, we can clearly see that the clump emission (red) is significantly colder than that of the ICM (magenta). It however does not allow us to estimate the gradient of radiation field within the ICM and within clumps. This is the most dramatic in the case of central illumination. In order to obtain a more realistic SED for this particular case, VD99 used an *ad hoc* prescription, assuming a power-law distribution of equilibrium grain temperatures controlled by several tuning parameters depending on the grain type.

III.1.1.4 Rigorous Solutions

The radiative transfer equation (Eq. III.16) can be solved numerically. There are two main classes of methods (Steinacker et al., 2013, for a review).

Monte-Carlo Radiative Transfer (MCRT) consists in simulating the random walk of photons, from their sources (stars, AGNs or thermal emission from dust grains) to the outside of the region, through their multiple scatterings.

Ray-tracing numerically solves the radiative transfer equation on a discretized grid along multiple sightlines. It is more difficult to implement than MCRT, and can be computationally more intensive. It however allows the user a better assessment of the numerical errors.

MCRT is by far the most popular method. In this section, we briefly review its principle and apply it to an example.

Setting the model. To solve the radiative transfer equation (Eq. III.16), we need to specify the following physical ingredients.

A 3D spatial grid of dust density has to be defined. Different coordinate systems can be chosen. In case there are steep density gradients (*e.g.* clumps), one has to make sure the transitions are finely enough sampled.

A 3D distribution of primary emitters, as well as their SED needs to be defined. In this section, we will consider only stars, but AGNs can be treated the same way. It is possible to account both for: *(i)* discrete emission, such as an individual star or a cluster; and *(ii)* diffuse emission, such as unresolved stellar distribution.

The dust properties need to include, at least: the opacity, the albedo and the asymmetry parameter. It is possible to account for a mixture of dust grains, with different compositions and sizes. The

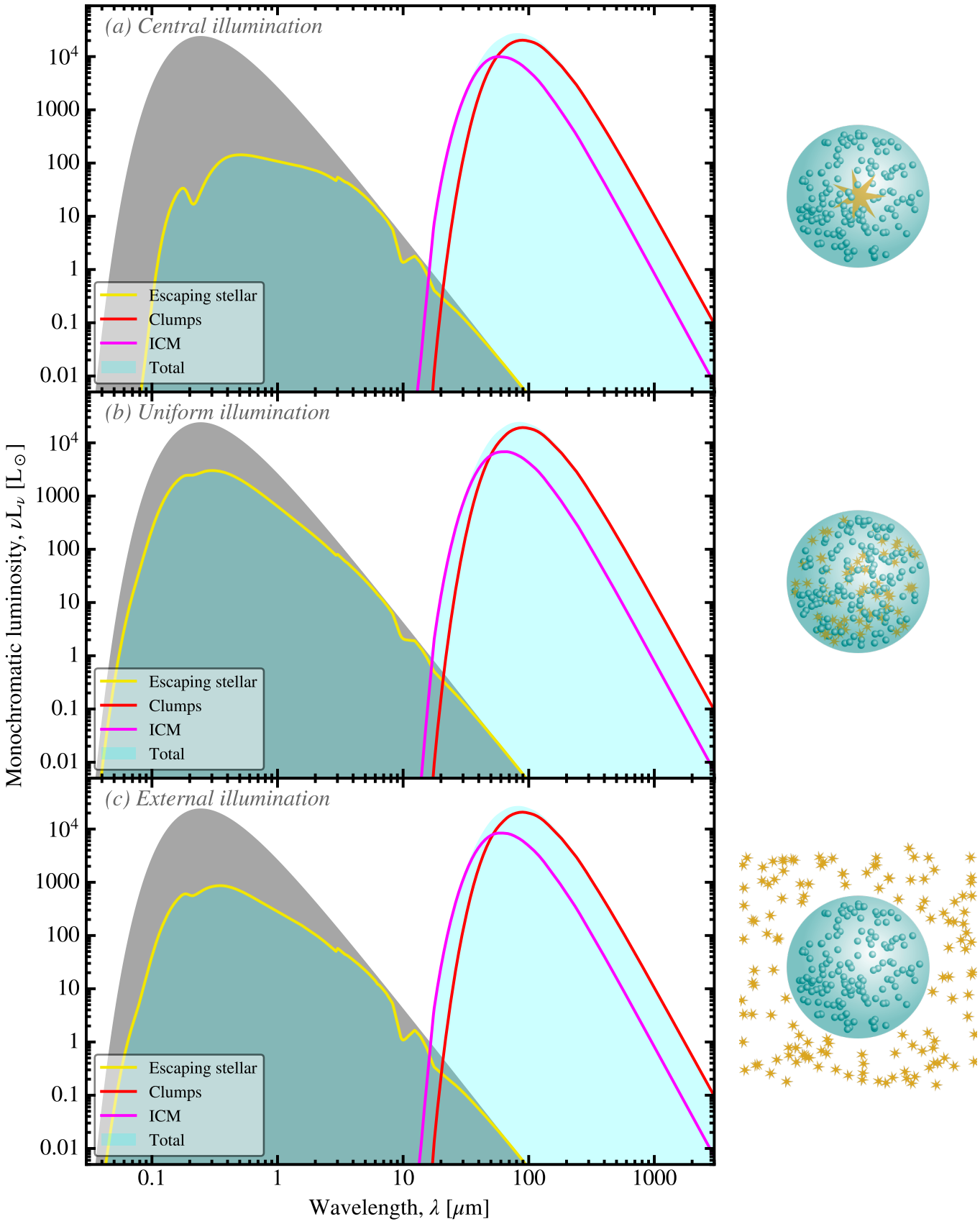

FIGURE III.5 – *Escaping SED from clumpy spherical clouds.* The three panels are the SED of a R_{cl} = 1 pc cloud, containing r_C = 0.05 pc clumps, computed with the mega-grains approximation. The density is n_{ICM} = 1000 cm^{-3} in the ICM and $n_C = 10^5$ cm^{-3} in the clumps (volume filling factor, f_V = 20 %). The grains have THEMIS optical properties and are assumed to be at thermal equilibrium. We have displayed: *(i)* the intrinsic stellar luminosity ($T_\star = 1.5 \times 10^4$ K; $L_\star = 3.3 \times 10^4$ $L_\odot$), in grey; *(ii)* the escaping stellar radiation, in yellow; *(iii)* the clump luminosity, in red; *(iv)* the ICM luminosity, in magenta; *(v)* the total escaping SED, in cyan. Licensed under CC BY-SA 4.0.

size-distribution-integrated quantities of Eqs. (II.19) – (II.22) are used for the transfer of stellar photons. It is however necessary to treat the thermal emission of individual species, especially if they are stochastically heated.

The principle of Monte-Carlo radiative transfer. To compute a MCRT model, we need to draw a large number of photons (typically $\simeq 10^6$ per wavelength bin), and execute the following steps. The procedure is schematically represented on Fig. III.6.

1. At each wavelength, photons are randomly drawn from primary emitters, proportionally to their specific intensity. The emission angle, (θ, ϕ), is randomly chosen, if the emitters are isotropic, which is the case for stars.
2. The interaction probability of a photon with a dust grain is then drawn from $1-\exp(-\tau)$, along the original direction of the photon. On interaction, one accounts for the probabilities of: *(i)* absorption (proportional to $1-\tilde{\omega}$); and *(ii)* scattering (proportional to $\tilde{\omega}$). We could randomly choose between absorption and scattering, and thus terminate the path of the photons $1-\tilde{\omega}$ of the times. However, forced scattering, the way it is shown in Fig. III.6, allows us to track the absorption and scattering probabilities at each interaction, in a numerically more efficient way. The scattering angle is randomly drawn from the scattering phase function (Eq. I.44), setting the new direction of the photon.
3. We iterate this process as long as needed, until the photon exits the nebula. The average number of interactions increases with the effective optical depth of the nebula. At each interaction, $(1-\tilde{\omega}) \times I_\nu$ is absorbed by the grain, and $\tilde{\omega} \times I_\nu$ is scattered. After N interactions, the scattered intensity is $\tilde{\omega}^N \times I_\nu$ and the absorbed power is proportional to $(1-\tilde{\omega}) \times \tilde{\omega}^{N-1}$. For a typical $\tilde{\omega} \simeq 0.5$, after three scatterings, the intensity is reduced by a factor $\simeq 0.13$.
4. Once all the photons at all wavelengths have been drawn, the thermal emission of all dust species within each cell can be computed. IR photons are then drawn and scattered through the nebula, the same way as stellar photons. The overall opacity and albedo are usually much lower in the IR. The computation of IR radiative transfer is thus usually much faster. In the most embedded regions, the IR radiation absorbed by dust grains can be significant. One therefore has to recompute the IR transfer a few times, until an energy balance is reached.

These steps constitute the most basic implementation of MCRT. Numerous optimizations have however been proposed in the last fifty years (*e.g.* Witt, 1977a,b,c; Witt & Oshel, 1977; Yusef-Zadeh et al., 1984; Whitney & Hartmann, 1992; Wood, 1997; Wood & Jones, 1997; Városi & Dwek, 1999; Baes & Dejonghe, 2001; Gordon et al., 2001; Misselt et al., 2001; Steinacker et al., 2002, 2006; Wood et al., 2008; Baes et al., 2011; Camps & Baes, 2015; Siebenmorgen et al., 2015; Natale et al., 2015; Juvela, 2019). Improvements and optimizations include: *(i)* massive parallelization, and the use of GPU; *(ii)* the production of synthetic photometric images; *(iii)* the treatment of polarization by scattering.

Numerical method to randomly draw photons. To simulate the random walk of a photon, there are two sets of random variables to draw: *(i)* random interaction events; and *(ii)* scattering angles.

Drawing interaction events along the path of a photon consists in drawing a path length from the following *Probability Density Function* (PDF):

$$p(l) = 1 - \exp\left(-\int_0^l \kappa\rho(l')\,l'\,\mathrm{d}l'\right). \tag{III.34}$$

For simplicity, l corresponds to the path length along the direction of the photon, starting at $l = 0$. Drawing a variable from this distribution can be achieved the following way (*e.g.* Városi & Dwek, 1999). It uses the *rejection method* (*cf.* Appendix C.2.3.1). These steps are represented on Fig. III.7.

1. First draw a uniform random variable between 0 and 1, Θ_1.

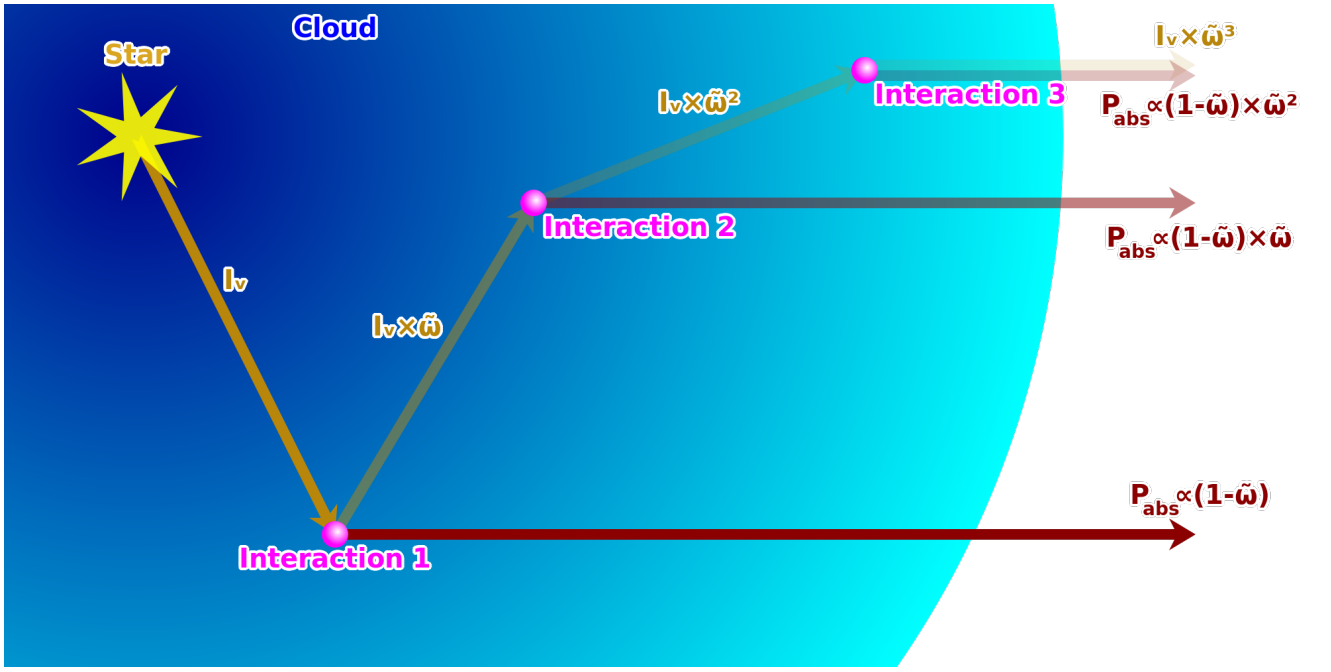

FIGURE III.6 – *Principle of Monte-Carlo radiative transfer.* The blue area represents a dust cloud. We follow the journey of a single photon emitted by a star into the cloud and scattered at different locations. A single photon will be either scattered or absorbed. However, for numerical efficiency, we consider both solutions, weighted by their probability (scattering: $\tilde{\omega}$; absorption: $1-\tilde{\omega}$). The dark red arrows correspond to emitted IR photons. In principle, these photons can also be scattered and absorbed by the cloud. The arrows exiting the cloud to the right represent what would be measured by an observer. Licensed under CC BY-SA 4.0.

2. Set $l_0 = -\ln(1-\Theta_1)/\kappa\rho_{max}$, where ρ_{max} is the maximum of the density along the path.
3. Draw a second uniform random variable between 0 and 1, Θ_2.
4. If $\Theta_2 \leq \rho(l_0)/\rho_{max}$, then the interaction is accepted, and a new scattering angle can be drawn. On the contrary, if $\Theta_2 > \rho(l_0)/\rho_{max}$, the interaction is rejected. One then needs to go back to the first step, starting from l_0, this time.

Scattering angles are drawn from the scattering phase function (Eq. I.44; Fig. III.8.a). If we place a spherical coordinate reference frame at the position of interaction with its z-axis aligned with the incoming direction of the photon, then the two spherical angle, (θ, ϕ), that will determine the new direction of the photon are drawn the following way.

1. The new polar angle, θ, is drawn by inverting the *Cumulative Distribution Function* (CDF) (*cf.* Appendix C.2.3.2). In case we use the Henyey & Greenstein (1941) phase function, the inverse of the CDF can be analytically derived (*cf.* Fig. III.8.b):

$$F^{-1}(\Theta_3) = \frac{1}{2g}\left[1+g^2-\left(\frac{1-g^2}{1-g+2g\Theta_3}\right)^2\right], \tag{III.35}$$

   where Θ_3 is a uniform random variable between 0 and 1.
2. The new azimuthal angle, ϕ, is simply drawn from a uniform distribution between 0 and 2π, because there is a symmetry of revolution around the direction of the photon.

Example of a clumpy medium. For this manuscript, we have developed a MCRT model, following the procedure previously described. We have applied it to a spherical clumpy cloud, similar to those discussed in Sect. III.1.1.3. The radius is $R_s = 1$ pc, with an ICM density, $n_{ICM} = 1000$ cm^{-3}. The $r_C = 0.05$ pc clumps have a density, $n_C = 10^5$ cm^{-3}, with a filling factor, $f_V = 20\,\%$. We assume

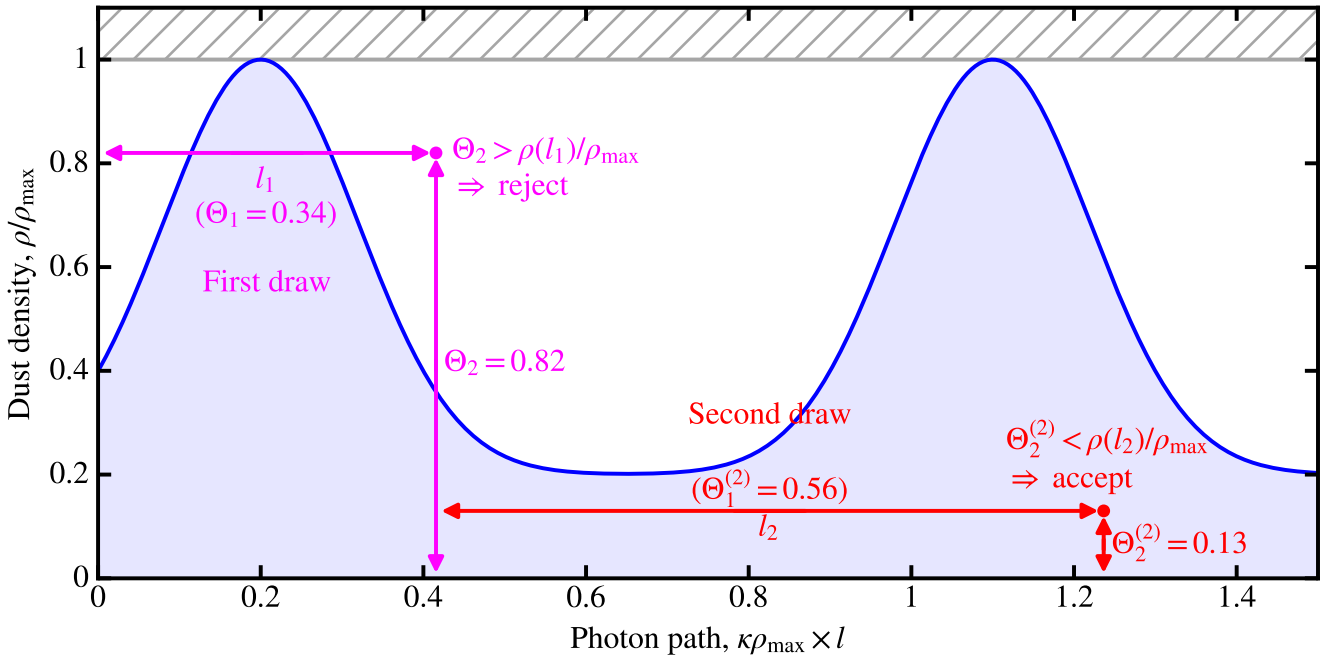

FIGURE III.7 – *Drawing photons in a Monte-Carlo radiative transfer model.* This figure shows the dust density of a medium (in blue; normalized to its peak value, $\rho_{\rm max}$), as a function of the path length of the photon, l, across the nebula. The x-axis is multiplied by $\kappa\rho_{\rm max}$ so that it corresponds to the optical depth the medium would have if the density was everywhere $\rho_{\rm max}$. Two random draws are represented. In magenta, we show a first draw, bringing the photon to $l_1 = -\ln(1-\Theta_1)/\kappa\rho_{\rm max}$. The interaction at l_1 is rejected because $\Theta_2 > \rho(l_1)/\rho_{\rm max}$. A second similar draw brings the photon at $l = l_1 + l_2$, where the interaction is accepted. After this draw, one needs to draw the scattering angle. Licensed under CC BY-SA 4.0.

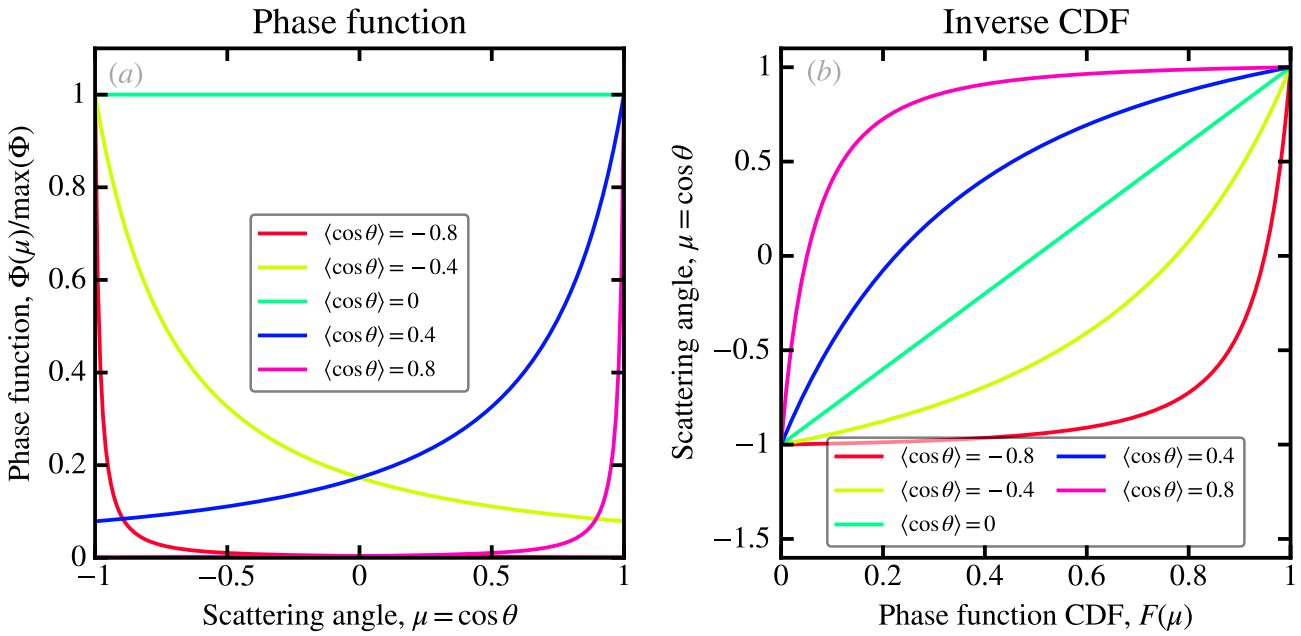

FIGURE III.8 – *Drawing scattering angles in a Monte-Carlo radiative transfer model.* Panel *(a)* shows the Henyey & Greenstein (1941) scattering phase function (Eq. I.44), for different values of the asymmetry parameter, $g = \langle\cos\theta\rangle$. Panel *(b)* shows the inverse CDF (Eq. III.35), for different values of g. Licensed under CC BY-SA 4.0.

THEMIS grain constitution, and assume all grains are at thermal equilibrium. This cloud is centrally illuminated by a $T_\star = 1.5 \times 10^4$ K star, with $L_\star = 3.3 \times 10^4\ L_\odot$.

The projected map of the dust mass surface density is shown in Fig. III.9.a. The average absorbed fraction, $\langle P_{abs} \rangle$ is shown in Fig. III.9.b. The latter quantity is the projected average of the absorbed fraction of photons passing through the cell. This fraction is highly concentrated in the central region, as most of the power is absorbed by clumps close to the star. Those clumps are hot, whereas clumps on the outskirt are colder, because they are essentially heated by fewer photons that have been multiply scattered. Fig. III.10 represents a few photon paths at three different wavelengths.

The total SED of this cloud is shown in Fig. III.11. We notice that a fraction of the dust emission is self-absorbed. This is mainly the 10 and 18 µm silicate emission of the hottest central clumps being absorbed by the outer ones. We have also compared our model to the mega-grains approximation (Sect. III.1.1.3; in dashed blue). We see this approximation is quite good in the UV-to-NIR range. It is however discrepant in the IR. This is because there is a very strong gradient of heating conditions, seen in Fig. III.9.b, whereas the mega-grains approximation accounts only for the total absorbed fraction in the clumps and the ICM [2].

Despite its intensive numerical requirements, MCRT is thus the most flexible and accurate way to compute the SED of an interstellar cloud. It is however important to make sure that the spatial resolution of the density grid is fine enough to resolve the shortest mean free path of photons. Otherwise, we would be smearing out a potential sub-grid temperature gradient. For the present model, we have 0.01 pc cells for $l_{mean}(U) \simeq 0.005$ pc.

> ☞ To accurately compute a radiative transfer model, it is necessary to resolve scale-lengths of the order of the mean free path of UV photons.

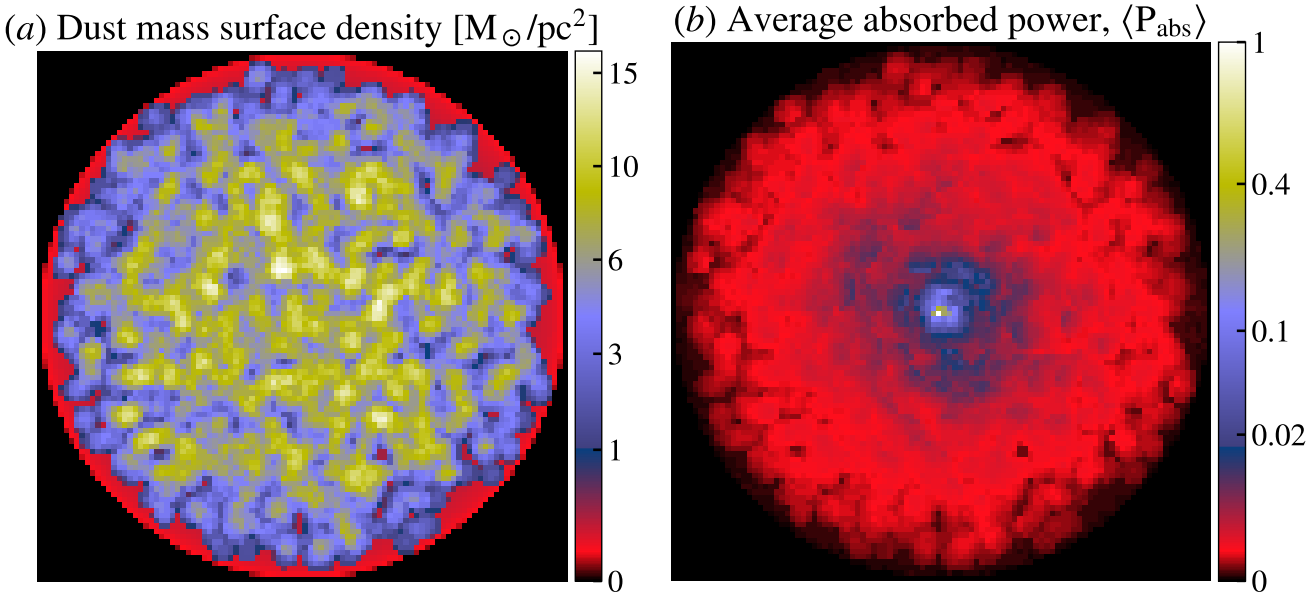

FIGURE III.9 – *Spatial distributions of the clumpy radiative transfer model.* Panel *(a)* shows the projected dust mass surface density of the cloud. Panel *(b)* shows the average projected absorbed fraction, $\langle P_{abs} \rangle$. The star is located at the center of the cloud. Notice that most of the power is absorbed in the central region.

2. VD99 solved this issue by assuming a power-law distribution of temperatures that we have discussed in Sect. III.1.1.3. This is however an *ad hoc* solution that needs to be calibrated for each dust species, by using an actual MCRT model. Our goal being to demonstrate what a MCRT model brings, we chose to compare it only to the SED that the mega-grains approximation allows us to derive, by itself.

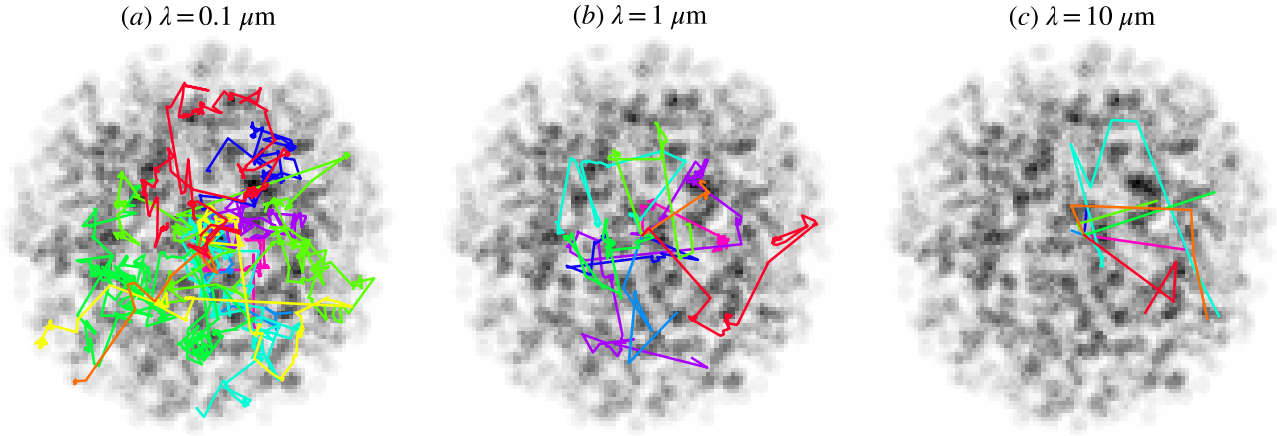

FIGURE III.10 – *Random photon path within a clumpy medium.* The three grey-scale images represent the projected column density of Fig. III.9.a. We have overlaid the random path of 10 photons before they exit the cloud, at three different wavelengths. These draws are those computed by the MCRT model. For a given wavelength, the different colors represent different photons. These figures demonstrate the fact that, at short wavelength, the mean free-path is shorter, resulting in a larger number of scatterings. Licensed under CC BY-SA 4.0.

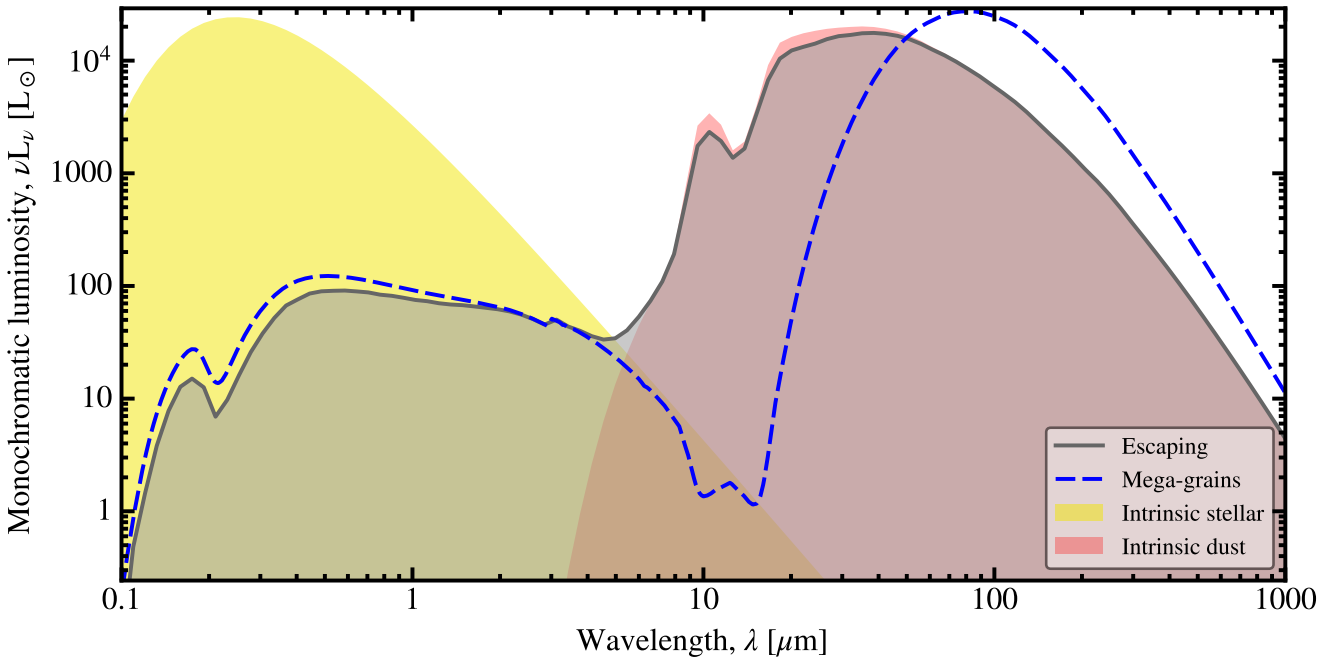

FIGURE III.11 – *Total SED from the clumpy radiative transfer model.* The yellow curve represents the intrinsic SED of the central star. The red curve is the intrinsic emission (non self-extincted) of the dust emission of the whole cloud. The grey curve shows the total escaping SED of the cloud. We have overlaid the mega-grains approximation (Sect. III.1.1.3), in dashed-blue, for comparison. Licensed under CC BY-SA 4.0.

III.1.2 Approximate Treatments of the Mixing of Physical Conditions

Ideally, each time we study a Galactic region or a galaxy, we should solve the radiative transfer equation (Eq. III.16). This is however, most of the time, impossible, because of the lack of constraints on the actual 3D structure of the region. Even if we have a collection of high-angular resolution multiwavelength images of our object, the matter and stellar distributions along the sightline have to be inferred. This inference is possible when the large-scale geometry of the object is quite regular, for instance: a protostellar disk and its jet, or a galactic disk and its bulge, *etc.* We will discuss the MCRT modeling of disk galaxies in Sect. III.1.3.2. Otherwise, most often, we need to adopt empirical approaches that allows us to constrain the dust properties, despite our uncertainty of the spatial structure of the region.

III.1.2.1 The Historical Model: the MBB

The MBB (*cf.* Sect. I.2.4.1) is historically the most widely-used dust SED model. It is controlled by the three following parameters (Eq. I.71 and Eq. I.73).

1. The dust mass, M_{dust}, is a scaling parameter.
2. The equilibrium temperature, T, controls the emission peak wavelength.
3. The *emissivity index*, β (Eq. I.73), controls the long-wavelength slope of the SED. This is demonstrated in Fig. III.12.a.

Its physical assumptions are simplistic: *(i)* the IR emission is optically thin; *(ii)* the dust is made of a single species of grains at thermal equilibrium with the ISRF; and *(iii)* the opacity is a power-law. By inferring both T and β, this model is designed to constrain both the dust excitation and its optical properties. This model was popularized by Hildebrand (1983), in the IRAS days (*cf.* Sect. II.1.2). At the time, it was well adapted, being a simple, but still physical model, with only three parameters to fit four broadbands (the four IRAS bands at 12, 25, 60 and 100 μm). It has however several limitations that are often disregarded in the literature.

The mixing of physical conditions is not accounted for by the MBB. It means that the SED fit of a complex region, containing a gradient of temperatures, is biased (*e.g.* Juvela & Ysard, 2012; Galliano et al., 2018). This is demonstrated in Fig. III.12.b. The grey-filled curve is the SED coming from a power-law distribution of temperatures (T = 15 to 60 K; the color curves). The intrinsic emissivity index of the grains making up this region is $\beta = 1.79$. Yet, fitting such a SED with a single MBB leads to a compromise temperature ($T = 45 \pm 8$ K) and a systematically lower emissivity index, $\beta = 1.12 \pm 0.30$. This is because a gradient of temperature tends to flatten the FIR slope, similarly to a lower β value.

> ☞ The emissivity index derived from a single MBB fit is always lower than its true, intrinsic value.

Stochastic heating is formally equivalent to a gradient of temperatures (*cf.* Sect. I.2.4.3). Stochastically heated grains dominate the emission at MIR wavelengths (*cf.* Fig. II.27). A single MBB is thus biased at short wavelengths by small grains, the same way it is biased at long wavelengths by cold dust. Solving this issue by fitting a linear combination of two or three MBBs can palliate this problem, but is usually not sufficient. In addition, fitting an out-of-equilibrium emission with equilibrium grains is physically incorrect. It renders the interpretation of the parameters of the hot MBB unreliable.

Realistic opacities are more complex than a power-law. Laboratory data show that emissivity indices of actual materials are wavelength-dependent quantities, $\beta(\lambda)$ (*cf. e.g.* Fig. II.22). Additionally, the somehow arbitrary choice of the two other parameters in Eq. (I.73) – the reference wavelength, λ_0, and the scaling of the opacity at this wavelength, κ_0 – have dramatic consequences on the derived dust mass. It is thus important to limit the potential range of variations of these parameters. The Kramers-Kronig relations (Sect. I.2.1.6) impose that $\beta \geq 1$, and

most compounds studied in the laboratory have $\beta < 2.5$ (*cf. e.g.* the Jena database). We recommend calibrating κ_0 on laboratory data or on well-constrained dust models (such as Eq. II.26). Contrary to what Hildebrand (1983) recommended, it is probably better to choose a reference wavelength, λ_0, around the peak of the FIR SED (between 100 and 300 µm), rather than in the submm. This way, variations of β will impact only moderately the derived dust mass.

☞ A MBB fit infers parameters whose physical meaning is difficult to assess.

The noise-induced degeneracy between T and β is well-documented (*e.g.* Shetty et al., 2009; Kelly et al., 2012; Galliano, 2018). A false negative correlation arises when a series of MBB fits are performed with standard least-squares, maximum likelihood, or non-hierarchical Bayesian methods. This degeneracy prevents to explore the potential correlation of these parameters that laboratory data and solid-state models suggest (*e.g.* Mennella et al., 1998; Meny et al., 2007). Luckily, hierarchical Bayesian methods are efficient at removing false, noise-induced correlations (*e.g.* Kelly et al., 2012; Galliano, 2018). Chap. V is entirely devoted to fitting techniques.

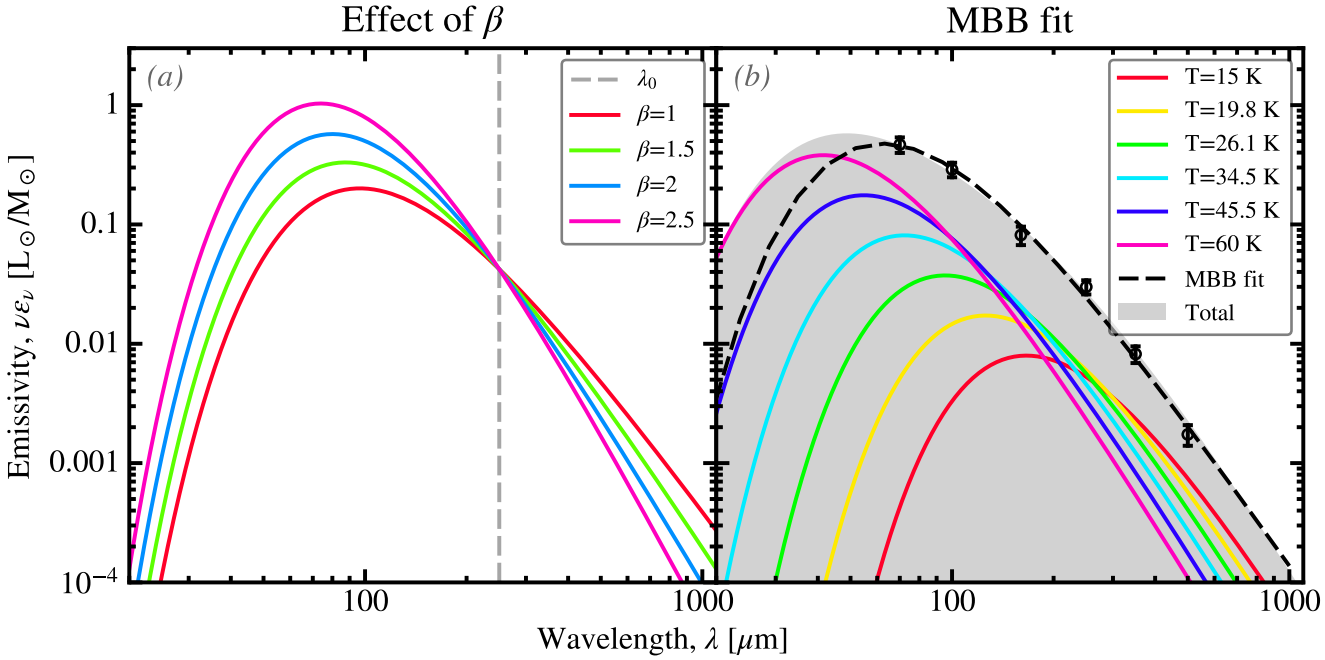

FIGURE III.12 – *MBB fitting.* Panel *(a)* demonstrate the effect of the emissivity index, β (Eq. I.73), on the SED of a MBB. The temperature is T = 30 K, with $\kappa(\lambda_0 = 250\ \mu m) = 0.64\ m^2/kg$ (Eq. II.26). Panel *(b)* illustrates the limitation of the isothermal assumption. The black error bars are synthetic observations (noise has been added). They are sampling the grey-filled curve, which is the integral of MBBs (color curves) times a power-law distribution of temperatures (T_{min} = 15 K, T_{max} = 60 K, and index 4). These MBBs have THEMIS optical properties (β = 1.79; Eq. II.26). Yet the fitted value (black dashed curve) is significantly lower: $\beta = 1.12 \pm 0.30$. The fitted temperature falls in the middle of the range, toward the high end: $T = 45 \pm 8$ K. Licensed under CC BY-SA 4.0.

III.1.2.2 A Phenomenological, Composite Approach

Dust models provide useful frameworks to model SEDs (Sect. II.3). Without the possibility to compute the radiative transfer, we are however facing the problem of the mixing of physical conditions. A prescription, proposed by Dale et al. (2001), has proven to be a powerful solution to this issue. It consists in assuming that the dust mass is distributed in regions with different starlight intensities,

U, following a power-law:

$$\frac{1}{M_{dust}}\frac{dM_{dust}}{dU} = U^{-\alpha} \times \left\{ \begin{array}{ll} \dfrac{1-\alpha}{(U_- + \Delta U)^{1-\alpha} - U_-^{1-\alpha}} & \text{if } \alpha \neq 1 \\ \dfrac{1}{\ln(U_- + \Delta U) - \ln U_-} & \text{if } \alpha = 1 \end{array} \right\} \text{for } U_- \leq U \leq U_- + \Delta U. \tag{III.36}$$

The idea is that the shape of the observed SED is used to constrain this distribution of ISRFs, assuming a dust mixture constitution. By lack of a better term, we call this approach the *composite* model. The free parameters are:

- the total dust mass, M_{dust}, acting as a scaling parameter;
- the power-law index, α;
- the minimum starlight intensity, U_-;
- the width of the starlight intensity distribution, ΔU.

It thus provides a way to account for the potential complexity of the region without having to model the radiative transfer. The model SED is then simply:

$$L_\nu^{dust}(\lambda) = \int_{U_-}^{U_- + \Delta U} \epsilon_\nu(\lambda, U) \frac{dM_{dust}}{dU} dU, \tag{III.37}$$

where $\epsilon_\nu(\lambda, U)$ is the monochromatic emissivity of the dust model, exposed to a single starlight intensity, U (Fig. II.24). Fig. III.13.a shows an example of a SED fit, using Eq. (III.36). We have a added a free-scaling black body, at $T_\star = 30{,}000$ K, to account for the stellar continuum that may be contaminating the MIR photometric bands. The composite approach is flexible enough to be usable in a diversity of environments. Dale et al. (2001) lists several simple geometries for which Eq. (III.36) is actually the solution. It is also adapted to more complex ISM topologies. For instance, Fig. III.13.b shows the dust mass distribution as a function of U, for each cell in the MCRT simulation of Sect. III.1.1.4. Despite the complex, clumpy structure of this cloud, it can be reasonably well-approximated by a power-law (shown in red).

The average starlight intensity. The parameters of Eq. (III.36) do not have a very clear physical meaning. Besides, they are often degenerate: the uncertainties on the three parameters U_-, ΔU and α are strongly correlated. It can be more efficient to quote the average of the distribution:

$$\langle U \rangle \equiv \frac{1}{M_{dust}} \int_{U_-}^{U_- + \Delta U} U \frac{dM_{dust}}{dU} dU = \left\{ \begin{array}{ll} \dfrac{1-\alpha}{2-\alpha} \times \dfrac{(U_- + \Delta U)^{2-\alpha} - U_-^{2-\alpha}}{(U_- + \Delta U)^{1-\alpha} - U_-^{1-\alpha}} & \text{if } \alpha \neq 1 \,\&\, \alpha \neq 2 \\ \dfrac{\Delta U}{\ln(U_- + \Delta U) - \ln U_-} & \text{if } \alpha = 1 \\ \dfrac{\ln(U_- + \Delta U) - \ln U_-}{U_-^{-1} - (U_- + \Delta U)^{-1}} & \text{if } \alpha = 2. \end{array} \right. \tag{III.38}$$

This parameter quantifies the *average starlight intensity*, heating the bulk of the dust mass. It is the equivalent of the equilibrium temperature of a MBB, as it controls the peak emission wavelength, except that it accounts for the mixing of physical conditions and the stochastic heating of small grains. The *Total InfraRed* (TIR) luminosity, L_{TIR}, can be expressed:

$$L_{TIR} \equiv \int_{3\,\mu m}^{1000\,\mu m} L_\lambda(\lambda)\, d\lambda \simeq \int_0^\infty L_\nu^{dust}(\nu)\, d\nu = \epsilon \times M_{dust} \times \langle U \rangle, \tag{III.39}$$

where the constant $\epsilon \equiv \int \epsilon_\nu \, d\nu$ is the bolometric emissivity of the dust model. For the THEMIS mixture, heated by the Mathis et al. (1983) ISRF, it is $\epsilon = 221\, L_\odot / M_\odot / U$ (Table II.7).

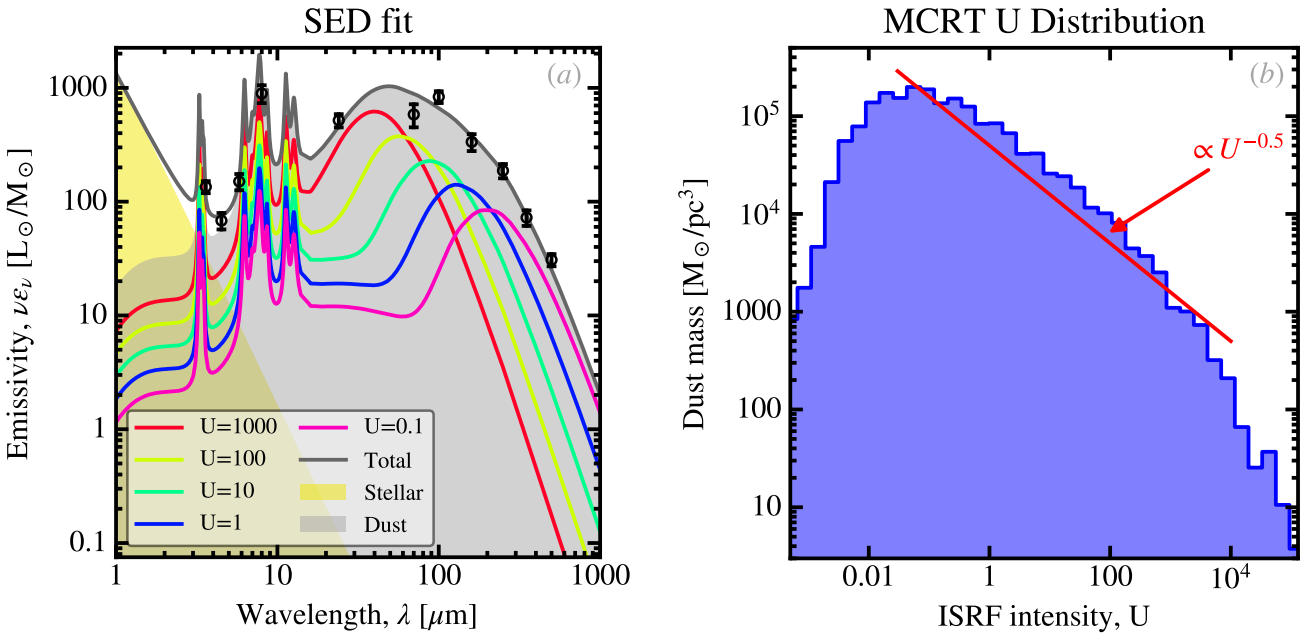

FIGURE III.13 – *Phenomenological mixing of physical conditions.* Panel *(a)* shows an example of SED fit using the composite approach (Eq. III.36). The black error bars represent synthetic observations (noise has been added). These observations have been fitted with the total model represented by the dark grey line. This total model is the sum of a stellar (in yellow) and a dust (in light grey) components. The dust component is the integral of dust models illuminated by different U (Eq. III.36). The rainbow curves represent several bins of ISRF. The sum of these rainbow curves is the light-grey-filled curve. The blue curve in panel *(b)* shows the distribution of dust mass per bin of ISRF intensity, U (Sect. I.2.4.2), for each cell in the MCRT simulation presented in Sect. III.1.1.4. The value of U has been derived from the grain equilibrium temperature, using Eq. (I.84). The red line shows a power-law approximation of this distribution. With the parametrization of Eq. (III.36), it would correspond to: $U_- = 0.03$, $\Delta U = 10^4$ and $\alpha = 0.5 + 1 = 1.5$ (the +1 comes from taking the derivative of $M_{dust}(U)$ to get Eq. III.36). Licensed under CC BY-SA 4.0.

Constraining the dust properties. The composite approach of Eq. (III.36) allows us to constrain parameters that are not extremely sensitive to radiative transfer effects (*i.e.* to variations of the local intensity and spectral shape of the ISRF; *cf. e.g.* Galliano et al., 2018, 2021, for a discussion).

The dust mass, M_{dust}, is dominated by large grains (*cf.* Table II.3). The heating of these large grains is sensitive only to the power they absorb, and not to the spectral shape of the ISRF, contrary to small grains (*cf.* Sect. I.2.4.3). The assumption of a constant ISRF shape therefore does not significantly bias M_{dust}.

The average starlight intensity, $\langle U \rangle$ (Eq. III.38), is empirically constrained by the shape of the FIR emission, dominated by large grains. This quantity is thus not particularly biased, similarly to M_{dust}. In addition, Eq. (III.39) tells us that $L_{TIR} \propto M_{dust}\langle U \rangle$. Yet, L_{TIR} is a weakly model-dependent quantity, as it is simply the integral of the SED model passing through the observed fluxes. L_{TIR} and M_{dust} being reliable, $\langle U \rangle$ has to be.

The mass fraction of PAH, q_{PAH} (or the mass fraction of small a-C(:H), q_{AF}, for the THEMIS model), discussed in Sect. II.3.3.1, controls the strength of the MIR aromatic features (*cf.* Sect. II.2.2.1). These features, being carried by small, stochastically heated grains, are sensitive to the spectral shape of the ISRF (*cf.* Fig. II.27.a). This is demonstrated in Fig. III.14. We have considered two extreme ISRFs (Fig. III.14.a). The bias on the aromatic feature emission is at most a factor $\simeq 1.8$ (Fig. III.14.b).

☞ Eq. (III.36) provides acceptable estimates of M_{dust}, $\langle U \rangle$ and q_{PAH} (or q_{AF}).

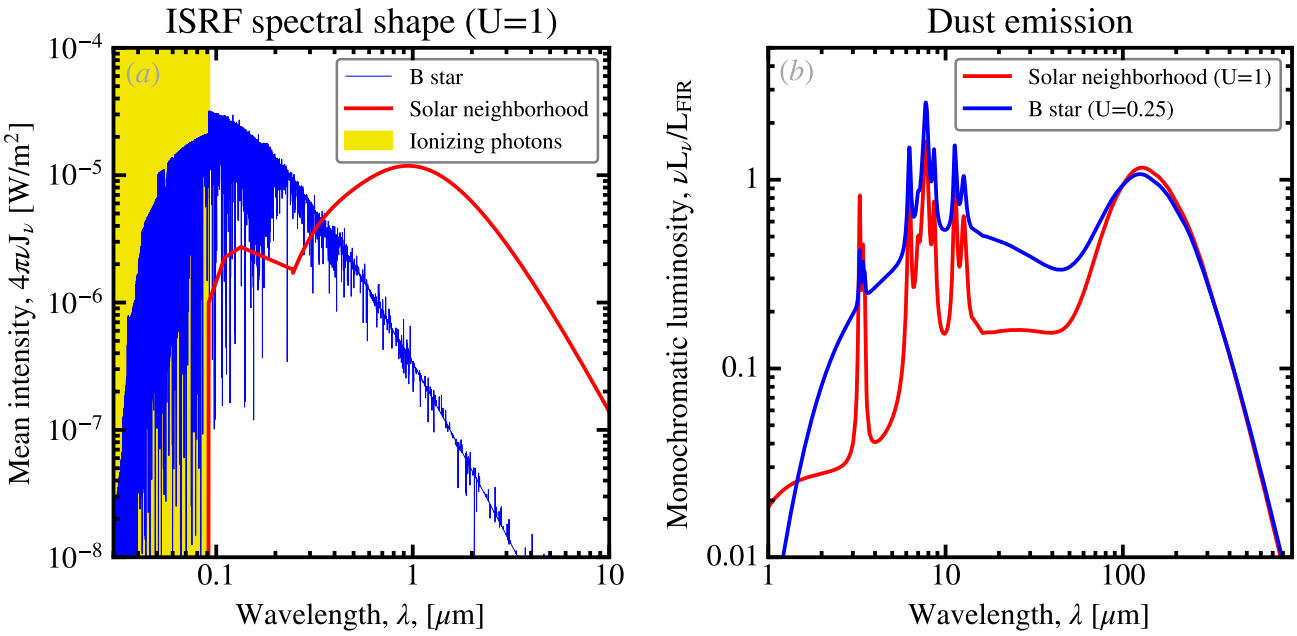

FIGURE III.14 – *Effect of the ISRF hardness on the SED.* Panel *(a)* represents different ISRFs: *(i)* the Solar neighborhood (red; Mathis et al., 1983); and *(ii)* a B star ($T_\star$ = 30 000 K; blue; Lanz & Hubeny, 2007). We have represented the spectral range of ionizing photons in yellow. Both ISRFs are normalized so that U = 1 (Eq. I.83). Panel *(b)* shows the SEDs of the THEMIS model, heated by the two ISRFs. We show the SED for different values of U, in order to obtain the same FIR SED, as this parameter is inferred by the fitter. The SEDs are normalized by the FIR luminosity, L_{FIR}, between $\lambda = 60$ and 200 µm. The B star heating leads to an increase in the $\lambda = 6 - 9$ µm emission by a factor $\simeq 1.8$, compared to the Solar neighborhood. Licensed under CC BY-SA 4.0.

Limitations of the composite approach. Using Eq. (III.36) to model typical broadband SEDs of Galactic regions and nearby galaxies is an efficient method. However, as any approximation, it has some limitations.

Variation of the grain constitution within the observed region is expected, as dust evolves with ISRF intensity and ISM density (*cf.* Chap. IV, which is devoted to dust evolution). The composite approach accounts for the fact that there are variations of the physical conditions within the region. However, assuming that the dust constitution is homogeneous biases the derived properties. The most problematic aspect is certainly the variation of the overall FIR opacity. If there is significant mantle accretion in dense regions, we might be mixing together regions with different κ (*cf.* Fig. I.21). This is unavoidable and this has to be pondered when discussing the modeling results.

The degeneracy between the grain size and ISRF distributions prevents constraining the former. This is because a MIR excess due to an enhancement of the small grain emission looks similar to the presence of hot equilibrium grains (such as compact H II regions) Fig. III.15 demonstrates this degeneracy. It shows the fit of the same synthetic observations, either varying the fraction of small grains, or the mixing of ISRFs. Additional constraints, on the geometry of the region and its radiation field, are necessary to attempt breaking this degeneracy (*cf.* Sect. III.1.3.4).

An alternative distribution. The starlight distribution of Eq. (III.36) is not the only possible one. Draine & Li (2007) proposed the following:

$$\left(\frac{1}{M_{dust}}\frac{dM_{dust}}{dU}\right)_{DL07} = \gamma \times \left(\frac{1}{M_{dust}}\frac{dM_{dust}}{dU}\right)_{Eq.\ (III.36)} + (1-\gamma) \times \delta(U - U_-), \tag{III.40}$$

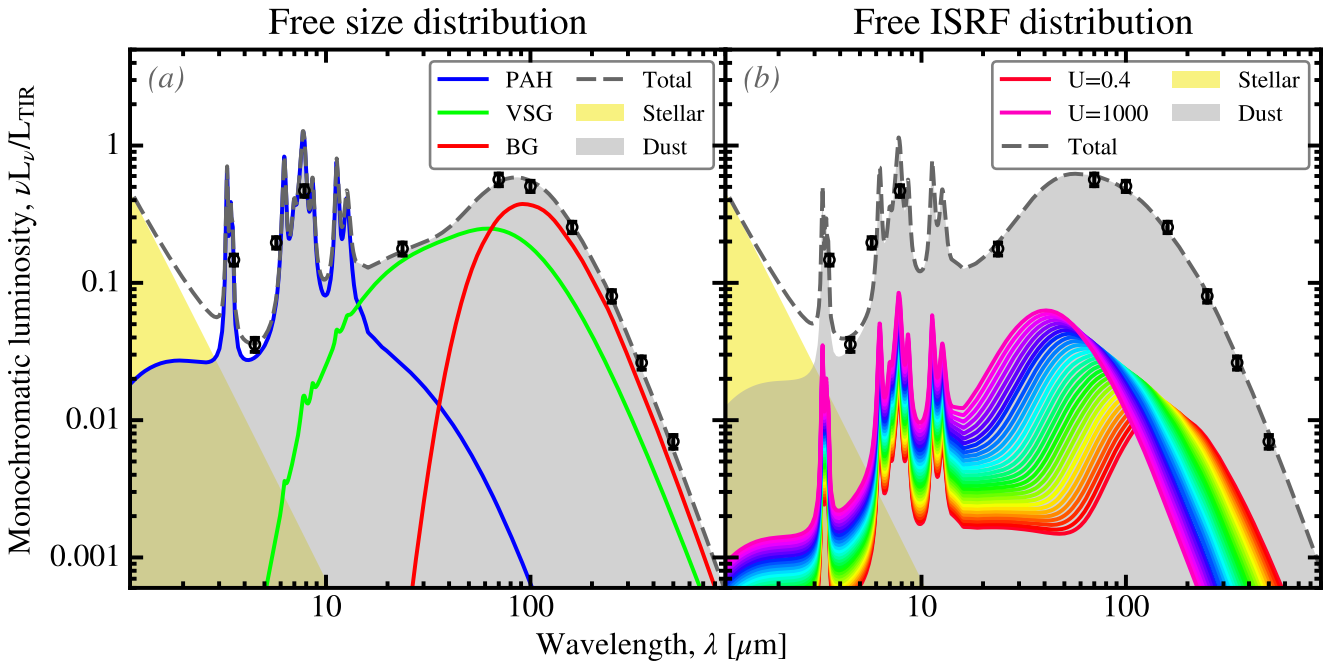

FIGURE III.15 – *Degeneracy of the grain size and ISRF distributions.* The two panels show the same synthetic observations (black error bars) fitted by two different models (Galliano et al., 2018). Panel *(a)* represents a fit by playing on the proportions of grains of different sizes: PAHs, VSGs and BGs. Panel *(b)* represents a fit using Eq. (III.36). In both cases, we have used the THEMIS dust mixture. Licensed under CC BY-SA 4.0.

which simply is the linear combination of the power-law distribution of Eq. (III.36), with a Dirac distribution centered at $U = U_-$, fixing $\alpha = 2$ and $U_- + \Delta U = 10^6$. The power-law distribution is supposed to account for star-forming regions, with a large gradient of starlight intensity, and the Dirac represents the diffuse ISM, uniformly illuminated. The parameter γ controls the relative weight of these two components. This distribution was elaborated when *Spitzer* data were being analyzed. There was no coverage beyond $\lambda = 160$ µm. There was thus no constraint on the Rayleigh-Jeans regime of the SED. The role of the Dirac component was to fit the SED peak, avoiding the dust mass to explode by lack of constraint on the cold dust distribution. This parametrization however became problematic when *Herschel* data arrived. The FIR-submm slope of the observed SED can indeed not be fitted as well with this model (Eq. III.40) as with the composite approach (Eq. III.36). This is because the model's slope is the intrinsic slope of the grain mixture. This is demonstrated in Fig. III.16.a. In Fig. III.16.b, we see that the starlight intensity distribution fit can not go down as low as the composite model. The Dirac component fits the FIR peak with a compromise U_-. This is reminiscent of the discussion we had about MBB fits, in Sect. III.1.2.1. This was demonstrated by G21, who compared different approaches by fitting the SEDs of about 800 galaxies of the DustPedia project (Davies et al., 2017) and *Dwarf Galaxy Sample* (DGS; Madden et al., 2013). Fig. III.17 compares the composite approach, as a reference, to the following models (see the complete discussion in G21).

A MBB with β free infers dust masses that are, on average over the whole sample, consistent with the composite approach (Fig. III.17.a). However, we see there is a bias as a function of the mass of the galaxy. The MBB approach tends to overestimate the mass of late-type galaxies (mostly the high-mass objects), and underestimates the mass of early-type galaxies. This is because the SED of early-type galaxies is fitted with a smaller β (thus a lower temperature, and a lower dust mass).

A MBB with β fixed tends to underestimate the dust mass on average. In Fig. III.17.b, the median of the ratio is $\simeq 0.85$. This is the effect we have discussed in Sect. III.1.2.1: the mixing of physical conditions is fitted by a compromise temperature, underestimating the coldest dust.

The Draine & Li (2007) distribution (Eq. III.40) results in a similar bias as the MBB. For the distribution in Fig. III.17.c, the median of the ratio is ≃ 0.71, even lower than in the case of the MBB. The reason is the same: the uniformly illuminated component dominating the FIR-submm SED can not account for the distribution of cold dust.

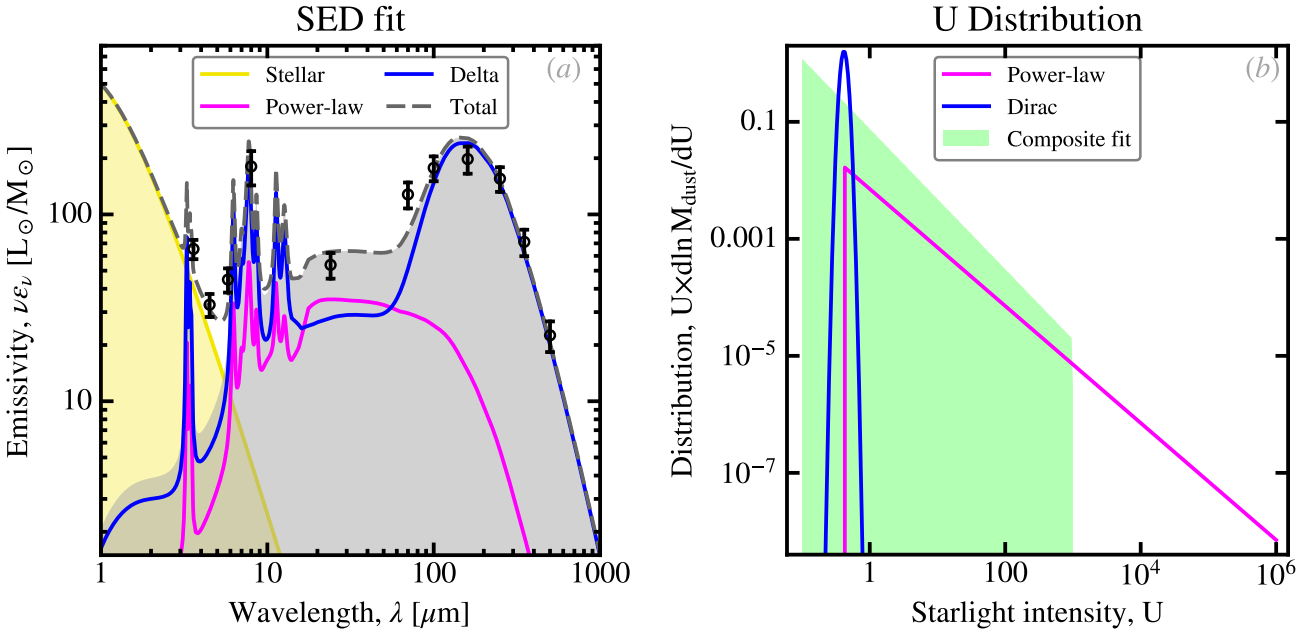

FIGURE III.16 – *SED fit with the Draine & Li (2007) starlight intensity distribution.* The black error bars in panel *(a)* are synthetic observations. They are fitted using Eq. (III.40): *(i)* the power-law component in magenta; *(ii)* the Dirac component in blue; and *(iii)* an additional stellar continuum in yellow. The corresponding starlight intensity distribution is shown in panel *(b)*, with the same color code. We have overlaid, in green, a composite model fit to the same synthetic observations. Licensed under CC BY-SA 4.0.

III.1.2.3 Panchromatic Empirical SED Models

Several codes in the literature model the *panchromatic*[3] SED of galaxies, with a simplified treatment of the radiative transfer (*e.g.* Silva et al., 1998; Charlot & Fall, 2000; Galliano et al., 2008a; da Cunha et al., 2008; Boquien et al., 2019; Fioc & Rocca-Volmerange, 2019). They include the emission by stellar populations, in addition to dust SEDs.

Stellar SEDs. Stars of different masses have different spectra and lifetimes. This is shown in Fig. III.18, in the form of a *Hertzsprung-Russell diagram*. Massive stars have: *(i)* the highest effective temperatures, their SEDs peaking in the UV; *(ii)* the highest luminosities; and *(iii)* the shortest lifetimes, of only a few million years. This is the opposite for low-mass stars: their SED peaks in the NIR, and they live longer than several hundred million years. These characteristics have a profound impact on the variation of stellar SEDs with time. The intrinsic emission of a stellar population can be simulated using *evolutionary synthesis* (*e.g.* Fioc & Rocca-Volmerange, 1997). This approach follows, at each time step, the formation and evolution of stars with different masses, $m_\star$. When these stars are born, all populations contribute to the SED. It is shown as the magenta curve in Fig. III.19. This initial SED is dominated by massive stars and peaks in the UV. Then, as the most massive stars, which also have the shortest lifetime, die, their contribution to the SED is suppressed. Consequently, when these stars disappear, the UV-side of the SED decreases. After several hundred million years, the SED

3. Literally for *all wavelengths*, from the X-rays to the radio.

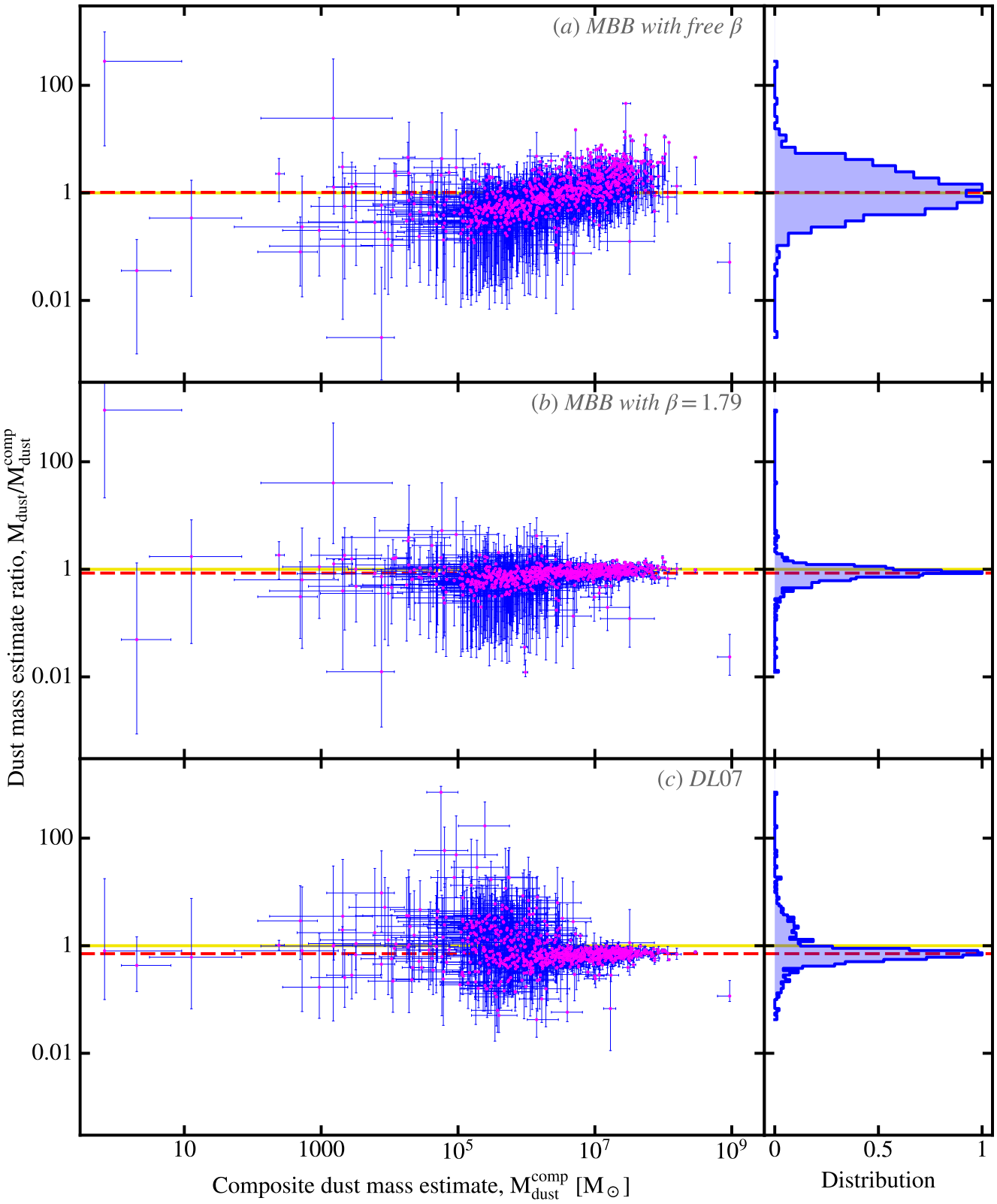

FIGURE III.17 – *Comparison of different SED models.* The data are from the SED modeling of the DustPedia and DGS nearby galaxies by Galliano et al. (2021, ≃ 800 galaxies of all types). The x-axis of the left panels shows the dust mass derived by fitting the SED of each galaxy using the composite approach (Eq. III.36). The y-axis shows the ratio of the x-axis and the dust mass estimate using one of the three alternate models: *(i)* MBB; *(ii)* MBB with fixed β = 1.79; *(iii)* Draine & Li (2007) distribution. Each point with an error bar corresponds to one particular galaxy. The yellow line shows the 1:1 ratio, and the dashed red line, the median of the sample. The right panels show the histogram of the distribution.

peaks in the NIR, as it originates only in low-mass stars (orange and red curves in Fig. III.19). There is also a drastic evolution of the emissivity as a function of time, as low-mass stars are significantly less luminous (*cf.* Fig. III.18). To compute such synthetic spectra, the following quantities need to be defined.

- The *Star Formation History* (SFH) expresses the variation as a function of time of the *Star Formation Rate* (SFR), $\psi(t) = \mathrm{d}m_\star/\mathrm{d}t$. Several forms are used in the literature: instantaneous burst, exponential, delayed, *etc.* (*e.g.* Lee et al., 2010).
- The *Initial Mass Function* (IMF) gives the PDF to form a star of mass $m_\star$. The historical IMF of Salpeter (1955) is less commonly used nowadays. For instance, an alternate IMF has been proposed by Chabrier (2003).

We will more extensively discuss these quantities in Sect. IV.3, when modeling the chemical evolution of galaxies. We have summarized in Table III.2 the main properties of the different stellar classes.

	Effective temperature, $T_{\rm eff}$	**Initial mass, $m_\star$**	**Initial luminosity, $L_\star$**	**Lifetime, $\tau(m_\star)$**
O	$\geq 30\,000$ K	≥ 16 M$_\odot$	$\geq 30\,000$ L$_\odot$	≤ 12 Myr
B	$10\,000 - 30\,000$ K	$2.1 - 16$ M$_\odot$	$25 - 30\,000$ L$_\odot$	12 Myr$-$1 Gyr
A	$7\,500 - 10\,000$ K	$1.4 - 2.1$ M$_\odot$	$5 - 25$ L$_\odot$	$1 - 3$ Gyr
F	$6\,000 - 7\,500$ K	$1.04 - 1.4$ M$_\odot$	$1.5 - 5$ L$_\odot$	$3 - 10$ Gyr
G	$5\,200 - 6\,000$ K	$0.8 - 1.04$ M$_\odot$	$0.6 - 1.5$ L$_\odot$	$10 - 25$ Gyr
K	$3\,700 - 5\,200$ K	$0.45 - 0.8$ M$_\odot$	$0.08 - 0.6$ L$_\odot$	...
M	$2\,400 - 3\,700$ K	$0.08 - 0.45$ M$_\odot$	≤ 0.08 L$_\odot$	...

TABLE III.2 – *Basic properties of the main stellar classes.*

Putting everything together. Empirical panchromatic SED models usually include the following physical ingredients.

One or several stellar populations are modeled. Their escaping radiation is fitted to the UV-to-NIR SED, allowing the user to constrain: the age, the SFH timescale, the SFR and the total stellar mass. The *attenuation*[4] is accounted for, by assuming simple topologies, such as those discussed in Calzetti et al. (1994). The intrinsic stellar power, $L_\star$, is derived from the *energy balance*: $L_\star = L_{\text{UV-NIR}} + L_{\text{TIR}}$, where $L_{\text{UV-NIR}}$ is the escaping UV-to-NIR power. This equation simply states that the intrinsic power emitted by stars is either escaping the galaxy in the UV-to-NIR range, or has been absorbed by dust. It implicitly assumes that the emission from the galaxy is isotropic, which is not necessarily the case for disk galaxies.

Dust emission is modeled, either by solving the radiative transfer equation (Eq. III.16) in a simple geometry, or by adopting a distribution of starlight intensities (*cf.* Sect. III.1.2.2). The dust properties are not always consistent with those used to account for attenuation.

Nebular emission, in the form of lines or continuum, can be included. In case of star-forming galaxies, it is dominated by H II regions (*e.g.* Charlot & Longhetti, 2001). Some models also include the gaseous emission from AGNs. These tracers are used to refine some of the diagnostics.

We illustrate this approach with the model of Galliano et al. (2008a), applied to two galaxies, in Fig. III.20. This particular model separates the emission from H II regions, which are powered by massive ionizing stars (cyan). The magenta curve shows the escaping radiation from H II regions. It includes

4. Attenuation is not equivalent to extinction. The extinction is the sum of scattering and absorption along the sight-line toward a point source, whereas the attenuation is a global account of the reddening of an ensemble of stars, potentially mixed with the dust. The extinction is directly linked to dust properties and is independent of geometry. The attenuation is a synthetic quantity depending both on the dust properties and on the ISM topology (*e.g.* Buat et al., 2019, for a recent discussion).

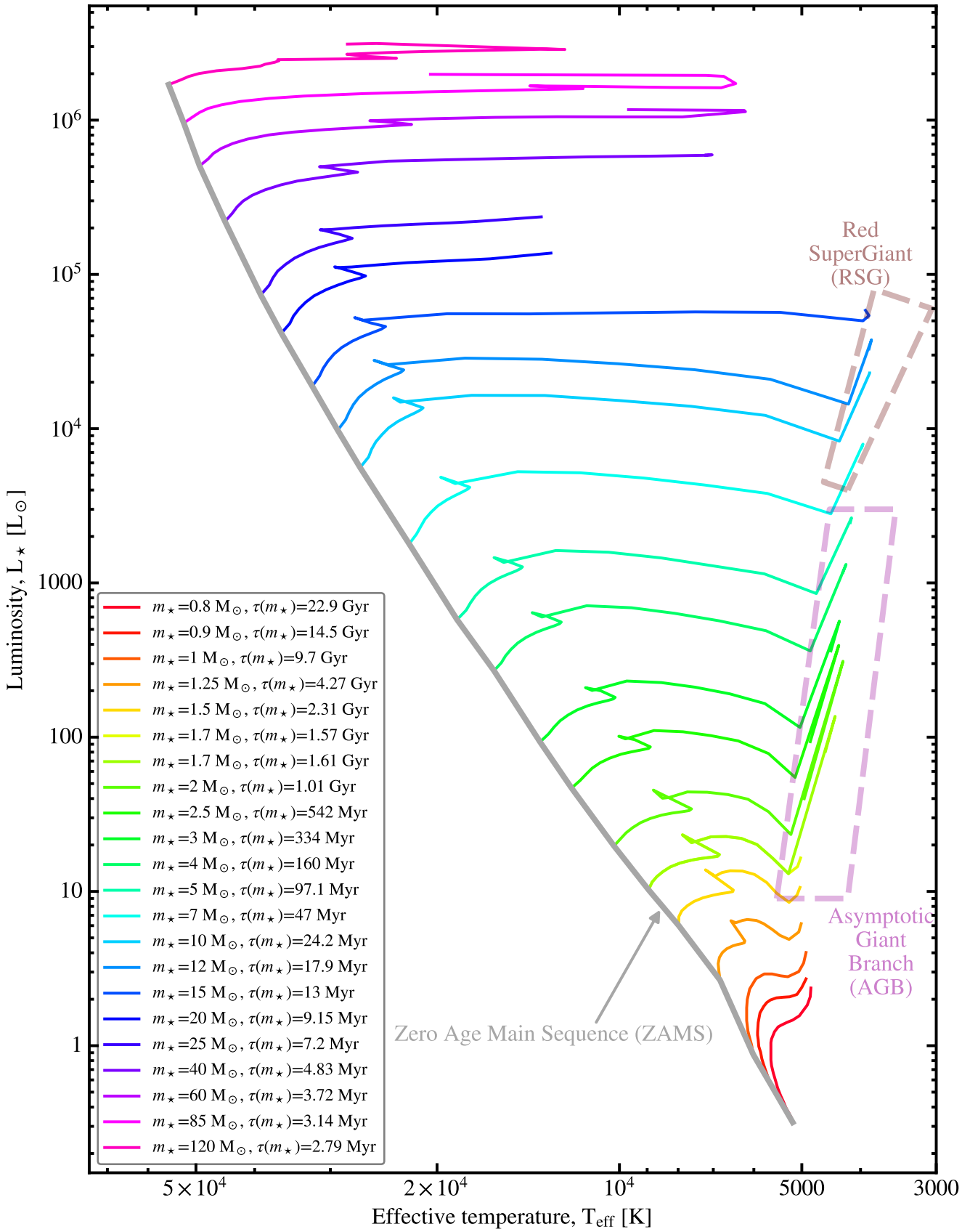

FIGURE III.18 – *Stellar isochrones.* This figure shows theoretical tracks of individual star evolution from the model of Schaller et al. (1992), at initial metallicity, Z = 0.008. This representation is known as a *Hertzsprung-Russell diagram.* Stars of a given mass, $m_\star$ (a given color), start from the *Zero Age Main Sequence* (ZAMS; grey) and evolve along their *Main Sequence* (MS) track until their death, after a time $\tau(m_\star)$. We have highlighted the late evolutionary stages: *(i)* red supergiants for massive stars; and *(ii)* AGB for *Low- and Intermedate-Mass Stars* (LIMS). Licensed under CC BY-SA 4.0.

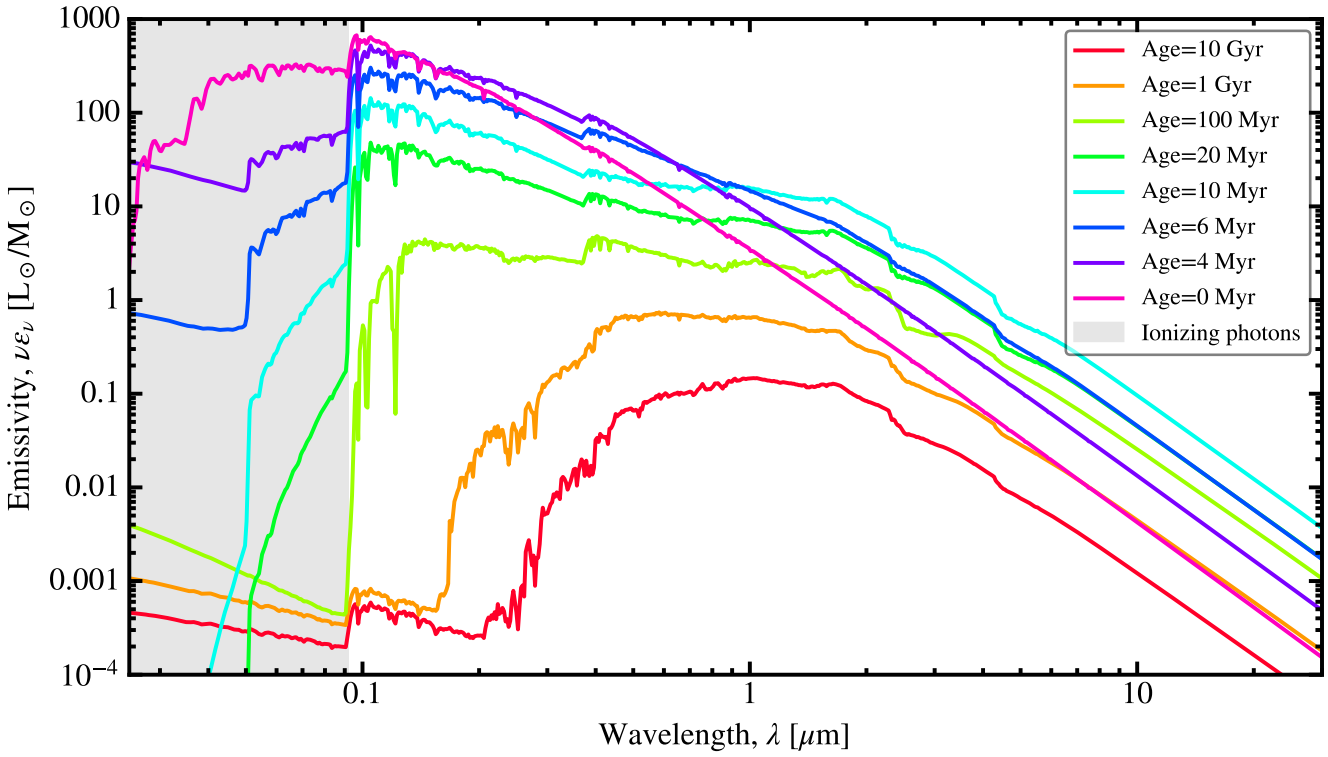

FIGURE III.19 – *Evolution of stellar SEDs as a function of time.* The different curves show the evolution, as a function of time, of the SED of a stellar population produced by an instantaneous burst, at Solar metallicity. We have assumed the Salpeter (1955) IMF. These models were generated using the code of Fioc & Rocca-Volmerange (1997). Notice, in particular, the fast decrease of ionizing photons with time. Licensed under CC BY-SA 4.0.

the dust emission and the free-free continuum. The escaping radiation from HII regions, as well as non-ionizing field stars (yellow), heat the neutral ISM (red). The degeneracy between both dust components was solved by using radio observations to constrain the level of the free-free emission. The gas density in HII regions, impacting the equilibrium temperature of large grains, is constrained by the MIR continuum. The remaining emission is thus assumed to come from the neutral ISM. We will discuss in more detail the results of this model, in Sect. IV.3.

Limitations of empirical panchromatic models. The approach we have just described has several advantages. In a single fit, it provides estimates of the SFR, the age of the stellar populations, the stellar mass, and the dust properties. Its major limitation however resides in the sensitivity of its results to the assumed ISM topology. The ISM indeed has a fractal structure, with several orders of magnitude of contrast density (*e.g.* Combes, 2000). The optical depth from the model thus probably underestimates the total dust column density (*cf.* Sect. III.1.1.3). In addition, the extinction and emission properties of these models are usually not consistent. The modeling of the microscopic grain constitution and of their macroscopic spatial distribution can differ from one side of the electromagnetic spectrum to the other. For instance, assuming a Calzetti et al. (1994) attenuation law and taking a mean radiation field to account for dust heating is virtually equivalent to decoupling the extinction and emission. Finally, the consistency brought by modeling all multi-wavelength tracers at once, which is *a priori* positive, leads to propagating the systematic uncertainties, due to arbitrary choices of ISM topologies, to parameters that could have been considered independent of these effects, if they had been modeled separately (M_{dust}, $\langle U \rangle$, q_{PAH}; Sect. III.1.2.2).

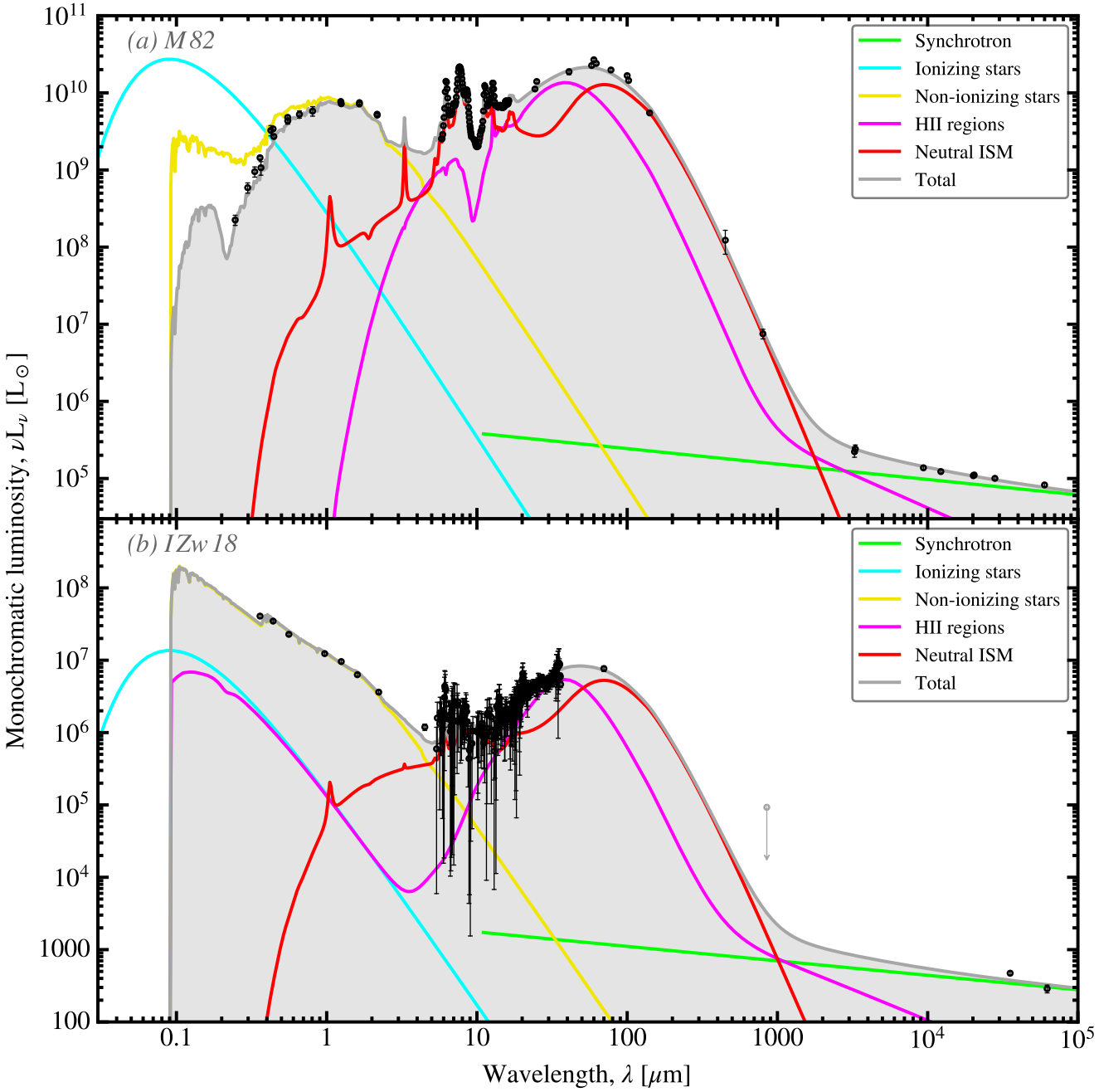

FIGURE III.20 – *Multiphase SEDs of galaxies.* This figure shows the SED of two galaxies, modeled by Galliano et al. (2008a): the prototypical starburst, M 82, and the lowest metallicity galaxy, I Zw 18. The black error bars represent the observed fluxes. The total SED model is shown in grey. The stars are split in two populations: *(i)* young, ionizing stars that are in H II regions; and *(ii)* older, non-ionizing stars that are in the rest of the galaxy. We show the intrinsic emission of both stellar components. The dust emission originates in: *(i)* H II regions, heated by ionizing stars; and *(ii)* the neutral ISM, heated by non-ionizing stars and by the escaping radiation from H II regions. Licensed under CC BY-SA 4.0.

III.1.2.4 The Matryoshka Effect

The main limitation of dust studies lies in the near impossibility to constrain at the same time the microscopic dust properties and their sub-pixel macroscopic spatial distribution. All the approaches we have discussed in this chapter face this problem. It can be illustrated with what Galliano et al. (2018) called the *matryoshka effect*. This empirical effect originates in the impact of the spatial resolution of the observations on the constrained parameters.

Demonstration on the LMC. Fig. III.21 demonstrates the effect with the modeling of the dust mass in a strip covering one fourth of the LMC, by Galliano et al. (2011). The different images on top show the spatial resolution that is used. The first image is one single large pixel. The second one is divided in four pixels, and so on. The curve in the bottom panel of Fig. III.21 shows the dust mass in the strip derived by summing all the pixels, at each resolution. We see that this mass increases with spatial resolution, until reaching a plateau around $\simeq 10$ pc. For this particular region, the discrepancy with the global mass is about $\simeq 50\,\%$. Galliano et al. (2011) interpreted this effect by noticing that the cold dust, which accounts for most of the mass and, at the same time, is the least luminous, is diluted into the warm dust emission when we sum all the regions together. With spatial resolution however, we can better separate the bright and cold regions. It is thus reasonable to assume that the most accurate estimate of the dust mass is the one obtained at the highest resolution. This assumption is confirmed by the fact that the length-scale at the growth curve plateau ($\simeq 10$ pc) corresponds roughly to the mean free-path of a U-band photon at a density $n_{\rm H} \simeq 100$ cm^{-3} (Table III.1; the LMC has a half-Solar metallicity; Pagel, 2003). This is the typical density of the CNM and diffuse H_2 phase (*cf.* Table III.6). It is possible that, if we could increase the resolution, we would see another plateau around $n_{\rm H} \simeq 10^4$ cm^{-3} ($\simeq 0.1$ pc), corresponding to dense H_2 clouds.

Generalization. This effect has been independently confirmed by Galametz et al. (2012), Roman-Duval et al. (2014) and Aniano et al. (2020), although it is less important if the maximum spatial resolution is not as high as ours.

> ☞ The dust mass derived at high spatial resolution is always larger than its global estimate.

III.1.3 Application to Nearby Galaxies

We now review the application of SED models to observations of nearby galaxies, aimed at constraining the grain properties in different environments. We illustrate the different aspects using our own projects and collaborations.

III.1.3.1 The Different Types of Galaxies

There is a wide diversity of galaxy types. Several systems of classification have been developed, through the years. In particular, the Hubble-de Vaucouleurs system, although outdated, is still used nowadays.

The outdated galaxy morphological classification. The most famous observational system of morphological classification is the *Hubble tuning fork* or *Hubble-de Vaucouleurs diagram*, represented in Fig. III.22. It was originally developed by Hubble (1936), and refined by de Vaucouleurs (1959). It is based on the morphological characteristics of galaxies in the visible range: presence and thickness of spiral arms, bars, rings, *etc.* There are essentially three classes of galaxies (left, center and right parts of Fig. III.22): *(i)* ellipticals, also called *Early-Type Galaxies* (ETG); *(ii)* spirals, also called *Late-Type Galaxies* (LTG); and *(iii)* irregulars and dwarf spheroidals. There are sub-categories with abstruse

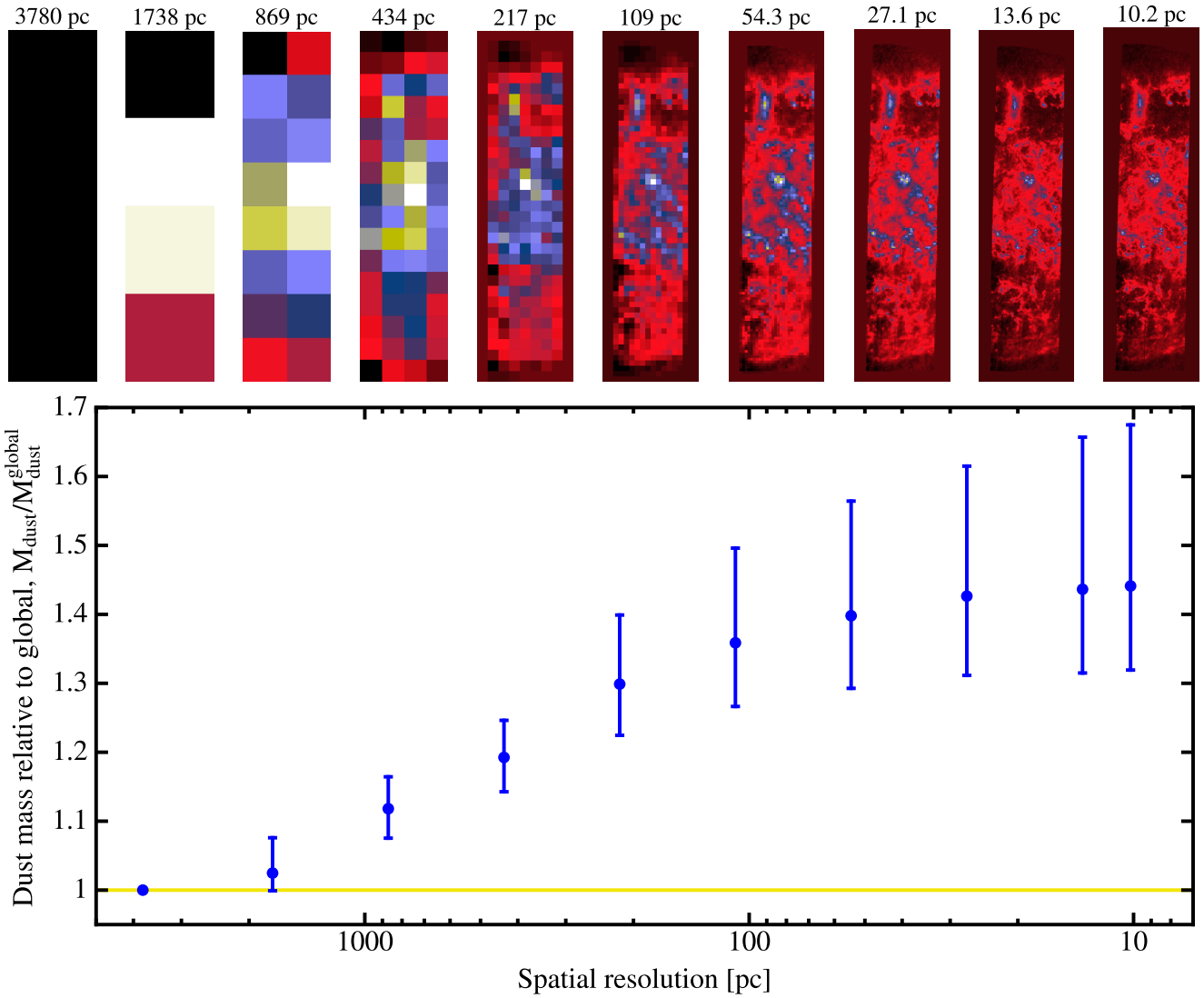

FIGURE III.21 – *Matryoshka effect demonstrated on the LMC.* On top are nine $SPIRE_{500\mu m}$ images of a strip covering about one fourth of the LMC, observed by Meixner et al. (2010). These images are rebinned at different spatial resolutions (indicated on the top). The bottom panel shows the dust mass derived by modeling the SED of each pixel of these images and summing them to derive the total mass in the strip (Galliano et al., 2011). It is normalized by the mass obtained when modeling the global (*i.e.* one pixel) SED of the strip, M_{dust}^{global}. Licensed under CC BY-SA 4.0.

notations (SAa, E2, *etc.*) that would be a waste of time to describe here. Overall, this is a mid-XX^{th}-century empirical classification, based on stellar dynamics, that does not take into account the IR information (especially the SF activity), nor the radio properties (presence of an AGN). Recently, with the DustPedia collaboration (Davies et al., 2017), we explored the sensitivity of dust properties to galaxy types (*e.g.* Davies et al., 2019; Bianchi et al., 2018; Nersesian et al., 2019). We did not find any clear systematic differences between adjacent sub-categories in Fig. III.22, and we found a large scatter within each class. There are overall trends between the three main categories, because they are linked to the gas fraction, metallicity and stellar populations. We will discuss those throughout this manuscript. The terminology "*late/early-type*" was introduced to denote the evolution of galaxies along the sequence. We now know that the sequence is reversed: early-type galaxies are the oldest objects, and late-types, the youngest ones. In addition, the most numerous galaxies in the local Universe, dwarf galaxies are under-represented in this diagram. They are part of the irregulars, which is a category by default. Finally, this Hubble-de Vaucouleurs classification was based on the local Universe, while galaxies at high redshift can exhibit different morphologies, such as clumpy chains and tadpoles (*e.g.* Elmegreen, 2015). We have developed an alternate, non-parametric classification,

taking into account IR morphology (Baes et al., 2020). It emphasizes the clumpy nature of the dust distribution in local galaxies.

☞ Stellar morphology is not particularly relevant to ISM studies.

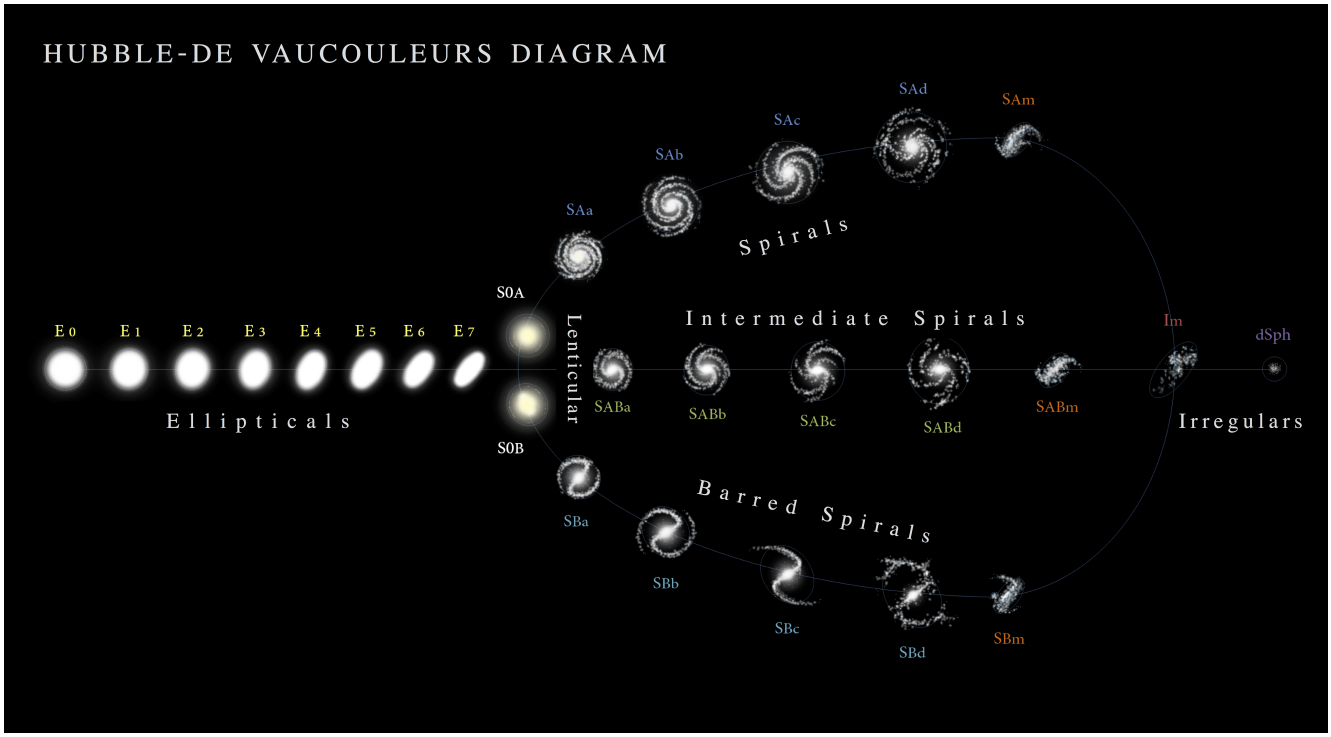

FIGURE III.22 – *Hubble-de-Vaucouleurs galaxy morphology diagram.* Credit: A. Ciccolella / M. De Leo, Wikipedia, licensed under CC BY-SA 3.0.

Galactic properties that matter to ISM studies. A few global quantities, such as the metallicity, the SFR or the gas fraction are more relevant to assess the general properties of the ISM of a galaxy. The three main categories of the Hubble-de Vaucouleurs diagram can be characterized the following way.

Irregular galaxies (*e.g.* Fig. III.23.a) can contain large amounts of atomic gas that typically extend to twice their Holmberg radius [5] (*e.g.* Huchtmeier et al., 1981).

At Solar metallicity, irregulars are rich in dust. Their visible and MIR scale-lengths are very similar (Hunter et al., 2006). The dust emission in irregular galaxies is clumpy and warm, with hot dust and UIB emissions mostly observed towards bright H II regions. This suggests that massive stars are a major source of heating in these environments (*e.g.* Hunter et al., 2006).

At low metallicity, irregulars are dwarf galaxies. Dustiness increases with metallicity (*cf.* Sect. IV.3; Rémy-Ruyer et al., 2014; Galliano et al., 2021). The ISM in these objects is less dusty and thus, more transparent. Similarly to irregular galaxies, massive stars are a major source of heating in these objects (*e.g.* Walter et al., 2007), and they are permeated by SN-triggered shock waves (*e.g.* Oey, 1996; Izotov et al., 2007). Finally, these galaxies exhibit large H I envelopes. The IR emitting region can correspond to only $\simeq 20-30\,\%$ of the total mass of the system (*e.g.* Walter et al., 2007). A particularly important type of dwarf galaxies are *Blue Compact Dwarf Galaxies* (BCD). These galaxies are actively star forming. As their name indicates, they have blue optical colors, because they contain several SSCs, rich in young massive stars, and they are weakly attenuated by dust.

5. The *Holmberg radius* is the radius within which the B-band surface brightness of the galaxy is 26.5 magnitudes per squared arcsecond.

Late-type galaxies (*e.g.* Fig. III.23.b) have a roughly Solar metallicity and an ISM accounting for ≃ 10 – 30 % of their baryonic mass.

Scale-lengths of disk galaxies are of the order of a few kpc (up to ≃ 10 kpc). Their diameter tends to be systematically smaller in the MIR than in the visible (Malhotra et al., 1996), whereas the arm/inter-arm contrast is larger in the MIR than in the visible (Vogler et al., 2005). This is also seen in ^{12}CO(J=1→0)$_{2.6mm}$, H$\alpha_{656.3nm}$ or radio continuum (Sauvage et al., 1996; Walsh et al., 2002; Vogler et al., 2005). This is because these different tracers are indicators of star formation activity, which is enhanced along the spiral arms. In the IR, the disk scale-length increases with wavelength (Hippelein et al., 2003), and is larger in the FIR than in the visible (Tuffs et al., 1996; Alton et al., 1998; Haas et al., 1998; Davies et al., 1999; Trewhella et al., 2000; Fritz et al., 2012; Casasola et al., 2017). This FIR colour gradient observed in the disk suggests that part of the FIR emission arises from grains heated by the radially decreasing diffuse ISRF, the extended parts of the disk being cold (Block et al., 1994; Stevens et al., 2005; Hinz et al., 2012). FIR scale-lengths do not vary strongly as a function of galaxy type and are on average ≃ 10 % larger than the stellar scale-lengths (*e.g.* Muñoz-Mateos et al., 2009; Hunt et al., 2015).

Scale heights of disk galaxies are typically of the order of a few hundred parsecs. Outside our Milky Way, edge-on galaxies are ideal objects to constrain this parameter (*e.g.* Xilouris et al., 1999). Radiative transfer codes are robust tools to derive such structural parameters (*cf.* Sect. III.1.3.2).

Early-type galaxies (*e.g.* Fig. III.23.c) possess very little dust: the average dust-to-stellar mass ratio is ≃ 50 times lower than that of spiral galaxies (Smith et al., 2012; Galliano et al., 2021). Dust lanes are, however, commonly detected in elliptical galaxies (*e.g.* Sadler & Gerhard, 1985; Gomez et al., 2010). Jura et al. (1987) for instance found that half of nearby ellipticals are detected at IRAS wavelengths. Smith et al. (2012) found that elliptical galaxies detected at 250 µm tend to have higher X-ray luminosities. This was further explored by G21. We will come back to this point in Sect. IV.2.2.2.

III.1.3.2 Large-Scale Dust Distribution in Galaxies

The dust spatial distribution, that is the value of various dust parameters in different regions or pixels of a galaxy, can be determined in the MW and nearby galaxies. This determination however requires good quality, homogenized multi-wavelength images of the studied objects. This is therefore significantly more complex than modeling the SED of a point source.

Homogeneous multi-wavelength data sets. To accurately model SEDs of galaxies, the observed fluxes must originate, at each wavelength, in the same region, and must trace only the emission we are modeling (*i.e.* the dust emission, the escaping stellar emission, *etc.*). The following artifacts can be encountered.

Contaminations in the telescope beam can have several origins. Most of them are displayed in Fig. III.24.

Foreground zodiacal emission originates in dust grains from the Solar system (*e.g.* Fixsen & Dwek, 2002; Reach et al., 2003; Rowan-Robinson & May, 2013; Krüger et al., 2019). Its intensity depends greatly on the angle above the planetary disk. It is prominent in the MIR (*cf.* Fig. III.24). The zodiacal emission is quite homogeneous at the typical angular scale of nearby galaxies (a few degrees or less). It can thus be efficiently subtracted, using the emission outside the target. Otherwise, several models compute its synthetic spectrum (*e.g.* Krüger et al., 2019).

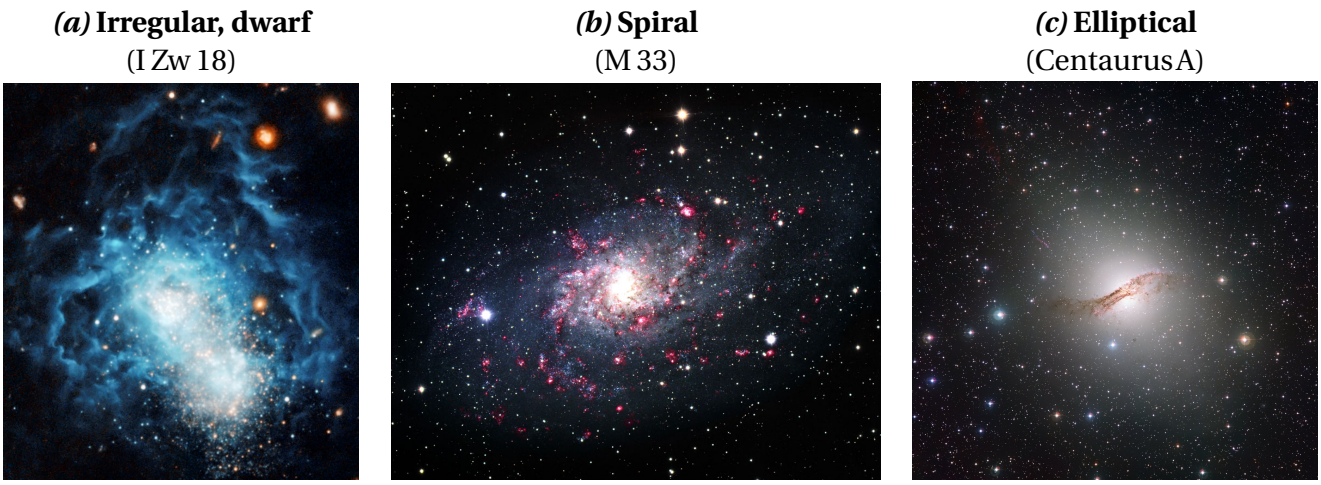

FIGURE III.23 – *Visible-range image of three nearby galaxies.* Panel *(a)* shows an image of the extremely low-metallicity, dwarf galaxy, I Zw 18, obtained with the instrument ACS onboard the HST (Aloisi et al., 2007). Panel *(b)* shows the spiral galaxy, M 33. Star-forming regions, traced by the $H\alpha_{656.3nm}$ line, are shown in red. Panel *(c)* shows the elliptical galaxy, Centaurus A. It has a warped dust lane and an AGN. Credit: *(a)* Cignoni & Tosi (2009), licensed under CC BY-SA 3.0; *(b)* Image Data: Subaru Telescope (NAOJ), Hubble Space Telescope – Image Processing: Robert Gendler – Additional Data: BYU, Robert Gendler, Johannes Schedler, Adam Block – Copyright: Robert Gendler, Subaru Telescope, NAOJ, with permission from Robert GENDLER; *(c)* courtesy of ESO, licensed under CC BY 4.0.

Foreground Galactic emission originates in dust grains from cirrus clouds within the MW. Its spectrum does not vary significantly with pointing direction, as the Galactic ISRF is relatively homogeneous. However, its total intensity scales with the column density of the ISM between the observer and the target galaxy. The H column density is the lowest at high Galactic latitude ($N_H \simeq 10^{24}$ H/m^2). The fractal structure of interstellar clouds (*e.g.* Elmegreen & Falgarone, 1996) results in a high degree of structure at small angular scales. In other words, it is difficult to subtract this emission using off-target areas. This contamination can not always be subtracted. Surface brightness being independent of distance, the emission from the diffuse ISM of nearby galaxies is similar to that of the MW, making the study of the former particularly challenging.

Background galaxy emission constitutes the CIB (*e.g.* Dole et al., 2006). Its SED looks similar to the diffuse Galactic ISM (*cf.* Fig. III.24). Spatially, it is granular, as it is the sum of numerous point sources. It is difficult to accurately subtract. It is thus another component that makes studying the diffuse ISM of nearby galaxies challenging.

Cosmological background emission is a T = 2.73 K black body (*cf.* Sect. I.2.4.2; Mather et al., 1994). It contaminates essentially the mm regime. Its emission is globally isotropic with some fluctuations. The amplitude of these fluctuations is shown as a solid red line in Fig. III.24. These fluctuations are a bit more difficult to subtract. However, in general this source of contamination is not the most challenging to remove.

Non-dusty contamination, such as gas-phase line emission or the radio continuum need to be subtracted. For instance, in the submm regime, the CO lines and the free-free continuum can account for 10 – 20 % of the emission around $\lambda \simeq 1$ mm (*cf.* Fig. II.10 and *e.g.* Galliano et al., 2003, 2005). Additional independent constraints are necessary, such as spectroscopic observations of the contaminating lines, and long-wavelength radio continuum fluxes that probe the free-free and synchrotron emission.

Differences in angular resolution are due to variations of the beam size across the observed SED. If

not corrected, this can have dramatic consequences, especially if the studied region has large gradients of emission on scales of the order of the largest beam size. It is however easy to correct. One needs to identify, among the instruments used, which one has the largest beam, $\Omega_{\rm max}$. One then simply needs to degrade the angular resolution of all the other wavelengths, to the resolution $\Omega_{\rm max}$. This degradation is performed by convolving the images by a kernel, which is the $\Omega_{\rm max}$ beam deconvolved by the beam at the nominal wavelength. Such kernels are provided, for instance, by Aniano et al. (2011) for a wide variety of instruments.

Differences in field of view come from the fact that the different instruments do not necessarily have the same orientation on the sky and the same pixel size. To model a spatially-resolved SED, it is thus necessary to reproject every image on a single grid. Numerous methods are available to perform this reprojection (*e.g.* Bertin et al., 2002). It can become problematic only when there are missing areas, such as incomplete maps or masked regions (*e.g.* because of saturation). The linear pixel size of the final grid can be as low as $\simeq 1/3$ of the largest beam size (Nyquist sampling).

Uncertainties must be taken into account as rigorously as possible. Ideally, we should not only determine the uncertainties of each pixel at each wavelength, but also their correlations. This can be simplified by separating the two major sources of uncertainties: noise and calibration effects. The noise comes from the instrument. It is usually provided by the data reduction pipeline. It thus needs to be propagated through the various sources of homogenization we have discussed. In particular, resolution degradation increases the median signal-to-noise ratio, as it has an averaging effect on the noise spatial distribution. It also creates correlations between pixels. To our knowledge, the best method to propagate noise uncertainties, which is also the simplest to implement, is by way of Monte-Carlo simulations (*e.g.* Galliano et al., 2011). The principle is the following.

1. We generate a large number, $N \simeq 100$, of images with flux:
$$F_\nu^{(i)}(x,y,\lambda) = F_\nu(x,y,\lambda) + \delta(i,x,y,\lambda) \times \sigma_\nu(x,y,\lambda) \tag{III.41}$$
($i = 1, N$), where F_ν and σ_ν are the flux and uncertainty coming from the data reduction pipeline. The random variable, δ, is independent, normal with mean 0 and standard deviation 1.
2. We then perform the different homogenization steps (contamination subtraction, degradation, reprojection) on each random samples.
3. We now have, for each pixel and each wavelength of the final homogenized maps, a distribution of N values. The standard deviation of this distribution gives the uncertainty and we can compute correlation coefficients between different pixels or wavelengths.

Calibration uncertainties can be computed afterwards, as they are proportional to the flux. These uncertainties are fully correlated between pixels and partially correlated between wavelengths (*e.g.* G21).

This technical data preparation can be tedious, but it is crucial as dust model results directly rely on it. A significant effort has been put into providing homogenized databases of nearby galaxies. Among them, the most important surveys are the following.

- SAGE/HERITAGE (Meixner et al., 2006, 2013) were a series of surveys of the Magellanic clouds with *Spitzer* and *Herschel*.
- The DGS (Madden et al., 2013; Rémy-Ruyer et al., 2013) was a survey of nearby dwarf galaxies with *Herschel*, for which we also added *Spitzer* and ancillary data (Bendo et al., 2012; Rémy-Ruyer et al., 2015).
- SINGS/KINGFISH (Kennicutt et al., 2003, 2011) was a series of *Spitzer* and *Herschel* surveys of nearby galaxies.
- DustPedia (Davies et al., 2017; Clark et al., 2018) was a European collaboration project, which built a homogenized sample of all available data for $\simeq 800$ nearby galaxies.

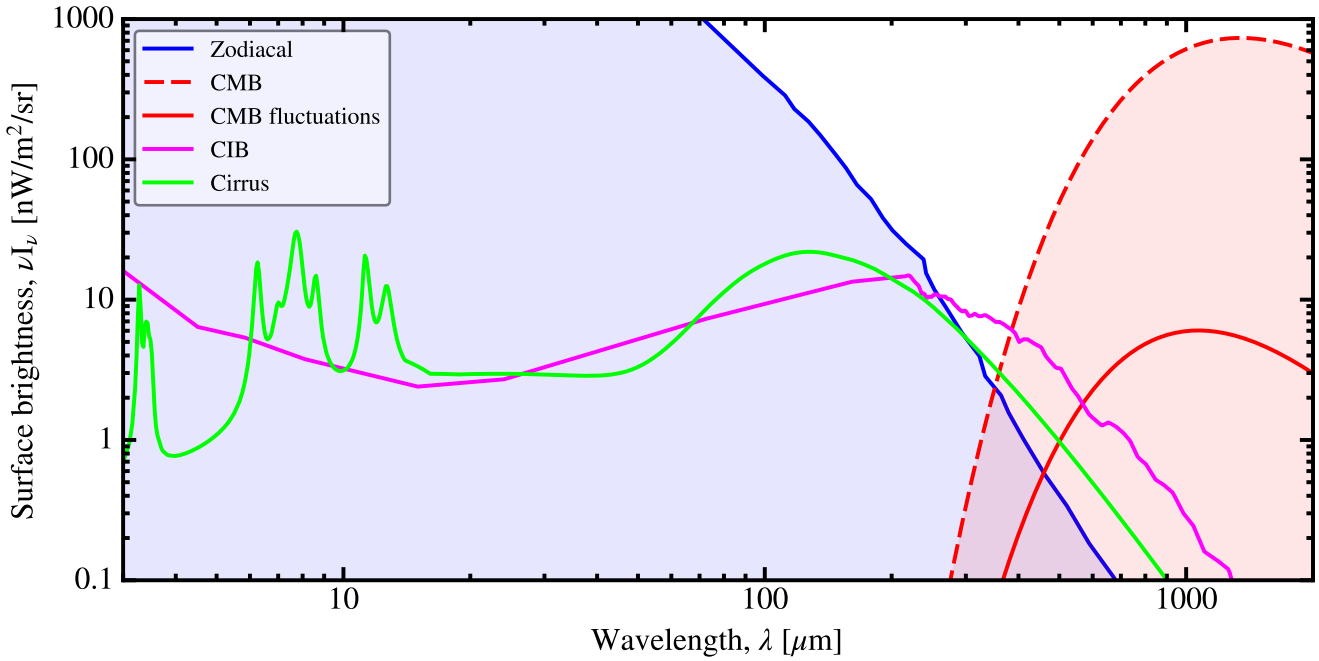

FIGURE III.24 – *Principal sources of contaminations encountered when modeling SEDs.* The zodiacal spectrum (blue) has been computed using the model of Fixsen & Dwek (2002). The CMB spectrum is a T = 2.73 K black body (red dashed line). The solid red line corresponds to the level of CMB fluctuations. The CIB (green) comes from the compilation of Dole et al. (2006). The Galactic cirrus emission is the THEMIS model scaled by a column density $N_H = 10^{24}$ H/m^2. Licensed under CC BY-SA 4.0.

Properties of individual galaxies. Numerous studies have presented the SED modeling of nearby galaxies, and their derived dust properties, either globally or spatially-resolved. We have participated to several such projects (*e.g.* Whaley et al., 2009; Galametz et al., 2009; Boselli et al., 2010; Galametz et al., 2010; O'Halloran et al., 2010; Eales et al., 2010; Cortese et al., 2010; Sauvage et al., 2010; Bendo et al., 2010; Roussel et al., 2010; Gordon et al., 2010; Davies et al., 2010; Boquien et al., 2010; Skibba et al., 2012; De Looze et al., 2012a; Galametz et al., 2013; Ciesla et al., 2014; Gordon et al., 2014; Galametz et al., 2016; Bianchi et al., 2018; Nersesian et al., 2019). Reviewing them would be unwieldy, here. In general, these studies provide dust parameters (mass, starlight intensity, PAH mass fraction, *etc.*) of different objects, which can be used in combination with other tracers to refine our understanding of the studied source. They also provide scaling relations and calibrations of various diagnostics such as SFR tracers. These results can also be used to train machine-learning models that could predict the SED of a poorly-observed galaxy (*e.g.* Dobbels et al., 2020).

Identifying dust heating sources. A particular question, that has been tackled by several studies, is the identification of the sources responsible for dust heating within galaxies. In the MW, 3D reconstruction of the ISM distribution showed that the heating by young, O/B stars (Table III.2) was prominent in molecular regions, whereas the atomic phase was mainly heated by lower-mass stars (*e.g.* Sodroski et al., 1997; Paladini et al., 2007). In nearby galaxies, this depends on the SF activity of the galaxy. For instance, we showed that PAHs were essentially heated by field stars in the quiescent galaxy NGC 2403. These molecules are however heated by the escaping radiation from H II regions in the more actively star-forming object, M 83 (Jones et al., 2015). More generally, with the DustPedia sample, we found that dust in ETGs was mainly heated by old stars (Nersesian et al., 2019). It is only when considering more gas-rich galaxies that the contribution of young stars becomes more important. It can account for up to ≃ 60 % of the dust luminosity in extreme late-type galaxies (Sm–Irr, Fig. III.22; Nersesian et al., 2019). These different heating sources have an impact on the global escape fraction (*i.e.* the fraction of stellar radiation leaving the galaxy unattenuated). Massive stars being embedded in molecular cocoons, they have a lower escape fraction than *Low- and Intermediate-*

Mass Stars (LIMS) which occupy lower density regions. In the DustPedia sample, we showed that the escape fraction was on average ≃ 81 %, with mild variations across galaxy types (Bianchi et al., 2018). It is slightly lower in LTGs (≃ 75 %). We emphasize that this nearby galaxy sample lacks the deeply enshrouded star formation of LIRGs and ULIRGs, where the global escape fraction can drop down to ≃ 1 % (*e.g.* Clements et al., 1996). The question of the dust heating contribution can now be tackled with more accuracy using 3D MCRT models.

Large-scale radiative transfer models of galaxies. Applying a 3D MCRT model to reproduce the spatial flux distribution of galaxies, in all wavebands, is not straightforward. Indeed, the observations provide only 2D projected constraints. This is why most studies favor edge-on galaxies, as the images of such objects provide constraints on both the radial and azimuthal distributions, assuming axisymmetry (Fig. III.25). Several studies have modeled the effect of extinction on the optical data of disk galaxies using such codes (*e.g.* Xilouris et al., 1999; Alton et al., 2004; Bianchi, 2007). They were able to answer the recurring question about the optical thickness of disk galaxies (Disney et al., 1989). In particular, Xilouris et al. (1999) found that the face-on optical depth of typical spiral galaxies is less than one, in all optical bands. Concerning dust heating, recent progress has been made, especially by the DustPedia collaboration, using the MCRT code SKIRT (Baes & Camps, 2015).

- In M 31, Viaene et al. (2017) showed that 90 % of the dust could be heated by the evolved stellar populations.
- Nersesian et al. (2020a) showed that dust heating by young stars accounts on average for ≃ 60 % in four face-on barred spirals.
- Viaene et al. (2020) modeled the strong AGN NGC 1068. We showed that ≃ 80 % of the heating is coming from young stars, and only a few percents from the central engine. However, dust heating by AGN represent about ≃ 90 % within the central ≃ 100 pc.
- Nersesian et al. (2020b) studied M 51, showing that globally ≃ 71 % of the heating was coming from young stars. Surprisingly, we also found that NGC 5195, the companion of M 51 was responsible for ≃ 6 % of this heating.

A model such as SKIRT can also be used to model the radiative transfer in simulations of galaxies (*e.g.* Trčka et al., 2020). Finally, these models account for the energy balance between the escaping UV-visible light and the re-emitted IR-submm radiation. Interestingly enough, several studies report a deficit of modeled FIR emission by a factor ≃ 3 – 4, compared to the observations (Alton et al., 2000, 2004; Dasyra et al., 2005; De Looze et al., 2012a,b). This discrepancy is thought to result from a lack of detail in modeling the geometry. In particular, the presence of young stars, deeply embedded in molecular clouds, at sub-grid resolutions, could compensate for this deficit without significantly altering the extinction (*cf. e.g.* Baes et al., 2010).

III.1.3.3 Constraining the Grain Opacity

Dust masses derived from SED fits directly depend on the assumed grain opacity. Using the MBB parametrization (Eq. I.73), both the scaling, κ_0, and the emissivity index, β, are important. There are particular situations, where we can reverse the process and constrain these two parameters:

1. if we are observing a region that we can assume uniformly illuminated, then we can infer β;
2. if we have an independent constraint on the dust mass, then we can infer κ_0.

Studies of the emissivity index. There are numerous publications presenting MBB fits of nearby galaxies. However, as discussed in Sect. III.1.2.1, the derived emissivity index, β, is degenerate with temperature mixing. The best constraints on the intrinsic β are obtained in the submm regime, where only massive amounts of very cold dust ($T \lesssim 10$ K) could bias the value. Table III.3 lists *effective emissivity indices*, $\beta_{\rm eff}$, for several objects, obtained with *Planck*, with constraints up to 850 µm. It

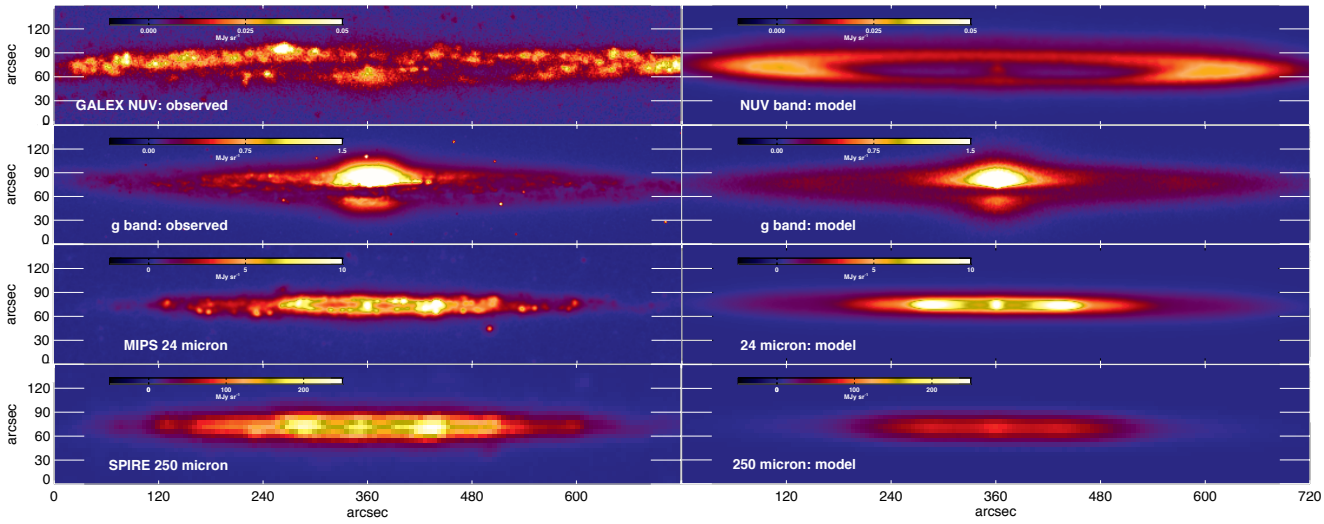

FIGURE III.25 – *Radiative transfer modeling of NGC 4565.* The observations (left column) are compared to the modeled flux distribution (right column). Credit: De Looze et al. (2012a).

appears that all the values are lower than 2, and that low-metallicity systems have a lower $\beta_{\rm eff}$ than higher metallicity galaxies. Boselli et al. (2012), studying a volume-limited sample with *Herschel* (up to 500 µm), also found an average $\beta_{\rm eff} \simeq 1.5$, and hinted that low-metallicity objects tend to have $\beta_{\rm eff} < 1.5$. In M 33, $\beta_{\rm eff}$ derived from *Herschel* observations is around 2 in the center and decreases down to 1.3 in the outer parts (Tabatabaei et al., 2014). On the other hand, the outer regions of M 31 exhibit a steeper slope ($\beta_{\rm eff} \simeq 2.3$) than in its center (Draine et al., 2014). This contradictory behaviour does not appear to originate in fit biases, as both increasing and decreasing trends of $\beta_{\rm eff}$ with radius are found in the sample of Hunt et al. (2015).

	Milky Way	M 31	LMC	SMC
Temperature	19.7 ± 1.4 K	18.2 ± 1.0 K	21.0 ± 1.9 K	22.3 ± 2.3 K
$\beta_{\rm eff}$	1.62 ± 0.10	1.62 ± 0.11	1.48 ± 0.25	1.21 ± 0.27
Reference	*Planck* (2014a)	*Planck* (2015a)	*Planck* (2011a)	*Planck* (2011a)

TABLE III.3 – *Free emissivity index MBB fits of nearby galaxies by the Planck collaboration.*

Grain opacity in the LMC. An important result, that has often been misunderstood, concerns the grain opacity in the LMC. Galliano et al. (2011), modeling a strip covering one fourth of the LMC (*cf.* Fig. III.21), with the composite approach (Sect. III.1.2.2), found that the dustiness distribution in this galaxy was most of the time larger than the maximum value it could in principle reach. This maximum value is set by the elemental abundances. The fraction of elements locked-up in grains can indeed not be larger than the amount available in the ISM. The metallicity of the LMC is $Z_{\rm LMC} \simeq 1/2\, Z_\odot$ (Pagel, 2003). The maximum dustiness of the LMC is thus $Z_{\rm dust}^{\rm max} \simeq Z_{\rm LMC} \simeq 0.007$. The dust mixture that was used is an update of the Zubko et al. (2004, BARE-GR-S). It is essentially based on the Draine & Li (2007) optical properties, a pre-*Herschel* model. This discrepancy is shown in Fig. III.26 (the red histogram). The only explanation is that this grain mixture is not emissive enough to account for the observed FIR-submm emission. We thus proposed an alternate dust model, simply replacing graphite by amorphous carbons (the ACAR sample of Zubko et al., 1996), without altering the total carbon fraction. This simple modification boosts the emissivity by a factor [6] $\simeq 2-3$. With this new model, most of the dustiness distribution is centered around its expected value, and is clear from

6. This factor is not precise, as the slope of the opacity is also changed. The difference in emissivity is thus not a sole scaling.

the forbidden range (yellow). It was called the *AC model* (blue histogram in Fig. III.26). The tail of the distribution in the forbidden zone originates in cold regions, where the uncertainty is large. The conclusion of this modeling was that LMC grains must be a factor $\simeq 2-3$ more emissive than the Draine & Li (2007) model. We actually presented a preliminary version of this result during *Herschel*'s science demonstration phase (Meixner et al., 2010).

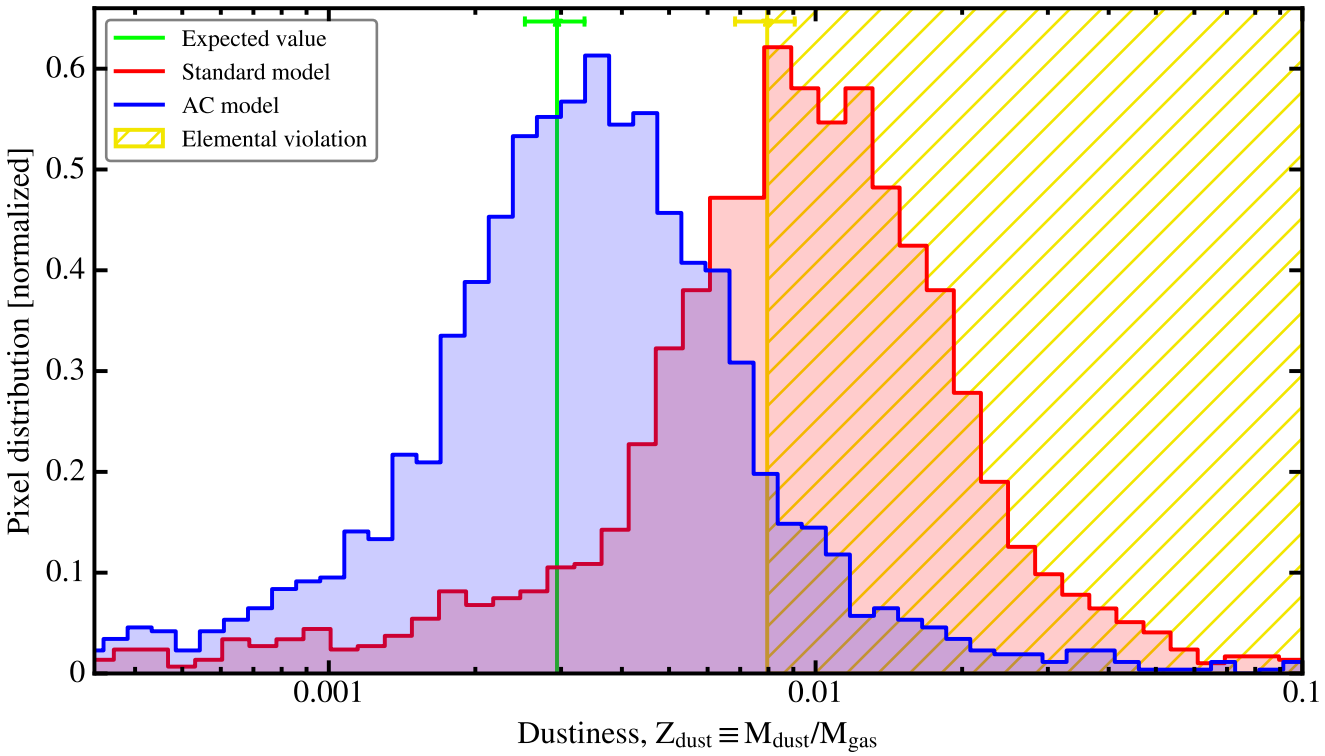

FIGURE III.26 – *Dust mass discrepancy in the LMC.* The histograms are the pixel distribution of the dustiness in the LMC strip of Galliano et al. (2011). We show two models: *(i)* the "*standard model*" (red), based on the Draine & Li (2007) optical properties; *(ii)* the "*AC model*" (blue), replacing graphite by amorphous carbon to boost the emissivity. Most pixels of the standard model are in the hatched area, thus violating the constraints put by heavy element abundances. We also show the uncertainties on the limit dustiness (yellow error bar) and on the expected one (green error bar).

Confirmation in other systems. The conclusion of the Galliano et al. (2011) study was that grains in the LMC had to be more emissive than in the MW, because the Draine & Li (2007) model was at the time consistent with the MW. This last statement however happened to be inexact. Planck Collaboration et al. (2016c) modeled the all sky dust emission, using also the Draine & Li (2007) model. The A(V) estimated along the sightlines of $\gtrsim 200\,000$ *Quasi-Stellar Objects* (QSO) was systematically lower than their dust-emission-derived A(V). Their comparison of emission and extinction thus indicates that the Galactic opacity is in fact also a factor of $\simeq 2$ higher than previously assumed. In addition, in M 31, Dalcanton et al. (2015) derived a high spatial resolution map of A(V). As in the Galaxy, the emission-derived A(V) map (Draine et al., 2014) was found to be a factor of $\simeq 2.5$ higher. We emphasize that, although each of these studies found evidence of local variations of the emissivity as a function of the density (*cf.* Sect. IV.2.1.1), the overall opacity seems to be scaled up compared to Draine & Li (2007). In other words, in all the environments where enough data is available to constrain κ, it is found a factor of $\simeq 2-3$ higher than the original Draine & Li (2007) properties. Dust models therefore need to use an opacity consistent with these constraints. This is the case of the THEMIS model. Its FIR-submm opacity is very close to our AC model (*cf.* Fig. 4 of Galliano et al., 2018).

☞ It is reasonable to adopt the THEMIS grain opacity (*cf.* Sect. II.3.3), when modeling galaxies.

The opacity in nearby galaxies. The DustPedia collaboration conducted several studies aimed at constraining the grain opacity in nearby galaxies. First, Bianchi et al. (2019) studied the actual emissivity of 204 late-type galaxies, that is the ratio of IR emission to H column density. We found an emissivity $\epsilon_\nu(250\,\mu m) \simeq 0.82 \pm 0.07$ MJy/sr/(1020 H/cm^2), consistent with the MW, except for the hottest sources. These estimates were derived using global fluxes, integrated over the whole galaxy. In parallel, Clark et al. (2019) modeled in details the two face-on galaxies, M 74 and M 83. We could map the grain opacity. This was done by converting metallicity maps into oxygen depletion maps, and comparing those to the dust mass. The derived opacities were quoted at $\lambda = 500\,\mu m$: $\kappa(500\,\mu m) \simeq 0.11 - 0.25$ m^2/kg in M 74, and $\kappa(500\,\mu m) \simeq 0.15 - 0.80$ m^2/kg in M 83. These values are consistent with the *Herschel*-*Planck*-revised opacities of the THEMIS model ($\kappa(500\,\mu m) \simeq 0.19$ m^2/kg; *cf.* Fig. II.26).

III.1.3.4 Constraining the Size Distribution

We have seen in Sect. III.1.2.2 that there is a degeneracy between the grain size and starlight intensity distributions. This degeneracy arises from the fact that it is observationally difficult to distinguish the MIR emission of a hot region from the MIR emission of small grains. In the early 2000s, we did not know it was impossible, so we did it (Galliano et al., 2003, 2005). We modeled the SED of the following four BCDs: NGC 1569 ($Z \simeq 1/4\,Z_\odot$), II Zw 40 ($Z \simeq 1/6\,Z_\odot$), He 2-10 ($Z \simeq 1\,Z_\odot$)and NGC 1140 ($Z \simeq 1/3\,Z_\odot$), to infer their size distribution. We interpreted these results in light of shock processing.

Grain processing by shock waves. Shock waves from SNe process dust grains, while sweeping the ISM.

- At high velocity, $v_{shock} \gtrsim 1000$ km/s, they vaporize most of the dust (*e.g.* Dwek, 1998; Slavin et al., 2015).
- At intermediate velocity, $50\text{ km/s} \lesssim v_{shock} \lesssim 200$ km/s, shattering and fragmentation become dominant, altering the size distribution (*e.g.* Jones et al., 1996; Bocchio et al., 2014).

Fig. III.27 shows the model of Jones et al. (1996) for graphite and silicates. In both panels, the grey curve is the initial, MRN size distribution. The color curves show the size distribution obtained after the mixture has been swept by a shock of velocity, v_{shock}. The main effect of the blast wave is to fragment and shatter grains, turning large grains into smaller grains. The qualitative effect is similar for both compositions. This is best seen at low velocity (blue curves). Large grains are depleted and there is an excess of small grains. At higher velocity, the distribution tends toward a log-normal centered around $a \simeq 10$ nm (magenta curve). Vaporization also leads to a net loss of dust mass. This model has since then been refined by Bocchio et al. (2014), who applied it to THEMIS grains. We will discuss more extensively dust processing by SN blast waves in Chap. IV.

The modeling strategy. Galliano et al. (2003, 2005) modeled the UV-to-mm global SED of the four BCDs, using the DBP90 dust model, the stellar evolutionary synthesis code PÉGASE (Fioc & Rocca-Volmerange, 1997, Fig. III.19), and the photoionization code, CLOUDY (Ferland et al., 1998). The modeling scheme was the following.

1. We assume that the ISM is concentrated in a spherical shell. At the center of this shell are the stellar populations.
2. We model the escaping UV-visible SED with two PÉGASE stellar populations, a young and an old one.

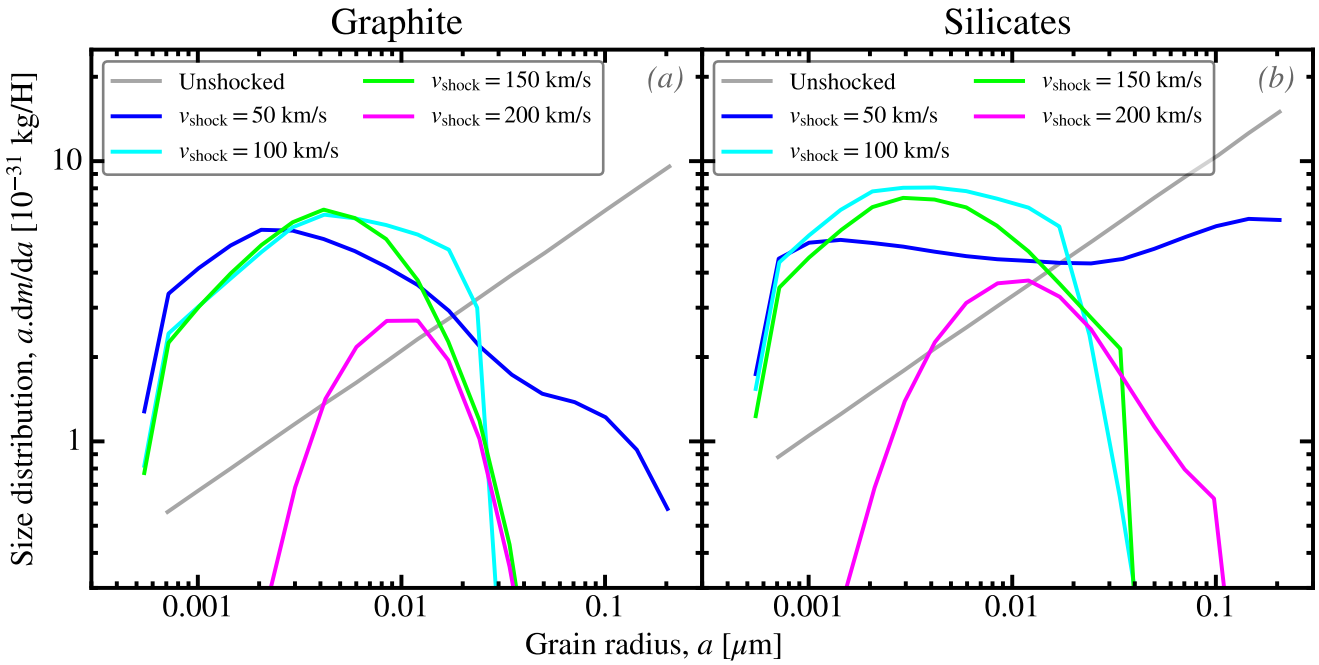

FIGURE III.27 – *Effect of a blast wave on the grain size distribution.* In both panels, we demonstrate the processing of a MRN size distribution (grey) by shock waves of different velocities, v_{shock}. Panel *(a)* shows graphite, and panel *(b)*, silicates, both from the Jones et al. (1996) model. Licensed under CC BY-SA 4.0.

3. We further constrain the UV-visible fit by selecting intrinsic stellar spectra that have the appropriate hardness. The hardness of the ISRF is constrained by matching the observed ISO $[\mathrm{Ne\,III}]_{15.56\mu m}/[\mathrm{Ne\,II}]_{12.81\mu m}$ and $[\mathrm{S\,IV}]_{10.51\mu m}/[\mathrm{Ne\,III}]_{15.56\mu m}$ ratios, using CLOUDY.
4. The intrinsic ISRF is then used to heat the DBP90 dust mixture. We fit the dust emission to the IR-to-mm observations, by varying the size distribution.
5. We iterate this process a few times, as the dust size distribution impacts the extinction curve, which is circularly used to constrain the stellar populations.

This model is self-consistent *per se*. It however avoids the degeneracy between size and ISRF distributions by assuming a simple geometry (the shell). The dust is thus uniformly illuminated in this model, which is an unrealistic assumption for a star-forming galaxy. It is therefore likely that some of the emission we have attributed to small grains originates in hot regions. The results Galliano et al. (2003, 2005) obtained, that we will discuss in the following paragraphs, are nevertheless qualitatively consistent with the properties we expect in these environments. It is possible that only a fraction of the MIR emission originates in compact H II regions, not excluding an overabundance of small grains.

The grain size distribution in four dwarf galaxies. The inferred size distribution, in the four BCDs, are shown in Fig. III.28. We display the three components of the DBP90 model: PAHs, VSGs and BGs (*cf.* Sect. II.1.2.5). The most striking features, common to the four objects, are the following.

- PAHs are under-abundant, compared to the MW. This was one of the first attempt at constraining the PAH abundance in low-metallicity environments. Nowadays, there are overwhelming evidence of a general trend between the aromatic feature strength and metallicity. We will come back to this point in Sect. IV.2.2.1.
- The global grain size distribution is dominated by small grains with radii of a few nanometers. These size distributions are thus qualitatively consistent with shock-processed grains. This is encouraging, as we know that these environments are permeated by numerous SN blast waves, coming from their young stellar populations (*e.g.* Oey, 1996; Izotov et al., 2007).

Two studies used a similar approach, assuming uniform illumination, and fitting the SED varying the size distribution of the DBP90 model, in NGC 1569 (Lisenfeld et al., 2002) and in the LMC (Paradis et al., 2009). They also concluded to an overabundance of small grains.

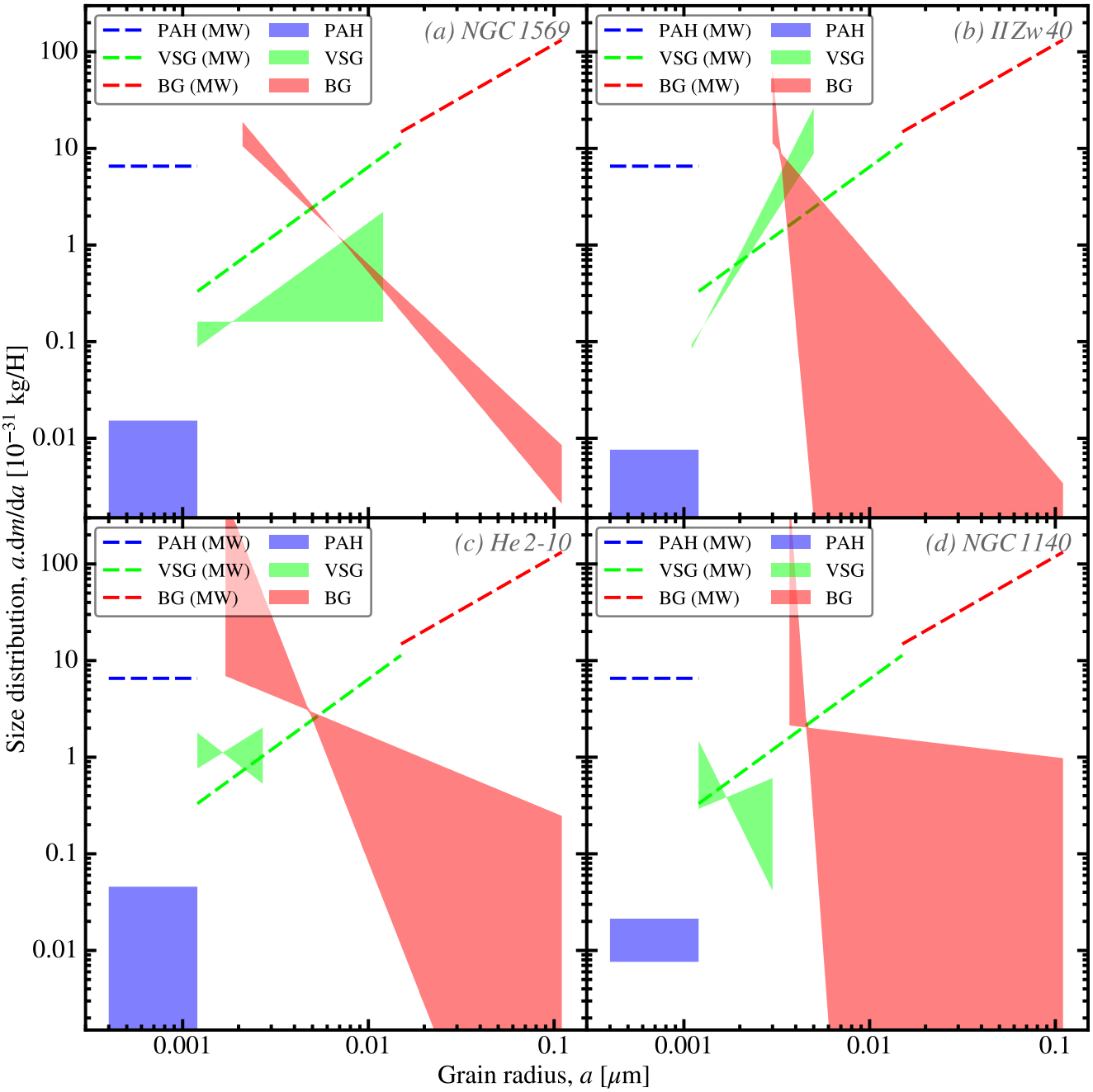

FIGURE III.28 – *Grain size distribution in four dwarf galaxies.* In each panel, we show the MW grain size distribution of the DBP90 model, as dashed lines. Those are the three components presented in Sect. II.1.2.5: PAH, VSG and BG. The filled curves show the likely range of size distribution inferred by the SED fits of Galliano et al. (2003, 2005). Licensed under CC BY-SA 4.0.

Consequence on the extinction curves. We have briefly mentioned in Sect. II.1.2.2 that the extinction curves in the Magellanic clouds were systematically different from the MW. Fig. III.29.a compares the extinction towards different sightlines in the LMC and SMC, to the range of extinction curves in the MW. We see that the LMC ($Z \simeq 1/2\ Z_\odot$) is on average (red curve) similar to the MW. However, toward the massive star-forming region 30 Doradus (LMC2 supershell; green curve), it is steeper, with a weaker 2175 Å bump. When we go to the SMC ($Z \simeq 1/5\ Z_\odot$; blue curve), the difference is more pronounced: the extinction curve has a very steep UV-rise and lacks the 2175 Å bump. The origin of these

variations are still debated. Our four BCDs brought an interesting perspective on this open question. The extinction curves derived from the size distributions of Fig. III.28 are shown in Fig. III.29.b. We can see that they are systematically steeper than the average MW (R(V) = 3.1). They also have a 2175 Å that is either weaker (NGC 1569, He 2-10 and NGC 1140) or similar (II Zw 40) to the MW[7]. In other words, these extinction curves lie between the LMC and SMC, consistent with the metallicity range of these BCDs. The modeling of Galliano et al. (2003, 2005) therefore provides a coherent view of the grain properties in these environments, where shock waves have an instrumental role in shaping the grain sizes.

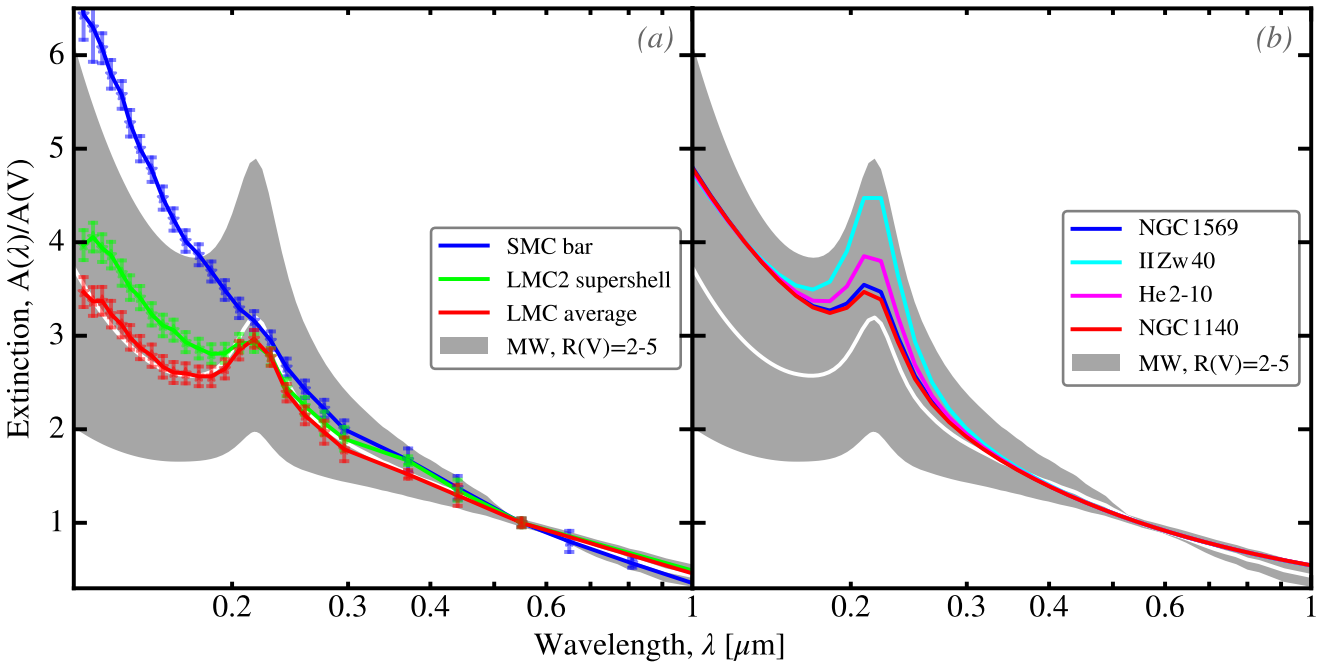

FIGURE III.29 – *Extinction curves of low-metallicity environments.* In both panels, we show as a reference the range of Galactic extinction curves, with R(V) = 2 – 5, from the Fitzpatrick et al. (2019) sample (*cf.* Fig. II.11), in grey. The white curve is the average Galactic extinction, with R(V) = 3.1. In panel *(a)*, we overlay several extinction curves within the Magellanic clouds, from the Gordon et al. (2003) sample: *(i)* the average of the LMC (red); *(ii)* the LMC2 supershell (green), near the massive star-forming region 30 Doradus; and *(iii)* the SMC bar (blue). In panel *(b)*, we show the extinction of the four BCDs modeled by Galliano et al. (2003, 2005). Licensed under CC BY-SA 4.0.

III.2 Studies Focussing on Specific Spectral Domains

Sect. III.1 was devoted to modeling the whole IR SED, which is necessary to estimate the total dust content of galaxies. There are however several other important properties that can be self-consistently studied by focussing on a particular wavelength range.

III.2.1 Scrutinizing Mid-IR Spectra

Mid-IR spectra have been extensively observed since the first light of ISO. *Spitzer* and AKARI have extended our knowledge of this spectral range and the JWST will likely revolutionize it.

7. We note that the strength of the bump is controlled by the carbon-to-silicate grain ratio, a parameter that is poorly constrained by the SED fit.

III.2.1.1 The Aromatic Feature Spectrum

Until now, we have discussed PAHs from a general point of view, and how to estimate their mass fraction. We now focus on the information that the analysis of their detailed MIR emission spectrum can bring. In what follows, we interchangeably use the terms UIBs, aromatic features and PAH bands. The only case where these terms are not equivalent is when discussing the UIBs around 3 µm, coming from a mixture of aromatic and aliphatic features, that can not be solely attributed to PAHs.

MIR spectra of galaxies. Fig. III.30 illustrates the diversity of MIR spectra encountered in different environments. It shows three extreme galaxies from the Hu et al., *in prep.* sample.

Gas-rich, Solar-metallicity galaxies, such as NGC 1097 (green spectrum in Fig. III.30), have bright aromatic features. These features are emitted by both their diffuse ISM and their PDRs. The level and steepness of their MIR continuum, longward 10 µm, depend on their SFR. Galaxies with a low SF-activity tend to have a flatter continuum, as the emission from hot equilibrium grains in H II regions is lower.

Low-metallicity galaxies, such as NGC 1569 (blue spectrum in Fig. III.30), have an integrated spectrum very similar to an H II region (*e.g.* Peeters et al., 2002b; Martín-Hernández et al., 2002). They have weak or undetected aromatic features, which we will extensively discuss in Sect. IV.2.2.1. Their strong ionic lines result from the combination of their young stellar population and lower dust screening. For the same reason, their MIR continuum is significantly steeper than Solar-metallicity objects having the same *specific Star Formation Rate* (sSFR $\equiv$ SFR/M$_\star$). In addition to small, stochastically-heated grains, the MIR continuum of BCDs originates partly in large grains at thermal equilibrium with the radiation field in H II regions. The latter grains are indeed hot enough to significantly emit at shorter wavelengths than Solar-metallicity objects.

AGNs, such as CentaurusA (red spectrum in Fig. III.30), have a rather flat NIR-to-MIR continuum (*e.g.* Laurent et al., 2000; Spoon et al., 2007). This continuum originates in the strong gradient of temperature due to the central illumination by the AGN (this is the same qualitative effect as in our MCRT simulation; Sect. III.1.1.4). In particular, temperatures of the underlying continuum can reach higher values in the central region, than normal galaxies. It explains why the NIR continuum does not drop to zero. These central hot regions produce a bright MIR continuum, attenuated by the entire disk, resulting in deep silicate absorption bands.

Laboratory and theoretical PAH physics. Although we do not know the exact composition of the interstellar carbon grain mixture responsible for the aromatic feature emission, the brightest bands have been attributed to the main vibrational modes of PAHs. There are still some debates about the origin of the weakest features (*cf. e.g.* Allamandola et al., 1999; Verstraete et al., 2001; Tielens, 2008; Boersma et al., 2010; Jones et al., 2013). In Fig. III.30, we have labeled the different bands with a given mode. These modes are schematically represented in Fig. III.31.a.

The charge of the molecules is one of the most important parameters controlling the ratio between the C–H and C–C bands. Fig. III.32.a shows the laboratory data of Allamandola et al. (1999). The two spectra are the sum of several neutral and cationic molecules. It is clear that C–C and C–C–C bands (6.2, 7.7 and 17 µm complexes) are predominantly carried by ionized PAHs, whereas C–H bands (3.3, 11.3 and 12.7 µm complexes) are carried essentially by neutral PAHs.

Dehydrogenation has a similar effect to ionization. However, for PAHs with more than $\simeq$ 25 C atoms (*i.e.* the bulk of interstellar PAHs), hydrogenation through reactions with abundant atomic H is more important than H loss through unimolecular dissociation (*cf. e.g.* Hony et al., 2001). Thus, dehydrogenation does not have a detectable effect on the UIB spectrum.

The molecular structure is another factor. C–H *Out-Of-Plane* (OOP) bending modes have different frequencies, depending on the number of H atom per aromatic cycle (*cf.* Fig. III.31.b). The

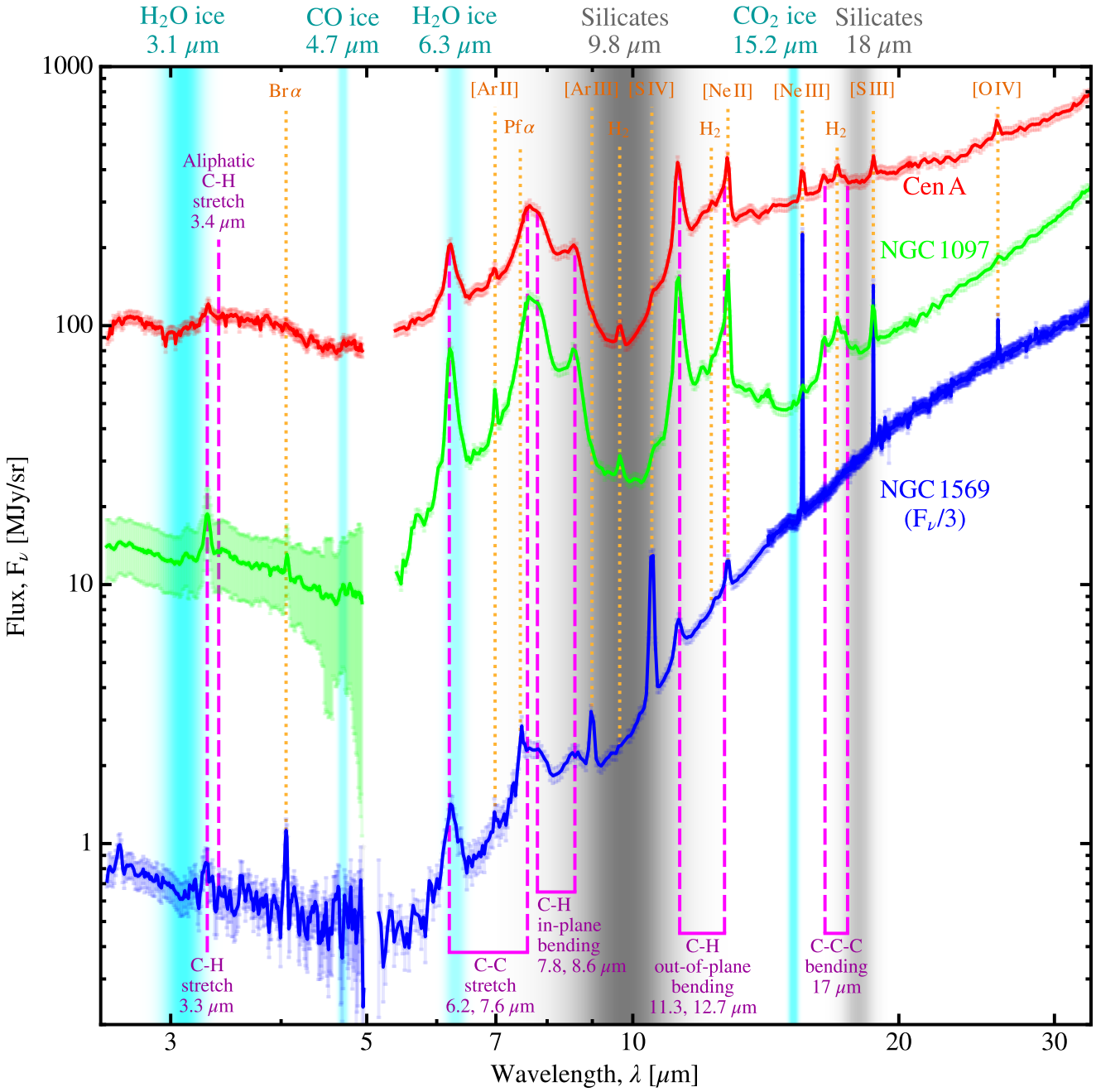

FIGURE III.30 – *MIR spectra of galaxies.* We show the AKARI and *Spitzer* spectra of three galaxies: *(i)* Centaurus A (red) is an ETG with a powerful AGN; *(ii)* NGC 1097 (green) is a LTG with a low-luminosity AGN; and *(iii)* NGC 1569 (blue) is BCD that we have scaled down by a factor of 3. These spectra were prepared for Galliano et al. (2018). We have indicated most of the relevant features. Silicate absorption bands are shown in grey, and ice absorption bands in cyan (*cf.* Sect. II.2.1.2). Gas-phase emission lines are indicated in orange, and carbon-dust emission features, in magenta.

11.3 µm band corresponds to a solo H, found on straight molecular edges, whereas the 12.7 µm one corresponds to a trio, found on corners of the molecules. The solo-to-trio intensity ratio, $I_{11.3}/I_{12.7}$, is thus an indicator of PAH compactness (I_λ being the integrated intensity of the feature centered at λ µm).

The size of the PAHs affects the relative intensity of the different bands. This is demonstrated in Fig. III.32.b. Small PAHs (magenta and red spectra) fluctuate up to temperatures higher than large ones (blue and cyan spectra). Short-wavelength bands are therefore more pumped in small PAHs, whereas large PAHs emit predominantly long-wavelength features.

ISRF hardness has an effect similar to the size, as a higher mean photon energy causes the grain to fluctuate up to higher temperatures (Sect. III.2.1.3 and *e.g.* Galliano et al., 2008b). We have however seen, in Fig. III.14, that this effect was probably less than a factor ≃ 2, in astrophysically relevant cases.

☞ The charge and size of the PAHs are the main parameters controlling their emission spectrum.

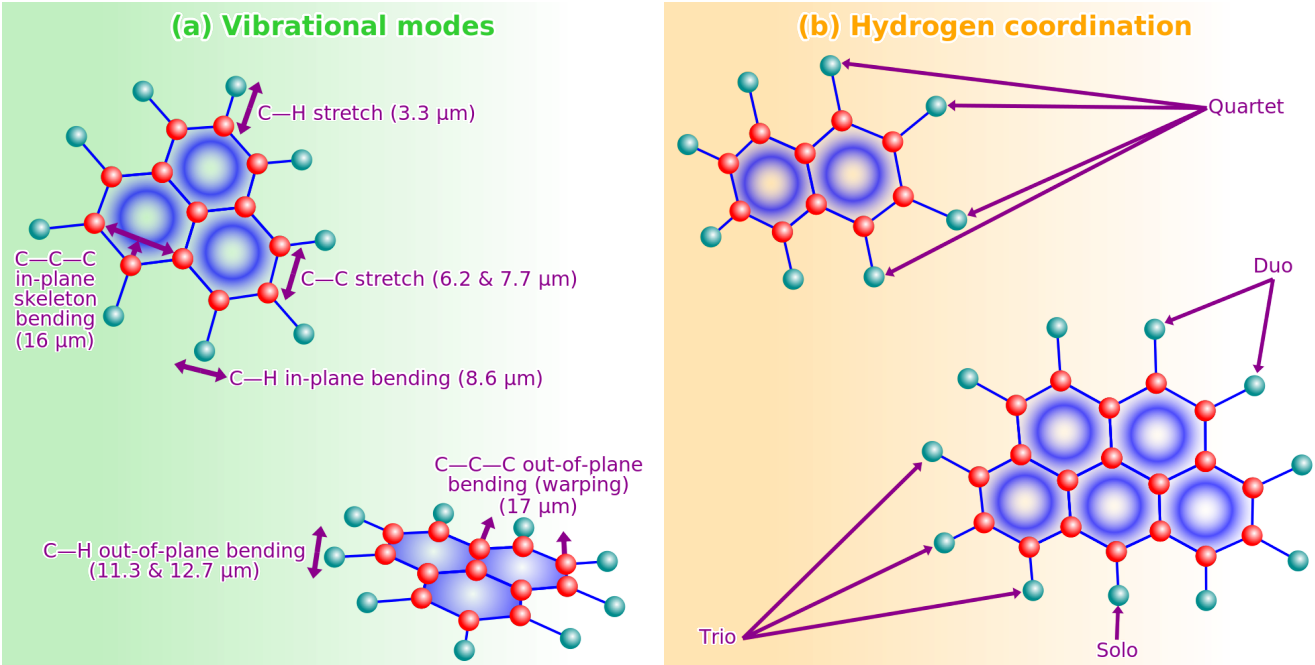

FIGURE III.31 – *Vibrational modes of PAHs.* Panel *(a)* represents the main in-plane and out-of-plane vibrational modes. Panel *(b)* gives examples of solo, duo, trio and quartet H sites. In both panels, red spheres represent C atoms, and cyan spheres, H atoms. Licensed under CC BY-SA 4.0.

III.2.1.2 Spectral Decomposition Methods

To study variations of the aromatic feature spectrum with environmental conditions, one needs to measure the intensity of each band. This task is not as simple as it appears. There are indeed several challenges.

- Aromatic bands are broad features with large wings. They are usually modeled with Lorentz or Drude profiles (*e.g.* Smith et al., 2007; Galliano et al., 2008b; Lai et al., 2020). Their intensity drops quite slowly, away from their peak. Consequently, deblending adjacent features and distinguishing features from the continuum is difficult.
- The exact number and spectral shape of the different aromatic features is not precisely known (*e.g.* Verstraete et al., 1996; Boulanger et al., 1998). High-spectral-resolution, high-signal-to-noise-ratio spectra allow us to identify up to ≃ 40 individual bands, some being very weak. The

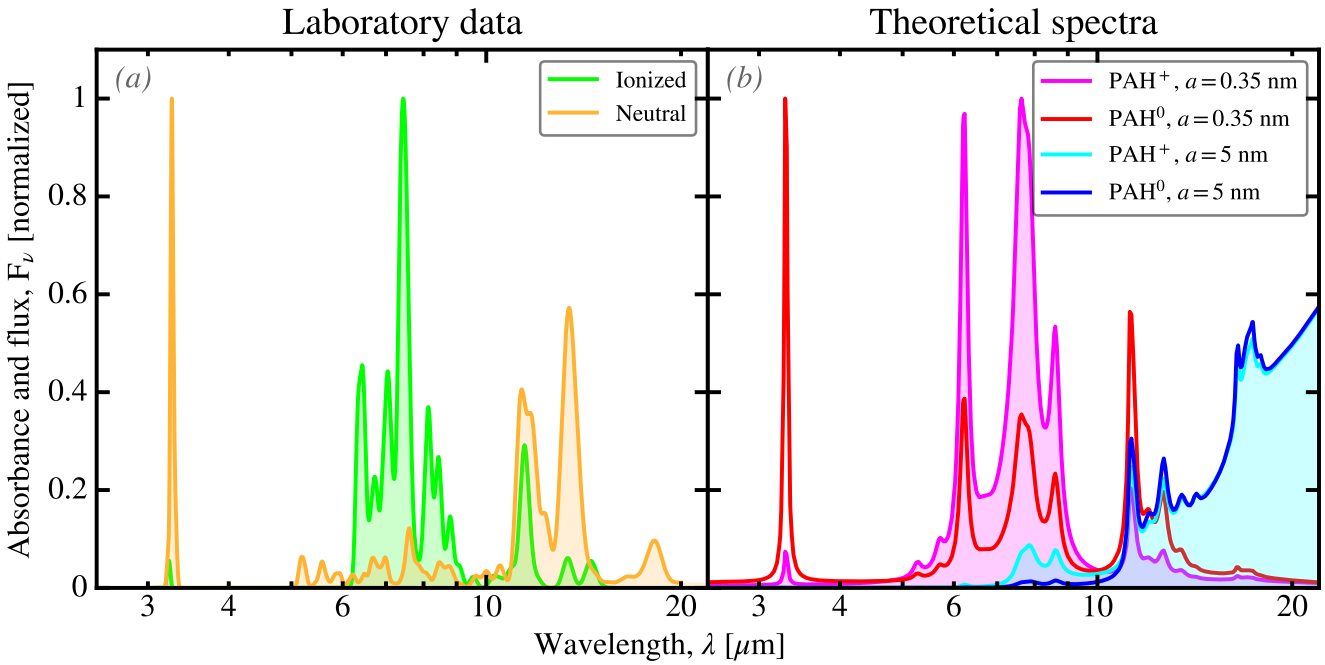

FIGURE III.32 – *Laboratory and theoretical PAH spectra.* Panel *(a)* shows the absorption coefficient of neutral and cationic PAHs measured in the laboratory by Allamandola et al. (1999). Panel *(b)* shows theoretical emission spectra of neutral and cationic PAHs, with radii $a = 0.35$ nm and $a = 5$ nm. We have used the Draine & Li (2007) optical properties and computed the stochastic heating for the Solar neighborhood ISRF (U = 1). Licensed under CC BY-SA 4.0.

assumption about the number and spectral properties of these bands therefore adds another layer of uncertainties.

- Absorption by silicates and ices introduce a degeneracy between A(V) and the band strength. In particular, unless the 9.8 μm band is deep enough to be unambiguously constrained (such as in Cen A; Fig. III.30), the 8 – 12 μm region can equivalently be modeled with: *(i)* 8.6 μm and 11.3 μm bands and no extinction; or *(ii)* weaker 8.6 μm and 11.3 μm bands, a higher underlying continuum and some extinction.

MIR spectral decomposition methods are therefore an essential tool to properly study PAH features.

Calibrating feature properties. Since the properties of the different UIBs are not *a priori* known, we need to empirically infer them. In our work, we parametrize the band spectral profile with a *split-Lorentz function* (Hu et al., 2021a):

$$\mathrm{F}_\nu = \mathrm{I} \times \begin{cases} \dfrac{2}{\pi} \dfrac{\Delta\nu_s^2}{\Delta\nu_s + \Delta\nu_l} \dfrac{1}{(\nu - \nu_0)^2 + \Delta\nu_s^2} & \text{for } \nu \geq \nu_0 \\ \dfrac{2}{\pi} \dfrac{\Delta\nu_l^2}{\Delta\nu_s + \Delta\nu_l} \dfrac{1}{(\nu - \nu_0)^2 + \Delta\nu_l^2} & \text{for } \nu < \nu_0, \end{cases} \tag{III.42}$$

where ν_0 is the central frequency of the feature, and $\Delta\nu_s$ and $\Delta\nu_l$ are its widths on the short- and long-wavelength sides. Having an asymmetric feature is indeed necessary to accurately fit good quality spectra. This asymmetry may originate in the anharmonicity of the transition responsible for the band, or may be due to unresolved blended features. The parameters characterizing each individual features, ν_0, $\Delta\nu_s$ and $\Delta\nu_l$, could be derived from each fit. However, most of them would be quite uncertain, using an average *Spitzer* spectrum. For that reason, we have calibrated these parameters (*i.e.* inferred their reference value), using high-resolution, high-signal-to-noise-ratio spectra of Galactic regions. This calibration is demonstrated in Fig. III.33.

1. We have first fitted the ISO/SWS spectrum of the reflection nebula, the *Red Rectangle*, in order to calibrate the narrow bands (*cf.* Fig. III.33.a). The very wide bands, also called *plateaus*, are not very prominent in this region.
2. We then fix the narrow band parameters and infer the $\lambda \simeq 8$ µm and $\lambda \simeq 12$ µm plateau parameters by fitting the ISO/SWS spectrum of the planetary nebula, NGC 7027 (*cf.* Fig. III.33.b). The $\lambda \simeq 17$ µm complex is too weak to be calibrated using this spectrum.
3. The $\lambda \simeq 17$ µm complex is calibrated by fitting the IRS spectrum of the PDR, M 17 (*cf.* Fig. III.33.c).
4. The aromatic and aliphatic bands in the $\lambda \simeq 3$ µm region are calibrated by fitting the $\lambda = 3 - 5$ µm spectrum of NGC 7027 (*cf.* Fig. III.33.d). The continuum in this range is indeed clean and there are no other blended bands.

Table III.4 gives the resulting band parameters. With these parameters fixed, we can fit even low-signal-to-noise-ratio spectra varying only the intensity of each band (parameter I in Eq. III.42).

Fitting every feature at once. The total MIR spectrum contains the emission from different physical processes that have to be separated in order to accurately measure UIB intensities (*cf.* Fig. III.30). Several models have tackled this problem since the ISO days (*e.g.* Verstraete et al., 1996; Boulanger et al., 1998; Laurent et al., 2000; Madden et al., 2006; Smith et al., 2007; Galliano et al., 2008b; Mori et al., 2012; Lai et al., 2020).

Individual UIBs can be fitted with Lorentz profiles (*e.g.* Galliano et al., 2008b), Drude profiles (*e.g.* Smith et al., 2007) or split-Lorentz profiles (*cf.* Table III.4 and Fig. III.33; *e.g.* Hu et al., *in prep.*).

The dust continuum can be fitted with a linear combination of grey bodies. The opacity of these grey bodies can be a simple MBB power-law (*e.g.* Smith et al., 2007) or the opacity of realistic materials (*e.g.* Hu et al., *in prep.*). This dust continuum likely originates in a combination of small, stochastically-heated grains, and large, hot equilibrium grains. The fitted parameters (mass and temperature) of each grey body therefore have to be considered as nuisance variables. They can not be interpreted physically, because of the uncertainty of their heating mechanism. They are employed only to decompose the continuum and UIB emissions.

Gas lines can be fitted with Gaussian profiles. Table III.5 lists the most prominent MIR gas lines and their central wavelengths. The width of the profile is determined by the spectral resolution of the instrument, except at very high spectral resolution ($R \equiv \lambda/\Delta\lambda \gtrsim 30\,000$), where the true width of the line can be resolved.

The stellar continuum only contributes at short wavelength, and can be modeled with a Rayleigh-Jeans law.

The extinction, which is essentially absorption at these wavelengths, can be modeled with a general extinction curve (*cf. e.g.* Fig. II.24), assuming a simple geometry (*cf. e.g.* Sect. III.1.1.2). The most prominent dust features are the two silicate bands at 9.8 and 18 µm (*cf.* Fig. III.30). Ice absorption can also be non negligible. They can be taken into account the same way, as icy band profiles are well-constrained (*cf.* Fig. II.12.b). The optical depth ratio between different ice species and the silicates however varies from one source to the other (*e.g.* Yamagishi et al., 2015). The optical depth therefore has to be independently estimated for each species (*i.e.* one needs to derive $\tau_{\rm dust}$, $\tau_{\rm H_2O}$, $\tau_{\rm CO}$, *etc.*).

Fig. III.34.a demonstrates such a fitting method on the total spectrum of M 82 (Galliano et al., 2008b). It is labeled as the *Lorentzian method*, as the UIBs are modeled with Lorentz profiles. This earlier model did not use all the bands given in Table III.4, that we are now using.

Alternative methods. Several other MIR spectral fitting methods have been dicussed in the literature. The two following ones are worth mentioning.

λ_0	$\Delta\lambda_s$	$\Delta\lambda_l$	Type
3.291 µm	0.020 µm	0.019 µm	Main
3.399 µm	0.011 µm	0.024 µm	Main
3.499 µm	0.077 µm	0.071 µm	Small
5.239 µm	0.025 µm	0.058 µm	Small
5.644 µm	0.040 µm	0.080 µm	Small
5.749 µm	0.040 µm	0.080 µm	Small
6.011 µm	0.040 µm	0.067 µm	Small
6.203 µm	0.031 µm	0.060 µm	Main
6.267 µm	0.037 µm	0.116 µm	Main
6.627 µm	0.120 µm	0.120 µm	Small
6.855 µm	0.080 µm	0.080 µm	Small
7.079 µm	0.080 µm	0.080 µm	Small
7.600 µm	0.480 µm	0.502 µm	Plateau
7.617 µm	0.119 µm	0.145 µm	Main
7.870 µm	0.170 µm	0.245 µm	Main
8.362 µm	0.016 µm	0.016 µm	Small
8.620 µm	0.183 µm	0.133 µm	Main
9.525 µm	0.107 µm	0.600 µm	Small
10.707 µm	0.100 µm	0.100 µm	Small
11.038 µm	0.027 µm	0.073 µm	Small
11.238 µm	0.053 µm	0.153 µm	Main
11.400 µm	0.720 µm	0.637 µm	Plateau
11.796 µm	0.021 µm	0.021 µm	Small
11.950 µm	0.080 µm	0.222 µm	Small
12.627 µm	0.200 µm	0.095 µm	Main
12.761 µm	0.081 µm	0.140 µm	Main
13.559 µm	0.160 µm	0.161 µm	Small
14.257 µm	0.152 µm	0.059 µm	Small
15.893 µm	0.178 µm	0.200 µm	Small
16.483 µm	0.100 µm	0.059 µm	Small
17.083 µm	0.496 µm	0.562 µm	Plateau
17.428 µm	0.100 µm	0.100 µm	Small
17.771 µm	0.031 µm	0.075 µm	Small
18.925 µm	0.037 µm	0.116 µm	Small

TABLE III.4 – *UIB profile parameters.* These are the parameters of Eq. (III.42). We have converted the frequencies in wavelengths: $\nu_0 \equiv c/\lambda_0$, $\Delta\nu_s \equiv c/(\lambda_0 - \Delta\lambda_s) - c/\lambda_0$, $\Delta\nu_l \equiv c/\lambda_0 - c/(\lambda_0 + \Delta\lambda_l)$. These are the parameters used for the work of Hu et al. (*in prep.*).

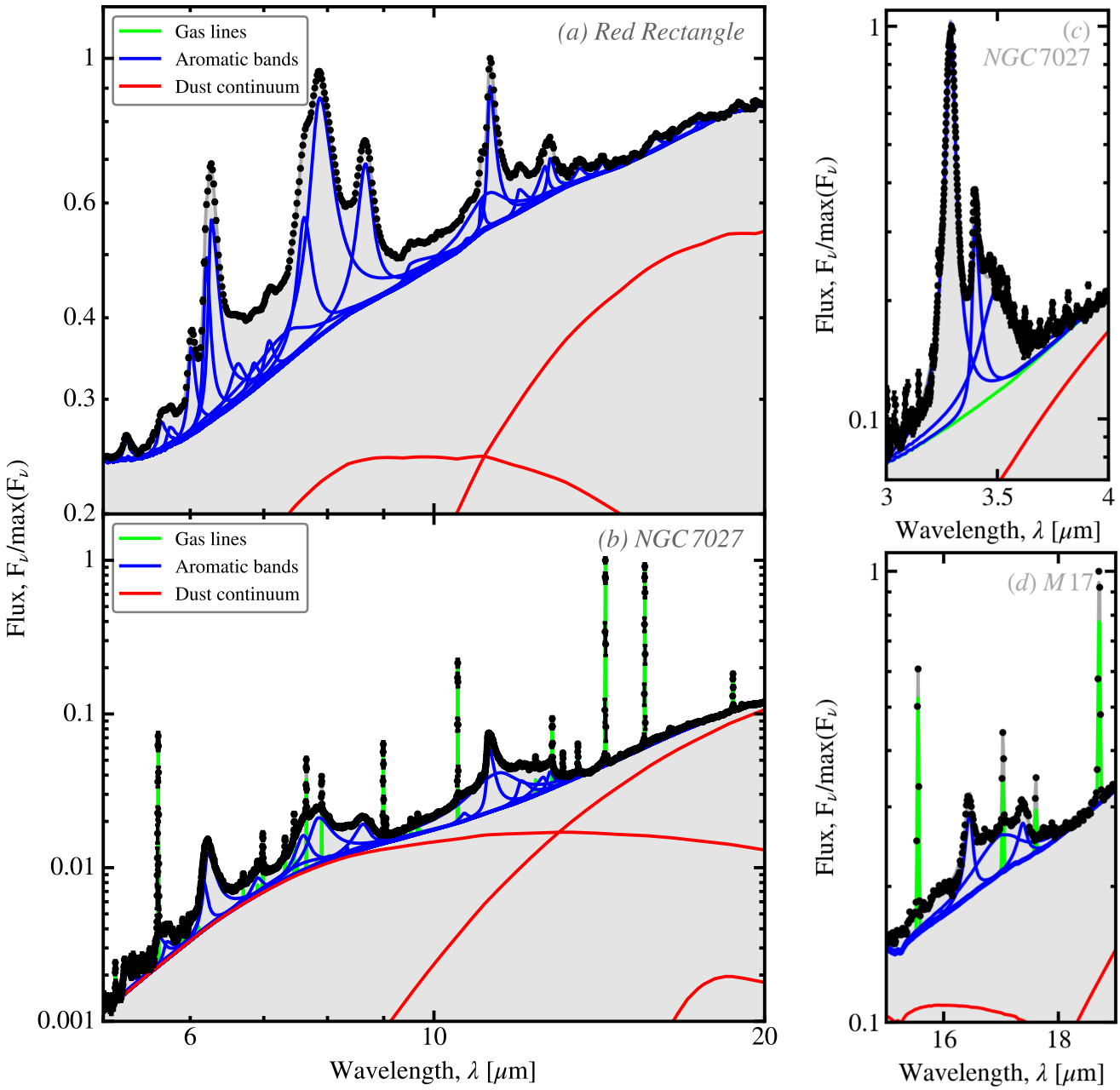

FIGURE III.33 – *Empirical calibration of UIB profiles.* In each panel, the black dots with error bars (barely visible) represent the observations. These are ISO/SWS spectra except for M 17, which is a *Spitzer*/IRS spectrum. The fitted model is the sum of the different individual components: *(i)* grey bodies for the dust continuum; *(ii)* Gaussian profiles for gas lines; and *(iii)* split-Lorentz profiles (Eq. III.42) for UIBs. Licensed under CC BY-SA 4.0.

The spline method consists in interpolating the spectrum under the main band complexes, using spline functions (*e.g.* Vermeij et al., 2002; Galliano et al., 2008b). It is demonstrated in Fig. III.34.b. A first spline interpolation defines the continuum and a second one defines the band plateaus. The areas between the two continua (magenta filled) represent the plateaus in Fig. III.34.b. The bands are then simply the intensity above the plateaus (cyan filled). The advantages of this method are: *(i)* it is simple to implement; *(ii)* it is very fast to run; and *(iii)* it does not suffer from the degeneracies between blended features, or between band wings and the continuum. It has however several limitations: *(i)* the choice of the spline anchor points is arbitrary, which results in systematic differences with other methods; *(ii)* at medium-spectral resolution (typical of ISO/CAM or *Spitzer*/IRS SL-LL modes) it is impossible to deblend features and lines, such as the 12.7 µm UIB and the [Ne II]$_{12.81\mu m}$ line; and *(iii)* this method does

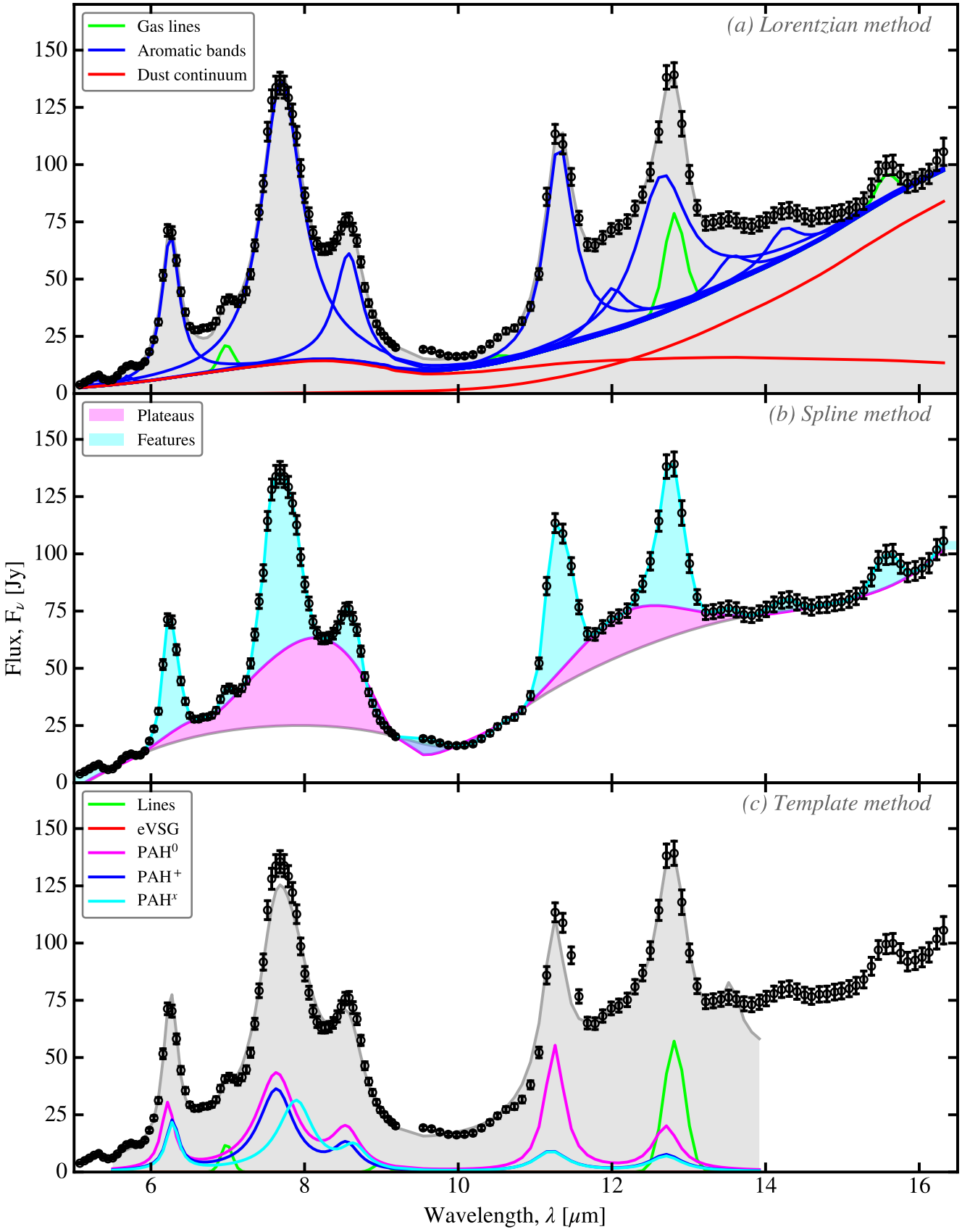

FIGURE III.34 – *MIR spectral fitting methods.* Demonstration of the three MIR fitting methods, described in this manuscript, on the total ISO/CAM spectrum of the starburst galaxy, M 82 (Galliano et al., 2008b). The observations (the black error bars) are identical in each panel. The models of panels *(a)* and *(c)* are least-squares fits, whereas panel *(b)* is a spline interpolation. Panels *(a)* and *(b)* are from Galliano et al. (2008b). The fit of panel *(c)* has been performed only up to λ = 14 μm, using `PAHtat` (Pilleri et al., 2012). In addition to the four components of Fig. III.35, a continuum and the main gas lines are simultaneously fitted.

Central wavelength	Species	Transition	Type
4.052 µm	H I	Brackett α	recombination
5.511 µm	H_2	0–0 S(7)	ro-vibrational
5.908 µm	H I	Humphreys γ	recombination
6.109 µm	H_2	0–0 S(6)	ro-vibrational
6.910 µm	H_2	0–0 S(5)	ro-vibrational
6.985 µm	Ar II	$2P^{3/2}$–$2P^{1/2}$	forbidden
7.460 µm	H I	Pfund α	recombination
7.502 µm	H I	Humphreys β	recombination
8.025 µm	H_2	0–0 S(4)	ro-vibrational
8.991 µm	Ar III	$3P^2$–$3P^1$	forbidden
9.665 µm	H_2	0–0 S(3)	ro-vibrational
10.511 µm	S IV	$2P^{3/2}$–$2P^{1/2}$	forbidden
12.279 µm	H_2	0–0 S(2)	ro-vibrational
12.369 µm	H I	Humphreys α	recombination
12.814 µm	Ne II	$2P^{3/2}$–$2P^{1/2}$	forbidden
15.555 µm	Ne III	$3P^2$–$3P^1$	forbidden
17.035 µm	H_2	0–0 S(1)	ro-vibrational
18.713 µm	S III	$3P^2$–$3P^1$	forbidden
21.829 µm	Ar III	$3P^1$-$3P^0$	forbidden
25.890 µm	O IV	$2P^{3/2}$–$2P^{1/2}$	forbidden
28.219 µm	H_2	0–0 S(0)	ro-vibrational
33.481 µm	S III	$3P^1$–$3P^0$	forbidden
34.815 µm	Si II	$2P^{3/2}$–$2P^{1/2}$	forbidden
35.349 µm	Fe II	$6D^{5/2}$–$6D^{7/2}$	forbidden
36.014 µm	Ne III	$3P^1$–$3P^0$	forbidden

TABLE III.5 – *Most prominent MIR gas lines.*

not provide meaningful uncertainty estimates. Galliano et al. (2008b) performed a systematic comparison of the Lorentzian and spline methods, and found that, although band intensities were different, the trends between band intensities or band ratios were consistent with the two methods.

The template method consists in fitting a small number of synthetic spectra characteristics of different regions or different species. We have demonstrated this method in Fig. III.34.c using `PAHtat` (Pilleri et al., 2012). This method uses four main components. These components were extracted from a sample of Galactic PDRs and PNe, using blind-signal separation methods (Berné et al., 2007; Joblin et al., 2008). In that sense, they are empirical, synthetic small grain spectra. These components are the following.

Neutral PAHs (PAH^0) are shown in Fig. III.35.a. Their brightest C–C band is centered at $\lambda \simeq 7.65$ µm.

Ionized PAHs (PAH^+) are shown in Fig. III.35.b. They have similar band centers as PAH^0, but different intensity ratios, as we have previously seen (*cf.* Fig. III.32). Both PAH^0 and PAH^+ have similar spectral characteristics as class $\mathscr{A}$ spectra of Peeters et al. (2002a), found in H II regions, and thought to be "*processed*" PAHs.

Large ionized PAHs (PAH^x), shown in Fig. III.35.c, have a peculiar redshifted C–C band at $\lambda \simeq 7.9$ µm, observed in PNe by Joblin et al. (2008). They are assumed to be $\simeq 100$ C atom

grains. Those are reminiscent of the class $\mathscr{B}$ spectra of Peeters et al. (2002a).

Evaporating VSGs (eVSGs), shown in Fig. III.35.d, are thought to be PAH clusters of ≃ 500 C atoms. Their spectra have the characteristics of class $\mathscr{C}$ of Peeters et al. (2002a) seen in post-AGB stars, with a broad 7.9 µm band and no 8.6 µm feature. Peeters et al. (2002a) conjectured these could be "*freshly-formed*" carbon grains. The carrier of the broad 7.9 µm band could be destroyed by the ionizing radiation, during its journey in the ISM (*e.g.* Joblin et al., 2008). In this scenario, PAHs are formed by the destruction of VSGs at the UV-illuminated edges of molecular clouds. Class $\mathscr{C}$ is not well studied. Some novae show spectra similar to Class $\mathscr{C}$, and could be due to nitrogen impurities in hydrocarbon compounds (Endo et al., 2021).

The advantages of this method are that: *(i)* fits are not extremely degenerate, even at low signal–to-noise ratios, because of the small number of free parameters, compared to the Lorentzian method; *(ii)* the four different classes are physically meaningful, providing a clear interpretation of the results. However, its lack of flexibility prevents accurate fits, that could overlook new information present in the observations.

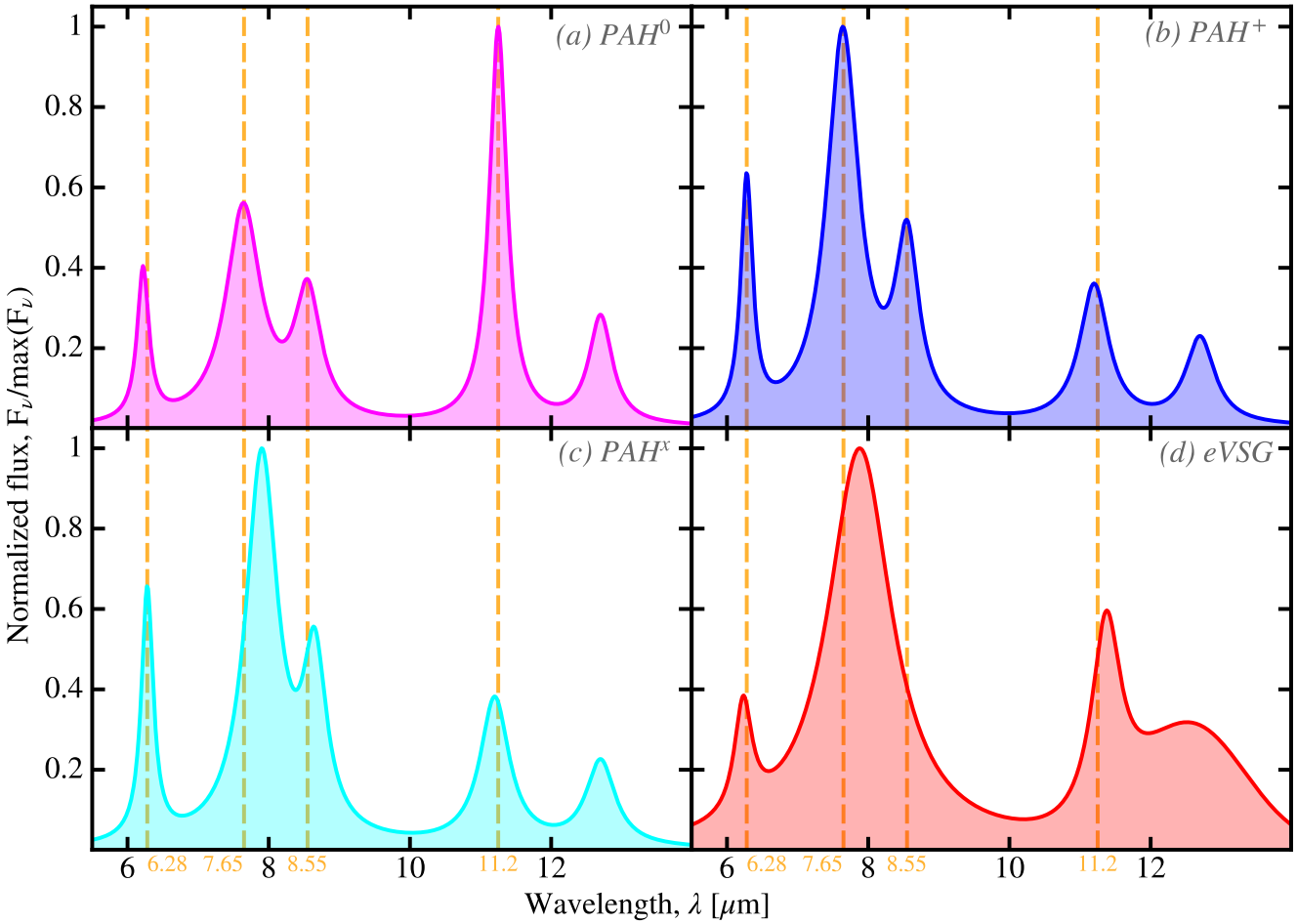

FIGURE III.35 – *PAH and small grain templates.* We show the four components of `PAHtat` (Pilleri et al., 2012). Vertical yellow dashed lines indicate the same wavelengths in the four panels, helping visualizing the band shifts of some components. Licensed under CC BY-SA 4.0.

III.2.1.3 PAH Band Ratio Studies

Applying a spectral decomposition method to a set of MIR spectra allows us to study the variations of several band ratios that contain physical information about the small carbon grain properties.

Observed band ratios in galaxies. Fig. III.36 demonstrates the diversity of spectra among galaxies (panel *a*) or within one (panel *b*). This figure emphasizes the differences in terms of aromatic band intensity. All these spectra are normalized by the 11.3-µm feature intensity. Yet, they exhibit large variations of their 6-to-9-µm features. This can be more precisely quantified by studying the correlation between specific band ratios, such as in Fig. III.37 (Galliano et al., 2008b). The quantity I(λ) is simply the intensity of the feature centered at λ µm. The bottom two panels show the results for integrated galaxies and Galactic regions, whereas the bottom two panels show the results for a few spatially-resolved sources. Overall the trends are similar for both types. It means that this is a multiscale relation, valid at sub-pc scales (within the Orion bar or M 17) and ≃ 10 kpc scales (among integrated galaxies). These three displayed band ratios span about an order of magnitude, and are linearly correlated with each other. It implies that the 6.2, 7.7 and 8.6 µm features are tied together, while the 11.3 µm can vary independently. This is what was illustrated in Fig. III.36. The only parameter that can explain such a variation is the charge of the PAHs (*cf.* Fig. III.32).

☞ The variation of the PAH charge can explain most of the UIB variations observed in the nearby Universe.

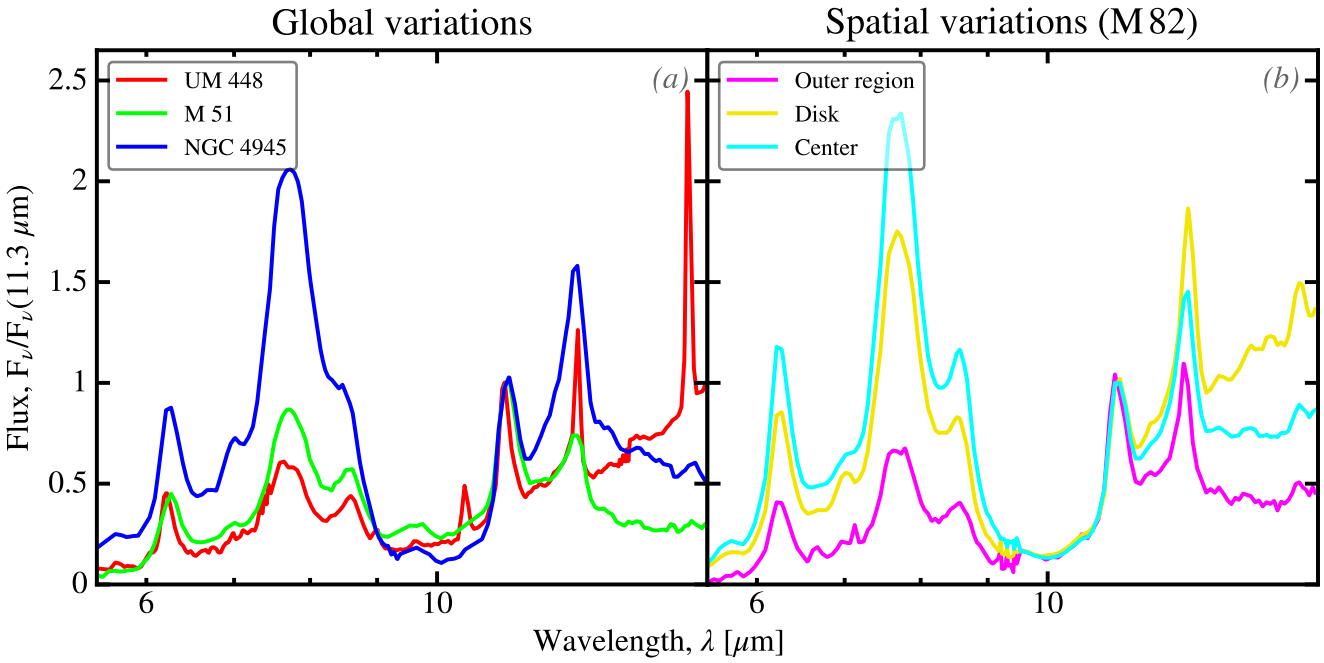

FIGURE III.36 – *Diversity of MIR spectra among and within galaxies.* Panel *(a)* shows the integrated spectra of three galaxies: *(i)* UM 448, a BCD; *(ii)* M 51, a prototypical LTG; and *(iii)* NGC 4945, a LIRG. Panel *(b)* shows the spectra of three different regions within the starbursting irregular galaxy, M 82. In both panels, the monochromatic flux is normalized to its value at 11.3 µm, in order to demonstrate band ratio variations. These are ISO spectra (Galliano et al., 2008b). Licensed under CC BY-SA 4.0.

Effects of ionization and size. Although ionization is the main driver of the UIB relative variations in galaxies, other effects can play a role in specific environments. The most important one of these secondary effects is the PAH size distribution. Fig. III.38 shows numerical simulations of several key UIB ratios (Hu et al., 2021a). We have varied: *(i)* the minimum PAH size expressed in number of C atoms, N_C^{min}, highlighted in Fig. III.38.a; *(ii)* the PAH charge fraction, f_+, highlighted in Fig. III.38.b; *(iii)* the ISRF intensity and hardness. To illustrate the last effect, we have computed the model grid for the Solar neighborhood ISRF (Mathis et al., 1983). This values are the bright grid points. We have also computed the grid for a hot star spectrum, with U = 10^4 (the faint grid points). The effect of the ISRF is non negligible, but it is less drastic than that of the charge and size. Most astrophysically relevant ISRFs will be intermediate between the two extreme cases we have displayed. Fig. III.38 illustrates

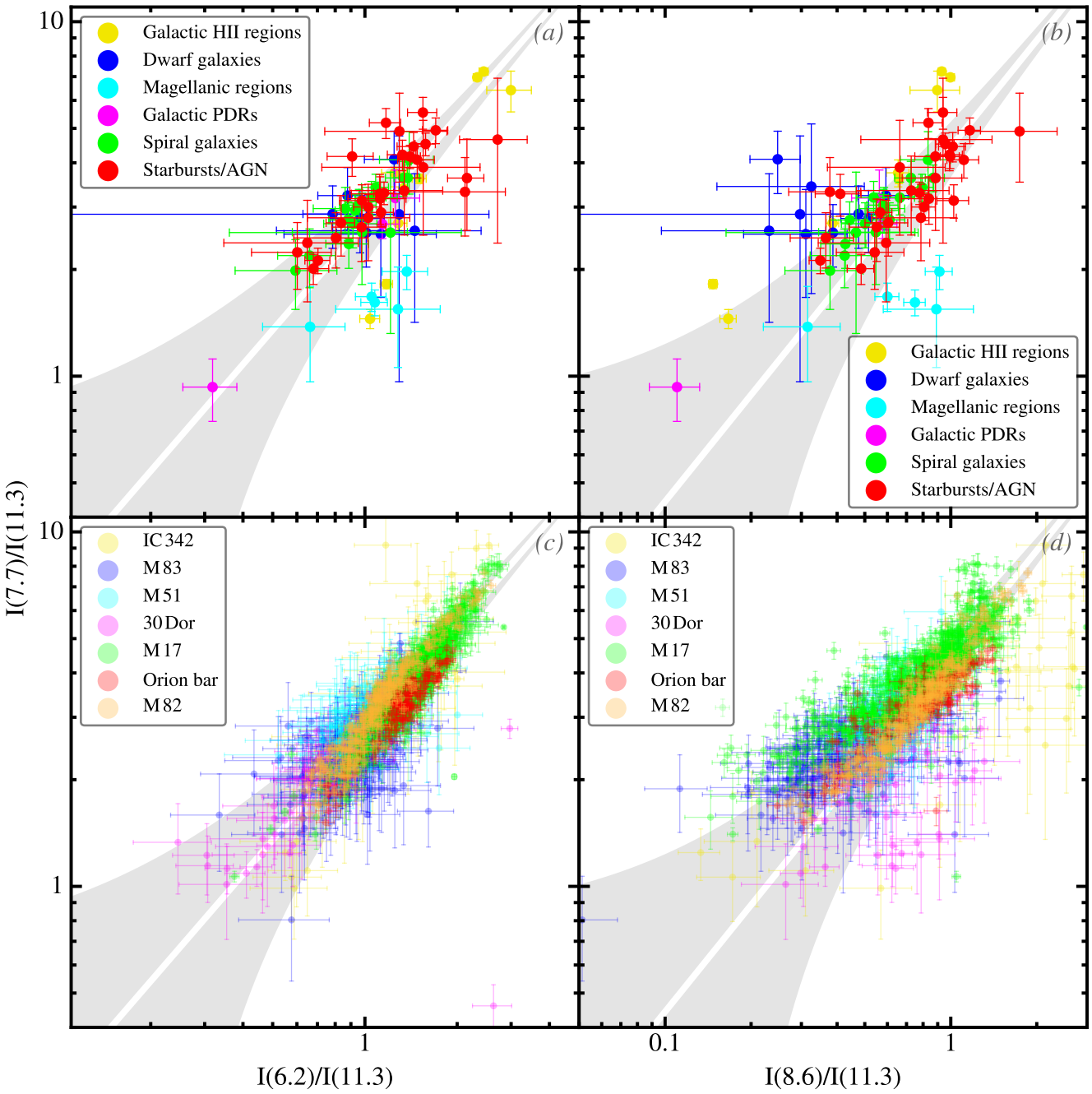

FIGURE III.37 – *PAH band ratio correlations inside and among galaxies.* The top two panels show the values of the ratios derived from integrated spectra of galaxies, as well as Galactic and Magellanic regions. The bottom two panels show pixel distribution of the same ratios, within a variety of objects. These data are a combination of ISO/CAM and *Spitzer*/IRS spectra, fitted using the Lorentzian method (Galliano et al., 2008b). The grey-filled curves represent the ±1σ linear fit to the integrated source correlations (*cf.* Table 2 of Galliano et al., 2008b). The grey curves are identical in panels *(a)* and *(c)* and in panels *(b)* and *(d)*, to guide the eye when comparing integrated and resolved correlations. Licensed under CC BY-SA 4.0.

the following points (see also Rigopoulou et al., 2021, for a more complete calculation using *Density Functional Theory*).

I(3.3)/I(11.3) is mainly a size tracer. Both 3.3 and 11.3 µm bands (C–H modes) are indeed primarily emitted by neutral PAHs. Charge thus does not significantly impact this ratio. The 3.3 µm feature is mainly carried by the smallest PAHs, whereas the 11.3 µm feature is carried by intermediate sizes.

I(7.7)/I(11.3), on the opposite, is essentially a charge tracer. It is still sensitive to the size, because of the relatively large difference in wavelength of both features. The degeneracy due to this additional dependence can be broken, using I(3.3)/I(11.3).

Such band ratio diagrams have been used to demonstrate systematic variations of the PAH size distribution in various environments. We studied the spatial variations of I(3.3)/I(11.3) in NGC 1097 (Fig. III.30) and showed it was systematically lower in the central region, close to the AGN (Wu et al., 2018b). The most likely explanation is that the hard radiation field from the central engine is selectively destroying the smallest PAHs. This effect was also shown by Smith et al. (2007) and Sales et al. (2010), on global scales.

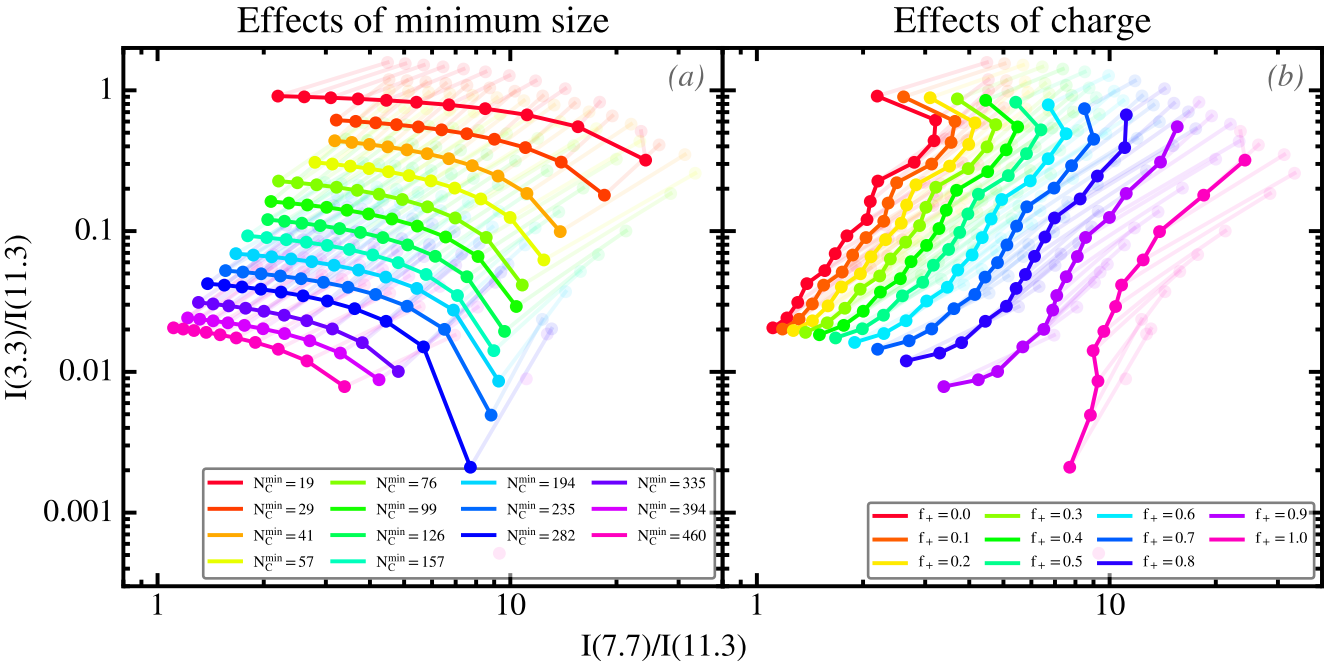

FIGURE III.38 – *Theoretical MIR band ratio variations.* Both panels show the same grid points, but are highlighted differently. Each circle is the theoretical band ratio estimated from the stochastic emission spectrum of a PAH mixture having the Draine & Li (2007) optical properties and the Zubko et al. (2004, BARE-GR-S) size distribution. The solid color symbol are mixtures heated with the Solar neighborhood ISRF (Fig. I.28) with U = 1, whereas the pastel symbols are heated by a black body at T = 30 000 K with U = 10^4. In panel *(a)*, we highlight the effect of changing the minimum size cut-off, in number of C atoms, N_C^{min}. In panel *(b)*, we show the effect of the charge fraction, f_+. Licensed under CC BY-SA 4.0.

The particular case of low-metallicity environments. In low-metallicity systems, band ratio variations can be more difficult to probe, as the band equivalent widths are lower, and thus more uncertain (*cf.* Sect. III.2.1.4). In the LMC, Mori et al. (2012) found different trends in neutral and ionized sightlines. Toward the latter, there are evidences that PAHs have a lower charge (as a consequence of the higher recombination rate) and are on average larger (due to the destruction of the smallest PAHs). In contrast, in the SMC, Sandstrom et al. (2012) found very weak I(6 – 9)/I(11.3) ratios and weak 8.6 and 17 µm bands, implying small weakly ionized PAHs. This last point is consistent with the trend

of I(17)/I(11.3) with 12 + log(O/H) found by Smith et al. (2007). This was also noted by Galliano et al. (2008b), who found that low-metallicity systems tends to lie on average toward the lower left corner of Fig. III.37, whereas the upper left corner is essentially populated by Solar-metallicity sources. However, Hunt et al. (2010) argued that BCDs exhibit a deficit of small PAHs. If there is a smooth variation of PAH size distribution with metallicity, these results are in contradiction. Sandstrom et al. (2012) noted that these BCDs are more extreme environments than the SMC, and that photodestruction could dominate the PAH processing (*cf.* Sect. IV.2.2.1). We note that the solution to this apparent controversy might alternatively reside in the difference in studied spatial scales. In the Magellanic Clouds, *Spitzer* spectroscopy gives a spatial resolution of a few parsecs, compared to a few hundred in nearby BCDs. The fact is that the LMC and SMC exhibit strong spatial variations of their UIB spectrum. Whelan et al. (2013) showed a diversity of MIR spectral properties in the SMC. In this study, we demonstrated that the PAH emission in a region like N66 is dominated by its diffuse component, and not by its bright clumps, where PAHs are destroyed. At the other extreme, the molecular cloud SMC-B1#1 shows unusually high UIB equivalent widths (Reach et al., 2000). Also, the I(11.2)/I(12.7) ratio indicates that PAHs are more compact in 30 Doradus and more irregular outside (Vermeij et al., 2002). All these elements suggest that there is a complex balance of processes shaping the MIR spectra throughout low-metallicity environments.

UIBs as diagnostics of the physical conditions. The fact that ionization dominates the UIB variation in galaxies opens the possibility to use specific observed band ratios to quantify the physical conditions. The charge of an ensemble of molecules is indeed the balance between: *(i)* the ionizing photon rate; and *(ii)* the electronic recombination rate. The first quantity is usually quantified by the variable G_0, defined as the integral of the ISRF in the FUV (*e.g.* Hollenbach & Tielens, 1997):

$$G_0 \equiv \frac{\int_{6\,\mathrm{eV}}^{13.6\,\mathrm{eV}} I_E(E)\,dE}{1.6\times10^{-6}\,\mathrm{W/m^2}}. \tag{III.43}$$

The recombination rate is roughly proportional to $n_e/\sqrt{T_{gas}}$ (n_e being the electron density, and T_{gas}, the gas temperature; *e.g.* de Jong, 1977). The ratio of these two rates, often called the *photoionization parameter*, therefore quantifies this equilibrium (*e.g.* Chap. 5 of Tielens, 2005):

$$\gamma \equiv \frac{G_0}{n_e}\sqrt{T_{gas}}. \tag{III.44}$$

The electron density can be related to the total H density by considering that most electrons in the neutral gas come from the photoionization of C. We thus have $n_e \simeq (C/H)\,n_H \simeq 2\times10^{-4}\,n_H$ (*cf.* Sect. II.2.3.1). Galliano et al. (2008b) measured the I(6.2)/I(11.3) ratio in Galactic regions where G_0, n_H and T_{gas} had been reliably estimated (Fig. III.39.a). It allowed us to propose an empirical relation between γ and I(6.2)/I(11.3):

$$\frac{I(6.2)}{I(11.3)} \simeq \frac{G_0/(n_e/1\,\mathrm{cm^{-3}})\sqrt{T_{gas}/10^3\,\mathrm{K}}}{1990} + 0.26 \pm 0.16. \tag{III.45}$$

In other words, measuring I(6.2)/I(11.3) provides an estimate of γ. With such a relation, the diagrams of Fig. III.37 can now be turned into the diagnostics of Fig. III.40. This relation has, since then, been refined by several studies, especially Boersma et al. (2016). Although unique, the diagnostics of Eq. (III.45) has however the following limitations.

- The average value of a quantity such as γ is problematic to interpret. If the observation includes a mix of regions with different densities and ISRF intensities, the weight of these different regions in $\langle\gamma\rangle$ will be non-trivial.
- As we have seen in Sect. III.2.1.2, there are systematic discrepancies between different fitting methods. The calibration of Eq. (III.45) is therefore specific to the details of the fitting method used.

- The I(6.2)/I(11.3) has a relatively narrow dynamical range. It varies at most by one order of magnitude in our sample. The relation is unclear outside this range.

Finally, the calibration of Eq. (III.45) can also be estimated theoretically. Fig. III.39.b shows the theoretical I(6.2)/I(11.3) ratio as a function of G_0 and n_e (Galliano, 2009). It has been derived by computing the stochastic emission of PAHs within the PDR model of Kaufman et al. (2006). Such model indeed computes the charge balance of PAHs at each point within the cloud, where G_0 and n_e are known. One grid point value corresponds to a whole cloud.

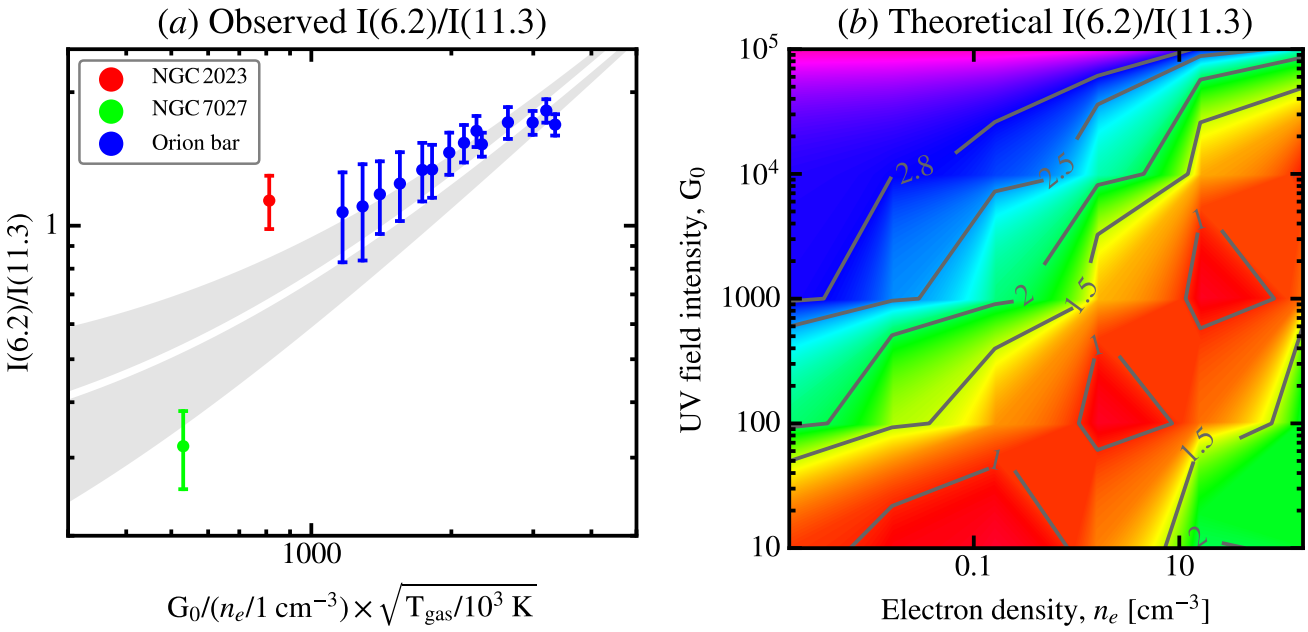

FIGURE III.39 – *Calibration of PAH ratio diagnostics.* Panel *(a)* shows the empirical correlation between the observed 6.2-to-11.3 µm ratio and the modeled parameter, γ (Eq. III.44), in three galactic PDRs (Galliano et al., 2008b). Panel *(b)* shows the theoretical variation of the band ratio as a function of G_0 and n_e (Galliano, 2009). This parameter grid was computed implementing stochastic heating in the PDR model of Kaufman et al. (2006), using a fixed PAH size distribution (the BARE-GR-S of Zubko et al., 2004). Licensed under CC BY-SA 4.0.

Other properties. We end this section by briefly reviewing other properties that can be studied with observations of UIBs.

PAH compactness can be probed by studying the relative variations of C–H OOP bending modes (*cf.* Fig. III.31.a). These bending modes depend on the number of H atoms per aromatic cycle (*cf.* Fig. III.31.b). We have seen in Sect. III.2.1.1 that, in particular, the solo-to-trio intensity ratio, $I_{11.3}/I_{12.7}$, is an indicator of PAH compactness. This ratio was scrutinized in Galactic regions (evolved stars, H II regions, reflection nebulae and YSOs) by Hony et al. (2001). Their results are consistent with the scenario where large ($\simeq 100-150$ C atoms), compact PAHs are formed in winds of evolved stars, and degraded into smaller, irregular molecules in the ISM.

Small a-C(:H) hydrogenation can be studied with the I(3.4)/I(3.3) ratio. There is a debate whether aromatic features are carried by PAHs or small a-C(:H). The 3.4 µm aliphatic feature however can not be carried by pure PAHs, it must come from either a-C(:H) grains (Jones et al., 2013) or *Hydrogenated PAHs* (HPAH) with one of several aliphatic groups (*e.g.* Fig. 1 of Marciniak et al., 2021). The I(3.4)/I(3.3) aliphatic-to-aromatic ratio shows regional variations in the ISM, as the result of structural changes in the hydrocarbons through UV processing (*e.g.* Jones et al., 2013). Mori et al. (2014) showed that the I(3.4)/I(3.3) decreases with the ionization of PAHs, in Galactic H II regions. Yamagishi et al. (2012) detected the 3.4 µm feature in the superwind of M 82.

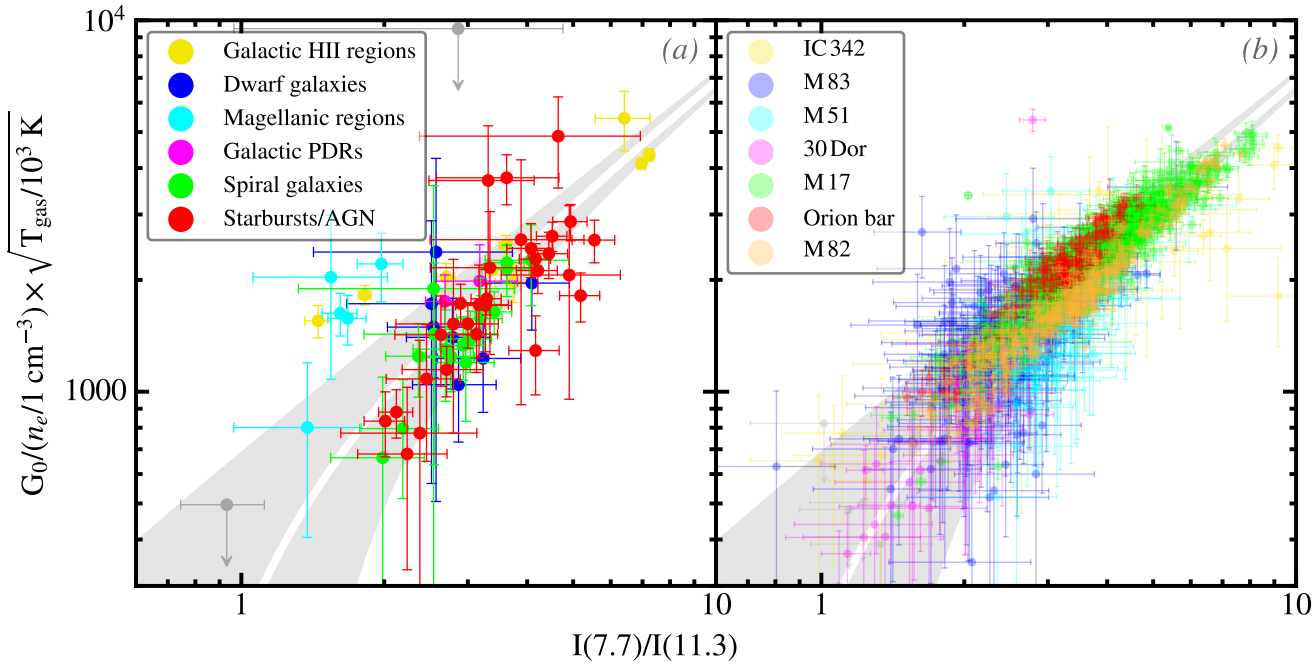

FIGURE III.40 – *PAH band ratio as diagnostics of the physical conditions.* These are the data shown in Fig. III.37 where the I(6.2)/I(11.3) ratio as been converted to $G_0/n_e \times \sqrt{T}$ using Eq. (III.45) (Eq. (5) of Galliano et al., 2008b). Licensed under CC BY-SA 4.0.

They found that the I(3.4)/I(3.3) ratio increases with distance from the center. They interpreted this trend as the production of small a-C(:H), by shattering of larger grains in this harsh halo. Similarly, Kondo et al. (2012) found a higher I(3.4)/I(3.3) ratio in the nuclear bar of NGC 1097, suggesting that the gas flow towards the center could lead to the formation of small a-C(:H) by shattering. We note that, alternatively, the I(3.4)/I(3.3) ratio can increase with the accretion of a-C(:H) mantles in denser regions (Jones et al., 2013). This feature can also be seen in extinction, in AGNs (*e.g.* Mason et al., 2007). Hu et al. (*in prep.*) modeled the spatially resolved AKARI and *Spitzer* spectra in M 82. In this study, we found a negative correlation between the I(3.4)/I(3.3) and $[\mathrm{S\,IV}]_{10.51\mu m}/[\mathrm{Ne\,II}]_{12.81\mu m}$ ratios. The latter is a ISRF hardness indicator. This result thus demonstrates the dehydrogenation of a-C(:H) grains by hard ISRFs.

SFR indicators are one of the most sought after astrophysical diagnostics. It happens that UIBs can be used to that purpose. Peeters et al. (2004) showed that the 6.2 µm feature intensity correlates well with SFR, making it a reliable estimator. Alternatively, Shipley et al. (2016) have calibrated a SFR estimator based on the integrated power of the 6.2, 7.7 and 11.3 µm features. The reason of this correlation is the same as for the TIR-SFR correlation (*e.g.* Kennicutt & Evans, 2012, for a review). At first order, the UIB strength is indeed correlated with TIR. Peeters et al. (2004) however note that UIBs are biased towards B stars. In addition, we note that such a tracer will be underestimating the SFR at low metallicity, because of the variation of the relative UIB strength, as we will see in Sect. III.2.1.4.

III.2.1.4 Variations of the Aromatic Feature Strength

The evolution of the shape of the UIB spectrum, probed by studying band ratio variations, is not the only diagnostics of the small carbon grain properties. The overall aromatic feature strength, relative to the continuum (*i.e.* to the emission of the rest of the dust populations) shows drastic variations across environments (*cf.* Fig. III.30). These variations trace the evolution of the mass fraction of their carriers – PAH or small a-C(:H).

Effect of ISRF hardness. PAH and small a-C(:H) are known to be sensitive to hard an intense radiation fields. They tend to evaporate near massive stars, and can be assumed to be fully depleted in H II regions (*e.g.* Cesarsky et al., 1996b; Galametz et al., 2013; Galliano et al., 2018). This effect can be quantified by studying the variation of the aromatic feature strength with a tracer of the ISRF hardness.

1. The aromatic feature strength can be traced with I(PAH)/I(cont), the PAH-to-MIR-continuum ratio, where I(PAH) is the sum of the intensities of every aromatic feature, and I(cont) is the integrated intensity of the continuum, over an arbitrary wavelength range (10-16 µm in the case of Madden et al., 2006).
2. The hardness of the ISRF can conveniently be traced by the $[\mathrm{Ne\,III}]_{15.56\mu m}/[\mathrm{Ne\,II}]_{12.81\mu m}$ ratio, as both of these MIR lines are usually bright. Madden et al. (2006) demonstrated, using a photoionization model, that $[\mathrm{Ne\,III}]_{15.56\mu m}/[\mathrm{Ne\,II}]_{12.81\mu m}$ is around unity when the ISM is heated by a young star cluster, and drops rapidly after a few million years, as massive stars die.

Such a trend is shown on Fig. III.41, with the Madden et al. (2006) results[8]. It clearly indicates that PAHs are less abundant in regions permeated with a hard ISRF, at all spatial scales down to ≃ 0.1 pc. Note however that both tracers do not come from the same physical region: *(i)* PAH being destroyed in H II regions are tracing the neutral gas; *(ii)* $[\mathrm{Ne\,III}]_{15.56\mu m}$ and $[\mathrm{Ne\,II}]_{12.81\mu m}$ obviously come from the ionized gas. The correlation therefore reflects the mixing of phases within the beam.

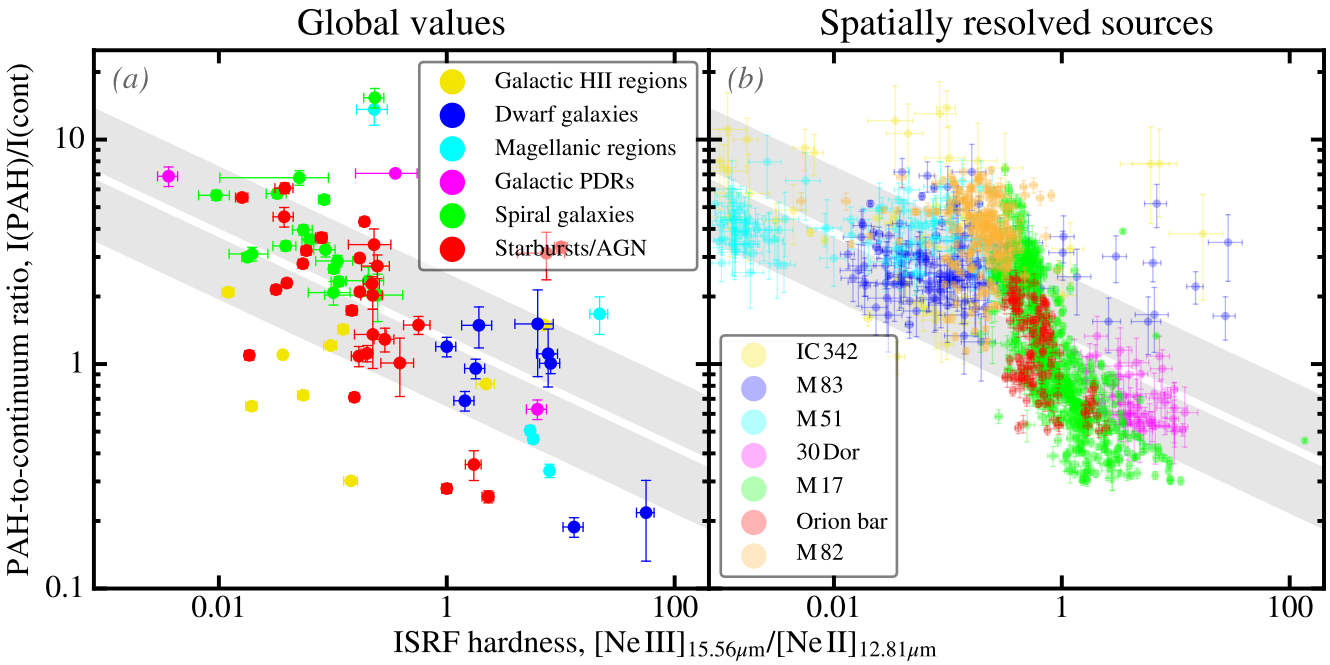

FIGURE III.41 – *Effect of ISRF hardness on PAH strength.* These results are from the spectral decomposition of Madden et al. (2006) and Galliano et al. (2008b). Panel *(a)* shows integrated sources, whereas panel *(b)* shows pixel-by-pixel distributions. The white line with the grey band shows the affine fit to the global values, ±1σ, in log-log space. It is the same in both panels. Licensed under CC BY-SA 4.0.

Effect of metallicity. The effects of ISRF and metallicity are often degenerate, as at low metallicity: *(i)* stars of a given mass have a systematically higher effective temperature, because of line blanketing effects; *(ii)* the ISM is less opaque, because of the lower dustiness, and thus more permeated by UV radiation. The highest $[\mathrm{Ne\,III}]_{15.56\mu m}/[\mathrm{Ne\,II}]_{12.81\mu m}$ ratios are found in BCDs, as well as the lowest

8. The results of Madden et al. (2006) consisted in a first spectral decomposition of ISO/CAM spectra, that we have refined in Galliano et al. (2008b), and added *Spitzer*/IRS spectra to the sample.

I(PAH)/I(cont). Fig. III.42.a shows the evolution of I(PAH)/I(cont) as a function of metallicity (Madden et al., 2006). There is a paucity of PAHs in low-metallicity environments. The questions is whether this is the result of their increased destruction, or if they have not been produced. We will come back to this question, when discussing dust evolution in Sect. IV.2.2.1.

☞ PAHs are under-abundant in low-metallicity environments.

The absence of metallicity threshold. The relation of Madden et al. (2006) was the first spectroscopy-based demonstration of the effect. Shortly before, Engelbracht et al. (2005) showed the broadband correlation of $F_\nu(8\,\mu m)/F_\nu(24\,\mu m)$ as a function of metallicity. They showed both quantities were clearly correlated. They however argued there were essentially two populations, below and above $12+\log(O/H)\simeq 8$. Galliano et al. (2008a) showed that this was a bias due to the saturation of $IRAC_{8\mu m}$ as a PAH tracer at low metallicity. When the aromatic feature strength becomes indeed low, $F_\nu(8\,\mu m)/F_\nu(24\,\mu m)$ is not anymore a measure of I(PAH)/I(cont), but is a measure of the temperature of the continuum. This is illustrated on Fig. III.42.b. We show that when the actual mass fraction of small a-C(:H) drops below $\simeq 10\,\%$, $F_\nu(8\,\mu m)/F_\nu(24\,\mu m)$ becomes insensitive to its value.

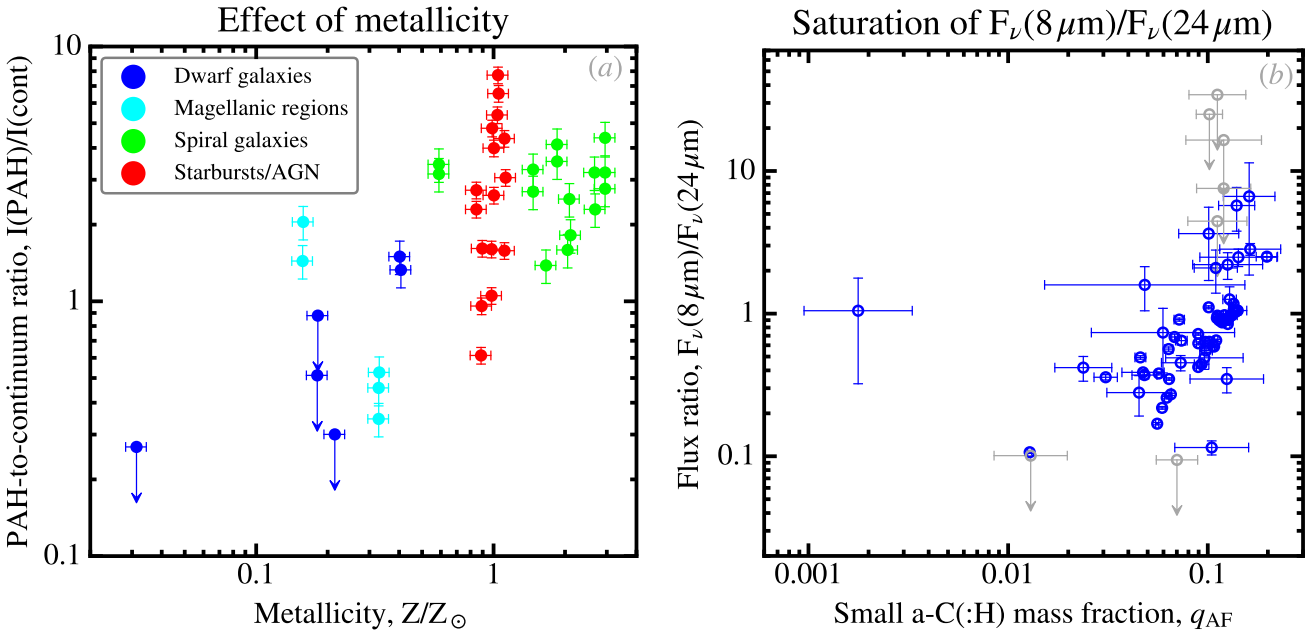

FIGURE III.42 – *Effect of metallicity on the PAH strength.* Panel *(a)* shows the trend of PAH relative strength with metallicity, by Madden et al. (2006). This was the first spectroscopy-based demonstration of this relation. Panel *(b)* illustrates the bias of the $F_\nu(8\,\mu m)/F_\nu(24\,\mu m)$ ratio as a tracer of PAH strength. It shows the flux ratio as a function of the modeled fraction of small a-C(:H) (the grains carrying the aromatic features), q_{AF}, in the DustPedia sample (G21). Only galaxies with both $IRAC_{8\mu m}$ and $MIPS_{24\mu m}$ fluxes are displayed. Licensed under CC BY-SA 4.0.

III.2.2 Long-Wavelength Properties

At long wavelengths, in the submm-to-cm range, dust emission does not always behave as the extrapolation from the Rayleigh-Jeans law ($F_\nu \propto \nu^{2+\beta}$). Two peculiar phenomena have been widely discussed in the literature: *(i)* the *submillimeter excess*; and *(ii)* the *Anomalous Microwave Emission* (AME).

III.2.2.1 The Elusive Submillimeter Excess

An excess emission above the modeled dust continuum is often observed, longward $\lambda \simeq 500$ µm. The most significant reports of this *submm excess* can not be accounted for by: *(i)* thermal dust emission; *(ii)* free-free and synchrotron continua; and *(iii)* molecular line emission (*cf.* Fig. III.43; Galliano et al., 2003).

1. The first occurrence of such an excess was unveiled by Reach et al. (1995), studying the COBE observations of the Milky Way. Their IR–submm SED could be fitted with a MBB ($\beta = 2$; *cf.* Sect. III.1.2.1), and an additional 4 – 7 K component.
2. A few years later, Lisenfeld et al. (2002) and Galliano et al. (2003) found a statistically significant excess in the dwarf galaxy NGC 1569, at 850 µm and 1.3 mm. It is shown in Fig. II.10.
3. Several subsequent studies confirmed the presence of an excess in other late-type galaxies (*e.g.* Dumke et al., 2004; Bendo et al., 2006; Zhu et al., 2009; Galametz et al., 2009, 2011), including the global SEDs of the Magellanic clouds (Israel et al., 2010; Bot et al., 2010).
4. *Herschel* and *Planck* opened the way to more detailed characterizations.

Studying this excess is important, as: *(i)* it could bias dust mass estimates; *(ii)* it potentially contains untapped physical information about the ISM.

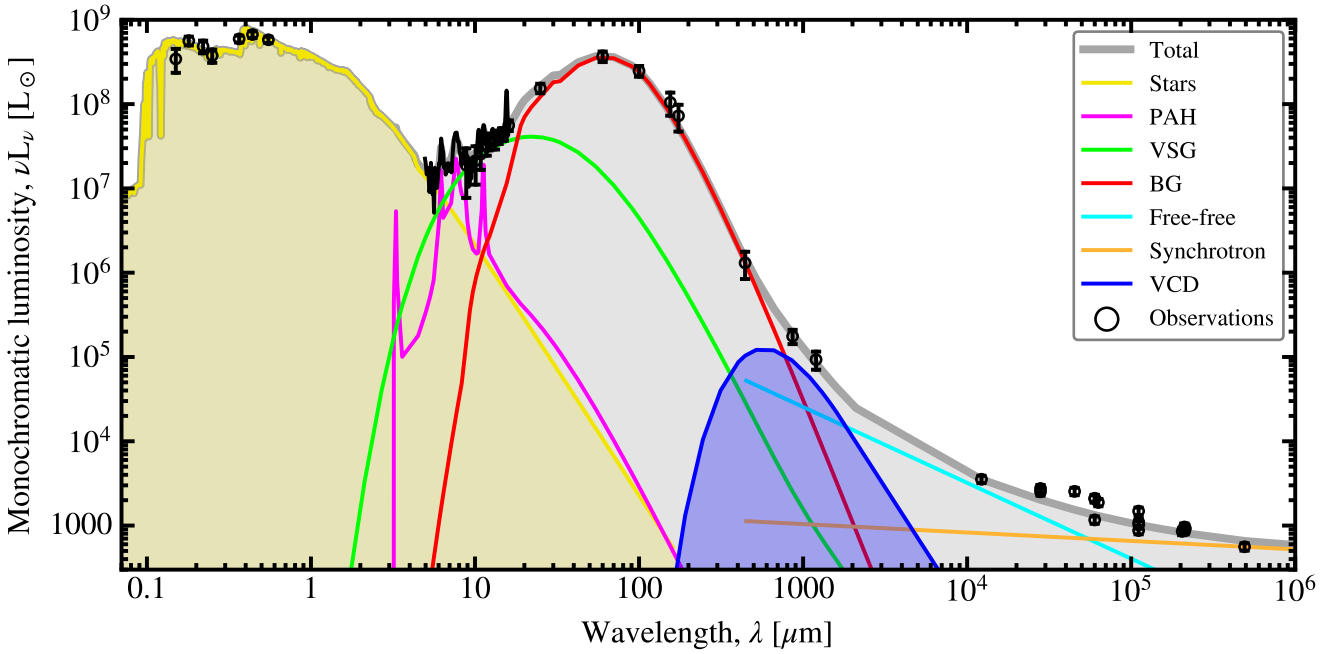

FIGURE III.43 – *Submillimeter excess in NGC 1569.* This is the best fit model of Galliano et al. (2003), discussed in Sect. III.1.3.4. We focus here on the blue component, which is a T = 5 K, $\beta = 1$ MBB accounting for ≃ 80 % of the dust mass of the galaxy. This component has been fitted to account for the submm excess. Licensed under CC BY-SA 4.0.

Possible explanations. The origin of the submm excess is currently debated. The following explanations have been proposed. These different scenarios are not exclusive.

Very cold dust (VCD), that is equilibrium grains colder than T ≃ 10 K, can be used to fit the excess. The emission of such a grain population indeed peaks in the submm range. Cold dust being weakly emissive, this scenario however leads to massive amounts of grains (40 – 80 % of the total dust mass; *e.g.* Galliano et al., 2003, 2005). Galliano et al. (2003) showed that VCD would be realistic only if this component was distributed in a few number of dense, parsec-size clumps. The existence of such cold dust indeed requires it to be shielded from all UV-visible light. Using the spatially resolved observations of the 500 µm excess in the LMC, Galliano et al. (2011)

concluded that this explanation is unrealistic, as it would require at least one clump in each of the ≃ 90 000 pixels of this study.

Temperature-dependent emissivity. Laboratory measures on cosmic grain analogs exhibit an increase of the FIR-submm opacity as a function of temperature (*e.g.* Mennella et al., 1998; Demyk et al., 2017a,b). Meny et al. (2007) designed the so-called *Disordered Charge Distribution/Two-Level System* (DCD/TLS) model, predicting an increase of $\kappa(\lambda_0)$ and a decrease of β with the temperature of amorphous grains. It reproduces the submm excess observed in the Galaxy by Paradis et al. (2012) and in the LMC by Bot et al. (2010, coupled with spinning grains; *cf.* Sect. III.2.2.2). However, this model can not account for the submm excess in the SMC (Bot et al., 2010).

Magnetic grains. Draine & Hensley (2012) showed that the submm excess of the SMC could be attributed to magnetic nanoparticles (Fe, Fe_3O_4, γ-Fe_2O_3 [9]). Thermal fluctuations in the magnetization of these grains can produce strong magnetic dipole emission, since ferromagnetic materials are known to have large opacities at microwave frequencies. This hypothesis seems to be consistent with the observed elemental abundances of the SMC and could also be responsible for the excess detected in other environments. These magnetic nanoparticles could be free-flying or inclusions in larger grains.

Empirical properties of the excess. Since the origin of the submm excess is still unknown, most studies focus on characterizing its observed properties.

Low-metallicity systems are the environments where the excess appears the be the most prominent. This is the reason why it has been detected in most nearby BCDs (*e.g.* Galliano et al., 2003; Dumke et al., 2004; Galliano et al., 2005; Galametz et al., 2009; Bot et al., 2010; Galametz et al., 2011). Galliano et al. (2011) have shown, using spatially-resolved observations of the LMC, that the $\mathrm{SPIRE}_{500\mu m}$ excess, r_{500}, varies up to ≃ 40 % in certain regions. It is correlated with the mean starlight intensity, $\langle U \rangle$, and anticorrelated with the dust surface density, as shown in Fig. III.44. The correlation with $\langle U \rangle$ could be a confirmation of the DCD/TLS effect, as $\langle U \rangle$ directly controls the temperature of the grains. The correlation with surface density is however significantly better than with ISRF, a trend that the DCD/TLS model alone fails to explain.

In the Milky Way, Paradis et al. (2012) showed that the $\mathrm{SPIRE}_{500\mu m}$ excess becomes significant in the peripheral regions (> 35°), as well as towards some H II regions. This is qualitatively consistent with the trend we found in the LMC, as these peripheral regions are also the most diffuse ones. The relative amplitude of the excess can rise up to ≃ 20 %.

In other galaxies, the excess is more difficult to detect (*e.g.* Rémy-Ruyer et al., 2015; Dale et al., 2017). When resolved in non-barred spirals, the submm excess is primarily detected in the disk outskirts, thus at low-surface density (*e.g.* Hunt et al., 2015).

☞ The submm excess is more prominent in low-metallicity environments, and in diffuse regions.

Reality of the phenomenon. The reality of the submm excess has been questioned for the two following reasons. We try to address these criticisms in order to support its likeliness.

The excess is model-dependent. Different dust opacities lead to different amplitudes of the excess. Some over-parametrized models have found excesses virtually everywhere. For instance, the *Broken-Emissivity Modified Black Body* (BEMBB) is a MBB with two free-varying emissivity indices, β_1 and β_2, below and above $\lambda = \lambda_b$ (Gordon et al., 2014). With such a model, any excess

9. γ-Fe_2O_3 is the notation to design ferromagnetic Fe_2O_3, called *maghemite*. It must be distinguished from its non-magnetic form, noted α-Fe_2O_3, called *hematite*. Both have distinct crystalline structures: cubic lattice for maghemite; trigonal crystals for hematite (*e.g.* Łęcznar, 1977).

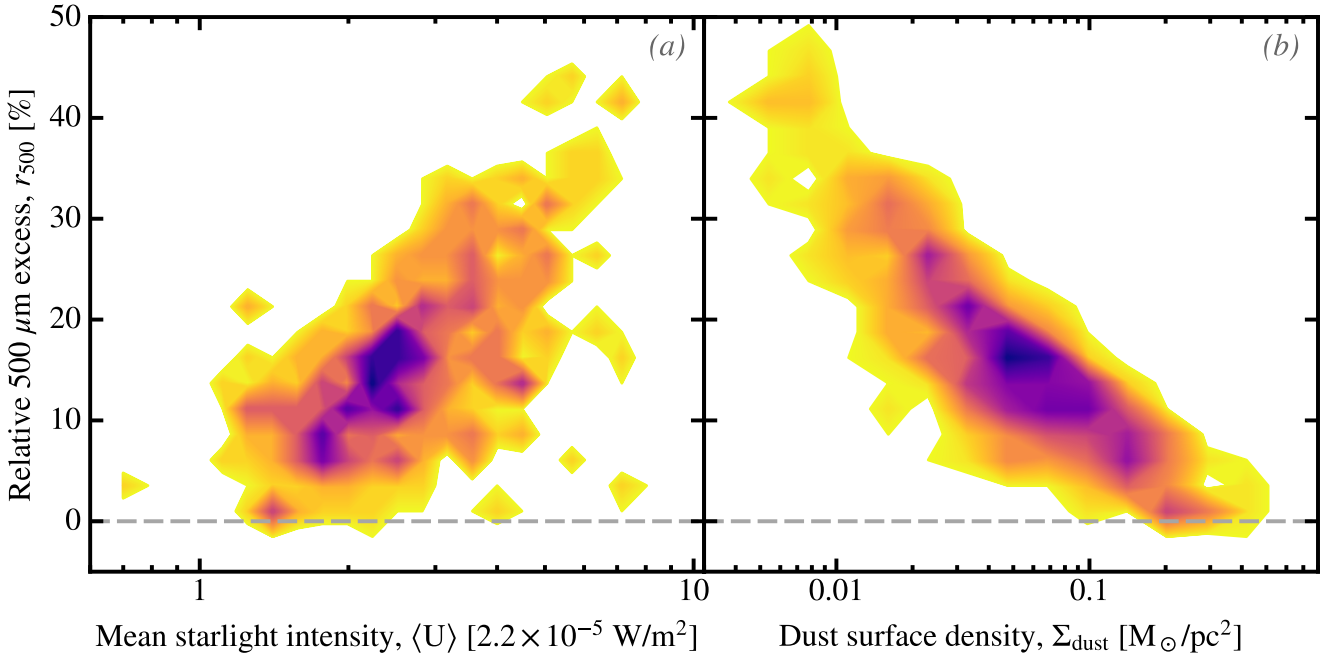

FIGURE III.44 – *Spatially-resolved submm excess in the LMC.* In both panels, the color density represents the number of pixels per bin of parameters in the star-forming region N 44 of the LMC (Galliano et al., 2011). The SPIRE$_{500\mu m}$ excess is shown as a function of: *(a)* mean starlight intensity (Eq. III.38); and *(b)* dust mass surface density. Licensed under CC BY-SA 4.0.

can be fitted, but the derived β_1, β_2 and λ_b do not necessarily correspond to existing solids. This model is also extremely degenerate, as shown by Galliano (2018). A BEMBB fit of the diffuse Galactic ISM SED (*cf.* Fig. II.25.d) by Gordon et al. (2014) gives a $r_{500} \simeq 48 \pm 11$ % excess starting at $\lambda_b \simeq 300 \pm 30$ µm. Yet, this is the SED that everyone uses to calibrate dust models. It does not exhibit an actual excess. It illustrates that probing the submm excess with models which are not based on realistic optical properties is a non-sense. It must be studied with a model as physical as possible.

The technically-challenging nature of submm-mm observations is also questioning the reality of the excess: *(i)* observations in this regime are difficult from the ground (*cf.* Sect. II.1.1.1); *(ii)* the calibration of these observations is often uncertain; *(iii)* data reduction methods have problems dealing with the diffuse emission, which is where the excess appears to be the most prominent. In particular, *Planck* data have lead to revise the calibration of the COBE/FIRAS FIR-submm spectrum of the diffuse Galactic ISM (Planck Collaboration et al., 2014c). With this new calibration, the excess of Reach et al. (1995), discussed earlier, is not significant anymore. There are however several sound indications that these concerns are not enough to doubt the reality of the phenomenon.

- The SED shape of low-metallicity systems is well characterized in this regime. It has been observed at different wavelengths, with different instruments. It is still present with the latest *Herschel* calibration (Dale et al., 2017).
- Reports of a deficit are very rare.
- In the Magellanic clouds, Planck Collaboration et al. (2011a) showed that, while the submm excess in the integrated SED of the LMC was consistent with CMB fluctuations, the SMC excess was significantly above this level.

III.2.2.2 The Anomalous Microwave Emission

As we have seen in Sect. II.2.2.3, the AME is a centimeter continuum excess that can not be accounted for by: *(i)* the extrapolation of dust thermal emission; *(ii)* molecular line emission; and *(iii)* free-free

and synchrotron continua (Fig. II.10). Its SED looks like a bump peaking around $\lambda = 1$ cm (*cf.* Fig. II.10). It is commonly attributed to the dipole emission of fastly rotating, small dust grains. The faster grains rotate, the shorter the frequency of the emission peak is.

The AME in extragalactic environments. In nearby galaxies, the first unambiguous detection of an AME has been obtained in an outer region of NGC 6946 (Murphy et al., 2010; Scaife et al., 2010). Follow up observations showed evidence for AME in eight regions of this galaxy (Hensley et al., 2015). This study showed that the spectral shape of this AME is consistent with spinning dust, but with a stronger AME-to-PAH-surface-density ratio, hinting that other grains could be the carriers. Overall, the AME fraction is highly variable, in nearby galaxies. Peel et al. (2011) put upper limits on the AME in M 82, NGC 253 and NGC 4945. These upper limits suggest that AME/100 µm is lower than in the Milky Way, in these objects. In M 31, Planck Collaboration et al. (2015a) report a 2.3σ *measurement* of the AME, consistent with the Galactic properties. Finally, Bot et al. (2010), fitting the NIR-to-radio SED of the LMC and SMC, tentatively explained the submm/mm excess with the help of spinning dust, in combination with a modified submm dust emissivity (*cf.* Sect. III.2.2.1). They concluded that, if spinning grains are responsible for this excess, their emission must peak at 139 GHz (LMC) and 160 GHz (SMC), implying large ISRF intensities and densities. Draine & Hensley (2012) argued that such fastly rotating grains would need a PDR phase with a total luminosity more than two orders of magnitude brighter than the SMC.

Controversy about the carriers of the AME. Although PAHs have been considered the most likely carriers of the AME, Hensley & Draine (2017) argued that nanosilicates could be a viable alternative. They showed that nanosilicates can indeed account for the AME, without violating the other observational constraints (depletions, emission, extinction; *cf.* Sect. II.2). This claim relies on the earlier findings of Hensley et al. (2016), showing that AME correlates better with dust radiance, $\mathscr{R}$ [10], in the MW. Hensley et al. (2016) also found some fluctuations in the PAH emission relative to the AME intensity, traced by $\mathrm{WISE}_{12\mu m}$. The fact is that there is no observational evidence of nanosilicates in the ISM. In particular, these grains would emit the 9.8 and 18 µm features, as they would be stochastically heated. These bands would eventually remain diluted in the aromatic feature emission, provided the abundance of nanosilicates is low enough. We can however note that in HII regions, where PAHs are destroyed, we can see the underlying continuum, and silicate features in emission are rarely present (*e.g.* Peeters et al., 2002b). They can be seen only in the most compact HII regions, and their 9.8-to-18 µm ratio indicates that they originate in large equilibrium grains. A weak correlation does not always indicate an absence of causality. This issue might reside in the fact that Hensley et al. (2016) used the $\mathrm{WISE}_{12\mu m}$ band as a tracer of PAH intensity, whereas this broad photometric band also encompasses a significant fraction of the underlying continuum, and is biased towards neutral PAHs. We have tried to address this controversy by refining the constraints on the PAH emission.

Correlation with charged PAHs. Bell et al. (2019) focussed on the 10°-wide Galactic molecular ring surrounding the O-type star, λ-Orionis (*cf.* Fig. III.45). We chose this region, because the *Planck* data indicate there is a large gradient of AME intensity. We fitted the spatially-resolved SED, at 0.25° angular sampling, using the AKARI 9 µm and IRAS 12 µm bands to constrain the PAH abundance, and longer wavelength bands for the rest of the emission. We used the dust SED code `HerBIE` (*HiERarchical Bayesian Inference for dust Emission;* Galliano, 2018, *cf.* Sect. V.3.3). We were able to address the controversy, thanks to the combination of: *(i)* rigorous SED fitting, allowing us to account for all the available information, not only a few broadbands; *(ii)* better observational constraint on the PAH emission (9 and 12 µm); and *(iii)* focussing on a clean region rather than the whole sky. Our results are shown in Fig. III.46. We have found very good pixel-to-pixel correlations between the AME intensity, derived by Planck Collaboration et al. (2016a), and the dust and PAHs surface densities from

10. The radiance is the spectral integral of the specific intensity: $\mathscr{R} \equiv \int I_\nu \, d\nu$.

SED fitting (*e.g. cf.* Fig. III.46.a). Our analysis however show that, if the dust mass per pixel is very well correlated with the intensity of AME per U, I_{AME}/U ($\rho \simeq 0.88$), the correlation is better with the mass of PAHs, and even better with the mass of ionized PAHs ($\rho \simeq 0.92$; *cf.* Fig. III.46.b). Our Bayesian results also show that there is a 0 probability that the total dust could correlate better with AME than with PAHs. Our impression is that the study of Hensley et al. (2016) may have too quickly interpreted a poor correlation as an absence of causality. The scatter in $WISE_{12\mu m}$ was likely not the result of an intrinsic scatter of the PAH/AME correlation, but rather a combination of observational artefacts: *(i)* noise; *(ii)* contribution of the continuum and ionic lines. Our SED model and our better MIR coverage allowed us to more accurately recover the true PAH column density.

☞ AME correlates better with charged PAHs.

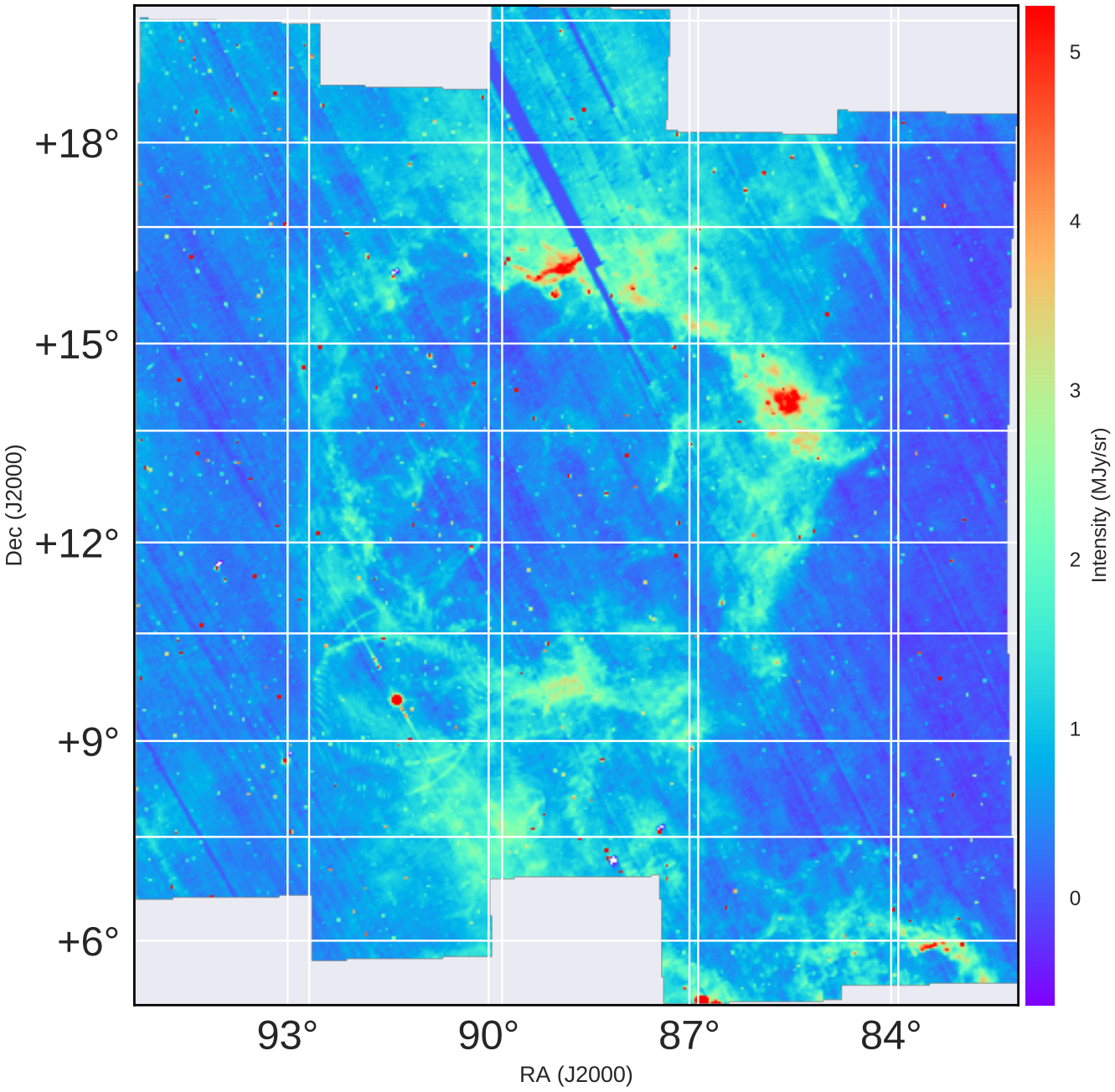

FIGURE III.45 – *AKARI 9* µm *map of* λ*-Orionis.* This is a mosaic of broadband photometric images of PAHs within this Galactic molecular ring. Credit: Bell et al. (2019).

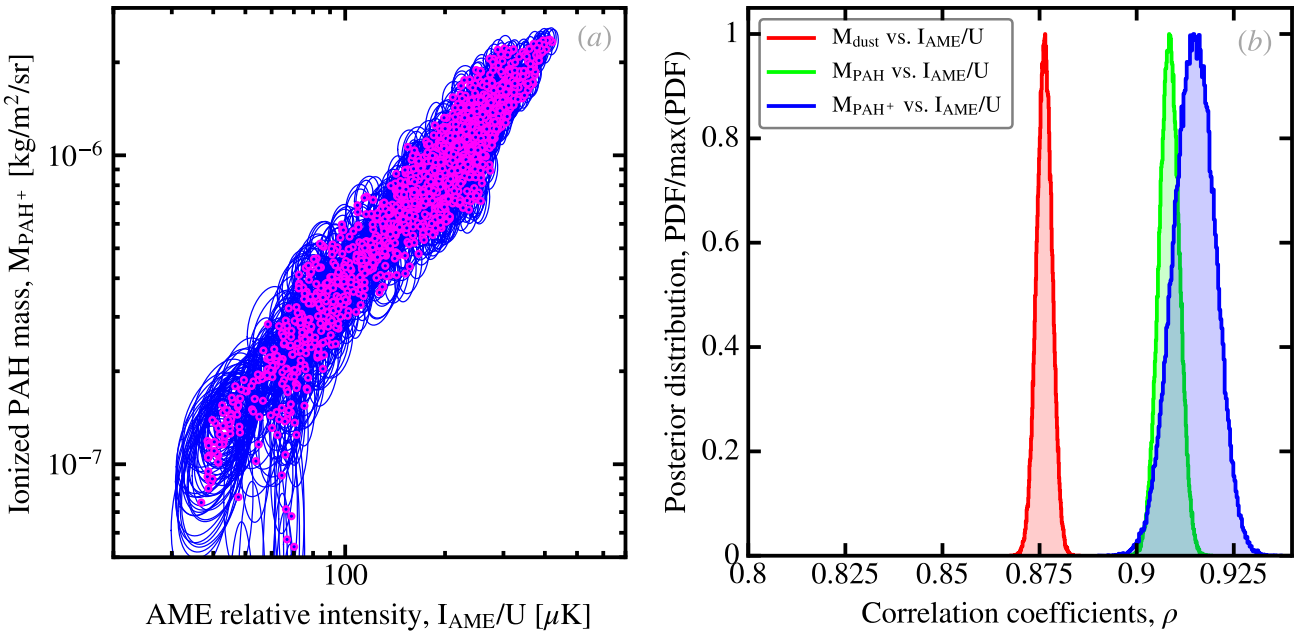

FIGURE III.46 – *AME correlation with ionized PAHs in λ-Orionis.* Panel *(a)* shows the pixel correlation between I_{AME}/U and M_{PAH+}, derived from the SED modeling of (Bell et al., 2019). Each point and its uncertainty ellipse represent the posterior PDF of a pixel. Panel *(b)* shows the posterior PDFs of the correlation coefficients between two sets of parameters (such as panel *a*). The correlation between I_{AME}/U and M_{PAH+} is the best of our study, and it is significantly better than with M_{dust}. Licensed under CC BY-SA 4.0.

III.3 Dust in Relation with the Gaseous and Stellar Contents

We end this chapter with a short introduction to *ISMology*, since the knowledge of the ISM as a whole is crucial to understanding ISD. We discuss a few of our results in this domain and illustrate the way dust can be used to better understand the gas. The video lectures and accompanying slides of the 2021 "*ISM of galaxies*" summer school (35 hours of lecture in total), that we have organized, can provide a good introduction to this subject. Otherwise, the books of Spitzer (1978), Tielens (2005) and Draine (2011) are references.

III.3.1 The Phases of the ISM

The ISM is intrinsically a *multi-phase* medium, with large contrast densities and differences in temperatures. The order of magnitude of its average density is $n_{gas} \simeq 1$ cm^{-3}. We list the physical characteristics of the main phases in Table III.6. We will discuss each phase individually in the rest of this section.

The cooling function. The way the gas cools across phases has a decisive impact on the multiphase structure of the ISM. It is possible to estimate its cooling rate as a function of temperature, or, in other words, how the thermal energy of the gas is converted into radiation. This quantity is called the *cooling function*. It is represented on Fig. III.47. We have highlighted the dominant processes in the different temperature regimes.

- At low-temperatures, in neutral atomic regions, $[CII]_{158\mu m}$ is the main coolant.
- Around $T_{gas} \simeq 10^4$ K, there is drastic increase of cooling efficiency, thanks to the $Ly\alpha_{121.6nm}$ line of H.
- Above $T_{gas} \gtrsim 10^4$ K, the gas becomes rapidly ionized. The cooling is then channelled through various ions.

	Density	Temperature	Volume filling factor
HIM	$\simeq 3 \times 10^{-3}$ cm^{-3}	$\simeq 10^6$ K	$\simeq 50\,\%$
H II regions	$\simeq 1 - 10^5$ cm^{-3}	$\simeq 10^4$ K	$\lesssim 1\,\%$
WIM	$\simeq 0.1$ cm^{-3}	$\simeq 10^4$ K	$\simeq 25\,\%$
WNM	$\simeq 0.3$ cm^{-3}	$\simeq 10^4$ K	$\simeq 30\,\%$
CNM	$\simeq 30$ cm^{-3}	$\simeq 100$ K	$\simeq 1\,\%$
Diffuse H_2	$\simeq 100$ cm^{-3}	$\simeq 50$ K	$\simeq 0.1\,\%$
Dense H_2	$\simeq 10^3 - 10^6$ cm^{-3}	$\simeq 10$ K	$\simeq 0.01\,\%$

TABLE III.6 – *Phases of the ISM.* Adapted from Tielens (2005) and Draine (2011). The sum of the filling factors is slightly larger than 100 %, because these estimates are rough.

- At $T_{gas} \gtrsim 10^7$ K, in coronal phases, the gas cools mainly *via* free-free emission.

The exact shape of this cooling function can vary sensibly. It depends on: *(i)* metallicity, as this parameter impacts the relative abundances of the different species; and *(ii)* the radiation field, which impacts the ionization state of the gas.

III.3.1.1 The Neutral Atomic Gas

The neutral atomic gas is the most abundant phase in the MW: it accounts for $\simeq 60\,\%$ of the total ISM mass, and $\simeq 8\,\%$ of the total baryonic mass (stars and ISM). It fills up about $\simeq 30\,\%$ of the MW volume. The neutral gas is far from thermal equilibrium, but it is roughly in pressure equilibrium, with:

$$\frac{P_{gas}}{k} = n_{gas} \times T_{gas} \simeq 3000\,\mathrm{K/cm^3}. \tag{III.46}$$

The photoelectric heating. In neutral regions, the direct heating of the gas by absorption of stellar UV photons is not efficient, because only a small fraction of these photons can be absorbed through the different available atomic lines. In these regions, the heating of the gas is indirect. Dust grains absorb much more efficiently UV photons, with their spectrally continuous cross-section. The absorption of an energetic photon (of a few eV) can lead to the ejection of an electron, *via* the photoelectric effect. This electron will then collide with the gas and heat it. This is the *photoelectric heating* of the gas (de Jong, 1977; Draine, 1978; Bakes & Tielens, 1994; Weingartner & Draine, 2001b; Kimura, 2016). We have schematically represented this process in Fig. III.48. The overall efficiency of this process is related to the integrated surface of dust grains. According to Table II.3, this surface is dominated by small grains. The smallest grains, especially PAHs, are therefore responsible for most of this heating. Wolfire et al. (1995) give an expression for the photoelectric heating rate:

$$n_{gas}\Gamma \simeq \epsilon_{PE}(\gamma, T_{gas}) \times G_0 \times \frac{n_{gas}}{1\,\mathrm{cm^{-3}}} \times 10^{-25}\,\mathrm{W/m^{-3}}, \tag{III.47}$$

where ϵ_{PE} is the efficiency of conversion of FUV energy into gas heating (it is a few percents), and G_0 and γ have been defined in Eqs. (III.43) – (III.44).

The two stable neutral atomic phases. For simplicity, let's assume the heating of the neutral ISM is assured only by photoelectric heating. Let's also use Eq. (III.47) with a fixed value of the photoelectric heating efficiency, $\epsilon_{PE} = 4.9\,\%$, and $G_0 = 1.7$. The equilibrium is obtained when cooling and heating are balanced:

$$n_{gas}\Gamma = n_{gas}^2 \Lambda(T), \tag{III.48}$$

which becomes, using Eq. (III.46):

$$P_{gas}/k = \frac{\Gamma \times T}{\Lambda(T)}. \tag{III.49}$$

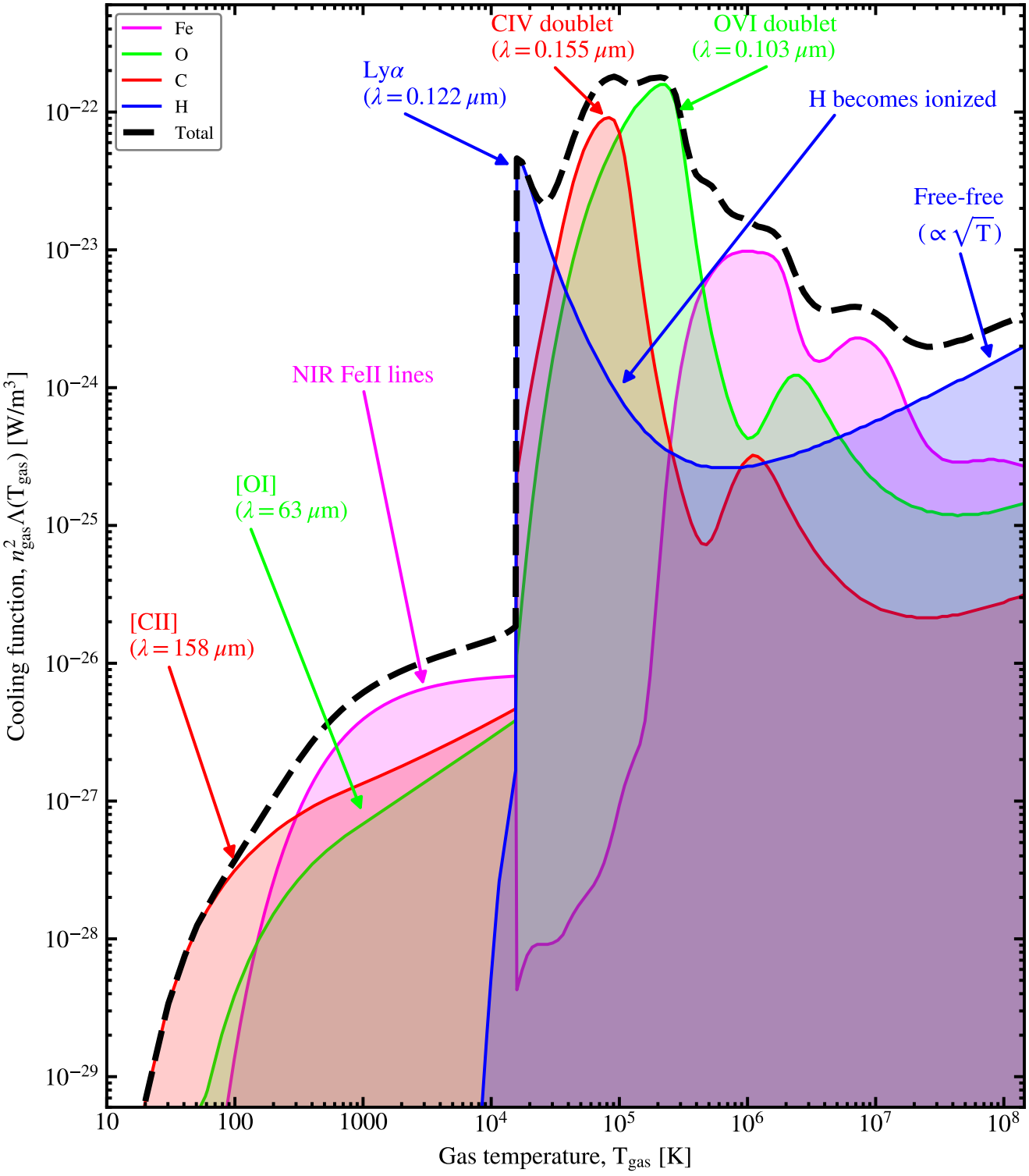

FIGURE III.47 – *Cooling function of the ISM at Solar metallicity.* The data below $T_{gas} = 10^4$ K is from Dalgarno & McCray (1972), and above, from Schure et al. (2009). We have highlighted the main cooling elements. In the neutral regime, we have assumed an electron fraction of $x \equiv n_e/n_H = 10^{-4}$.

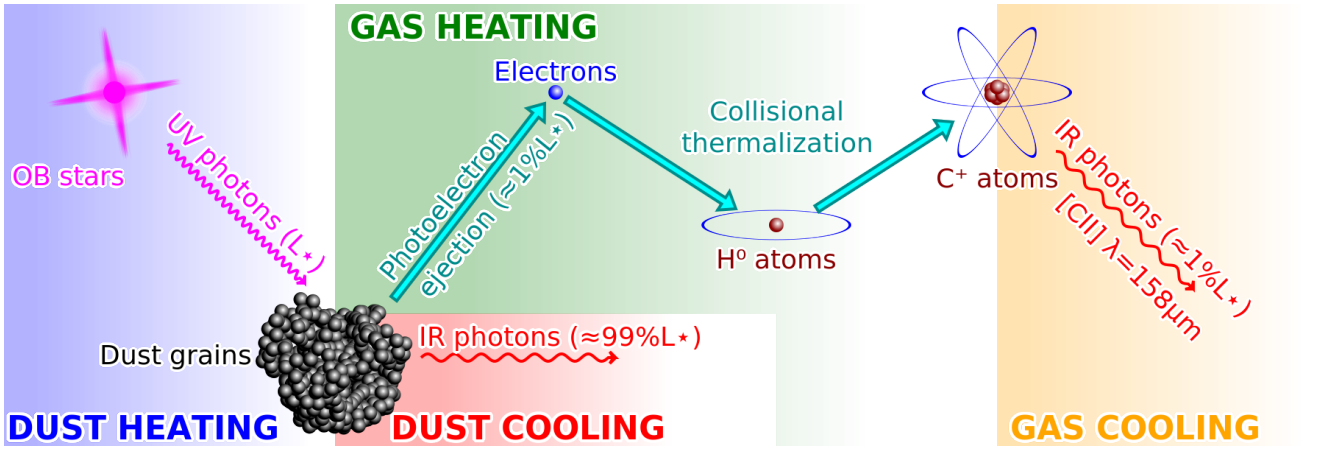

FIGURE III.48 – *Photoelectric heating in PDRs.* We have implicitly assumed that the stellar power, $L_\star$, is also the total power absorbed by dust, as PDRs are mostly optically thick at UV wavelengths. Licensed under CC BY-SA 4.0.

This is the black line we have represented in Fig. III.49. There are three pressure equilibrium positions (the three dots), at the value of Eq. (III.46). We have hatched in grey the regime corresponding to unstable solutions. In this regime, the pressure indeed decreases with density. Thus, a small pressure increase, above the green dot, will decrease the density. It will thus make the gas expand and its temperature increase, moving further away from the green dot. On the opposite, a small decrease of the pressure, below the green dot, will increase the gas density, and make its temperature decrease, at the same time. The gas will thus collapse and move further away from the green dot. The two only stable solutions correspond to the two main neutral atomic phases of the ISM.

The Warm Neutral Medium (WNM) is a diffuse phase with density of the order of $n_{\rm gas} \simeq 0.3$ cm^{-3} and temperature $T_{\rm gas} \simeq 10^4$ K. It is heated essentially by the photoelectric effect, and also by cosmic rays. It cools via UV-optical emission lines, essentially Ly$\alpha_{121.6\rm nm}$.

The Cold Neutral Medium (CNM) is a denser phase with density of the order of $n_{\rm gas} \simeq 30$ cm^{-3} and temperature $T_{\rm gas} \simeq 100$ K. It is heated essentially by the photoelectric effect, and also by cosmic rays. It cools essentially *via* fine-structure lines, [C II]$_{158\mu\rm m}$ and also [O I]$_{63\mu\rm m}$.

Both of these phases are observed with [H I]$_{21\,\rm cm}$, and UV-optical absorption lines.

☞ There are two distinct neutral atomic phases in pressure equilibrium: the WNM and the CNM.

III.3.1.2 The Ionized Gas

The ionized gas accounts for a moderate mass fraction of the ISM in the MW, but fills up a large volume. It is ≃ 23 % of the ISM mass and ≃ 3 % of the total baryonic mass (stars and ISM).

The Hot Ionized Medium (HIM). The HIM is a coronal gas ($n_{\rm gas} \simeq 3 \times 10^{-3}$ cm^{-3}, $T_{\rm gas} \simeq 10^6$ K; Table III.6) filling up ≃ 50 % of the MW volume. It is at pressure equilibrium with the WNM and CNM. McKee & Ostriker (1977) showed that this phase was heated by SN shockwaves. It is composed of overlapping SN bubbles, and is sometimes referred to as the *intercloud medium*. This gas, which pervades everywhere, can be found significantly above the Galactic disk, contrary to the other phase, which are contained to the disk. It is observed through FUV absorption lines of ions, and diffuse soft X-ray and synchrotron emissions.

H II regions. H II regions are short-lived dense ionized regions around OB star associations. The gas is ionized by photons from the massive stars. These regions are not in equilibrium, they are

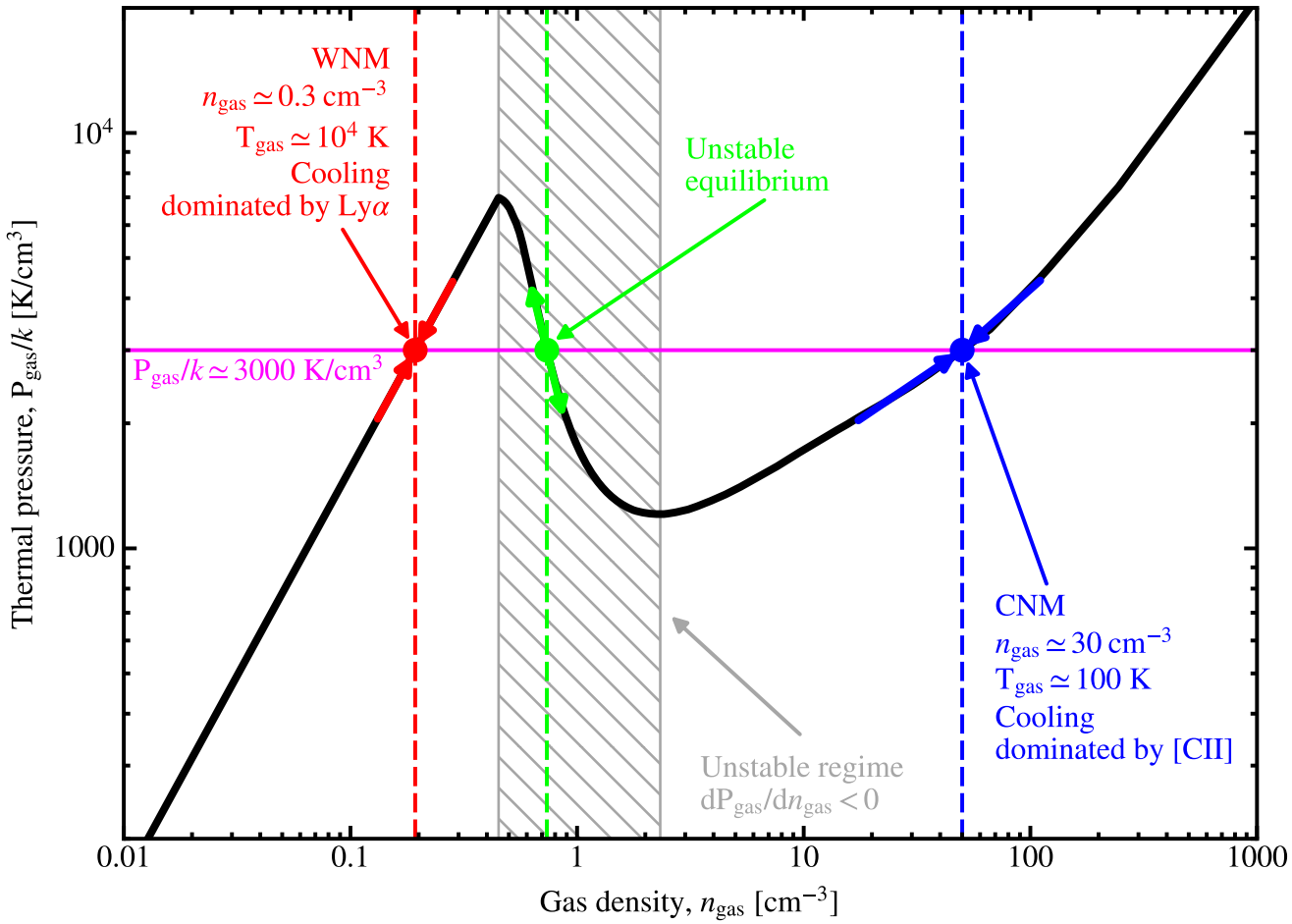

FIGURE III.49 – *Neutral ISM phase diagram.* The black line is Eq. (III.49), with the cooling function of Fig. III.47. The horizontal magenta line is the typical pressure of the ISM (Eq. III.46). There are three pressure equilibrium solutions (the three dots), but one (the green dot) lies in the unstable regime (grey hatched). The arrows along each curve, near the dots, show the direction the gas would move if there was a perturbation around the equilibrium. Licensed under CC BY-SA 4.0.

expanding. Strömgren (1939) has estimated the radius of an homogeneous sphere of ionized gas, around a star of H-ionizing photon rate, Q_0. Such a sphere is called a *Strömgren sphere*. Its radius, R_s, can be estimated by balancing photoionization and recombination:

$$\underbrace{Q_0}_{\text{total ionization rate}} = \underbrace{\frac{4\pi}{3} R_s^3 n_p}_{\text{number of protons}} \times \underbrace{n_e \alpha_B}_{\text{recombination rate}} , \tag{III.50}$$

where α_B is the *case B recombination rate*. The product $n_e \alpha_B$ is the electronic recombination rate to any H level $n \geq 2$:

$$\alpha_B(T_e) \simeq 2.6 \times 10^{-13} T_e^{-3/4} \text{cm}^3/\text{s}. \tag{III.51}$$

Recombination down to $n = 1$ will indeed produce an ionizing photon that will be absorbed by another H atom. Rearranging Eq. (III.50), Strömgren's radius is thus:

$$R_s = \left(\frac{3 Q_0}{4\pi n_{gas}^2 \alpha_B} \right)^{1/3} . \tag{III.52}$$

For an O5 star, with $n_{gas} = 10^3$ cm^{-3}, $R_s \simeq 1$ pc. This estimate can be refined, accounting for He and other atomic species, as well as dust screening (*e.g.* Osterbrock, 1989, for an extensive lecture).

The Warm Ionized Medium (WIM). The WIM is a diffuse phase ($n_{gas} \simeq 0.1$ cm^{-3}, $T_{gas} \simeq 10^4$ K; Table III.6) filling up about $\simeq 25\%$ of the MW volume. It is roughly in pressure equilibrium with the other thermal phases, although it can be found expanding in some regions. This gas is photoionized by photons from OB star associations, escaping from H II regions. The electrons ejected by this photoionization provide the main heating source. It is observed through optical lines, essentially $H\alpha_{656.3nm}$, as well as some fine-structure lines and free-free emission.

III.3.1.3 The Molecular Gas

The molecular gas constitutes only a moderate fraction of the ISM mass and a small fraction of its volume. It is however crucial, as it is where stars are formed. In the MW, $\simeq 17\%$ of the ISM mass is molecular, which corresponds to $\simeq 2\%$ of the total baryonic mass (stars and ISM).

Molecular hydrogen formation. The formation of the most abundant molecule of the Universe, H_2, is inefficient in the gas phase. This is because the freshly formed molecule needs to evacuate 4.5 eV to remain stable. Yet, due to its symmetry, H_2 does not have rotational transitions that would allow it to radiate at these energy levels. H_2 formation thus takes place on grain surfaces (*e.g.* Bron et al., 2014, for a review). We have represented the two main processes on Fig. III.50: the so-called *Langmuir-Hinshelwood* (physisorption) and *Eley-Rideal* (chemisorption) mechanisms. In both cases, the grain serves as a catalyst and helps evacuate the formation energy when the newly formed molecule is released in the gas phase. Similarly to the photoelectric heating, this process happening on grain surfaces, it takes place primarily on small grains. Temperature fluctuations therefore play an important role in its efficiency (*e.g.* Le Bourlot et al., 2012).

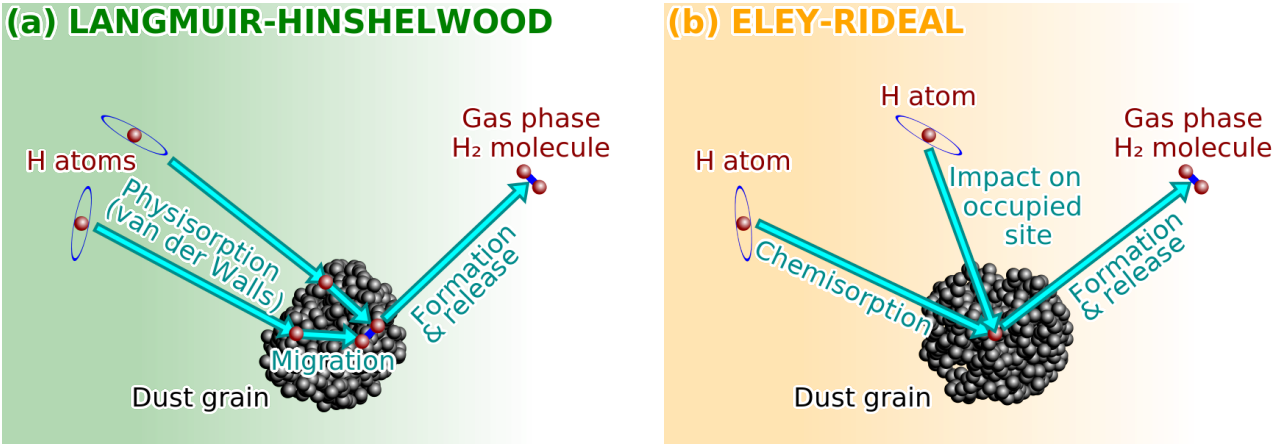

FIGURE III.50 – *H_2 formation on grain surface.* Panel *(a)* illustrates the *Langmuir-Hinshelwood mechanism*, which is driven by physisorption. H atoms are first captured by the grains and migrate to form H_2. The energy released by the formation liberates the molecule. Panel *(b)* demonstrates the *Eley-Rideal mechanism*, which is driven by chemisorption. In this case, an H atom is absorbed at a site where another H atom is already present. See Bron (2014) for more details. Licensed under CC BY-SA 4.0.

The diffuse molecular gas. Molecular gas can be observed at moderate densities ($n_{gas} \simeq 100$ cm^{-3}; Table III.6). This is often associated with the CNM with large enough column densities to allow H_2 to be self-shielded (*i.e.* its UV electronic lines are optically thick). It is also heated by photoelectric effect and cosmic rays. It cools primarily *via* $[C\,II]_{158\mu m}$ and can be observed through UV absorption lines.

Photodissociation regions. Same as H II regions, PDRs are a phase defined by the presence of massive stars in their vicinity. They are not a stable phase of the ISM, but they are very important since

they are the interface between the HII region and the molecular cloud (*e.g.* Hollenbach & Tielens, 1997, for a review). Because of their high density and their high G_0, they absorb a significant fraction of the FUV radiation by OB stars and reradiate it in the IR, as dust thermal emission and fine structure lines. Since they are the regions where molecules are being dissociated by FUV photons and subsequently recombine, they are the place of many important chemical reactions. Fig. III.51 shows the structure of a typical PDR. We have performed an isobaric run with the *Meudon PDR code* (Le Petit et al., 2006), for $P_{gas} = 10^7$ K/cm^3 and $G_0 = 10^5$. We show the variation of the abundances of the main species, and we represent in the upper part the HI/H_2 and CII/CI/CO transitions. This figure demonstrates that H_2, being efficiently self-shielded, exists at lower A(V), whereas CO appears deeper into the cloud.

Dense molecular clouds. Dense molecular clouds ($n_{gas} \simeq 10^3 - 10^6$ cm^{-3}; Table III.6) contain most of the molecular gas, concentrated in a small volume. These molecular clouds are gravitationally bound. Their structure is clumpy and filamentary. The gas motions are controlled by turbulence. They can be arranged in *molecular complexes* of sizes up to $\simeq 100$ pc (*e.g.* Solomon et al., 1987). The densest cores are collapsing and will lead to star formation. One of the most challenging issue of ISMology is the difficulty to measure the mass of molecular clouds. As we have mentioned earlier, H_2 is a symmetric molecule. It thus does not have any dipole moment allowing rotational transitions. Its first transitions are its rovibrational levels (H_2 0-0 S(0)$_{28.3\mu m}$, H_2 0-0 S(1)$_{17.0\mu m}$ and so on) that need temperatures of a few hundred K to be pumped. Cold molecular clouds are thus primarily traced by the second most abundant molecule, CO, which is asymmetric. CO rotational lines, ^{12}CO(J=1→0)$_{2.6mm}$ and ^{12}CO(J=2→1)$_{1.3mm}$, are the most commonly observed transitions. The conversion of an observed ^{12}CO(J=1→0)$_{2.6mm}$ line intensity, I_{CO}, to a H_2 column density requires the knowledge of a *CO-to-H_2 conversion factor*, X_{CO}, such that (*e.g.* Bolatto et al., 2013):

$$N(H_2) \simeq X_{CO} \times I_{CO}. \tag{III.53}$$

The X(CO) factor has been calibrated on Galactic molecular clouds: $X(CO) \simeq 2 \times 10^{20}$ cm^{-2}(K.km/s)$^{-1}$. This value is however metallicity dependent, as we will see in Sect. III.3.2.3.

III.3.2 Dust as a Diagnostic Tool

We have already discussed the potential of dust as a tracer of the physical conditions in the ISM, especially in Sect. III.2.1.3. We review here a few examples where dust tracers were used to refine the results of studies dedicated to star formation or gas physics.

III.3.2.1 Dust to Study Star Formation

Star formation rates. Dust-related SFR tracers rely on the fact that young stars are extremely luminous and are enshrouded with dust. If the clouds are optically thick and if their covering factor is unity, the OB star luminosity is: $L_{OB} \simeq L_{TIR}$. Contrary to a common misconception, this is independent of dust properties. Assuming a typical IMF, burst age and metallicity, L_{OB} can be converted to: $SFR \simeq 10^{-10} \times L_{TIR}/L_\odot$ (*e.g.* Kennicutt, 1998a). The contribution of old stars to L_{TIR} is negligible for high enough SFRs. Alternatively, monochromatic SFR indicators have been proposed. Calzetti et al. (2007) and Li et al. (2010) found that the 24 and 70 µm monochromatic luminosities were good local SFR indicators (on spatial scales of $\simeq 0.5 - 1$ kpc): $SFR \simeq 2611 \times [L_\nu(24\ \mu m)/(L_\odot/Hz)]^{0.885}$ and $SFR \simeq 1547 \times L_\nu(70\ \mu m)/(L_\odot/Hz)$. We have discussed the use of aromatic features as SFR tracers in Sect. III.2.1.3. Finally, several composite indicators have been calibrated (Hao et al., 2011). By combining FUV or H$\alpha_{656.3nm}$ measurements with the 24 µm or TIR indicators, they account for the fact that star-forming regions are not completely opaque.

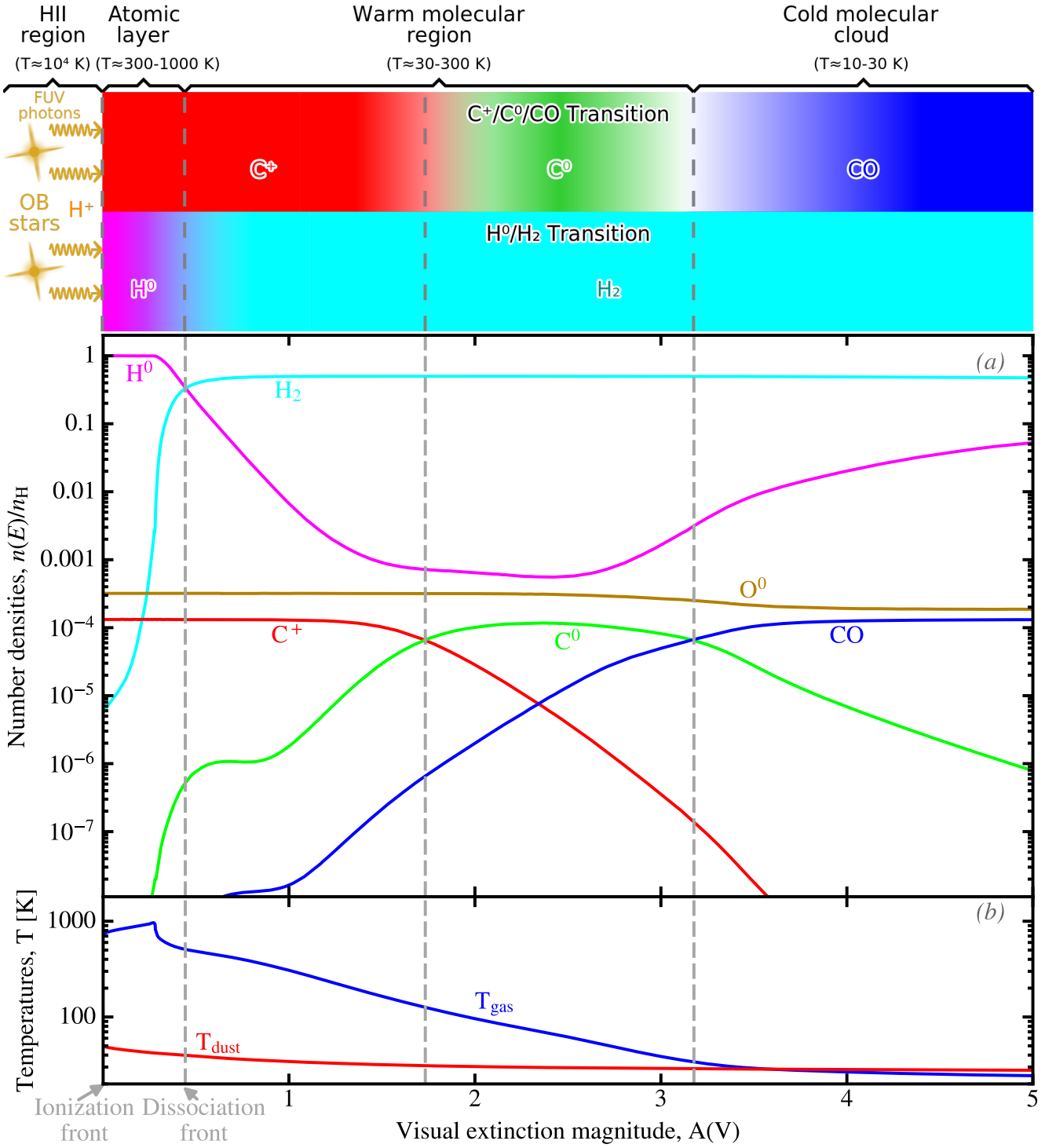

FIGURE III.51 – *Structure of a PDR.* The top drawing schematically represents the structure of a PDR. The ionizing stars are illuminating the cloud from the left. In the H II region, H is fully ionized. We enter the PDR at the ionization front. H is essentially neutral and atomic in this layer. We then pass the dissociation front around A(V) ≃ 0.5 – 1, where H is essentially molecular (H_2). Around A(V) ≃ 1.5 – 2, C becomes neutral, and around A(V) ≃ 3, CO becomes the dominant carbon-bearing species. We are at this stage in the cold molecular cloud. The two bottom panels show the results of an isobaric PDR model for $P_{gas} = 10^7$ K/cm^3 and $G_0 = 10^5$ (using the `Meudon PDR code`; Le Petit et al., 2006). Panel *(a)* shows the evolution as a function of A(V) of the densities of the most important species. These densities are normalized by the total H density, $n_H \equiv n(H^+) + n(H^0) + 2n(H_2)$. Panel *(b)* shows the evolution of the gas and dust temperatures. The exact densities, A(V) and temperatures are specific to the particular model we have run, but they give a rough idea of the typical values of these parameters.

Resolving star formation. Hony et al. (2015) performed a comparison of different SFR estimators with the actual stellar content of the star-forming region N 66, in the SMC. In this study, we derived the stellar surface density, $\Sigma_\star$, based on individual star counts from HST photometry. When compared to the dust mass surface density, Σ_{dust}, derived from SED modeling, we found a significant scatter, at $\simeq 6$ pc linear resolution. The SFRs derived from Σ_{dust} or $H\alpha_{656.3nm}$ underestimate the more reliable, $\Sigma_\star$-derived SFR, by up to a factor of $\simeq 10$. This is likely due to ionizing photons escaping the region [11]. Finally, converting our Σ_{dust} map to a gas mass surface density map, Σ_{gas}, we found that the pixels of our region are lying above the *Schmidt-Kennicutt relation* [12]. This might be due to low density gas, inefficient at forming stars, that is included in global Schmidt-Kennicutt relations, but absent when zooming on star-forming regions.

III.3.2.2 Photodissociation Regions

PDR Properties. We have participated to numerous studies aiming at constraining the PDR properties in low-metallicity environments (Cormier et al., 2010, 2012; Lebouteiller et al., 2012; Cormier et al., 2015; Chevance et al., 2016; Lebouteiller et al., 2017; Wu et al., 2018a; Cormier et al., 2019; Lebouteiller et al., 2019). The common point of these studies is their use of numerous fine structure lines observed by *Herschel* and *Spitzer*, as well as the dust emission, to constrain the main parameters of a PDR model (G_0, n_{gas}, filling factor). The challenge lies in the multiple degeneracies, due to the fact that a given line can trace several phases. For instance, $[CII]_{158\mu m}$ comes from the ionized gas, the neutral gas and from an important fraction of molecular clouds (Fig. III.51). Such a degeneracy can be solved by using additional lines to constrain the properties of these different phases. Dust tracers are also useful, either as a constraint or as a self-consistency test. As an example, Chevance et al. (2016) modeled the gas properties in 30 Doradus and derived the typical depth of PDRs, in terms of visual extinction magnitude, $A_{PDR}(V)$. Fig. III.52 shows the comparison of $A_{PDR}(V)$ to the value of this parameter, derived from SED modeling, $A_{dust}(V)$. We can see that both quantities are in good agreement, validating the PDR results.

Photoelectric heating. Assuming that $[CII]_{158\mu m}$ is the main gas coolant, the *photoelectric efficiency*, that we already discussed in Sect. III.3.1.1, ϵ_{PE}, can be approximated by the gas-to-dust cooling ratio: $\epsilon_{PE} \simeq L_{CII}/L_{TIR}$. Detailed studies usually add other lines to the gas cooling rate, like $[OI]_{63\mu m}$, to have a more complete estimate (*e.g.* Lebouteiller et al., 2012; Cormier et al., 2015; Lebouteiller et al., 2019). Overall, Smith et al. (2017) found that $0.1\,\% \lesssim \epsilon_{PE} \lesssim 1\,\%$, with an average of $\langle\epsilon_{PE}\rangle \simeq 0.5\,\%$, in a sample of 54 nearby galaxies. It appears that ϵ_{PE} is lower when the dust temperature is higher (Rubin et al., 2009; Croxall et al., 2012). This is not likely the result of the destruction of the UIB carriers, as their intensity correlates the best with the $[CII]_{158\mu m}$ emission (*e.g.* Helou et al., 2001). It is rather conjectured to be due to the saturation of grain charging in UV-bright regions. The shape of the ISRF also has a consequence on the accuracy with which L_{TIR} represents the true UV, photoelectric-efficient flux. Indeed, Kapala et al. (2017) showed that the variations of ϵ_{PE} in M 31 could be explained by the contribution of old stars to L_{TIR}. Finally, one of the most puzzling features is that ϵ_{PE} is higher at low metallicity (Poglitsch et al., 1995; Madden et al., 1997; Cormier et al., 2015; Smith et al., 2017; Madden et al., 2020), while the UIB strength drops in these systems (Sect. IV.2.2.1). This is currently poorly understood. However, in the extreme case of I Zw 18 ($Z \simeq 1/35\,Z_\odot$), where no UIB is detected (*e.g.* Wu et al., 2006) and the photoelectric heating is estimated to be negligible, the gas-cooling-to-TIR ratio is still $\simeq 1\,\%$ (Lebouteiller et al., 2017). In this instance, we have shown the gas could be heated by X-rays.

11. We saw a similar discrepancy in the center of M 83, where the $[NII]_{122\mu m}$ line was significantly more extended than other SFR tracers (Wu et al., 2015).

12. The Schmitt-Kennicutt relation is the empirical correlation between Σ_{SFR} and Σ_{gas} for a wide diversity of galaxies (Schmidt, 1959; Kennicutt, 1998b).

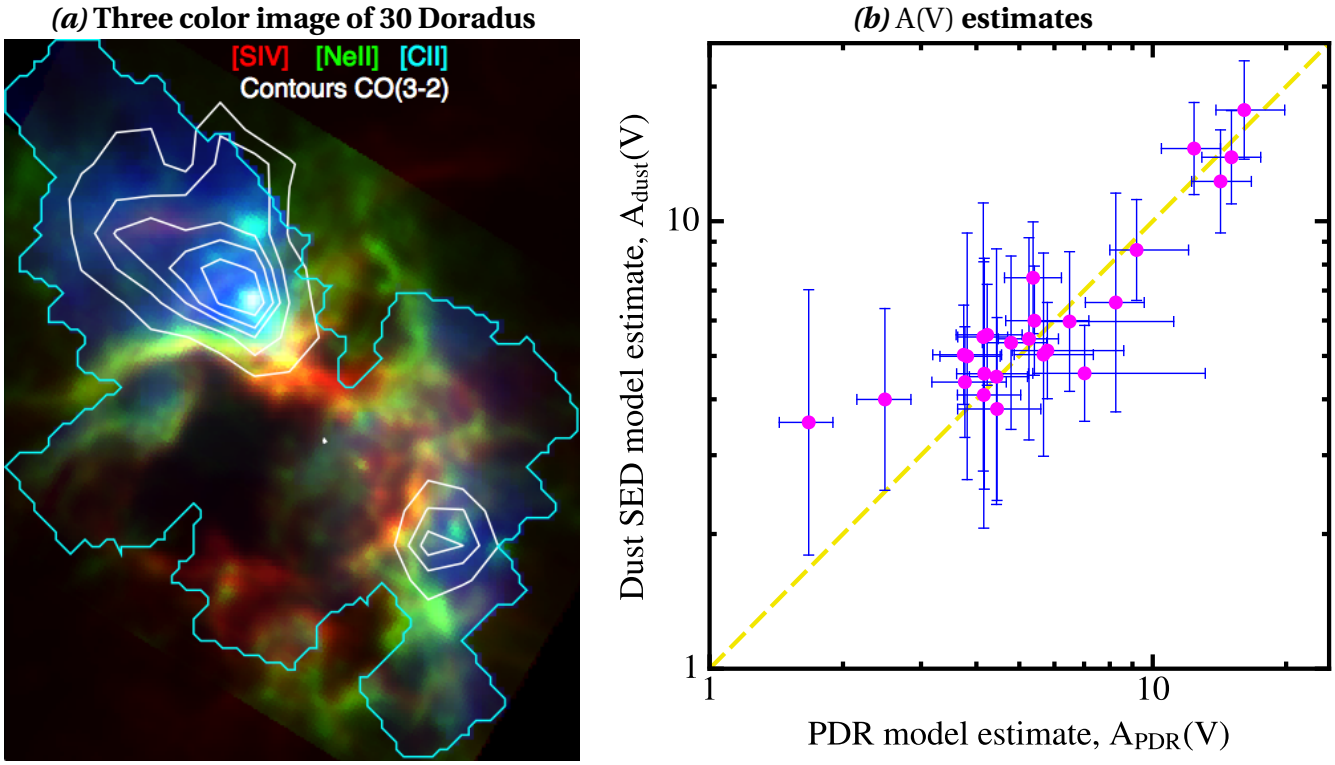

FIGURE III.52 – *Comparison of visual extinctions in 30 Doradus.* Panel *(a)* shows a map of 30 Doradus, seen through: *(i)* $[SIV]_{10.51\mu m}$ (red; heavily-ionized gas; Indebetouw et al., 2009); *(ii)* $[NeII]_{12.81\mu m}$ (green; moderately ionized gas; Indebetouw et al., 2009); *(iii)* $[CII]_{158\mu m}$ (blue; neutral gas; Chevance et al., 2016); and *(iv)* $^{12}CO(J=3\rightarrow2)_{867\mu m}$ (white contours; molecular gas; Minamidani et al., 2011). At the center of the image lies the SSC, R136. Panel *(b)* shows the comparison between the estimates of the visual extinction magnitudes, A(V) (Eq. II.4), in different regions of panel *(a)*. The *x*-axis shows the A(V) value derived from the PDR modeling of the available gas lines, whereas the *y*-axis shows the value of A(V) inferred from dust SED modeling. Credit: *(a)* Chevance et al. (2016); *(b)* licensed under CC BY-SA 4.0.

III.3.2.3 The Molecular Gas and its Dark Layer

The dark gas. We have discussed in Sect. III.3.1.3 that the photodissociation of H_2 and CO at different depths into molecular clouds leads to biases in gas mass estimates. H_2 is indeed self-shielded. It therefore exists at column densities roughly independent of metallicity. On the contrary, CO, which is significantly less abundant, is not self-shielded (*i.e.* its electronic lines remain optically thin at large column densities). Consequently, CO needs to be shielded by dust to survive. It thus exists only deeper into molecular clouds. The H_2 gas that exists in regions where CO is photodissociated is often referred to as the *CO-dark molecular gas*. Other tracers can be used to constrain this dark gas: *(i)* dust emission (*e.g.* Israel, 1997; Leroy et al., 2011); *(ii)* $[CII]_{158\mu m}$ (*e.g.* Madden et al., 1997); *(iii)* and γ-rays (*e.g.* Grenier et al., 2005). Using I_{CO} to derive $N(H_2)$ with Eq. (III.53) can therefore be biased if the dark gas fraction is significantly larger than in the MW, where X(CO) has been calibrated. This is what happens in low-metallicity systems, where the dustiness is lower, because of the lower abundance of heavy elements (*cf.* Sect. IV.3.1). This is represented in Fig. III.53. We see that in the low-metallicity cloud (on the right), CO cores are much smaller, because of the increased photodissociation of this molecule, compared to the left cloud (Solar metallicity). It results that the mass of CO-dark H_2 is significantly larger at low metallicity. We have investigated this ISM component in the LMC, using dust mass surface density, concluding it could account between ≃ 10 % and ≃ 100 % of the total molecular gas mass (Galliano et al., 2011). Recently, we studied dark gas in the star-forming region N11 of the LMC, modeling the full set of IR emission lines (Lebouteiller et al., 2019). We showed that most of

the molecular gas in this region is CO-dark and that $[CII]_{158\mu m}$ traces mostly this component. We extended this analysis to a sample of nearby dwarf galaxies (Madden et al., 2020). We found that $\simeq 70-100\,\%$ of the molecular gas mass is not traced by $^{12}CO(J{=}1{\rightarrow}0)_{2.6mm}$.

☞ The molecular gas content of low-metallicity systems is dominated by dark gas.

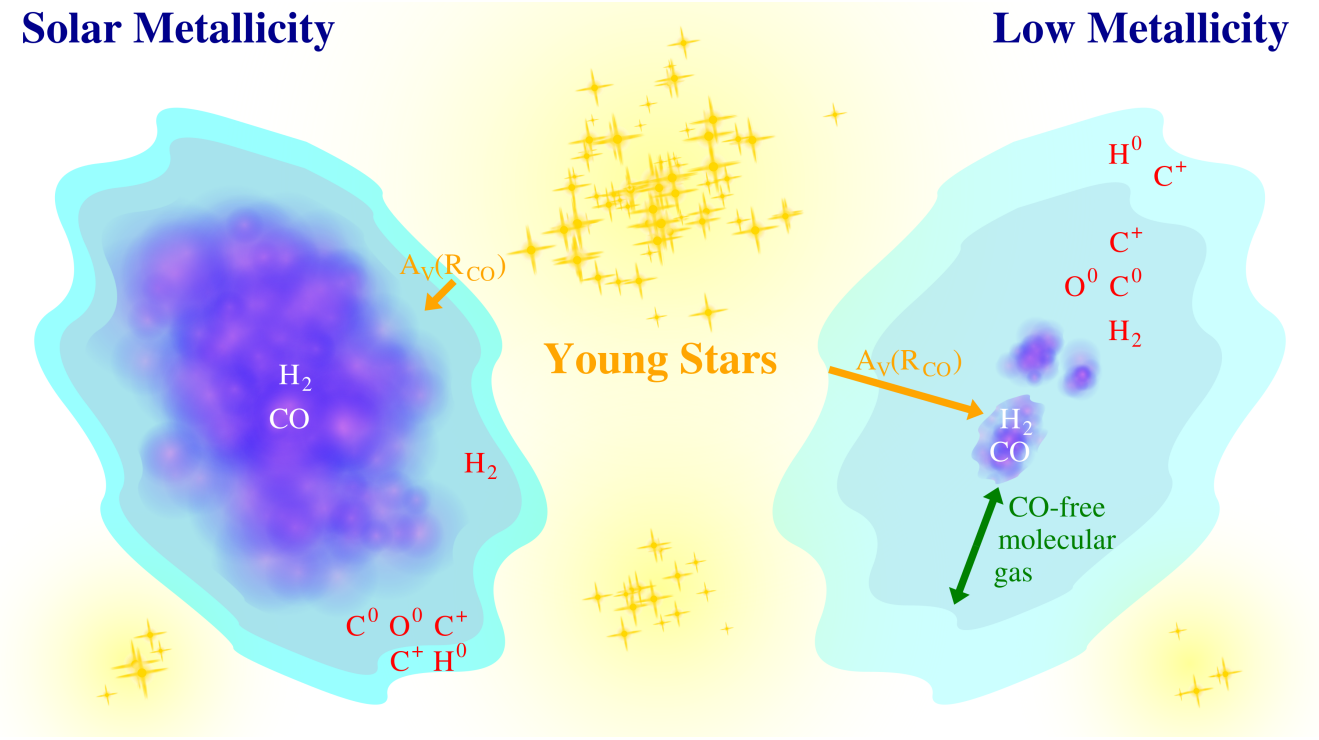

FIGURE III.53 – *Metallicity effect on the CO-dark gas.* We have represented two molecular clouds photodissociated by nearby OB star associations. The left cloud has a Solar metallicity. Its CO core is efficiently shielded by dust. This is not the case for the right cloud, which has a low metallicity. In this cloud, the lower grain abundance causes a lower dust screening. Consequently, CO is photodissociated deeper into the cloud, whereas H_2 remains self-shielded. Credit: Madden et al. (2020).

Pressure and radiation field. The pressure in molecular clouds can be significantly larger than in the pressure equilibrium phases of the ISM: $P_{gas} \simeq 6\times10^7$ K/cm^{-3} in the Orion bar (Goicoechea et al., 2016); compared to $P_{gas} \simeq 3000$ K/cm^{-3} in the HIM, WIM and CNM (Eq. III.46). We have studied the physical conditions of the molecular gas in the central region of the starbursting galaxy, M 83 (Wu et al., 2015). We used the CO *Spectral Line Energy Distribution* (SLED) observed by *Herschel* to estimate its column density and pressure, N(CO) and P_{CO}, in different regions. We have also performed SED modeling to estimate the mean starlight intensity heating the grains, $\langle U\rangle$ (Eq. III.38). This allowed us to show that both quantities are correlated (*cf.* Fig. III.54.a). We also noted that the pressure gradient was oriented along a chain of radio sources, corresponding to a radio jet (Fig. III.54.b). We derived a similar correlation between the ISRF strength and the gas thermal pressure in the Carina nebula (Wu et al., 2018a). Such a correlation was also found by Joblin et al. (2018) in the Orion bar. They argue that the photoevaporation of the PDR can explain this relation.

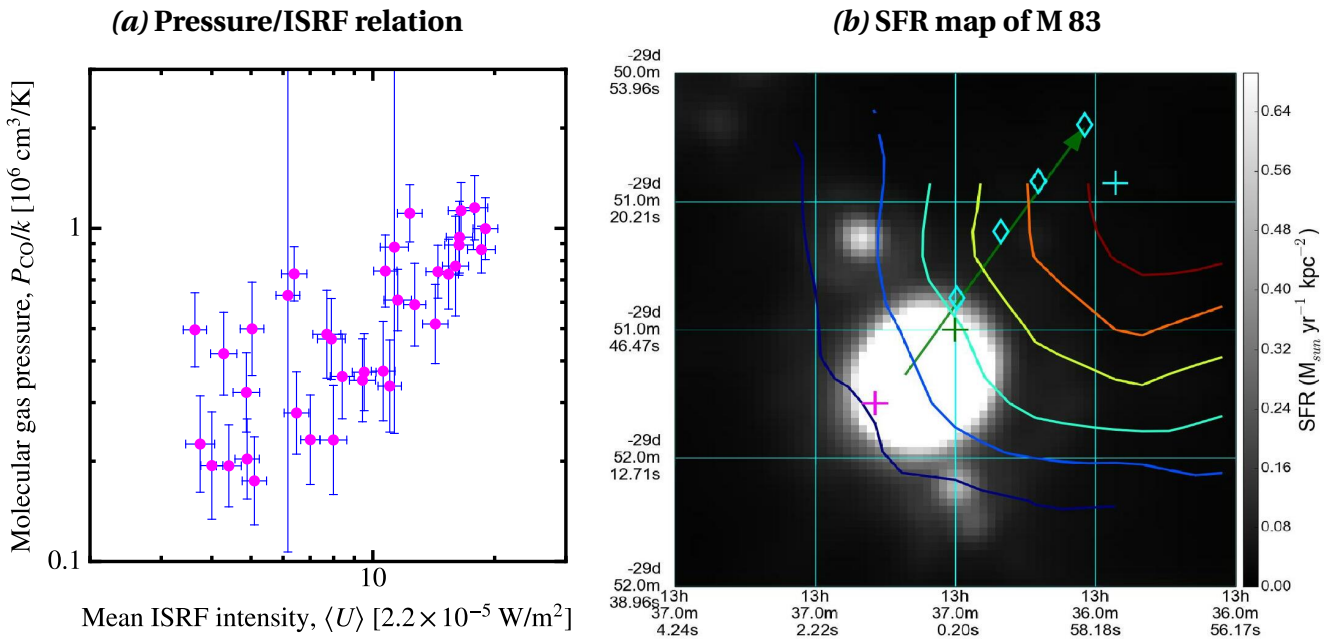

FIGURE III.54 – *Molecular gas pressure in the center of M 83.* Panel *(a)* displays the relation between the average starlight intensity derived from SED modeling, and the molecular gas pressure, inferred from CO SLED modeling, in different regions in the center of M 83 (Wu et al., 2015). Panel *(b)* shows the SFR map of the central region of M 83. The color contours represent the molecular gas pressure, from $P_{CO} = 4 \times 10^5$ K/cm^3 (blue) to $P_{CO} = 2.4 \times 10^6$ K/cm^3 (red). The four diamonds indicates the position of the four radio sources reported by Maddox et al. (2006). Credit: *(a)* licensed under CC BY-SA 4.0; *(b)* Wu et al. (2015).

Chapter IV

Modeling Cosmic Dust Evolution

This is not a new result – Draine & Salpeter (1979) reached the conclusion that grain destruction was rapid and that regrowth of dust in the ISM was required to explain the observed depletions. The numbers basically haven't changed appreciably since then; the argument has been reiterated a number of times (...). Nevertheless, some authors continued to hold the view that the solids in the interstellar medium were primarily formed in stars.

(Bruce T. DRAINE; Draine, 2009)

Contents

IV.1 Stellar Evolution . . . 180
IV.1.1 The Fate of Stars of Different Masses . . . 180
IV.1.1.1 Nucleosynthesis . . . 180
Nuclear binding energies. . . . 180
Primordial nucleosynthesis. . . . 180
Stellar nucleosynthesis. . . . 180
IV.1.1.2 Brief Outline of Stellar Evolution . . . 181
The Main Sequence. . . . 181
The late stages of massive stars. . . . 182
The late stages of LIMS. . . . 182
IV.1.1.3 Parametrizing Star Formation . . . 183
Initial mass functions. . . . 183
Parametric star formation histories. . . . 183
IV.1.2 Elemental and Dust Yields . . . 185
IV.1.2.1 Injection of Heavy Elements in the ISM . . . 186
Stellar elemental yields. . . . 186
Metallicity estimates. . . . 188
IV.1.2.2 Production of Stardust . . . 188
AGB stars. . . . 188
SN II. . . . 188
Indirect evidence. . . . 189
IV.2 Dust Evolution Processes in the ISM . . . 189
IV.2.1 Grain Formation and Transformation . . . 189
IV.2.1.1 Evidence of Grain Growth and Coagulation in the ISM . 190
The evidence brought by depletions. . . . 190
FIR opacity variations. . . . 190

IV.2.1.2 Studies of the Magellanic Clouds . . . 190
Spatially-resolved SED fitting of LMC-N44 and SMC-N66. 191
Derived dust-gas relations. . . . 191
IV.2.1.3 Quantifying Grain Growth . . . 192
Accretion timescale. . . . 193
Grain growth in different ISM phases. . . . 194
Relation to global parameters. . . . 194
IV.2.2 Grain Destruction . . . 195
IV.2.2.1 Photodestruction of Small Grains . . . 195
Photodesorption and sublimation. . . . 195
Evidence in resolved regions. . . . 196
IV.2.2.2 Thermal Sputtering . . . 196
Sputtering times. . . . 198
Early-type galaxies. . . . 199
IV.2.2.3 Destruction by SN Blast Waves . . . 199
Evidence in resolved regions. . . . 200
Global model prescription. . . . 200
The destruction efficiency. . . . 200
IV.3 Cosmic Dust Evolution . . . 201
IV.3.1 Constraining the Dust Build-Up in Galaxies . . . 201
IV.3.1.1 Cosmic Dust Evolution Models . . . 202
Physical ingredients and assumptions. . . . 202
The ejected masses. . . . 203
The equations of evolution. . . . 203
Dust evolution tracks. . . . 204
Effects of the individual parameters. . . . 204
IV.3.1.2 Empirical Inference of Dust Evolution Timescales . . . 206
Fitting dust scaling relations. . . . 206
Evolutionary timescales as a function of metallicity. . . . 208
Methodological remarks. . . . 210
The controversy about stardust. . . . 211
Limitations of our approach. . . . 212
IV.3.2 Evolution of the Aromatic Feature Carriers . . . 212
IV.3.2.1 The Different Evolution Scenarios . . . 213
Enhanced destruction at low metallicity. . . . 213
Inhibited formation efficiency at low metallicity. . . . 213
IV.3.2.2 The Observed Trends . . . 214
A better correlation with metallicity. . . . 214
The global point of view. . . . 214
The potential of quiescent very-low-metallicity galaxies. . 215

This chapter focusses on the study of dust evolution in all interstellar environments, at all spatial scales. Dust evolution is the variation of the constitution of a grain mixture with time, under the effects of its environment. The timescales of evolution being significantly longer than the career of a scientist, we usually study spatial variations of the dust content in a region, or the variations among a sample of galaxies. These different observations are then compared, being considered as snapshots at different evolutionary stages. The environmental parameters that are commonly used to quantify dust evolution are: *(i)* the ISM density and the ISRF intensity and hardness, for spatially-resolved studies; *(ii)* the metallicity and star formation rate, for global galactic studies. The main processes responsible for dust evolution are represented on Fig. IV.1.

Grain Formation is the dust mass build-up by:

- grain condensation in the ejecta of core-collapse SNe and AGB stars (*i.e.* making grains from scratch by condensing atoms);
- grain (re-)formation in the CNM and molecular clouds, by accretion of atoms and molecules onto grains: *(i)* grain growth; *(ii)* mantle accretion; and *(iii)* ice formation.

Grain Processing is the alteration of the grain constitution in the ISM by:

- shattering and fragmentation by grain-grain collisions in low-velocity shocks (modification of the size distribution);
- structural modifications by high energy photons or cosmic ray impacts;
- grain-grain coagulation in cold regions.

Grain Destruction is the full or partial removal of the elements constituting the grains by:

- erosion and evaporation by thermal or kinetic sputtering (gas-grain collision in a hot gas or a shock);
- photodesorption of atoms and molecules;
- thermal evaporation;
- astration (incorporation into stars).

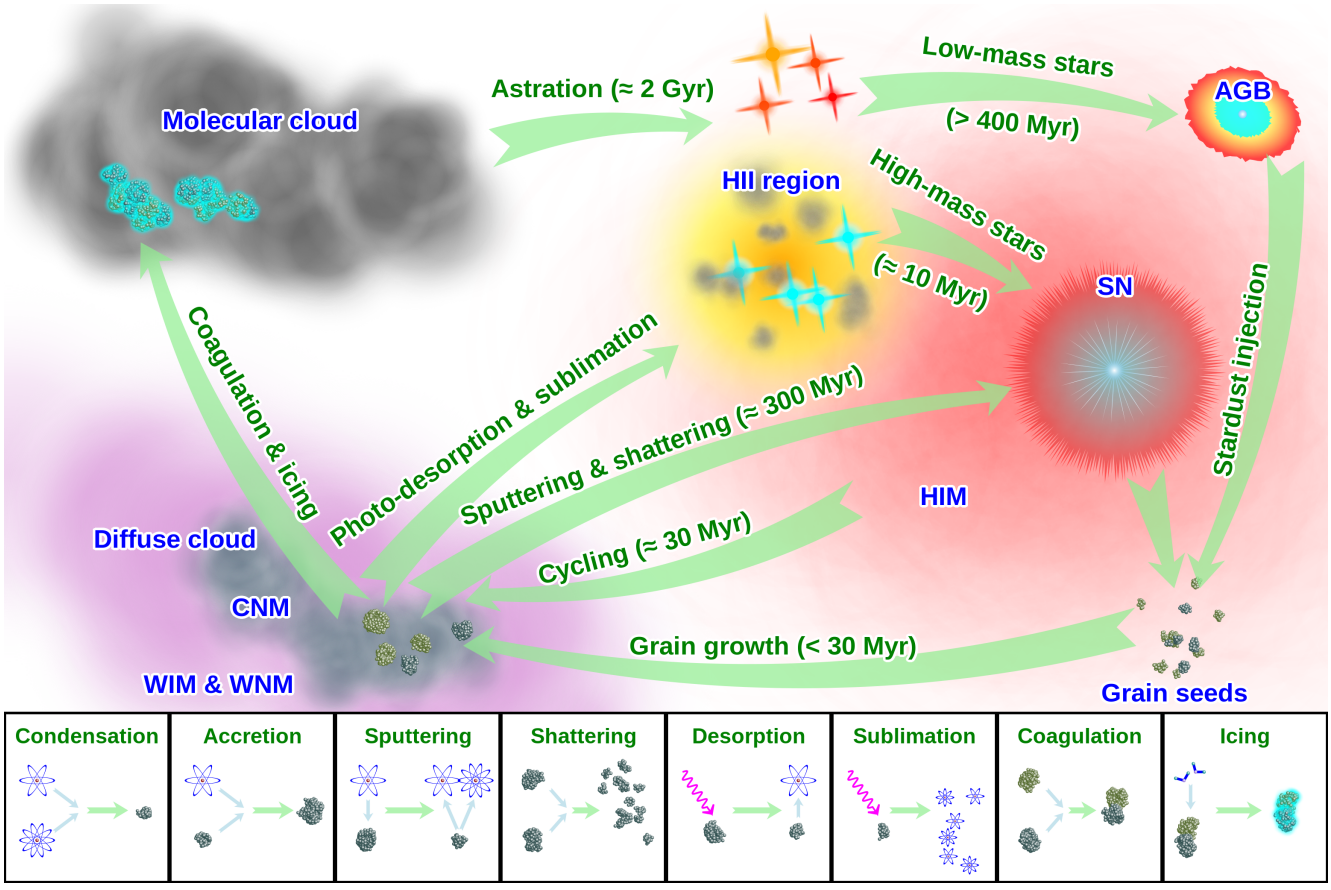

FIGURE IV.1 – *The interstellar dust lifecycle.* This is the schematic representation of dust evolution through the ISM. The upper part illustrates the different sources, sinks and environments where grains are processed. The timescales are indicative and will be discussed in the rest of this chapter. The eight small bottom panels focus on the microscopic processes. Licensed under CC BY-SA 4.0.

IV.1 Stellar Evolution

Stars have a crucial impact on ISD: *(i)* they synthesize the heavy elements that constitute dust grains (Fig. II.16); *(ii)* they also directly produce dust seeds in their ejecta; *(iii)* the shock waves of SNe erode and vaporize the grains; *(iv)* the radiative and mechanical feedback of massive stars carve the ISM and process the grains.

IV.1.1 The Fate of Stars of Different Masses

A star can be conceptualized as a sphere of gas in hydrostatic equilibrium, where the gravity is counterbalanced by the thermal pressure sustained by nuclear reactions in its core (*e.g.* Degl'Innocenti, 2016, for an introduction). The energy produced in the core is carried out through radiation, convection or conduction. The initial mass of a star, and in a lesser extent its initial metallicity, determine its future evolution.

IV.1.1.1 Nucleosynthesis

The nuclear reactions in stellar interiors, on top of being the fuel of stars, lead to the production of heavy elements. A fraction of these freshly synthesized elements are injected back into the ISM, during the final stages of stellar evolution.

Nuclear binding energies. A fundamental quantity to determine the efficiency of nuclear reactions to sustain the thermal pressure within a star is the nuclear binding energy of an element of mass A (number of nucleons; *cf. e.g.* Chaps. 1-2 of Pagel, 1997, for a review). This quantity is represented in Fig. IV.2 for the most relevant nuclei. To have an exothermic reaction, that will be able to counterbalance gravity, one needs to synthesize elements of higher binding energies. The curve of Fig. IV.2 reaches a maximum around ^{56}Fe.

Fusion of elements lighter than ^{56}Fe is exothermic. Since the initial composition of a star is $\simeq 3/4$ H and $\simeq 1/4$ He, stellar nucleosynthesis takes this way.

Fission of elements heavier than ^{56}Fe is exothermic. This is the process implemented in nuclear reactors to generate electricity (through heat).

Primordial nucleosynthesis. Before the first stars appeared, ^{2}H and ^{4}He, as well as elements up to ^{7}Li, were synthesized during the first 15 minutes after the big bang (*e.g.* Pagel, 1997; Calura & Matteucci, 2004; Johnson, 2019). The temperature was at this time around $T \simeq 10^9$ K. This primordial nucleosynthesis was brief, as the Universe was expanding and cooling. It is estimated that after 20 minutes, the temperature was too low to synthesize new elements. The *primordial abundances* refer to the elements produced during these first minutes (*cf.* Eq. II.11):

$$X_{\rm primordial} \simeq 0.76, \quad Y_{\rm primordial} \simeq 0.24, \quad Z_{\rm primordial} \simeq 0.00. \tag{IV.1}$$

Stellar nucleosynthesis. Once the temperature at the center of a collapsing protostar becomes high enough ($T \simeq 10^7$ K), *thermonuclear* reactions [1] are initiated. Several chains and cycles of reactions occur in stars, at different stages. The most important ones are the following (*e.g.* Filippone, 1986; Pagel, 1997; Silva Aguirre, 2018).

Proton fusion, also called *p-p chain*, is a series of nuclear reactions converting $4\,^{1}$H into ^{4}He. This reaction chain has three branches cycling through various light elements (D, Li, B, Be). It is the dominant process in stellar interiors with $T \lesssim 2 \times 10^7$ K, that is for stars with mass $m_\star \lesssim 1\,M_\odot$. [2]

1. In thermonuclear reactions, the high temperature gives nuclei enough kinetic energy to overcome their Coulomb barrier, and allows them to fuse with each other.
2. The Sun's core is at $T \simeq 1.5 \times 10^7$ K.

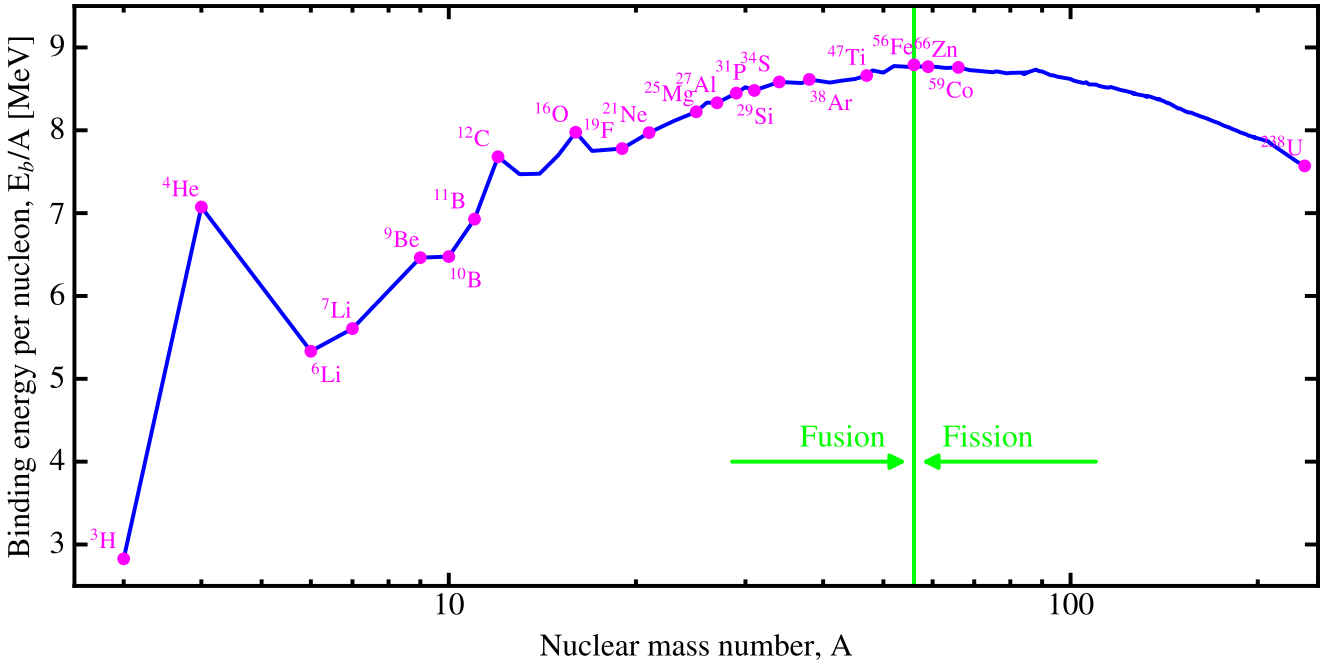

FIGURE IV.2 – *Average nuclear binding energies per nucleon.* We have displayed the experimental data compiled by Ghahramany et al. (2012). The most stable elements are around ^{56}Fe. Below, fusion is exothermic, above, it is fission. Licensed under CC BY-SA 4.0.

CNO cycle is another series of nuclear reactions converting $4\,^{1}$H into ^{4}He. Contrary to the p-p chain, this cycle requires pre-existing C, N or O (*i.e.* it requires a non-zero-metallicity star). This cycle can be broken into: *(i)* a *CN cycle*, starting with ^{12}C and $4\,^{1}$H, ending with ^{12}C and ^{4}He; and *(ii)* a *NO cycle*, starting with ^{15}N and $3\,^{1}$H, ending with ^{14}N and ^{4}He. This cycle is more efficient than the p-p chain for $T \gtrsim 2 \times 10^7$ K, that is for stars with $m_\star \gtrsim 1\,M_\odot$. In practice, both happen simultaneously, but with different efficiencies.

The triple α process is a series of nuclear reactions converting $3\,^{4}$He into ^{12}C (the ^{4}He nucleus is indeed called the α *particle*). It also produces ^{16}O and ^{20}Ne as byproducts. This process starts when the star has converted ≃ 10 % of its H into He. It requires temperatures of $T \simeq 10^8$ K.

Heavier element fusion happens essentially in massive stars ($m_\star \gtrsim 8\,M_\odot$), when the temperature of the core reaches $T \simeq 10^9$ K. Several successive phases are then possible: C burning, Ne burning and O burning, producing up to ^{28}Si. The last series of reactions are the α ladder, which produce elements up to Fe and Ni.

☞ *H burning*, which encompasses both the p-p chain and the CNO cycle, represents the longest phase in the lifetime of a star, whereas *He burning* lasts only ≃ 10 % of its existence.

IV.1.1.2 Brief Outline of Stellar Evolution

Stars are born from the collapse of molecular clouds into protostars (*e.g.* Motte et al., 2018, for a review). Protostars accrete matter until their winds and radiation pressure stops this process, leading to a *pre-main sequence star* (pre-MS). Pre-MS stars exhibit violent winds and bipolar jets, clearing away the remaining molecular cocoon they were born in. They contract until the temperature in their core is high enough to initiate H fusion ($T \simeq 10^7$ K). Below $m_\star \leq 0.08\,M_\odot$, we get a *brown dwarf*, which is a compact object not massive enough to sustain nuclear reactions. Fig. IV.3 schematically represents the different stages of evolution of low- and high-mass stars.

The Main Sequence. Once nuclear reactions ignite, stars are on the *Zero-Age Main Sequence* (ZAMS; grey line in Fig. III.18). We have already briefly discussed stellar evolution in Sect. III.1.2.3. The dif-

ferent types of stars, their mass, luminosities and lifetimes are given in Fig. III.18 and in Table III.2.

1. As long as stars are in their H burning phase (*cf.* Sect. IV.1.1.1) they are *Main Sequence* (MS) stars. They move slowly along their tracks in Fig. III.18.
2. Once the core has exhausted its H, it contracts by lack of fuel. This contraction increases the temperature, allowing the He burning to start (*cf.* Sect. IV.1.1.1). Due to the increase of central temperature, the outer layers expand. The star is now a *red giant*.
3. This process repeats, with He burning (triple α process; Sect. IV.1.1.1).

The late stages of massive stars. Massive stars ($8\ M_\odot \leq M_\star < 120\ M_\odot$) are the hottest and most luminous ones (*cf.* Table III.2). They are short-lived ($\tau(m_\star) \lesssim 30$ Myr; Fig. III.18).

1. The process of burning heavier elements is repeated beyond C, resulting in an "*onion*" structure (*cf.* Fig. IV.3.a). The combustion of each element is exponentially faster. These stars are, at this point, *red supergiants* (*cf.* Fig. III.18).
2. Once the core is made of Fe, the star can not anymore produce energy by nuclear fusion. It therefore collapses (*e.g.* Heger et al., 2003).

   If $m_\star \lesssim 40\ M_\odot$, the collapse is halted by the *degeneracy pressure*[3] of neutrons. The outer layers of the stars then explode as a *type II supernova* (SN II) or *core-collapse supernova*, leaving a *Neutron Star* (NS) in the center.

   If $m_\star \gtrsim 40\ M_\odot$, the degeneracy pressure of the neutron core is not sufficient to sustain the collapse. The remnant is not anymore a NS, but a *Black Hole* (BH). This is also the approximate mass range where the star leaves a remnant without exploding as a SN, ending as a *collapsar* (Heger et al., 2003). These two phenomena (ending as a collapsar and leaving a BH) are not necessarily concomitant. The exact masses above which these two phenomena occur are not accurately known and depend on other parameters, such as stellar rotation. For simplicity, we have represented both phenomena on the same branch in Fig. IV.3.

The late stages of LIMS. *Low- and Intermediate-Mass Stars* (LIMS; $0.08\ M_\odot \leq M_\star < 8\ M_\odot$) are less luminous than massive stars, but they are the most numerous. Their lower gravity allow them to burn their elements slower than massive stars, and therefore to live longer (several Gyrs, on average; Fig. III.18).

1. Their mass does not allow them to start C burning. LIMS enter the *Asymptotic Giant Branch* (AGB; *cf.* Fig. III.18; *e.g.* van Winckel, 2003; Herwig, 2003, for reviews). They are larger and more luminous than red giants and are thermally pulsing.
2. The contraction of the core is halted by electron degeneracy pressure. The thermal pulses lead the outer shell to expand progressively, creating a *Planetary Nebula* (PN), leaving a *White Dwarf* (WD) in the center.
3. The maximum mass a white dwarf can reach is the *Chandrasekar mass*, $m_{\rm Chandra} \simeq 1.4\ M_\odot$. If a white dwarf of mass $m_{\rm WD}$ happens to be in a binary system with another red giant, it will accrete some of its mass.

   If $m_{\rm WD} \gtrsim m_{\rm Chandra}$, the excess of mass above the Chandrasekar limit re-ignites the thermonuclear reactions. It follows a *type Ia SN* (SN Ia), which disrupts the binary system.

   If $m_{\rm WD} \lesssim m_{\rm Chandra}$, thermonuclear reactions are ignited at the surface of the white dwarf. It ensues a *nova*, that does not disrupt the binary system.

3. The degeneracy pressure is due to the fact that fermions can not occupy the same state. In very dense environments, this leads to a pressure: electron degeneracy pressure in white dwarfs; neutron degeneracy pressure in neutron stars.

IV.1.1.3 Parametrizing Star Formation

Star formation is a complex process involving stars of different masses being formed at different times. At the scale of a star-forming region or an entire galaxy, SF can be described statistically.

Initial mass functions. *Initial Mass Functions* (IMF) express the number distribution of stars of mass $m_\star$ born at a given time: $\phi(m_\star) \equiv \mathrm{d}N_\star/\mathrm{d}m_\star$. IMFs are usually expressed in $\mathrm{M}_\odot^{-1}$, and are normalized as [4]:

$$\int_{m_-}^{m_+} \phi(m_\star)\,\mathrm{d}m_\star = 1, \tag{IV.2}$$

where $m_- = 0.1\,\mathrm{M}_\odot$ and $m_+ = 100\,\mathrm{M}_\odot$ are the lower and upper masses. The average stellar mass is defined as:

$$\langle m_\star \rangle \equiv \int_{m_-}^{m_+} m_\star \phi(m_\star)\,\mathrm{d}m_\star. \tag{IV.3}$$

The fraction of stars ending their life as a core-collapse SN is:

$$f_{\mathrm{SN}} \equiv \int_{m_-^{\mathrm{SN}}}^{m_+^{\mathrm{SN}}} \phi(m_\star)\,\mathrm{d}m_\star, \tag{IV.4}$$

with $m_-^{\mathrm{SN}} = 8\,\mathrm{M}_\odot$ and $m_+^{\mathrm{SN}} = 40\,\mathrm{M}_\odot$ (*e.g.* Heger et al., 2003). Several IMFs have been proposed in the literature (see also Kroupa, 2001).

The Salpeter IMF (Salpeter, 1955) was the first one proposed. It is defined as:

$$\phi_{\mathrm{Salp}}(m_\star) \equiv \frac{(1-\alpha)\times m_\star^{-\alpha}}{m_+^{1-\alpha} - m_-^{1-\alpha}}, \quad \text{with} \quad \alpha = 2.35 \tag{IV.5}$$

where the lower and upper masses, m_- and m_+, are usually taken as $m_- = 0.1\,\mathrm{M}_\odot$ and $m_+ = 100\,\mathrm{M}_\odot$, although the original Salpeter (1955) study constrained the index of the power-law only up to $m_+ = 10\,\mathrm{M}_\odot$.

The Chabrier IMF (Chabrier, 2003) for individual stars is defined, within the same mass range, as:

$$\phi_{\mathrm{Chab}}(m_\star) \equiv \begin{cases} 0.16033 \times m_\star^{-2.3} & \text{for } m_\star > 1\,\mathrm{M}_\odot \\ \dfrac{0.5718}{m_\star} \exp\left(-\dfrac{(\log_{10}(m_\star) + 1.1023729)^2}{0.9522}\right) & \text{for } m_\star \leq 1\,\mathrm{M}_\odot. \end{cases} \tag{IV.6}$$

The top-heavy IMF (*e.g.* Dwek et al., 2007) is often invoked at high-redshift. It is defined as:

$$\phi_{\mathrm{Top}}(m_\star) \equiv \frac{(1-\alpha)\times m_\star^{-\alpha}}{m_+^{1-\alpha} - m_-^{1-\alpha}}, \quad \text{with} \quad \alpha = 1.50 \tag{IV.7}$$

These IMFs are compared in Fig. IV.4. Some of their properties are listed in Table IV.1. The IMF is thought to be a universal property of interstellar media. The different IMFs of Table IV.1 have consequences on the stellar properties. The current consensus is that the Chabrier IMF might be more appropriate than Salpeter's, at least at low redshift.

Parametric star formation histories. We have already briefly discussed *Star Formation Histories* (SFH) in Sect. III.1.2.3. The SFH quantifies the SFR, $\psi(t)$, as a function of time, t, of a star-forming region or galaxy. Several parametric forms are commonly used in the literature. As we will see in Sect. IV.3, their parameters can be inferred by fitting a set of observations.

The exponential SFH (*cf.* Fig. IV.5.a) is parametrized by a timescale, τ_{SF}, and a SFR at $t = 0$, ψ_0:

$$\psi_{\mathrm{exp}}(t) \equiv \psi_0 \exp\left(-\frac{t}{\tau_{\mathrm{SF}}}\right). \tag{IV.8}$$

4. Careful though, some authors quote IMFs, normalized as $\int m_\star \phi(m_\star)\,\mathrm{d}m_\star = 1$.

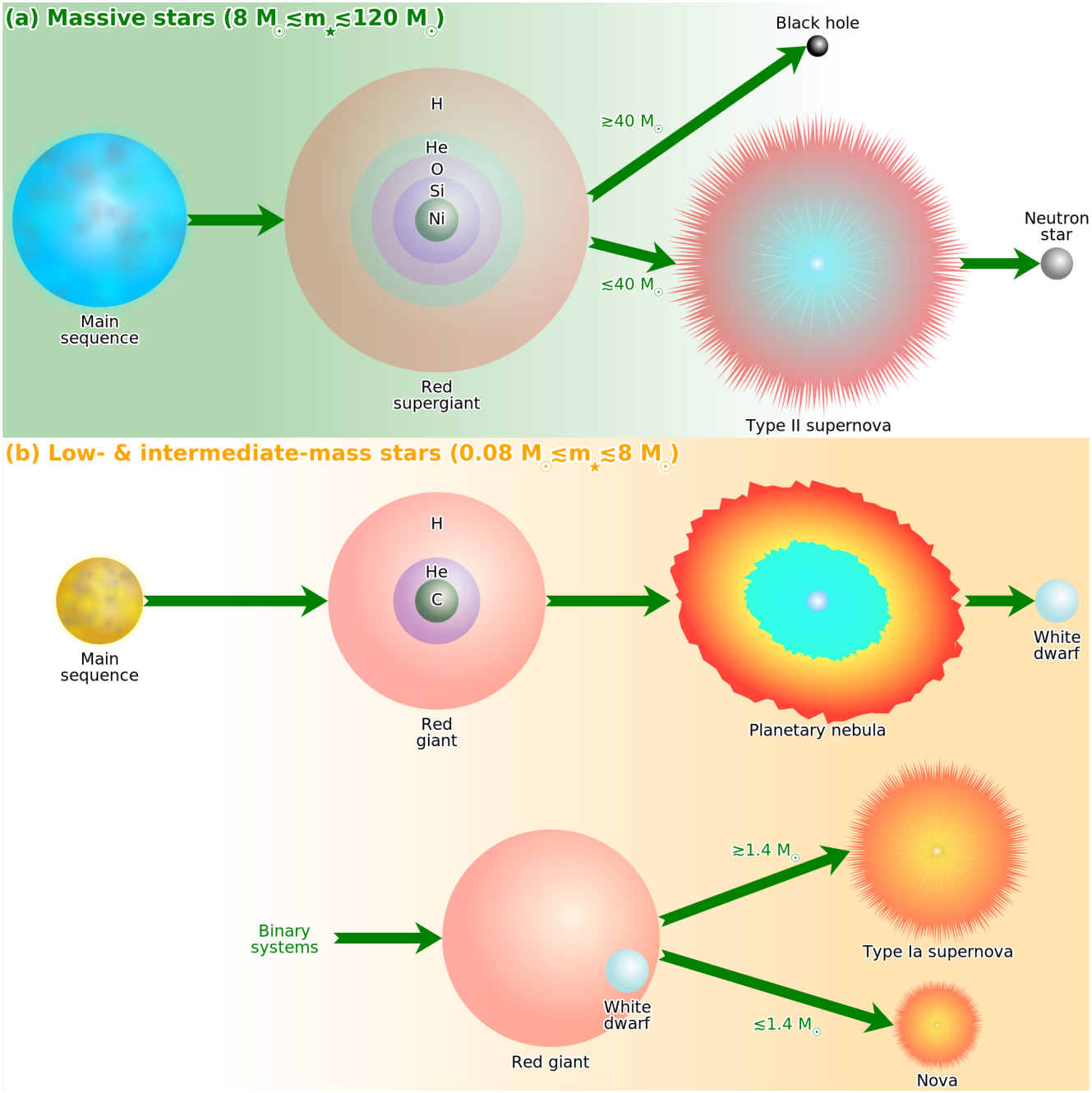

FIGURE IV.3 – *Schematic representation of stellar evolution.* Licensed under CC BY-SA 4.0.

	Salpeter	Chabrier	Top-Heavy
Average mass, $\langle m_\star \rangle$	0.351 $M_\odot$	0.673 $M_\odot$	3.16 $M_\odot$
SN II fraction, f_{SN}	0.239 %	0.724 %	6.38 %
Mass fraction of massive stars	13.9 %	22.6 %	74.1 %
LIMS luminosity ($t_\star = 0$, Z = 0.008)	4.81 $L_\odot/M_\odot$	13.9 $L_\odot/M_\odot$	55.3 $L_\odot/M_\odot$
Massive star luminosity ($t_\star = 0$, Z = 0.008)	180 $L_\odot/M_\odot$	579 $L_\odot/M_\odot$	1.38×10^4 $L_\odot/M_\odot$
Total luminosity ($t_\star = 0$, Z = 0.008)	185 $L_\odot/M_\odot$	593 $L_\odot/M_\odot$	1.38×10^4 $L_\odot/M_\odot$

TABLE IV.1 – *IMF properties.* These properties are integrated over three different IMFs: Salpeter (Eq. IV.5); Chabrier (Eq. IV.6); and Top-heavy (Eq. IV.7). For the last three lines, we used the ZAMS stellar luminosities of Fig. III.18 (initial metallicity Z = 0.008).

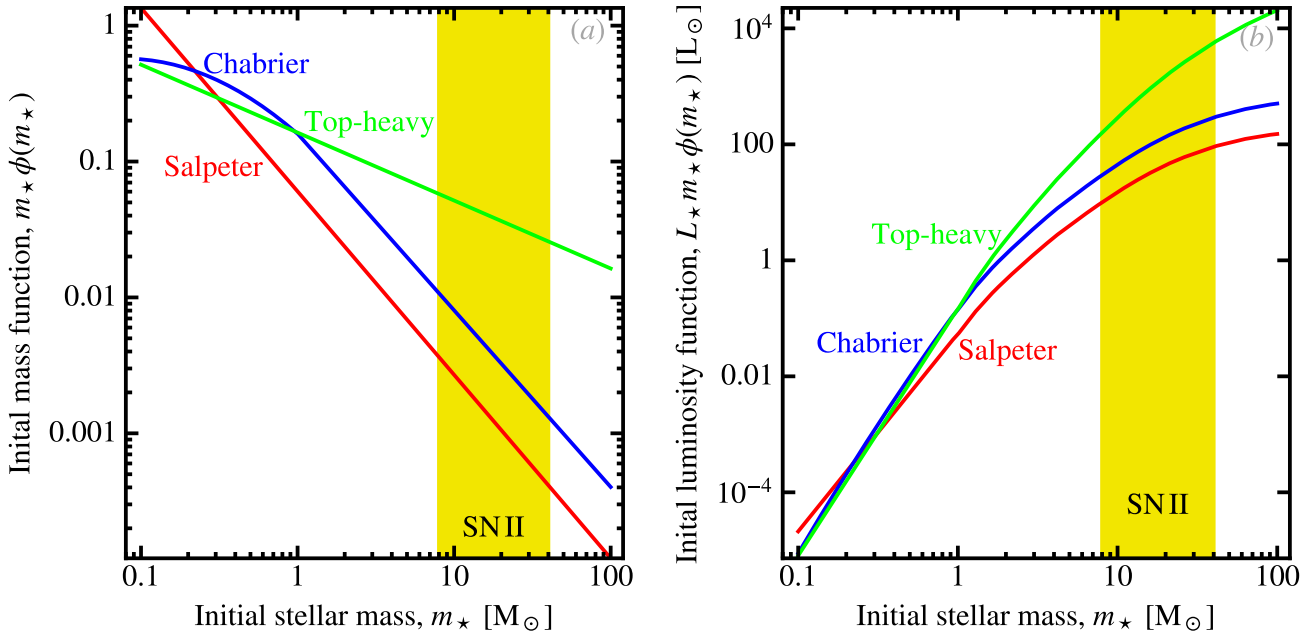

FIGURE IV.4 – *Initial mass functions.* We compare the three IMFs discussed in the text: *(i)* Salpeter (1955) (Eq. IV.5); *(ii)* Chabrier (2003) (Eq. IV.6); and *(iii)* Top-heavy (Eq. IV.7). Panel *(a)* shows the number distribution of stars, $m_\star\phi(m_\star)$. Panel *(b)* shows the luminosity distribution, $L_\star m_\star\phi(m_\star)$, where $L_\star$ comes from Fig. III.18. We have indicated in yellow the range $8 \leq m_\star < 40\,M_\odot$, corresponding to SN II. Licensed under CC BY-SA 4.0.

The delayed SFH (*cf.* Fig. IV.5.b; Lee et al., 2010) has the same number of parameters as the exponential SFH, but its SFR peak is *delayed* at $t = \tau_{SF}$:

$$\psi_{del}(t) \equiv \psi_0 \frac{t}{\tau_{SF}} \exp\left(-\frac{t}{\tau_{SF}}\right). \tag{IV.9}$$

It is possible to combine several SFHs to account for the complex history of a galaxy. A useful quantity, deriving from the SFH, is the *stellar birth rate*, which is the average number of stars born per unit time:

$$B(t) \equiv \frac{\psi(t)}{\langle m_\star \rangle}. \tag{IV.10}$$

The rate of SN II, $R_{SN}(t)$, can be approximated from this quantity:

$$R_{SN}(t) \equiv \int_{m_-^{SN}}^{m_+^{SN}} B\,(t - \tau(m_\star)) \times \phi(m_\star)\,dm_\star \simeq B(t)\,f_{SN}, \tag{IV.11}$$

where $\tau(m_\star)$ is the lifetime of a star of mass $m_\star$ (*cf.* Fig. III.18). The approximation, in the second part of Eq. (IV.11), comes from the fact that the lifetime of massive stars ($\tau(m_\star) \lesssim 30$ Myr) is usually much smaller than the SF timescale: $\tau(m_\star) \ll \tau_{SF}$.

IV.1.2 Elemental and Dust Yields

Stars, in their late stages, return to the ISM a fraction of the heavy elements they have synthesized. Stellar ejecta are: *(i)* stellar winds; *(ii)* planetary nebulae; *(iii)* novae; *(iv)* SN Ia; and *(v)* SN II. In addition, the temperature in these ejecta can be low enough (*cf.* Fig. II.17.b) to condense grains, that we refer to as *stardust*.

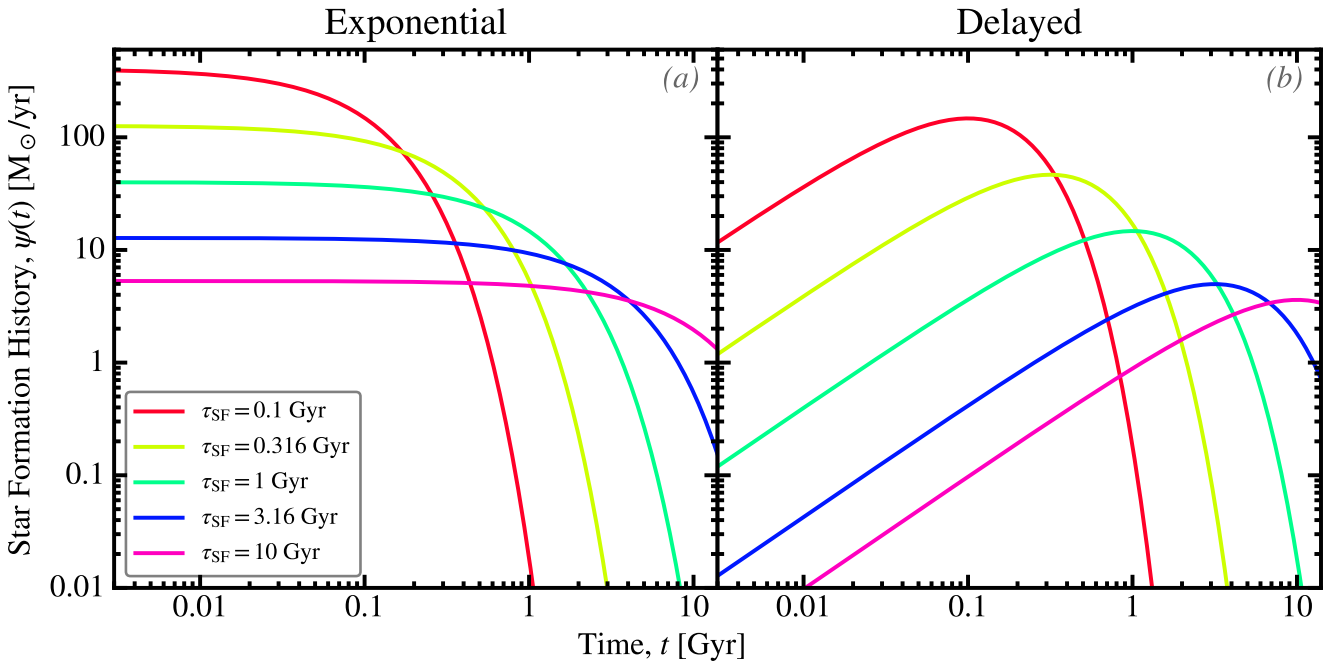

FIGURE IV.5 – *Parametric star formation histories.* Panel *(a)* represents the exponential SFH (Eq. IV.8), for different values of τ_{SF}. Panel *(b)* represents the delayed SFH (Eq. IV.9), for the same grid of τ_{SF}. In both panels, the SFHs are normalized so that the integrated mass of stars formed in Δt = 14 Gyr (about the age of the Universe) is $M_\star = 4 \times 10^{10}$ $M_\odot$ (roughly the MW stellar mass).

IV.1.2.1 Injection of Heavy Elements in the ISM

Fig. IV.6 gives the approximate fraction of each element produced in different environments, for the Solar neighborhood (*e.g.* Johnson, 2019). These proportions depend on the past SFH of the system we are considering.

Primordial nucleosynthesis (*cf.* Sect. IV.1.1.1) is responsible for the production of most of the light elements.

SN II account for most of the ISD-relevant elements, except C.

AGB ejecta (*i.e.* LIMS winds and PNe) account for a significant fraction of C and N, and heavier elements we have not displayed here.

SN Ia are responsible for synthesizing a significant fraction of the metals around Fe.

Other processes, such as cosmic ray fission and merging neutron stars, are not very relevant to ISD.

Stellar elemental yields. A stellar yield, $Y_E(m_\star)$, is the mass of an element E injected into the ISM by a star of mass $m_\star$, at the end of its lifetime. These yields can be constrained observationally, but they are essentially determined theoretically (*e.g.* Karakas & Lattanzio, 2014, for a review). Fig. IV.7.a shows the yields of the most important elements. An important quantity determining the type of dust grains that will form in the ejecta is the C/O ratio. Indeed, when the temperature cools down enough, C and O tend to combine to form CO molecules. The excess atom will thus be the only one left to form stardust. Therefore, stellar ejecta with C < O will form primarily O-rich grains (silicates and oxides), whereas stellar ejecta with C > O will form mainly carbon grains and SiC. Fig. IV.7.b compares the number abundances of C and O ejected by stars of different masses. We can see that carbon grains originate mainly in LIMS around $m_\star \simeq 3\,M_\odot$.

> ☞ SN II are responsible for most O-rich stardust, while LIMS produce most C-rich grain seeds.

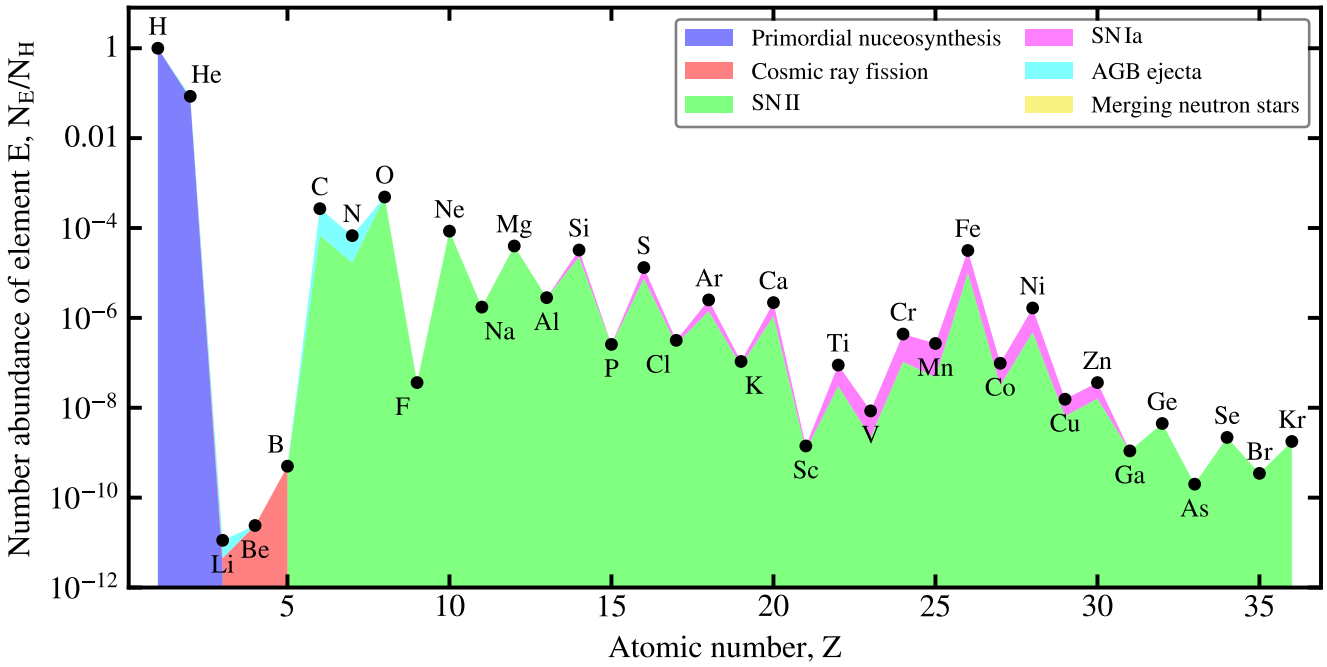

FIGURE IV.6 – *Nucleosynthesis origin of the main elements.* This curve represents the Solar abundances of Asplund et al. (2009) that we have shown in Fig. II.16. We have indicated the fraction of the different sources of nucleosynthesis where these elements originate from (Table S1 of Johnson, 2019). Since we have stopped at Z = 36, none of the elements shown are coming from merging neutron stars. Licensed under CC BY-SA 4.0.

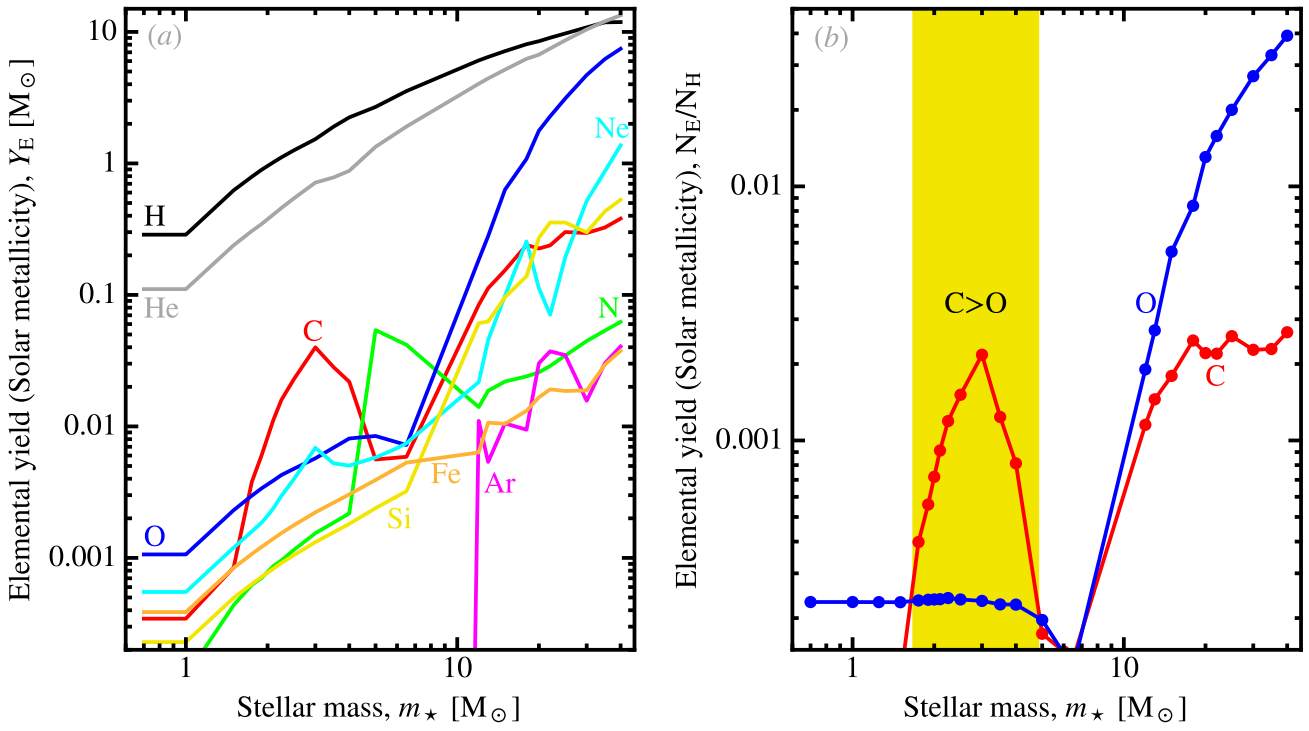

FIGURE IV.7 – *Solar metallicity elemental stellar yields.* Panel *(a)* shows the mass of the most abundant elements ejected by stars of different masses. Panel *(b)* focusses on the stellar mass range where the number abundance of C exceeds that of O (in yellow). These data are the yields used by the chemical evolution model of Galliano et al. (2008a). They are an homogenization of the yields of Karakas & Lattanzio (2003a,b), for LIMS, and of Woosley & Weaver (1995), for high-mass stars. Licensed under CC BY-SA 4.0.

Metallicity estimates. The heavy elements injected by the successive stellar populations increase the metallicity of the ISM, Z. In that sense, the metallicity is an indicator of "*the fraction of baryonic matter that has been converted into heavier elements by means of stellar nucleosynthesis*" (Kunth & Östlin, 2000), such that:

$$\left\{\begin{array}{lcl} X_{primordial} & \simeq & 0.76 \\ Y_{primordial} & \simeq & 0.24 \\ Z_{primordial} & \simeq & 0.00 \end{array}\right. \longrightarrow \left\{\begin{array}{lcl} X_{\odot} & \simeq & 0.74 \\ Y_{\odot} & \simeq & 0.25 \\ Z_{\odot} & \simeq & 0.01. \end{array}\right. \tag{IV.12}$$

The measure of metallicity is not completely straightforward and is vigorously debated (*e.g.* Kewley et al., 2019, for a review). In external galaxies, it is usually estimated by modeling observations of nebular optical lines, coming from H II regions. Several methods, allowing an observer to convert a few line ratios into a metallicity estimate, have been proposed. These methods have been calibrated on particular H II regions, modeling the photoionization, making unavoidable assumptions about the stellar populations and the topology of the gas. We have systematically compared several calibrations over the DustPedia sample (De Vis et al., 2019). We have favored the "S" calibration from Pilyugin & Grebel (2016), as it is the most reliable down to low metallicities.

IV.1.2.2 Production of Stardust

At the scale of a galaxy, the two most important sources of stardust are: *(i)* AGB stars, encompassing both LIMS winds and PNe; and *(ii)* SN II.

AGB stars. Most of the dust production in LIMS is believed to occur during the *Thermally-Pulsing Asymptotic Giant Branch* (TPAGB) phase (Gail et al., 2009). In addition, LIMS with $m_{\star} \lesssim 1\,M_{\odot}$ do not condense grains (*e.g.* Ferrarotti & Gail, 2006). Theoretical models concur that only a fraction of the available heavy elements will go into stardust (Morgan & Edmunds, 2003; Ventura et al., 2012):

$$\delta_{LIMS} \equiv \frac{m^{ej}_{stardust}}{m^{ej}_{Z}} \simeq 10-40\,\%, \tag{IV.13}$$

$m^{ej}_{stardust}$ and m^{ej}_{Z} being the ejected mass of stardust and heavy elements. Observations and modeling of the circumstellar envelopes of post-AGB stars are consistent with these values (*e.g.* Ladjal et al., 2010).

SN II. There is solid evidence that grains form in *SuperNova Remnants* (SNR), as the ejected gas cools down. Theoretical estimates of the net dust yield of a single SN II range in the literature from $Y_{SN} \simeq 10^{-3}$ to $Y_{SN} \simeq 1\,M_{\odot}/SN$ (*e.g.* Todini & Ferrara, 2001; Ercolano et al., 2007; Bianchi & Schneider, 2007; Bocchio et al., 2016; Marassi et al., 2019). From an observational point of view, measuring the dust mass produced *in situ* by a single SN II is quite difficult, as it implies disentangling the freshly-formed dust from the surrounding ISM. It also carries the usual uncertainty about dust optical properties. A decade ago, the largest dust yield ever measured was $Y_{SN} \simeq 0.02\,M_{\odot}$ (in SN 2003gd; Sugerman et al., 2006). The *Herschel* space telescope has been instrumental in estimating the cold mass of SNRs. The yields of the three most well-studied SNRs are now an order of magnitude higher:

Cassiopeia A: $Y_{SN} \simeq 0.04-1.1\,M_{\odot}$ (Barlow et al., 2010; Arendt et al., 2014; De Looze et al., 2017; Bevan et al., 2017; Priestley et al., 2019);

The Crab nebula: $Y_{SN} \simeq 0.03-0.23\,M_{\odot}$ (Gomez et al., 2012; Temim & Dwek, 2013; De Looze et al., 2019);

SN 1987A: $Y_{SN} \simeq 0.45-0.8\,M_{\odot}$ (Dwek & Arendt, 2015; Matsuura et al., 2015).

Most of the controversy however lies in the fact that, while large amounts could form in SN II ejecta (*e.g.* Matsuura et al., 2015; Temim et al., 2017), a large fraction of freshly formed grains would not survive the reverse shock ($v \simeq 1000$ km/s; *e.g.* Nozawa et al., 2006; Micelotta et al., 2016; Kirchschlager

et al., 2019). In all the cases we have listed above, the newly-formed grains have indeed not yet experienced the reverse shock (Bocchio et al., 2016). The net yield is thus expected to be significantly lower. Even if $\simeq 10-20\,\%$ of the dust condensed in an SN II ejecta survives its reverse shock (*e.g.* Nozawa et al., 2006; Micelotta et al., 2016; Bocchio et al., 2016), we have to also consider the fact that massive stars are born in clusters. The freshly-formed dust injected by a particular SN II, having survived the reverse shock, will thus be exposed to the forward shock waves of nearby SNe (*e.g.* Martínez-González et al., 2018). Overall, SN II dust yields are largely uncertain. We will extensively discuss their empirical constraint, from a statistical point of view, in Sect. IV.3. We will show that we can infer the average dust yield per SN II, $\langle Y_{SN} \rangle$. The corresponding timescale is then simply:

$$\frac{1}{\tau_{\text{SN-cond}}(t)} \equiv \frac{\langle Y_{SN} \rangle}{M_{\text{dust}}(t)} R_{SN}(t). \tag{IV.14}$$

Indirect evidence. The best constraints on the fraction of ISD which is stardust might be indirect. The clear correlation between the depletion factor, $F_\star$, and the average density of the ISM, $\langle n_H \rangle$, that we have discussed in Fig. II.17.a, has been shown to require rapid destruction and reformation into the ISM (*e.g.* Draine & Salpeter, 1979; Tielens, 1998; Draine, 2009). The rest of the grains needs to form in the ISM. Draine (2009, D09) gives a series of additional arguments concluding that, in the MW, stardust has to be less than 10 % of ISD.

1. A first argument given by D09 is based on the typical lifetime of ISD.
   - *a)* From the literature, the stardust injection rate is roughly $\dot{M}_{\text{stardust}} \simeq 5 \times 10^{-3}\,M_\odot/\text{yr}$.
   - *b)* Noting that the typical lifetime of a dust grain in the MW is $\tau_{ISD} \simeq 3 \times 10^8$ yr (*cf.* Sect. IV.2.2.3; Jones et al., 1996), the present stardust mass in the ISM should be: $M_{\text{stardust}} \simeq \dot{M}_{\text{stardust}} \times \tau_{ISD} \simeq 1.5 \times 10^6\,M_\odot$.
   - *c)* The ISD mass in the MW is roughly $M_{ISD} \simeq M_{ISM}/183 \simeq 2.7 \times 10^7\,M_\odot$ (*cf.* Table II.4).

   Stardust is thus only $M_{\text{stardust}}/M_{ISD} \simeq 5\,\%$ of the total ISD.
2. A second argument given by D09 is based on the study of IDPs in meteorites (*cf.* Sect. II.2.4).
   - *a)* Stardust silicate grains in meteorites, identified with their isotopic anomalies (*cf.* Fig. II.19), appear to be $\simeq 20\,\%$ crystalline.
   - *b)* Silicates in the ISM are less than $\lesssim 2\,\%$ crystalline (*cf.* Sect. II.2.1.2; Kemper et al., 2004).

   Therefore, the fraction of stardust is only less than $\lesssim 2/20 \simeq 10\,\%$ of ISD. Also, the fact that ISD is mainly amorphous, whereas circumstellar grains are essentially crystalline, is another argument in favor of rapid destruction and reformation in the ISM.

☞ In the MW, stardust represents only a few percents of the ISD content.

IV.2 Dust Evolution Processes in the ISM

Most of the important dust evolution processes occur in the ISM. These effects can be studied by looking at spatial variations of the dust properties in a region.

IV.2.1 Grain Formation and Transformation

Grain formation is the transfer of elements from the gas phase to the dust phase, therefore increasing the dustiness.

IV.2.1.1 Evidence of Grain Growth and Coagulation in the ISM

We have just discussed stardust (*cf.* Sect. IV.1.2.2) which is thought to produce grain seeds onto which mantle can grow. We now focus on the dominant process in Solar metallicity systems: the accretion of gas phase atoms and molecules. Grain-grain coagulation does not result in grain formation *per se*, as it does not affect the dustiness. It however follows grain growth and has similar effects on the FIR opacity.

The evidence brought by depletions. As we have discussed in Sect. IV.1.2.2, the clearest evidence of grain growth in the ISM is provided by the good correlation between the depletion factor and the average density of the ISM (*cf.* Fig. II.17.a). It implies that atoms and molecules from the gas phase are progressively building up grain mantles, when going into denser regions. This observed behaviour is also consistent with the progressive de-mantling and disaggregation of cloud-formed, mantled and coagulated grains injected into the low density ISM, following cloud disruption. It is perhaps not unreasonable to hypothesise that dust growth in the ISM occurs on short timescales during cloud collapse rather than by dust growth in the quiescent diffuse ISM. In this alternative interpretation, the arrow of time is in the opposite sense and requires rapid dust growth, through accretion and coagulation, in dense molecular regions and slow de-mantling and disaggregation in the diffuse ISM (*e.g.* Jones, 2009). Given that astronomical observations provide only single-time snapshots, it will seemingly be difficult to determine the direction of the time-arrow of dust evolution.

FIR opacity variations. We have seen in Fig. I.21 that the growth of mantles has an impact on the FIR opacity (*cf.* Köhler et al., 2014, 2015). Yet, there is clear evidence of FIR opacity variations in the MW. The main factor seems to be the density of the medium. For instance, both Stepnik et al. (2003) and Roy et al. (2013) found that the FIR dust cross-section per H atom increases by a factor of $\simeq 3$ from the diffuse ISM to the molecular cloud they targeted. Stepnik et al. (2003) noticed that this opacity variation is accompanied by the disappearance of the small grain emission. They concluded that grain coagulation could explain these variations. In the diffuse ISM, Ysard et al. (2015) showed that the variation of emissivity, including the $\beta - T$ relation (*cf.* Sect. III.1.2.1), could be explained by slight variations of the mantle thickness of the THEMIS model. For that reason, the THEMIS model aims at describing the evolution of grain mantles as a function of density and ISRF, as we have seen in Fig. I.21: *(i)* in the diffuse ISM, the grains are supposed to have a thin a-C mantle, largely dehydrogenated (aromatic) by UV photons; *(ii)* in denser regions, the mantle thickness is hypothesized to increase and to become more hydrogenated (aliphatic), because of the progressive shielding of stellar photons; *(iii)* in molecular clouds, grains are thought to be coagulated and iced. The THEMIS model predicts a factor of $\simeq 2.5$ dust mass increase in going from MW diffuse to dense clouds. This would correspond to a factor up to $\simeq 7$ in terms of dust emissivity per H atom (Köhler et al., 2015).

IV.2.1.2 Studies of the Magellanic Clouds

In nearby galaxies, studies of the local grain processing are difficult to conduct, as the emissivity variations are smoothed out by the mixing of dense and diffuse regions. Even when potential evolutionary trends are observed, their interpretation is often degenerate with other factors. The Magellanic clouds are the most obvious systems where this type of study can be attempted. The insights provided by depletion studies (*cf.* Sect. II.2.3) show that there are clear variations of the fraction of heavy elements locked-up in dust, and these variations correlate with the density (Tchernyshyov et al., 2015; Jenkins & Wallerstein, 2017). Since the coagulation and the accretion of mantles lead to an increase of FIR emissivity (*cf.* Fig. I.21; Köhler et al., 2015), we should expect emissivity variations in the Magellanic clouds. Indeed, Roman-Duval et al. (2017) studied the trends of gas surface density (derived from HI and CO) as a function of dust surface density (derived from the IR emission), in these galaxies. They found that the observed dustiness of the LMC increases smoothly by a factor of $\simeq 3$ from the diffuse to the dense regions. In the SMC, the same variation occurs, with a factor of $\simeq 7$. They argue

that optically thick HI and CO-free H_2 gas (*cf.* Sect. III.3.2.3) can not explain these trends, and that grain growth is thus the most likely explanation.

Spatially-resolved SED fitting of LMC-N44 and SMC-N66. We have conducted a similar study, focussing on two massive star-forming regions, rather than the whole galaxies[5]: *(i)* N44 in the LMC; and *(ii)* N66 in the SMC (Galliano, 2017). Our maps were 200 pc wide regions, with a spatial resolution of ≃ 15 pc. The MIR-to-submm data were coming from the SAGE/HERITAGE surveys (*Spitzer* and *Herschel* data; Meixner et al., 2006, 2013). We used the hierarchical Bayesian SED model, `HerBIE`, with the AC dust composition of Galliano et al. (2011, *cf.* Sect. III.1.3.3). The goal was to perform a spatially-resolved modeling of the dust properties, in a region with a strong gradient of physical conditions, in order to probe dust processing, as a function of density, ISRF and metallicity. The wide range of physical conditions can be estimated by looking at the range of SEDs shown in Fig. IV.8. In both panels, the faintest pixels show a rather cold SED, peaking around λ ≃ 100 µm, whereas the brightest pixels peak around λ ≃ 60 µm, with a very broad FIR bump, indicating a wide range of ISRF intensities, typical of compact SF regions (*cf.* Sect. III.1.2.2).

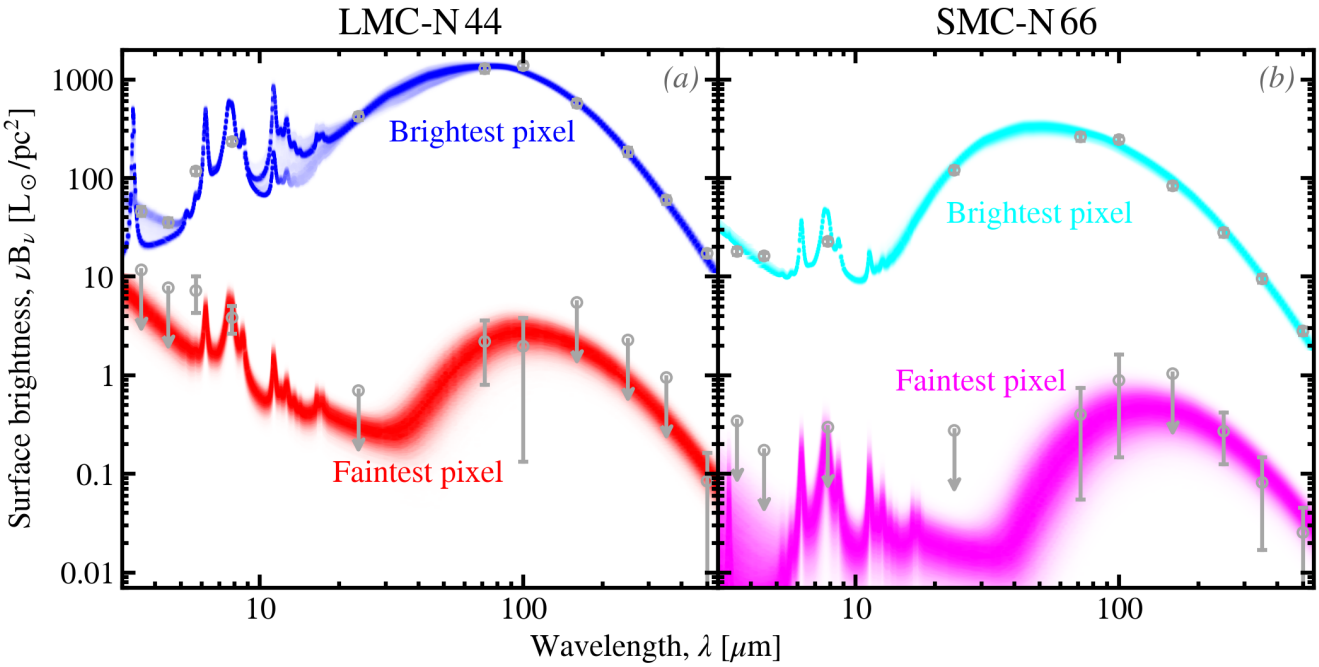

FIGURE IV.8 – *Spatially-resolved SED fits in N44 and N66.* In both panels, we show the brightest and the faintest pixels of our entire map. The grey error bars are the observations, and the colored densities are the Bayesian posterior distributions of SED models (Galliano, 2017). Licensed under CC BY-SA 4.0.

Derived dust-gas relations. We have compared the derived dust and total gas column densities. The latter was estimated from the $[HI]_{21\,cm}$ and $^{12}CO(J{=}1{\rightarrow}0)_{2.6mm}$ measurements (Meixner et al., 2006; Gordon et al., 2011; Meixner et al., 2013). The results are displayed in Fig. IV.9. The orange line represents the Galactic dustiness (*cf.* Table II.4) scaled by the metallicity, therefore representing the Galactic dust-to-metal mass ratio. This line corresponds to the values we would expect if the dust constitution was close to the diffuse ISM of the MW and was not evolving with density. The most diffuse pixels in both regions are consistent with this value. The hatched yellow area corresponds to a dustiness larger than the metallicity, that is requiring more heavy elements in dust than what is available in the ISM. Overall, the trends of Fig. IV.9 indicate a non-linear dust-to-gas relation, with a variation of the observed dustiness by a factor of ≃ 3, similar to the studies we have reviewed at the

5. As a reminder, the metallicities of the Magellanic clouds are: $Z_{LMC} \simeq Z_\odot/2$ and $Z_{SMC} \simeq Z_\odot/5$ (Pagel, 2003).

beginning of this section. The high density pixels lie in the forbidden zone. The possible causes are the following.

Grain growth: a part of this trend is likely the result of the evolution of the *true* dustiness, due to mantle accretion in denser regions. The yellow hatched area can however be considered as a hard upper limit, as in practice, not all heavy elements are refractory: even in the densest molecular clouds, there are gas phase CO, HCN, *etc.* This sole factor is therefore probably not sufficient to explain the full extent of the *observed* dustiness variation.

Emissivity increase: grain growth and coagulation are accompanied by an increase of FIR emissivity (*cf.* Fig. I.21; Köhler et al., 2015). This effect is naturally expected and would amplify the increase of the *observed* dustiness with density, as the constant emissivity assumption of our SED model would lead us to overestimate the dust mass of dense regions.

Contribution of dark gas: we have not accounted for CO-dark gas (*cf.* Sect. III.3.2.3). This component can potentially bias the molecular gas mass estimate in translucent regions by up to a factor ≃ 100 (Madden et al., 2020). It could also explain a part of the trend, as it would result in an underestimate of the total gas mass. This effect should however be significative at intermediate column densities, and decrease toward the densest regions, where CO would dominate. It might thus not be the main cause of the non-linearity of our trends.

☞ There is multiple evidence of dust evolution as a function of density, consistent with grain growth and coagulation, and the consequent increase of emissivity.

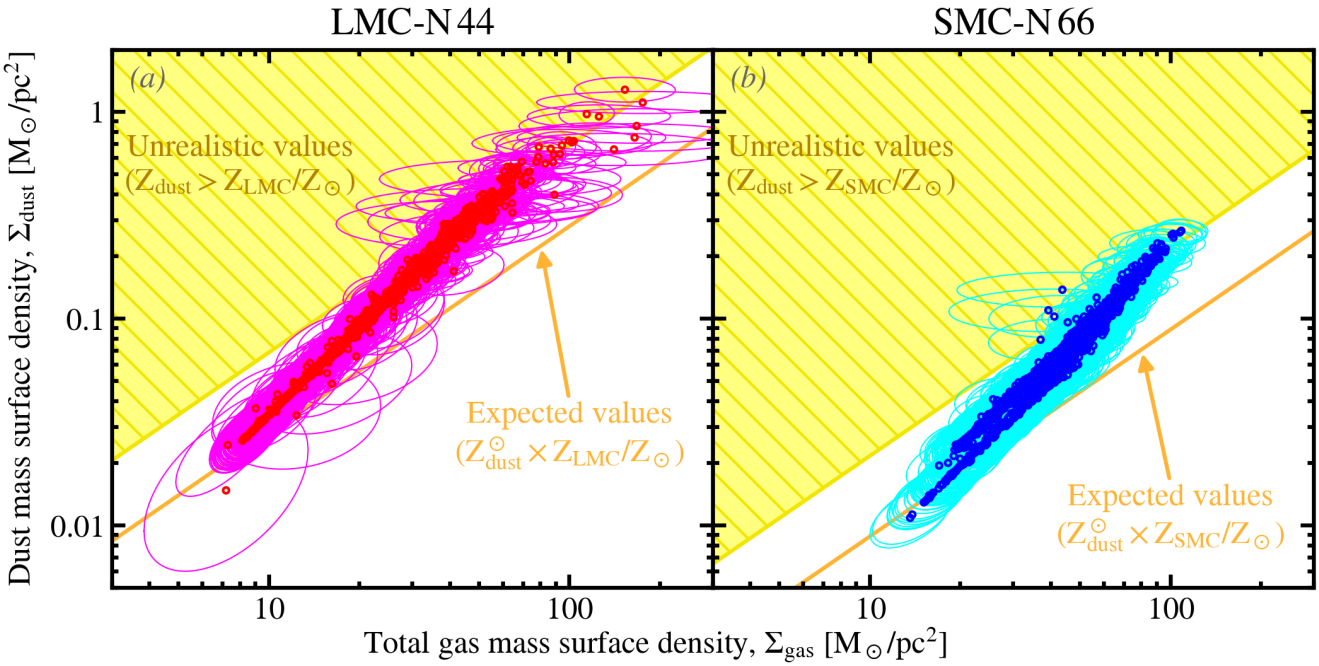

FIGURE IV.9 – *Dust-to-gas mass surface density relation in N44 and N66.* In both panels, we show the trends of dust mass surface density as a a function of the total gas mass (atomic and molecular) surface density derived from the SED fitting of Fig. IV.8 (Galliano, 2017). Each point, with its uncertainty ellipse, corresponds to ≃ 15 pc pixel. The orange line corresponds to the dustiness of the MW (*cf.* Table II.4) scaled by the metallicity of the region. The yellow hatched area corresponds to a dustiness larger than the metallicity, that is an unrealistic value requiring more heavy elements being locked up in grains than what is available in the ISM. Licensed under CC BY-SA 4.0.

IV.2.1.3 Quantifying Grain Growth

We now discuss the way grain growth can be approximately quantified. The following relations are rather uncertain, because of the lack of constraint on grain structure and composition. They however

provide a framework to study grain growth efficiency.

Accretion timescale. Timescales for grains to accrete atoms are widely discussed in the literature (*e.g.* Dwek, 1998; Edmunds, 2001; Draine, 2009; Hirashita & Kuo, 2011; Zhukovska et al., 2016; Priestley et al., 2021). First, the collision rate of an atom E of mass $m_{\rm E}$, with a grain of radius a is:

$$\frac{1}{\tau_{\rm coll}(a,{\rm E})} \equiv \underbrace{\pi a^2}_{\text{grain cross-section}} \times \underbrace{n_{\rm E}}_{\text{gas density of E}} \times \underbrace{\sqrt{\frac{8kT_{\rm gas}}{\pi m_{\rm E}}}}_{\text{Maxwellian velocity of E}} . \tag{IV.15}$$

In this equation, we have implicitly neglected Coulomb interaction (*i.e.* we have assumed that the grain and the atom are both neutral, which is a reasonable assumption in the CNM). Second, the growth rate of a grain of mass $m_{\rm d}(a)$, due to accretion following these collisions, can be written:

$$\left(\frac{{\rm d}m_{\rm d}}{{\rm d}t}\right)_{\rm acc}(a,{\rm E}) = \underbrace{\mathscr{S}}_{\text{sticking probability}} \times \underbrace{\frac{m_{\rm E}}{f_{\rm E}}}_{\text{gained mass}} \times \underbrace{\frac{1}{\tau_{\rm coll}(a,{\rm E})}}_{\text{rate}}, \tag{IV.16}$$

where $0 \leq \mathscr{S} \lesssim 1$ is the *sticking coefficient*, that is the probability the atom will be bound with the grain after the collision. The factor $f_{\rm E}$ is the mass fraction of element E within the grain. We choose E as a *key element* (Zhukovska et al., 2008), that is the element in the grain make-up that will have the longest collision time.

For silicates, the key element is Si, with $f_{\rm Si} \simeq 0.16$ for olivine and $f_{\rm Si} \simeq 0.24$ for pyroxene (assuming Fe:Mg=1:1). In other words, for each collision with Si, there are more collisions with O, Fe and Mg. Therefore, the dust mass gained between two Si collisions is the mass of a full crystal unit (SiO_4MgFe for olivine $SiO_3Mg_{0.5}Fe_{0.5}$ for pyroxene; *cf.* Sect. I.1.4.1).

For carbon grains, the mass is essentially C, as H is negligible. We thus have $f_{\rm C} \simeq 1$.

Finally, it is convenient to express this quantity as an *accretion timescale*, $\tau_{\rm acc}(a)$:

$$\frac{1}{\tau_{\rm acc}(a)} \equiv \frac{1}{m_{\rm d}(a)}\left(\frac{{\rm d}m_{\rm d}}{{\rm d}t}\right)_{\rm acc}(a,{\rm E}) = \mathscr{S}\frac{\sqrt{m_{\rm E}}}{f_{\rm E}}\frac{3n_{\rm E}}{2a\rho}\sqrt{\frac{2kT_{\rm gas}}{\pi}}, \tag{IV.17}$$

where we have simply developed $m_{\rm d}(a) = 4/3\pi a^3\rho$ in the second equality, ρ being the mass density of the grain. The density of the element E can be written as a function of the total H density, assuming its abundance scales with metallicity:

$$n_{\rm E} \simeq \left(\frac{\rm Z}{\rm Z_\odot}\right)\left(\frac{\rm E}{\rm H}\right)_\odot n_{\rm H}. \tag{IV.18}$$

We therefore see that the grain growth timescale roughly obeys the following proportionality (assuming $\mathscr{S} = 1$ and olivine composition of silicates):

$$\tau_{\rm acc}(a) \simeq \frac{100\,{\rm cm^{-3}}}{n_{\rm H}} \times \frac{\rm Z_\odot}{\rm Z} \times \sqrt{\frac{100\,{\rm K}}{T_{\rm gas}}} \times \frac{a}{100\,{\rm nm}} \times \begin{cases} 57\,{\rm Myr} & \text{for silicates} \\ 41\,{\rm Myr} & \text{for carbon grains.} \end{cases} \tag{IV.19}$$

As said above, these estimates are uncertain. We especially have no idea of the sticking probability, $\mathscr{S}$. Eq. (IV.19) however provides a description of the sensitivity of grain growth to density, size and metallicity. It is also indicative of the lower limit of these timescales.

Grain growth in different ISM phases. Fig. IV.10 displays Eq. (IV.19) for carbon and silicate grains in the most relevant ISM phases. Timescales longer than the typical destruction timescales by SN II blast waves are irrelevant. That is the reason why this range is hatched in yellow in Fig. IV.10.

In the WNM, only the smallest grains ($a \lesssim 10$ nm) could grow. The WNM is thus not very suitable for grain growth.

In the CNM, all grain sizes can grow in less than 300 Myr. The CNM is thus a phase where dust growth could happen.

In diffuse molecular clouds, growth timescales are roughly similar to the CNM. The same conclusion therefore applies.

In dense molecular clouds, all relevant interstellar grain sizes can grow in less than $\simeq 10$ Myr, which is also the typical lifetime of these clouds, in star-forming regions.

These timescales are consistent with the picture painted by the variation of elemental depletions across phases (*cf.* Fig. II.17.a). To estimate a global growth timescale, let's consider the radius corresponding to the average mass of the THEMIS model, in Table II.3:

$$\sqrt[3]{\langle a^3 \rangle_a} \simeq \begin{cases} 31\,\text{nm} & \text{for silicates} \\ 28\,\text{nm} & \text{for large a-C(:H).} \end{cases} \tag{IV.20}$$

With these sizes, a typical accretion time in the CNM would be $\tau_{\text{acc}} \simeq 58$ Myr for silicates, and $\tau_{\text{acc}} \simeq 38$ Myr for large a-C(:H).

☞ Grains can possibly grow in the CNM, on timescales of $\gtrsim 30 - 60$ Myr, and faster in molecular clouds.

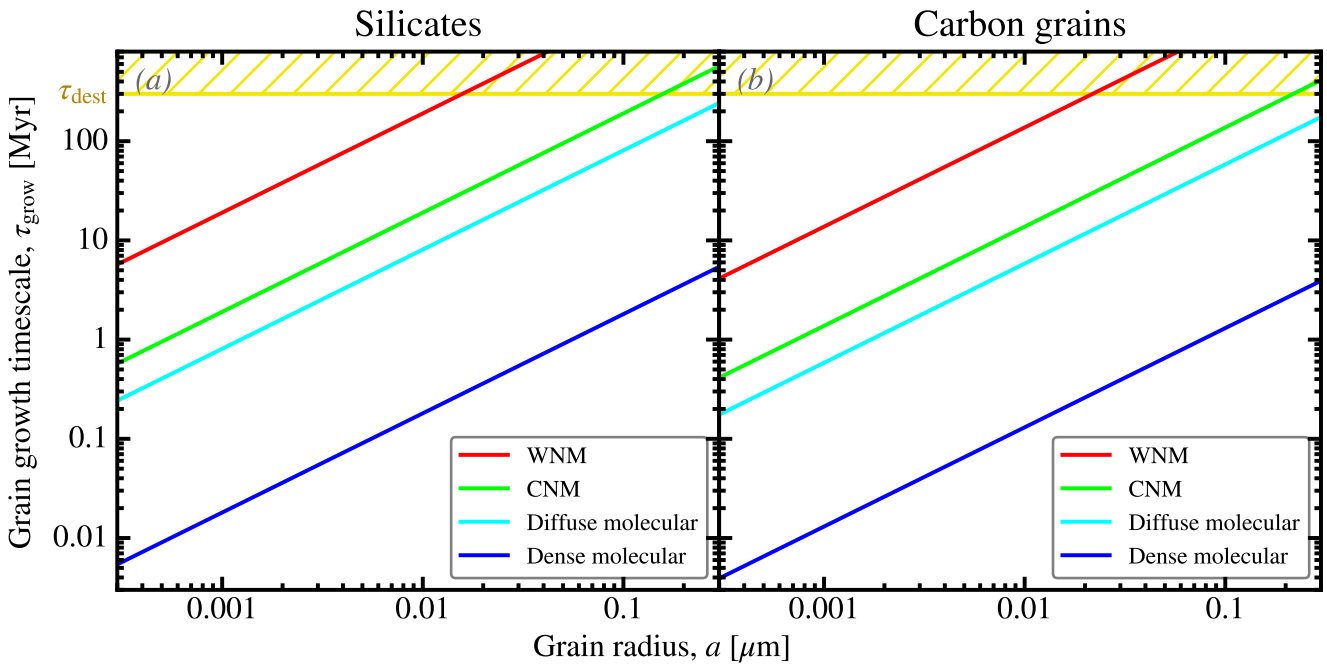

FIGURE IV.10 – *Grain growth timescales.* Both panels represent Eq. (IV.19) for several of the phases in Table III.6 (taking $n_{\text{H}} = 10^4$ cm^{-3} for the dense molecular phase). We have assumed $\mathcal{S} = 1$ for both silicates and carbon grains. We have highlighted timescales longer than the typical shock destruction timescale, $\tau_{\text{SN-dest}} \simeq 300$ Myr (*cf.* Sect. IV.2.2.3), in hatched yellow. Licensed under CC BY-SA 4.0.

Relation to global parameters. As we will see in Sect. IV.3, it is convenient to relate the grain growth timescale to global galaxy parameters. Mattsson et al. (2012) proposed a relation based on the following assumptions.

1. Most of grain growth happens in molecular clouds. The mass surface density of these molecular clouds, $\Sigma_{\rm mol}$, is proportional to the SFR surface density, $\Sigma_{\rm SFR}$ (*e.g.* Kennicutt, 1998b). Grain growth rate is thus proportional to $\Sigma_{\rm SFR}$:
$$\frac{\Sigma_{\rm gas}}{\tau_{\rm grow}} \propto \Sigma_{\rm SFR}. \tag{IV.21}$$
2. The grain growth rate is also proportional to the fraction of available heavy elements in the gas. It implies that:
$$\frac{\Sigma_{\rm gas}}{\tau_{\rm grow}} \propto \Sigma_{\rm SFR} \times \left(1 - \frac{Z_{\rm dust}}{Z}\right) Z, \tag{IV.22}$$
where $Z_{\rm dust}$ is the dustiness, and $Z_{\rm dust}/Z$, the dust-to-metal mass ratio (*cf.* Sect. II.2.3.2). By subtracting $Z_{\rm dust}/Z$, we account for the fact that the fraction of heavy elements already locked up in grains does not contribute to grain growth.
3. The other parameters in Eq. (IV.19) are assumed to not vary significantly. These parameters are the mean grain size, the mean gas velocity and mean density of molecular clouds.

The grain growth rate proposed by Mattsson et al. (2012) can thus be parametrized as a function of global galactic quantities and a phenomenological, dimensionless parameter, $\epsilon_{\rm grow}$, containing all our uncertainties. The goal is to empirically infer $\epsilon_{\rm grow}$, as we will see in Sect. IV.3. Eq. (IV.22) thus becomes:
$$\frac{1}{\tau_{\rm grow}(t)} = \epsilon_{\rm grow} \frac{\psi(t)}{M_{\rm gas}(t)} (Z(t) - Z_{\rm dust}(t)), \tag{IV.23}$$
where we have replaced the ratio of surface densities by the ratio of the quantities, and have explicited the temporal dependencies. In the case of the MW ($\psi \simeq 1.3\,M_\odot/{\rm yr}$; $M_{\rm gas} \simeq 7 \times 10^9\,M_\odot$), a grain growth timescale of $\tau_{\rm grow} \simeq 60$ Myr (Eq. IV.19) corresponds to $\epsilon_{\rm grow} \simeq 10^4$.

IV.2.2 Grain Destruction

We now discuss grain destruction, that is the return of heavy elements from the grains to the gas phase. Note that fragmentation and shattering by shock waves (at $v \lesssim 200$ km/s), that we have discussed in Sect. IV.2.2.3, simply rearrange the size distribution without destroying the dust. Shocks however have a pulverization effect, accompanying the other processes, that are difficult to differentiate from an observational point of view.

IV.2.2.1 Photodestruction of Small Grains

Due to thermal spikes, small grains have a certain probability that one of their atom will be ejected. This is a runaway process leading to the complete sublimation of the dust grain.

Photodesorption and sublimation. Following the formalism of Guhathakurta & Draine (1989), we consider a cluster X_N containing N atoms of X (X can be C, Fe, Si, O, *etc.*). The ejection of an atom from the grain is balanced by the return of an atom from the gas phase. The rate of the reaction $X_N + X \leftrightarrows X_{N+1}$ is $R_N A_N$, where the total grain surface is $A_N = 4\sigma_N \simeq 4\pi a^2$. Guhathakurta & Draine (1989) write the sublimation rate as:
$$\frac{dN}{dt} = -R_N(T) \times S_N(T) \times A_N, \tag{IV.24}$$
and provide the following rates for graphite and silicate:
$$R^{\rm gra}_{N+1}(T) \simeq 4.6 \times 10^{33} \left(\frac{\alpha_N}{0.1}\right) \exp\left(-\frac{B_{\rm gra}}{kT}\right) {\rm m}^{-2}\,{\rm s}^{-1}, \tag{IV.25}$$
$$R^{\rm sil}_{N+1}(T) \simeq 4.9 \times 10^{34} \left(\frac{\alpha_N}{0.1}\right) \exp\left(-\frac{B_{\rm sil}}{kT}\right) {\rm m}^{-2}\,{\rm s}^{-1}, \tag{IV.26}$$

with the binding energy per atom:

$$B_{gra}/k = 81\,200 - 20\,000N^{-1/3}\,K, \quad \text{(IV.27)}$$

$$B_{sil}/k = 68\,100 - 20\,000N^{-1/3}\,K. \quad \text{(IV.28)}$$

The sticking coefficients, α_N, is unknown and is arbitrarily chosen by the authors to be $\alpha_N \simeq 0.1$. Assuming the surface free energy is about 2×10^4 K, the term $-20\,000N^{-1/3}$ accounts for the surface tension, making it easier to release an atom when the grain is smaller. Finally, the *suppression factor*, $S_N(T) < 1$, accounts for the suppression of the thermal fluctuations in a thermally isolated particle. This factor is:

$$S_N(T) = \left(\frac{1+\gamma}{\gamma}\right)^b \frac{\Gamma(\gamma f+1)\Gamma(\gamma f+f-b)}{\Gamma(\gamma f-b+1)\Gamma(\gamma f+f)}, \quad \text{(IV.29)}$$

where $f = 3N-6$ is the number of vibrational degrees of freedom (*cf.* Sect. I.2.3). In addition, the mean number of quanta per degree of freedom is $\gamma = H(T)/(\hbar\omega_0 f)$, and the number of quanta necessary to release a particle is $b = B/(\hbar\omega_0)$. Guhathakurta & Draine (1989) take $\hbar\omega_0 = 0.75\Theta$, where Θ is the Debye temperature (taking $\Theta_{gra} = 420$ K and $\Theta_{sil} = 470$ K; *cf.* Sect. I.2.3.2). The mean lifetime is then integrated over the temperature distribution:

$$\frac{1}{\tau_{subl}} = \int \frac{dP}{dT} R_N(T) S_N(T) A_N \, dT. \quad \text{(IV.30)}$$

Guhathakurta & Draine (1989) assume that a grain does not survive if it has a lifetime $\lesssim 10^{13}$ s $\simeq$ 0.3 Myr. Fig. IV.11 displays these lifetimes for silicates and graphite bathed in the Mathis et al. (1983) ISRF. Although the exact numbers are to be taken with caution, we can conclude the following.

1. In the diffuse ISM of the MW ($U = 1$), silicates larger than $a \simeq 4.5$ Å and graphite $a \simeq 3.5$ Å can survive.
2. When a increases, the lifetimes become exponentially longer, meaning that for grains larger than $a \gtrsim 6$ Å, the survival of these grains will not be very sensitive to the assumptions in Eq. (IV.30).

The hardness of the ISRF, that we have not represented here, will however increase the minimum size a grain needs to have in order to survive. The vicinity of OB associations will thus be environments where the smallest grains can be photodestroyed.

Evidence in resolved regions. This last point is observationally verified in countless regions. It can be conveniently witnessed, as the smallest grains are the carriers of the MIR continuum, which is well separated from the rest of the emission (*cf.* Fig. II.27.b). In addition, small carbon grains carry the series of aromatic features (*cf.* Sect. III.2.1.1). The disappearance of these features in regions of enhanced ISRF is very likely the sign of the destruction of these grains by hard UV photons. This is, for instance, evident in one of our studies of the massive star-forming region, N 11, in the LMC (Galametz et al., 2016). This region contains several blobs, with embedded star clusters. The maps of the PAH mass fraction, q_{PAH} (*cf.* Sect. III.1.2.2), is shown in Fig. IV.12.a. It has been derived by modeling the spatially-resolved SED of *Spitzer* and *Herschel* images. Comparing this image to the mean starlight intensity in Fig. IV.12.b, we see that PAHs are strongly depleted in the blobs where $\langle U \rangle$ is enhanced. The photodestruction is evident. In the case of this massive region, a bright star cluster such as N 11B can clear PAHs out over a region of typically $\simeq 50$ pc.

☞ Aromatic features are severely depleted around star-forming regions.

IV.2.2.2 Thermal Sputtering

Another destruction mechanism is grain erosion and vaporization by collisions with energetic ions, either in coronal plasmas (*thermal sputtering*; $T \gtrsim 10^6$ K), or in shock waves (*kinetic sputtering*; $v \gtrsim$

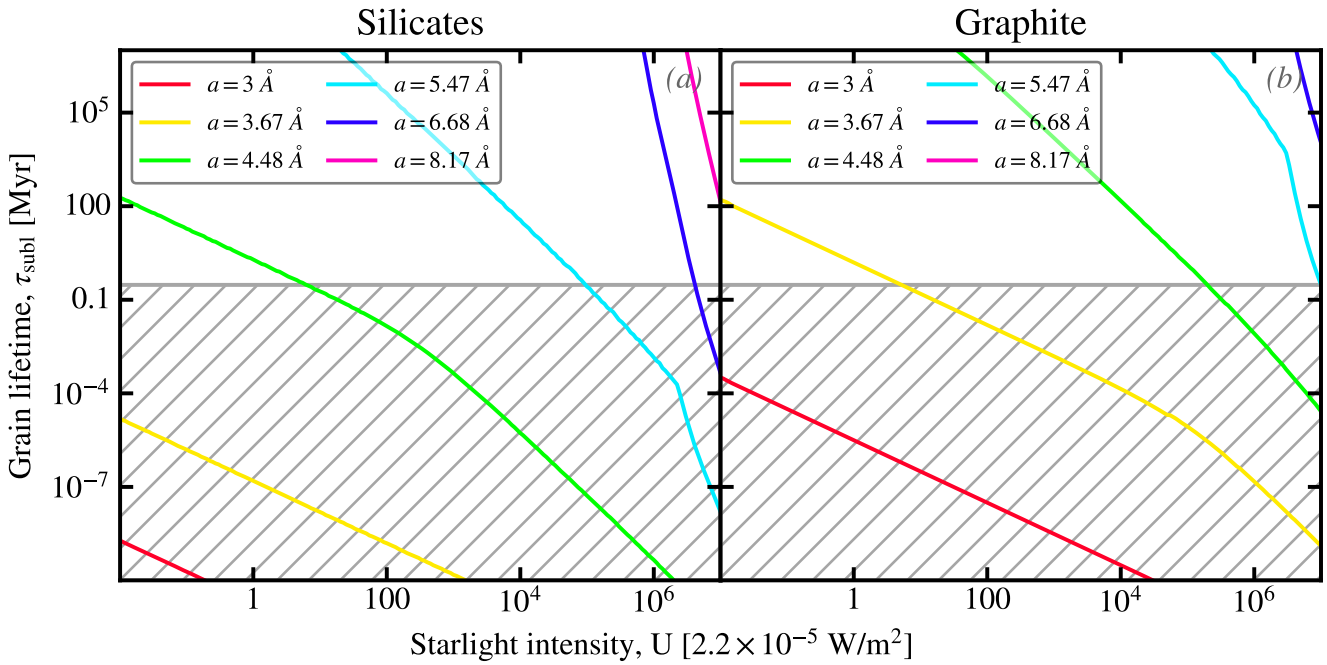

FIGURE IV.11 – *Lifetimes of small grains in a radiation field.* In both panels, we plot the mean sublimation times from Eq. (IV.30), for different grain radii (color lines), as a function of the starlight intensity of the Mathis et al. (1983) ISRF: *(a)* for the silicates of Weingartner & Draine (2001a); and *(b)* for the graphite of Laor & Draine (1993). Licensed under CC BY-SA 4.0.

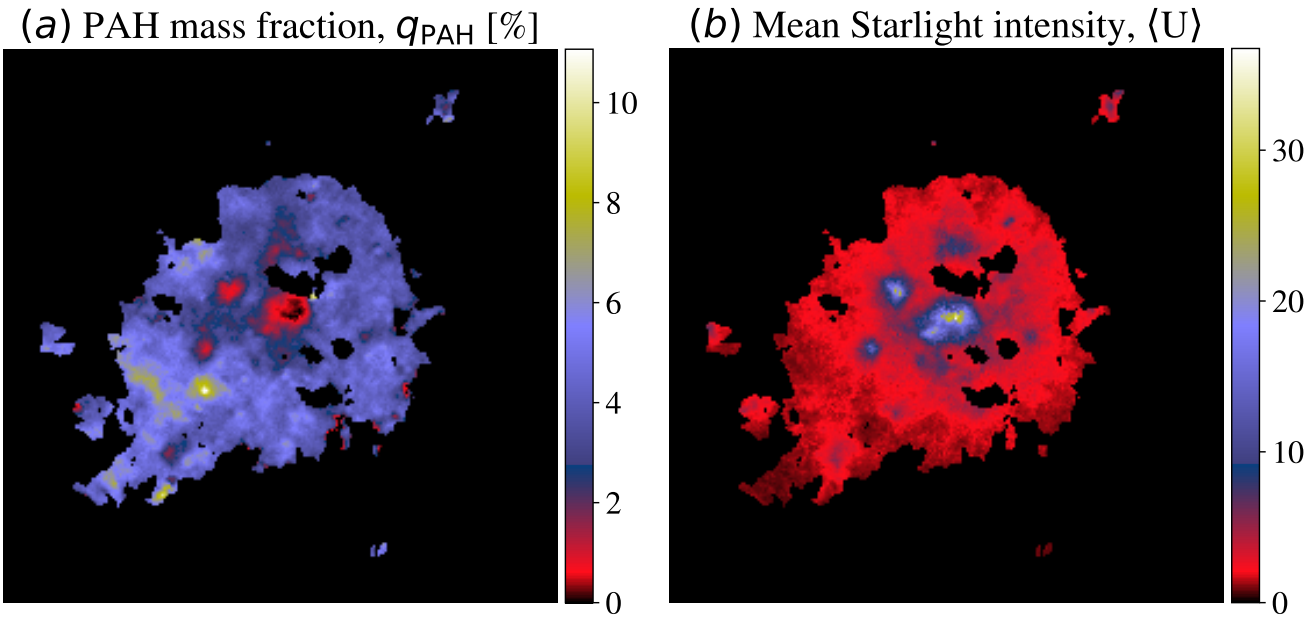

FIGURE IV.12 – *Carving out of PAHs by UV photons in N11.* Both maps have identical fields of view, centered on the star cluster N11B (LH10; Lucke & Hodge, 1970), and are 400 pc wide. The quantities displayed are the results from the spatially-resolved SED modeling, with the composite approach (*cf.* Sect. III.1.2.2; Galametz et al., 2016): *(a)* the PAH mass fraction, $q_{\rm PAH}$; and *(b)* the mean starlight intensity, $\langle U \rangle$, in units of 2.2×10^{-5} W/m^2. The black areas have been masked. Licensed under CC BY-SA 4.0.

100 km/s). There is an abundant literature on the subject (*e.g.* Draine & Salpeter, 1979; Dwek & Scalo, 1980; Tielens et al., 1994; Jones et al., 1996; Jones, 2004; Nozawa et al., 2006; Micelotta et al., 2010; Bocchio et al., 2012, 2014; Hu et al., 2019, see also the review by Dwek & Arendt, 1992). We start by discussing thermal sputtering in this section, and will review kinetic sputtering in Sect. IV.2.2.3.

Sputtering times. The evolution of a grain of radius, a, and mass, $m_{\rm d}(a) = 4/3\pi a^3 \rho$, subjected to sputtering in a gas of density $n_{\rm H}$, can be expressed (*e.g.* Hu et al., 2019):

$$\frac{{\rm d}m_{\rm d}(a)}{{\rm d}t} = 3m_{\rm d}(a)\frac{1}{a}\frac{{\rm d}a}{{\rm d}t} = 3\frac{m_{\rm d}(a)}{a} n_{\rm H} {\rm Y}_{\rm sput}({\rm T}_{\rm gas}, \upsilon_{\rm s}), \tag{IV.31}$$

where we have hidden all the microphysics into the *sputtering yield*, ${\rm Y}_{\rm sput}({\rm T}_{\rm gas}, \upsilon_s) \equiv {\rm d}a/{\rm d}t/n_{\rm H}$. This quantity depends on: *(i)* the gas temperature, ${\rm T}_{\rm gas}$, in case of thermal sputtering; or *(ii)* the shock velocity, υ_s, in case of kinetic sputtering. A detailed derivation of ${\rm Y}_{\rm sput}$ can be found in Nozawa et al. (2006, Sect. 5). For our simple discussion, we will adopt their yields, for silicate and carbon grains, fitted by Hu et al. (2019). In the thermal case, the *sputtering rate* can be expressed as:

$$\frac{1}{\tau^{\rm th}_{\rm sput}(a, {\rm T}_{\rm gas}, n_{\rm H})} \equiv \frac{1}{m_{\rm d}}\frac{{\rm d}m_{\rm d}}{{\rm d}t} = \frac{3n_{\rm H}}{a}{\rm Y}_{\rm sput}({\rm T}_{\rm gas}). \tag{IV.32}$$

Fig. IV.13.a shows the lifetimes of grains in a coronal plasma. With Eq. (IV.32), in the HIM (*cf.* Table III.6), typical grains (Eq. IV.20) have lifetimes of: *(i)* $\tau^{\rm th}_{\rm sput} \simeq 11$ Myr, for silicates; and *(ii)* $\tau^{\rm th}_{\rm sput} \simeq 16$ Myr, for carbon grains. In the case of SN II blastwaves, grains stay in post-shock conditions for only $\simeq 10^4$ yr. Dust destruction by thermal sputtering is thus not the dominant process in the shocked ISM.

☞ Grains have short lifetimes in coronal plasmas.

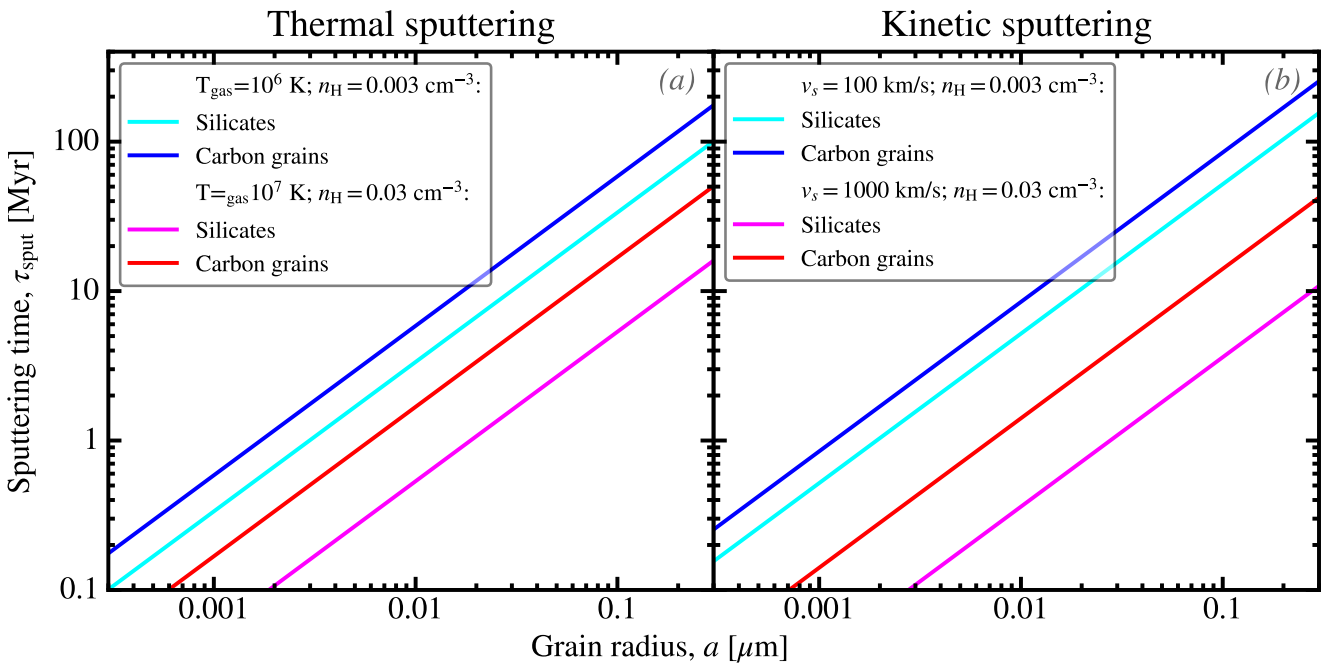

FIGURE IV.13 – *Thermal and kinetic sputtering times of silicates and carbon grains.* Panel *(a)* show the mean lifetimes of grains in a hot gas, computed from Eq. (IV.32), using the sputtering yields of Nozawa et al. (2006) fitted by Hu et al. (2019). Panel *(b)* show the mean lifetimes of grains in a shock of velocity υ_s, computed from Eq. (IV.33), using the same sputtering yields. Licensed under CC BY-SA 4.0.

Early-type galaxies. We have seen in Sect. III.1.3.1 that ETGs tend to be characterized by a diffuse X-ray emission, originating in a permeating coronal gas. This HIM is likely filling most of their ISM. This has consequences on the dust properties. This can be seen in Fig. IV.14.a, looking at a classic scaling relation between the dustiness and the *specific gas mass*[6], $s\mathrm{M_{gas}} \equiv \mathrm{M_{gas}}/\mathrm{M_\star}$. Most ETGs appear to be distributed on a vertical branch, below the main trend. They appear to be depleted in dust, at a given specific gas mass. Investigating the contribution of the X-ray emitting coronal gas, we have displayed the specific dust mass, as a function of the X-ray-luminosity-to-dust-mass ratio, $\mathrm{L_X}/\mathrm{M_{dust}}$, in Fig. IV.14.b (G21). The $\mathrm{L_X}/\mathrm{M_{dust}}$ ratio quantifies the X-ray photon rate per dust grain. We see that ellipticals occupy the lower right corner of this relation: they have a high photon rate per dust grain and a low specific dust mass. We have just shown that grains in a hot gas have a short lifetime (Eq. IV.32). The correlation of Fig. IV.14.b is thus likely the result of enhanced thermal sputtering in ETGs.

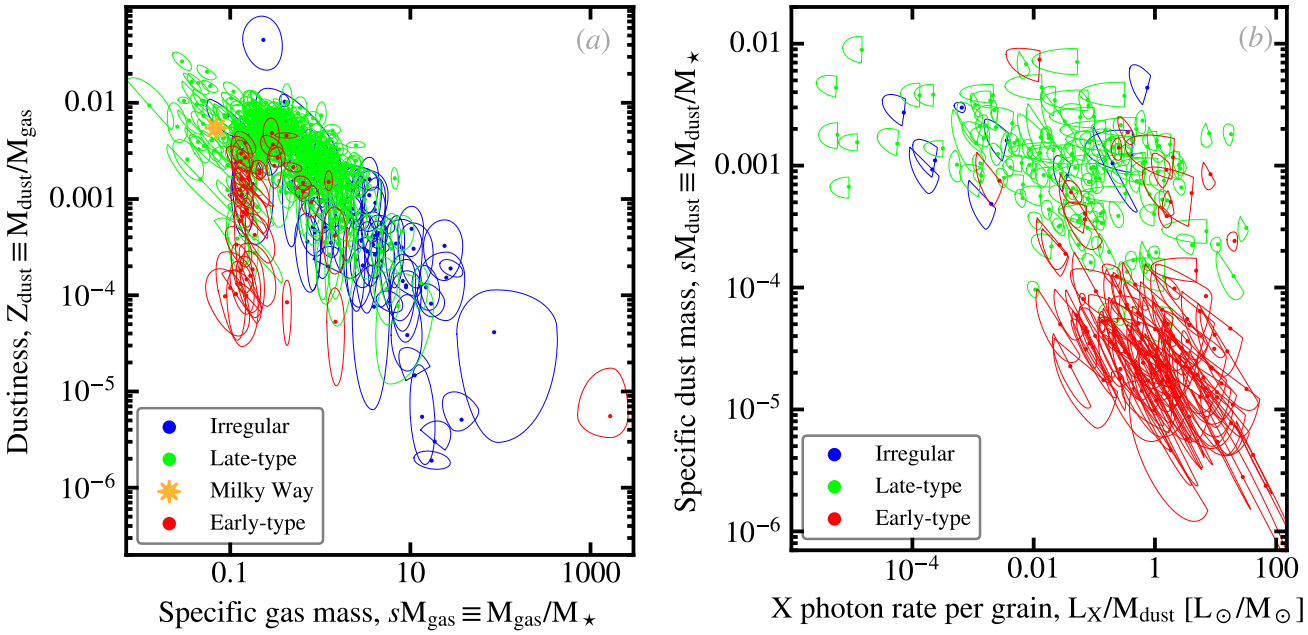

FIGURE IV.14 – *Evidence of thermal sputtering in elliptical galaxies.* Both panels show the results of the SED fitting of 800 nearby galaxies (G21), that we have started to discuss in Sect. III.1.2.2. We have represented the measurements as *Skewed Uncertainty Ellipses* (SUE; Appendix F of G21). Each SUE corresponds to one whole galaxy. Galaxies are color coded according to their Hubble stage, T: *(i)* ETGs ($\mathrm{T} \leq 0$) in red; *(ii)* LTGs ($0 < \mathrm{T} < 9$) in green; and *(iii)* Irregulars ($\mathrm{T} \geq 9$) in blue. Panel *(a)* shows how the dustiness scales with the specific gas mass. We see that most ETGs (red) are distributed along a vertical branch, below the main trend. Panel *(b)* shows how the specific dust mass varies with X-ray luminosity, $\mathrm{L_X}$, over dust mass, $\mathrm{M_{dust}}$. ETGs occupy the lower right corner of this relation. Licensed under CC BY-SA 4.0.

IV.2.2.3 Destruction by SN Blast Waves

We now focus on the effect of kinetic sputtering. This process leads to erosion and vaporization of grains in SN II blast waves. As we will see, this happens to be the major dust grain destruction mechanism. The kinetic sputtering rate is similar to the thermal case (Eq. IV.32), except that the sputtering yield now depends on the shock velocity, v_s (*cf.* Fig. IV.13.b):

$$\frac{1}{\tau^{\mathrm{kin}}_{\mathrm{sput}}(a, v_s, n_\mathrm{H})} = \frac{3 n_\mathrm{H}}{a} \mathrm{Y_{sput}}(v_s). \tag{IV.33}$$

6. Given an extensive quantity, Q, it is common, in extragalactic astronomy, to define the corresponding intensive *specific* quantity, $s\mathrm{Q} \equiv \mathrm{Q}/\mathrm{M_\star}$, by dividing by the stellar mass.

In addition, grain shattering in grain-grain collisions is an important dust destruction mechanism in SN II blast waves (*e.g.* Kirchschlager et al., 2021).

Evidence in resolved regions. Although the efficiency of the process is debated, the reality of dust destruction by SN II shock waves is rather consensual. This process can even be observed in spatially-resolved SNRs. In particular, ISO and *Spitzer* MIR spectra of pre-shock and post-shock matter show systematic differences in, for instance: *(i)* 3C391 (Reach et al., 2002); *(ii)* SN 1987A (Dwek et al., 2008; Arendt et al., 2016); and *(iii)* Puppis A (Arendt et al., 2010). The post-shock ISM exhibits:

- the disappearance of the aromatic features;
- the disappearance of the dust continuum.

Global model prescription. Similarly to what we did for grain growth (Eq. IV.23), it is convenient to express the dust destruction rate as a function of global galactic quantities. Such a formula was proposed by Dwek & Scalo (1980):

$$\frac{1}{\tau_{\text{SN-dest}}(t)} = \frac{m_{\text{gas}}^{\text{dest}}}{\text{M}_{\text{gas}}(t)} \text{R}_{\text{SN}}(t), \tag{IV.34}$$

where $\text{R}_{\text{SN}}(t)$ is the SN II rate (Eq. IV.11), and $m_{\text{gas}}^{\text{dest}}$ is an empirical parameter quantifying the destruction efficiency. The latter represents the gas mass swept by a single SN II blast wave, within which all grains are destroyed. Eq. (IV.34) can be understood the following way.

1. A single SN II destroys a mass $\text{Z}_{\text{dust}} \times m_{\text{gas}}^{\text{dest}}$ of dust.
2. Knowing the SN II rate, the dust mass destroyed per unit time is therefore:

$$\left(\frac{\text{dM}_{\text{dust}}}{\text{d}t}\right)_{\text{dest}} = \text{Z}_{\text{dust}} m_{\text{gas}}^{\text{dest}} \times \text{R}_{\text{SN}}(t). \tag{IV.35}$$

3. The dust destruction rate is then simply $1/\tau_{\text{SN-dest}} = (\text{dM}_{\text{dust}}/\text{d}t)_{\text{dest}} / \text{M}_{\text{dust}}$, which gives Eq. (IV.34).

The destruction efficiency. The dust destruction efficiency, quantified by the parameter $m_{\text{gas}}^{\text{dest}}$ in Eq. (IV.34), ranges in the literature between $\simeq 100\ \text{M}_\odot$ and $\simeq 1000\ \text{M}_\odot$. It can be roughly estimated with the following arguments (Draine, 2009, slightly adapting his numbers):

1. In a ISM of density $n_{\text{H}} \simeq 1\ \text{cm}^{-3}$, a SN II, with energy $\text{E}_0 \simeq 10^{43}$ J (10^{51} erg), produces a blast wave that stays in the Sedov-Taylor phase (adiabatic expansion), until reaching a velocity $v_s \simeq 200$ km/s (Eq. 39.22 of Draine, 2011).
2. Grains are primarily destroyed in the Sedov-Taylor phase. At the end of this phase, the radius of our blast wave is $\text{R}_{\text{Sedov}} \simeq 24$ pc (Eq. 39.21 of Draine, 2011), corresponding to a total gas mass of $\text{M}_{\text{Sedov}} \simeq 1900\ \text{M}_\odot$, which is a rough estimate of our efficiency parameter, $m_{\text{gas}}^{\text{dest}}$.
3. At solar metallicity (using the dustiness of Table II.4), this corresponds to $\text{M}_{\text{dust}}^{\text{dest}} \simeq 10\ \text{M}_\odot$.

This estimate corresponds to a dust lifetime of $\tau_{\text{SN-dest}} \simeq 370$ Myr, in the MW. This is a value close to what is found by more detailed, theoretical studies (*e.g.* Jones et al., 1996). Note however that a recent re-estimate, using hydrodynamical simulations, and accounting for the role of dust mantles found: *(i)* a shorter lifetime for carbon grains; but *(ii)* a significantly longer lifetime ($\tau_{\text{SN-dest}} \simeq 2-3$ Gyr) for silicates (Slavin et al., 2015). We will give our own take on this timescale in Sect. IV.3.1.2.

> ☞ A single SN II blast wave can destroy up to $\lesssim 10\ \text{M}_\odot$ of dust, at Solar metallicity, resulting in a dust lifetime of $\tau_{\text{SN-dest}} \gtrsim 400$ Myr.

IV.3 Cosmic Dust Evolution

Cosmic dust evolution is the modeling of dust evolution from a global point of view, at the scale of a galaxy, over cosmic times [7]. At galaxy-wide scales, most dust evolution processes can be linked to star formation: *(i)* formation of molecular clouds and their subsequent evaporation; *(ii)* stellar ejecta; *(iii)* SN shock waves; *(iv)* UV and high-energy radiation. The characteristic timescale of these processes is relatively short (of the order of the lifetime of massive stars; $\tau \lesssim 10$ Myr) and their effect is usually localized around star-forming regions. For these reasons, the sSFR is an indicator of sustained dust processing. However, the dust lifecycle is a hysteresis. There is a longer term evolution, resulting from the progressive elemental enrichment of the ISM, which becomes evident on timescales of $\simeq 1$ Gyr. This evolutionary process can be traced by the metallicity. Fig. IV.15 illustrates these two timescales by comparing the SEDs of a few galaxies.

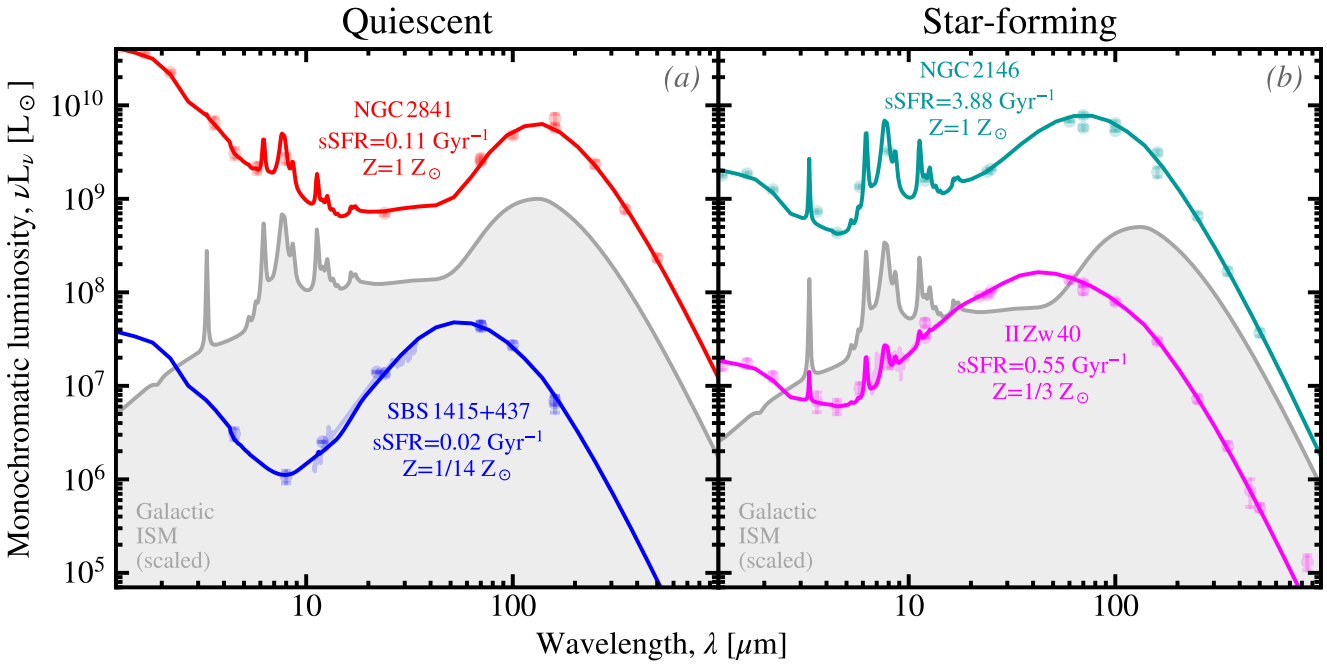

FIGURE IV.15 – *Effects of dust evolution on the SEDs of galaxies.*. Each panel displays the observations and the SED model of two nearby galaxies (Rémy-Ruyer et al., 2015), on top of the SED of the diffuse Galactic ISM (in grey). The red curve in panel *(a)* shows a quiescent Solar-metallicity galaxy. Apart from the stellar continuum, it is identical to the diffuse ISM. In contrast, the blue curve represents a low-metallicity quiescent system. Its dust properties are notably different: *(i)* weak or absent UIBs; *(ii)* overall hotter dust (FIR peaks at shorter wavelengths); *(iii)* a somehow broader FIR spectrum, resulting from a distribution of starlight intensities and/or an overabundance of small grains (*cf.* Sect. III.1.2.2). This SED is qualitatively similar to the SED of a compact H II region (*e.g.* Peeters et al., 2002b). The red curve in panel *(b)* shows a Solar-metallicity galaxy with a sustained star formation activity. Compared to its quiescent counterpart, it has a much hotter and broader FIR emission, originating at least partly in bright PDRs. The starbursting low-metallicity galaxy (blue curve in panel *b*) has the same features as its quiescent counterpart, with a broader FIR emission. Licensed under CC BY-SA 4.0.

IV.3.1 Constraining the Dust Build-Up in Galaxies

We start by focussing on the build-up of the total dust mass. We will discuss the evolution of small carbon grains in Sect. IV.3.2. For terminological consistency of the rest of the discussion, let's define the following metallicity regimes:

7. We assume that the age of the Universe is $t_{\rm present} \simeq 14$ Gyr (*e.g.* Hogg, 1999).

Very low metallicity: $Z \lesssim 0.2 \times Z_\odot$;

Low metallicity: $0.2 \times Z_\odot \lesssim Z \lesssim 0.45 \times Z_\odot$;

Normal metallicity: $Z \gtrsim 0.45 \times Z_\odot$.

We will see in Sect. IV.3.1.2 that these ranges correspond to dust evolution regimes of nearby galaxies.

IV.3.1.1 Cosmic Dust Evolution Models

The first model accounting for the evolution of the gas content of galaxies and its cycle with star formation was presented by Schmidt (1959). The Eqs. 7-9 of Schmidt (1959) are the basic equations for the evolution of the gas mass as a result of the successive waves of star formation. Subsequent studies included the heavy element enrichment of the gas, therefore accounting for the chemical evolution of galaxies (*e.g.* Audouze & Tinsley, 1976, for an early review). Dwek & Scalo (1980) then initiated the first cosmic dust evolution model, by including grain processing in the gas enrichment modeling. Dwek (1998) modeled the radial trends in the MW, accounting for the individual elemental yields by stars of different initial masses. Such models have since then been refined (*e.g.* Morgan & Edmunds, 2003; Dwek et al., 2007; Zhukovska et al., 2008; Galliano et al., 2008a; Hirashita & Kuo, 2011; Asano et al., 2013; Rowlands et al., 2014; Zhukovska, 2014; Feldmann, 2015; De Looze et al., 2020; Galliano et al., 2021). These models are nowadays used to account for subgrid physics in numerical simulations of galaxy evolution (*e.g.* Hou et al., 2017; Aoyama et al., 2020).

Physical ingredients and assumptions. The different cosmic dust evolution models we have just cited above all have differences. They however have a common set of physical ingredients and assumptions. In what follows, we describe the model of G21, which is well representative of the diversity found in the literature.

Star-formation regulation: the evolution is driven by the SFH of the galaxy (*cf.* Sect. IV.1.1.3), considered as a box, where the mixing of freshly injected elements and grains is assumed instantaneous. This box can be closed or include the effects of *infall* and *outflow*. The infall and outflow rates are usually assumed to be proportional to the SFR:

$$R_{in}(t) \equiv \delta_{in} \times \psi(t) \quad \text{(IV.36)}$$

$$R_{out}(t) \equiv \delta_{out} \times \psi(t). \quad \text{(IV.37)}$$

Stellar evolution and ejecta: in each time interval, $[t_0, t_0+\Delta t]$, a mass $\psi(t_0)\Delta t$ of stars is formed. The fraction of stars of different initial masses, $m_\star$, is given by the particular IMF we have assumed (usually Salpeter or Chabrier; *cf.* Sect. IV.1.1.3). These stars have different lifetimes, $\tau(m_\star)$ (*cf.* Fig. III.18). They return to the ISM a fraction of their gas, freshly formed heavy elements and dust grain seeds, after a time $t_0 + \tau(m_\star)$. This is called the *delayed injection* process. After this time $t_0+\tau(m_\star)$, a fraction of the initial stellar mass is locked in a remnant (white dwarf, neutron star or black hole; *e.g.* Ferreras & Silk, 2000).

Dust evolution: grain sources and sinks are estimated with the formulae we have discussed earlier in this chapter:

Stardust condensation is accounted for by assuming a mean fraction of ejected dust by LIMS and SN II: *(i)* for LIMS, we have used $\delta_{LIMS} = 15\,\%$ (Eq. IV.13); *(ii)* for SN II, we use Eq. (IV.14).

Grain growth is accounted for by Eq. (IV.23).

SN blast wave destruction is accounted for by Eq. (IV.34).

Astration is simply the fraction of dust consumed by SF, at a rate $Z_{dust}(t) \times \psi(t)$.

The ejected masses. The dust evolution differential equations we will discuss below depend on the gas, heavy element and dust masses ejected by stars, at time t:

$$e(t) = \int_{\min[m_\star(t-\tau(m_\star))]}^{m_+} [m_\star - r(m_\star)] \times \mathrm{B}(t-\tau(m_\star)) \times \phi(m_\star)\,\mathrm{d}m_\star \quad \text{(IV.38)}$$

$$e_\mathrm{Z}(t) = \int_{\min[m_\star(t-\tau(m_\star))]}^{m_+} \mathrm{Y_Z}(m_\star) \times \mathrm{B}(t-\tau(m_\star)) \times \phi(m_\star)\,\mathrm{d}m_\star \quad \text{(IV.39)}$$

$$\begin{aligned} e_\mathrm{dust}(t) &= \int_{\min[m_\star(t-\tau(m_\star))]}^{m_-^\mathrm{SN}} \mathrm{Y_Z}(m_\star)\delta_\mathrm{LIMS} \times \mathrm{B}(t-\tau(m_\star)) \times \phi(m_\star)\,\mathrm{d}m_\star \\ &+ \int_{\min[m_\star(t-\tau(m_\star)),m_-^\mathrm{SN}]}^{m_+^\mathrm{SN}} \langle \mathrm{Y_{SN}} \rangle \times \mathrm{B}(t-\tau(m_\star)) \times \phi(m_\star)\,\mathrm{d}m_\star. \end{aligned} \quad \text{(IV.40)}$$

These three equations are essentially the integral of the products of three terms: $\int f(m_\star) \times \mathrm{B}(t-\tau(m_\star)) \times \phi(m_\star)\,\mathrm{d}m_\star$.

1. The term $f(m_\star)$ is the mass of gas, heavy elements and dust ejected by a star of initial mass, $m_\star$. For the gas mass, we have subtracted the remnant mass, $r(m_\star)$. The term $\mathrm{Y_Z}(m_\star)$ is the total heavy element yield (*cf.* Fig. IV.7).
2. The term $\mathrm{B}(t-\tau(m_\star))$ is the stellar birth rate, $\tau(m_\star)$ ago. It gives the number of stars of initial mass $m_\star$, dying at time t.
3. The third term is the IMF, giving the number of stars per mass bin. It is the number density we integrate over.
4. In Eqs. (IV.38) – (IV.40), the lower bound of the integrals, $m_\star(\tau = t-\tau(m_\star))$, is the mass of stars having a lifetime $t-\tau(m_\star)$. We thus take the minimum mass of stars dying at time t (assuming star formation has started at $t=0$). Low-mass stars ($m_\star \lesssim 0.9\,\mathrm{M_\odot}$) are irrelevant for chemical evolution, as their lifetime is longer than the age of the Universe.

The equations of evolution. The physical ingredients and assumptions we have discussed earlier in this section translate into four coupled differential equations describing the temporal evolution of the stellar, gas, heavy element and dust masses, $\mathrm{M_\star}$, $\mathrm{M_{gas}}$, $\mathrm{M_Z}$ and $\mathrm{M_{dust}}$:

$$\frac{\mathrm{dM_\star}}{\mathrm{d}t} = \psi(t) - e(t) \quad \text{(IV.41)}$$

$$\frac{\mathrm{dM_{gas}}}{\mathrm{d}t} = -\psi(t) + e(t) + \mathrm{R_{in}}(t) - \mathrm{R_{out}}(t) \quad \text{(IV.42)}$$

$$\frac{\mathrm{dM_Z}}{\mathrm{d}t} = -\mathrm{Z}(t)\psi(t) + e_\mathrm{Z}(t) + 0 \times \mathrm{R_{in}}(t) - \mathrm{Z}(t)\mathrm{R_{out}}(t) + \frac{\mathrm{M_{dust}}}{\tau_\mathrm{SN\text{-}dest}(t)} - \frac{\mathrm{M_{dust}}}{\tau_\mathrm{grow}(t)} \quad \text{(IV.43)}$$

$$\frac{\mathrm{dM_{dust}}}{\mathrm{d}t} = \underbrace{-\mathrm{Z_{dust}}(t)\psi(t)}_{\text{astration}} + \underbrace{e_\mathrm{dust}(t)}_{\text{ejecta}} + \underbrace{0 \times \mathrm{R_{in}}(t)}_{\text{infall}} - \underbrace{\mathrm{Z_{dust}}(t)\mathrm{R_{out}}(t)}_{\text{outflow}} - \underbrace{\frac{\mathrm{M_{dust}}}{\tau_\mathrm{SN\text{-}dest}(t)}}_{\text{SN destruction}} + \underbrace{\frac{\mathrm{M_{dust}}}{\tau_\mathrm{grow}(t)}}_{\text{grain growth}}. \quad \text{(IV.44)}$$

Eqs. (IV.41) – (IV.44) simply express the time derivative of the mass, on the left-hand side, and the sum of the different individual rates on the right-hand side, some positive, some negative. We can note a few points.

1. We have neglected metallicity variations in the total gas mass (Eq. IV.42), as it represents at most $\simeq 2\,\%$.
2. We have assumed that the infalling gas was free of heavy elements and dust. It is therefore 0 in Eqs. (IV.43) – (IV.44).
3. On the contrary, the outflowing gas is carrying away heavy elements and dust. This is the reason why we loose these quantities at rates $\mathrm{Z.R_{out}}$ and $\mathrm{Z_{dust}.R_{out}}$, respectively.

4. Dust destruction by SN II removes mass to the dust content, at a rate $M_{dust}/\tau_{SN\text{-}dest}$, but returns it as gas-phase heavy elements.
5. This is the opposite for grain growth which removes mass to gas-phase heavy elements, at a rate M_{grow}/τ_{grow}, and puts it into grains.

Dust evolution tracks. We now present a set of solutions to Eqs. (IV.41) – (IV.44). For simplicity, we adopt the Chabrier IMF (Eq. IV.6) and the delayed SFH (Eq. IV.9). The total baryonic, initial mass of the galaxy is assumed to be $M_{ini} = 4 \times 10^{10}\ M_\odot$. Fig. IV.16 shows the time evolution of the main quantities, for a MW-like galaxy. We have adopted the following parameters:

$$\tau_{SFH} = 3\ \text{Gyr} \quad \text{(Eq. IV.9)} \tag{IV.45}$$
$$\psi_0 = 20\ M_\odot/\text{yr} \quad \text{(Eq. IV.9)} \tag{IV.46}$$
$$\delta_{in} = 0.05 \quad \text{(Eq. IV.36)} \tag{IV.47}$$
$$\delta_{out} = 0.05 \quad \text{(Eq. IV.37)} \tag{IV.48}$$
$$\langle Y_{SN} \rangle = 0.007\ M_\odot/\text{SN} \quad \text{(Eq. IV.14)} \tag{IV.49}$$
$$\epsilon_{grow} = 1000 \quad \text{(Eq. IV.23)} \tag{IV.50}$$
$$m_{gas}^{dest} = 1000\ M_\odot/\text{SN} \quad \text{(Eq. IV.34)}. \tag{IV.51}$$

Fig. IV.16.a shows the SFH we have adopted. The time evolution of the individual quantities are represented in Fig. IV.16.b. We can note the following points.

1. The total baryonic content is conserved: $M_{ini} = M_\star + M_{gas}$. The stellar mass is increasing with time, while the gas gets depleted. In this particular simulation, they cross over around $t_{cross} \simeq 5$ Gyr.
2. The mass of heavy elements follows the stellar mass at $t \lesssim t_{cross}$, two orders of magnitude lower, as it is controlled by the accumulative stellar enrichment. Above $t \gtrsim t_{cross}$, the net mass of heavy elements decreases due to astration, as the ISM becomes more tenuous.
3. The dust mass follows the trend of heavy elements two orders of magnitude lower, for $t \lesssim 3$ Gyr, as it is dominated by dust production by SN II. Around $t \simeq 3$ Gyr, the metallicity is high enough to render grain growth efficient. This is what Asano et al. (2013) have conceptualized as the *critical metallicity*. This is an important quantity, that depends on the SFH. It roughly delineates the two regimes dominated by SN II production and grain growth in the ISM. In the particular case of Fig. IV.16, it is $Z_{crit} \simeq Z_\odot/3$. Above $t \gtrsim t_{cross}$, dust production is dominated by grain growth, and $M_{dust}/M_Z \simeq 0.5$, which is roughly the Galactic dust-to-metal mass ratio (*cf.* Table II.4).

Effects of the individual parameters. We end this section by demonstrating the effects of the seven parameters of Eqs. (IV.45) – (IV.51) on dust evolution. We vary each parameter, one by one, keeping the other ones to their values in Eqs. (IV.45) – (IV.51). We represent the dustiness, as a function of: *(i)* metallicity; *(ii)* sSFR; and *(iii)* gas fraction, $f_{gas} \equiv M_{gas}/(M_\star + M_{gas})$. For completeness, we have represented the four SFH-related parameters in Fig. IV.17. Our center of interest is however the three dust evolution tuning parameters, represented in Fig. IV.18.

The SN II dust yield, $\langle Y_{SN} \rangle$ (Eq. IV.14), has essentially a scaling effect on the dustiness, below the critical metallicity, and has no effect above (Fig. IV.18.a-c). This is the reason why constraining this parameter requires very-low-metallicity objects. In the very-low-metallicity regime, dust and heavy elements directly come from stellar ejecta. Both quantities are thus roughly proportional, using our simple prescriptions. When $\langle Y_{SN} \rangle \lesssim 0.003\ M_\odot/\text{SN}$, this parameter is so low, that stardust injection by LIMS becomes dominant, below the critical metallicity.

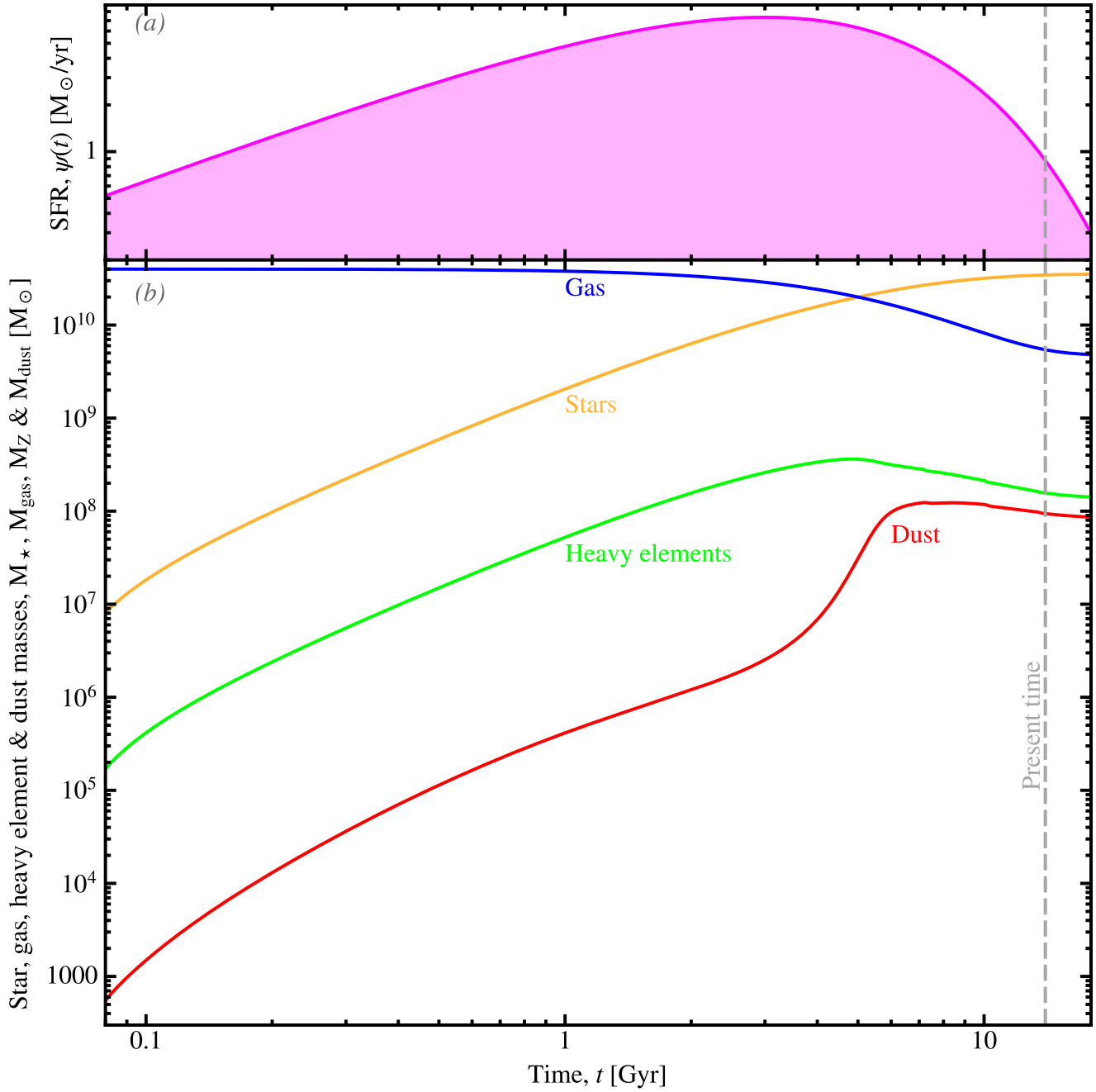

FIGURE IV.16 – *Dust evolution tracks for a MW-like galaxy.* Panel *(a)* displays the adopted SFH. Panel *(b)* shows the evolution as a function of time of the four quantities of Eqs. (IV.41) – (IV.44). These quantities approximately reach the MW values at $t = t_{\rm present}$. The parameters are those of Eqs. (IV.45) – (IV.51). Licensed under CC BY-SA 4.0.

The grain growth efficiency, $\epsilon_{\rm grow}$ (Eq. IV.23), has also a scaling effect on the dustiness, but above the critical metallicity (Fig. IV.18.d-f). It has no effect at very low metallicity, because $1/\tau_{\rm grow} \propto Z$ (Eq. IV.23 with $Z \gg Z_{\rm dust}$). The tracks for the lowest values of $\epsilon_{\rm grow}$ (in red on Fig. IV.18) exhibit a quasi-linear dustiness-trend with metallicity, over the whole range[8], because grain growth never reaches the efficiency of stardust condensation, in these extreme cases. The timescale ratio between SN II production and ISM grain growth is (using Eq. II.2, Eq. IV.10, Eq. IV.11, Eq. IV.14 and Eq. IV.23):

$$\frac{\tau_{\rm SN\text{-}cond}}{\tau_{\rm grow}} = \frac{\epsilon_{\rm grow}\langle m_\star\rangle}{f_{\rm SN}\langle Y_{\rm SN}\rangle} Z_{\rm dust}(Z - Z_{\rm dust}). \quad \text{(IV.52)}$$

8. The sawtooth features in Fig. IV.18.d-f, for the two lowest values of $\epsilon_{\rm grow}$ (red and orange), are numerical artefacts due to the fact that grain growth is so low, that SN II can clear dust faster than our time resolution.

Since we usually have $Z \gtrsim 2 \times Z_{dust}$, we can write the rough proportionality: $\tau_{SN\text{-}cond}/\tau_{grow} \propto Z \times Z_{dust}$, with Z_{dust} being a steep function of Z. This is the reason why the relative efficiency of the two processes is so strongly metallicity dependent.

The SN II destruction efficiency, m_{gas}^{dest} (Eq. IV.34), has the effect of decreasing the dustiness, at low to normal metallicity (Fig. IV.18.g-i). It however has no noticeable effect at very low metallicity. This is because the average dust mass destroyed by a single SN II blast wave is $m_{dust}^{dest} = Z_{dust} \times m_{gas}^{dest}$ and $Z_{dust} \ll 1$.

IV.3.1.2 Empirical Inference of Dust Evolution Timescales

We now discuss some empirical estimates of the three main grain evolution parameters ($\langle Y_{SN} \rangle$, ϵ_{grow} and m_{gas}^{dest}), derived from fitting dust scaling relations. This is not a new topic. Several studies have attempted to tackle this issue (*e.g.* Lisenfeld & Ferrara, 1998; Morgan & Edmunds, 2003; Galliano et al., 2008a; Mattsson & Andersen, 2012; Rémy-Ruyer et al., 2014; De Vis et al., 2017; Nanni et al., 2020; De Looze et al., 2020). We have recently published such a study (G21). We will try to demonstrate the progress it has brought to the field.

Fitting dust scaling relations. We have used the SED modeling results of the DustPedia/DGS sample we have already discussed in Fig. III.17 and Sect. IV.2.2.2 (G21). These results were obtained using the *composite approach* (Sect. III.1.2.2), with the THEMIS grain properties, and a hierarchical Bayesian model (Sect. V.3.3). These results are an estimate of: *(i)* the dust mass, M_{dust}, for all galaxies (G21); *(ii)* the stellar mass, $M_\star$ and SFR for most of them (Rémy-Ruyer et al., 2015; Nersesian et al., 2019); *(iii)* the metallicity, Z, for about half the sample (Madden et al., 2013; De Vis et al., 2019). The dust evolution model of Sect. IV.3.1.1 has then been fitted to our estimates of $M_\star$, M_{gas}, M_{dust}, Z and SFR. We have adopted a hierarchical Bayesian approach (*cf.* Sect. V.3.3), varying the following set of parameters.

The SFH-related parameters, τ_{SFH} (Eq. IV.9), ψ_0 (Eq. IV.9), δ_{in} (Eq. IV.36) and δ_{out} (Eq. IV.37) are varied individually for each galaxy. In other words, we have assumed that each galaxy has a particular, independent SFH.

The dust evolution tuning parameters, $\langle Y_{SN} \rangle$ (Eq. IV.14), ϵ_{grow} (Eq. IV.23) and m_{gas}^{dest} (Eq. IV.34) were varied, assuming they were common to every galaxy. In other words, we have assumed that the efficiencies of the dust evolution processes were universal.

Fig. IV.19 shows the fitted dustiness-metallicity relation, from our study (G21). We have represented the estimated observed quantities (SUEs) on top of the posterior PDF of our dust evolution model. This figure clearly shows the physical origin of the three regimes we had arbitrarily defined at the beginning of Sect. IV.3.1.

1. At very low metallicity ($Z \lesssim 0.2 \times Z_\odot$), grain production is dominated by condensation in SN II ejecta. We see a roughly-linear dustiness trend with metallicity, with a rather low dust-to-metal mass ratio ($Z_{dust}/Z \simeq 10^{-4}$):

$$\frac{Z_{dust}}{Z_{dust}^\odot} \simeq 10^{-4} \times \frac{Z}{Z_\odot} \quad \text{for} \quad Z \lesssim 0.2 \times Z_\odot. \tag{IV.53}$$

2. At low metallicity ($0.2 \times Z_\odot \lesssim Z \lesssim 0.45 \times Z_\odot$), we are in what we have called the critical metallicity regime. The dustiness rises sharply with metallicity, as grain growth in the ISM kicks in. The critical metallicity regime of individual galaxies is usually narrower (*cf.* Figs. IV.17 – IV.18). It is broadened here, because the PDF is the superimposition of all the galaxies, having different SFHs.

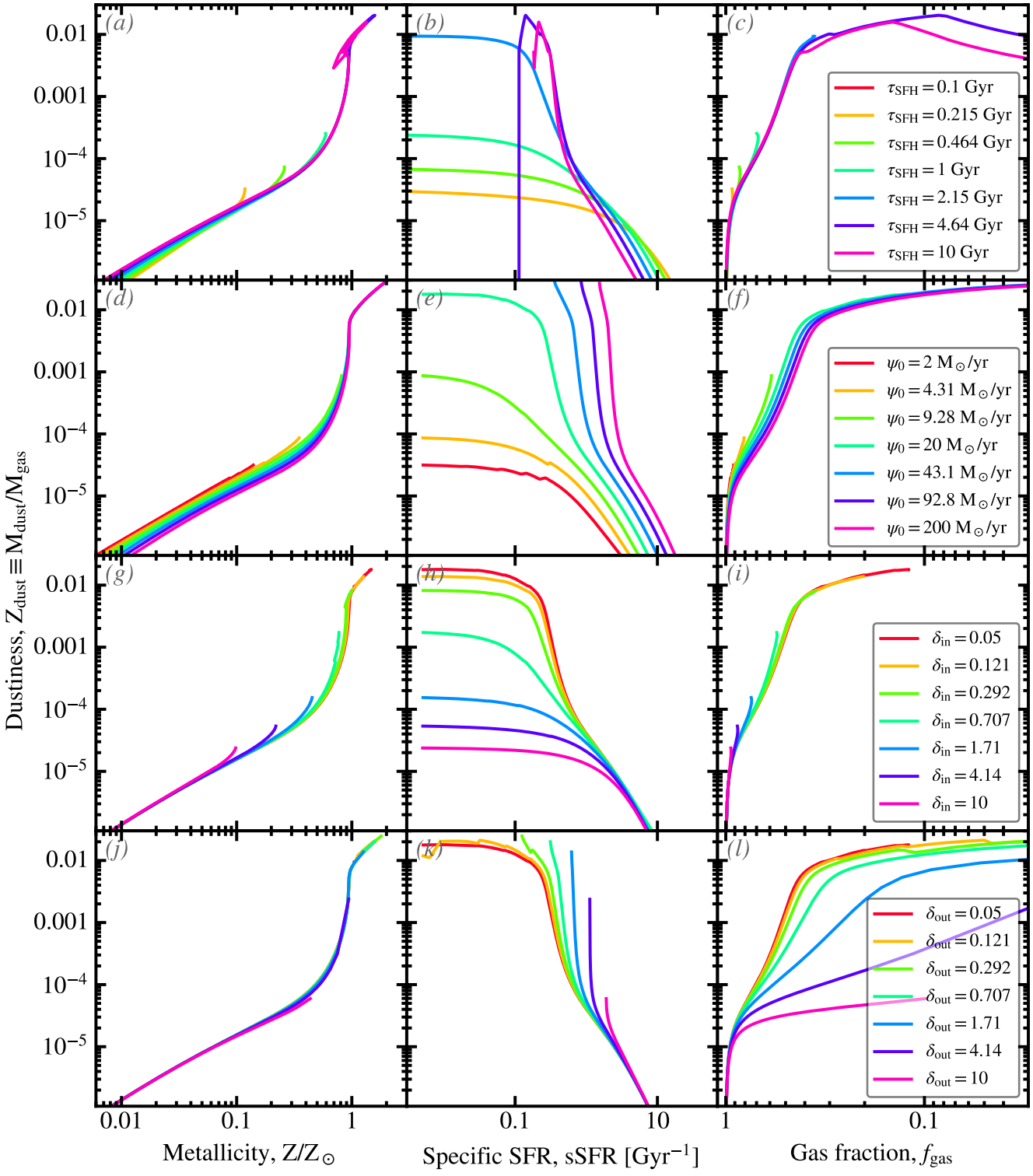

FIGURE IV.17 – *Effects of SFH-related parameters on dust evolution.* Each row of panels represents the evolution of the dustiness as a function of metallicity, sSFR and gas fraction. In each row, we vary a particular parameter, whose values are given in the right panel. The other parameters are kept to their values in Eqs. (IV.45) – (IV.51).

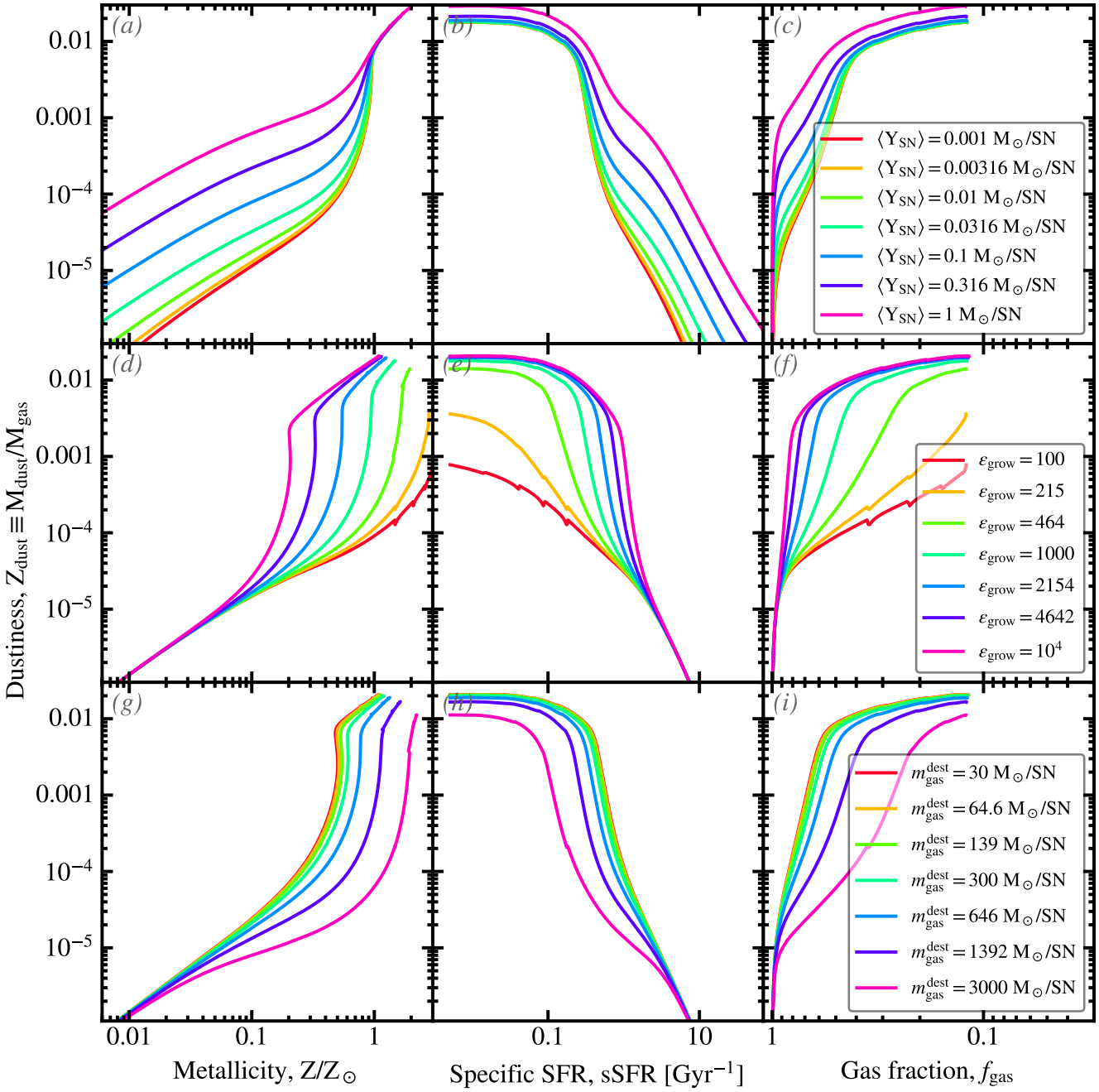

FIGURE IV.18 – *Effects of tuning parameters on dust evolution.* This figure is similar to Fig. IV.17, except that we have varied the dust evolution tuning parameters. Licensed under CC BY-SA 4.0.

3. At normal metallicity ($Z \gtrsim 0.45 \times Z_\odot$), we have another roughly-linear dustiness trend with metallicity, sustained by grain growth in the ISM, with a Galactic dust-to-metal mass ratio ($Z_{dust}/Z \simeq 0.5$):

$$\frac{Z_{dust}}{Z_{dust}^\odot} \simeq \frac{Z}{Z_\odot}. \quad \text{for} \quad Z \gtrsim 0.45 \times Z_\odot. \tag{IV.54}$$

Evolutionary timescales as a function of metallicity. The dust evolution fitting of Fig. IV.19 allowed us to infer the values of the three tuning parameters. Accounting for possible systematic biases, we concluded the following (G21):

$$\langle Y_{SN} \rangle \lesssim 0.03\ M_\odot/SN, \qquad \epsilon_{grow} \gtrsim 3000, \qquad m_{gas}^{dest} \gtrsim 1200\ M_\odot/SN. \tag{IV.55}$$

These efficiencies can be translated into timescales of the three dust evolution processes, in each galaxy. We have represented these timescales as a function of metallicity, in Fig. IV.20. The derived

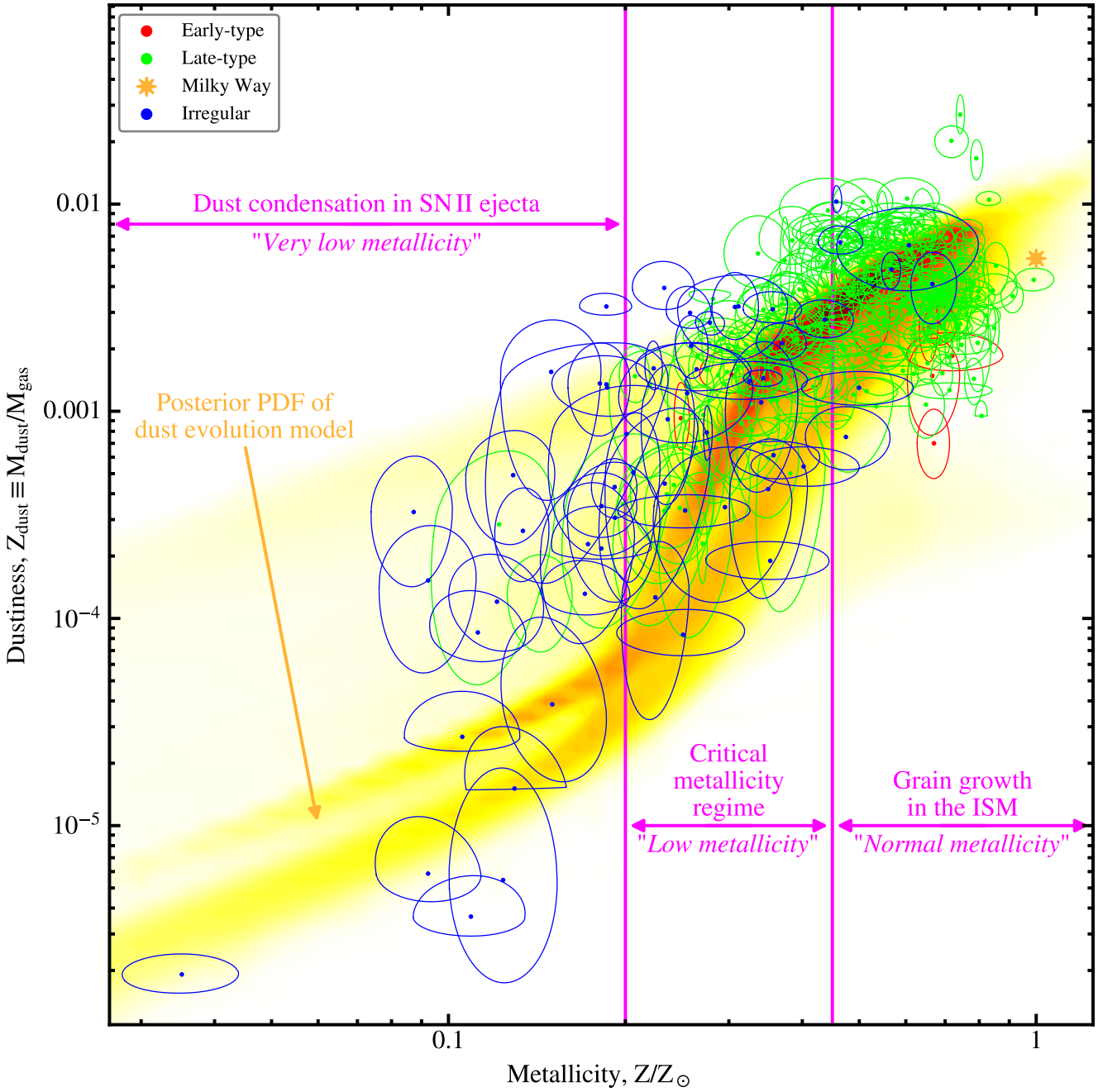

FIGURE IV.19 – *Dustiness-metallicity relation fitted with a dust evolution model.* The SUEs are the results of the SED fitting of the DustPedia/DGS sample. Each SUE represents one galaxy, color-coded according to its type (*cf.* Fig. IV.14). We have overlaid the posterior probability distribution of the dust evolution model of Eqs. (IV.41) – (IV.44) as a yellow-orange density. This fit was used by G21 to infer the values of the three dust evolution tuning parameters. This is only a sub-sample of our 800 galaxies, as not all of them had reliable metallicity measurements. Licensed under CC BY-SA 4.0.

timescales for the MW are represented as a yellow star, although they were not used in the fit. We note the following points

1. The timescale for dust condensation in SN II ejecta rises very abruptly with metallicity (*cf.* Fig. IV.20.a). It is realistic (*i.e.* shorter than the age of the Universe) only for very-low- and low-metallicity systems. At normal metallicity, another process needs to be invoked. Eq. (IV.52) can be approximated by (assuming our limits in Eq. IV.55 are close to the true values):

$$\frac{\tau_{\text{SN-cond}}}{\tau_{\text{grow}}} \simeq 1000 \times \frac{Z}{Z_\odot} \times \frac{Z_{\text{dust}}}{Z_{\text{dust}}^\odot}. \tag{IV.56}$$

At low very metallicity ($Z \lesssim 0.2 \times Z_\odot$), Eq. (IV.53) gives $\tau_{\text{SN-cond}}/\tau_{\text{grow}} \simeq 0.1 \times (Z/Z_\odot)^2 \ll 1$, which is another way to show that grain growth is inefficient in this regime.

At normal metallicity ($Z \gtrsim 0.45 \times Z_\odot$), Eq. (IV.54) gives $\tau_{\text{SN-cond}}/\tau_{\text{grow}} \simeq 1000 \times (Z/Z_\odot)^2 \gg 1$, which is another way to show that grain growth is now dominant.

2. The grain growth and blast wave destruction timescales (*cf.* Fig. IV.20.b-c) have rather similar features, because their ratio is (using Eq. IV.10, Eq. IV.11, Eq. IV.34 and Eq. IV.23):

$$\frac{\tau_{\text{SN-dest}}}{\tau_{\text{grow}}} = \frac{\epsilon_{\text{grow}} \langle m_\star \rangle}{f_{\text{SN}} m_{\text{gas}}^{\text{dest}}} (Z - Z_{\text{dust}}) \simeq 4 \times \frac{Z}{Z_\odot}. \tag{IV.57}$$

The two processes thus balance each other around $Z_{\text{crit}} \simeq Z_\odot/4$. This is where our value of the critical metallicity comes from. We note that, for the MW, we find $\tau_{\text{grow}}^{\text{MW}} \simeq 80$ Myr and $\tau_{\text{SN-dest}}^{\text{MW}} \simeq 300$ Myr, close to the values we had expected in Sect. IV.2.1.3 and Sect. IV.2.2.3. Yet, we did not put any prior on the Galactic values. This is a indication in favor of the consistency of our analysis.

3. The ratio of the timescales for dust condensation in SN II ejecta and destruction by SN II blast waves is (using Eq. IV.14 and Eq. IV.34):

$$\frac{\tau_{\text{SN-cond}}}{\tau_{\text{SN-dest}}} = \frac{m_{\text{gas}}^{\text{dest}}}{\langle Y_{\text{SN}} \rangle} Z_{\text{dust}} \simeq 500 \times \frac{Z_{\text{dust}}}{Z_{\text{dust}}^\odot}. \tag{IV.58}$$

At very low metallicity ($Z \lesssim 0.2 \times Z_\odot$), Eq. (IV.53) gives $\tau_{\text{SN-cond}}/\tau_{\text{SN-dest}} \simeq 0.5 \times (Z/Z_\odot) \ll 1$, showing that SN II are net dust producers.

At normal metallicity ($Z \gtrsim 0.45 \times Z_\odot$), Eq. (IV.54) gives $\tau_{\text{SN-cond}}/\tau_{\text{SN-dest}} \simeq 500 \times (Z/Z_\odot) \gg 1$, showing that SN II are net dust destroyers.

☞ SN II are net dust destroyers, except at very low metallicity.

Methodological remarks. The study this section relies on (G21) was the first rigorous empirical determination of the dust evolution tuning parameters in Eq. (IV.55), using a wide enough metallicity range to unambiguously constrain these quantities. We emphasize two important points.

Fitting dust evolution models is instrumental. Numerous studies, trying to tackle the issues of cosmic dust evolution, simply overlaid dust evolution tracks (such as those in Figs. IV.17 – IV.18), on top of dust scaling relations (such as those in Fig. IV.14.a and Fig. IV.19). The issue with this approach is that two quantities of a given galaxy could be fitted with two different SFHs, at different ages. This is obviously inconsistent, but can give the appearance a good agreement with the data. We have avoided this pitfall with our hierarchical Bayesian approach. It allows us to avoid mutually inconsistent explanations of different trends and correlations. Overall, performing a rigorous fit does not help getting better solutions, but it definitely helps avoiding bad ones.

Low-metallicity systems are crucial. As we have shown in Fig. IV.18, the effect of dust condensation in SN II ejecta can only be probed at very low metallicity. It is therefore necessary to have a good enough sampling of this regime. Without a good coverage at very low metallicity, the solution will consequently be degenerate. It will be impossible to disentangle the contributions of grain growth and stardust production. The relevance of dwarf galaxies here is not necessarily that they can be considered as analogs of primordial distant galaxies, but that they sample a particular, key dust production regime.

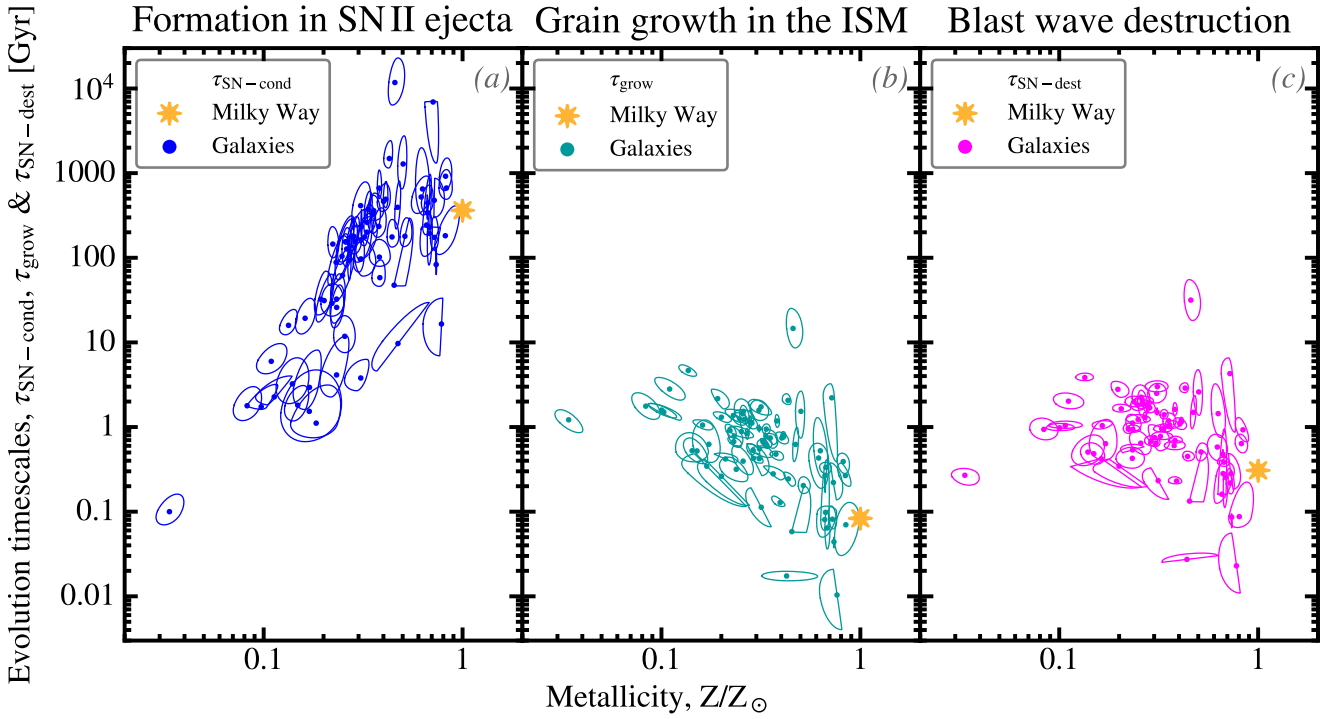

FIGURE IV.20 – *Empirical estimates of dust evolution timescales as a function of metallicity.* The three panels represent the dust evolution timescales inferred from the fit of Fig. IV.19 (G21): *(a)* $\tau_{\text{SN-cond}}$ (Eq. IV.14); *(b)* τ_{grow} (Eq. IV.23); and *(c)* $\tau_{\text{SN-dest}}$ (Eq. IV.34). Each SUE corresponds to one galaxy. Licensed under CC BY-SA 4.0.

The controversy about stardust. We have opened this chapter with a citation of D09, about the belief that ISD could be mainly stardust. It is unfortunate that this discussion can sometimes turn into an ideological debate, in the literature.

In the nearby Universe, for instance, De Looze et al. (2020) recently tried to show that SN II could be net dust producers at normal metallicity. They used a rather similar approach to ours. The only difference is that they did not have very-low-metallicity constraints. Their results were therefore clearly degenerate, but they forced their interpretation in favor of stardust. We will come back to these issues, from an epistemological point of view, in Chap. V.

In the distant Universe, this debate is also vigorous, as dusty galaxies are found at high redshifts ($z \gtrsim 6$; *e.g.* Dwek et al., 2007; Valiante et al., 2009; Dwek et al., 2014; Laporte et al., 2017). At this time, we are only ≃ 400 Myr after the reionization. We thus need a rapid source of dust, and stardust is seriously considered. However, our results confirm that grain growth can happen on timescales shorter than $\lesssim$ 100 Myr, provided that the ISM has been enriched by a first generation of stars, up to the critical metallicity. This therefore provides a simple solution to this conundrum.

In between, measurements in absorption by *Damped Lyman-Alpha systems* (DLA), along the sight-line towards a QSO or a *Gamma-Ray Burst* (GRB), can be used to estimate the metallicity and depletion of some elements in these systems, by comparing volatile and refractory abundances (*e.g.* De Cia et al., 2016). These data produce a quasi-linear dustiness-metallicity trend, much flatter than Fig. IV.19 (*e.g.* Fig. 10 of G21). If this trend is correct, it is consistent with stardust production at all metallicities. It is however difficult to understand the discrepancy between these systems and nearby galaxies. G21 conjectured it was possible that these estimates could be biased due to the dilution of heavy element absorption lines in near-pristine clouds, along the sightline, within the same velocity bin.

To try to rise above a mere ideological debate, we should not lose sight of the big picture, as the truth is the whole. Table IV.2 summarizes the observational evidence in favor of one scenario and the other.

	Stardust origin	ISM origin
Elemental depletions (*cf.* Sect. II.2.3 & Sect. IV.2.1.1)		✓
Nearby galaxy dustiness-metallicity trend (*cf.* Sect. IV.3.1.2)		✓
Individual SNRs (before the reverse shock; *cf.* Sect. IV.1.2.2)	(✓)	
Individual SNRs (accounting for the reverse shock; *cf.* Sect. IV.1.2.2)		✓
Isotopic ratios of IDPs in meteorites (*cf.* Sect. IV.1.2.2)		✓
Distant dusty galaxies (*cf.* Sect. IV.3.1.2)	(✓)	(✓)
DLA dustiness-metallicity trend (*cf.* Sect. IV.3.1.2)	(✓)	
ISD is mainly amorphous, while CSD is crystalline (*cf.* Sect. IV.1.2.2)		(✓)
Emissivity variation as a function of ISM density (*cf.* Sect. IV.2.1.1)		(✓)

TABLE IV.2 – *Summary of the observational evidence about interstellar dust origin at normal metallicity.* Check marks between parenthesis indicate uncertain evidence.

Limitations of our approach. Although our approach was successful in providing a unique, rigorous estimate of the dust evolution tuning parameters, and in deriving timescales as a function metallicity, it has several limitations.

Systematic uncertainties of the data could bias the observed dustiness of our galaxy, displayed in Fig. IV.19. We have estimated the different potential biases on both the dust and gas mass estimates (Sect. 4.1.3 of G21). At normal metallicity, our measurements are consistent with the MW. At very low metallicity, we could suffer from: *(i)* the possible overestimate of the gas mass because of the extended gas halo of dwarf galaxies (Sect. III.1.3.1); *(ii)* the systematic variation of the grain opacity with metallicity (Sect. IV.2.1.1); *(iii)* the potential overabundance of small grains at very low metallicity (Sect. III.1.3.4); and *(iv)* the possible presence of unaccounted for VCD (Sect. III.2.2.1). G21 concluded that these biases can not, in total, be larger than a factor of $\simeq 4$, which is consequent, but not sufficient to produce a linear dustiness-metallicity relation, that would be consistent with SN II dust production at all epochs.

The universality of the tuning parameters is a questionable assumption. As we have shown in Sect. IV.2, all these parameters hide information about, in particular: *(i)* the typical grain size distribution; *(ii)* sticking coefficients, which are dependent on grain structure and composition; *(iii)* the topology of the ISM; *(iv)* stellar evolution. Exploring these variations with environment is however premature. We need independent estimates of the different factors we have just listed.

The simplicity of the dust evolution model can cause discrepancies when trying to account for the observed SFRs. In particular, our model failed at reproducing the trend of sM_{dust} with sSFR (*cf.* Sect. 5.2.3 of G21). The likely explanation is that our parametric SFH is too simple. This could be solved by adding another SF component, to account for a potential recent burst.

IV.3.2 Evolution of the Aromatic Feature Carriers

We close this chapter with a discussion about the trend followed by the grains carrying the aromatic feature emission. We have already discussed this point in Sect. III.2.1.4, from a spectroscopic point of view. We now give a more general point of view, based on SED modeling, and discuss the different scenarios. We remind the reader that aromatic features can be emitted by PAHs [9] or small a-C(:H)s. This is a debated modeling choice (*cf.* Sect. II.3). In the present section, we will assume that small a-C(:H)s are the carriers. Their mass fraction is q_{AF} (*cf.* Sect. II.3.3.1). Small a-C(:H) and PAHs emit similar aromatic feature strengths if $q_{PAH} \simeq 0.45 \times q_{AF}$ (G21).

9. Alternative acronym: *Poor-people's Amorphous Hydrocarbon...*

IV.3.2.1 The Different Evolution Scenarios

Aromatic features are significantly weaker in low-metallicity systems, compared to normal galaxies (*cf.* Sect. III.2.1.4). This fact could indicate an increasing formation efficiency as a function of Z. However, low-metallicity environments have also their ISM bathed with a hard, permeating ISRF (*cf.* Sect. III.3.2.3). Knowing that small a-C(:H)s are massively destroyed by such an ISRF (*cf.* Sect. IV.2.2.1), this trend could result from the increased suppression of aromatic features at low metallicity. Several scenarios have been proposed to explain these trends.

Enhanced destruction at low metallicity. Madden et al. (2006) proposed that small a-C(:H)s are more efficiently destroyed at low metallicity. This was supported by the relation in Fig. III.41, between the strength of the aromatic features and the $[\mathrm{Ne\,III}]_{15.56\mu m}/[\mathrm{Ne\,II}]_{12.81\mu m}$ tracing the hardness of the ISRF. The fact that dwarf galaxies have in general harder, more intense ISRF is linked to the following facts.

- Low-metallicity stars, at a given initial mass, tend to be hotter, because of line-blanketing effects, therefore emitting a harder ISRF (*e.g.* Martins et al., 2002).
- The opacity of the ISM is lower at low metallicity, because of the low dustiness, allowing photons to travel farther away from ionizing stars (*e.g.* Madden et al., 2020).
- Most observational samples are biased, because they tend to select starburst or post-starburst dwarf galaxies, quiescent dwarf galaxies being challenging to observe at IR wavelengths. We will address this selection effect in Sect. IV.3.2.2.

Another mechanism, proposed by O'Halloran et al. (2006), is the destruction of aromatic feature carriers by SN II blast waves. However, this scenario is less satisfactory, as blast waves tend to destroy all dust species (*e.g.* Reach et al., 2002). They therefore do not constitute a consistent explanation for the selective destruction of small a-C(:H)s.

Inhibited formation efficiency at low metallicity. Several scenarios based on metallicity-dependent production mechanisms, in stellar ejecta or in the ISM, have been proposed.

The delayed injection of C, by LIMS in their post-AGB phase, was proposed by Dwek (2005). Galliano et al. (2008a) conducted a quantitative comparison, using a dust evolution model comparable to Eqs. (IV.41) – (IV.44). We showed that it provided a consistent account of the observed trend of q_{AF} with metallicity. We also took into account the small a-C(:H) photodestruction in H II regions, in the SED modeling, and estimated it was not sufficient to produce the trend. One major problem of this scenario is however that the volatility of small a-C(:H)s, that we see spatially, requires a mechanism to reform them in the ISM.

Shattering of large C grains leads to the formation of small a-C(:H)s. Seok et al. (2014) have implemented this process in a cosmic dust evolution model and showed it could reproduce the q_{AF}-Z trend. The range of SFHs required to cover the whole $q_{\mathrm{AF}} - \mathrm{Z}$ trend is however wider than that needed to reproduce the dustiness-metallicity trend of the same sample (*cf.* our discussion in Sect. IV.3.1.2 about the importance of fitting dust evolution models).

Formation in molecular clouds is another interesting scenario, as the molecular mass fraction is known to rise with metallicity (*e.g.* Schruba et al., 2012). Greenberg et al. (2000) proposed that aromatic feature carriers could form on grain surfaces in molecular clouds and be photoprocessed in the diffuse ISM. Sandstrom et al. (2010) and Chastenet et al. (2019) showed that the spatial distribution of q_{AF} is consistent with this scenario in the Magellanic clouds: q_{AF} is higher in molecular clouds.

IV.3.2.2 The Observed Trends

G21 have derived q_{AF} in each galaxy of the DustPedia/DGS sample, that we have already amply discussed earlier in this chapter. Fig. IV.21 shows the evolution of this quantity with: *(a)* the metallicity, Z; and *(b)* the mean starlight intensity, ⟨U⟩ (Eq. III.38).

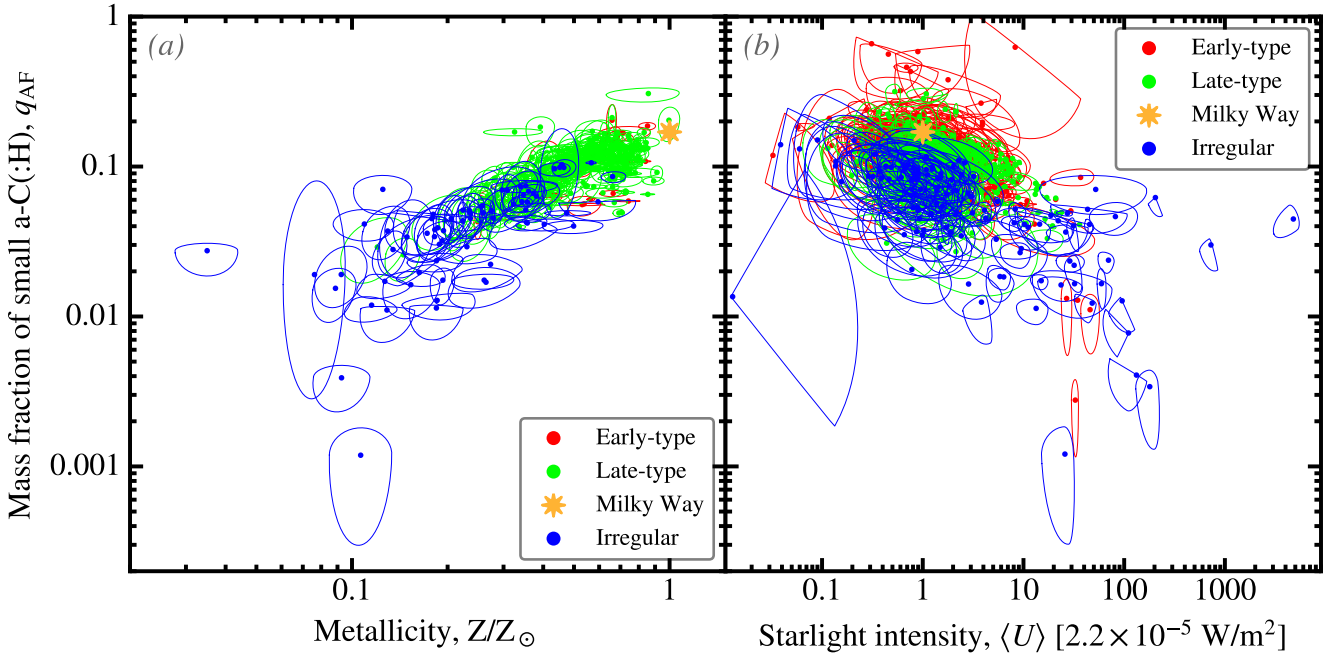

FIGURE IV.21 – *Evolution of the mass fraction of small a-C(:H) grains with metallicity and starlight intensity.* In both panels, we show the mass fraction of aromatic-feature-emitting grains, q_{AF} (*cf.* Sect. II.3.3.1) derived from the SED fit of G21. This quantity is displayed as a function of metallicity and mean starlight intensity, ⟨U⟩ (Eq. III.38). Each SUE corresponds to one galaxy, color-coded according to its type (*cf.* Fig. IV.14). Licensed under CC BY-SA 4.0.

A better correlation with metallicity. Fig. IV.21.a shows a clear linear rising trend of q_{AF} with metallicity (Eq. 9 of G21), and a decreasing trend of q_{AF}, with ⟨U⟩ quantifying the intensity of the ISRF. Both correlations could be explained by any of the scenarios discussed in Sect. IV.3.2.1. We have however found that the correlation with metallicity is significantly better (*cf.* detailed discussion in Sect. 4.2.2 of G21). This result is worth noting, especially since several studies focussing on a narrower metallicity range concluded the opposite (*e.g.* Gordon et al., 2008; Wu et al., 2011). It probably relies on the fact the metallicities we have adopted in this study (De Vis et al., 2019) correspond to well-sampled galaxy averages, while in the past a single metallicity, often central, was available and may have not been representative of the entire galaxy. This result suggests that photodestruction, although real at the scale of star-forming regions, might not be the dominant mechanism at galaxy-wide scales and that one needs to invoke one of the inhibited formation processes discussed in Sect. IV.3.2.1.

> ☞ At global scales, the mass fraction of small a-C(:H) seems to correlate better with metallicity than with the ISRF.

The global point of view. Overall, the $q_{AF}-Z$ trend might have several origins. We think we can be confident about the following facts.

Small a-C(:H) photodestruction is real and it is enhanced at low metallicity. It is however difficult to firmly establish if it is sufficient or not to explain the $q_{AF}-Z$ trend.

The C/O ratio varies as a function of metallicity (*e.g.* Pagel, 2003). For instance, in the SMC, $(C/O) \simeq 1/4\times(C/O)_\odot$. It means that if the a-C(:H)-to-metal mass ratio is Galactic, the abundance of small a-C(:H)s will be at most 1/4 Galactic.

In terms of filling factors of a multiphase ISM, we can assume that small a-C(:H)s are absent of the HIM, WIM and H II regions, and are present in the other phases. Yet, the ISM of low-metallicity systems appears to be permeated with ionized gas, and their molecular cloud filling factor is lower.

What makes this question difficult to tackle is the diversity of spatial scales needed to properly balance the different processes. Ideally, we would indeed need to account for the following.

- A large fraction of the aromatic feature power comes from the UV-illuminated edge of molecular clouds (sub-pc-scales). This is the region where small a-C(:H) will have the higher emissivity, and it is at the edge of the region where they are massively destroyed.
- Most of the mass of small a-C(:H) is in the diffuse, weakly-illuminated phases, filling an important volume of the galaxy (100 kpc-scales).

To know the origin of the q_{AF} – Z trend, we would need to reliably estimate the contribution to the integrated emission of both of these components, resolving sub-pc scales, in order to account for the enhanced emissivity in PDRs. This is out of reach of current facilities.

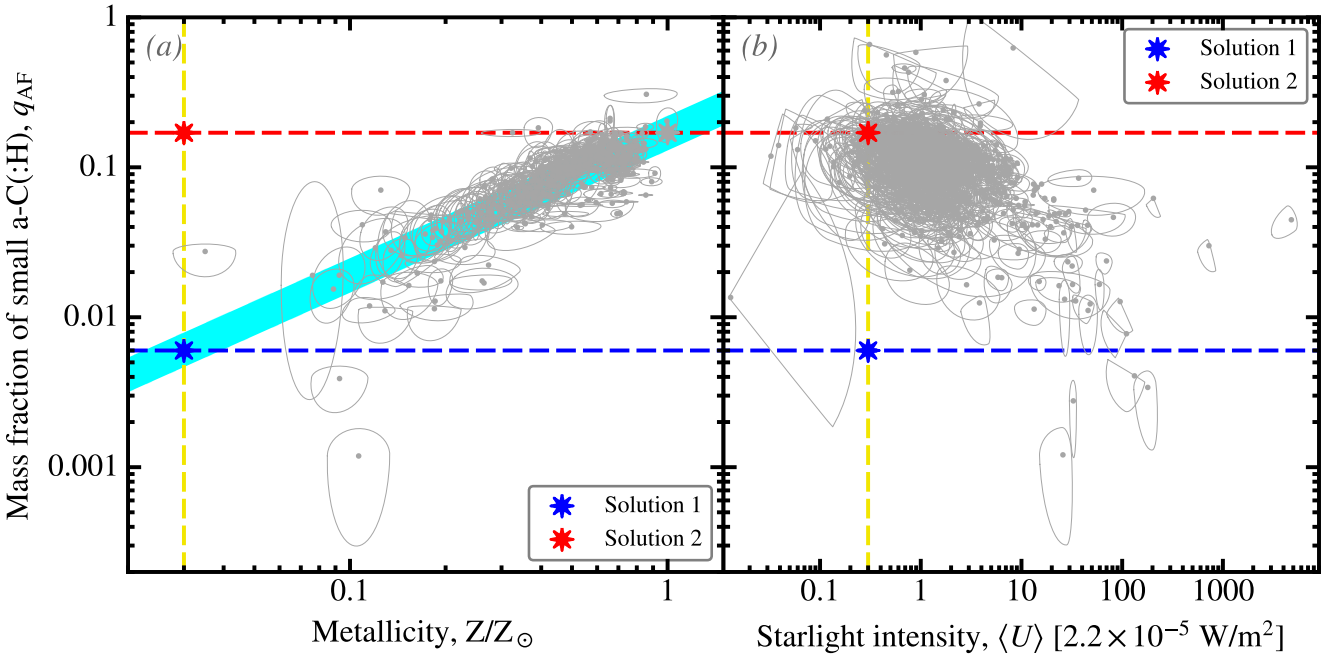

FIGURE IV.22 – *The potential of quiescent very-low-metallicity galaxies to understand the origin of small a-C(:H) grains.* The data in both panels are identical to Fig. IV.21. We have simply added the hypothetical observations of a quiescent very-low-metallicity galaxy (solutions 1 and 2). The cyan stripe in panel *(a)* is the analytical fit of the trend given in Eq. (10) of G21.

The potential of quiescent very-low-metallicity galaxies. An alternative would be to observe quiescent very-low-metallicity systems. We know such a population of galaxies exist (*e.g.* Lara-López et al., 2013). Let's assume that we can estimate q_{AF} for a galaxy with $Z \simeq 0.03\ Z_\odot$ and $\langle U \rangle \simeq 0.3$. We have represented the two possible solutions on Fig. IV.22. We see that:

1. if we find $q_{AF} \simeq 0.006$, it will be consistent with the Z trend (Fig. IV.22.a), but not with the $\langle U \rangle$ trend (Fig. IV.22.b); or
2. if we find $q_{AF} \simeq 0.17$, it will be consistent with the $\langle U \rangle$ trend (Fig. IV.22.b), but not with the Z trend (Fig. IV.22.a).

Such observations would require a sensitive MIR-to-FIR observatory, such as what SPICA (van der Tak et al., 2018b) could have been.

Chapter V

Methodological Effort and Epistemological Reflection

(...) the Bayesian method is easier to apply and yields the same or better results. (...) the orthodox results are satisfactory only when they agree closely (or exactly) with the Bayesian results. No contrary example has yet been produced. (...) We conclude that orthodox claims of superiority are totally unjustified; today, the original statistical methods of Bayes and Laplace stand in a position of proven superiority in actual performance, that places them beyond the reach of mere ideological or philosophical attacks. It is continued teaching and use of orthodox methods that is in need of justification and defense.

(Edwin T. JAYNES; Jaynes, 1976)

Contents

V.1 Understanding the Opposition between Bayesians and Frequentists . . 219
V.1.1 Two Conceptions of Probability and Uncertainty 220
V.1.1.1 The Concept of Conditional Probability 220
The meaning of conditional probabilities. 220
All probabilities are conditional. 220
Bayes' rule. 221
V.1.1.2 The Bayesian and Frequentist Assumptions 221
The Bayesian viewpoint. 221
The frequentist viewpoint. 222
V.1.2 Comparison of the Two Approaches on Simple Cases 223
V.1.2.1 Simple Case: When the Two Approaches Agree 223
The Bayesian solution. 224
The frequentist solution. 224
A few remarks. 225
V.1.2.2 Benefits of Using an Informative Prior 225
The Bayesian improvement. 225
Accumulation of data. 226
V.1.2.3 Case Where the Two Approaches Differ: Non Gaussianity and Few Data 227
Flux with a non-linear detector. 227
The solutions. 227
The reason of the frequentist failure. 228

V.1.3 Numerical Methods to Solve Bayesian Problems . . . 229
V.1.3.1 Sampling the Posterior Distribution . . . 229
Markov Chains Monte-Carlo. . . . 229
The Metropolis-Hastings algorithm. . . . 229
Gibbs sampling. . . . 232
V.1.3.2 Post-Processing MCMCs . . . 232
Assessing convergence. . . . 232
Parameter inference. . . . 233
Quantifying the goodness of a fit. . . . 234
V.1.4 Decision Making and Limitations of the Frequentist Approach . 238
V.1.4.1 Hypothesis Testing . . . 238
Bayesian hypothesis testing. . . . 238
Frequentist hypothesis testing. . . . 240
The Jeffreys-Lindley's paradox. . . . 240
The recent controversy about frequentist significance tests. 241
V.1.4.2 Pros and Cons of the two Approaches . . . 241
Hypotheses and information that can be taken into account. . . . 241
Analysis and interpretation. . . . 242
Overall applicability. . . . 243
V.2 Bayesianism, an Alternative to Popper's Scientific Method . . . 243
V.2.1 Bayes Formula Throughout History . . . 243
V.2.1.1 The Origins . . . 243
The emergence of the concept of probability. . . . 243
The discovery of Bayes. . . . 244
The contribution of Laplace. . . . 245
V.2.1.2 The Frequentist Winter . . . 245
The rejection of Laplace's work. . . . 245
The golden age of frequentism (1920-1930). . . . 245
The Bayesian resistance. . . . 246
V.2.1.3 The Bayesian Renaissance . . . 246
After World War II. . . . 246
The great numerical leap forward. . . . 247
Bayesian techniques, nowadays. . . . 247
V.2.2 Bayesian and Popperian Epistemologies . . . 248
V.2.2.1 The Epistemological Debate at the Beginning of the XXth Century . . . 248
Scientific positivism. . . . 248
Conventionalism and verificationism. . . . 248
V.2.2.2 Popper's Logic of Scientific Discovery . . . 249
The criticism of induction. . . . 249
Falsifiability. . . . 249
Reproducibility. . . . 249
Parsimony (Ockham's razor). . . . 250
Popper's epistemology is frequentist. . . . 250
V.2.2.3 Verifiability, Holisticity and Parsimony: the Bayesian Alternative . . . 250
Falsifiability and the limits of Platonic logic. . . . 250
Parsimony is hard-coded in Bayes' rule. . . . 251
Comparison of the Bayesian and Popperian methods. . . . 252

V.3 Relevance for Interstellar Dust Studies . . . 253
V.3.1 The Particularities of Interstellar Dust Studies . . . 254
V.3.1.1 Complexity of the Physics . . . 254
Degeneracy between microscopic and macroscopic properties. . . . 254
Heterogeneity of the empirical constraints. . . . 254
V.3.1.2 Entanglement of the Observations . . . 254
The observables are weakly informative. . . . 254
Contaminations are challenging to subtract. . . . 255
V.3.2 The Principles of Hierarchical Bayesian Inference . . . 255
V.3.2.1 Non-Hierarchical Bayesian Formalism for SED Modeling 255
Posterior of a single source. . . . 255
Modeling several sources together. . . . 255
V.3.2.2 The Introduction of Nuisance Variables . . . 256
Calibration uncertainties. . . . 256
Introduction into the posterior. . . . 256
V.3.2.3 The Role of the Hyperparameters . . . 257
Accounting for the evidence brought by each source. . . . 257
The hierarchical posterior. . . . 258
V.3.3 Hierarchical Bayesian Models for ISD Studies . . . 258
V.3.3.1 Efficiency and Comparison to Other Methods . . . 258
Close look at a fit. . . . 258
Comparison between different approaches. . . . 260
The emissivity-index-temperature degeneracy of MBBs. . . 262
V.3.3.2 The Role of the Prior . . . 262
Linking the different sources. . . . 262
Holistic prior. . . . 263
V.3.3.3 Other Developments . . . 264
Cosmic dust evolution. . . . 264
MIR spectral decomposition. . . . 265

We have stressed earlier that ISD studies were essentially empirical, because of the complexity of their subject. Most of the time, they consist in interpreting data with formulae and models. Yet, comparing observations to models is a very wide methodological topic. It also has *epistemological*[1] consequences. All the knowledge we derive about ISD depends on the way it was inferred. The question of the methods we use, and the way we articulate different results to build a comprehensive picture of the ISM, is thus of utmost importance.

V.1 Understanding the Opposition between Bayesians and Frequentists

Historically, two competitive visions of the way empirical data should be quantitatively compared to models have emerged, the *(i)* Bayesian, and *(ii)* frequentist methods. We personally follow the Bayesian method and will try to give arguments in favor of its superiority. An efficient way to present the Bayesian approach is to compare it to its alternative, and to show how both methods differ. There is a large literature on the subject. The book of Gelman et al. (2004) is a reference to learn Bayesian concepts and techniques. The posthumous book of Jaynes (2003) is more theoretical, but very en-

1. Epistemology is the philosophical study of the nature, origin and limits of human knowledge. By extension, it is the philosophy of science.

lightening. Otherwise, several reviews have been sources of inspiration for what follows (Jaynes, 1976; Loredo, 1990; Lindley, 2001; Bayarri & Berger, 2004; Wagenmakers et al., 2008; Hogg et al., 2010; Lyons, 2013; VanderPlas, 2014). A good introduction to frequentist methods can be found in the books of Barlow (1989) and Bevington & Robinson (2003).

V.1.1 Two Conceptions of Probability and Uncertainty

Bayesian and frequentist methods differ by: *(i)* the meaning they attribute to probabilities; and *(ii)* the quantities they consider random. Their radically different approaches and the various bifurcations the two methods take to address a given problem originate from these sole conceptions.

V.1.1.1 The Concept of Conditional Probability

The concept of *conditional probability* is central to what follows. As we will see, Bayesian and frequentist approaches differ on this aspect.

The meaning of conditional probabilities. If A and B are two logical propositions, the conditional probability, noted $p(\mathrm{A}|\mathrm{B})$, is the probability of A being true, knowing B is true. To give an astronomical example, let's assume that:

- A is the probability per unit time to observe a SN Ia, when pointing a telescope at a random star; and
- B is the probability to observe a binary system, when pointing a telescope at a random star.

Since most stars are LIMS, and that they have a lifetime $\langle\tau\rangle \simeq 10$ Gyr, we can estimate the probability to observe a SN Ia, knowing we are observing a binary system:

$$p\left(\mathrm{SN\,Ia}\middle|\mathrm{binary}\right) \simeq 0.1\ \mathrm{Gyr}^{-1}. \tag{V.1}$$

On the contrary the probability to observe a binary system, knowing we are observing a SN Ia is:

$$p\left(\mathrm{binary}\middle|\mathrm{SN\,Ia}\right) = 1, \tag{V.2}$$

because SN Ia happen only in binary systems. We see that $p(\mathrm{A}|\mathrm{B}) \neq p(\mathrm{B}|\mathrm{A})$. In our example, the two quantities do not even have the same units.

All probabilities are conditional. In practice, all probabilities are conditional. In the previous example, we have implicitly assumed that our *possibility space*, that is the ensemble of cases we can expect out of the experiment we are conducting, contained all the events where we are actually observing a star, when we are pointing our telescope at its coordinates. However, what if there is suddenly a cloud in front of the telescope? We would then need to account for these extra possibilities, which is equivalent to adding conditions. For instance, if we are conducting the same experiment from a ground-based telescope in London, during winter, we will get:

$$p\left(\mathrm{SN\,Ia}\middle|\mathrm{binary} \wedge \mathrm{London} \wedge \mathrm{winter}\right) \ll 0.1\ \mathrm{Gyr}^{-1}, \tag{V.3}$$

where the symbol $\wedge$ denotes the logical "*and*".

> ☞ All probabilities are conditional and the possible conditions are limited by our own knowledge.

Bayes' rule. Thomas BAYES derived, in the middle of the XVIII$^{\text{th}}$ century, a formula to reverse the event and the condition, in conditional probabilities. Fig. V.1 shows a *Venn diagram*, that is a graphic representation of a possibility space. We have shown an arbitrary event A, in red, and another event B, in blue. The intersection of A and B, numbered (2), can be written A ∧ B. The probability of A, knowing B, is the probability of A, when B is considered as the new possibility space. In other words:

$$p(\mathrm{A}|\mathrm{B}) = \frac{(2)}{(2)+(3)} = \frac{p(\mathrm{A}\wedge\mathrm{B})}{p(\mathrm{B})}. \tag{V.4}$$

We therefore have: $p(\mathrm{A}\wedge\mathrm{B}) = p(\mathrm{A}|\mathrm{B})\,p(\mathrm{B})$. By symmetry of A and B, we have $p(\mathrm{A}\wedge\mathrm{B}) = p(\mathrm{B}\wedge\mathrm{A})$, thus $p(\mathrm{A}|\mathrm{B})\,p(\mathrm{B}) = p(\mathrm{B}|\mathrm{A})\,p(\mathrm{A})$, which gives *Bayes' rule*:

$$p(\mathrm{A}|\mathrm{B}) = \frac{p(\mathrm{B}|\mathrm{A})\,p(\mathrm{A})}{p(\mathrm{B})}. \tag{V.5}$$

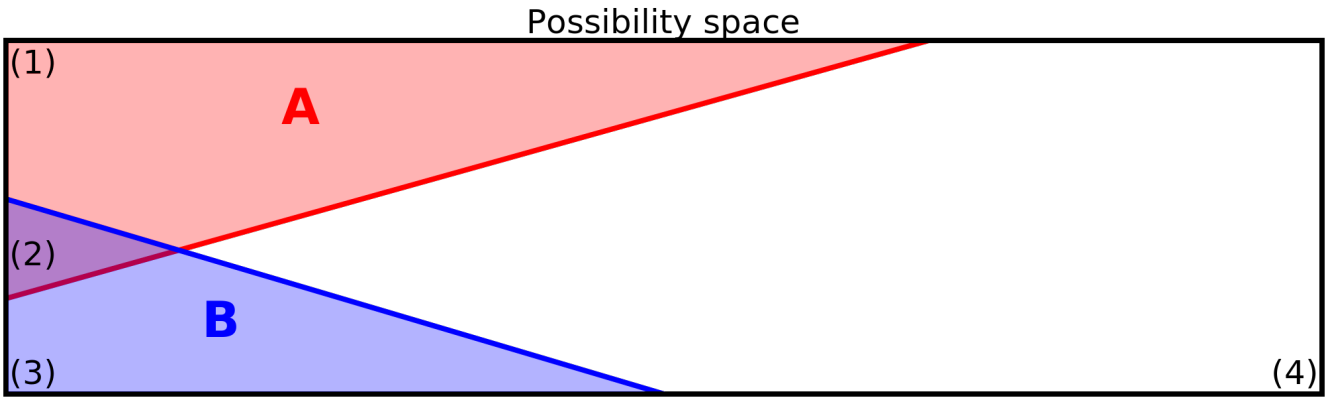

FIGURE V.1 – *Venn diagram to demonstrate Bayes' rule.* Licensed under CC BY-SA 4.0.

V.1.1.2 The Bayesian and Frequentist Assumptions

We review here the assumptions of both methods, in a general, abstract way. We will illustrate this presentation with concrete examples in Sect. V.1.2. Let's consider we are trying to estimate a list of n physical parameters, $\vec{x} = (x_i)_{i=1,\dots,n}$, using a set of m observations, $\vec{d} = (d_j)_{j=1,\dots,m}$. Let's also assume that we have a model, f, predicting the values of the observables, $\vec{d}_{\text{mod}}$, for any value of $\vec{x}$: $\vec{d}_{\text{mod}} = f(\vec{x})$.

The Bayesian viewpoint. The Bayesian approach considers that there is an objective truth, but that our *knowledge* is only partial and subjective. Bayesians thus assume the following.

Probabilities quantify the plausibility of a proposition, when we only have incomplete knowledge. With this assumption, probabilities can be assigned to parameters and hypotheses. More precisely, the true value of a parameter is considered fixed and an hypothesis is either true or false, but our knowledge of the value of this parameter, or of the plausibility of this hypothesis, can be described by random variables. Probabilities are therefore used to quantify our partial, subjective knowledge.

The method then consists in sampling the probability distribution of the parameters, conditional on the data, using Bayes' rule:

$$\underbrace{p\left(\vec{x}\middle|\vec{d}\right)}_{\text{posterior}} \propto \underbrace{p\left(\vec{d}\middle|\vec{x}\right)}_{\text{likelihood}} \times \underbrace{p(\vec{x})}_{\text{prior}}. \tag{V.6}$$

Compared to Eq. (V.5), Eq. (V.6) misses the denominator, $p\left(\vec{d}\right)$. This is because this distribution is independent of our variables, that are the physical parameters. If we were to explicit it, it would be:

$$p\left(\vec{d}\right) = \int p\left(\vec{d}\middle|\vec{x}\right) p\left(\vec{x}\right) \mathrm{d}^n\vec{x}, \tag{V.7}$$

which is simply the normalization factor of $p\left(\vec{x}\middle|\vec{d}\right)$. This factor can thus be estimated by numerically normalizing the posterior, hence the proportionality we have used in Eq. (V.6). The three remaining terms are the following.

The posterior distribution, $p\left(\vec{x}\middle|\vec{d}\right)$, is what we are interested in. It is literally the PDF of the physical parameters (what we want), knowing the data (what we have).

The likelihood, $p\left(\vec{d}\middle|\vec{x}\right)$, is the probability of the data, for a fixed value of the parameters. It can be computed using our model, $f\left(\vec{x}\right)$. For instance, assuming that our observations are affected by uncorrelated, Gaussian noise, with standard deviations $\vec{\sigma} = \left(\sigma_j\right)_{j=1,\dots,m}$, we can write:

$$p\left(\vec{d}\middle|\vec{x}\right) = \frac{1}{(2\pi)^{m/2}\prod_{j=1}^{m}\sigma_j} \exp\left(-\sum_{j=1}^{m}\frac{\left(f_j(\vec{x})-d_j\right)^2}{2\sigma_j^2}\right). \tag{V.8}$$

The prior distribution, $p\left(\vec{x}\right)$, is a unique feature of the Bayesian approach. It literally quantifies all our prior knowledge about the values of $\vec{x}$. We will give concrete examples of what that could mean in the following sections.

The result of the Bayesian approach is the posterior, as it contains all the information we want on the parameters, informed by the observations and our prior knowledge. We can then decide to synthesize this information by, for instance:

- quoting moments of the posterior: means, $\left\langle x_i\middle|\vec{d}\right\rangle$, standard deviation, $\sigma\left(x_i\middle|\vec{d}\right)$, *etc.*;
- quoting their correlation coefficient: $\rho\left(x_i, x_j\middle|\vec{d}\right)$, *etc.*;
- testing hypotheses: $\mathrm{P}\left(x_i > \mathrm{const}\middle|\vec{d}\right)$, *etc.*;
- and so on.

The frequentist viewpoint. The frequentist approach also considers that there is an objective truth, but it differs with the Bayesian viewpoint by rejecting its subjectivity. Frequentists thus assume the following.

Probabilities are the limit to infinity of the *occurrence frequency* of an event, in a sequence of repeated experiments, under identical conditions[2]. This repeated event can be, for instance, the measure of a quantity. The rejection of the use of probabilities as a quantification of knowledge forbids frequentists to consider parameters or hypotheses as random variables. In other words, physical quantities have a single, true value, and hypotheses are either true or false. Only the data, which are tainted with uncertainties, can be considered as random variables.

The method then consists in using the likelihood, $p\left(\vec{d}\middle|\vec{x}\right)$, to perform several tests, the most well-known being the *maximum likelihood*. We can see here that frequentists consider the probability distribution of the data, given the physical parameters. The data are thus considered as *variables*, and the physical parameters, fixed.

The results consist in describing what values of the physical parameters we would find if we were to repeat the experiment in the same conditions. Frequentists then compute the uncertainties on their estimate of the parameters by simulating new data that could have been obtained in

2. It is often considered as the scientific definition of probabilities, while we will show later that the Bayesian definition has more practical applications.

the same conditions. We thus end-up with a distribution of parameter values, that is not a probability distribution. For instance, hypothesis testing can not be performed the Bayesian way, because we dot not have a conditional probability of the parameter. We will see in Sect. V.1.4.1 that we need to resort to the infamous significance tests, instead.

☞ Bayesians do not tamper with the data, whereas frequentists account for hypothetical data that have not actually been obtained.

V.1.2 Comparison of the Two Approaches on Simple Cases

We now compare the two approaches on a series of simple examples, in order to demonstrate in which situations the two approaches may differ.

V.1.2.1 Simple Case: When the Two Approaches Agree

Let's assume we are trying to estimate the flux of a star, $\mathrm{F}_\star$, in a given photometric filter, with the following assumptions.

- The true flux of the star is $\mathrm{F}_{\mathrm{true}} = 42$ (in arbitrary units).
- We have performed $m = 3$ repeated measures, $d_j = \mathrm{F}_j$ $(j = 1, \ldots, m)$.
- Each flux has Gaussian *independent, identically distributed* (iid) uncertainties: $\sigma_j = \sigma_\mathrm{F} = 14$ $(\forall\, j = 1, \ldots, m)$.
- The physical quantity we want to estimate is simply the value of the flux, $\mathrm{F}_\star$. This corresponds thus to the simplest case, where we have only $n = 1$ parameter and the model is the identity: $\mathrm{F}_{\mathrm{mod}} = f(x) = x$.

This is represented in Fig. V.2. There is an analytic solution to this simple case:

$$\mathrm{F}_\star \simeq \frac{\sum_{j=1}^{m} \mathrm{F}_j}{m} \pm \frac{\sigma_\mathrm{F}}{\sqrt{m}} = 53.9 \pm 8.1. \tag{V.9}$$

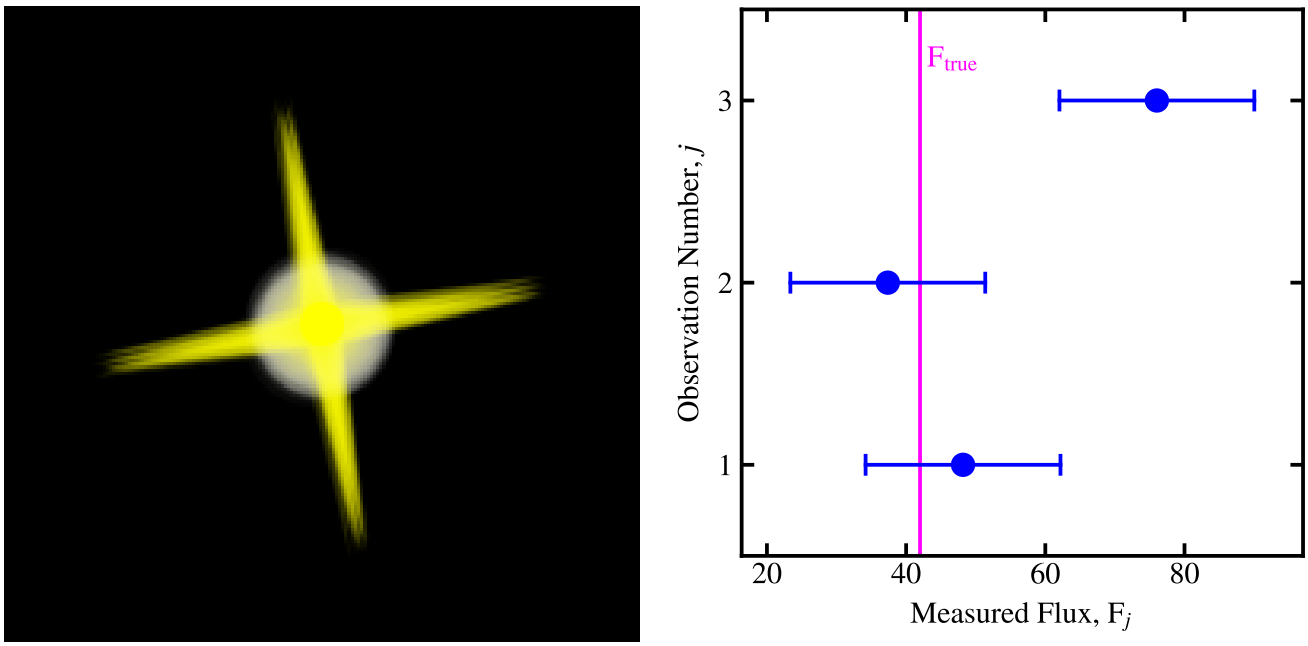

FIGURE V.2 – *Simulation of the measure of a stellar flux to compare Bayesian and frequentist methods.* The blue dots with error bars represent the successive measures and their uncertainties. The magenta line shows the true value. The units are arbitrary. Licensed under CC BY-SA 4.0.

The Bayesian solution. The Bayesian solution is obtained by sampling the posterior distribution in Eq. (V.6): $p(F_\star|F_1,F_2,F_3)$.

The likelihood term is exactly Eq. (V.8), in our case, as we have Gaussian iid uncertainties.

The choice of the prior is the arbitrary part of the Bayesian model. For this first example, let's assume that we have no idea what the flux should be. We thus take a flat, *uninformative prior*, $p(F_\star) \propto 1$. This is a subjective choice that has the following consequences.

1. This particular choice is called an *improper prior*, meaning it can not be normalized, as: $\int_{-\infty}^{\infty} p(F_\star)\,dF_\star = \infty$. In practice, we thus need to choose lower and upper bounds, $[F_-,F_+]$, beyond which the prior is 0. Since we are measuring a positive quantity[3], we can take $F_- = 0$ as the lower bound. The upper bound could be taken as several times the flux of a 120 $M_\odot$ star at the distance of the source. We thus have:

$$p(F_\star) = \begin{cases} \dfrac{1}{F_+ - F_-} & \text{for } F_- \leq F_\star \leq F_+ \\ 0 & \text{otherwise.} \end{cases} \tag{V.10}$$

2. This prior is also subjective, as it depends on the choice of the variable. If we decide to study $\ln F_\star$, instead of $F_\star$, it will lead to a different result. We will address this issue in Sect. V.1.4.1. We can summarize it the following way.
   - If the choice of the prior matters in the final solution, it means that the weight of evidence brought by the data is weak. It is therefore natural that the way we decide to quantify our prior knowledge is important. This is an aspect of the Bayesian method we need to embrace.
   - On the opposite, if the weight of evidence brought by the data is large, the choice of the prior will not matter significantly. In other words, if the width of the likelihood is much narrower than a dex, the difference between multiplying by $p(F_\star)$ or $p(\ln F_\star)$ will be negligible.

The solution is represented in Fig. V.3.a. We have sampled the posterior using a *Markov Chain Monte-Carlo* method (MCMC; using the code `emcee` by Foreman-Mackey et al., 2013). We will come back to MCMC methods in Sect. V.1.3. The estimated value is $F_\star \simeq 53.9 \pm 8.1$ (1σ uncertainty). This is exactly the analytical solution in Eq. (V.9). The 95 % *credible range*, that is the range centered on $\langle F_\star \rangle$ containing a 95 % probability, is $CR_{95\,\%}(F_\star) = [37.8, 69.8]$.

The frequentist solution. There are different ways to approach this problem in the frequentist tradition. The most common solution would be to use a *Maximum-Likelihood Estimation* (MLE) method.

Maximum-likelihood value. There are numerical tools to compute the MLE of complex models. We have used a *Levenberg-Marquardt algorithm* (*e.g.* Markwardt, 2009). The MLE value of $F_\star$ we derive is $F_{ML} = 53.9$, which is in agreement with the analytical solution in Eq. (V.9). It however does not provide uncertainties.

Uncertainty estimates. A common solution to estimate the uncertainties on F_{ML} would be to perform *bootstrapping*. Following the frequentist conception of probabilities, we randomly draw new observations around the MLE value, a large number of times. We thus obtain a set of synthetic repeated measures, assuming the population distribution has F_{ML} for mean. For each new set, we derive a new MLE value, $\bar{F}_{ML}^{(k)}$ ($k = 1,\ldots,3000$). The first four draws are represented in Fig. V.3.b-e. The standard deviation of this sample is 8.1, in agreement with Eq. (V.9). We can also compute the 95 % *confidence interval*, from this sample: $CI_{95\,\%}(F_\star) = [37.8, 69.8]$.

3. Our variable is the true flux. It is positive. Measured fluxes can occasionally be negative because of noise fluctuations.

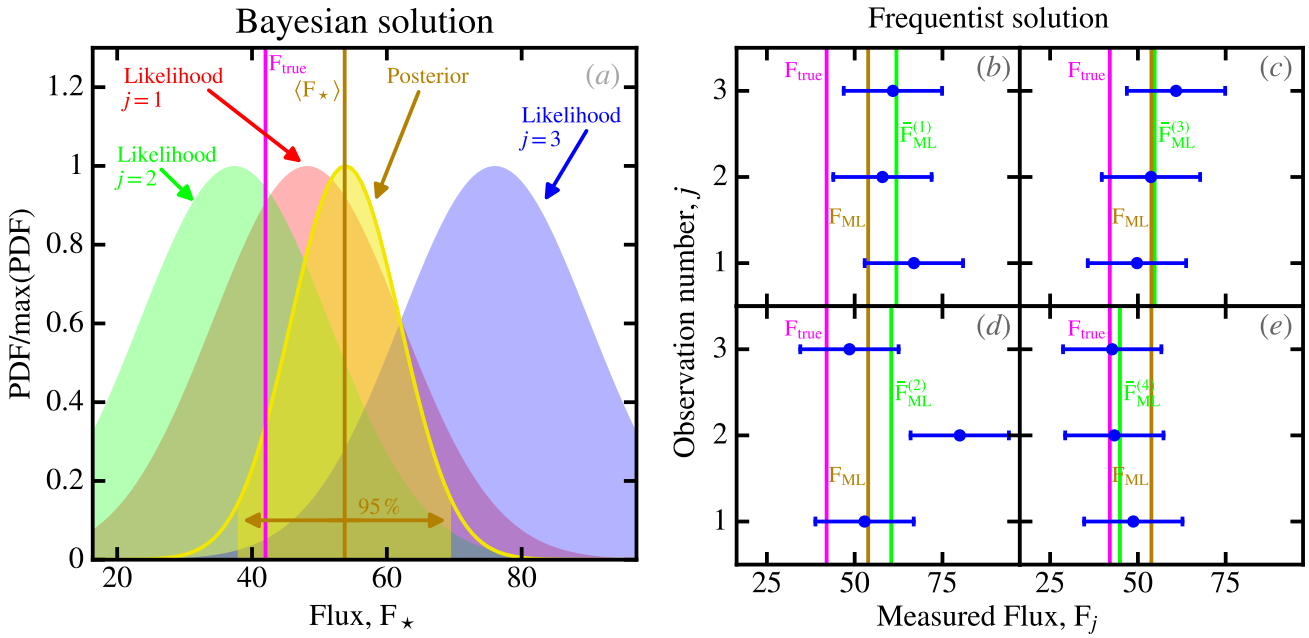

FIGURE V.3 – *Bayesian and frequentist solutions to the problem of Fig. V.2.* Panel *(a)* shows the likelihood of the individual measures, in red, green and blue. The posterior, which is the product of the three likelihoods, is shown in yellow. We have filled its area corresponding to the 95 % credible range. The posterior average, $\langle F_\star \rangle$ is shown in dark yellow. Panels *(b-e)* shows random reproduction of the measures. The blue dots with error bars are randomly drawn around the maximum likelihood, F_{ML}, using a bootstrapping method. The estimated value of $F_\star$ resulting from these draws, $\bar{F}^{(k)}_{ML}$, is shown in green. In all panels, the true value, F_{true}, is shown in magenta.

A few remarks. We can see that both methods give the same exact result, which is also consistent with the analytical solution (Eq. V.9). This is because the assumptions were simple enough to make the two approaches equivalent:

1. by assuming a flat prior, we removed the effect of this Bayesian peculiarity;
2. the symmetry and the iid nature of the noise made the sampling of the likelihood as a function of the parameters, or as a function of the data, identical.

Note also our subtle choice of terminology: *(i)* we talk about *credible range* in the Bayesian case, as this term designates the quantification of our beliefs; while *(ii)* we talk about *confidence interval* in the frequentist case, as it concerns our degree of confidence in the results, if the experiment was repeated a large number of times, assuming the population mean is the maximum likelihood.

V.1.2.2 Benefits of Using an Informative Prior

A first way to find differences between the Bayesian and frequentist approaches is to explore the effect of the prior. To that purpose, let's keep the same experiment as in Sect. V.1.2.1, but let's assume now that the star we are observing belongs to a cluster, and we know its distance.

The Bayesian improvement. Contrary to Sect. V.1.2.1, where we had to guess a very broad, flat prior, we can now refine this knowledge, based on the expected luminosity function, scaled at the known distance of the cluster. This is represented on Fig. V.4. The posterior distribution (yellow) is now the product of the likelihood (green) and prior (blue). The frequentist solution has not changed, as it can not account for this kind of information. We can see that the maximum *a posteriori* is now closer to the true value than the maximum likelihood. This can be understood the following way.

The true flux has been drawn from the luminosity function, because we have randomly targetted a star in this cluster. This is the definition of the luminosity function, which we happen to have chosen as the prior. This is often noted $F_{true} \sim p(F_\star)$, the $\sim$ symbol meaning "*distributed as*".

The observed flux has then been drawn from a normal law centered on F_{true} with variance σ_F^2, that can be written: $F_j|F_{true} \sim \mathcal{N}(F_{true}, \sigma_F^2)$. This is equivalent to saying that the observed flux has been drawn from the posterior $p(F_\star) \times \mathcal{N}(F_{true}, \sigma_F^2)$. Sampling this distribution is thus the best choice we can make, considering the information we have. This is why we get an advantage over the frequentist result.

If we perform several such measures, there will be some Bayesian solutions that will get corrected farther away from the true flux. This is a consequence of stochasticity. On Fig. V.4, keeping our value of F_{true}, this will be the case if the noise fluctuation, $-\delta F$ is negative, that is if the observed flux is lower than F_{true} ($F_j = F_{true} - \delta F < F_{true}$). However, this deviation will be less important than the correction we would benefit from if the same fluctuation was positive, because the prior would be higher: $p(F_{true} - \delta F) > p(F_{true} + \delta F)$ (*cf.* Fig. V.4). The prior would therefore correct less the likelihood on the left side, in this particular case. Thus, on average, taking into account this informative prior will improve the results.

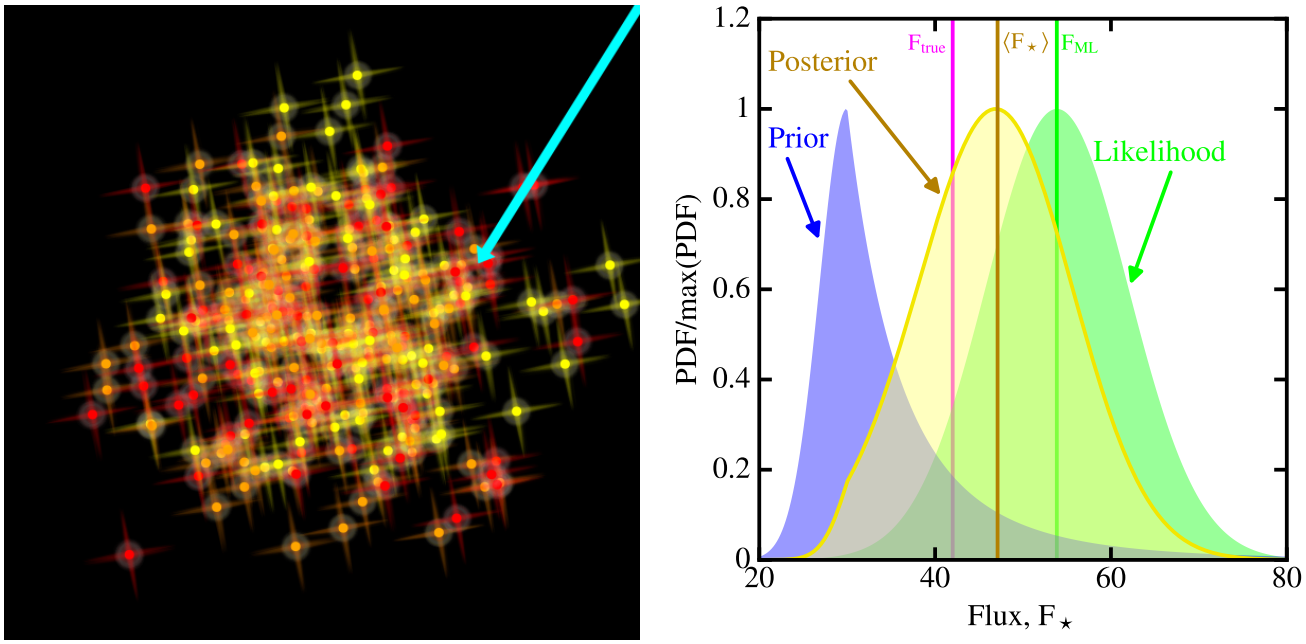

FIGURE V.4 – *The benefits of using an informative prior.* The green curve shows the total likelihood. It is identical to the yellow curve in Fig. V.3. The prior, which is taken as the luminosity function of the cluster, is represented in blue. The posterior, in yellow, is the product of these two distributions.

Accumulation of data. In this case and the previous one (Sect. V.1.2.1), we had three observations of the same flux. The posterior distribution we sampled was:

$$p(F_\star|F_1, F_2, F_3) \propto p(F_\star) \times p(F_1|F_\star) \times p(F_2|F_\star) \times p(F_3|F_\star)\,. \tag{V.11}$$

This is because we considered the three measures as part of the same experiment. However, we could have chosen to analyze the data as they were coming. After the first flux, we would have inferred:

$$p(F_\star|F_1) \propto p(F_\star) \times p(F_1|F_\star)\,. \tag{V.12}$$

This posterior would have been wider (*i.e.* more uncertain), as we would have had only one data point. Note that such an inference would have not been possible with a frequentist method, as we

would have had one parameter for one constraint (*i.e.* zero degree of freedom). What is interesting to note is that the analysis of the second measure, can be seen as taking into account the first measure in the prior:

$$p(\mathrm{F}_\star|\mathrm{F}_1,\mathrm{F}_2) \propto p(\mathrm{F}_\star)\, p(\mathrm{F}_1|\mathrm{F}_\star) \times p(\mathrm{F}_2|\mathrm{F}_\star) = \underbrace{p(\mathrm{F}_\star|\mathrm{F}_1)}_{\text{new prior}} \times p(\mathrm{F}_2|\mathrm{F}_\star)\,, \tag{V.13}$$

and so on. For the third measure, the new prior would be $p(\mathrm{F}_\star|\mathrm{F}_1,\mathrm{F}_2)$:

$$p(\mathrm{F}_\star|\mathrm{F}_1,\mathrm{F}_2,\mathrm{F}_3) \propto \underbrace{p(\mathrm{F}_\star|\mathrm{F}_1,\mathrm{F}_2)}_{\text{new prior}} \times p(\mathrm{F}_3|\mathrm{F}_\star)\,. \tag{V.14}$$

which is formally equivalent to Eq. (V.11), but is a different way of looking at the prior. Notice that the original prior, $p(\mathrm{F}_\star)$, appears only once in the product. The more we accumulate data, the less important it becomes.

> ☞ The Bayesian approach is an optimal framework to account for the accumulation of knowledge.

V.1.2.3 Case Where the Two Approaches Differ: Non Gaussianity and Few Data

The other reason why the two approaches might differ is because Bayesians sample $p\left(\vec{x}\middle|\vec{d}\right)$, whereas frequentists produce a series of tests based on $p\left(\vec{d}\middle|\vec{x}\right)$. The difference becomes evident when we consider non-Gaussian errors with small data sets.

Flux with a non-linear detector. Let's assume that we are measuring again the flux from the same star ($\mathrm{F}_\star = 42$), with $m = 3$ repetitions, but that our detector is now highly non-linear. This non-linearity translates into a heavily-skewed split-normal noise distribution (*cf.* Sect. C.2.2):

$$p(\mathrm{F}_j|\mathrm{F}_\star) = \begin{cases} \dfrac{1}{\sqrt{2\pi}\lambda} \exp\left(-\dfrac{(\mathrm{F}_j-\mathrm{F}_\star)^2}{2\lambda^2}\right) & \text{if } \mathrm{F}_j \leq \mathrm{F}_\star \\ \dfrac{1}{\sqrt{2\pi}\lambda\tau} \exp\left(-\dfrac{(\mathrm{F}_j-\mathrm{F}_\star)^2}{2\lambda^2\tau^2}\right) & \text{if } \mathrm{F}_j > \mathrm{F}_\star. \end{cases} \tag{V.15}$$

with $\lambda = 0.3$ and $\tau = 50$. This noise distribution is the red curve in Fig. V.5.a. In practice, this could for example be a very accurate detector suffering from transient effects. The measured value would be systematically higher than the true flux[4]. We have simulated three such measures in Fig. V.5.a, in blue. This problem was adapted from example 5 of Jaynes (1976).

The solutions. Knowing that the measured flux is always greater than or equal to the true flux, it is obvious that the solution should be lower than the lowest measured flux: $\mathrm{F}_\star \leq \min_j \mathrm{F}_j = 47.6$, in our particular case. This flux range, corresponding to inconsistent values, has been hatched in grey, in Fig. V.5.

The Bayesian solution is obtained the same way as before, by sampling the posterior. We again assume a flat prior, and take the likelihood in Eq. (V.15). The posterior is shown in yellow, in Fig. V.5.b. It has zero probability in the range that we qualified as "*inconsistent*", and the true value falls in a high probability domain. The mean and standard deviation of the posterior give us $\mathrm{F}_\star \simeq 43.8 \pm 3.6$, with $\mathrm{CR}_{95\,\%}(\mathrm{F}_\star) = [34.6, 47.9]$.

4. The distribution in Fig. V.5.a has a very narrow tail on the lower side of $\mathrm{F}_{\mathrm{true}}$. It can thus in principle be lower, but this is such a low probability event that, for the clarity of the discussion, we will assume this is unlikely.

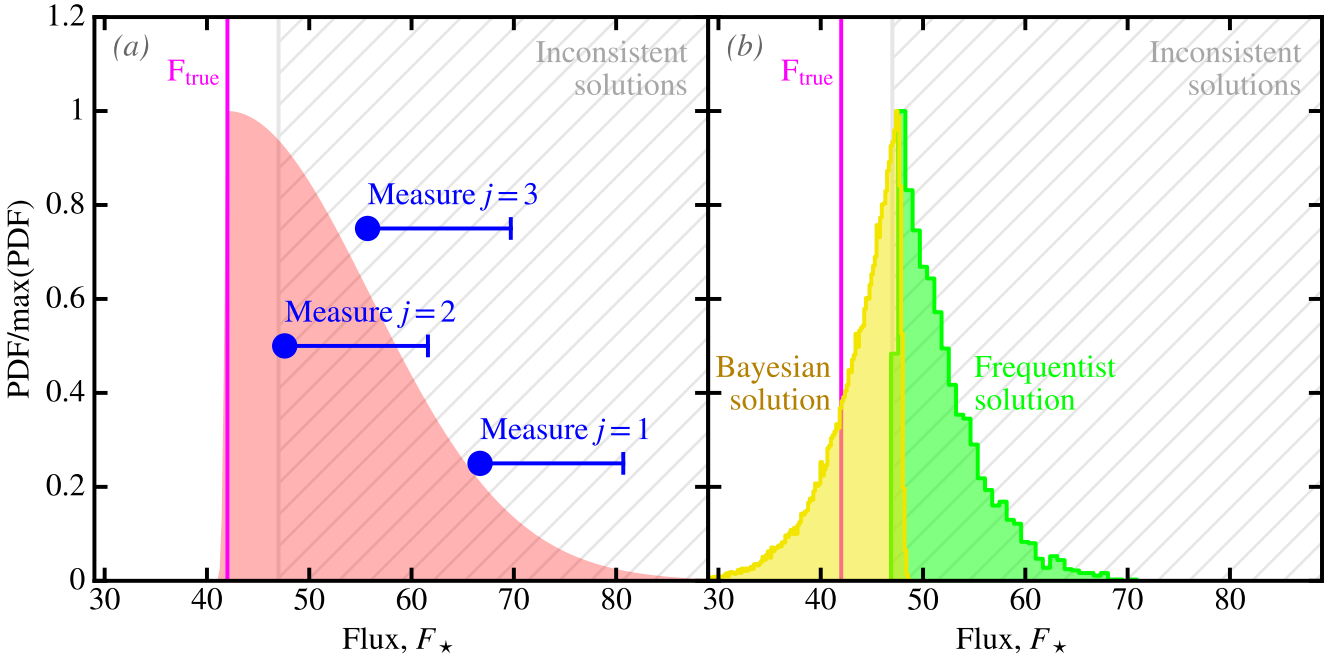

FIGURE V.5 – *Flux measures with a non-linear detector.* Panel *(a)* shows the noise distribution, in red, and the three observations in blue. Panel *(b)* displays the Bayesian posterior in yellow and the frequentist bootstrapping in green. In both panels, the true flux is shown in magenta and the zone of inconsistent solutions is hatched in grey. Licensed under CC BY-SA 4.0.

The frequentist solution is obtained the same way as before. The maximum likelihood and the whole bootstrapping sample however falls in the "*inconsistent*" domain. We get $F_\star \simeq 51.9 \pm 4.0$, with $CI_{95\,\%}(F_\star) = [47.4, 62.5]$. We see here that the frequentist solutions fails at inferring the true flux. On top of that, it gives only "*inconsistent*" solutions. In this particular case, this is because of the asymmetry of the noise, which breaks the symmetry between $p(F_j|F_\star)$ and $p(F_\star|F_j)$ that we had in Sect. V.1.2.1. This can be seen in Fig. V.5.b. The frequentist solution is the mirror symmetric of the Bayesian posterior for that reason.

When m increases, the frequentist solution gets closer and closer to the true flux. However, a bootstrapping analysis will reject the true flux in 100 % of the cases.

The reason of the frequentist failure. The failure of the frequentist approach is a direct consequence of its conception of probability (*cf. e.g.* VanderPlas, 2014, for a more detailed discussion and more examples). The frequentist method actually succeeds in returning the result it pretends to give: predicting a confidence interval where the solution would fall 95 % of the time, if we repeated the same procedure a large number of times. This is however not equivalent to giving the credible range where the true value of the parameter has a 95 % probability to be (the Bayesian solution). With the frequentist method, we have no guarantee that the *true* flux will be in the confidence interval, only the *solution*. We can see that the main issue with the frequentist approach is that it is difficult to interpret, even in a simple problem such as that of Fig. V.5. "*Bayesians address the question everyone is interested in by using assumptions no-one believes, while Frequentists use impeccable logic to deal with an issue of no interest to anyone*" (Lyons, 2013). In the previous citation, the "*assumption no-one believes*" is the subjective choice of the prior, and the "*issue of no interest to anyone*" is the convoluted way frequentists formulate a problem, to avoid assigning probabilities to parameters.

☞ Frequentist results can be inconsistent in numerous practical applications, and they never perform better than Bayesian methods.

V.1.3 Numerical Methods to Solve Bayesian Problems

Bayesian problems are convenient to formulate as they consist in laying down all the data, the model, the noise sources and the nuisance variables to build a posterior, using Bayes' rule. The Bayesian results are also convenient to interpret as they all consist in using the posterior, which gives the true probability of the parameters. However, in between, estimating the average, standard deviation, correlation coefficients of parameters, or testing hypotheses can be challenging, especially if there are a lot of parameters or if the model is complex. Fortunately, several numerical methods have been introduced to make these tasks simpler. Most of these methods are based on *Markov Chain Monte-Carlo* (MCMC [5]), which are a class of algorithms for sampling PDFs.

V.1.3.1 Sampling the Posterior Distribution

Markov Chains Monte-Carlo. A MCMC draws samples from the posterior. In other words, it generates a *chain* of N values of the parameters, $\vec{x}_k$ ($k = 1, \ldots, \mathrm{N}$). These parameter values are not uniformly distributed in the parameter space, but their number density is proportional to the posterior PDF. Consequently, there are more points where the probability is high, and almost none where the probability is low. It has several advantages.

- Contrary to grid-based sampling or standard Monte-Carlo techniques, we spend most of our computing time estimating our model (which can be costly) where it matters, and not much time where it does not.
- From the MCMC, it is very simple and easy to estimate moments of a given parameter, marginalizing over the other ones. For instance, if we have two parameters, x and y, the average of x, marginalizing over y would be:

$$\langle x \rangle \equiv \iint x.p(x,y)\,\mathrm{d}x\,\mathrm{d}y \simeq \frac{1}{\mathrm{N}} \sum_{k=1}^{\mathrm{N}} x_k, \tag{V.16}$$

  where the second equality is simply the average of the sample. We could do the same for the standard deviation, or the correlation coefficient.
- It also makes hypothesis testing very easy. For instance, if we want to know the probability that $x > y$, we literally compute the fraction of points in the MCMC, where $x_k > y_k$.

All these operations would have been much more expensive, in terms of computing time, if we had to numerically solve the integral. In particular, computing the normalization of the whole posterior would have been costly. From a technical point of view, a MCMC is a random series of values of a parameter where the value at step k depends only the value at step $k-1$. We briefly discuss below the two most used algorithms. A good presentation of these methods can be found in the book of Gelman et al. (2004) or in the *Numerical recipes* (Press et al., 2007).

The Metropolis-Hastings algorithm. To illustrate this method and the next one, let's consider again the measure of the flux of our star, with the difference, this time, that we would be observing it through two different photometric filters.

- Let's call $\mathrm{F}_\star$ and $\mathrm{G}_\star$ the fluxes in these two bands, with uncertainties $\sigma_\mathrm{F} = 12$ and $\sigma_\mathrm{G} = 10$.
- Let's assume that the uncertainties in the filters are correlated, with a correlation coefficient, $\rho = 0.8$, because, for instance, of the way the calibration was performed.

5. Numerous authors publish articles claiming to have solved a problem using "*MCMC methods*". This is not the best terminology to our mind, especially knowing that MCMCs can be used to sample any distribution, not only a Bayesian posterior. These authors should state instead to have solved a problem in a Bayesian way (what), using a MCMC numerical method (how). The same way, we tell our students to say that they "*modeled the photoionization*", rather than they "*used Cloudy*".

- Let's assume that we make only $m = 1$ measure in each band, with observed fluxes $F_1 = 42$ and $G_1 = 36$. The posterior, assuming a flat prior, is simply a bivariate normal distribution centered on the observed flux, with covariance matrix:

$$V = \begin{pmatrix} \sigma_F^2 & \rho\sigma_F\sigma_G \\ \rho\sigma_F\sigma_G & \sigma_G^2 \end{pmatrix}. \tag{V.17}$$

The posterior is thus, noting $\vec{x} = (F_\star, G_\star)$ and $\vec{d} = (F_1, G_1)$:

$$p\left(\vec{x}\middle|\vec{d}\right) \propto \exp\left(-\frac{1}{2}(\vec{x}-\vec{d})^T V^{-1}(\vec{x}-\vec{d})\right). \tag{V.18}$$

Contours of this distribution are represented in Fig. V.6.a-b.

The algorithm proposed by Metropolis et al. (1953) and generalized by Hastings (1970) is the most popular method to sample any PDF. This is a *rejection method*, similar to what we have discussed for MCRTs, in Sect. III.1.1.4 (*cf.* also Appendix C.2.3.1).

A proposal distribution, $p(\vec{x}_k|\vec{x}_{k-1})$, first needs to be chosen. The choice of this distribution is instrumental in the sampling efficiency: *(i)* if it is too wide, a lot of draws will be rejected; *(ii)* if it is too narrow, the sampling steps are going to be small, and more iterations are going to be necessary to sample the posterior. For our present example, we choose a bivariate normal distribution, centered on $\vec{x}_{k-1}$, whose width is the noise of our data, $s_F = \sigma_F$ and $s_G = \sigma_G$:

$$p(\vec{x}_k|\vec{x}_{k-1}) \propto \exp\left[-\frac{1}{2}\left(\frac{F_{\star,k}-F_{\star,k-1}}{s_F}\right)^2 - \frac{1}{2}\left(\frac{G_{\star,k}-G_{\star,k-1}}{s_G}\right)^2\right] \tag{V.19}$$

The method then consists in the following steps, iterated N times.

1. At each iteration, k, we draw a new set of parameters, $\vec{x}_k$, from the proposal distribution: $\vec{x}_k \sim p(\vec{x}_k|\vec{x}_{k-1})$.
2. With this new value, we compute the *acceptance probability*, defined as:

$$\alpha_k = \min\left(1, \frac{p\left(\vec{x}_k\middle|\vec{d}\right) p(\vec{x}_{k-1}|\vec{x}_k)}{p\left(\vec{x}_{k-1}\middle|\vec{d}\right) p(\vec{x}_k|\vec{x}_{k-1})}\right). \tag{V.20}$$

The min function is here to make sure we get a result between 0 and 1. In our case, we have chosen a symmetric proposal distribution. Eq. (V.19) thus implies that:

$$\frac{p(\vec{x}_{k-1}|\vec{x}_k)}{p(\vec{x}_k|\vec{x}_{k-1})} = 1 \quad\Rightarrow\quad \alpha_k = \min\left(1, \frac{p\left(\vec{x}_k\middle|\vec{d}\right)}{p\left(\vec{x}_{k-1}\middle|\vec{d}\right)}\right). \tag{V.21}$$

We just need to estimate our posterior at one position (assuming we saved the value of $p\left(\vec{x}_{k-1}\middle|\vec{d}\right)$, after the previous iteration). In addition, since we need only the ratio of two points in the posterior, we do not need to normalize it. This is the reason why this algorithm is so efficient.

3. To update $\vec{x}_k$, we draw a random variable, θ_k, uniformly distributed between 0 and 1.
   - If $\theta_k \leq \alpha_k$, we accept the new value, $\vec{x}_k$.
   - If $\theta_k > \alpha_k$, we reject the new value and keep the old one, $\vec{x}_k = \vec{x}_{k-1}$.

The initial value of the chain has to be a best guess.

The sampling of Eq. (V.18) with the Metropolis-Hastings method is shown in Fig. V.6.a.

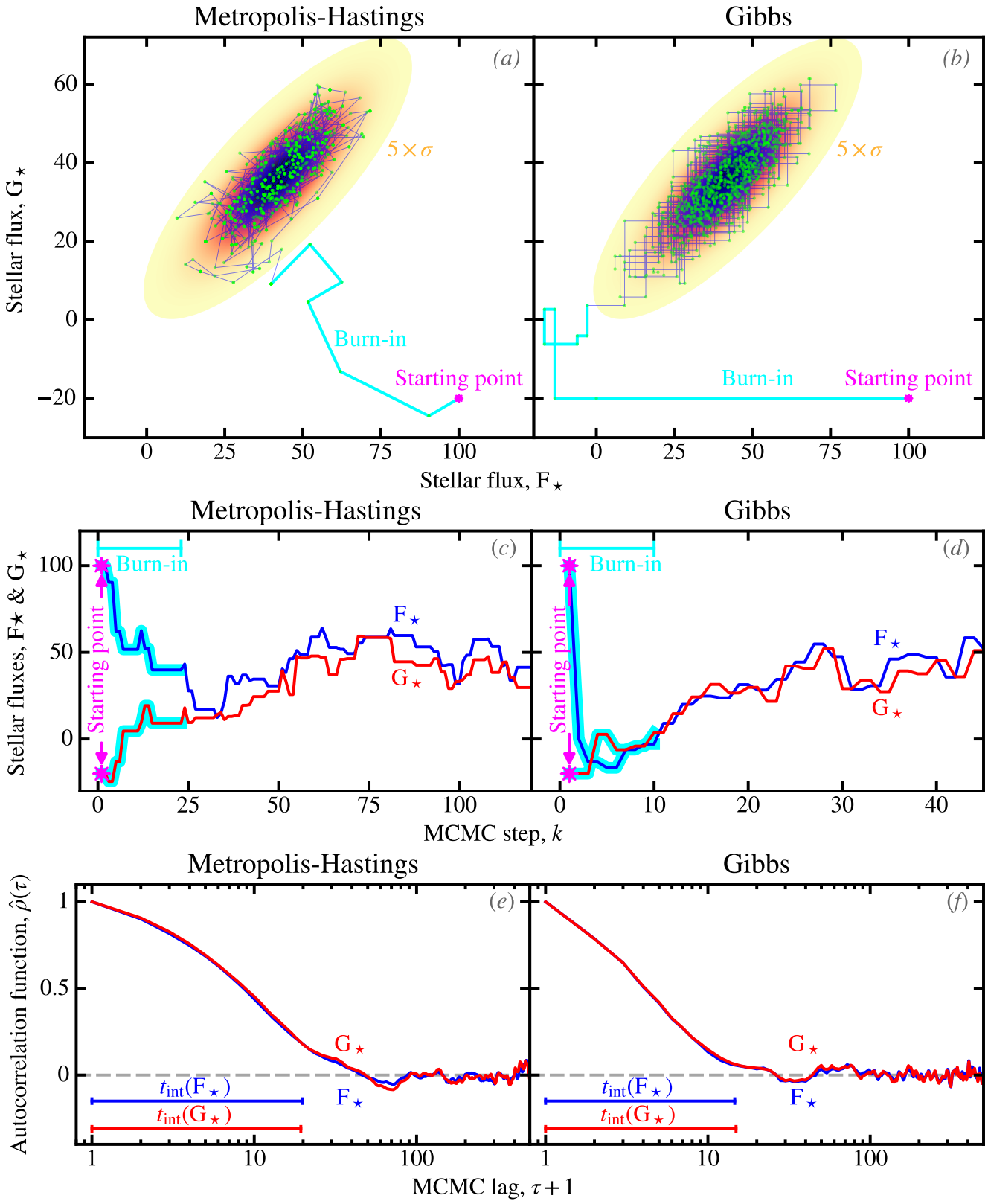

FIGURE V.6 – *Markov Chain Monte-Carlo algorithms.* Panels *(a)* and *(b)* show contours, up to 5σ, of the posterior distribution of Eq. (V.18). In both panels, the blue line with the green dots represent the MCMC, for the first 1000 steps, starting from the magenta star. The burn-in phase is highlighted in cyan. Panels *(c)* and *(d)* represent the MCMCs of the two parameters, at the start of the chain. We have highlighted the burn-in phase in cyan. Panels *(e)* and *(f)* represent the ACFs of both parameters. We have also quoted the integrated autocorrelation times, $t_{\rm int}$. As indicated, left panels demonstrate the Metropolis-Hastings algorithm, while right panels show Gibbs sampling.

Gibbs sampling. The number of parameters, n, determines the dimension of the posterior. The higher this number is, the smaller the *support of the function* is (*i.e.* the region where the probability is non negligible). Metropolis-Hastings methods therefore will have a high rejection rate, if $n \gg 1$, requiring longer chains to ensure convergence. *Gibbs sampling* (Geman & Geman, 1984) provides an alternative MCMC method, where all draws are accepted. Its drawback is that it requires normalizing, at each iteration, the *full conditional distribution*:

$$p\left(x_i \middle| \vec{x}_-, \vec{d}\right) \equiv p\left(x_i \middle| x_1, \ldots, x_{i-1}, x_{i+1}, \ldots, x_n, \vec{d}\right) \tag{V.22}$$

that is the posterior fixing all parameters except one. This is only a one dimensional PDF, though, much less computing-intensive than the whole posterior. The method consists, at each iteration k, to cycle through the different parameters, and draw a new value from Eq. (V.22):

$$x_{i,k} \sim p\left(x_{i,k} \middle| \underbrace{x_{1,k}, \ldots, x_{i-1,k}}_{\text{already updated}}, \underbrace{x_{i+1,k-1}, \ldots, x_{n,k-1}}_{\text{not yet updated}}, \vec{d}\right). \tag{V.23}$$

Since this distribution has an arbitrary form, random drawing can be achieved numerically using the *CDF inversion method* (Appendix C.2.3.2). Fig. V.6.b represents the Gibbs sampling of Eq. (V.18). The squared pattern comes from the fact that we alternatively sample each parameter, keeping the other one fixed.

V.1.3.2 Post-Processing MCMCs

Assessing convergence. One of the most crucial questions, when using a MCMC method, is how long a chain do we need to run. To answer that question, we need to estimate if the MCMC has converged toward the stationary posterior. Concretely, it means that we want to make sure the sampling of the posterior is homogeneous, and that the moments and hypothesis testing we will perform will not be biased, because some areas of the parameter space have only been partially explored. The reason why the sampling of the parameter space might be incomplete is linked to the two following factors.

The burn-in refers to the first drawn values, before the MCMC could find the support of the posterior. This can be seen in Fig. V.6.a-b (highlighted in cyan). The arbitrary starting value (magenta star) is outside the 5σ contour of the PDF. The MCMC thus walks a few steps before finding the probable region. This burn-in phase is also highlighted in cyan, in Fig. V.6.c-d. This burn-in phase could actually be significantly longer, for several non-exclusive reasons: *(i)* a larger number of parameters; *(ii)* a more degenerate model, with several local maxima; *(iii)* a less lucky choice of initial conditions; or *(iv)* a very well-constrained model, resulting in a very small support over the whole parameter space. There is no universal method to identify burn-in, it needs to be investigated carefully, most of the time. Running several MCMCs, starting from initial conditions distributed over the whole parameter space, is usually efficient.

The autocorrelation of the MCMC results from the fact that the parameter value at step $k+1$ depends on step k. If several successive iterations stay in the same region of the posterior, this will create a portion of correlated values. The *AutoCorrelation Function* (ACF; *e.g.* Sokal, 1996) is an essential tool to determine the correlation length of a MCMC. The ACF, $\hat{\rho}$, of a given parameter, depends on the *lag*, τ, that is the number of steps between two arbitrary iterations:

$$\hat{\rho}(\tau) \equiv \frac{N}{N-\tau} \frac{\sum_{k=1}^{N-\tau} (x_k - \langle x \rangle)(x_{k+\tau} - \langle x \rangle)}{\sum_{k=1}^{N} (x_k - \langle x \rangle)^2}. \tag{V.24}$$

This is the correlation coefficient of the parameter with itself, shifted by τ steps. The ACFs of our example are displayed in Fig. V.6.e-f. We can see that the ACF starts at 1, for $\tau = 0$. It then drops over a few steps and oscillates around 0. The typical lag after which the ACF has dropped to 0, corresponds to the average number of steps necessary to draw independent values. This typical lag can be quantified, by the *integrated autocorrelation time*, $t_{\rm int}$ [6]:

$$t_{\rm int} \equiv 1 + 2 \sum_{i=\tau}^{N} \hat{\rho}(\tau). \tag{V.25}$$

It is represented in Fig. V.6.e-f. It corresponds roughly to the average number of steps needed to go from one end of the posterior to the other. Different parameters of a given MCMC can in principle have very different $t_{\rm int}$ (*e.g.* Galliano, 2018). To make sure that our posterior is properly sampled, we thus need to let our MCMC run a large number of steps, times $t_{\rm int}$, after burn-in. The *effective sample size*, $N_{\rm eff} \equiv N / t_{\rm int}$, quantifies the effective number of steps that can be considered independent. We need $N_{\rm eff} \gg 1$.

With the Metropolis-Hastings algorithm, the integrated autocorrelation time will depend heavily on the choice of the proposal distribution. We have explored the effect of the width of this distribution on $t_{\rm int}$. In Eq. (V.19), instead of taking $s_F = \sigma_F$ and $s_G = \sigma_G$, we have varied this parameter. Fig. V.7.a represents the mean rejection rate as a function of $\sqrt{s_F s_G / (\sigma_F \sigma_G)}$.

- When $\sqrt{s_F s_G / (\sigma_F \sigma_G)} \ll 1$, the proposal is much narrower than the posterior. The proposed steps are thus very small, and a lot of them are necessary to cross the posterior. This is why $t_{\rm int}$ is very large in this case (*cf.* Fig. V.7.b).
- When $\sqrt{s_F s_G / (\sigma_F \sigma_G)} \gg 1$, the proposal distribution is much larger than the posterior. Most proposals therefore falls outside the support of the posterior. They are therefore rejected close to 100 % of the times. This is why $t_{\rm int}$ is also very large in this case.

Fig. V.7.b shows that the only range where $t_{\rm int}$ is reasonable is when the width of the proposal distribution is comparable to the width of the posterior.

Parameter inference. Numerous quantities can be inferred from a MCMC. We have previously seen that the average, uncertainties, and various tests can be computed using the posterior of the parameters of a source. This becomes even more powerful when we are analyzing a sample of sources. To illustrate this, let's assume we are now observing $N_\star = 5$ stars, through the same photometric bands as before. Fig. V.8.b shows the posterior PDF of the two parameters of the five stars. It is important to distinguish the following two types of distributions.

The posterior of individual stars are represented in Fig. V.8. The error bars in panel *(b)* correspond to the mean and standard deviation of the marginal distributions in panels *(a)* and *(c)*. They represent the uncertainty on the measured fluxes of each individual star. They are the moments of a given parameter, over the whole MCMC. This is what we have focussed on, until now.

The statistic distribution across the sample is represented in Fig. V.9. In panel *(a)*, we have shown the distribution of the standard deviation of the sample, at each step k in the MCMC:

$$\sigma(F_\star)_k \equiv \frac{1}{N_\star - 1} \sum_{i=1}^{N_\star} \left(F_{i,k} - \frac{1}{N_\star} \sum_{j=1}^{N_\star} F_{j,k} \right)^2, \tag{V.26}$$

where $F_{i,k}$ is the observed flux of the star i, at the MCMC iteration k. It is how we can quantify the dispersion of the sample. We can thus quote the sample dispersion as (*cf.* Fig. V.9.a):

$$\sigma(F_\star) \simeq \langle \sigma(F_\star) \rangle \pm \sigma \left[\sigma(F_\star) \right]. \tag{V.27}$$

6. This quantity is problematic to compute. Sokal (1996) and Foreman-Mackey et al. (2013) discuss an algorithm to evaluate it numerically.

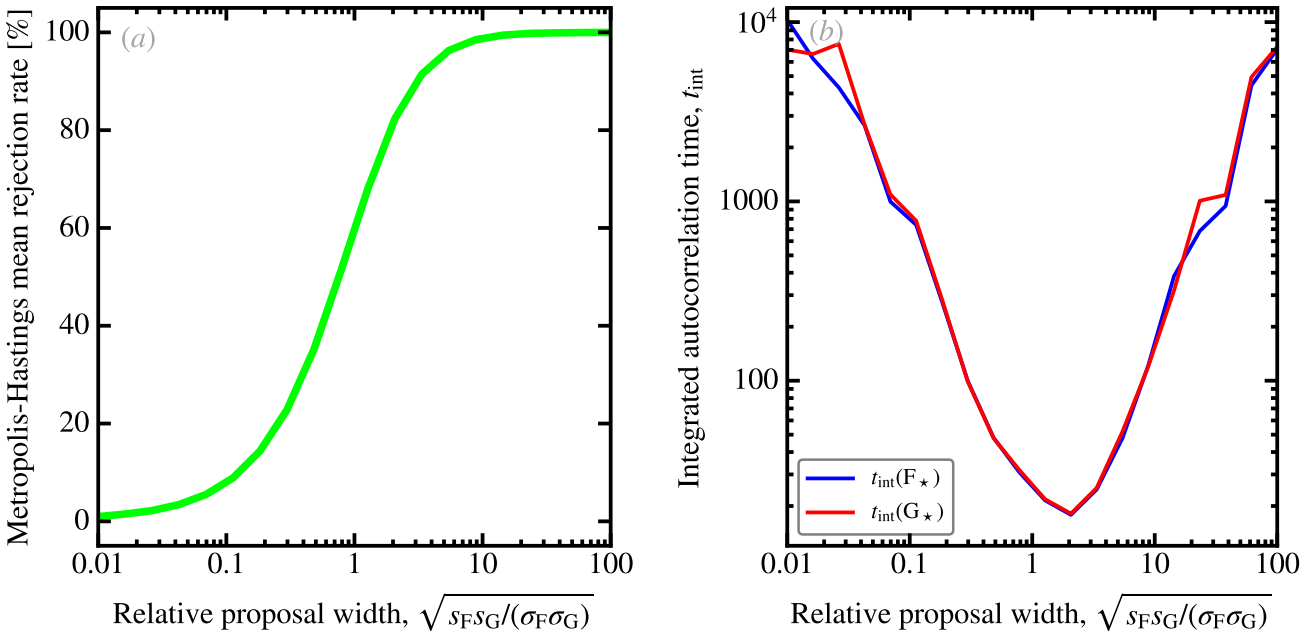

FIGURE V.7 – *Importance of the choice of the Metropolis-Hastings proposal distribution.* Panel *(a)* represents the Metropolis-Hastings mean rejection rate, varying the width of the proposal distribution (Eq. V.19), when sampling Eq. (V.18). Panel *(b)* represents the corresponding integrated autocorrelation time for the two parameters. Licensed under CC BY-SA 4.0.

In our example, we have: $\sigma(F_\star) \simeq 13.8 \pm 1.6$ and $\sigma(G_\star) \simeq 6.8 \pm 1.0$. We can see that these values correspond roughly to the intrinsic scatter between individual stars, in Fig. V.8.b, but they are larger than the uncertainty on the flux of individual stars. We can do the same for the correlation coefficient, as shown in Fig. V.9.b: $\rho(F_\star, G_\star) \simeq -0.63 \pm 0.15$. Notice that it is negative, because the correlation between stellar *fluxes*, in Fig. V.8.b, points toward the lower right corner. However, the correlation between the *uncertainties* on $F_\star$ and $G_\star$ is positive: the individual ellipses point in the other direction, toward the upper right corner. We have deliberately simulated data with these two opposite correlations to stress the difference between the individual likelihood properties and those of the ensemble. Finally, we could have done the same type of estimate for the mean of the sample: $\langle F_\star \rangle \simeq 52.2 \pm 1.5$ and $\langle G_\star \rangle \simeq 26.0 \pm 1.0$.

Quantifying the goodness of a fit. It is important, in any kind of model fitting, to be able to assess the quality of the fit. In the frequentist approach, this is done with the chi-squared test, which is limited in its assumptions to normal iid noise, without nuisance parameters. In the Bayesian approach, the same type of test can be done, accounting for the full complexity of the model (non-Gaussian errors, correlations, nuisance parameters, priors). This test is usually achieved by computing *posterior predictive p-values* (ppp; *e.g.* Chap. 6 of Gelman et al., 2004). To illustrate how ppps work, let's consider now that we are observing the same star as before, through four bands (R, I, J, H) and are performing a blackbody Bayesian fit to this SED, varying the temperature, $T_\star$, and the dilution factor, $\Omega_\star$. This is represented in Fig. V.10.b. The principle is the following.

1. We generate a set of *replicated data*, $\vec{d}_{rep}$, from our posterior:

$$p\left(\vec{d}_{rep}\middle|\vec{d}\right) \equiv \int p\left(\vec{d}_{rep}\middle|\vec{x}\right) p\left(\vec{x}\middle|\vec{d}\right) \mathrm{d}\vec{x}. \tag{V.28}$$

If we sampled our posterior with a MCMC, this integral can simply be computed by evaluating our model (the blackbody, in the present case), for values of our drawn parameters: $\vec{d}_{rep} = \{f(\vec{x}_k)\}_{k=1}^{N}$.

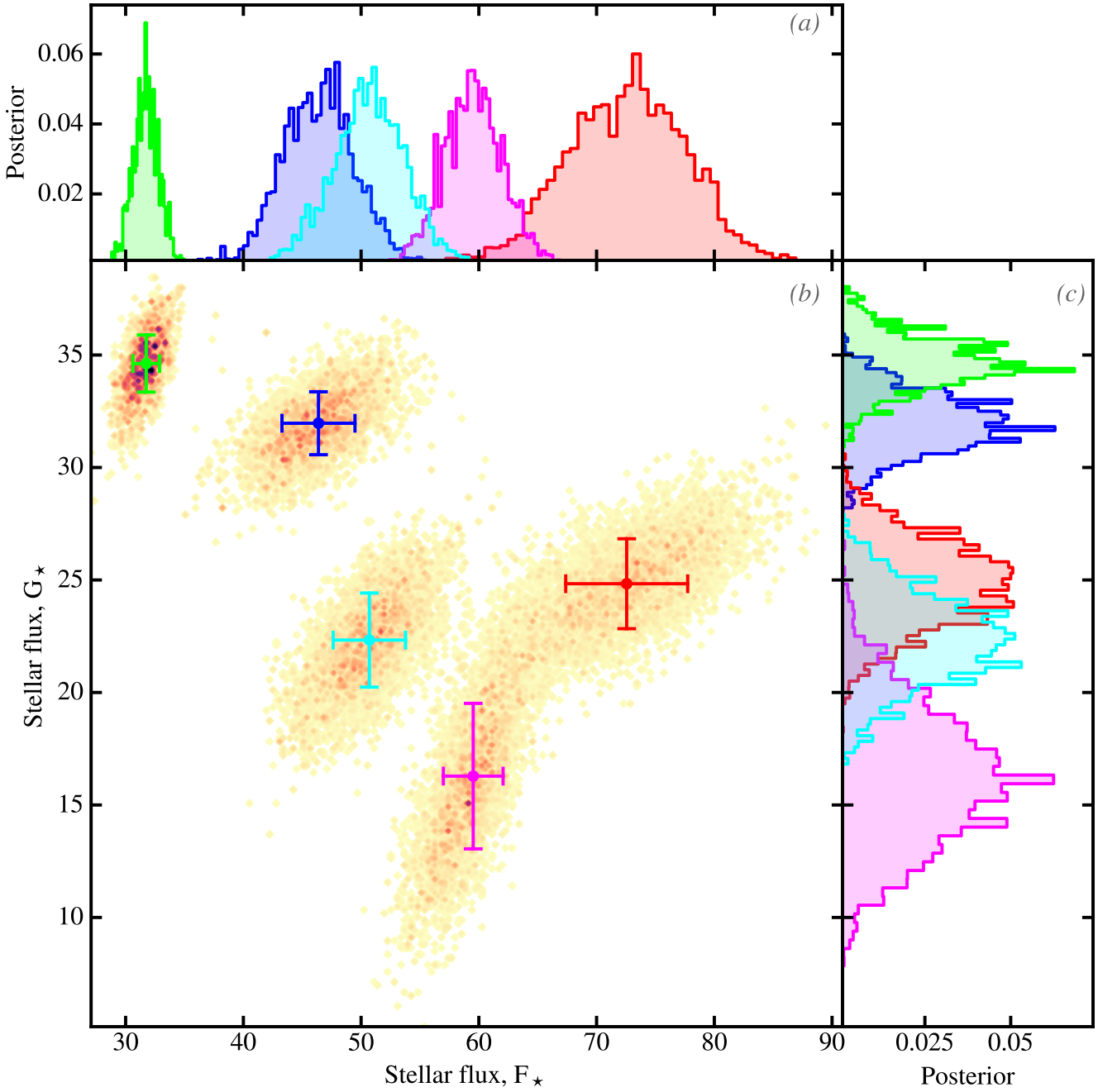

FIGURE V.8 – *Post-processing of the MCMC of a sample of sources.* In panel *(b)*, the contours represent the posterior of five stars, observed through the two photometric bands (fluxes $F_\star$ and $G_\star$). The margin plots represent the marginalized distribution of the posterior of each individual star. The error bars in panel *(b)* are plotted from the mean and standard deviations of the posterior. Licensed under CC BY-SA 4.0.

2. We evaluate the mean and standard deviation of this replicated data set, $\left\langle \vec{d}_{\text{rep}} \middle| \vec{x} \right\rangle$ and $\sigma\left(\vec{d}_{\text{rep}} \middle| \vec{x}\right)$. These quantities are the average and the dispersion of the predicted flux in the different bands. They will serve as position and scale references, when comparing model and observations.
3. We compute a *discrepancy metric*, $T\left(\vec{d} \middle| \vec{x}\right)$. Several choices are possible, but the most common is to adopt a chi-squared equivalent:

$$T\left(\vec{d} \middle| \vec{x}\right) \equiv \sum_{j=1}^{m} \frac{\left[d_j - \langle d_j | \vec{x} \rangle\right]^2}{\sigma\left(d_j | \vec{x}\right)^2}. \tag{V.29}$$

We compute this quantity both for the replicated set, $T\left(\vec{d}_{\text{rep}} \middle| \vec{x}\right)$, which is the blue distribution

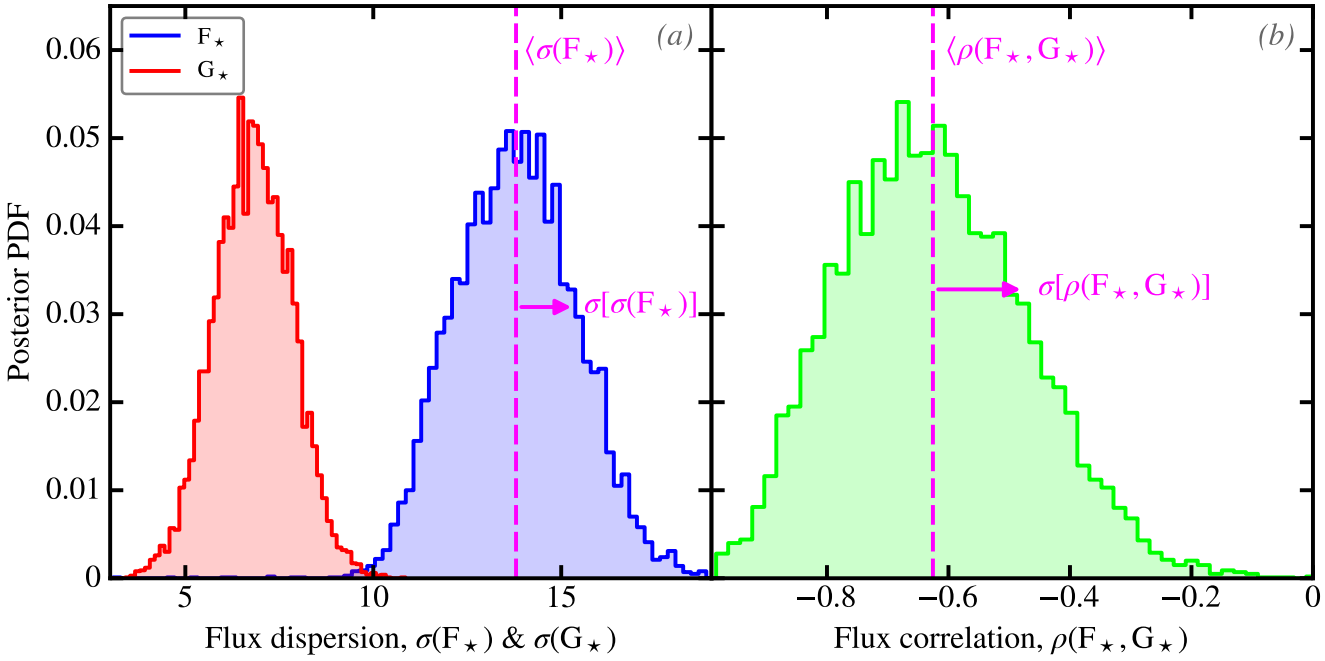

FIGURE V.9 – *MCMC statistics of a sample of sources.* Panel *(a)* represents the posterior of the standard deviation of the sample in Fig. V.8. It represents the PDF of the dispersion of the sample, not the width of individual PDFs. Similarly, panel *(b)* represents the correlation coefficient of the flux distribution.

in Fig. V.10.e, and for the observations, $\mathrm{T}\left(\vec{d}\middle|\vec{x}\right)$, which is the red line in Fig. V.10.e (it is a single value). To be clear, only the data term in Eq. (V.29) changes between $\mathrm{T}\left(\vec{d}_{\mathrm{rep}}\middle|\vec{x}\right)$ and $\mathrm{T}\left(\vec{d}\middle|\vec{x}\right)$. The quantities $\langle d_j|\vec{x}\rangle$ and $\sigma\left(d_j|\vec{x}\right)$ are identical in both cases.

4. The quality of the test is assessed by comparing both quantities. To that purpose, we compute the following probability:

$$p_{\mathrm{B}} \equiv p\left(\mathrm{T}\left(\vec{d}_{\mathrm{rep}}\middle|\vec{x}\right) \geq \mathrm{T}\left(\vec{d}\middle|\vec{x}\right)\middle|\vec{d}\right). \tag{V.30}$$

If the difference between the replicated set and the data is solely due to statistical fluctuations, we should have on average $p_{\mathrm{B}} \simeq 50\,\%$. The fit is considered bad, at the 95 % level, if $p_{\mathrm{B}} < 2.5\,\%$ or $p_{\mathrm{B}} > 97.5\,\%$.

We have illustrated this test in Fig. V.10, varying the number of parameters and observational constraints, in order to explore the different possible cases.

A good fit is shown in Fig. V.10.b. We have varied both $\mathrm{T}_\star$ and $\Omega_\star$ to fit the 4 fluxes. Fig. V.10.e shows that $\mathrm{T}\left(\vec{d}\middle|\vec{x}\right)$ falls in the high probability range of $\mathrm{T}\left(\vec{d}_{\mathrm{rep}}\middle|\vec{x}\right)$. In other words, the average deviation of the replicated data, relative to the reference we have chosen, $\left\langle \vec{d}_{\mathrm{rep}}\middle|\vec{x}\right\rangle$, is comparable to the deviation of the actual data relative to the same reference. The observations could thus have likely been drawn from our posterior.

A poor fit is shown in Fig. V.10.a. We have intentionally fixed the temperature of the fit at $\mathrm{T}_\star = 7000$ K, while the true value is $\mathrm{T}_\star = 6000$ K. We see that $p_{\mathrm{B}} \simeq 1$, in Fig. V.10.d. The difference between the observations and the model, can thus not be explained by the scatter of the model. It is the sign of a bad fit. In our case, it is because the model is bad (wrong choice of fixed temperature).

An overfit is shown in Fig. V.10.c. This time we fit only two fluxes. With a chi-squared fit, we would have 0 degrees of freedom. We see that $p_{\mathrm{B}} \simeq 0$, in Fig. V.10.f. The average model therefore gets too close to the observations. The ppp tells us this is very unlikely. It is however not an issue in terms of derived parameters. We can see that the true model (green) is well among the sampled model (blue), and the inferred parameters are consistent with their true values.

There is no issue with fitting even fewer constraints than parameters, with a Bayesian approach. The consequence is that the posterior is going to be very wide along the dimensions corresponding to the poorly constrained parameters. However, the results will be consistent, and the derived probabilities will be meaningful.

☞ Contrary to the frequentist approach, we can fit Bayesian models with more parameters than data points.

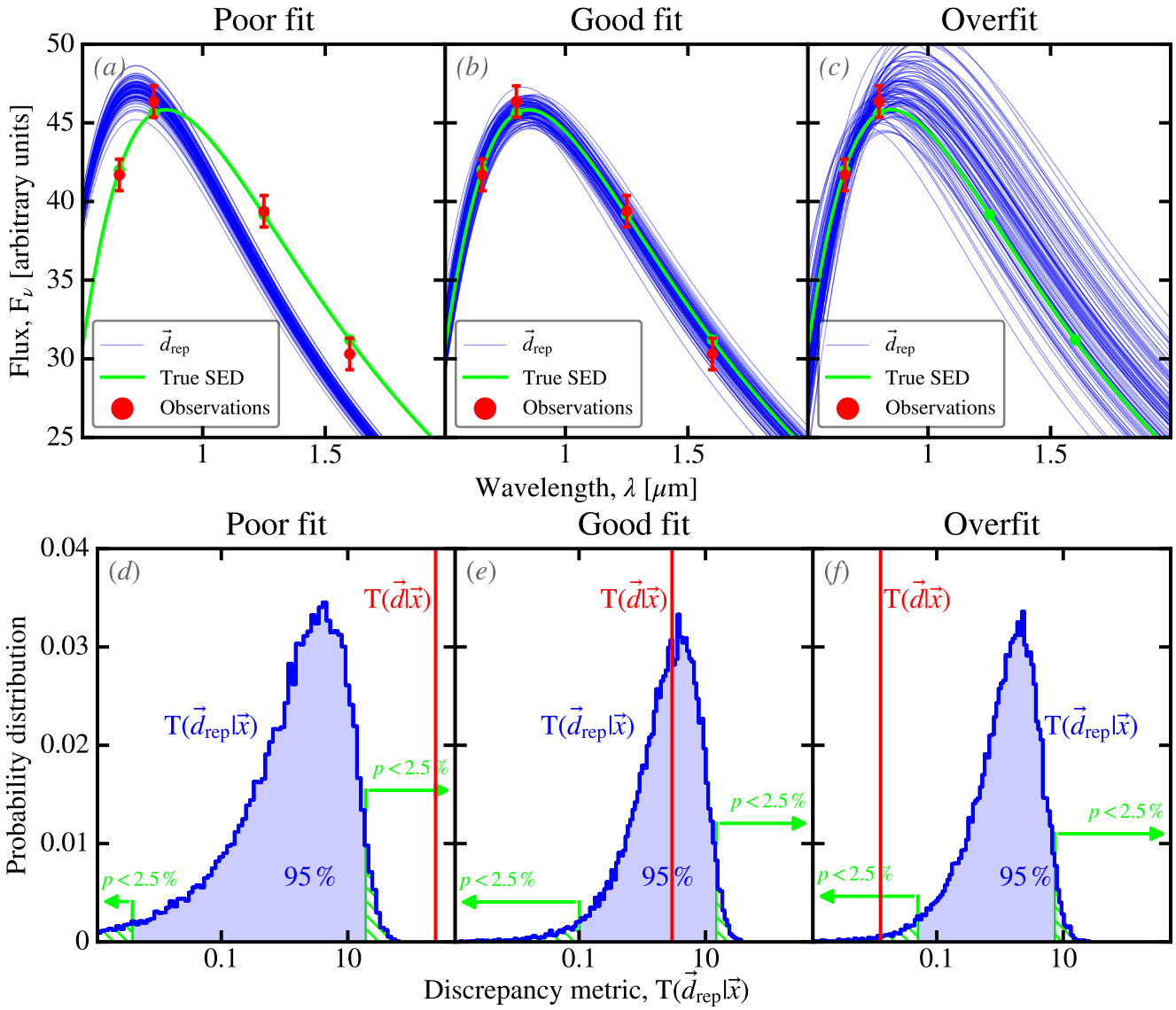

FIGURE V.10 – *Demonstration of the use of posterior predictive p-values.* The top three panels show the fit of an observed stellar SED (red error bars) with a blackbody. The true model ($T_\star$ = 6000 K) is shown in green. The blue lines are a subsample of the inferred model (at different steps in the MCMC). In panel *(a)*, we have fixed the temperature to $T_\star$ = 7000 K, different from its true value. We thus vary only $\Omega_\star$, resulting in a poor fit. In panel *(b)*, we let both $T_\star$ and $\Omega_\star$ vary, in order to get a good fit. In panel *(c)*, we fit only two fluxes, with our two parameters. We are thus overfitting the data. The three bottom panels show the distribution of the discrepancy metric for the replicated data set (in blue), corresponding to the upper panels. We compare it to $T\left(\vec{d}\middle|\vec{x}\right)$, in red. The low probability ranges are hatched in green. This example has been generated using `emcee` (Foreman-Mackey et al., 2013). Licensed under CC BY-SA 4.0.

V.1.4 Decision Making and Limitations of the Frequentist Approach

We now resume our comparison of the Bayesian and frequentist approaches, started in Sect. V.1.2. We focus more on the interpretation of the results and synthesize the advantages and inconveniences of both sides.

V.1.4.1 Hypothesis Testing

Until now, we have seen how to estimate parameters and their uncertainties. It is however sometimes necessary to be able to make decisions, that is to choose an outcome or its alternative, based on the observational evidence. Hypothesis testing consists in assessing the likeliness of a *null hypothesis*, noted H_0. The *alternative hypothesis* is usually noted H_1, and satisfies the logical equation $\mathrm{H}_1 = \neg\mathrm{H}_0$, where the $\neg$ symbol is the logical negation. The priors necessarily obey $p(\mathrm{H}_0) + p(\mathrm{H}_1) = 1$. To illustrate this process let's go back to our first example, in Sect. V.1.2. We are observing a star with true flux $\mathrm{F}_{\mathrm{true}}$, m times, with an uncertainty σ_F on each individual flux measurements, F_i. This time, we want to know if $\mathrm{F}_{\mathrm{true}} \leq \mathrm{F}_{\mathrm{test}}$, for a given $\mathrm{F}_{\mathrm{test}}$.

Bayesian hypothesis testing. Bayesian hypothesis testing consists in computing the *posterior odds* of the two complementary hypotheses:

$$\underbrace{\frac{p\left(\mathrm{H}_1\middle|\vec{d}\right)}{p\left(\mathrm{H}_0\middle|\vec{d}\right)}}_{\text{posterior odds}} = \underbrace{\frac{p\left(\vec{d}\middle|\mathrm{H}_1\right)}{p\left(\vec{d}\middle|\mathrm{H}_0\right)}}_{\text{Bayes factor}} \times \underbrace{\frac{p(\mathrm{H}_1)}{p(\mathrm{H}_0)}}_{\text{prior odds}}. \tag{V.31}$$

The posterior odds is the ratio of the posterior probabilities of the two hypotheses. It is literally the odds we would use for gambling (*e.g.* a posterior odd of 3 corresponds to a 3:1 odd in favor of H_1). The important term in Eq. (V.31) is the *Bayes factor*, usually noted $\mathrm{BF}_{10} \equiv p\left(\vec{d}\middle|\mathrm{H}_1\right) / p\left(\vec{d}\middle|\mathrm{H}_0\right)$. It quantifies the weight of evidence, brought by the data, *against* the null hypothesis. It tells us how much our observations changed the odds we had against H_0, prior to collecting the data. Table V.1 gives a qualitative scale to decide upon Bayes factors. We see that it is a continuous credibility range going from rejection to confidence. The posterior of our present example, assuming a wide flat prior, is:

$$p(\mathrm{F}_\star|\mathrm{F}_1,\ldots,\mathrm{F}_m) = \frac{1}{\sqrt{2\pi}\sigma_\mathrm{F}/\sqrt{m}} \exp\left(-\frac{1}{2}\frac{(\mathrm{F}_\star - \langle\mathrm{F}\rangle)^2}{\sigma_\mathrm{F}^2/m}\right), \tag{V.32}$$

where $\langle\mathrm{F}\rangle = \sum_{i=1}^{m} \mathrm{F}_i/m$. The posterior probability of $\mathrm{H}_0 = (\mathrm{F}_{\mathrm{true}} \leq \mathrm{F}_{\mathrm{test}})$ is then simply:

$$p(\mathrm{H}_0|\mathrm{F}_1,\ldots,\mathrm{F}_m) = \int_{-\infty}^{\mathrm{F}_{\mathrm{test}}} p(\mathrm{F}_\star|\mathrm{F}_1,\ldots,\mathrm{F}_m)\,\mathrm{dF}_\star = \frac{1}{2}\left[1 + \mathrm{erf}\left(\frac{1}{\sqrt{2}}\frac{\mathrm{F}_{\mathrm{test}} - \langle\mathrm{F}\rangle}{\sigma_\mathrm{F}/\sqrt{m}}\right)\right]. \tag{V.33}$$

It is represented in Fig. V.11.a. This PDF is centered in $\langle\mathrm{F}\rangle$, since, as usual in the Bayesian approach, it is conditional on the data. Fig. V.11.a shows the complementary posteriors of H_0 (red) and H_1 (blue), which are the incomplete integrals of the PDF. When we vary $\mathrm{F}_{\mathrm{test}}$, the ratio of the two posteriors, BF_{10}, changes. Assuming we have chosen a very wide, flat prior, such that $p(\mathrm{H}_1)/p(\mathrm{H}_0) \simeq 1$, the Bayes factor becomes:

$$\mathrm{BF}_{10} \simeq \frac{1}{p(\mathrm{H}_0|\mathrm{F}_1,\ldots,\mathrm{F}_m)} - 1. \tag{V.34}$$

Fig. V.11.b represents the evolution of the Bayes factor as a function of the sample size, m. In this particular simulation, H_0 is false. We see that, when m increases, we accumulate evidence against H_0, going through the different levels of Table V.1. The evidence is decisive around $m \simeq 60$, here.

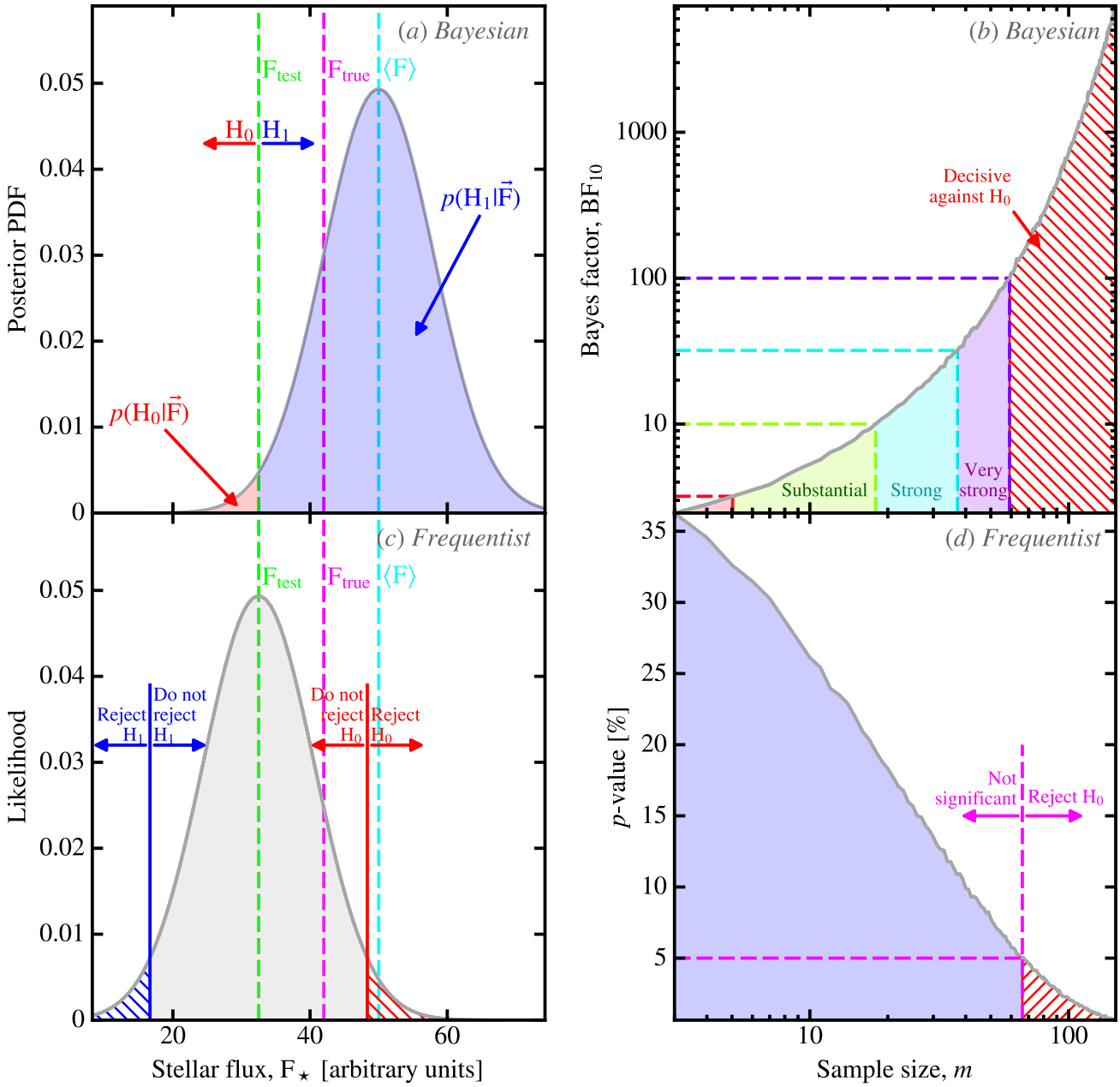

FIGURE V.11 – *Bayesian and frequentist hypothesis testing.* Panel *(a)* represents the calculation of the posterior odds (Eq. V.31). Notice the distribution is centered on the average of the observed fluxes, $\langle F \rangle$, and we consider F_{test} as a variable. We want to assess the null hypothesis, $H_0 = (F_{true} \leq F_{test})$. In the particular example we have plotted, H_0 is false. The Bayes factor is simply the ratio of the blue and red areas. Panel *(c)* represents NHST for the same problem. Notice, this time, the distribution is centered on F_{test}, which is considered fixed, and the observations, $\langle F \rangle$, are considered variable. We have plotted the two-tailed p-value decisions. The alternative to rejection is not acceptance, but the absence of significance. The two right panels illustrate the variation of the Bayes factors and p-values, as a function of the sample size, m. In these particular examples, we have chosen a fixed $F_{test} = 38$ and $F_{true} = 42$, such that H_0 is false. The uncertainty is $\sigma_F = 14$. The more we have data, the more we can constrain the solution. We can see that both Bayesian and frequentist methods conclude the right solution (H_0 is false), around the same sample size ($m \simeq 60 - 70$ in our case). Below this value, both methods are inconclusive. The Bayesian credibility scale is however more continuous than the frequentist NHST, though. The latter tells us our data are useless below $m \simeq 70$. To avoid stochastic fluctuations, that would make the figure less easy to read, we have randomly drawn 10 000 samples for each value of m and we show the averages.

Bayes factor, BF_{10}	Strength of evidence against H_0
1–3.2	Barely worth mentioning
3.2–10	Substantial
10–32	Strong
32–100	Very strong
>100	Decisive

TABLE V.1 – *Jeffreys strength of evidence scale.* This scale translates the value of a Bayes factor in a qualitative decision (Jeffreys, 1939). Below one, we consider BF_{01} instead, and discuss the evidence in favor of H_0.

Frequentist hypothesis testing. Instead of computing the credibility of H_1 against H_0, the frequentist approach relies on the potential rejection of H_0. It is called *Null Hypothesis Significance Test* (NHST; *e.g.* Ortega & Navarrete, 2017). It consists in testing if the observation average, $\langle F \rangle$, could have confidently been drawn out of a population centered on F_{test}. In that sense, it is the opposite of the Bayesian case. This is demonstrated in Fig. V.11.c. We see that the distribution is centered on F_{test}, which is assumed fixed, and the observations, $\langle F \rangle$, are assumed variable. Since frequentists can not assign a probability to F_{test}, they estimate a p-value, that is the probability of observing the data at hands, assuming the null hypothesis is true. It is based on the following statistics:

$$t_m \equiv \frac{\langle F \rangle - F_{test}}{\sigma_F / \sqrt{m}}. \tag{V.35}$$

The p-value of this statistics is then simply:

$$p_0 = \frac{1}{2}\left[1 + \mathrm{erf}\left(\frac{t_m}{\sqrt{2}}\right)\right]. \tag{V.36}$$

Notice it is identical to Eq. (V.33), but different from the Bayes factor (Eq. V.34). It however does not mean the same thing. A significance test at $p_0 = 0.05$ does not tell us that the probability that the null hypothesis is 5 %. It means that the null hypothesis will be rejected 5 % of the time [7]. NHST decision making is represented in Fig. V.11.c. It shows one of the most common misconceptions about NHST: the absence of rejection of H_0 does not mean that we can accept it. It just mean that the results are not significant. Accepting H_0 requires rejecting H_1, and vice versa. Fig. V.11.d shows the effect of sample size on the p-value, using the same example as we have discussed for the Bayesian case. The difference is that the data are not significant until $m \simeq 70$.

The Jeffreys-Lindley's paradox. Although the method and the interpretations are different, Bayesian and frequentist tests give consistent results, in numerous applications. There are however particular cases, where both approaches are radically inconsistent. This ascertainment was first noted by Jeffreys (1939) and popularized by Lindley (1957). Lindley (1957) demonstrated the discrepancy on an experiment similar to the example we have been discussing in this section, with the difference that a *point* null hypothesis is tested: $H_0 = (F_{true} = F_{test})$. Lindley (1957) shows that there are particular cases, where the posterior probability of H_0 is $1 - \alpha$, and H_0 is rejected at the α level, at the same time. This "*statistical paradox*", known as the *Jeffreys-Lindley's paradox* has triggered a vigorous debate, that is still open nowadays (*e.g.* Robert, 2014). The consensus about the paradox is that *there is no paradox*. The discrepancy simply arises from the fact that both approaches answer different questions, as we have been illustrating at several occasions in this chapter, and that these different interpretations can sometimes be inconsistent.

7. The acceptance of a wrong hypothesis (false positive) is called "*type I error*", whereas the rejection of a correct hypothesis (false negative) is called "*type II error*".

The recent controversy about frequentist significance tests. NHST has recently been at the center of an important controversy across all empirical sciences. We have already discussed several of the issues with frequentist significance tests. Let's summarize them here (*e.g.* Ortega & Navarrete, 2017).

1. Frequentist tests are conditional on model parameters and thus consider data that have not actually been observed. The general frequentist approach is difficult to grasp, even for advanced statisticians. It can easily lead to false interpretations.
2. NHST is prone to overestimates and can state effects even if none exist. If we repeat an experiment a sufficient number of times, we will always end up rejecting H_0. This potentially leads to a large number of false positives.
3. There is a variety of statistics that one can test, and they are not all going to give the same result. In addition, the significance level is subjective and there are no clear rules how to choose the p-value ($p = 0.05$, $p = 0.01$, *etc.*). There is therefore some subjectivity in the frequentist approach. It is not in the prior, it is in the significance assessment.

Data dredging or *p-hacking* has come into the spotlight during the last twenty years, although it was known before (*e.g.* Smith & Ebrahim, 2002; Simmons et al., 2011; Head et al., 2015). It points out that numerous scientific studies could be wrong, and several discoveries could have been false positives. This is particularly important in psychology, medical trials, *etc.*, but could affect any field using p-values. In 2016, the *American Statistical association* published a "*Statement on statistical significance and p-values*" (Wasserstein & Lazar, 2016), saying that: "*widespread use of 'statistical significance' (generally interpreted as 'p<0.05') as a license for making a claim of a scientific finding (or implied truth) leads to considerable distortion of the scientific process*". They suggested "*moving toward a 'post p<0.05' era*". While some recommendations have been proposed to use p-values in a more controlled way (*e.g.* Simmons et al., 2011), by deciding the sample size and significance level before starting the experiment, some researchers have suggested abolishing NHST (*e.g.* Loftus, 1996; Anderson et al., 2000). Several journals have stated that they will no longer publish articles reporting p-values (*e.g.* *Basic & Applied Social Psychology*, in 2015, and *Political Analysis*, in 2018).

☞ Frequentist p-values are to be used with caution.

V.1.4.2 Pros and Cons of the two Approaches

We finish this section by summarizing the advantages and inconveniences of both approaches. This comparison is synthesized in Table V.2.

Hypotheses and information that can be taken into account. The two methods diverge on what information can be included in the analysis.

Bayesian models can account for a maximum amount of information:

- all types of noise and uncertainties, whether non-Gaussian, partially or fully correlated (*cf.* Sect. V.1.2.3);
- nuisance parameters, that are parameters necessary to estimate the model, but whose values are not relevant (we will give an example in Sect. V.3.3.1);
- complex, non-linear models with more parameters than observational constraints (*cf.* Sect. V.1.3.2);
- any kind of prior information (*cf.* Sect. V.1.2.2).

Frequentist analysis is limited in that way:

- complex, correlated noise is difficult to include in the likelihood;
- nuisance parameters can not be included and we can not have more parameters than observations;

Bayesian approach	Frequentist approach
CON choice of prior is subjective	PRO likelihood is not subjective
PRO can account for non-Gaussian errors, nuisance parameters, complex models & prior information	CON very limited in terms of the type of noise, the complexity of the model & can not deal with nuisance parameters
PRO the posterior makes sense (conditional on the data) & is easy to interpret	CON samples non-observed data, arbitrary choice of estimator & p-value
PRO probabilistic logic ⇒ continuum between skepticism & confidence	CON boolean logic ⇒ a proposition is either true or false, which leads to false positives
PRO based on a master equation (Bayes' rule) ⇒ easier to learn & teach	CON difficult to learn & teach (collection of *ad hoc* cooking recipes)
CON heavy computation	PRO fast computation
PRO works well with small samples & heterogeneous data sets	CON does not work well with small samples, can not mix samples & require fixing the sample size and significance level before experimenting
PRO holistic & flexible: can account for all data & theories	CON strict: can account only for data related to a particular experiment
PRO conservative	CON can give ridiculous answers

TABLE V.2 – *Pros and cons of the Bayesian and frequentist methods.*

- complex models, with a lot of degeneracies fail frequentist approaches, such as maximum likelihood methods;
- no prior information can be included.

In favor of the frequentist approach, we can note that the likelihood is perfectly objective, whereas the choice of the prior is subjective. The subtlety is however that this choice is *subjective*, as it depends on the knowledge we believe we have prior to the observation, but it is not *arbitrary*, as a prior can be rationally constructed. In addition, when the strength of evidence is large, the prior becomes unimportant. The prior is important only when the data are very noisy or unconvincing. In that sense, the prior does not induce a *bias of confirmation*.

Analysis and interpretation. As we have seen throughout Sect. V.1, the point of view of the two approaches is very different.

Inference is performed on the posterior, in the Bayesian approach. It gives the probability of the parameters, knowing the data. It makes sense and is easy to interpret. On the contrary, frequentists sample data that have not actually been observed and base their results on arbitrary choices of statistics and estimators. The results are difficult to interpret, as they consist in describing what could be the observations, for a given set of model parameters (*cf.* Sect. V.1.4.1).

The underlying logic is probabilistic, in the Bayesian approach. There is a continuum between skepticism and confidence that makes any data worth taking into account. Bayes factors quantify the strength of evidence brought by these data (*cf.* Sect. V.1.4.1). On the contrary, frequentist logic is *Platonic*, a proposition is either true or false. With real-life uncertainties and stochasticity, this leads to false positives. By refusing to assign probabilities to parameters and hypotheses, frequentists rely on p-values, while those are only one particular tool of the Bayesian analysis (*e.g.* Sect. V.1.3.2). Credibility is progressive whereas significance is dichotomic.

Learning and teaching of the Bayesian method is considerably easier, because it is based on a master equation, Bayes' rule. All Bayesian problems start with Eq. (V.5), which is developed to ac-

count for all the details we are modeling. On the contrary, frequentists methods are a collection of *ad hoc* cooking recipes, whose derivation is often obscure (*e.g.* R. Fisher's book, "*Statistical methods for research workers*"; Fisher, 1925).

Computation of Bayesian problems is intensive, as sampling the posterior is challenging (*cf.* Sect. V.1.3). One of the advantages of frequentist methods is that they are usually fast. Even a Bayesian can use them, for instance, to find good MCMC starting points (*e.g.* Galliano, 2018, Sect. 4.2.1) or compute quick estimators (*e.g.* Galliano et al., 2021, Appendix F.2).

Overall applicability. In practice, choosing one approach over the other depends on the situation. There are however a lot of arguments in favor of the Bayesian point of view.

Sample size and data collection are one of the major issues with frequentist methods. We have seen that NHST was problematic in that aspect, and that the stopping condition of an experiment could bias its significance. It is recommended to use large samples, and decide of the size and significance level, before conducting the measures. Consequently, contrary to Bayesians, frequentists can not *(i)* analyze partial data sets, as the stopping point could be instrumental in forcing one outcome over another (concept of p-hacking discussed in Sect. V.1.4.1), or *(ii)* combine heterogeneous data sets, as the limiting frequency would not have any sense.

Consistency of the results is also an issue with the frequentist approach, as it can only account for data related to a particular experiment. On the contrary, the Bayesian approach is more flexible. We will even discuss in Sect. V.3.3.2 that it is potentially holistic. It is at the same time more conservative, as the prior tends to prevents aberrant results, while we have seen that frequentist methods can give ridiculous answers (*cf.* Sect. V.1.2.3).

☞ For all these reasons, the Bayesian approach is more well-suited for most problems encountered in empirical sciences.

V.2 Bayesianism, an Alternative to Popper's Scientific Method

The Bayesian and frequentist approaches lead to radically different epistemological points of view, that have important consequences on the way we study ISD. We start by briefly brushing the history of the competition between these two systems. We then discuss their consequences on the scientific method.

V.2.1 Bayes Formula Throughout History

The History of the introduction of probability in sciences and the subsequent competition between Bayesians and frequentists is epic. The book of McGrayne (2011) gives an invaluable overview of this controversy, that started two centuries ago.

V.2.1.1 The Origins

The emergence of the concept of probability. In antique societies, randomness was interpreted as the language of the gods. Hacking (2006) argues that the notion of probability emerged around 1660, in western Europe. Before this date, "*probable*" meant only "*worthy of approbation*" or "*approved by authority*". In a few years, during the Renaissance, there was a transition of the meaning of "*probable*" from "*commonly approved*" to "*probed by evidence*", what Gaston BACHELARD would have called an *epistemological break*. The time was ready for the idea. The *Thirty Years' War* (1618–1648), which had caused several millions of deaths throughout western Europe, had just ended. It consolidated the division into Catholic and Lutheran states of a continent that had been religiously homogeneous for almost a thousand years. "*Probabilism is a token of the loss of certainty that characterizes the*

Renaissance, and of the readiness, indeed eagerness, of various powers to find a substitute for the older canons of knowledge. Indeed the word 'probabilism' has been used as a name for the doctrine that certainty is impossible, so that probabilities must be relied on" (Hacking, 2006, page 25). The first book discussing the concept of probability, applied to games of fortune, was published in 1657 by Christiaan HUYGENS (Huygens, 1657). It is however Blaise PASCAL (*cf.* Fig. V.12.a) who is considered the pioneer in the use of probability as a quantification of beliefs. His *wager*[8] is known as the first example of decision theory (Pascal, 1670).

(a) Blaise PASCAL (1623–1662)

(b) Thomas BAYES (1702–1761)

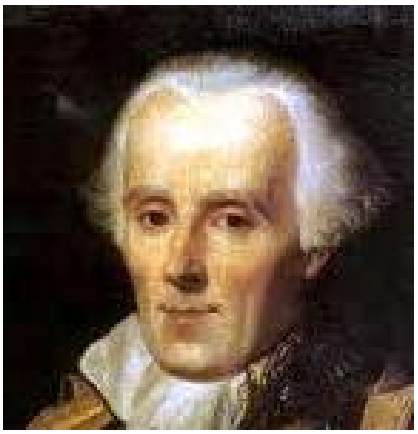

(c) Pierre-Simon LAPLACE (1749–1827)

FIGURE V.12 – *The probability pioneers.* Credit: *(a)* Wikipedia, public domain; *(b)* Wikipedia, public domain; *(c)* Wikipedia, public domain.

The discovery of Bayes. Thomas BAYES (*cf.* Fig. V.12.b) was an XVIIIth English Presbyterian minister. Coming from a nonconformist family, he had read the work of Isaac NEWTON, David HUME and Abraham DE MOIVRE (McGrayne, 2011). His interest in game theory led him to imagine a thought experiment.

His thought experiment was developed between 1746 and 1749. He was trying to infer the position of a ball on a pool table behind him, that he could not see. His idea was to be able to start from a guess and refine it using some information.

1. His assistant would throw on the table a first ball, whose position is to be inferred.
2. His assistant would then throw a second ball and tell him if it landed on the left or the right of the first one.
3. This procedure would be repeated until Bayes could infer the quadrant were the first ball is.

He derived Eq. (V.5) to solve this problem.

The essay presenting his formula (Bayes, 1763) was published after his death by Richard PRICE. Bayes defined the probability of an event as "*the ratio between the value at which an expectation depending on the happening of the event ought to be computed, and the value of the thing expected upon its happening*". Richard PRICE added that his formula provides the *probability of causes* and can thus be applied to prove the existence of God.

8. Pascal's wager states that it is rational to act as if God existed. If God indeed exists, we will be rewarded, which is a big win. If He doesn't, we will have only renounced to some material pleasures, which is not a dramatic loss.

The contribution of Laplace. Pierre-Simon LAPLACE (*cf.* Fig. V.12.c) was the son of a small estate owner, in Normandie. His father pushed him towards a religious career, that led him to study theology. He however quit at age 21 and moved to Paris, where he met the mathematician Jean LE ROND D'ALEMBERT, who helped him to get a teaching position. Laplace then had a successful scientific and political career (*cf.* Hahn, 2005, for a complete biography). Among his many other scientific contributions, Laplace is the true pioneer in the development of statistics using Bayes' rule. Some authors even argue that we should call the approach presented in Sect. V.1 "*Bayesian-Laplacian*" rather than simply "*Bayesian*". After having read the memoir of Abraham DE MOIVRE, he indeed understood that probabilities could be used to quantify experimental uncertainties. His 1774 memoir on "*the probability of causes by events*" (Laplace, 1774) contains the first practical application of Bayes' rule. His *rule of succession*, giving the probability of an event knowing how many times it happened previously, was applied to give the probability that the Sun will rise again. Laplace rediscovered Bayes' rule. He was only introduced to Bayes' essay in 1781, when Richard PRICE came to Paris. Laplace had a Bayesian conception of probabilities: "*in substance, probability theory is only common sense reduced to calculation; it makes appreciate with accuracy what just minds can feel by some sort of instinct, without realizing it*" (Laplace, 1812).

V.2.1.2 The Frequentist Winter

The rejection of Laplace's work. The frequentist movement was initiated by British economist John Stuart MILL, only ten years after the death of Laplace. There were several reasons for this reaction (Loredo, 1990; McGrayne, 2011).

- The idea that probability should represent a *degree of plausibility* seemed too vague to provide the foundation for a mathematical theory. People also realized there was no clear way to assign priors.
- The computation of Bayesian solutions by hand was crippling.
- Laplace was despised in England for his support to Napoléon.

Mill's disdain for the Bayesian approach was unhinged: "*a very slight improvement in the data, by better observations, or by taking into fuller consideration the special circumstances of the case, is of more use than the most elaborate application of the calculus of probabilities founded on the data in their previous state of inferiority. The neglect of this obvious reflection has given rise to misapplications of the calculus of probabilities which have made it the real opprobrium of mathematics.*" (Mill, 1843). The early anti-Bayesian movement was led by English statistician Karl PEARSON (*cf.* Fig. V.13.a). Pearson developed: *(i)* the chi-squared test; *(ii)* the standard-deviation; *(iii)* the correlation coefficient; *(iv)* the p-value; *(v)* the *Principal Component Analysis* (PCA). His book, "*The Grammar of Science*" (Pearson, 1892), was very influential, in particular to the young Albert EINSTEIN. Despite these great contributions, Pearson was a social Darwinist and a eugenicist.

The golden age of frequentism (1920-1930). Ronald FISHER (*cf.* Fig. V.13.b) followed the way opened by Pearson. He is the most famous representative of the frequentist movement. He developed: *(i)* the maximum likelihood; *(ii)* NHST; *(iii)* the F-distribution and the F-test. His 1925 book, "*Statistical Methods for Research Workers*" (Fisher, 1925), was widely used in academia and industry. Despite the criticism we can address to the frequentist approach, Fisher's contributions gave guidelines to rigorously interpret experimental data, that brought consistency to science. Fisher, who was like Pearson a eugenicist, was also paid as a consultant by the "*Tobacco Manufacturer's Standing Committee*". He spoke publicly against a 1950 study showing that tobacco causes lung cancer, by resorting to "*correlation does not imply causation*" (Fisher, 1957). Besides Pearson and Fisher, Jerzy NEYMAN (*cf.* Fig. V.13.c) was also a prominent figure of frequentism at this time. These scientists, also known for their irascibility, made sure that nobody revived the methods of Laplace. McGrayne (2011) estimates that this golden era culminated in the 1920s-1930s.

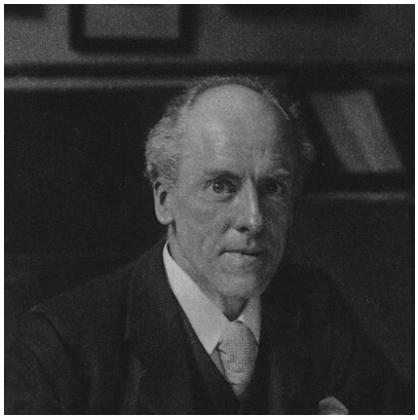

(a) Karl PEARSON (1857–1936)

(b) Ronald FISHER (1890–1962)

(c) Jerzy NEYMAN (1894–1981)

FIGURE V.13 – *The frequentist promoters.* Credit: *(a)* Wikipedia, public domain; *(b)* Bibmath, public domain; *(c)* Wikipedia, licensed under CC BY-SA 2.0 DE.

The Bayesian resistance. Several prominent scientists, who were not intimidated by Fisher and his colleagues, perpetuated the Bayesian approach (McGrayne, 2011). Among them, we can cite the following two.

Harold JEFFREYS (*cf.* Fig. V.14.a) was a British geophysicist and mathematician. In 1926, he performed a Bayesian analysis of earthquake records and inferred that the Earth had a liquid core. This discovery could not have been possible with the frequentist approach, as the data were very scarce. Jeffreys initiated the Bayesian revival and was an early critic of NHST. His book, "*Theory of probability*" (Jeffreys, 1939), popularized the use of Bayes factors, as we have seen in Sect. V.1.4.1.

Alan TURING (*cf.* Fig. V.14.b) was the founder of theoretical computer science and artificial intelligence. He also brilliantly put into practice Bayesian techniques during World War II. He secretly worked at Bletchley Park, near London, to decode the communications between German U-boats, that were using the cryptographic *Enigma* machine. Turing built a mechanical computer, called "*The Bomb*", which he used to test combinations. He used Bayesian priors to reduce the number of combinations, looking for frequent German words and meteorological terms. He even developed a unit quantifying the weight of evidence (Bayes factor), named the "*ban*", after the city of Banbury where punch cards were printed.

V.2.1.3 The Bayesian Renaissance

After World War II. The first computers were built during the war. Bayesian techniques were now becoming feasible. Their use rapidly increased in the early 1950s. McGrayne (2011) note a few of them.

Competitive businesses, that usually favor pragmatic solutions over ideology, turned naturally to the Bayesian approach. Arthur BAILEY was a pioneer in applying Bayes' rule to estimate insurance premiums. This was the only way to calculate the probability of catastrophic events, that had never happened before. This is the type of situations were frequentist methods are unusable. Howard RAIFFA and Robert SCHLAIFER taught Bayes' rule for business and decision-making.

Nuclear security is another example of a discipline requiring to estimate the probability of rare, unprecedented events. Frequentist studies concluded that nuclear plant incidents were unlikely, but would be catastrophic if they happened. In the 1970s, Norman RASMUSSEN estimated, in a Bayesian way, that it was the opposite: they were likely, but not necessarily catastrophic. The

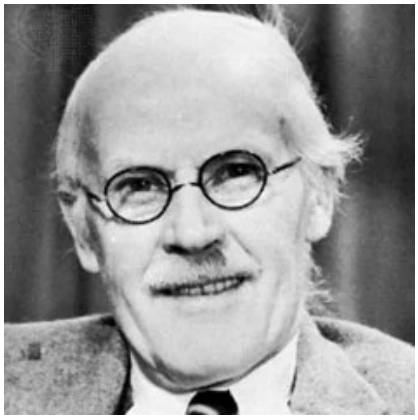

(a) Harold JEFFREYS (1891–1989)

(b) Alan TURING (1912–1954)

(c) Edwin Thompson JAYNES (1922–1998)

FIGURE V.14 – *The Bayesian resistance.* Credit: *(a)* Encyclopedia Britannica, used for non-commercial, educational purpose; *(b)* Wikipedia, public domain; *(c)* Wikipedia, public domain.

Three Mile Island incident (1979) proved him right. In another area, Bayesian search algorithms were used to find lost nuclear bombs and Russian nuclear submarines.

Epidemiological studies, using Bayesian techniques, were pioneered by Jerome CORNFIELD, who ridiculed Fisher's attempt at minimizing the link between smoking and lung cancer.

In academia, Dennis LINDLEY and Jimmie SAVAGE were actively promoting Bayesian methods and showing the limitations of frequentist techniques, claiming that "*Fisher is making Bayesian omelet without breaking Bayesian eggs*".

The great numerical leap forward. In the 1970s, the increasing power of computers opened new horizons to the Bayesian approach. The Metropolis-Hastings algorithm (*cf.* Sect. V.1.3; Hastings, 1970) provided a fast, easy-to-implement method, which rendered Bayesian techniques more attractive. Gibbs sampling (*cf.* Sect. V.1.3; Geman & Geman, 1984), which can be used to solve complex problems, put Bayes' rule into the spotlight. We can note the following achievements.

The human genome was decoded using Bayesian methods (Beaumont & Rannala, 2004).

In astrophysics, Bayesian techniques were first applied to analyze the neutrino flux from SN 1987A (Loredo & Lamb, 1989).

At the same time, Edwin JAYNES (*cf.* Fig. V.14.c) was working at solidifying the mathematical foundations of the Bayesian approach. It culminated in his posthumous book, "*Probability Theory: The Logic of Science*" (Jaynes, 2003).

Bayesian techniques, nowadays. Looking at the contemporary literature, it appears that Bayesians have won over frequentists [9]. In a lot of cases, this is however only a fashion trend due to the fact that the word "*Bayesian*" became hip in the 2010s, in astrophysics. There are already misuses of Bayesian methods. This is unavoidable. This might result from the fact that there is still a generation of math teachers and the majority of statistical textbooks ignoring the Bayesian approach. The difference with p-hacking is that Bayesian-hacking is easier to spot, because interpreting posterior distributions is less ambiguous than NHST. The supremacy of Bayesian techniques is ultimately demonstrated by the success of *Machine-Learning* (ML). ML has Bayesian foundations. It is a collection of probabilistic methods. Using ML can be seen as performing posterior inference, based on the evidence gathered during the training of the neural network.

9. There are still a few frequentist trolls roaming Wikipedia's mathematical pages.

V.2.2 Bayesian and Popperian Epistemologies

The following epistemological considerations have been expressed in several texts (*e.g.* Good, 1975; Loredo, 1990; Jaynes, 2003; Hoang, 2020). The book of Jaynes (2003) is probably the most rigorous on the subject, while the book of Hoang (2020) provides an accessible overview.

V.2.2.1 The Epistemological Debate at the Beginning of the XXth Century

Epistemology treats several aspects of the development of scientific theories, from their imagination to their validation. We will not discuss here how scientists can come up with ground-breaking ideas. We will only focus on how a scientific theory can be experimentally validated.

Scientific positivism. The epistemological point of view of Auguste COMTE (*cf.* Fig. V.15.a) had a considerable influence on the XIXth century epistemology, until the beginning of the XXth century. Comte was a French philosopher and sociologist, who developed a complex classification of sciences and theorized their role in society. What is interesting for the rest of our discussion is that he was aiming at *demarcating* sciences from theology and metaphysics. He proposed that we need to renounce to understand the absolute *causes* (why), to focus on the mathematical *laws* of nature (how). In that sense, his system, called *positivism*, is not an empiricism (*e.g.* Grange, 2002). Comte stressed that a theoretical framework is always necessary to interpret together different experimental facts. His approach is a reconciliation of empiricism and idealism, where both viewpoints are necessary to make scientific discoveries. Positivism is not scientism, either. Comte's view was, in substance, that science provides a knowledge that is rigorous and certain, but at the same time only partial and relative.

(a) Auguste COMTE (1798–1857)

(b) Henri POINCARÉ (1854–1912)

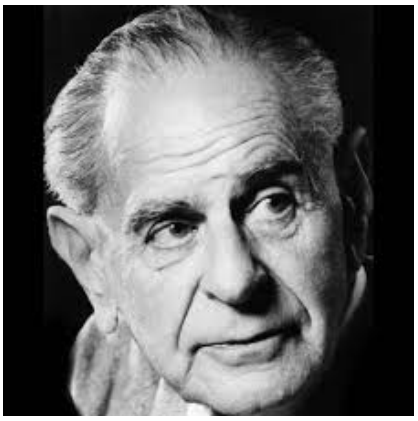

(c) Karl POPPER (1902–1994)

FIGURE V.15 – *Three figures of modern epistemology.* Credit: *(a)* Wikipedia, public domain; *(b)* Est Republicain, public domain; *(c)* Wikipedia, not licensed.

Conventionalism and verificationism. At the beginning of the XXth century, two complementary epistemological points of view were debated.

Conventionalism was represented, in physics and mathematics, by Henri POINCARÉ (*cf.* Fig. V.15.b). This philosophy considers that human intuitions about the physical world are possibly flawed. Some of our scientific principles are only *conventions*. Poincaré, having worked on Lobachevskian geometries, was taking Euclidean geometry as an example (*e.g.* Bland, 2011). These conventions should thus be chosen so that they agree with the physical reality.

Verificationism is another doctrine deriving from scientific positivism (*e.g.* Okasha, 2001). It postulates that a proposition has a cognitive meaning only if it can be *verified* by experience.

V.2.2.2 Popper's Logic of Scientific Discovery

We now review the epistemology developed by Karl POPPER (*cf.* Fig. V.15.c), which is the center of our discussion. Popper was an Austrian-born British philosopher who had a significant impact on the modern scientific method [10]. His concepts of falsifiability and reproducibility are still considered as the standards of the scientific method, nowadays. His major book, "*The Logic of Scientific Discovery*" (Popper, 1959), was originally published in German in 1934, and rewritten in English in 1959. Before starting, it is important to make the distinction between the following two terms.

Deduction is inferring the truth of a specific case from a general rule. For instance, knowing that SN Ia occur only in binary systems, if we observe a SN Ia, we can *deduce* that it originates from a binary system.

Induction is inferring a general conclusion based on individual cases. For instance, if we observe a few SNRs with massive amounts of freshly-produced dust, we can *induce* that SNe produce massive amounts of dust.

The criticism of induction. Popper's reflection focusses on the methods of empirical sciences. The foundation of his theory is the rejection of inductive logic, as he deems that it does not provide a suitable *criterion of demarcation*, that is a criterion to distinguish empirical sciences from mathematics, logic and metaphysics. According to him, the conventionalist and verificationist approaches are not rigorous enough. Popper argues that only a deductivist approach provides a reliable empirical method: "*hypotheses can only be empirically tested and only after they have been advanced*" (Popper, 1959, Sect. I.1). Deductivism is however not sufficient in Popper's mind.

Falsifiability. Popper criticizes conventionalists who "*evade falsification by using ad hoc modifications of the theory*". For that reason, verifiability is not enough. Empirical theories must be *falsifiable*, that is they must predict experimental facts that, if empirically refuted, will prove them wrong. His system, which was afterward called *falsifiabilism*, is the combination of: *(i)* deductivism; and *(ii) modus tollens*. The *modus tollens* is the following logical proposition:

$$((\mathrm{T} \Rightarrow \mathrm{D}) \wedge \neg \mathrm{D}) \Rightarrow \neg \mathrm{T}. \tag{V.37}$$

Put in words, it can be interpreted as: if a theory T predicts an observational fact D, and this fact D happens to be wrong, then we can *deduce* that the theory T is wrong. This principle is to be strictly applied: "*one must not save from falsification a theory if it has failed*" (Popper, 1959, Sect. II.4). Let's take a pseudo-science example to illustrate Popper's point. Let's assume that a "*ghost expert*" pretends a ghost inhabits a given haunted house. The verificationist approach would consist in saying that, to determine if there is really a ghost, we need to go there and see if it shows up. Popper would argue that, if the ghost did not appear, our expert would claim that it was because it was intimidated or it felt our skepticism. Falsifiabilism would dictate to set experimental conditions beforehand by agreeing with the expert: if the ghost does not appear in visible light, in this house, at midnight, on a particular day, then we will deduce that this ghost theory is wrong. The ghost expert would probably not agree with such strict requirements. Popper would thus conclude that ghostology is not an empirical science.

Reproducibility. A difficulty of the empirical method is relating perceptual experiences to concepts. Popper argues that the objectivity of scientific statements lies in the fact that they can be *intersubjectively* tested. In other words, if several people, with their own subjectivity, can perform the same empirical tests, they will rationally come to the same conclusion. This requires *reproducibility*. Only repeatable experiments can be tested by anyone. Reproducibility is also instrumental in avoiding coincidences.

10. If journalists are reading these lines, we stress that the *peer-review process* has nothing to do with the scientific method. It is just a convenient editorial procedure that filters poorly thought-out studies.

Parsimony (Ockham's razor). A fundamental requirement of scientific theories is that they should be the simplest possible. Unnecessarily complex theories should be eliminated. This is the *principle of parsimony*. Popper is aware of that and includes it in his system. This is however not the most convincing point of his epistemology. His idea is that a simple theory is a theory that has a high *degree of falsifiability*, which he calls "*empirical content*" (Popper, 1959, Sect. II.5). In other words, according to him, the simplest theories are those that have the highest prior improbability, whereas complex theories tend to have special conditions that help them evade falsification.

Popper's epistemology is frequentist. It is obvious that Popper's system has a frequentist frame of mind. It was indeed conceived at the golden age of frequentism (*cf.* Sect. V.2.1.2).

The requirement of falsifiability is reminiscent of NHST (*cf.* Sect. V.1.4.1). Frequentists only accept a hypothesis by rejecting (*i.e.* falsifying) its alternative. Rigorous NHST requires setting up the detailed experimental procedure, the stop condition and the significance of the outcome beforehand. This is exactly what Popper requires to make sure the conditions of falsifiability are not tampered with. This makes it impossible to test several theories with a single experiment, contrary to the Bayesian approach.

Platonic logic is at the center of Popper's epistemology. The last third of his book (Popper, 1959) is actually devoted to probabilities. He favors their *objective* interpretation, in terms of frequency. This is because he does not even conceive the possibility to assign a probability to a theory. This is also the weakness of the frequentist approach (*cf.* Sect. V.1).

Repeatability is the necessary condition to satisfy the assumption that experimental uncertainties are the limiting frequency of the result's fluctuations. This also makes it impossible to account for sparse or unique constraints.

Accumulation of knowledge is impossible in this approach, as each individual experiment must be considered independently. It is impossible to account for prior knowledge. The Popperian approach, if it was actually applied by scientists, would even lead to a decrease of knowledge. Indeed, if we indefinitely try to falsify a theory, we will end up by rejecting it, just by luck [11].

V.2.2.3 Verifiability, Holisticity and Parsimony: the Bayesian Alternative

We now discuss how the Bayesian approach provides an alternative to Popper's epistemology. Jaynes (2003) demonstrates that probabilities, in the Bayesian sense, could be the foundation of a rigorous scientific method. Hoang (2020) even argues that Bayes' rule is the optimal way to account for experimental data.

Falsifiability and the limits of Platonic logic. The refusal of Popper and frequentists to adopt probabilistic logic is the reason why their decision upon experimental evidence is so convoluted. The application of Platonic logic to the physical reality indeed presents some issues. One of the most famous aporias is "*Hempel's paradox*" (Hempel, 1945). It states the following.

Hempel's paradox: if a logical *proposition* is true, its *contraposition* is necessarily true:

$$\underbrace{(A \Rightarrow B)}_{\text{proposition}} \Leftrightarrow \underbrace{(\neg B \Rightarrow \neg A)}_{\text{contraposition}}. \tag{V.38}$$

The example taken by Hempel (1945), is "*all ravens are black*" (raven ⇒ black). The contraposition is "*anything that is not black is not a raven*" (¬black ⇒ ¬raven). From an experimental point of view, if we want to *corroborate* that all ravens are black, we can either: *(i)* find black ravens (*i.e.* verifying the proposition); or *(ii)* find anything that is neither black nor a raven, such as a red apple (*i.e.* verifying the contraposition). The second solution is obviously useless

11. This could be called "*P(opper)-hacking*".

in practice. To take an astrophysical example, finding a quiescent H I cloud would be considered as a confirmation that star formation occurs only in H_2 clouds. This is one of the reasons why Popper requires falsifiability.

A Bayesian solution to the paradox was proposed by Good (1960, who was Turing's collaborator at Bletchley Park). First, in probabilistic logic:

$$(\mathrm{A} \Rightarrow \mathrm{B}) \Leftrightarrow p\,(\mathrm{B}|\mathrm{A}) = 1. \tag{V.39}$$

The difference is that, with probabilities, we can deal with uncertainty, that is $0 < p\,(\mathrm{B}|\mathrm{A}) < 1$. Second, Bayes factors quantify the strength of evidence (*cf.* Sect. V.1.4.1), and it is different in the case of a black raven or a red apple. Good (1960) shows that the strength of evidence is negligible in the case of a red apple. The Bayesian solution is thus the most sensible one. Bayes factors are therefore the tool needed to avoid requiring falsifiability. We can adopt a verificationist approach and discuss if our data brought significant evidence.

☞ Bayesianism does not require falsifiability. Bayes factors provide a way to quantify the strength of evidence brought by any data set.

Parsimony is hard-coded in Bayes' rule. The principle of parsimony is directly implied by the use of Bayes factors. To illustrate this point, let's assume we are fitting a two-parameter model to a data set, $\vec{d}$, and we want to know if we can fix the second parameter (model M_1) or let it free (model M_2). The Bayes factor (Eq. V.31) is simply:

$$\mathrm{BF}_{21} = \frac{p\left(\vec{d}\middle|\mathrm{M}_2\right)}{p\left(\vec{d}\middle|\mathrm{M}_1\right)} = \frac{\iint p\left(\vec{d}\middle|x_1,x_2\right) p\,(x_1,x_2|\mathrm{M}_2)\,\mathrm{d}x_1\,\mathrm{d}x_2}{\int p\left(\vec{d}\middle|x_1\right) p\,(x_1|\mathrm{M}_1)\,\mathrm{d}x_1}. \tag{V.40}$$

Let's assume that we have a Gaussian model. We can write the product of the prior and the likelihood, in this case:

$$\underbrace{p\left(\vec{d}\middle|x_1\right)}_{\text{likelihood}}\underbrace{p\,(x_1|\mathrm{M}_1)}_{\text{prior}} = \underbrace{\frac{1}{(\sqrt{2\pi}\sigma)^m}\exp\left(-\frac{\chi^2}{2}\right)}_{\text{likelihood}}\underbrace{\frac{1}{\Delta_1}}_{\text{prior}}, \tag{V.41}$$

where we have assumed that the prior was flat over Δx_1 and that we had m observations with uncertainty σ. Notice that the product in Eq. (V.41) is proportional but not equal to the posterior. We indeed have not divided it by $p\left(\vec{d}\right)$, as this is the quantity we want to determine. If we approximate the posterior by a rectangle, we obtain the following rough expression, using the notations in Fig. V.16.a:

$$p\left(\vec{d}\middle|x_1\right) p\,(x_1|\mathrm{M}_1) \simeq \frac{\delta_1}{\Delta_1}\exp\left(-\frac{\chi^2_{\mathrm{max}}}{2}\right). \tag{V.42}$$

Let's assume that adding parameter x_2 does not improve the fit. The χ^2_{max} thus stays the same. This is represented in Fig. V.16.b. With the same assumptions as in Eq. (V.42), we obtain:

$$p\left(\vec{d}\middle|x_1,x_2\right) p\,(x_1,x_2|\mathrm{M}_2) \simeq \frac{\delta_1\delta_2}{\Delta_1\Delta_2}\exp\left(-\frac{\chi^2_{\mathrm{max}}}{2}\right). \tag{V.43}$$

Eq. (V.40) thus becomes:

$$\mathrm{BF}_{21} \simeq \frac{\delta_2}{\Delta_2} \ll 1. \tag{V.44}$$

It thus tell us that model M_1 is more credible. The penalty of adding the extra parameter is δ_2/Δ_2. More generally, we can encounter the three following situations.

1. If the fit is indeed better, we will have: $\mathrm{BF}_{21} \simeq \delta_2/\Delta_2 \exp[-(\chi^2_2 - \chi^2_1)/2]$. Model M_2 will be more credible only if the increased chi-squared compensates the penalty.

2. If the fit is not better, but parameter x_2 is not constrained, we will have $\delta_2 \simeq \Delta_2$, and $BF_{21} \simeq 1$. Both models will be equivalent because we will not have changed our prior knowledge about x_2.

3. If the fit is not better, but parameter x_2 has a smaller support than its prior, model M_2 will be less credible than M_1. This is the example of Fig. V.16.

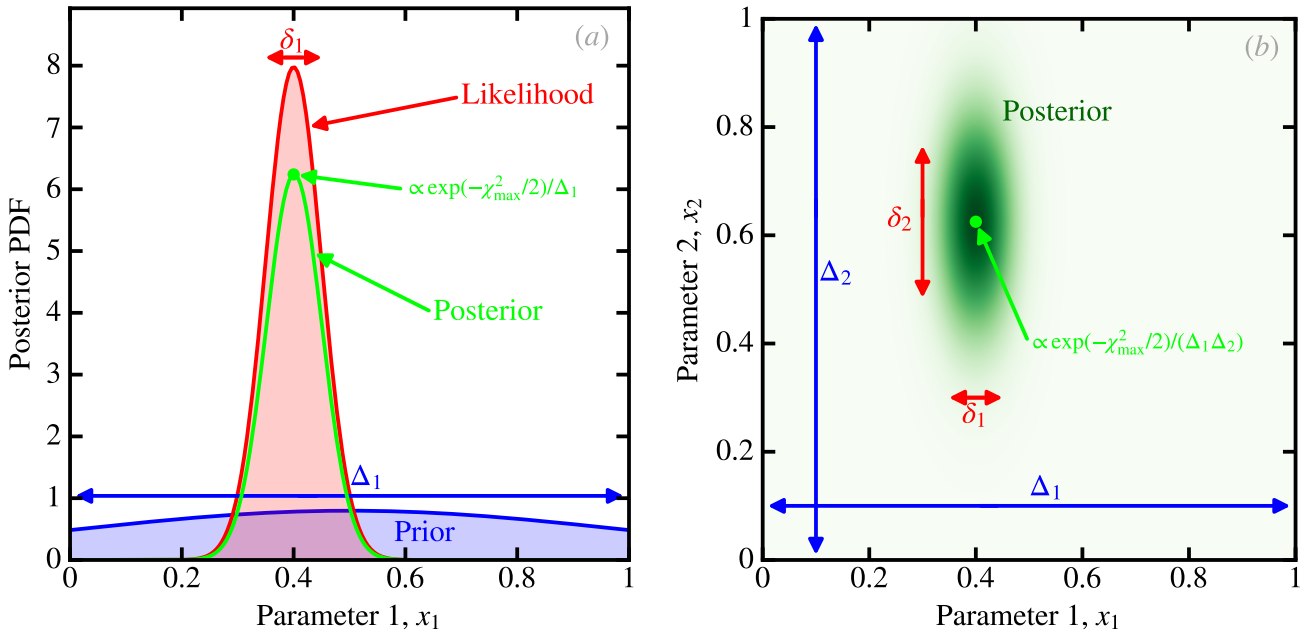

FIGURE V.16 – *Bayes factors and parsimony.* Panel *(a)* represents the likelihood of a one-parameter model, in red. Its width is δ_1. The prior is shown in blue and is wider (width Δ_1). The posterior, in green, is the product of the two. Its peak, the green dot, is roughly proportional to $\exp(-\chi^2_{\text{max}}/2)/\Delta_1$ (Eq. V.42). Panel *(b)* represents the same model, adding an extra model parameter, x_2. In the case we have represented, the parameter does not improve the fit, so that the chi-squared is similar. The maximum *a posteriori* is the green dot. It is roughly proportional to $\exp(-\chi^2_{\text{max}}/2)/(\Delta_1\Delta_2)$ (Eq. V.43).

Comparison of the Bayesian and Popperian methods. We can now compare both approaches. The following arguments are summarized in Table V.3.

Theory corroboration requires falsifiability, in the Popperian approach. Experiments need to be reproducible and the detailed procedure needs to be defined before starting acquiring data. The Bayesian approach is more flexible because falsifiability is not required and heterogeneous data sets can be accounted for. For instance, the first detection of gravitational waves (LIGO collaboration et al., 2016) and the first direct image of a black hole (Event Horizon Telescope Collaboration et al., 2019), combined, bring a large weight of evidence in favor of general relativity. On the contrary, a strict Popperian would argue that: *(i)* both experiments are independent and should not be mixed together; and *(ii)* these experiments are not falsifiable, as an absence of detection could have been blamed on their complexity. In that sense, the Popperian approach, if it was actually put in practice, would be extremely wasteful and would slow down the progress of science. Fortunately, the majority of scientists do not apply the Popperian method, most of them unconsciously. Our impression is that most scientists apply the Bayesian principles, at least qualitatively. This is probably because our own brain is Bayesian (*e.g.* Meyniel & Dehaene, 2017).

Reproducibility is a requirement of the Popperian approach [12], whereas Bayesians can account for unique, unreproducible data, such as earthquakes, SNe, GRBs, *etc.* The Bayesian approach will benefit from reproducible experiments, as they will increase the strength of evidence, but it is not a requirement.

Accumulation of knowledge is natural in Bayesianism, as the prior is there to account for what any previous experience has taught us. This is what we demonstrated in Sect. V.1.2.2:

$$\underbrace{p\left(\vec{x}\right)}_{\text{new prior}} = \underbrace{1}_{\text{initial prior}} \times \underbrace{p\left(\vec{d}_1\middle|\vec{x}\right) \times \ldots \times p\left(\vec{d}_N\middle|\vec{x}\right)}_{\text{accumulated previous data}}. \tag{V.45}$$

Logical decision is Platonic for Popperians. They see theories either right or wrong, until proven otherwise. The probabilistic logic of Bayesians is more progressive, because it uses a continuous credibility scale and accounts for all previous data. It makes it more conservative. Yet, Epistemological breaks are still possible if new data bring a large strength of evidence in favor of a new theory.

Scientist or lawyer? The Popperian approach forces scientists to design experiments to test a single theory, whereas Bayesians can naturally compare several theories and use all available data. The latter favors a less doctrinal attitude, less ideological, that should be promoted in science. On the contrary, Popperians have an attitude closer to that of lawyers, as they are forced to defend one particular case, by attacking (falsifying) the alternatives [13].

	Bayesian	**Popperian**
Corroboration	Verifiability & strength of evidence	Requires falsifiability
Logic	Probabilistic: continuity between skepticism & confidence	Platonic: theories are either true or false at a given time
Repeatability	Can account for unique data	Requires reproducibility
Experimental data	Can account for small, heterogeneous data sets	Experimental settings need to be defined beforehand
External data	Holistic approach	No possibility to account for any data outside of the experiment
Parsimony	Bayes factors eliminate unnecessary complex theories	The most falsifiable theories are preferred
Knowledge growth	Prior accounts for past knowledge	Each experiment is independent
Attitude	Universal approach: can test any theory	Partial approach: only one theory can be tested
Application	Most scientists are unconsciously pragmatic Bayesians	Strict Popperians are rare & probably not very successful

TABLE V.3 – *Comparison of Bayesian and Popperian epistemologies.*

V.3 Relevance for Interstellar Dust Studies

We now demonstrate what the Bayesian methods, which constitute a true epistemological approach, can bring to ISD studies. In particular, we advocate that hierarchical Bayesian models are an even better application of this approach. We illustrate this point with our own codes.

12. Nowadays, scientists call "*reproducibility*" the action of providing the data and the codes a publication was prepared with. This is a good practice, but this is not Popper's reproducibility. It should rather be qualified as "*open source*".

13. Concerning the topics discussed in Sect. IV.3, we have seen this attitude in a small group of people trying to prove ISM dust is stardust, constantly ignoring the big picture summarized in Table IV.2.

V.3.1 The Particularities of Interstellar Dust Studies

We have discussed throughout this manuscript the difficulty to constrain dust properties using a variety of observational constraints. For instance, we have seen that there is a degeneracy between small and hot equilibrium grains in the MIR (*cf.* Sect. III.1.2.2), or between the effects of the size and charge of small a-C(:H) (*cf.* Sect. III.2.1.3). In a sense, we are facing what mathematicians call an *ill-posed problem*, with the difference that we do not have the luxury of rewriting our equations, because they are determined by the observables. We detail these issues below.

V.3.1.1 Complexity of the Physics

Degeneracy between microscopic and macroscopic properties. When we observe a $[\mathrm{C\,II}]_{158\mu\mathrm{m}}$ line, we know it comes from a C^+ atom, and we can characterize very precisely the physical nature of this atom. On the contrary, if we observe thermal grain emission, we know it can come from a vast diversity of solids, with different sizes, shapes, structures, and composition. Even if we observe a feature, such as the 9.8 µm silicate band or an aromatic feature, we still have a lot of uncertainty about the physical nature of its carrier. This is the fundamental difference between ISM gas and dust physics. The complexity of gas modeling comes from the difficulty to determine the variation of the environmental conditions within the telescope beam. This difficulty thus comes from our uncertainty about the *macroscopic* distribution of ISM matter and of the energy sources (stars, AGNs, *etc.*) in galaxies. We also have the same issue with dust. When studying ISD, we therefore constantly face uncertainties about both the *microscopic* and *macroscopic* properties. Assuming we have a model that accounts for variations of both the dust constitution and the spatial distribution of grains relative to the stars, the Bayesian approach is the only way to consistently explore the credible regions of the parameter space, especially if several quantities are degenerate. We will give some examples in Sect. V.3.3.

Heterogeneity of the empirical constraints. A dust model, such as those discussed in Sect. II.3, has been constrained from a variety of observables (*cf.* Sect. II.2): *(i)* from different physical processes, over the whole electromagnetic spectrum; *(ii)* originating from different regions in the MW; *(iii)* with prior assumptions coming from studies of laboratory analogues and meteorites. When we use such a model to interpret a set of observations, we should in principle account for all the uncertainties that went into using these constraints:

- the uncertainties on the observations used to design the model (depletions, extinction curves, *etc.*);
- the uncertainties on the laboratory data (opacity, density, *etc.*);
- the prior probability of the different assumptions.

Obviously, only the Bayesian approach can account for these, especially knowing that these different uncertainties will likely be non-Gaussian and partially correlated. This is however an ambitious task, and it has been done only approximately (*e.g.* Sect. 4.1.3 of Galliano et al., 2021). This is a direction that future dust studies should take.

V.3.1.2 Entanglement of the Observations

The observables are weakly informative. Another issue with ISD studies is that the observables, taken individually, bring a low weight of evidence. A single broadband flux is virtually useless, but a few fluxes, strategically distributed over the FIR SED, can unlock the dust mass and starlight intensity (*cf.* Sect. III.1.2.2). Yet, these different fluxes come from different observation campaigns, with different instruments. If we add that the partially-correlated calibration uncertainties of the different instruments often dominate the error budget, we understand that the Bayesian approach is the only one that can rigorously succeed in this type of analysis. We will discuss the treatment of calibration uncertainties in Sect. V.3.2.2.

Contaminations are challenging to subtract. The different sources of foreground and background contaminations, that we have discussed in Sect. III.1.3.2, will become more and more problematic with the increasing sensitivity of detectors. Indeed, probing the diffuse ISM of galaxies requires to observe surface brightnesses similar to the MW foreground. In addition, the CIB is even brighter at submm wavelengths (*cf.* Fig. III.24). These two contaminations, the MW and the CIB, have very similar SEDs and a complex, diffuse spatial structure. Accurately separating these different layers therefore requires probabilistic methods, using redundancy on large-scales (*e.g.* Planck Collaboration et al., 2016a). It requires modeling every component at once. Bayesian and ML methods are the most obvious solutions.

V.3.2 The Principles of Hierarchical Bayesian Inference

We now discuss the formalism of hierarchical Bayesian inference, applied to SED modeling. This method has been presented by Kelly et al. (2012) and Galliano (2018).

V.3.2.1 Non-Hierarchical Bayesian Formalism for SED Modeling

Posterior of a single source. Let's assume that we are modeling a single observed SED (*e.g.* one pixel or one galaxy), sampled in m broadband filters, that we have converted to monochromatic luminosities: $\mathrm{L}_\nu^{\mathrm{obs}}(\lambda_j)$ $(j = 1,\dots,m)$. Let's assume that these observations are affected by normal iid noise, with standard-deviation $\sigma_\nu^{\mathrm{noise}}(\lambda_j)$. If we have a SED model, depending on a set of parameters $\vec{x}$, such that the predicted monochromatic luminosities in the observed bands is $\mathrm{L}_\nu^{\mathrm{mod}}(\lambda_j,\vec{x})$, we can write that:

$$\mathrm{L}_\nu^{\mathrm{obs}}(\lambda_j) = \mathrm{L}_\nu^{\mathrm{mod}}(\lambda_j,\vec{x}) + \epsilon(\lambda_j)\sigma_\nu^{\mathrm{noise}}(\lambda_j), \tag{V.46}$$

where $\epsilon(\lambda_j) \overset{\mathrm{iid}}{\sim} \mathcal{N}(0,1)$. In other words, our observations are the model fluxes plus some random fluctuations distributed with the properties of the noise. The distribution of the parameters, $\vec{x}$, is what we are looking for. We can rearrange Eq. (V.46) to isolate the random variable:

$$\epsilon(\lambda_j,\vec{x}) = \frac{\mathrm{L}_\nu^{\mathrm{obs}}(\lambda_j) - \mathrm{L}_\nu^{\mathrm{mod}}(\lambda_j,\vec{x})}{\sigma_\nu^{\mathrm{noise}}(\lambda_j)}. \tag{V.47}$$

Since we have assumed iid noise, the likelihood of the model is the product of the likelihoods of each individual broadbands:

$$p\left(\vec{\mathrm{L}}_\nu^{\mathrm{obs}}\middle|\vec{x}\right) = \prod_{j=1}^{m} p\left(\epsilon(\lambda_j,\vec{x})\right), \tag{V.48}$$

were $\vec{\mathrm{L}}_\nu^{\mathrm{obs}} \equiv \{\mathrm{L}_\nu^{\mathrm{obs}}(\lambda_j)\}_{j=1,\dots,m}$. If we assume a flat prior, the posterior is (Eq. V.6):

$$p\left(\vec{x}\middle|\vec{\mathrm{L}}_\nu^{\mathrm{obs}}\right) \propto \prod_{j=1}^{m} p\left(\epsilon(\lambda_j,\vec{x})\right). \tag{V.49}$$

The difference is that: *(i)* in Eq. (V.48), the parameters, $\vec{x}$, are assumed fixed, the different $p\left(\epsilon(\lambda_j,\vec{x})\right)$ are thus independent; whereas *(ii)* in Eq. (V.49), the observations, $\vec{\mathrm{L}}_\nu^{\mathrm{obs}}$, are assumed fixed, the different terms in the product are now correlated, because each $p\left(\epsilon(\lambda_j,\vec{x})\right)$ depends on all the parameters.

Modeling several sources together. If we now model n sources with observed luminosities, $\vec{\mathrm{L}}_\nu^{\mathrm{obs},i}$ $(i = 1,\dots,n)$, to infer a set of parameters, $\vec{x}_i$, the posterior of the source sample will be:

$$p\left(\vec{x}_1,\dots,\vec{x}_n\middle|\vec{\mathrm{L}}_\nu^{\mathrm{obs},1},\dots,\vec{\mathrm{L}}_\nu^{\mathrm{obs},n}\right) \propto \prod_{i=1}^{n}\prod_{j=1}^{m} p(\epsilon_i(\lambda_j,\vec{x}_i)) = \prod_{i=1}^{n} p\left(\vec{x}_i\middle|\vec{\mathrm{L}}_\nu^{\mathrm{obs},i}\right). \tag{V.50}$$

Notice that, in the second equality, the different $p\left(\vec{x}_i\middle|\vec{\mathrm{L}}_\nu^{\mathrm{obs},i}\right)$ are independent, as each one depends on a distinct set of parameters, $\vec{x}_i$. The sampling of the whole posterior distribution will thus be rigorously equivalent to sampling each individual SED, one by one.

☞ With a non-hierarchical Bayesian approach, the sources in a sample are independently modeled.

V.3.2.2 The Introduction of Nuisance Variables

Nuisance variables are parameters we need to estimate to properly compare our model to our observations. The particular value of these variables is however not physically meaningful, and we end up marginalizing the posterior over them. The Bayesian framework is particularly well-suited for the treatment of nuisance parameters.

Calibration uncertainties. Calibration errors originate from the uncertainty on the conversion of detector readings to astrophysical flux (typically ADU/s to Jy/pixel). Detectors are calibrated by observing a set of *calibrators*, that are bright sources with well-known fluxes. The uncertainties in the observations of these calibrators and on the true flux of the calibrators translate into a *calibration uncertainty*.

Correlation between sources: the offset resulting from this uncertainty will be the same for every observations made with a given detector. For instance, if an instrument's calibration factor is 5 % higher than what it should be [14], all high signal-to-noise measures made with this instrument will report a flux higher by 5 % than its true value. The calibration uncertainty, for a given broadband filter, will thus be perfectly correlated between all our sources.

Partial correlation between wavelengths: instruments are often cross-calibrated and use similar calibrators. The correlation procedure will thus induce a partial correlation between different broadband fluxes. An example of this type of correlation is discussed in Appendix A of Galliano et al. (2021).

Introduction into the posterior. To account for calibration uncertainties, we can rewrite Eq. (V.47) as:

$$\epsilon(\lambda_j, \vec{x}, \delta_j) = \frac{\mathrm{L}_\nu^{\mathrm{obs}}(\lambda_j) - \mathrm{L}_\nu^{\mathrm{mod}}(\lambda_j, \vec{x}) \times (1+\delta_j)}{\sigma_\nu^{\mathrm{noise}}(\lambda_j)}. \tag{V.51}$$

We have now multiplied the model by $(1+\delta_j)$, where $\delta_j \sim \mathcal{N}(0, \mathbb{V}_{\mathrm{cal}})$ is a random variable following a centered multivariate normal law [15] with covariance matrix, $\mathbb{V}_{\mathrm{cal}}$. This random variable, which represents a correction to the calibration factor, is multiplicative: it scales the flux up and down. $\mathbb{V}_{\mathrm{cal}}$ contains all the partial correlations between wavelengths (*cf.* Appendix A of Galliano et al., 2021). The important point to notice is that the δ_j do not depend on the individual object (index i), they are unique for the whole source sample. The posterior of Eq. (V.50) now becomes:

$$p\left(\vec{x}_1, \ldots, \vec{x}_n, \vec{\delta} \middle| \vec{\mathrm{L}}_\nu^{\mathrm{obs},1}, \ldots, \vec{\mathrm{L}}_\nu^{\mathrm{obs},n}\right) \propto p\left(\vec{\delta}\right) \times \prod_{i=1}^{n} \frac{\underbrace{p\left(\vec{x}_i \middle| \vec{\mathrm{L}}_\nu^{\mathrm{obs},i}, \vec{\delta}\right)}}{\prod_{j=1}^{m} p\left(\epsilon_i(\lambda_j, \vec{x}_i, \delta_j)\right)}, \tag{V.52}$$

where $p\left(\vec{\delta}\right) = \mathcal{N}(0, \mathbb{V}_{\mathrm{cal}})$ is the prior on δ. We can make the following remarks.

1. The prior on the calibration *errors*, $\vec{\delta}$, is the calibration *uncertainty*, $p\left(\vec{\delta}\right)$, quoted by the different instrument teams (all the information is included in $\mathbb{V}_{\mathrm{cal}}$). It means that, by sampling Eq. (V.52), we will infer values of $\vec{\delta}$ that are potentially more accurate than the calibration coefficients provided by the instrument teams. In practice, this is however not the case, because: *(i)* the calibration sources are usually the brightest and the most well-constrained, it is unlikely

14. In this example, 5 % is not the calibration *uncertainty*, but the *error* made because of the calibration uncertainty.
15. We could have taken a different distribution, such as a Student's t (*e.g.* Eq. 31 of Galliano, 2018).

to reach the same accuracy observing galaxies; *(ii)* observations of galaxies suffer from contaminations adding several biases that are difficult to take into account; and *(iii)* models used to interpret observations of galaxies are not as accurate as models of typical calibrators, such as stars or Uranus.

2. By sampling Eq. (V.52), we are inferring a single value of the δ_j factors. This is because the calibration has been done only once, and stays the same. The randomness it introduces is a single draw. It is not a reproducible event. The calibration uncertainty can not be considered as the limiting frequency of a repeated procedure. This is why frequentists could not treat these uncertainties.

3. The calibration factors in Eq. (V.52) link the posteriors of the individual sources together. We have noted that they were independent in Eq. (V.50). This is not the case anymore, as they all depend on $\vec{\delta}$. Thus: *(i)* inferring $\vec{\delta}$ is made possible by simultaneously sampling several sources, sharing the same calibration coefficients; *(ii)* the presence of $\vec{\delta}$, at the same time, improves the fit of individual SEDs.

The posterior of the parameters is, in the end, the marginalization over $\vec{\delta}$ of Eq. (V.52):

$$p\left(\vec{x}_1,\dots,\vec{x}_n\middle|\vec{\mathrm{L}}_\nu^{\mathrm{obs,1}},\dots,\vec{\mathrm{L}}_\nu^{\mathrm{obs,n}}\right)=\int p\left(\vec{x}_1,\dots,\vec{x}_n,\vec{\delta}\middle|\vec{\mathrm{L}}_\nu^{\mathrm{obs,1}},\dots,\vec{\mathrm{L}}_\nu^{\mathrm{obs,n}}\right)\mathrm{d}^m\vec{\delta}. \tag{V.53}$$

☞ Calibration errors can be rigorously taken into account as nuisance parameters.

V.3.2.3 The Role of the Hyperparameters

Accounting for the evidence brought by each source. In Sect. V.1.2.2, we have stressed that, when performing a sequential series of measure, we can use the previous posterior as the new prior. Yet, the posterior in Eq. (V.52) does not allow us to do so, as: *(i)* the posteriors of individual sources all depend on $\vec{\delta}$, they must therefore be sampled at once; and *(ii)* the parameters, $\vec{x}_i$, are not identical, we are not repeating the same measure several times as in Eq. (V.14), we are observing different sources. Accounting for the accumulation of evidence is thus not as straightforward as in Eq. (V.14). There is however a way to use an informative prior, consistently constrained by the sample. It is the *Hierarchical Bayesian* (HB) approach. To solve the conundrum that we have just exposed, we can make the following assumptions.

1. We can assume that the parameters of the different sources are drawn from a *common distribution*, but this distribution is unknown. For instance, the dust masses in the pixels of a galaxy span only a few dexes. They are not arbitrarily distributed. Their distribution results from the complex physics at play: dynamics, star formation, dust evolution, *etc.*

2. We can reasonably approximate this common distribution with a particular functional form, such as a multivariate Gaussian or a Student's t. Such a distribution is parametrized by its average, $\vec{\mu}$, and its covariance matrix, $\mathbb{V}$. These parameters are called *hyperparameters*, because they control the distribution of physical parameters. This is why this approach is called *hierarchical*. There are two layers of modeling: *(i)* the common distribution of parameters, controlled by a set of hyperparameters; *(ii)* the SED model controlled by as many sets of parameters as there are sources. The average $\vec{\mu}$ will therefore represent the mean of each SED model parameters ($\mathrm{M_{dust}}$, $\langle\mathrm{U}\rangle$, q_{AF}, *etc.*; *cf.* Sect. III.1.2.2) and, $\mathbb{V}$, their intrinsic scatter and correlations (such as the correlation between $\langle\mathrm{U}\rangle$ and q_{AF}; *cf.* Sect. IV.3.2).

3. This common distribution, controlled by hyperparameters, is treated as the prior of our SED model parameters. We can then infer the values of the hyperparameters when sampling the whole posterior and marginalize over them in the end.

The hierarchical posterior. With the HB approach, the full posterior of our source sample is:

$$p\left(\vec{x}_1,\dots,\vec{x}_n,\vec{\delta},\vec{\mu},\mathbb{V}\middle|\vec{L}_\nu^{\mathrm{obs,1}},\dots,\vec{L}_\nu^{\mathrm{obs,n}}\right)\propto\prod_{i=1}^{n}\underbrace{p\left(\vec{L}_\nu^{\mathrm{obs,i}}\middle|\vec{x}_i,\vec{\delta}\right)}_{\text{source likelihoods}}\times\underbrace{p\left(\vec{x}_i\middle|\vec{\mu},\mathbb{V}\right)}_{\text{parameter prior}}\times\underbrace{p\left(\vec{\mu}\right)p\left(\mathbb{V}\right)}_{\text{hyperparameter prior}}\times\underbrace{p\left(\vec{\delta}\right)}_{\text{calibration prior}}. \tag{V.54}$$

The hyperprior: compared to Eq. (V.52), we have introduced a new term: $p\left(\vec{x}_i\middle|\vec{\mu},\mathbb{V}\right)\times p\left(\vec{\mu}\right)p\left(\mathbb{V}\right)$. This is the hierarchical prior. The term $p\left(\vec{x}_i\middle|\vec{\mu},\mathbb{V}\right)$ is what we have previously called the *common distribution* of parameters. It is the actual prior on the parameters, and it is parametrized by the hyperparameters. The other terms, $p\left(\vec{\mu}\right)p\left(\mathbb{V}\right)$ are the necessary priors on $\vec{\mu}$ and $\mathbb{V}$, that we can assume rather flat (*cf.* Sect. 3.2.4 of Galliano, 2018, for more details). The elements of $\vec{\mu}$ are drawn one by one, using Gibbs sampling (*cf.* Sect. V.1.3). Regarding the elements of $\mathbb{V}$, we independently draw each standard-deviation and correlation coefficient (*cf.* Sect. 3.2.4 of Galliano, 2018).

The parameter space corresponding to Eq. (V.54) has dimension (noting q the number of SED model parameters):

$$\mathrm{N_{dim}}=\underbrace{n\times q}_{\text{SED model parameters}}+\underbrace{q}_{\text{elements of }\vec{\mu}}+\underbrace{q}_{\text{diagonal of }\mathbb{V}}+\underbrace{q\times(q-1)/2}_{\text{number of correlations}}+\underbrace{m}_{\text{calibration errors}}. \tag{V.55}$$

For the *composite* model ($q=7$; *cf.* Sect. III.1.2.2), constrained by $m=10$ wavelengths, and for $n=1000$ sources or pixels, we would have to sample a $\mathrm{N_{dim}}\simeq 7000$ dimension parameter space.

V.3.3 Hierarchical Bayesian Models for ISD Studies

We now present practical illustrations of SED modeling with the HB approach. The first HB dust SED model was presented by Kelly et al. (2012). It was restrained to single MBB fits. Veneziani et al. (2013) then presented a HB model that could be applied to a combination of MBBs. The *HiERarchical Bayesian Inference for dust Emission* code (`HerBIE`; Galliano, 2018), was the first HB model, and to this day the only one to our knowledge, to properly account for full dust models, with: *(i)* realistic optical properties; *(ii)* complex size distributions; *(iii)* rigorous stochastic heating; *(iv)* mixing of physical conditions; *(v)* photometric filter and color corrections; and *(vi)* partially-correlated calibration errors. The following examples have been computed with `HerBIE`.

V.3.3.1 Efficiency and Comparison to Other Methods

To demonstrate the efficiency of the HB method and the fact that it performs better than its alternatives, we rely on the simulations presented by Galliano (2018). These simulations are simply obtained by randomly drawing SED model parameters from a multivariate distribution, for a sample of sources. This distribution is designed to mimic what we observe in typical star-forming galaxies. The SED model used is the *composite* approach (*cf.* Sect. III.1.2.2), except when we discuss MBBs. Each set of parameters result in an observed SED, that we integrate into the four IRAC, the three PACS and the three SPIRE bands. We add noise and calibration errors. This way we can test fitting methods and assess their efficiency by comparing the inferred and the true values.

Close look at a fit. Fig. V.19.a-b shows the posterior SED PDF of the faintest and brightest pixels in a simulation, fitted in a HB fashion.

For the faintest pixel (Fig. V.19.a), we can see that the PDF is wider, because it is less constrained. Half of the observations (green) are indeed only upper limits. The SED looks however realistic and matches very well its truth (in red). This is one of the advantages of the HB approach: when a source is poorly constrained, its posterior is dominated by the prior, which has been informed by the whole sample. Thus, despite few information on this particular source, we

obtain realistic parameters and SED, because the rest of the sample is providing information about the typical shape of an SED in that luminosity range.

For the brightest pixel (Fig. V.19.b), the SED is much tighter. There are however spectral domains where the uncertainty can increase. For instance, notice that there is a wider spread around 3 µm and around 11 µm. This is because the charge of the PAHs gives the model a degree of freedom in this range (*cf.* Sect. III.2.1.3). Yet, the model is poorly constrained. The true SED lies in the tail of the distribution. It is still consistent, though.

The calibration errors are shown in Fig. V.19.c. The red dots represent the biases we have introduced into the synthetic observations. These biases are the same for each pixel in the simulation. These errors are treated as nuisance parameters in Eq. (V.54). The blue error bars show the inference of these biases. We see that they are most of the time consistent within 1σ. We also see that they are most of the time consistent with zero. This is what we discussed in Sect. V.3.2.2: typical galaxy observations are not accurate enough to refine the calibration of the instruments. The only outlier is the $\mathrm{SPIRE}_{350\mu m}$ point. It is however less than 3σ away from zero.

The posterior distribution of these two pixels is shown in Fig. V.18.b. We have represented the PDF of two parameters, M_{dust} and $\langle U \rangle$, marginalizing over the rest. We see that the faintest pixel has a larger uncertainty, and that both posteriors are close to their true values (red dots). If we now compare these results to the same exact simulation fitted in a standard, non-hierarchical Bayesian way (Fig. V.18.a), we notice that the PDF of the brightest pixel is very much the same, but the PDF of the faintest pixel is now much wider, covering a large fraction of the parameter space. This is because, as we have noted earlier, sources are individually fitted with a standard Bayesian method, they thus do not benefit from the information provided by the rest of the sample, through the prior.

☞ In a HB model, the least-constrained sources are more corrected by the prior than the brightest ones.

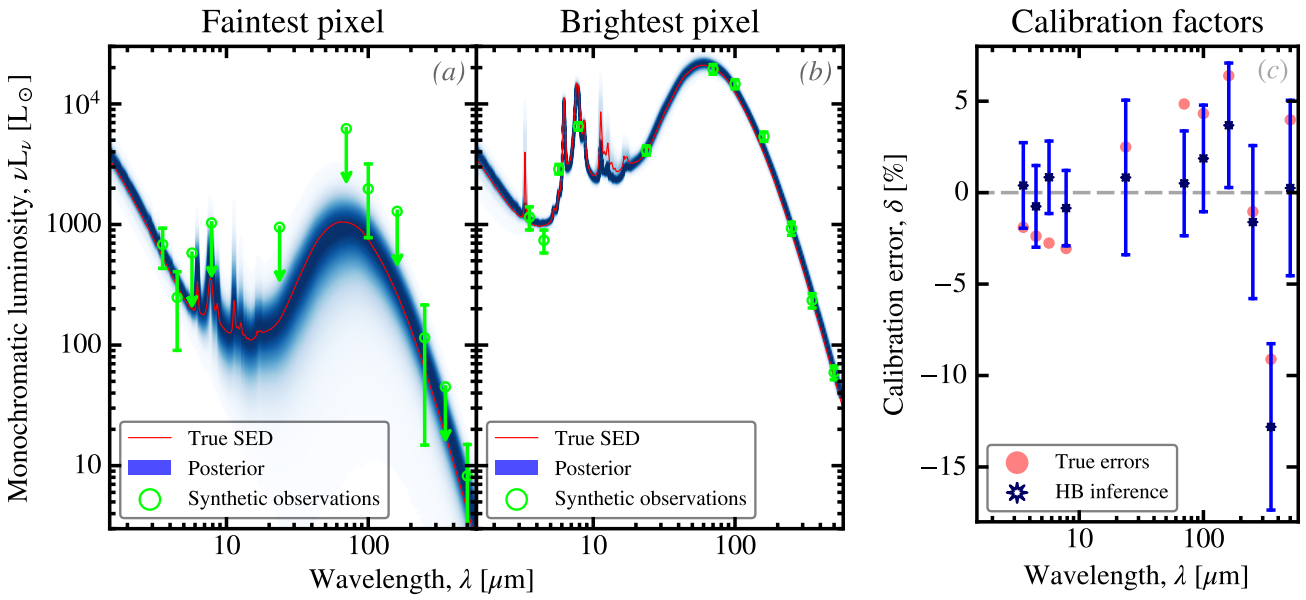

FIGURE V.17 – *Example of hierarchical Bayesian SED fits.* The blue contours in panels *(a)* and *(b)* represent the posterior SED of the faintest and brightest pixels in a simulation presented by Galliano (2018). This simulation reproduces typical conditions in star-forming galaxies. The synthetic observations, including noise and calibration errors, are in green. The true model is shown in red, for reference. Panel *(c)* shows the simulated calibration errors in red, and their inferred posterior values, in blue. Licensed under CC BY-SA 4.0.

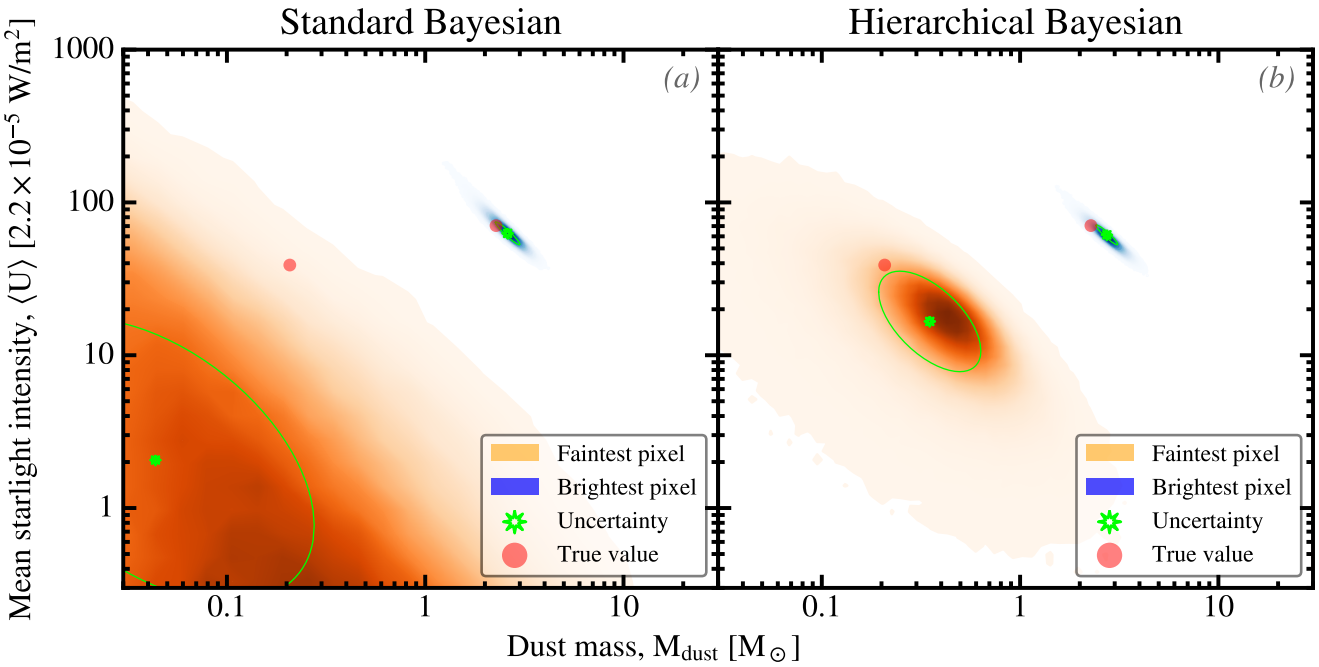

FIGURE V.18 – *Posterior distributions with standard and hierarchical Bayesian methods.* In each panel, we show the marginalized posterior of the dust mass, M_{dust}, and mean starlight intensity, $\langle U \rangle$ (Eq. III.38), for the two pixels in Fig. V.17. Panel *(a)* corresponds to the case of a non-hierarchical Bayesian fit, and panel *(b)*, to a full hierarchical fit. In both panels, the orange contours represent the faintest pixel and the blue contours, the brightest one. The uncertainty ellipses corresponding to these posteriors are the green ellipses. The true values are the red dots. Licensed under CC BY-SA 4.0.

Comparison between different approaches. We have been discussing the two extreme pixels of our simulation. Let's now look at the whole source sample and compare several methods. Fig. V.19 shows the same parameter space as in Fig. V.18, but for all sources, with different methods.

The least-squares method, which is frequentist, is shown in green, in Fig. V.19.a. We note the following points.

1. The inferred parameters have large individual uncertainties (*i.e.* big ellipses).
2. The overall sample is quite scattered, covering three orders of magnitude, while the true values are within a dex.
3. There is a false negative correlation between M_{dust} and $\langle U \rangle$.

This false correlation is typical of frequentist methods, but not exclusive. It is the equivalent of the $\beta-T$ degeneracy we have already discussed in Sect. III.1.2.1. Because of the way the model is parametrized, if we slightly overestimate the dust mass, we will indeed need to compensate by decreasing $\langle U \rangle$, to account for the same observed fluxes, and vice versa. This false correlation is thus induced by the noise.

The non-hierarchical Bayesian method, in Fig. V.19.b, provides a more accurate fit of the brightest sources (high M_{dust} and high $\langle U \rangle$). The faintest sources are however quite scattered. There is still a false correlation, due to the same reasons as for the least-squares, but it is less significant.

The hierarchical Bayesian method, in Fig. V.19.c, on the contrary, provides an unbiased statistical account of the sample. We note the following points.

1. The uncertainty of individual sources (blue ellipses) is moderate. It is never larger than the scatter of the true sample.
2. The inferred mean and scatter of the sample properties are very close to their true values. Their comparison is given in Table V.4.

3. There is no false correlation. The inferred correlation coefficient is consistent with zero, its true value.

From a general point view, a HB method is efficient at removing the scatter between sources that is due to the noise. In addition, the inferred uncertainties on the parameter of a source are never larger than the intrinsic scatter of the sample, because this scatter is also the width of the prior. For instance, in Fig. V.19.c, the lowest signal-to-noise sources (lower left side of the distribution) have uncertainties (blue ellipses) similar to the scatter of the true values (red points), because the width of the prior matches closely this distribution. On the opposite, the uncertainties of high signal-to-noise sources (upper right side) are much smaller, they are thus not significantly affected by the prior.

☞ HB methods are efficient at recovering the true, intrinsic scatter of parameters and their correlations.

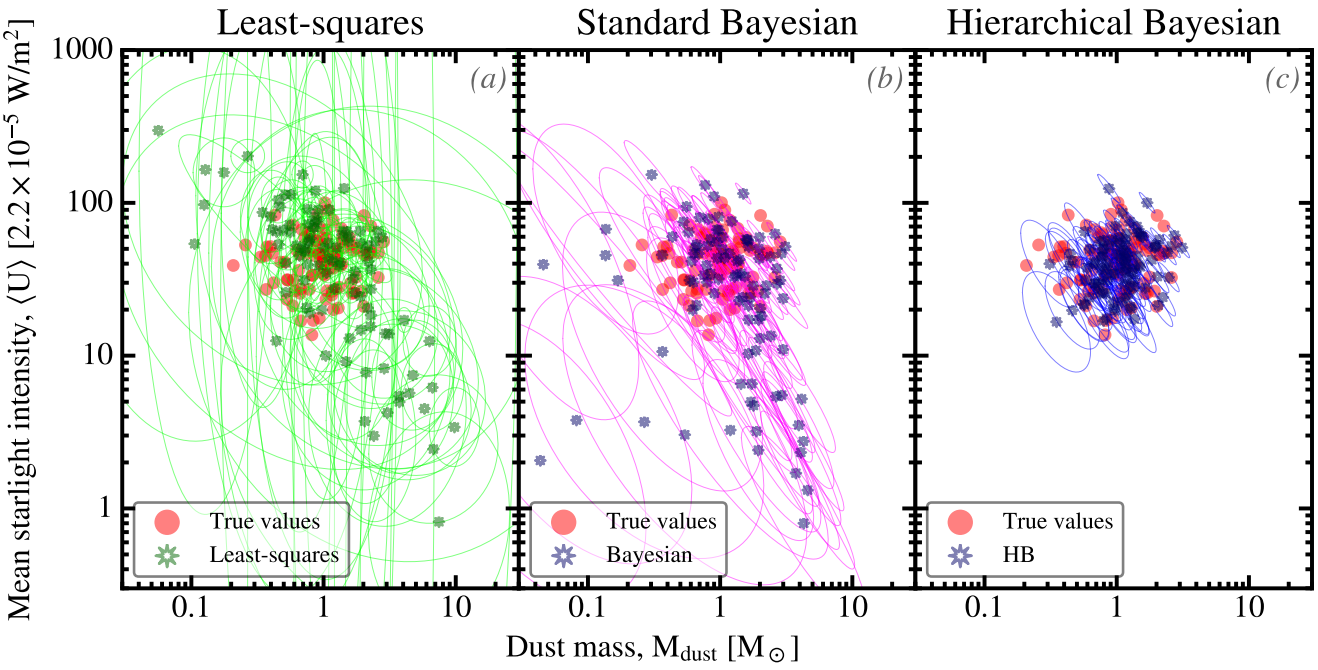

FIGURE V.19 – *Comparison of least-squares, standard Bayesian and HB methods.* Each panel shows the full simulation of Fig. V.19, fitted with three different methods. The true values are the red dots. They are identical in the three panels. We have 100 sources. We represent the same parameter space as in Fig. V.18. The ellipses represent the posterior of: *(a)* a least-squares fit; *(b)* the non-hierarchical Bayesian fit of Fig. V.18.a; and *(c)* the hierarchical Bayesian fit of Fig. V.18.c.

	HB	**True**
$\langle \ln M_{dust} \rangle$	0.053 ± 0.136	0
$\sigma(\ln M_{dust})$	0.477 ± 0.065	0.5
$\langle \ln \langle U \rangle \rangle$	3.64 ± 0.29	3.742
$\sigma(\ln \langle U \rangle)$	0.65 ± 0.20	0.4
$\rho(\ln M_{dust}, \ln \langle U \rangle)$	-0.088 ± 0.144	0

TABLE V.4 – *Inferred statistical properties of the HB model in Fig. V.19.c.* These quantities are the inferred moments of the source distribution.

The emissivity-index-temperature degeneracy of MBBs. We have just seen that HB methods are efficient at removing false correlations between inferred properties. We emphasize that HB methods do not systematically erase correlations if there is a true one between the parameters (*cf.* the tests performed in Sect. 5.1 of Galliano, 2018, with intrinsic positive and negative correlations). This potential can obviously be applied to the infamous β – T correlation discussed in Sect. III.1.2.1. This false correlation has been amply discussed by Shetty et al. (2009). Kelly et al. (2012) showed, for the first time, that HB methods could be used to solve the degeneracy. Fig. V.20 shows the results of Galliano (2018) on that matter. We can see that the false β – T negative correlation obtained with a least-squares fit (Fig. V.20.a) is completely eliminated with a HB method (Fig. V.20.b).

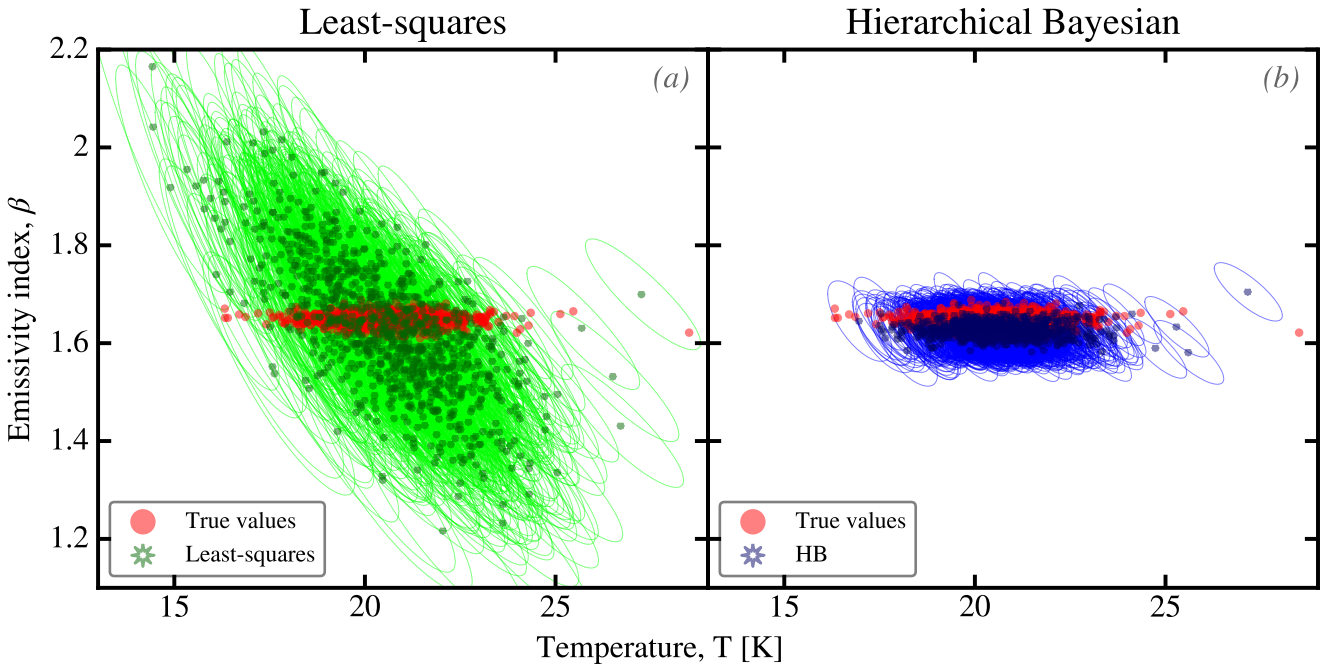

FIGURE V.20 – *Solving the emissivity-index-temperature degeneracy of MBBs with a HB model.* The red dots in both panels represent a MBB simulation of 1000 sources in the T – β plane (Galliano, 2018). Noise and calibration uncertainties have been added to the synthetic SEDs corresponding to these values. They have been fitted with: *(a)* a least-squares method, in green; and *(b)* a HB method, in blue. Licensed under CC BY-SA 4.0.

V.3.3.2 The Role of the Prior

We now further develop and illustrate the instrumental role of the hierarchical prior.

Linking the different sources. We have noted in Eq. (V.54) that the hierarchical prior was breaking the independency between the different sources in the sample, encountered in the non-hierarchical Bayesian case. This is because the properties of the prior (the hyperparameters) are inferred from the source distribution, and the properties of the individual sources are affected, in return, by this prior. This is illustrated in Fig. V.21. This figure shows the HB fits of three simulations, varying the median signal-to-noise ratio of the sample. We have represented a different parameter space, this time.

At high signal-to-noise (Fig. V.21.a), we see that the uncertainty of individual sources is significantly smaller than the scatter of their properties. The prior thus does not play an important role. This is a case where a non-hierarchical Bayesian fit would give very similar results.

At intermediate signal-to-noise (Fig. V.21.b), the brightest sources (on the right side) still have small uncertainties. However, most of the points now have uncertainties comparable to the sample scatter, because the posterior of each individual source starts to be dominated by the prior. We note that the maximum *a posteriori* (cyan stars) starts to cluster in the center.

At low signal-to-noise (Fig. V.21.c), the inferred values of $q_{\rm PAH}$ (green stars) are now almost similar for every source. We are in the case where the uncertainty on each individual source is so large that we can not recover their individual values. We can however give their most likely value, based on the distribution of the sample. This type of result has to be interpreted in a Bayesian way, to be consistent (*i.e.* performing tests on the MCMC). The fact that the inferred values of $q_{\rm PAH}$ all collapsed on a single point does not mean we would deduce that the points all have the same value. If we were performing some tests, we would realize that they are uncorrelated: if we were randomly drawing parameter values from the posterior, they would be scattered with a distribution similar to the true values. In a sense, we obtain here a result similar to stacking the sources, but in a smarter way, as some parameters are better constrained than others. For instance, in Fig. V.21.c, we see that we have only access to $\langle q_{\rm PAH}\rangle$ (y-axis), but we resolve the $\langle$U$\rangle$ of individual sources (x-axis).

☞ HB methods are useful when the parameter uncertainty of some sources is comparable to or larger than the scatter of this property over the whole sample.

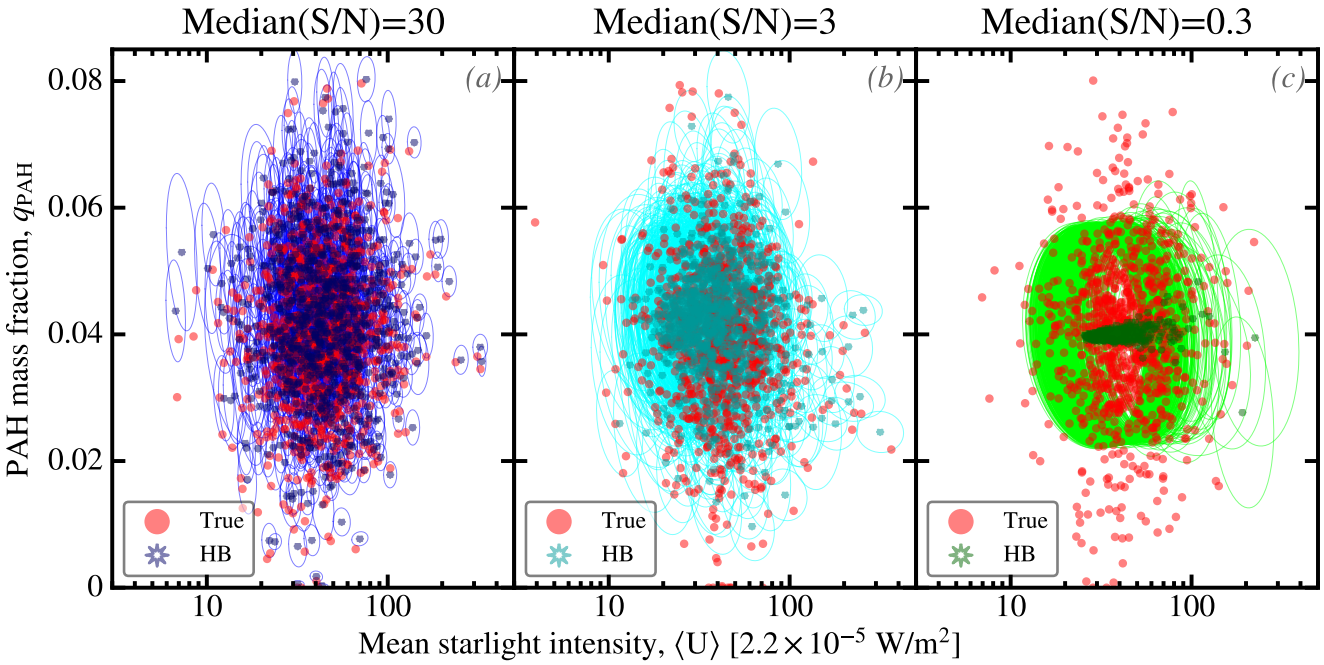

FIGURE V.21 – *Demonstration of the effect of the prior in a HB model.* The red dots in the different panels represent three simulations of 1000 sources, with similar physical properties, similar calibration uncertainties, but different signal-to-noise ratios (S/N). Each simulation has been fitted with our HB code (Galliano, 2018). We represent the marginalized posterior of the PAH mass fraction, $q_{\rm PAH}$, and mean starlight intensity, $\langle$U$\rangle$ (*cf.* Sect. III.1.2.2). Licensed under CC BY-SA 4.0.

Holistic prior. From a statistical point of view, it is always preferable to treat all the variables we are interested in as if they were drawn from the same multivariate distribution, however complex it might be. Stein (1956) showed that the usual estimator of the mean ($\sum_i X_i/N$) of a multivariate normal variable is inadmissible (for more than two variables), that is we could always find a more accurate one. In other words, if we were interested in analyzing together several variables, not necessarily correlated, such as the dust and stellar masses, it would always be more suitable to use estimators that combine all of them. This is known as *Stein's paradox*. Although Stein (1956)'s approach was frequentist, this is a general conclusion. From a Bayesian point of view, it means that we should put all the variables we are interested in analyzing, even if they are not SED model parameters, in the prior. In addition, if these external variables happen to be correlated with some SED model parameters, they will help refining their estimates. This is illustrated in Fig. V.22. We show in both panels a simulation

of the correlation between the dust mass, which is a SED model parameter, and the gas, which is not. When performing a regular HB fit, and plotting the correlation as a function of M_{gas}, we obtain the correlation in Fig. V.22.a. We see that the agreement with the true values breaks off at low mass (also the lowest signal-to-noise). If we now include M_{gas} in the prior [16], we obtain the correlation in Fig. V.22.b. It provides a much better agreement with the true values. This is because adding M_{gas} in the prior brought some extra information. The information provided by a non-dusty parameter helped refine the dust SED fit. For instance, imagine that you have no constraints on the dust mass of a source, but you know its gas mass. You could infer its dust mass by taking the mean dustiness of the rest of the sample. This *holistic* prior does that, in a smarter way, as it accounts for all the correlations in a statistically consistent way.

☞ The HB approach allows an optimal, holistic treatment of all the quantities of interest, even if they are not related to the dust.

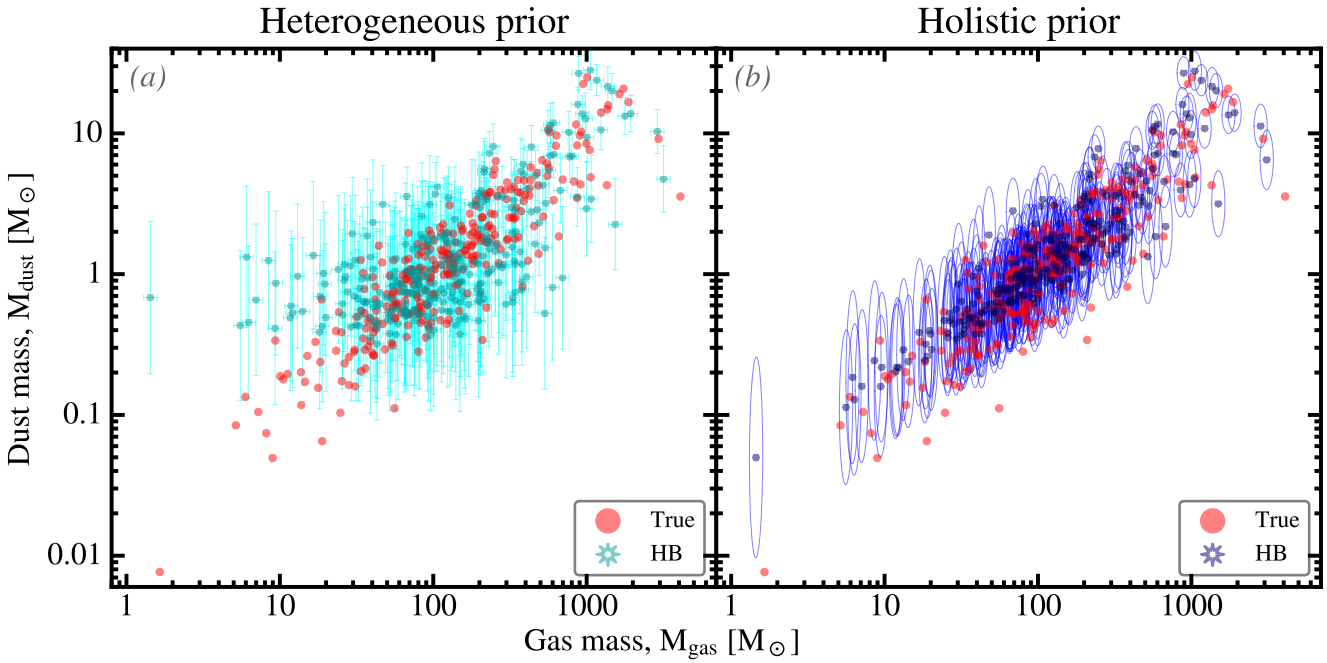

FIGURE V.22 – *The holistic approach: inclusion of external parameters into the prior.* Both panels represent the same simulation (red dots) of 300 sources, with physical properties typical of star-forming galaxies, including noise and calibration errors (Galliano, 2018). We have added a parameter that is external to our SED model, the gas mass, M_{gas}. In panel *(a)*, we show the HB inference of the dust mass as a function of the synthetic observations of the gas mass (cyan error bars). In panel *(b)*, we show the HB inference of the parameters when they are both in the prior (blue ellipses). Licensed under CC BY-SA 4.0.

V.3.3.3 Other Developments

SED modeling is far from the only possible application of HB methods. We briefly discuss below two other models we have developed.

Cosmic dust evolution. The dust evolution model we have discussed in Sect. IV.3 has been fitted to galaxies by Galliano et al. (2021), in a HB way. To be precise, we have used the output of `HerBIE`,

16. From a technical point of view, *including* an external parameter in the prior, such as M_{gas}, can be seen as adding an identity model component: $M_{gas} = f(M_{gas})$. Concretely, it means that, at each iteration, we sample M_{gas} from its uncertainty distribution, and the distribution of M_{gas} and its potential correlations with the other parameters inform the prior.

M_{dust}, M_{gas}, $M_\star$, SFR and metallicity, as observables. We then have modeled the SFH-related parameters in a HB way, and have assumed that the dust efficiencies were common to all galaxies (*i.e.* we inferred one single value for the whole sample). These *common* parameters were not in the hierarchical prior, because their value is the same for all galaxies. They were however sampled with the other parameters, in a consistent way. We were successful at recovering dust evolution timescales consistent with the MW at Solar metallicity (*cf.* Sect. IV.3.1.2). One important improvement would be to treat everything within the same HB model: *(i)* the SED; *(ii)* the stellar and gas parameters; and *(iii)* the dust evolution. This is something we plan to achieve in the near future.

MIR spectral decomposition. The type of MIR spectral decomposition that we have discussed in Sect. III.2.1.2 could also benefit from the HB approach. Although the model is mostly linear, there are a lot of degeneracies between the uncertainties of adjacent blended bands, such as the 7.6 and 7.8 µm features. In addition, plateaus and weak features are usually poorly constrained and their intensity can considerably bias the fit at low signal-to-noise. Hu et al. (*in prep.*) have developed such a HB MIR spectral decomposition tool. Its efficiency has been assessed on simulated data, and it is now being applied to M 82. This model will be valuable to analyze the spectra from the JWST.

Chapter VI

Conclusion and Prospective

We look at the present through a rear view mirror. We march backwards into the future.

(Marshall MCLUHAN; McLuhan, 1967)

Contents

VI.1 What Have We Learned About ISD in the Past Decade? . . . 268
VI.1.1 About Dust Properties . . . 268
Grain opacity. . . . 268
Scaling relations. . . . 268
Dust properties of low-metallicity systems. . . . 268
The Submillimeter excess. . . . 268
The AME. . . . 269
Stoichiometry and grain structure. . . . 269
Dust models. . . . 269
Polarization. . . . 269
Laboratory data. . . . 269
VI.1.2 About Dust Evolution . . . 269
Dust sources. . . . 269
Evolution of the Aromatic Feature Carriers. . . . 269
Thermal sputtering. . . . 270
Emissivity Variations in the ISM. . . . 270
Distant objects. . . . 270
VI.2 What Are the Open Questions for the Next Decade? . . . 270
VI.2.1 Extragalactic Dust . . . 270
Studies of diffuse dust in nearby galaxies. . . . 270
Quiescent low-metallicity galaxies. . . . 270
Circumgalactic dust. . . . 271
VI.2.2 Dust Evolution Modeling . . . 271
Local evolution modeling. . . . 271
Cosmic dust evolution models. . . . 271
VI.2.3 Dusty Epiphenomena . . . 271
Long-wavelength properties. . . . 271
DIBs. . . . 271
VI.2.4 The Need for a New FIR Observatory . . . 272
VI.2.5 The Public Image of Interstellar Dust . . . 272
VI.3 Current Future Projects . . . 272

VI.3.1 The *Modelosaur* Approach 272
VI.3.2 Out-of-the-Box Idea Bin 273

VI.1 What Have We Learned About ISD in the Past Decade?

We have seen in Sect. V.3.1 that ISD studies were particular because of the inherent complexity of the dust make-up and of the low weight of evidence provided by individual observables. This sometimes leads colleagues from other fields to think that our subject is messy and stalling. If we however integrate over a large number of studies, we can delineate some clear breakthroughs. I try the exercise of listing them here [1]. This is of course a subjective account of the progress, biased by my own interests. The observations acquired by *Herschel* and *Planck* played an instrumental role in these.

VI.1.1 About Dust Properties

Grain opacity. *Herschel* and *Planck* have brought invaluable information about the FIR and submm optical properties of dust grains, in the MW and nearby galaxies (*cf.* Sect. III.1.3.3). Before that, the commonly-used opacities were a factor of $\simeq 2-3$ lower, biasing the dust masses one would estimate. We still do not know the exact constitution of interstellar grains and its evolution, but we know relatively well the zero level FIR-submm opacity they should have in the diffuse ISM of the MW and a few nearby galaxies.

Scaling relations. The large number of galaxies observed by *Herschel* and the effort to build homogeneous ancillary data samples have provided consistent estimates of the dust, stellar and gaseous properties for a large number of objects, with spatial resolution in numerous cases (*cf.* Sects. IV.2 – IV.3). These relations provide snapshots of galaxy evolution at different stages. They are now well sampled over most of the parameter space (metallicity, gas fraction and specific star formation rate). They are the main benchmarks dust evolution models must account for. The most important ones and the information they convey are the following.

- The dustiness-metallicity relation exhibits two distinct regimes of dust production: *(i)* at very low metallicity, dominated by stardust; and *(ii)* at high metallicity, dominated by grain growth in the ISM.
- The dustiness-gas-fraction relation links the gas depletion timescale and the evolution probed by the dustiness-metallicity relation.
- Scaling relations linking the dust content to the diffuse X-ray emission are promising tools to constrain grain sputtering timescales.

Dust properties of low-metallicity systems. I have emphasized in Sect. IV.3 that low-metallicity systems (*i.e.* dwarf galaxies) were crucial to constrain dust evolution models, because they sample a different grain production regime than higher metallicity objects. *Herschel* has provided us with the first FIR SEDs of extremely low-metallicity galaxies that were decisive in understanding the early stages of dust evolution.

The Submillimeter excess. Twenty years after its discovery the submm excess is still a mysterious epiphenomenon (*cf.* Sect. III.2.2.1). In the last years: *(i)* several studies have hinted that it could be more prominent in diffuse regions of galaxies; and *(ii)* a new physical process that could explain its origin has been proposed (magnetic grains).

1. I have, with many others, contributed to the first 5 items of Sect. VI.1.1 and to the first 4 items of Sect. VI.1.2.

The AME. The AME has, for the first time, been detected in extragalactic systems (*cf.* Sect. III.2.2.2). To our humble opinion, the debate about its origin (PAHs or nanosilicates) is closed, in favor of PAHs.

Stoichiometry and grain structure. Important progress has been made constraining the grain structure and stoichiometry using X-ray edge absorption. The results are sometimes difficult to understand, such as the high crystalline fraction discussed in Sect. II.2.1.3. The technics are however promising and will revolutionize our understanding of the dust constitution, when ATHENA will be observing.

Dust models. A few dust models have been published in the last decade. The THEMIS model (*cf.* Sect. II.3.2.2) is, in our opinion, the most innovative for the following reasons.

- It is designed as an evolution model. Some fundamental properties of the constitution of the grain mixture (a-C(:H) hydrogenation, size distribution, mantle thickness) can be varied to account for different observables. This way, we have a few physically-grounded parameters to empirically explore the effects of dust evolution. It is an important progress over classic, static models.
- It is laboratory-data based.
- The model can be adapted to account for polarization constraints.
- It is the only recent model accounting for the 3.4 µm aliphatic feature.
- It is one of the only models to be consistent with the revised FIR-submm opacity that I have mentioned earlier.

Polarization. Whole-sky submm polarized emission maps have been produced by *Planck*, at several wavelengths (*cf.* Sect. II.2.2.2). On top of permitting unprecedented studies of the magnetic field, they provide evidence that the bulk of the large grain emission is homogeneous in size and composition.

Laboratory data. Long-wavelength (FIR-submm) measures of a diversity of dust analogues have been produced (*cf.* Sect. II.2.4.3). They provide the necessary data that, when consistently included in dust models, will help us to: *(i)* better constrain the evolution of grain mantles; and *(ii)* characterize more precisely the submm excess.

VI.1.2 About Dust Evolution

Dust sources. Our understanding of the dust production mechanisms has considerably progressed, thanks to *Herschel* (*cf.* Sects. IV.2 – IV.3).

The modeling of scaling relations, in particular the dustiness-metallicity relation, provides clear evidence that: *(i)* dust growth in the ISM is the prominent grain production regime around Solar metallicity; and *(ii)* condensation in SN II ejecta dominates at very low metallicity.

Observations of individual SNRs have shown that large amounts of dust could be produced shortly after SN II explosions. It suggests that a large fraction of these freshly-formed grains must be destroyed by the reverse shock.

Evolution of the Aromatic Feature Carriers. Before the 2010s, ISO and *Spitzer* were crucial to understand the variations of the strength of the UIBs (*cf.* Sect. III.2.1.1). In the 2010s, the detailed modeling of the FIR SED permitted by *Herschel*, allowed us to understand more finely how the *abundance* of the grains carrying these features evolves. To our mind, the important points are that: *(i)* their mass fraction is better correlated with metallicity than with the strength of the ISRF; and *(ii)* they are spatially associated with molecular clouds.

Thermal sputtering. ETGs, due to the paucity of their ISM, had been poorly studied before *Herschel*. We have now been able to characterize their dust content. It appears that these environments exhibit a dust deficit due to grain destruction in their permeating coronal gas. They are thus potentially interesting laboratories to constrain sputtering timescales (*cf.* Sect. IV.2.2.2).

Emissivity Variations in the ISM. The good coverage and sensitivity of *Herschel* and *Planck* allowed us to better characterize the way the FIR-submm emissivity evolves from the diffuse ISM to dense regions, in the MW and the Magellanic clouds (*cf.* Sect. IV.2). It is now clear that the increase of emissivity with ISM density, resulting from mantle accretion and grain coagulation, is a universal process.

Distant objects. The dust content of numerous galaxies at very high redshifts ($z > 6$) has been constrained, thanks to ALMA. It appears that dust-rich objects existed only a few 100 Myrs after reionization, requiring fast grain build-up. In our opinion, this can be explained with rapid dust growth in the ISM (*cf.* Sect. IV.3).

VI.2 What Are the Open Questions for the Next Decade?

I now try to delineate a few open questions that should occupy us during the next decade. The list below is as subjective as Sect. VI.1. This is not everything we *should* do, but rather everything we *will be able* to do, knowing the available observing facilities.

VI.2.1 Extragalactic Dust

Studies of diffuse dust in nearby galaxies. The diffuse ISM of the MW is the only medium used to constrain dust models, because it provides simultaneous information about extinction, emission and elemental depletions (*cf.* Sect. II.3). The combination of these different constraints is crucial to solve the degeneracies between emissivity and size distribution. This is why dust models are calibrated on these data, and why we do not yet have reliable dust models for the SMC, for instance. Such observations are however available, in a fragmented way, in external systems such as the Magellanic clouds and M 31. An effort should be made to produce an homogeneous data set of similar constraints in a few external galaxies and to build dust models using it. This implies several challenges.

- The extraction of the emission from the diffuse ISM is required to make sure we have homogeneous physical conditions and are not biased by the variation of the FIR opacity. The large beam of *Planck* renders this task difficult in external galaxies, but can be compensated by using other observations (*e.g.* *Herschel* and ground-based submm data).
- Additional observations are probably needed to cover the missing information. Facilities such as the *Multi Unit Spectroscopic Explorer* (MUSE; Bacon et al., 2010, for abundances) and ALMA (for the submm continuum) provide exceptional data that have not yet been utilized to their full potential in our field.

Having different extragalactic dust models would allow us to: *(i)* understand how the diffuse dust properties vary as a function of metallicity; and *(ii)* have a more robust way to study external galaxies, by using models that take into account the effect of cosmic dust evolution on the grain mixture.

Quiescent low-metallicity galaxies. I have emphasized several times the crucial role low-metallicity systems play in constraining dust evolution. These objects are however faint and we usually observe those which are actively star-forming. We therefore suffer from a selection effect that hides the nature of low-metallicity *quiescent* systems. I have given an example of what such systems could bring to our understanding of the evolution of MIR features in Fig. IV.22. The question is in which

quadrant of this figure they will fall? Obtaining JWST spectra of these objects would probably be a game changer.

Circumgalactic dust. Grains present in the immediate vicinity of galaxies, either in the infalling or outflowing gas, are currently poorly known. Yet, infall and outflow might be an important mechanism regulating the dustiness of galaxies. JWST and ALMA observations might be able to characterize circumgalactic grain properties beyond the nearby Universe, because of their resolving power. For local objects, NIKA2 is currently acquiring mm maps of infalls and outflows in nearby galaxies.

VI.2.2 Dust Evolution Modeling

Local evolution modeling. I have emphasized that a dust model such as THEMIS provides a unique framework to model SEDs, taking into account dust evolution. Its current limitation is however that we lack a quantitative link between the evolution parameters (a-C(:H) hydrogenation, size distribution and mantle thickness) and the environmental conditions (density and ISRF intensity). This can be achieved by empirically calibrating the tuning parameters of the evolution processes discussed in Sect. IV.2. The goal would be to have a reliable dust model predicting the constitution of the grain mixture as a function of $n_{\rm gas}$ and G_0.

Cosmic dust evolution models. The empirical modeling of cosmic dust evolution, that was the center of Sect. IV.3, calls for several improvements that could greatly change our understanding of the matter.

1. If we want to be able to precisely constrain the grain growth and SN II blast-wave destruction timescales, we need the most accurate possible stellar elemental and dust yields. This is an effort asked to the circumstellar community, both modelers and observers.
2. We need to adopt a more consistent approach between the different physical elements involved (dust, gas and stellar emissions and evolutions; *cf.* Sect. V.3.3.3).
3. When modeling SEDs at scales of several tens of parsecs or larger, we need to properly account for the mixing of physical conditions. This is currently done phenomenologically (*cf.* Sect. III.1.2.2). Ideally, we should move toward fitting models accounting for the statistical distribution of dust and stars, with a wide range of topologies, accounting for: *(i)* dust evolution in the ISM, as a function of $n_{\rm gas}$ and G_0, as I have mentioned earlier; and *(ii)* radiative transfer.

VI.2.3 Dusty Epiphenomena

Long-wavelength properties. The current submm-to-cm ground-based observatories (such as NIKA2, ALMA, *etc.*) open windows to progress on our understanding of the submm excess (*cf.* Sect. III.2.2.1) and of the AME (*cf.* Sect. III.2.2.2). By combining these new observations with archival *Spitzer*, AKARI and *Herschel* data, we should be able to systematically test the different possible scenarios. In addition, this analysis should be performed with dust models including state-of-the-art submm-mm laboratory opacities of interstellar grain analogues, in order to provide a reliable baseline.

DIBs. DIBs have been extensively observed with Gaia. Since we do not know their nature, unbiased exploration of how their properties vary with all available ISM tracers should be performed, in a big data way.

VI.2.4 The Need for a New FIR Observatory

I have illustrated all along this manuscript what modeling the IR SED of various regions can bring. In particular, the FIR regime is crucial to properly constrain the peak of the large equilibrium grain emission. This is the only way we can quantify the total dust mass and its excitation conditions. These quantities are necessary to interpret any other observables, such as the strength of the aromatic features, the submm excess, *etc.* We currently have good archival data for most nearby galaxies. We however lack: *(i)* continuous MIR-to-FIR spectroscopy to better constrain SED models and study the various solid-state features in emission and absorption; and *(ii)* deep observations of quiescent low-metallicity systems (*cf.* Sect. VI.2.1). After the cancellation of SPICA, our community should regroup around a new project.

VI.2.5 The Public Image of Interstellar Dust

On a *public relation* viewpoint, we should think about the way our field is represented.

Among colleagues, there is still a distinction between *the ISM* (*i.e.* the MW) and the ISM of other galaxies. This hierarchy between *intragalactic* and *extragalactic* ISM is becoming less and less justified. In addition, *interstellar media* (extragalactic ISM) provide unique constraints on ISM physics, as I have illustrated along this manuscript. The plural is justified, as they are characterized by different heating and cooling mechanisms, different grain formation processes, *etc.* We should motivate the new generation of astronomers to consider ISMology as a field where, depending on the studied physical process, we can use a galaxy or a Galactic region as a laboratory.

To the outside world, "*dust*" physics is not very appealing. What we do is important, but we need a better name. The US environmental protection agency defines *nanoparticles* as having sizes roughly between 1 and 100 nm. This is very close to the range of sizes of interstellar grains (*cf.* Sect. II.3.3.1). We could thus call our object of study *Cosmic NanoParticles* (CNP), when talking to the outside world, and keep talking about *dust* between us.

VI.3 Current Future Projects

I finish by listing the future projects I am currently considering working on. These are motivated by the challenges I have listed in Sect. VI.2.

VI.3.1 The *Modelosaur* Approach

It is more and more becoming a necessity to consistently model the different processes (dust, gas and stellar physics), in a large Bayesian framework. I plan to progressively include more physical processes in `HerBIE` to account for a wider diversity of observables:

1. the modeling of stellar evolution;
2. the consistency between SED modeling, and dust and chemical evolution;
3. the account of local dust evolution and of the systematic uncertainties of the model (depending on the developers of `THEMIS`);
4. radiative transfer grids of different dust-star topologies;
5. including the constraints from photoionization and photodissociation lines.

A first step will be the project ICED (IAS-CEA Evolution of Dust) that I have put together. It will consist in modeling the spatial distribution of the dust properties in nearby galaxies, to constrain local grain evolution. This will be done with the data from DustPedia, as well as from the NIKA2 guaranteed time project IMEGIN.

VI.3.2 Out-of-the-Box Idea Bin

- One way to solve the degeneracy between size distribution and emissivity is to observe a given dust mixture illuminated by a time-varying ISRF. This way, we can see the same grains exposed to two different fields, at two different times. This is possible with the light echo of SNe (*e.g.* Arendt et al., 2016), but very limited. Nearby Cepheids provide periodic variable sources, that modern observatories give us access to. I am currently working on a feasibility study of the observations of their echo with the JWST and ALMA.
- I currently have an intern working on the feasibility of using *Natural Language Processing* (NLP) methods, in collaboration with IRIS.AI, to tackle the origin of DIBs. NLP is a machine-learning method that, when trained on a large corpus of scientific articles, can be used to find relations between concepts, formulate new research directions, *etc.* It is aimed at dealing with information overload. The idea of the project is to see if we can automatically find clues in the chemistry and material science literature that could be relevant to DIBs.
- I am planning to use machine-learning to accelerate the interpolation of large model grids in `HerBIE`. Machine-learning, trained on hydrodynamical simulations, could also be useful to simulate realistic dust-star topologies (accounting for clustering, *etc.*), for which we would solve the radiative transfer. These grids would be SED model building blocks.

Appendix A

List of Acronyms

Education is what is left after you have forgotten all you have learned.

(Forgotten author)

Contents

A.1 General Acronyms 275
A.2 Telescope and Instrument Acronyms 277
A.3 Model and Project Acronyms 278
A.4 Denomination of the Main Spectral Windows 279

A.1 General Acronyms

Acronym	Expression
3D	*3-Dimensional*
ACF	*AutoCorrelation Function*
AGB	*Asymptotic Giant Branch* stars
AGN	*Active Galactic Nucleus*
AME	*Anomalous Microwave Emission*
BCD	*Blue Compact Dwarf Galaxies*
BEMBB	*Broken-Emissivity Modified Black Body*
BG	*Big Grain*
BH	*Black Hole*
CCD	*Charge-Coupled Device*
CDF	*Cumulative Distribution Function*
CGS	*Centimetre-Gram-Second*
CIB	*Cosmic Infrared Background*
CMB	*Cosmic Microwave Background*
CNP	*Cosmic NanoParticles*
CNM	*Cold Neutral Medium*
DCD	*Disordered Charge Distribution*
DDA	*Discrete Dipole Approximation*
DGL	*Diffuse Galactic Light*
DGS	*Dwarf Galaxy Sample*
DIB	*Diffuse Interstellar Bands*
DLA	*Damped Lyman-Alpha systems*

Acronym	Expression
EMT	*Effective Medium Theory*
ERE	*Extended Red Emission*
ETG	*Early-Type Galaxy*
eVSG	*evaporating Very Small Grains*
FIR	*Far-InfraRed*
FUV	*Far-UltraViolet*
FWHM	*Full Width at Half Maximum*
GEMS	*Glass with Embedded Metals and Sulfides*
GRB	*Gamma-Ray Burst*
HB	*Hierarchical Bayesian*
HDR	*Habilitation à Diriger des Recherches*
HIM	*Hot Ionized Medium*
ICM	*InterClump Medium*
IDP	*Interplanetary Dust Particles*
iid	*independent, identically distributed*
IMF	*Initial Mass Function*
IR	*InfraRed*
ISD	*InterStellar Dust*
ISM	*InterStellar Medium*
ISRF	*InterStellar Radiation Field*
ISS	*International Space Station*
LIRG	*Luminous InfraRed Galaxies*
LMC	*Large Magellanic Cloud*
LIMS	*Low- and Intermediate-Mass Stars*
LTG	*Late-Type Galaxy*
MBB	*Modified Black Body*
MCRT	*Monte-Carlo Radiative Transfer*
MCMC	*Markov Chain Monte-Carlo*
MIR	*Mid-InfraRed*
MKS	*Meter-Kilogram-Second*
MKSA	*Meter-Kilogram-Second-Ampere*
ML	*Machine-Learning*
MLE	*Maximum-Likelihood Estimation*
MS	*Main Sequence*
MW	*Milky Way*
NHST	*Null Hypothesis Significance Test*
NIR	*Near-InfraRed*
NLP	*Natural Language Processing*
NS	*Neutron Star*
NUV	*Near-UltraViolet*
OOP	*Out-Of-Plane*
PAH	*Polycyclic Aromatic Hydrocarbon*
PCA	*Principal Component Analysis*
PDF	*Probability Density Function*
PDR	*PhotoDissociation Regions*
PN	*Planetary Nebula*
ppb	*part per billion*
ppp	*posterior predictive p-value*
QSO	*Quasi-Stellar Object*
RAT	*Radiative Alignment Torques*

Acronym	Expression
SSC	*Super Star Cluster*
SED	*Spectral Energy Distribution*
SF	*Star Formation*
SFH	*Star Formation History*
SFR	*Star Formation Rate*
SI	*International System of units*
SLED	*Spectral Line Energy Distribution*
SMC	*Small Magellanic Cloud*
SN	*SuperNova*
SN Ia	*Type Ia SuperNova*
SN II	*Type II SuperNova*
SNR	*SuperNova Remnant*
sSFR	*specific Star Formation Rate*
SUE	*Skewed Uncertainty Ellipse*
TIR	*Total InfraRed*
TLS	*Two-Level System*
TPAGB	*Thermally-Pulsing Asymptotic Giant Branch*
TMA	*Too Many Acronyms*
UIB	*Unidentified Infrared Bands*
ULIRG	*UltraLuminous InfraRed Galaxies*
UV	*UltraViolet*
VCD	*Very Cold Dust*
VSG	*Very Small Grain*
YSO	*Young Stellar Object*
WD	*White Dwarf*
WIM	*Warm Ionized Medium*
WNM	*Warm Neutral Medium*
WR	*Wolf Rayet* star
ZAMS	*Zero-Age Main Sequence*

TABLE A.1 – *List of acronyms used throughout the manuscript.*

A.2 Telescope and Instrument Acronyms

Acronym	Telescope or Instrument
ALMA	*Atacama Large Millimeter/submillimeter Array*
APEX	*Atacama Pathfinder Experiment*
ATHENA	*Advanced Telescope for High ENergy Astrophysics*
BLAST	*Balloon-borne Large Aperture Submillimeter Telescope*
COBE	*COsmic Background Explorer*
CSO	*Caltech Submilleter Observatory*
DIRBE	*Diffuse Infrared Background Experiment*
DMR	*Differential Microwave Radiometer*
FIRAS	*Far-InfraRed Absolute Spectrophotometer*
FIS	*Far-Infrared Surveyor*
FUSE	*Far Ultraviolet Spectroscopic Explorer*
FTS	*Fourier Transform Spectrometer*
HFI	*High Frequency Instrument*
HIFI	*Heterodyne Instrument for the Far-Infrared*
HST	*Hubble Space Telescope*

Acronym	Telescope or Instrument
IRAC	*InfraRed Array Camera*
IRAM	*Institut de RadioAstronomie Millimétrique*
IRAS	*InfraRed Astronomical Satellite*
IRC	*InfraRed Camera*
IRS	*InfraRed Spectrograph*
IRTF	*InfraRed Telescope Facility*
ISO	*Infrared Space Observatory*
IUE	*International Ultraviolet Explorer*
JCMT	*James Clerk Maxwell Telescope*
JWST	*James Webb Space Telescope*
KAO	*Kuiper Airborne Observatory*
LFI	*Low Frequency Instrument*
MIPS	*Multiband Imaging Photometer for Spitzer*
MIRI	*Mid-InfraRed Instrument*
MUSE	*Multi Unit Spectroscopic Explorer*
NCT	*Nuclear Compton Telescope*
NIKA2	*New IRAM Kids Arrays*
NIRcam	*Near-InfraRed Camera*
NIRISS	*Near-InfraRed Imager and Slitless Spectrograph*
NIRspec	*Near-InfraRed Spectrograph*
OAO	*Orbiting Astronomical Observatory*
PACS	*Photodetector Array Camera and Spectrometer*
PILOT	*Polarized Instrument for the Long-wavelength Observation of the Tenuous ISM*
PRONAOS	*PROjet National pour l'Observation Submillimétrique*
SOFIA	*Stratospheric Observatory for Infrared Astronomy*
SPICA	*SPace Infrared telescope for Cosmology and Astrophysics*
SPIRE	*Spectral and Photometric Imaging REceiver*
UKIRT	*United Kingdom InfraRed Telescope*
VLT	*Very Large Telescope*
WIRO	*Wyoming InfraRed Observatory*
WISE	*Wide-field Infrared survey Explorer*
WMAP	*Wilkinson Microwave Anisotropy Probe*

TABLE A.2 – *List of instrumental acronyms used throughout the manuscript.*

A.3 Model and Project Acronyms

Acronym	Model Name
DGS	*Dwarf Galaxy Survey*
DustPedia	*A definitive study of dust in the local Universe*
HerBIE	*HiERarchical Bayesian Inference for dust Emission*
HERITAGE	*HERschel Inventory of The Agents of Galaxy Evolution*
SAGE	*Surveying the Agents of Galaxy Evolution*
THEMIS	*The Heterogeneous Evolution Model for Interstellar Solids*

TABLE A.3 – *List of model acronyms used throughout the manuscript.*

A.4 Denomination of the Main Spectral Windows

Table A.4 gives the acronyms and spectral ranges of the most important electromagnetic domains. For each domain, we give the interval in photon wavelength, frequency and energy. There are slight variations of these intervals across the literature. The physical phenomena listed in the right column are indicative of the typical most dominant emission at the scale of a galaxy. Fig. A.1 shows where these different domains fall on the SED of a nearby galaxy.

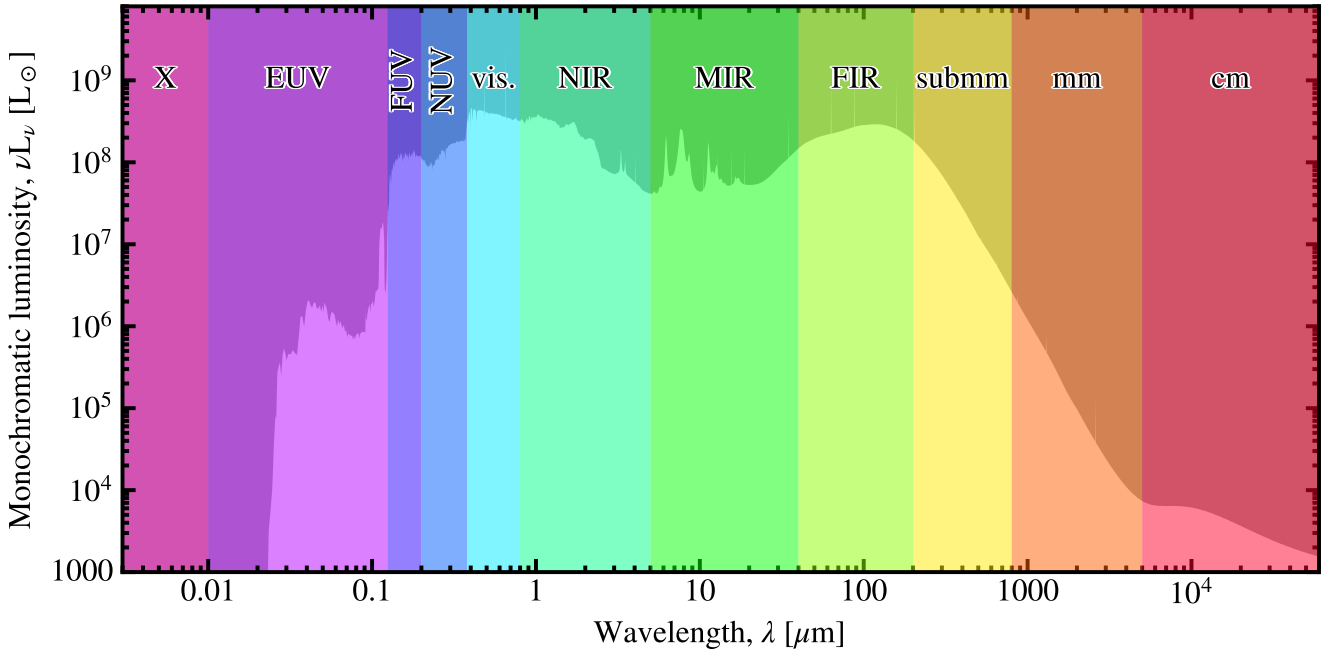

FIGURE A.1 – *Spectral domains represented over the SED of a nearby galaxy.* See Table A.4 for the acronyms. Licensed under CC BY-SA 4.0.

Abbreviation	Name	Spectral range Start	Spectral range End	Predominant physical origin
HIGH ENERGIES				
γ	γ rays	… … …	0.01 nm 30 EHz 0.12 GeV	Cosmic rays
X	X rays	0.01 nm 30 EHz 120 keV	10 nm 0.03 EHz 0.12 keV	Accretion disks & coronal plasmas
UV-VISIBLE				
EUV	Extreme-UV	10 nm 30 PHz 120 eV	124 nm 2.4 PHz 10 eV	Massive stars
FUV	Far-UltraViolet	124 nm 2.4 PHz 10 eV	200 nm 1.5 PHz 6.2 eV	Massive stars
NUV	Near-UV	200 nm 1.5 PHz 6.2 eV	380 nm 0.8 PHz 3.3 eV	Massive stars
vis.	Visible	0.38 µm 0.8 PHz 3.3 eV	0.8 µm 0.4 PHz 1.5 eV	Intermediate & low-mass stars
COLD UNIVERSE				
NIR	Near-InfraRed	0.8 µm 400 THz 1.5 eV	5µm 60 THz 0.25 eV	Circumstellar material
MIR	Mid-InfraRed	5 µm 60 THz 250 meV	40 µm 7.5 THz 30 meV	Aromatic features & hot dust
FIR	Far-InfraRed	40 µm 7.5 THz 30 meV	200 µm 1.5 THz 6 meV	Large ISM grains
submm	Submillimeter	200 µm 1.5 THz 6 meV	800 µm 0.4 THz 1.5 meV	Cold dust
RADIO/MICROWAVE				
mm	Millimeter	0.8 mm 400 GHz 1.5 meV	5 mm 60 GHz 0.25 meV	Cold dust & free-free
cm	Centimeter	0.5 cm 60 GHz 250 µeV	6 cm 5 GHz 20 µeV	Free-free & synchrotron

TABLE A.4 – *Denomination of the main spectral windows.*

Appendix B

Astronomers and Units

I hope all Americans will do everything in their power to introduce the French metrical system. (...) I look upon our English system as a wickedly, brain-destroying system of bondage under which we suffer. The reason why we continue to use it, is the imaginary difficulty of making a change.

(William THOMSON, Lord Kelvin; Thomson, 1889)

Contents

B.1 Brief History of Unit Systems 281
The necessity to unify disparate measures. 281
Measuring the Earth. 281
The introduction of the metric system. 282
Difficulty of adoption. 282
The international system. 282
B.2 Working with Units 282

B.1 Brief History of Unit Systems

The necessity to unify disparate measures. During Antiquity and the Middle Age, measures of weight, length and duration were varying from one place to another. The first government in History to try and homogenize measures was under king Henri III, in England. The 1297 version of the *Magna Carta* (originally signed in 1215), expressed the will to define standards for measuring weights and distances. "*Article 25. One measure of Wine shall be through our Realm, and one measure of Ale, and one measure of Corn, that is to say, the Quarter of London; and one breadth of dyed Cloth, Russets, and Haberjects, that is to say, two Yards within the lists. And it shall be of Weights as it is of Measures.*" The rest of the world kept using different yards and pounds, for several centuries.

Measuring the Earth. In France, the *Académie royale des sciences* was funded in 1666 by Jean-Baptiste COLBERT, under king Louis XIV, influenced by his secretary for sciences and arts, Charles PERRAULT (Débarbat & Quinn, 2019). In 1667, the royal observatory was created and astronomers were tasked with providing more accurate maps of the realm. Clergyman Jean PICARD performed a series of measures by triangulation, with a unique measuring board, and estimated the size of the Earth (Mesure de la Terre, 1671). During the XVIIIth century, several scientific expeditions in Latin America or the North Pole (by La Condamine, Maupertuis, *et al.*) refined the measurement of the size of the Earth and confirmed its flattening around the poles.

The introduction of the metric system. It is only during the French revolution (1789–1799) that the metric system was introduced. It was consistent with its time. It was aimed at erasing differences in an abstract way, with new standards independent of the old human references (foot, inch, *etc.*). One of its important features was that it was a decimal system, simplifying calculations. It can be traced back to the months before the revolution, in 1789. The *cahiers de doléances* (register of grievances) expressed the wish to have unified measures throughout the realm. In 1790, Charles-Maurice DE TALLEYRAND-PÉRIGORD, a bishop elected at the recent national assembly, submitted a memoir to adopt a new system of weights and measures, contributed by Marie-Jean-Antoine CRITAT DE CONDORCET and Joseph-Jérôme LEFRANÇOIS DE LALANDE (Débarbat & Quinn, 2019). In 1792, Jean-Baptiste DELAMBRE and Pierre-François MÉCHAIN were charged with measuring the length of the meridian between Dunkerque and Barcelona (Alder, 2015). The definition of the meter was then 1/10 000 000 of the distance between the North Pole and the equator. The kilogram was defined as the mass of one cubic decimeter of water.

Difficulty of adoption. The metric system was not adopted right away, even in France. It was mocked by Napoléon, although Laplace promoted the advantage of its decimal system to him. For a while, we kept "*mesure usuelles*", which were a standardization of imperial units. In Germany, around 1830, Carl-Friedrich GAUSS formalized the metric unit system in physics, and proposed to add the seconds to meters and kilograms, leading to the *CGS system* (Centimetre-Gram-Second). During the 1851 World's fair in London, France promoted the metric system to the world. It led to the "*Treaty of the Metre*", signed in Paris in 1875, by seventeen countries adopting the metric system. Great Britain, the Netherlands and Portugal were opposed. England, in particular, felt that adopting the French system would be a political defeat. A diplomatic solution was proposed in adopting the Greenwich meridian, during the 1883 Geodetic Congress: "*The Conference hopes that, if the whole world is agreed upon the unification of longitudes and hours in accepting the Greenwich meridian as the point of departure, Great Britain will find in this fact an additional motive to take on her side new steps in favour of the unification of weights and measures, by joining the Metrical Convention of May 20, 1875*" (The Geodetic Congress, 1883). The Greenwich meridian was finally adopted during the 1884 International Meridian Conference, but England did not adopt the metric system...

The international system. Since 1960, the *International System of units* (SI) is the *Meter-Kilogram-Second-Ampere system* (MKSA or MKS). Astronomers are one of the last communities to use CGS units (and the Gaussian system for electrodynamics; Table B.4). The continued use of a mix between imperial units and the CGS system is counterproductive. The most dramatic example is the crash of the 1999 *Mars Climate Observer* probe, because of a conversion mistake between imperial and metric units (Popular Mechanics, 2017). Table B.1 gives the correspondence between the MKS and CGS systems, and Tables B.2 – B.3 list the fundamental constants in both systems. Table B.4 compares the MKSA and Gaussian systems for electrodynamics.

B.2 Working with Units

My personal experience in working with units led me to the following advices.

Adopt specific units for each problem, so that the quantities one have to deal with are close to unity (in orders of magnitude). This is particularly important to avoid numerical problems. In ISMology, the µm is a good wavelength unit, and the cm^{-3} a good density unit, and the pc a good distance unit.

Deciding which quantity should be logarithmic must be based on the way the uncertainty on this quantity has been estimated. The conversion between linear and logarithmic quantities indeed is not straightforward. Keeping the same 1σ range is a good practice, but it is not rigorously

Quantity	International units (MKS)		Astronomer's units (CGS)	
		General		
Length	1	m (meter)	10^2	cm (centimeter)
Force	1	N (Newton)	10^5	dyn (dynes)
Energy	1	J (joule)	10^7	erg
Power	1	W (watt)	10^7	erg/s
Flux (1 Jansky)	10^{-26}	W/m^2/Hz	10^{-23}	erg/s/cm^2/Hz
		Electromagnetism		
Charge	1	C (Coulomb)	$2.997\,924\,58 \times 10^9$	esu (electrostatic unit)
Current	1	A (Ampere)	$2.997\,924\,58 \times 10^9$	esu/s
Electric potential	1	V (volt)	$1/299.792\,458$	statV (statvolt)
Electric field	1	V/m	$1/299\,79.245\,8$	statV/cm
Magnetic field	1	T (Tesla)	10^4	G (Gauss)
Magnetic flux	1	Wb (Weber)	10^8	G.cm^2
Auxiliary field H	1	A/m	$4\pi \times 10^{-3}$	Oe (Oersted)
		Angular distance		
1 arcsec	4.848×10^{-6}	rad		
1 arcsec at 1 Mpc	4.848	pc		

Table B.1 – *Unit conversion.*

equivalent:

$$\log X \pm \sigma_{\log X} \quad \Leftrightarrow \quad X^{+(10^{\sigma_{\log X}}-1)X}_{-(1-10^{-\sigma_{\log X}})X}. \tag{B.1}$$

The underlying probability law is different in both cases. It is preferable to choose a representation of the quantity so that its uncertainty is the closest to a normal law. If we are estimating the uncertainty on a parameter, the dynamical range is important. If a quantity varies by more than one order of magnitude, it is often a good choice to treat the logarithm of this quantity in a Bayesian model. Concerning fluxes, the magnitude system is logarithmic, but it is not a decimal system (it uses a cumbersome 2.5 factor), and it relies on arbitrary zero-point fluxes (*cf.* Table B.5). The only useful formula concerning magnitudes is to get out of them:

$$F_\nu(\lambda_0) = F_{\nu,0} \times 10^{-0.4 m(\lambda_0)}. \tag{B.2}$$

Perform conversions through the SI, and avoid CGS units, which are are already deprecated outside astronomy. CGS are indeed boomer units, so is the Gaussian unit system in electrodynamics. In terms of computing, it is important to have a reliable conversion module in the different programming languages that one uses, to avoid stupid mistakes.

Quantity	International units (MKS)		Astronomer's units (CGS)	
		UNIVERSAL		
Light speed, c	$2.999\,792\,458 \times 10^{8}$	m/s	$2.999\,792\,458 \times 10^{10}$	cm/s
Newton constant, $\mathcal{G}$	$6.674\,28 \times 10^{-11}$	$m^3/kg/s^2$	$6.674\,28 \times 10^{-8}$	$cm^3/g/s^2$
Planck constant, h	$6.626\,068\,96 \times 10^{-34}$	J.s	$6.626\,068\,96 \times 10^{-27}$	erg.s
$\hbar \equiv h/2\pi$	$1.054\,571\,628 \times 10^{-34}$	J.s	$1.054\,571\,628 \times 10^{-27}$	erg.s
Magnetic constant, $\mu_0 \equiv 4\pi \times 10^{-7}$	$1.256\,637\,061\,4 \times 10^{-6}$	N/A^2		
Electric constant, $\epsilon_0 \equiv 1/\mu_0 c^2$	$8.854\,187\,817 \times 10^{-12}$	F/m		
Elementary charge, e	$1.602\,176\,487 \times 10^{-19}$	C	$4.806\,529\,5 \times 10^{-10}$	esu
		ATOMIC		
Electron mass, m_e	$9.109\,382\,15 \times 10^{-31}$	kg	$9.109\,382\,15 \times 10^{-28}$	g
$m_e c^2$	$8.187\,104\,38 \times 10^{-14}$	J	$8.187\,104\,38 \times 10^{-7}$	erg
$m_e c^2/e$	0.510 998 910	MeV		
Proton mass, m_p	$1.672\,621\,637 \times 10^{-27}$	kg	$1.672\,621\,637 \times 10^{-24}$	g
$m_p c^2$	$1.503\,277\,359 \times 10^{-10}$	J	$1.503\,277\,359 \times 10^{-3}$	erg
$m_p c^2/e$	0.938 272 013	GeV		
Rydberg, $R_\infty \equiv \alpha^2 m_e c/2h$	10 973 731.568 527	m^{-1}	109 737.315 685 27	cm^{-1}
$R_\infty c$	$3.289\,841\,960\,361 \times 10^{15}$	Hz		
$R_\infty hc$	$2.179\,871\,97 \times 10^{-18}$	J	$2.179\,871\,97 \times 10^{-11}$	erg
$R_\infty hc/e$	13.605 691 93	eV		
		MACROSCOPIC		
Boltzmann constant, k	$1.380\,650\,4 \times 10^{-23}$	J/K	$1.380\,650\,4 \times 10^{-16}$	erg/K
k/e	$8.617\,343 \times 10^{-5}$	eV/K		
k/eh	$69.503\,56 \times 10^{10}$	Hz/K		
Atomic mass unit, $m_u \equiv m(^{12}C)/12$	$1.660\,538\,782 \times 10^{-27}$	kg	$1.660\,538\,782 \times 10^{-24}$	g
Avogadro number, $\mathcal{N}_A$	$6.022\,141\,79 \times 10^{23}$	mol^{-1}		
Molar gas constant, $R \equiv k\mathcal{N}_A$	8.314 472	J/mol/K	$8.314\,472 \times 10^{7}$	erg/mol/K

TABLE B.2 – *Fundamental constants.*

Quantity	International units (MKS)		Astronomer's units (CGS)	
	GENERAL			
Astronomical unit, a.u. $\equiv \langle \odot - \oplus \rangle$	$1.495\,979 \times 10^{11}$	m	$1.495\,979 \times 10^{13}$	cm
Parsec, pc $\equiv 1$ a.u./$1''$	$3.085\,678 \times 10^{16}$	m	$3.085\,678 \times 10^{18}$	cm
	SOLAR SYSTEM			
Solar radius, $R_\odot$	$6.959\,9 \times 10^{8}$	m	$6.959\,9 \times 10^{10}$	cm
Solar mass, $M_\odot$	$1.988\,9 \times 10^{30}$	kg	$1.988\,9 \times 10^{33}$	g
Solar luminosity, $L_\odot$	3.846×10^{26}	W	3.846×10^{33}	erg/s
Earth radius, $R_\oplus$	$6.378\,140 \times 10^{6}$	m	$6.378\,140 \times 10^{8}$	cm
Earth mass, $M_\oplus$	5.974×10^{24}	kg	5.974×10^{27}	g
	GALAXY			
Solar velocity around G.C., $\Theta_\circ$	220	km/s		
Distance sun-G.C., $R_\circ$	8.0	kpc		
Local disk density, ρ_{disk} n_{disk}	$3 - 12 \times 10^{-21}$ $1 - 5 \times 10^{6}$	kg/m^3 m^{-3}	$3 - 12 \times 10^{-24}$ $1 - 5$	g/cm^3 cm^{-3}
Local halo density, ρ_{halo} n_{halo}	$2 - 13 \times 10^{-22}$ $10 - 60 \times 10^{4}$	kg/m^3 m^{-3}	$2 - 13 \times 10^{-25}$ $0.1 - 0.6$	g/cm^3 cm^{-3}
	COSMOLOGY			
Hubble expansion rate, H_0	71	km/s/Mpc		
Critical density, $\rho_c \equiv 3H_0^2/8\pi\mathcal{G}$	$1.399\,062 \times 10^{11}$	$M_\odot$/Mpc^3	9.472×10^{-30}	g/cm^3
Pressureless matter density, $\Omega_M \equiv \rho_M/\rho_c$	$0.15 \lesssim \Omega_M \lesssim 0.45$			
Baryon density, $\Omega_B \equiv \rho_B/\rho_c$	$0.019 \lesssim \Omega_B \lesssim 0.046$			
Cosmological constant, $\Omega_\Lambda \equiv \Lambda_c^2/3H_0^2$	$0.6 \lesssim \Omega_\Lambda \lesssim 0.8$			

TABLE B.3 – *Astronomical constants.*

Quantity	Rationalized MKSA	Gaussian units
Lorentz Force	$\vec{F} = q\left(\vec{E} + \vec{v} \wedge \vec{B}\right)$ $\frac{d\vec{F}}{dV} = \rho\vec{E} + \vec{j} \wedge \vec{B}$	$\vec{F} = q\left(\vec{E} + \frac{\vec{v}}{c} \wedge \vec{B}\right)$ $\frac{d\vec{F}}{dV} = \rho\vec{E} + \frac{\vec{j}}{c} \wedge \vec{B}$
Dielectric Constant & Permeability	$\epsilon_0 = \frac{10^7}{4\pi c^2} \quad \mu_0 = 4\pi 10^{-7}$	$\epsilon_0 = 1 \quad \mu_0 = 1$
Displacement & Magnetic Field	$\vec{D} = \epsilon\vec{E} + \vec{P}$ $\vec{H} = \frac{\vec{B}}{\mu} - \vec{M}$	$\vec{D} = \epsilon\vec{E} + 4\pi\vec{P}$ $\vec{H} = \frac{\vec{B}}{\mu} - 4\pi\vec{M}$
Maxwell Equations	$\vec{\nabla}.\vec{D} = \rho$ $\vec{\nabla} \wedge \vec{H} = \vec{j} + \frac{\partial\vec{D}}{\partial t}$ $\vec{\nabla} \wedge \vec{E} + \frac{\partial\vec{B}}{\partial t} = \vec{0}$ $\vec{\nabla}.\vec{B} = 0$	$\vec{\nabla}.\vec{D} = 4\pi\rho$ $\vec{\nabla} \wedge \vec{H} = \frac{4\pi}{c}\vec{j} + \frac{1}{c}\frac{\partial\vec{D}}{\partial t}$ $\vec{\nabla} \wedge \vec{E} + \frac{1}{c}\frac{\partial\vec{B}}{\partial t} = \vec{0}$ $\vec{\nabla}.\vec{B} = 0$
Poynting Vector	$\vec{\mathscr{P}} = \vec{E} \wedge \vec{H}$	$\vec{\mathscr{P}} = \frac{c}{4\pi}\vec{E} \wedge \vec{H}$
Electromagnetic Power	$P = \iint_S \vec{\mathscr{P}}.d\vec{S}$	$P = \iint_S \vec{\mathscr{P}}.d\vec{S}$
Energy Density	$U = \frac{1}{2}\left(\epsilon\vec{E}^2 + \frac{\vec{B}^2}{\mu}\right)$	$U = \frac{1}{8\pi}\left(\epsilon\vec{E}^2 + \frac{\vec{B}^2}{\mu}\right)$

TABLE B.4 – *Classical electrodynamics.*

	Central wavelength, λ_0	Zero-point flux, $F_{\nu,0}$
U	0.36 µm	1884 Jy
B	0.44 µm	4646 Jy
V	0.55 µm	3953 Jy
R	0.66 µm	2875 Jy
I	0.80 µm	2241 Jy
J	1.25 µm	1602 Jy
H	1.60 µm	1010 Jy
K	2.18 µm	630 Jy
L	3.45 µm	278 Jy
M	4.75 µm	153 Jy
N	10.6 µm	36.3 Jy

TABLE B.5 – *The magnitude system.*

Appendix C

Useful Formulae

There is no royal road to science, and only those who do not dread the fatiguing climb of its steep paths have a chance of gaining its luminous summits.

(Karl MARX; Marx, 1872)

Contents

C.1 3D Quantities and Volume Integrals . . . 290
C.1.1 Differential Operators . . . 290
C.1.1.1 Gradient . . . 290
C.1.1.2 Laplacian . . . 291
C.1.1.3 Divergence . . . 291
C.1.1.4 Curl . . . 291
C.1.2 Vectorial Analysis . . . 291
C.1.3 Integral Theorems . . . 292
C.1.4 Dust Heating and Cooling: Two Ways of Slicing the Pis . . . 292
C.1.4.1 Solution 1 . . . 293
C.1.4.2 Solution 2 . . . 293
C.2 Statistics . . . 293
C.2.1 General Formulae . . . 293
C.2.1.1 Moments of a PDF . . . 293
Definitions. . . . 293
Estimators. . . . 294
C.2.1.2 Marginalization . . . 294
C.2.1.3 Variable Change . . . 294
C.2.1.4 Combining Uncertainties . . . 294
Rant about systematics. . . . 295
C.2.2 Useful Probability Distributions . . . 295
C.2.2.1 Binomial Distribution . . . 295
C.2.2.2 Poisson Distribution . . . 295
C.2.2.3 Gaussian Distribution . . . 295
Multivariate form. . . . 295
Error function. . . . 296
C.2.2.4 Student's *t* Distribution . . . 296
C.2.2.5 Split-Normal Distribution . . . 296
C.2.2.6 Lorentzian Distribution . . . 296
C.2.3 Drawing random variables from an arbitrary distribution . . . 296

C.2.3.1 The Rejection Method . . . 296
C.2.3.2 Inverting the CDF . . . 297
C.3 Trigonometry . . . 297
C.3.1 Transformations . . . 298
C.3.1.1 Rotations . . . 298
C.3.1.2 Relations Between Functions . . . 298
C.3.2 Addition . . . 298
C.3.2.1 Summing Angles . . . 298
C.3.2.2 Inverse Relations . . . 298
C.3.3 Linearization . . . 298
C.3.3.1 Squares and Cubes . . . 298
C.3.3.2 Inverse Relations . . . 299

This appendix contains various unrelated formulae that I find useful in my daily practice, but that I do not necessarily remember. The problem is that gathering them here suppresses any incentive to memorize them, therefore making it essential to have them written here.

C.1 3D Quantities and Volume Integrals

C.1.1 Differential Operators

The three most common coordinate systems are represented in Fig. C.1. In what follows, we express the differential operators in these systems.

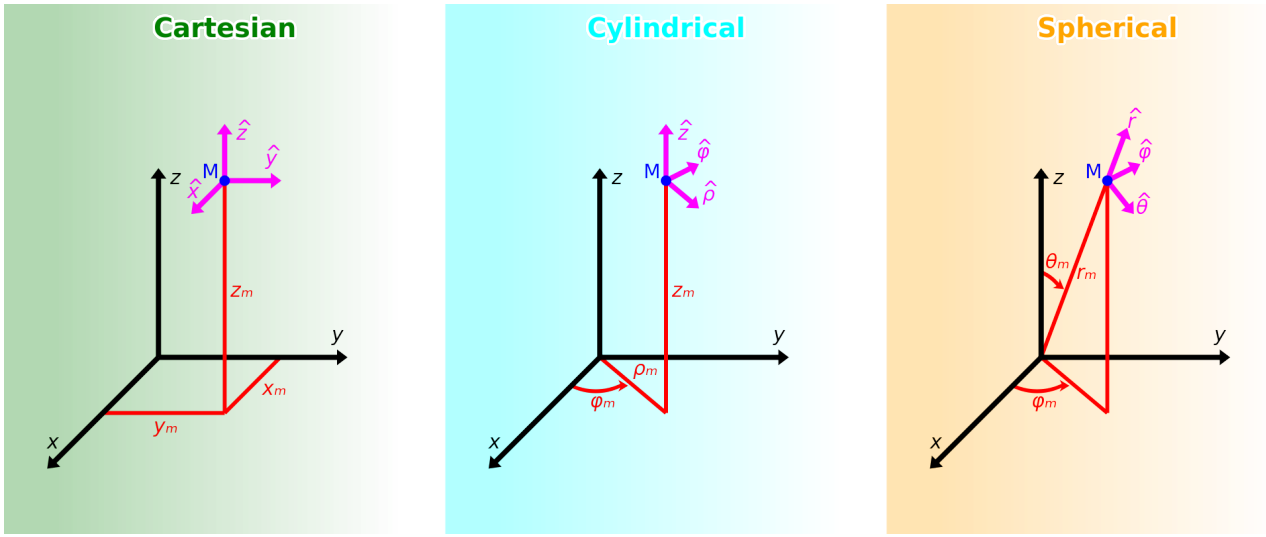

$dV = dx.dy.dz$ $dV = d\rho.d\phi.dz$ $dV = dr.d\phi.d\cos\theta$

FIGURE C.1 – *Most common coordinate systems.* Licensed under CC BY-SA 4.0.

C.1.1.1 Gradient

Cartesian: $\vec{\nabla} U = \frac{\partial U}{\partial x}\hat{x} + \frac{\partial U}{\partial y}\hat{y} + \frac{\partial U}{\partial z}\hat{z}.$

Cylindrical: $\vec{\nabla} U = \frac{\partial U}{\partial \rho}\hat{\rho} + \frac{1}{\rho}\frac{\partial U}{\partial \phi}\hat{\phi} + \frac{\partial U}{\partial z}\hat{z}.$

Spherical: $\vec{\nabla} U = \frac{\partial U}{\partial r}\hat{r} + \frac{1}{r}\frac{\partial U}{\partial \theta}\hat{\theta} + \frac{1}{r\sin\theta}\frac{\partial U}{\partial \phi}\hat{\phi}.$

C.1.1.2 Laplacian

Cartesian: $\vec{\nabla}^2 U = \dfrac{\partial^2 U}{\partial x^2} + \dfrac{\partial^2 U}{\partial y^2} + \dfrac{\partial^2 U}{\partial z^2}.$

Cylindrical: $\vec{\nabla}^2 U = \dfrac{1}{\rho}\dfrac{\partial}{\partial \rho}\left(\rho \dfrac{\partial U}{\partial \rho}\right) + \dfrac{1}{\rho^2}\dfrac{\partial^2 U}{\partial \phi^2} + \dfrac{\partial^2 U}{\partial z^2}.$

Spherical: $\vec{\nabla}^2 U = \dfrac{1}{r}\dfrac{\partial^2}{\partial r^2}(rU) + \dfrac{1}{r^2 \sin\theta}\dfrac{\partial}{\partial \theta}\left(\sin\theta \dfrac{\partial U}{\partial \theta}\right) + \dfrac{1}{r^2 \sin^2\theta}\dfrac{\partial^2 U}{\partial \phi^2}.$

C.1.1.3 Divergence

Cartesian: $\vec{\nabla}.\vec{A} = \dfrac{\partial A_x}{\partial x} + \dfrac{\partial A_y}{\partial y} + \dfrac{\partial A_z}{\partial z}.$

Cylindrical: $\vec{\nabla}.\vec{A} = \dfrac{1}{\rho}\dfrac{\partial}{\partial \rho}(\rho A_\rho) + \dfrac{1}{\rho}\dfrac{\partial A_\phi}{\partial \phi} + \dfrac{\partial A_z}{\partial z}.$

Spherical: $\vec{\nabla}.\vec{A} = \dfrac{1}{r^2}\dfrac{\partial}{\partial r}(r^2 A_r) + \dfrac{1}{r\sin\theta}\dfrac{\partial}{\partial \theta}(\sin\theta A_\theta) + \dfrac{1}{r\sin\theta}\dfrac{\partial A_\phi}{\partial \phi}.$

C.1.1.4 Curl

Cartesian: $\vec{\nabla} \wedge \vec{A} = \left(\dfrac{\partial A_z}{\partial y} - \dfrac{\partial A_y}{\partial z}\right)\hat{x} + \left(\dfrac{\partial A_x}{\partial z} - \dfrac{\partial A_z}{\partial x}\right)\hat{y} + \left(\dfrac{\partial A_y}{\partial x} - \dfrac{\partial A_x}{\partial y}\right)\hat{z}.$

Cylindrical: $\vec{\nabla} \wedge \vec{A} = \left(\dfrac{1}{\rho}\dfrac{\partial A_z}{\partial \phi} - \dfrac{\partial A_\phi}{\partial z}\right)\hat{\rho} + \left(\dfrac{\partial A_\rho}{\partial z} - \dfrac{\partial A_z}{\partial \rho}\right)\hat{\phi} + \dfrac{1}{\rho}\left(\dfrac{\partial \rho A_\phi}{\partial \rho} - \dfrac{\partial A_\rho}{\partial \phi}\right)\hat{z}.$

Spherical: $\vec{\nabla} \wedge \vec{A} = \dfrac{1}{r\sin\theta}\left(\dfrac{\partial \sin\theta A_\phi}{\partial \theta} - \dfrac{\partial A_\theta}{\partial \phi}\right)\hat{r} + \dfrac{1}{r\sin\theta}\left(\dfrac{\partial A_r}{\partial \phi} - \sin\theta \dfrac{\partial r A_\phi}{\partial r}\right)\hat{\theta} + \dfrac{1}{r}\left(\dfrac{\partial r A_\theta}{\partial r} - \dfrac{\partial A_r}{\partial \theta}\right)\hat{\phi}.$

C.1.2 Vectorial Analysis

$$\vec{A}.\left(\vec{B} \wedge \vec{C}\right) = \vec{B}.\left(\vec{C} \wedge \vec{A}\right) = \vec{C}.\left(\vec{A} \wedge \vec{B}\right) \tag{C.1}$$

$$\vec{A} \wedge \left(\vec{B} \wedge \vec{C}\right) = \left(\vec{A}.\vec{C}\right)\vec{B} - \left(\vec{A}.\vec{B}\right)\vec{C} \tag{C.2}$$

$$\left(\vec{A} \wedge \vec{B}\right).\left(\vec{C} \wedge \vec{D}\right) = \left(\vec{A}.\vec{C}\right)\left(\vec{B}.\vec{D}\right) - \left(\vec{A}.\vec{D}\right)\left(\vec{B}.\vec{C}\right) \tag{C.3}$$

$$\vec{\nabla} \wedge \vec{\nabla}\psi = \vec{0} \tag{C.4}$$

$$\vec{\nabla}.\left(\vec{\nabla} \wedge \vec{A}\right) = 0 \tag{C.5}$$

$$\vec{\nabla} \wedge \left(\vec{\nabla} \wedge \vec{A}\right) = \vec{\nabla}\left(\vec{\nabla}.\vec{A}\right) - \vec{\nabla}^2\vec{A} \tag{C.6}$$

$$\vec{\nabla}.\left(\psi\vec{A}\right) = \vec{A}.\vec{\nabla}\psi + \psi\vec{\nabla}.\vec{A} \tag{C.7}$$

$$\vec{\nabla} \wedge \left(\psi\vec{A}\right) = \vec{\nabla}\psi \wedge \vec{A} + \psi\vec{\nabla} \wedge \vec{A} \tag{C.8}$$

$$\vec{\nabla}\left(\vec{A}.\vec{B}\right) = \left(\vec{A}.\vec{\nabla}\right)\vec{B} + \left(\vec{B}.\vec{\nabla}\right)\vec{A} + \vec{A} \wedge \left(\vec{\nabla} \wedge \vec{B}\right) + \vec{B} \wedge \left(\vec{\nabla} \wedge \vec{A}\right) \tag{C.9}$$

$$\vec{\nabla}.\left(\vec{A} \wedge \vec{B}\right) = \vec{B}.\left(\vec{\nabla} \wedge \vec{A}\right) - \vec{A}.\left(\vec{\nabla} \wedge \vec{B}\right) \tag{C.10}$$

$$\vec{\nabla} \wedge \left(\vec{A} \wedge \vec{B}\right) = \vec{A}\left(\vec{\nabla}.\vec{B}\right) - \vec{B}\left(\vec{\nabla}.\vec{A}\right) + \left(\vec{B}.\vec{\nabla}\right)\vec{A} - \left(\vec{A}.\vec{\nabla}\right)\vec{B} \tag{C.11}$$

C.1.3 Integral Theorems

$$\iiint_V \vec{\nabla}.\vec{A}\,dV = \oiint \vec{A}.\vec{dS} \tag{C.12}$$

$$\iiint_V \vec{\nabla}\psi\,dV = \oiint \psi\vec{dS} \tag{C.13}$$

$$\iiint_V \vec{\nabla}\wedge\vec{A}\,dV = -\oiint \vec{A}\wedge\vec{dS} \tag{C.14}$$

$$\iiint_V \left(\phi\vec{\nabla}^2\psi + \vec{\nabla}\phi.\vec{\nabla}\psi\right) dV = \oiint \phi\vec{\nabla}\psi.\vec{dS} \tag{C.15}$$

$$\iiint_V \left(\phi\vec{\nabla}^2\psi - \psi\vec{\nabla}^2\phi\right) dV = \oiint \left(\phi\vec{\nabla}\psi - \psi\vec{\nabla}\phi\right).\vec{dS} \tag{C.16}$$

$$\iint_S \left(\vec{\nabla}\wedge\vec{A}\right).\vec{dS} = \oint_C \vec{A}.\vec{dl} \tag{C.17}$$

$$\iint_S \vec{\nabla}\psi\wedge\vec{dS} = -\oint_C \psi\vec{dl} \tag{C.18}$$

C.1.4 Dust Heating and Cooling: Two Ways of Slicing the Pis

One of the most elementary equations for a grain is the relation between its absorption efficiency and the power it absorbs or emits, given in Eq. (I.78) and Eq. (I.79). Yet, it often causes problems to newcomers, who, by trying to visualize the rays, get the numerical factor in the integrand ($4\pi^2 a^2$) wrong. I have seen several improper values: $16\pi^2 a^2$, $4\pi a^2$, *etc.* The solution is of course to explicitly write the integral, which I do below. I also provide two alternative visual solutions to count the factor the right way.

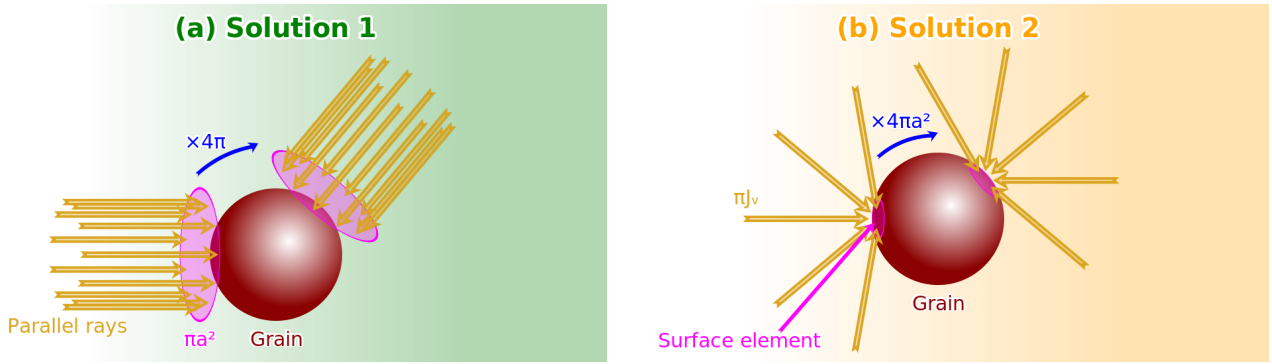

FIGURE C.2 – *Two ways of slicing the πs.* This figure represents the two possible orders to integrate the power absorbed by a grain. For the emitted power, the direction of the arrows is simply reversed. Licensed under CC BY-SA 4.0.

The power absorbed by a spherical grain of radius a, exposed to an isotropic ISRF with mean intensity J_ν, P_{abs}, can expressed as:

$$dP_{abs}(a,\theta,\phi) = \left(\int_0^\infty Q_{abs}(a,\nu)J_\nu(\nu)\,d\nu\right) dA\,d\Omega, \tag{C.19}$$

where dA and $d\Omega = d\cos\theta\,d\phi$ are the grain surface and solid angle elements. Ω indicates the direction of the incident rays. The possible orders of the integrals over these two elements is illustrated in Fig. C.2.

C.1.4.1 Solution 1

The case represented in Fig. C.2.a corresponds to the case where we first integrate over dA. Thus, parallel rays with a given direction (θ,ϕ) intercept the grain on a surface πa^2:

$$\mathrm{dP_{abs}}(a,\theta,\phi) = \pi a^2 \left(\int_0^\infty \mathrm{Q_{abs}}(a,\nu)\mathrm{J}_\nu(\nu)\,\mathrm{d}\nu \right) \mathrm{d}\Omega. \tag{C.20}$$

Then, we need to integrate over all the possible ray directions:

$$\begin{aligned} \mathrm{P_{abs}}(a) &= \pi a^2 \left(\int_0^\infty \mathrm{Q_{abs}}(a,\nu)\mathrm{J}_\nu(\nu)\,\mathrm{d}\nu \right) \iint_{\mathrm{sphere}} \mathrm{d}\Omega & \text{(C.21)} \\ &= \int_0^\infty 4\pi^2 a^2 \mathrm{Q_{abs}}(a,\nu)\mathrm{J}_\nu(\nu)\,\mathrm{d}\nu. & \text{(C.22)} \end{aligned}$$

C.1.4.2 Solution 2

The case represented in Fig. C.2.b corresponds to the case where we first integrate the flux over the ray directions, on an incident surface:

$$\begin{aligned} \mathrm{dP_{abs}}(a) &= \left(\int_0^\infty \mathrm{Q_{abs}}(a,\nu)\mathrm{J}_\nu(\nu)\,\mathrm{d}\nu \right) \int_0^1 \cos\theta\,\mathrm{d}\cos\theta \int_0^{2\pi} \mathrm{d}\phi & \text{(C.23)} \\ &= \pi \left(\int_0^\infty \mathrm{Q_{abs}}(a,\nu)\mathrm{J}_\nu(\nu)\,\mathrm{d}\nu \right). & \text{(C.24)} \end{aligned}$$

There is only a π factor here, as we integrate the flux on a surface element, somewhere on the grain. The rest of the grain shields this surface from the radiation coming from the other hemisphere. In addition, this integration is weighted by the inclination of the rays on the surface (this is the classical flux formula). We thus have the flux received by a surface element of the grain, from all possible ray directions. We now simply need to integrate over the whole grain surface: $4\pi a^2$:

$$\mathrm{P_{abs}}(a) = \int_0^\infty 4\pi^2 a^2 \mathrm{Q_{abs}}(a,\nu)\mathrm{J}_\nu(\nu)\,\mathrm{d}\nu. \tag{C.25}$$

C.2 Statistics

C.2.1 General Formulae

C.2.1.1 Moments of a PDF

Definitions. If we have a joint PDF, $p(x,y)$, of two variables, X and Y, the first moments are the following.

Normalization: $1 = \iint_{-\infty}^{\infty} p(x,y)\,\mathrm{d}x\,\mathrm{d}y.$

Mean: $\langle \mathrm{X} \rangle \equiv \iint_{-\infty}^{\infty} x\,p(x,y)\,\mathrm{d}x\,\mathrm{d}y.$

Variance: $\mathrm{V(X)} \equiv \iint_{-\infty}^{\infty} [x - \langle \mathrm{X} \rangle]^2\,p(x,y)\,\mathrm{d}x\,\mathrm{d}y.$

Skewness: $\gamma_1(\mathrm{X}) \equiv \iint_{-\infty}^{\infty} \left[\frac{x - \langle \mathrm{X} \rangle}{\sigma(\mathrm{X})} \right]^3 p(x,y)\,\mathrm{d}x\,\mathrm{d}y.$

Covariance: $\mathrm{V(X,Y)} \equiv \iint_{-\infty}^{\infty} [x - \langle \mathrm{X} \rangle] \times \left[y - \langle \mathrm{Y} \rangle \right] p(x,y)\,\mathrm{d}x\,\mathrm{d}y.$

Standard-deviation: $\sigma(\mathrm{X}) \equiv \sqrt{\mathrm{V(X)}}.$

Correlation coefficient: $\rho(\mathrm{X}) \equiv \mathrm{V(X,Y)}/\sigma(\mathrm{X})\sigma(\mathrm{Y}).$

Estimators. The most commonly used non-robust estimators are the following.

Mean: $\langle \mathrm{X} \rangle \simeq \frac{1}{\mathrm{N}} \sum_{i=1}^{\mathrm{N}} x_i \quad \left(\pm \frac{\sigma}{\sqrt{\mathrm{N}}} \right)$.

Standard-deviation: $\sigma(\mathrm{X}) \simeq \sqrt{\frac{1}{\mathrm{N}-1} \sum_{i=1}^{\mathrm{N}} (x_i - \langle \mathrm{X} \rangle)^2} \quad \left(\pm \frac{\sigma}{\sqrt{2(\mathrm{N}-1)}} \right)$.

Skewness: $\gamma_1(\mathrm{X}) \simeq \frac{\mathrm{N}}{(\mathrm{N}-1)(\mathrm{N}-2)} \sum_{i=1}^{\mathrm{N}} \left(\frac{x_i - \langle \mathrm{X} \rangle}{\sigma(\mathrm{X})} \right)^3$.

Correlation coefficient: $\rho(\mathrm{X},\mathrm{Y}) \simeq \frac{1}{\mathrm{N}-1} \sum_{i=1}^{\mathrm{N}} \left(\frac{x_i - \langle \mathrm{X} \rangle}{\sigma(\mathrm{X})} \right) \left(\frac{y_i - \langle \mathrm{Y} \rangle}{\sigma(\mathrm{Y})} \right)$.

C.2.1.2 Marginalization

Marginalizing over a parameter, θ:

$$p(y) = \int_{-\infty}^{\infty} p(\theta)\, p\left(y|\theta\right) \mathrm{d}\theta. \tag{C.26}$$

Comparing two data sets, y and $\tilde{y}$:

$$p\left(\tilde{y}|y\right) = \int_{-\infty}^{\infty} p\left(\tilde{y}|\theta\right) p\left(\theta|y\right) \mathrm{d}\theta. \tag{C.27}$$

C.2.1.3 Variable Change

If we have two sets of random variables, $\vec{u}$ and $\vec{v}$, such that $\vec{v} = f(\vec{u})$, then the relation between their PDF is:

$$p_v\left(\vec{v}\right) = |\mathbb{J}| \times p_u\left(f^{-1}\left(\vec{v}\right)\right), \tag{C.28}$$

where the Jacobian of the transformation is:

$$\mathbb{J}_{i,j} \equiv \frac{\partial u_i}{\partial v_j}. \tag{C.29}$$

C.2.1.4 Combining Uncertainties

If we have a set of random variables, $\vec{x}$, the uncertainty of an arbitrary function of these parameters, $f(\vec{x})$, is given by:

$$\sigma^2\left(f(\vec{x})\right) = \left(\vec{\nabla} f(\vec{x})\right)^{\mathrm{T}} \mathbb{V} \vec{\nabla} f(\vec{x}), \tag{C.30}$$

where $\mathbb{V}$ is the covariance matrix of the variable set. In the 2D case, posing $\vec{x} = (a, b)$, we have:

$$\vec{\nabla} f = \begin{pmatrix} \dfrac{\partial f}{\partial a} \\ \\ \dfrac{\partial f}{\partial b} \end{pmatrix} \quad \& \quad \mathbb{V} = \begin{pmatrix} \sigma_a^2 & \rho\sigma_a\sigma_b \\ \rho\sigma_a\sigma_b & \sigma_b^2 \end{pmatrix}, \tag{C.31}$$

and Eq. (C.30) gives the usual expression:

$$\sigma^2_{f(\vec{x})} = \left(\frac{\partial f}{\partial a}\right)^2 \sigma_a^2 + \left(\frac{\partial f}{\partial b}\right)^2 \sigma_b^2 + 2\left(\frac{\partial f}{\partial a}\right)\left(\frac{\partial f}{\partial b}\right) \rho\sigma_a\sigma_b. \tag{C.32}$$

Similarly, the covariance of two functions of the parameter set, $f(\vec{x})$ and $g(\vec{x})$, is:

$$\mathrm{V}(f(\vec{x}), g(\vec{x})) = \left(\vec{\nabla} f(\vec{x})\right)^{\mathrm{T}} \mathbb{V} \vec{\nabla} g(\vec{x}). \tag{C.33}$$

Rant about systematics. There is a long-lasting laboratorian legend that "*systematics must be non-quadratically summed*". This is true in some cases and false in others. Everything depends on what we are talking about.

1. If we are measuring a flux, F, with noise, $\sigma_{\rm noise}$, and calibration uncertainty (systematics), $\sigma_{\rm cal}$, the total uncertainty on the flux will be, according to Eq. (C.32): $\sigma_{\rm tot} = \sqrt{\sigma^2_{\rm noise} + \sigma^2_{\rm cal}}$. This is because $\rho = 0$. The fluctuations of the detector's signal at the time of the observation do not have anything to do with the error the instrument's team made by deriving the calibration factor.
2. Now, if we are summing the flux in two pixels with same flux and noise levels, we will get, using Eq. (C.32): $\sigma_{\rm tot} = \sqrt{2\sigma^2_{\rm noise} + 4\sigma^2_{\rm cal}}$, because the calibration factors of the pixels were correlated. The total calibration uncertainty is this time linearly summed: $\sigma_{\rm cal\,tot} = 2\sigma_{\rm cal}$, because $\rho = 1$ (the error due to the calibration uncertainty is the same for both pixels).
3. If we are now summing two systematics, such as the calibration and the background subtraction uncertainties, $\sigma_{\rm cal}$ and $\sigma_{\rm back}$, we will sum them quadratically: $\sigma_{\rm syst} = \sqrt{\sigma^2_{\rm cal} + \sigma^2_{\rm back}}$. This is because the error the instrument's team made deriving the calibration factor is independent of the error we have made by selecting a region in one of the corners of our map, assuming it was free of galaxy emission.

C.2.2 Useful Probability Distributions

C.2.2.1 Binomial Distribution

Discrete probability distribution to get r successes out of n tries, each one having a probability p:

$$\mathrm{P}_{\rm binomial}(r|p,n) \equiv \mathrm{C}^n_r\, p^r (1-p)^{n-r} = \frac{n!}{r!(n-r)!} p^r (1-p)^{n-r}, \tag{C.34}$$

with $\langle r\rangle = np$ and $\sigma(r) = \sqrt{np(1-p)}$.

C.2.2.2 Poisson Distribution

Discrete probability distribution to get r events per unit time knowing the mean expected number, λ, of such events per unit time:

$$\mathrm{P}_{\rm Poisson}(r|\lambda) \equiv \frac{e^{-\lambda}\lambda^r}{r!}, \tag{C.35}$$

with $\langle r\rangle = \lambda$ and $\sigma(r) = \sqrt{\lambda}$. The superposition of two Poissonian events (λ_a, λ_b) is also Poissonian with mean $\lambda = \lambda_a + \lambda_b$. It is the limit of the binomial distribution to large numbers:

$$\mathrm{P}_{\rm Poisson}(r|\lambda) = \lim_{n\to\infty} \mathrm{P}_{\rm binomial}\left(r\middle|\frac{\lambda}{n}, n\right). \tag{C.36}$$

C.2.2.3 Gaussian Distribution

$$\mathrm{P}_{\rm Gauss}(x|\mu,\sigma) \equiv \frac{1}{\sqrt{2\pi}\sigma} \exp\left(-\frac{(x-\mu)^2}{2\sigma^2}\right), \tag{C.37}$$

with $\langle x\rangle = \mu$, $\sigma(x) = \sigma$ and all superior moments equal to 0. It is the limit of a Poisson distribution when $\lambda \gg 1$: $\mathrm{P}_{\rm Poisson}(r|\lambda) = \lim_{\lambda\gg1} \mathrm{P}_{\rm Gauss}\left(r\middle|\lambda,\sqrt{\lambda}\right)$.

Multivariate form. A multivariate normal law of mean $\vec{\mu}$ and covariance matrix $\mathbb{V}$ is defined as:

$$\mathrm{P}_{\rm Gauss}(\vec{x}\,|\,\vec{\mu},\mathbb{V}) \equiv \frac{1}{(2\pi)^{n/2}\sqrt{|\mathbb{V}|}} \exp\left(-\frac{1}{2}(\vec{x}-\vec{\mu})^{\mathrm{T}}\mathbb{V}^{-1}(\vec{x}-\vec{\mu})\right). \tag{C.38}$$

Error function. Noting $\Phi(x)$ the CDF of a reduced normal law, the *error function* is defined such that:

$$\Phi(x) = \frac{1}{2}\left(1 + \mathrm{erf}\left(\frac{x}{\sqrt{2}}\right)\right). \tag{C.39}$$

It is thus:

$$\mathrm{erf}(x) \equiv \frac{2}{\sqrt{\pi}}\int_0^x e^{-t^2}\,\mathrm{d}t = 2\Phi\left(x\sqrt{2}\right) - 1. \tag{C.40}$$

C.2.2.4 Student's *t* Distribution

It is defined as:

$$\mathrm{P}_{\mathrm{Student}}(x|f) \equiv \frac{1}{\sqrt{f\pi}}\frac{\Gamma\left(\frac{f+1}{2}\right)}{\Gamma\left(\frac{f}{2}\right)}\left(1 + \frac{x^2}{f}\right)^{-\frac{f+1}{2}}, \tag{C.41}$$

with $f > 0$ being the *degree of freedom*. Its mean is 0 and its standard-deviation, for $f > 2$, is $\sigma = \sqrt{f/(f-2)}$.

C.2.2.5 Split-Normal Distribution

It is, to my mind, the most convenient asymmetric distribution:

$$\mathrm{P}_{\text{split-norm}}(x|\mu,\lambda,\tau) \equiv \sqrt{\frac{2}{\pi}}\frac{1}{\lambda(1+\tau)} \times \begin{cases} \exp\left(-\frac{1}{2}\left(\frac{x-\mu}{\lambda}\right)^2\right) & \text{if } x \leq \mu \\ \exp\left(-\frac{1}{2}\left(\frac{x-\mu}{\lambda\tau}\right)^2\right) & \text{if } x > \mu. \end{cases} \tag{C.42}$$

Posing:

$$b = \frac{\pi - 2}{\pi}(\tau - 1)^2 + \tau, \tag{C.43}$$

the first moments are:

$$\langle \mathrm{X} \rangle = \mu + \sqrt{\frac{2}{\pi}}\lambda(\tau - 1) \tag{C.44}$$

$$\sigma(\mathrm{X}) = \sqrt{b}\lambda \tag{C.45}$$

$$\gamma_1(\mathrm{X}) = b^{-3/2}\sqrt{\frac{2}{\pi}}(\tau - 1) \times \left[\left(\frac{4}{\pi} - 1\right)(\tau - 1)^2 + \tau\right]. \tag{C.46}$$

C.2.2.6 Lorentzian Distribution

$$\mathrm{P}_{\mathrm{Lorentz}}(x|\mu,\gamma) \equiv \frac{2}{\pi\gamma}\frac{1}{1 + \left(\frac{x-\mu}{\gamma/2}\right)^2}. \tag{C.47}$$

Its mean is μ, its FWHM is γ, but its standard-deviation is not defined.

C.2.3 Drawing random variables from an arbitrary distribution

C.2.3.1 The Rejection Method

The *rejection method* is a widely used technique to draw a random variable, x', from an arbitrary PDF, $f(x)$. It requires the ability to easily draw a random variable, x_1, from a *proposal distribution*, $g(x)$, such that $g(x) \geq f(x)\ \forall x$. In case $f(x)$ is finite over $[x_{\min}, x_{\max}]$, we can take:

$$g(x) = \begin{cases} \max(f) & \text{for } x_{\min} \leq x \leq x_{\max} \\ 0 & \text{elsewhere.} \end{cases} \tag{C.48}$$

The algorithm is the following.

1. Draw a random variable x_1 from $g(x)$.
2. Draw a uniform random variable between 0 and 1, Θ_1.
3. If $\Theta_1 < f(x_1)/g(x_1)$, then $x' = x_1$ is accepted. Otherwise, if $\Theta_1 \geq f(x_1)/g(x_1)$, this draw is rejected, and we need to go back to the first step.

The closer $g(x)$ is from $f(x)$, the lower the rejection rate will be, and the faster the method will be. It is illustrated in Fig. C.3.a.

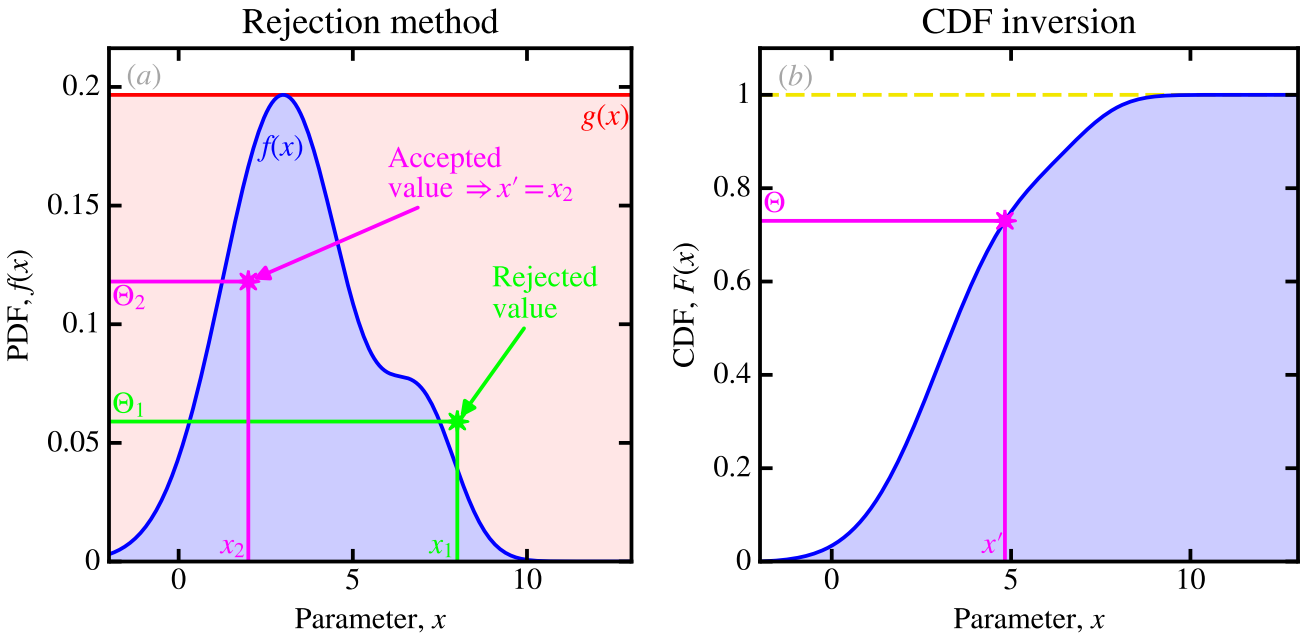

FIGURE C.3 – *Methods for drawing random numbers from arbitrary distributions.* Panel *(a)* represents the rejection method applied to the distribution in blue, with the proposal in red. We have represented a first rejected draw and a second accepted one. Panel *(b)* represents the CDF method applied to the distribution in panel *(a)*. Licensed under CC BY-SA 4.0.

C.2.3.2 Inverting the CDF

A general Monte-Carlo technique to draw a random variable, x', from an arbitrary PDF, $f(x)$, consists in drawing a uniform random variable between 0 and 1, Θ, and inverting the *Cumulative Distribution Function* (CDF) of $f(x)$:

$$\mathrm{F}(x) \equiv \int_{-\infty}^{x} f(y)\,\mathrm{d}y. \tag{C.49}$$

The desired random variable is then simply:

$$x' = \mathrm{F}^{-1}(\Theta). \tag{C.50}$$

It is illustrated in Fig. C.3.b.

C.3 Trigonometry

$$\cos a = \cos b \quad \Leftrightarrow \quad a = b\,[2\pi] \ \vee \ a = -b\,[2\pi] \tag{C.51}$$

$$\sin a = \sin b \quad \Leftrightarrow \quad a = b\,[2\pi] \ \vee \ a = \pi - b\,[2\pi] \tag{C.52}$$

$$\tan a = \tan b \quad \Leftrightarrow \quad a = b\,[2\pi] \tag{C.53}$$

C.3.1 Transformations

C.3.1.1 Rotations

$$\cos\left(\frac{\pi}{2}+x\right)=-\sin x \qquad \sin\left(\frac{\pi}{2}+x\right)=\cos x \tag{C.54}$$

$$\cos\left(\frac{\pi}{2}-x\right)=\sin x \qquad \sin\left(\frac{\pi}{2}-x\right)=\cos x \tag{C.55}$$

$$\cos(\pi-x)=-\cos x \qquad \sin(\pi-x)=\sin x \tag{C.56}$$

$$\cos(\pi+x)=-\cos x \qquad \sin(\pi+x)=-\sin x \tag{C.57}$$

$$\cos(-x)=\cos x \qquad \sin(-x)=-\sin x \tag{C.58}$$

C.3.1.2 Relations Between Functions

$$\cos^2 x+\sin^2 x=1 \qquad 1+\tan^2 x=\frac{1}{\cos^2 x} \tag{C.59}$$

$$\cos(2x)=\frac{1-\tan^2 x}{1+\tan^2 x} \qquad \sin(2x)=\frac{2\tan x}{1+\tan^2 x} \qquad \tan(2x)=\frac{2\tan x}{1-\tan^2 x} \tag{C.60}$$

C.3.2 Addition

C.3.2.1 Summing Angles

$$\cos(a-b)=\cos a.\cos b+\sin a.\sin b \qquad \cos(a+b)=\cos a.\cos b-\sin a.\sin b \tag{C.61}$$

$$\sin(a-b)=\sin a.\cos b-\cos a.\sin b \qquad \sin(a+b)=\sin a.\cos b+\cos a.\sin b \tag{C.62}$$

$$\tan(a-b)=\frac{\tan a-\tan b}{1+\tan a.\tan b} \qquad \tan(a+b)=\frac{\tan a+\tan b}{1-\tan a.\tan b} \tag{C.63}$$

C.3.2.2 Inverse Relations

$$\cos a.\cos b=\frac{1}{2}\left[\cos(a-b)+\cos(a+b)\right] \tag{C.64}$$

$$\cos a.\sin b=\frac{1}{2}\left[\sin(a+b)-\sin(a-b)\right] \tag{C.65}$$

$$\sin a.\sin b=\frac{1}{2}\left[\cos(a-b)-\cos(a+b)\right] \tag{C.66}$$

$$\cos a+\cos b=2\cos\left(\frac{a+b}{2}\right)\cos\left(\frac{a-b}{2}\right) \qquad \cos a-\cos b=-2\sin\left(\frac{a+b}{2}\right)\sin\left(\frac{a-b}{2}\right) \tag{C.67}$$

$$\sin a+\sin b=2\sin\left(\frac{a+b}{2}\right)\cos\left(\frac{a-b}{2}\right) \qquad \sin a-\sin b=2\sin\left(\frac{a-b}{2}\right)\cos\left(\frac{a+b}{2}\right) \tag{C.68}$$

C.3.3 Linearization

C.3.3.1 Squares and Cubes

$$\cos^2 x=\frac{1+\cos(2x)}{2} \qquad \sin^2 x=\frac{1-\cos(2x)}{2} \qquad \tan^2 x=\frac{1-\cos(2x)}{1+\cos(2x)} \tag{C.69}$$

$$\cos^3 x=\frac{\cos(3x)+3\cos x}{4} \qquad \sin^3 x=\frac{-\sin(3x)+3\sin x}{4} \qquad \tan^3 x=\frac{-\sin(3x)+3\sin x}{\cos(3x)+3\cos x} \tag{C.70}$$

C.3.3.2 Inverse Relations

$$\cos(2x) = \cos^2 x - \sin^2 x = 2\cos^2 x - 1 = 1 - 2\sin^2 x \tag{C.71}$$

$$\sin(2x) = 2\sin x.\cos x \qquad \tan(2x) = \frac{2\tan x}{1-\tan^2 x} \tag{C.72}$$

$$\cos(3x) = 4\cos^3 x - 3\cos x \qquad \sin(3x) = 3\sin x - 4\sin^3 x \qquad \tan(3x) = \frac{3\tan x - \tan^3 x}{1-3\tan^2 x} \tag{C.73}$$

Acknowledgements

Bien faire et laisser dire.

(devise d'Étienne François Sallé de Chou)

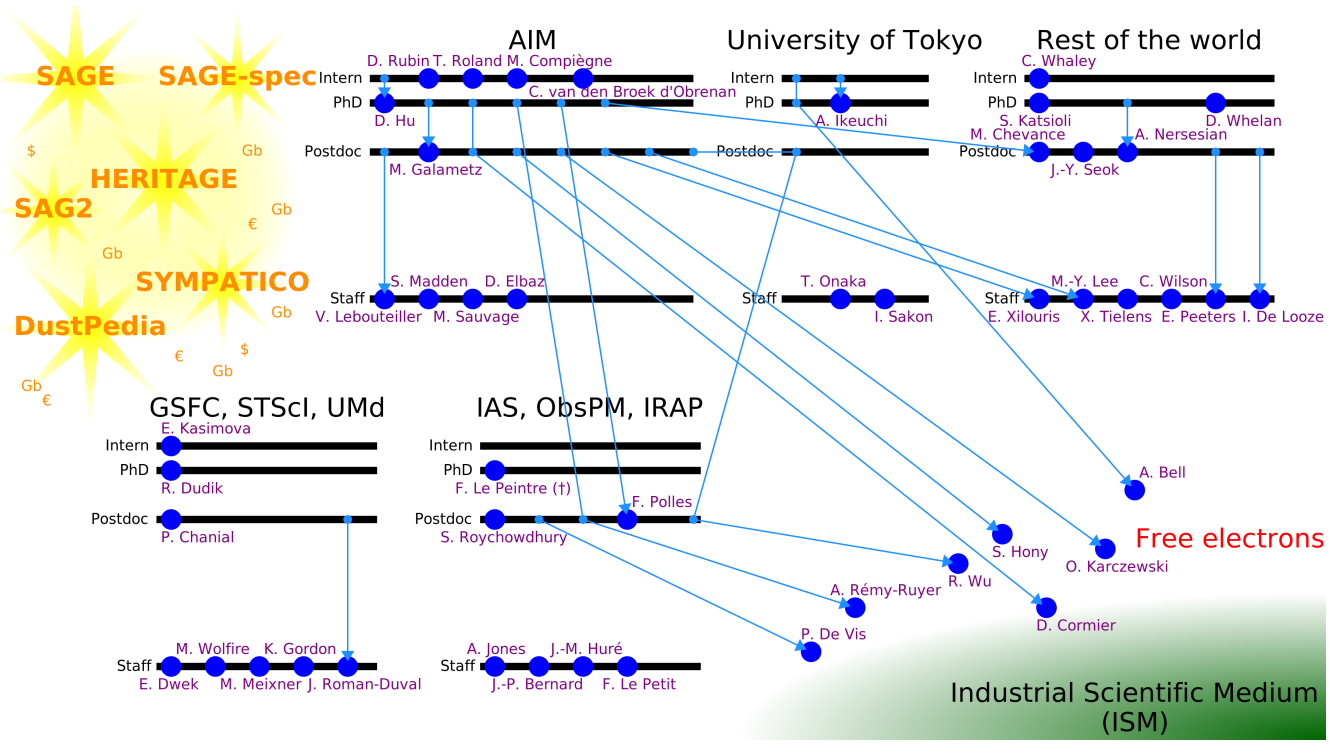

FIGURE D.1 – *Nerdy allegory of my collaboration network.* Large collaborations are sources of funding and of Gigabytes of data. They subsequently trigger transitions between levels in laboratories. Collaborators usually become more bound to their academic institution with time. We also notice some charge exchange and a few individuals becoming free electrons in the private sector. Licensed under CC BY-SA 4.0.

I am particularly grateful to the colleagues who have accepted to participate in my HDR committee and to read this whole manuscript: Véronique Buat, Vassilis Charmandaris, Thomas Henning, Laurent Verstraete, Stéphane Charlot and François-Xavier Désert. I thank them for their comments and the interesting discussions we had. I also thank Hervé Dole for handling the administrative procedure of this accreditation.

I thank the people who willingly provided me with useful comments, clarifying the text and correcting some errors: Dangning Hu, Anthony Jones, Vianney Lebouteiller, Suzanne Madden, Marc-Antoine Miville-Deschênes and Takashi Onaka. I also thank Christine Joblin for her insight on the 3.4 µm feature, and Matteo Bugli for a useful discussion about SNe and collapsars. I thank Anthony Jones and Nathalie Ysard for providing me with their DDA results, plotted in Fig. I.21, and Chia-Yu Hu for his sputtering yield polynomial fits used to make Fig. IV.13. I am finally grateful to all the

people who have granted me the permission to reproduce their figures in this manuscript: Lou ALLAMANDOLA, Jean-Philippe BERNARD, Robert GENDLER, Peter HOPPE, Tom JARRETT, Andy MATTIODA and Marc-Antoine MIVILLE-DESCHÊNES.

☞ No dust grains were harmed in the making of this work.

Bibliography

Abeles, B. & Gittleman, J. I. 1976, Appl. Opt., 15, 2328

Abergel, A., Verstraete, L., Joblin, C., Laureijs, R., & Miville-Deschênes, M.-A. 2005, Space Science Reviews, 119, 247

Alder, K. 2015, Mesurer le monde: 1792-1799: l'incroyable histoire de l'invention du mètre (Flammarion)

Allamandola, L. J., Hudgins, D. M., & Sandford, S. A. 1999, ApJ, 511, L115

Allamandola, L. J., Tielens, A. G. G. M., & Barker, J. R. 1985, ApJ, 290, L25

Aloisi, A., Clementini, G., Tosi, M., et al. 2007, ApJ, 667, L151

Altobelli, N., Postberg, F., Fiege, K., et al. 2016, Science, 352, 312

Alton, P. B., Trewhella, M., Davies, J. I., et al. 1998, A&A, 335, 807

Alton, P. B., Xilouris, E. M., Bianchi, S., Davies, J., & Kylafis, N. 2000, A&A, 356, 795

Alton, P. B., Xilouris, E. M., Misiriotis, A., Dasyra, K. M., & Dumke, M. 2004, A&A, 425, 109

Amelio, G. F., Tompsett, M. F., & Smith, G. E. 1970, The Bell System Technical Journal, 49, 593

Anderson, D., Burnham, K., & Thompson, W. 2000, The journal of wildlife management, 64, 912

Andersson, B.-G., Lazarian, A., & Vaillancourt, J. E. 2015, ARA&A, 53, 501

André, P., Men'shchikov, A., Bontemps, S., et al. 2010, A&A, 518, L102

Andriesse, C. D. 1978, A&A, 66, 169

Aniano, G., Draine, B. T., Gordon, K. D., & Sandstrom, K. 2011, PASP, 123, 1218

Aniano, G., Draine, B. T., Hunt, L. K., et al. 2020, ApJ, 889, 150

Aoyama, S., Hirashita, H., & Nagamine, K. 2020, MNRAS, 491, 3844

Arendt, R. G., Dwek, E., Blair, W. P., et al. 2010, ApJ, 725, 585

Arendt, R. G., Dwek, E., Bouchet, P., et al. 2016, AJ, 151, 62

Arendt, R. G., Dwek, E., Kober, G., Rho, J., & Hwang, U. 2014, ApJ, 786, 55

Asano, R. S., Takeuchi, T. T., Hirashita, H., & Inoue, A. K. 2013, Earth, Planets, and Space, 65, 213

Aschenbach, B. 1991, Reviews in Modern Astronomy, 4, 173

Ashcroft, N. & Mermin, N. 1976, Solid State Physics (Harcourt College Publishers)

Asplund, M., Grevesse, N., Sauval, A. J., & Scott, P. 2009, ARA&A, 47, 481

Atkins, P. 1992, General chemistry (Scientific American Books)

Atkins, P. & Friedman, R. 2005, Molecular quantum mechanics (Oxford University Press)

Audouze, J. & Tinsley, B. M. 1976, ARA&A, 14, 43

Bacon, R., Accardo, M., Adjali, L., et al. 2010, in Proceedings of SPIE - The International Society for Optical Engineering, Vol. 7735, 08

Baes, M. & Camps, P. 2015, Astronomy and Computing, 12, 33

Baes, M. & Dejonghe, H. 2001, MNRAS, 326, 733

Baes, M., Fritz, J., Gadotti, D. A., et al. 2010, A&A, 518, L39

Baes, M., Nersesian, A., Casasola, V., et al. 2020, A&A, 641, A119

Baes, M., Verstappen, J., De Looze, I., et al. 2011, ApJS, 196, 22

Bakes, E. L. O. & Tielens, A. G. G. M. 1994, ApJ, 427, 822

Bame, S. J., McComas, D. J., Barraclough, B. L., et al. 1992, A&AS, 92, 237

Barker, G. F. 1888, Bibliographical memoir of Heny Draper (Report of the National Academy of Sciences)

Barlow, M. J., Krause, O., Swinyard, B. M., et al. 2010, A&A, 518, L138

Barlow, R. J. 1989, Statistics: A Guide to the Use of Statistical Methods in the Physical Sciences (Manchester Physics Series), reprint edn. (WileyBlackwell)

Barnard, E. E. 1899, ApJ, 9, 157

Barnard, E. E. 1919, ApJ, 49, 1

Bauschlicher, Charles W., J., Ricca, A., Boersma, C., & Allamandola, L. J. 2018, ApJS, 234, 32

Bayarri, M. J. & Berger, J. O. 2004, Statistical Science, 19, 58

Bayes, T. 1763, Philosophical Transactions of the Royal Society of London, 53, 370–418

Beaumont, M. & Rannala, B. 2004, Nat Rev Genet, 5, 251–261

Bedell, M., Bean, J. L., Meléndez, J., et al. 2018, ApJ, 865, 68

Beichman, C. A. 1987, ARA&A, 25, 521

Beichman, C. A., Rieke, M., Eisenstein, D., et al. 2012, in Society of Photo-Optical Instrumentation Engineers (SPIE) Conference Series, Vol. 8442, Space Telescopes and Instrumentation 2012: Optical, Infrared, and Millimeter Wave, ed. M. C. Clampin, G. G. Fazio, H. A. MacEwen, & J. Oschmann, Jacobus M., 84422N

Bell, A. C., Onaka, T., Galliano, F., et al. 2019, PASJ, 71, 123

Bendo, G. J., Dale, D. A., Draine, B. T., et al. 2006, ApJ, 652, 283

Bendo, G. J., Galliano, F., & Madden, S. C. 2012, MNRAS, 423, 197

Bendo, G. J., Wilson, C. D., Pohlen, M., et al. 2010, A&A, 518, L65

Bennett, C. L., Larson, D., Weiland, J. L., et al. 2013, ApJS, 208, 20

Benoît, A., Ade, P., Amblard, A., et al. 2004, A&A, 424, 571

Berg, M., Sorensen, C., & Chakrabarti, A. 2011, Journal of Quantitative Spectroscopy & Radiative Transfer, 112, 1170–1181

Bernard, J. P., Ade, P., André, Y., et al. 2016, Experimental Astronomy, 42, 199

Berné, O., Joblin, C., Deville, Y., et al. 2007, A&A, 469, 575

Bertin, E., Mellier, Y., Radovich, M., et al. 2002, in Astronomical Society of the Pacific Conference Series, Vol. 281, Astronomical Data Analysis Software and Systems XI, ed. D. A. Bohlender, D. Durand, & T. H. Handley, 228

Bertoldi, F., Timmermann, R., Rosenthal, D., Drapatz, S., & Wright, C. M. 1999, A&A, 346, 267

Bevan, A., Barlow, M. J., & Milisavljevic, D. 2017, MNRAS, 465, 4044

Bevington, P. R. & Robinson, D. K. 2003, Data reduction and error analysis for the physical sciences (McGraw-Hill)

Bianchi, S. 2007, A&A, 471, 765

Bianchi, S., Casasola, V., Baes, M., et al. 2019, A&A, 631, A102

Bianchi, S., De Vis, P., Viaene, S., et al. 2018, A&A, 620, A112

Bianchi, S. & Schneider, R. 2007, MNRAS, 378, 973

Birkmann, S. M., Ferruit, P., Rawle, T., et al. 2016, in Society of Photo-Optical Instrumentation Engineers (SPIE) Conference Series, Vol. 9904, Space Telescopes and Instrumentation 2016: Optical, Infrared, and Millimeter Wave, ed. H. A. MacEwen, G. G. Fazio, M. Lystrup, N. Batalha, N. Siegler, & E. C. Tong, 99040B

Bisschop, S. E., Fuchs, G. W., van Dishoeck, E. F., & Linnartz, H. 2007, A&A, 474, 1061

Bland, S. 2011, Philosophia Scientiæ, 15-3, 47

Block, D. L., Witt, A. N., Grosbol, P., Stockton, A., & Moneti, A. 1994, A&A, 288, 383

Bocchio, M., Jones, A. P., & Slavin, J. D. 2014, A&A, 570, A32

Bocchio, M., Jones, A. P., Verstraete, L., et al. 2013, A&A, 556, A6

Bocchio, M., Marassi, S., Schneider, R., et al. 2016, A&A, 587, A157

Bocchio, M., Micelotta, E. R., Gautier, A.-L., & Jones, A. P. 2012, A&A, 545, A124

Boersma, C., Bauschlicher, C. W., Allamandola, L. J., et al. 2010, A&A, 511, A32

Boersma, C., Bregman, J., & Allamandola, L. J. 2016, ApJ, 832, 51

Boggess, A., Carr, F. A., Evans, D. C., et al. 1978, Nature, 275, 372

Boggess, N. W., Mather, J. C., Weiss, R., et al. 1992, ApJ, 397, 420

Bohren, C. F. & Huffman, D. R. 1983, Absorption and scattering of light by small particles (Wiley)

Boksenberg, A. 1982, Nature, 298, 795

Bolatto, A. D., Wolfire, M., & Leroy, A. K. 2013, ARA&A, 51, 207

Boogert, A. C. A., Gerakines, P. A., & Whittet, D. C. B. 2015, ARA&A, 53, 541

Boquien, M., Burgarella, D., Roehlly, Y., et al. 2019, A&A, 622, A103

Boquien, M., Duc, P.-A., Galliano, F., et al. 2010, AJ, 140, 2124

Borgman, J., van Duinen, R. J., & Koornneef, J. 1975, A&A, 40, 461

Boselli, A., Ciesla, L., Cortese, L., et al. 2012, A&A, 540, A54

Boselli, A., Eales, S., Cortese, L., et al. 2010, PASP, 122, 261

Bot, C., Ysard, N., Paradis, D., et al. 2010, A&A, 523, A20+

Boulanger, F., Boisssel, P., Cesarsky, D., & Ryter, C. 1998, A&A, 339, 194

Boulanger, F. & Perault, M. 1988, ApJ, 330, 964

Box, G. E. P. 1979, in Robustness in the strategy of scientific model building, ed. R. L. Launer & G. N. Wilkinson (Academic Press), 201–236

Bradley, J. P. 1994, Science, 265, 925

Bransden, B. & Joachain, C. 1983, Physics of atoms and molecules (Longman)

Bron, E. 2014, PhD thesis, LERMA, Observatoire de Paris, PSL Research University, CNRS, Sorbonne Universités, UPMC Univ. Paris 06, F-92190, Meudon, France

Bron, E., Le Bourlot, J., & Le Petit, F. 2014, A&A, 569, A100

Brownlee, D. E., Tsou, P., Anderson, J. D., et al. 2003, Journal of Geophysical Research (Planets), 108, 8111

Buat, V. 2015, Nature, 522, 422

Buat, V., Ciesla, L., Boquien, M., Małek, K., & Burgarella, D. 2019, A&A, 632, A79

Burrows, C. J., Holtzman, J. A., Faber, S. M., et al. 1991, ApJ, 369, L21

Calura, F. & Matteucci, F. 2004, MNRAS, 350, 351

Calzetti, D., Kennicutt, R. C., Engelbracht, C. W., et al. 2007, ApJ, 666, 870

Calzetti, D., Kinney, A. L., & Storchi-Bergmann, T. 1994, ApJ, 429, 582

Cami, J., Bernard-Salas, J., Peeters, E., & Malek, S. E. 2010, Science, 329, 1180

Campbell, E. K., Holz, M., Gerlich, D., & Maier, J. P. 2015, Nature, 523, 322

Camps, P. & Baes, M. 2015, Astronomy and Computing, 9, 20

Cardelli, J. A., Clayton, G. C., & Mathis, J. S. 1989, ApJ, 345, 245

Casasola, V., Cassarà, L. P., Bianchi, S., et al. 2017, A&A, 605, A18

Cauchy, A.-L. 1821, Cours d'analyse de l'École Royale Polytechnique, première partie, Analyse algébrique, Paris (J. Gabay (Sceaux))

Cayrel, R. & Schatzman, E. 1954, Annales d'Astrophysique, 17, 555

Cesarsky, C. J., Abergel, A., Agnese, P., et al. 1996a, A&A, 315, L32

Cesarsky, D., Lequeux, J., Abergel, A., et al. 1996b, A&A, 315, L309

Chabrier, G. 2003, PASP, 115, 763

Charlot, S. & Fall, S. M. 2000, ApJ, 539, 718

Charlot, S. & Longhetti, M. 2001, MNRAS, 323, 887

Chastenet, J., Sandstrom, K., Chiang, I. D., et al. 2019, ApJ, 876, 62

Chevance, M., Madden, S. C., Lebouteiller, V., et al. 2016, A&A, 590, A36

Chiappini, C., Romano, D., & Matteucci, F. 2003, MNRAS, 339, 63

Chiar, J. E. & Tielens, A. G. G. M. 2006, ApJ, 637, 774

Chlewicki, G. & Laureijs, R. J. 1988, A&A, 207, L11

Ciesla, L., Boquien, M., Boselli, A., et al. 2014, A&A, 565, A128

Cignoni, M. & Tosi, M. 2009, Advances in Astronomy, 2010

Clark, C. J. R., De Vis, P., Baes, M., et al. 2019, MNRAS, 489, 5256

Clark, C. J. R., Verstocken, S., Bianchi, S., et al. 2018, A&A, 609, A37

Clegg, P. E., Ade, P. A. R., Armand, C., et al. 1996, A&A, 315, L38

Clements, D. L., Sutherland, W. J., McMahon, R. G., & Saunders, W. 1996, MNRAS, 279, 477

Clerke, A. M. 1903, Problems in Astrophysics (London: A. & C. Black)

Code, A. D., Houck, T. E., McNall, J. F., Bless, R. C., & Lillie, C. F. 1970, ApJ, 161, 377

Cohen-Tannoudji, C., Diu, B., & Laloë, F. 1996, Mécanique quantique (Hermann)

Combes, F. 2000, in The Chaotic Universe, ed. V. G. Gurzadyan & R. Ruffini, 143–172

Compiègne, M., Verstraete, L., Jones, A., et al. 2011, A&A, 525, A103+

Cormier, D., Abel, N. P., Hony, S., et al. 2019, A&A, 626, A23

Cormier, D., Lebouteiller, V., Madden, S. C., et al. 2012, A&A, 548, A20

Cormier, D., Madden, S. C., Hony, S., et al. 2010, A&A, 518, L57+

Cormier, D., Madden, S. C., Lebouteiller, V., et al. 2015, A&A, 578, A53

Cortese, L., Bendo, G. J., Boselli, A., et al. 2010, A&A, 518, L63

Costantini, E., Pinto, C., Kaastra, J. S., et al. 2012, A&A, 539, A32

Croxall, K. V., Smith, J. D., Wolfire, M. G., et al. 2012, ApJ, 747, 81

da Cunha, E., Charlot, S., & Elbaz, D. 2008, MNRAS, 388, 1595

Dalcanton, J. J., Fouesneau, M., Hogg, D. W., et al. 2015, ApJ, 814, 3

Dale, D. A., Cook, D. O., Roussel, H., et al. 2017, ApJ, 837, 90

Dale, D. A., Helou, G., Contursi, A., Silbermann, N. A., & Kolhatkar, S. 2001, ApJ, 549, 215

Dalgarno, A. & McCray, R. A. 1972, ARA&A, 10, 375

Dartois, E., Alata, I., Engrand, C., et al. 2016, IAU Focus Meeting, 29B, 416

Dartois, E., Ding, J. J., de Barros, A. L. F., et al. 2013, A&A, 557, A97

Dartois, E., Muñoz Caro, G. M., Deboffle, D., Montagnac, G., & D'Hendecourt, L. 2005, A&A, 432, 895

Dasyra, K. M., Xilouris, E. M., Misiriotis, A., & Kylafis, N. D. 2005, A&A, 437, 447

Davies, J. I., Alton, P., Trewhella, M., Evans, R., & Bianchi, S. 1999, MNRAS, 304, 495

Davies, J. I., Baes, M., Bianchi, S., et al. 2017, PASP, 129, 044102

Davies, J. I., Nersesian, A., Baes, M., et al. 2019, A&A, 626, A63

Davies, J. I., Wilson, C. D., Auld, R., et al. 2010, MNRAS, 409, 102

Davis, Jr., L. & Greenstein, J. L. 1951, ApJ, 114, 206

De Cia, A., Ledoux, C., Mattsson, L., et al. 2016, A&A, 596, A97

de Graauw, T., Haser, L. N., Beintema, D. A., et al. 1996, A&A, 315, L49

de Graauw, T., Helmich, F. P., Phillips, T. G., et al. 2010, A&A, 518, L6

de Jong, T. 1977, A&A, 55, 137

De Looze, I., Baes, M., Bendo, G. J., et al. 2012a, MNRAS, 427, 2797

De Looze, I., Baes, M., Fritz, J., & Verstappen, J. 2012b, MNRAS, 419, 895

De Looze, I., Barlow, M. J., Bandiera, R., et al. 2019, MNRAS, 488, 164

De Looze, I., Barlow, M. J., Swinyard, B. M., et al. 2017, MNRAS, 465, 3309

De Looze, I., Lamperti, I., Saintonge, A., et al. 2020, MNRAS, 496, 3668

de Vaucouleurs, G. 1959, Handbuch der Physik, 53, 275

De Vis, P., Gomez, H. L., Schofield, S. P., et al. 2017, MNRAS, 471, 1743

De Vis, P., Jones, A., Viaene, S., et al. 2019, A&A, 623, A5

Debye, P. 1909, Annalen der Physik, 335, 57

Degl'Innocenti, S. 2016, Journal of Physics: Conference Series, 703, 012002

Demyk, K., Jones, A. P., Dartois, E., Cox, P., & D'Hendecourt, L. 1999, A&A, 349, 267

Demyk, K., Meny, C., Leroux, H., et al. 2017a, A&A, 606, A50

Demyk, K., Meny, C., Lu, X. H., et al. 2017b, A&A, 600, A123

Désert, F.-X., Boulanger, F., & Puget, J. L. 1990, A&A, 237, 215 (DBP90)

Desert, F. X., Boulanger, F., & Shore, S. N. 1986, A&A, 160, 295

D'Hendecourt, L., Jourdain de Muizon, M., Dartois, E., et al. 1996, A&A, 315, L365

Disney, M., Davies, J., & Phillipps, S. 1989, MNRAS, 239, 939

Diu, B., Guthmann, C., Lederer, D., & Roulet, B. 1997, Physique statistique (Hermann)

Do-Duy, T., Wright, C. M., Fujiyoshi, T., et al. 2020, MNRAS, 493, 4463

Dobbels, W., Baes, M., Viaene, S., et al. 2020, A&A, 634, A57

Dole, H., Lagache, G., Puget, J. L., et al. 2006, A&A, 451, 417

Dolginov, A. Z. & Mitrofanov, I. G. 1976, Ap&SS, 43, 291

Donn, B. 1968, ApJ, 152, L129

Dorschner, J. 1982, Ap&SS, 81, 323

Dorschner, J. 2003, in Astromineralogy, ed. T. K. Henning, Vol. 609, 1–54

Dorschner, J., Begemann, B., Henning, T., Jaeger, C., & Mutschke, H. 1995, A&A, 300, 503

Dowell, J. D., Buckalew, B. A., & Tan, J. C. 2008, AJ, 135, 823

Doyon, R., Hutchings, J. B., Beaulieu, M., et al. 2012, in Society of Photo-Optical Instrumentation Engineers (SPIE) Conference Series, Vol. 8442, Space Telescopes and Instrumentation 2012: Optical, Infrared, and Millimeter Wave, ed. M. C. Clampin, G. G. Fazio, H. A. MacEwen, & J. Oschmann, Jacobus M., 84422R

Draine, B. T. 1978, ApJS, 36, 595

Draine, B. T. 2003a, ARA&A, 41, 241

Draine, B. T. 2003b, ApJ, 598, 1017

Draine, B. T. 2003c, ApJ, 598, 1026

Draine, B. T. 2009, in Astronomical Society of the Pacific Conference Series, Vol. 414, Astronomical Society of the Pacific Conference Series, ed. T. Henning, E. Grün, & J. Steinacker, 453–+ (D09)

Draine, B. T. 2011, Physics of the Interstellar and Intergalactic Medium (Princeton University Press)

Draine, B. T. 2016, ApJ, 831, 109

Draine, B. T. & Anderson, N. 1985, ApJ, 292, 494

Draine, B. T., Aniano, G., Krause, O., et al. 2014, ApJ, 780, 172

Draine, B. T. & Flatau, P. J. 1994, J. Opt. Soc. Am. A, 11, 1491

Draine, B. T. & Hensley, B. 2012, ApJ, 757, 103

Draine, B. T. & Lazarian, A. 1998a, ApJ, 494, L19+

Draine, B. T. & Lazarian, A. 1998b, ApJ, 508, 157

Draine, B. T. & Lee, H. M. 1984, ApJ, 285, 89

Draine, B. T. & Li, A. 2001, ApJ, 551, 807

Draine, B. T. & Li, A. 2007, ApJ, 657, 810

Draine, B. T. & Malhotra, S. 1993, ApJ, 414, 632

Draine, B. T. & Salpeter, E. E. 1979, ApJ, 231, 438

Duley, W. W. & Seahra, S. 1998, ApJ, 507, 874

Duley, W. W. & Williams, D. A. 1981, MNRAS, 196, 269

Dulieu, F., Amiaud, L., Congiu, E., et al. 2010, A&A, 512, A30

Dumke, M., Krause, M., & Wielebinski, R. 2004, A&A, 414, 475

Dwek, E. 1986, ApJ, 302, 363

Dwek, E. 1987, ApJ, 322, 812

Dwek, E. 1998, ApJ, 501, 643

Dwek, E. 2005, in AIP Conf. Proc. 761: The Spectral Energy Distributions of Gas-Rich Galaxies: Confronting Models with Data, ed. C. C. Popescu & R. J. Tuffs, 103

Dwek, E. & Arendt, R. G. 1992, ARA&A, 30, 11

Dwek, E. & Arendt, R. G. 2015, ApJ, 810, 75

Dwek, E., Arendt, R. G., Bouchet, P., et al. 2008, ApJ, 676, 1029

Dwek, E., Arendt, R. G., Fixsen, D. J., et al. 1997, ApJ, 475, 565

Dwek, E., Galliano, F., & Jones, A. P. 2007, ApJ, 662, 927

Dwek, E. & Scalo, J. M. 1980, ApJ, 239, 193

Dwek, E., Staguhn, J., Arendt, R. G., et al. 2014, ApJ, 788, L30

Débarbat, S. & Quinn, T. 2019, Comptes Rendus Physique, 20, 6

Eales, S., Dunne, L., Clements, D., et al. 2010, PASP, 122, 499

Edmunds, M. G. 2001, MNRAS, 328, 223

Elbaz, D., Le Floc'h, E., Dole, H., & Marcillac, D. 2005, A&A, 434, L1

Elmegreen, B. G. & Falgarone, E. 1996, ApJ, 471, 816

Elmegreen, D. M. 2015, in Lessons from the Local Group, ed. K. Freeman, B. Elmegreen, D. Block, & M. Woolway (Cham: Springer International Publishing), 455–462

Elvey, C. T. & Roach, F. E. 1937, ApJ, 85, 213

Endo, I., Sakon, I., Onaka, T., et al. 2021, ApJ, 917, 103

Engelbracht, C. W., Gordon, K. D., Rieke, G. H., et al. 2005, ApJ, 628, L29

Ercolano, B., Barlow, M. J., & Sugerman, B. E. K. 2007, MNRAS, 375, 753

Erickson, E. F. & Meyer, A. W. 2013, in NASA's Kuiper Airborne Observatory, 1971–1995: An Operations Retrospective With a View to SOFIA (NASA)

Erickson, W. C. 1957, ApJ, 126, 480

Event Horizon Telescope Collaboration, Akiyama, K., Alberdi, A., et al. 2019, ApJ, 875, L1

Fan, H., Hobbs, L. M., Dahlstrom, J. A., et al. 2019, ApJ, 878, 151

Fazio, G. G., Hora, J. L., Allen, L. E., et al. 2004, ApJS, 154, 10

Feldmann, R. 2015, MNRAS, 449, 3274

Ferland, G. J., Korista, K. T., Verner, D. A., et al. 1998, PASP, 110, 761

Ferrara, A. & Dettmar, R.-J. 1994, ApJ, 427, 155

Ferrarotti, A. S. & Gail, H.-P. 2006, A&A, 447, 553

Ferreras, I. & Silk, J. 2000, ApJ, 532, 193

Filippone, B. W. 1986, Annual Review of Nuclear and Particle Science, 36, 717

Fioc, M. & Rocca-Volmerange, B. 1997, A&A, 326, 950

Fioc, M. & Rocca-Volmerange, B. 2019, A&A, 623, A143

Fisher, R. 1925, Statistical methods for research workers (Oliver & Boyd)

Fisher, R. A. 1957, BMJ, 2, 43

Fitzpatrick, E. L. & Massa, D. 2005, AJ, 130, 1127

Fitzpatrick, E. L., Massa, D., Gordon, K. D., Bohlin, R., & Clayton, G. C. 2019, ApJ, 886, 108

Fixsen, D. J. & Dwek, E. 2002, ApJ, 578, 1009

Flagey, N., Boulanger, F., Verstraete, L., et al. 2006, A&A, 453, 969

Foreman-Mackey, D., Conley, A., Meierjurgen Farr, W., et al. 2013, emcee: The MCMC Hammer, Astrophysics Source Code Library

Forrey, R. C., Woo, J. W., & Cho, K. 1998, ApJ, 505, 236

Fraser, H. J. & van Dishoeck, E. F. 2004, Advances in Space Research, 33, 14

Fritz, J., Gentile, G., Smith, M. W. L., et al. 2012, A&A, 546, A34

Gail, H. P., Zhukovska, S. V., Hoppe, P., & Trieloff, M. 2009, ApJ, 698, 1136

Galametz, M., Hony, S., Albrecht, M., et al. 2016, MNRAS, 456, 1767

Galametz, M., Hony, S., Galliano, F., et al. 2013, MNRAS, 431, 1596

Galametz, M., Kennicutt, R. C., Albrecht, M., et al. 2012, MNRAS, 425, 763

Galametz, M., Madden, S., Galliano, F., et al. 2009, A&A, 508, 645

Galametz, M., Madden, S. C., Galliano, F., et al. 2011, A&A, 532, A56

Galametz, M., Madden, S. C., Galliano, F., et al. 2010, A&A, 518, L55+

Galliano, F. 2009, in The Evolving ISM in the Milky Way and Nearby Galaxies

Galliano, F. 2017, Planet. Space Sci., 149, 38

Galliano, F. 2018, MNRAS, 476, 1445 (HerBIE)

Galliano, F., Dwek, E., & Chanial, P. 2008a, ApJ, 672, 214

Galliano, F., Galametz, M., & Jones, A. P. 2018, ARA&A, 56, 673

Galliano, F., Hony, S., Bernard, J.-P., et al. 2011, A&A, 536, A88

Galliano, F., Madden, S. C., Jones, A. P., Wilson, C. D., & Bernard, J.-P. 2005, A&A, 434, 867

Galliano, F., Madden, S. C., Jones, A. P., et al. 2003, A&A, 407, 159

Galliano, F., Madden, S. C., Tielens, A. G. G. M., Peeters, E., & Jones, A. P. 2008b, ApJ, 679, 310

Galliano, F., Nersesian, A., Bianchi, S., et al. 2021, A&A, 649, A18 (G21)

Gelman, A., Carlin, J., Stern, H., & Rubin, D. 2004, Bayesian Data Analysis (Chapman & Hall)

Geman, S. & Geman, D. 1984, IEEE Trans. Pattern Anal. Mach. Intell., 6, 721

Ghahramany, N., Gharaati, S., & Ghanaatian, M. 2012, Journal of Theoretical and Applied Physics, 8, 97

Gillett, F. C. & Forrest, W. J. 1973, ApJ, 179, 483

Gillett, F. C., Forrest, W. J., & Merrill, K. M. 1973, ApJ, 183, 87

Goicoechea, J. R., Pety, J., Cuadrado, S., et al. 2016, Nature, 537, 207

Gomez, H. L., Baes, M., Cortese, L., et al. 2010, A&A, 518, L45

Gomez, H. L., Krause, O., Barlow, M. J., et al. 2012, ApJ, 760, 96

Good, I. J. 1960, The British Journal for the Philosophy of Science, 11, 145

Good, I. J. 1975, Synthese, 30, 39

Gordon, K. D., Clayton, G. C., Misselt, K. A., Landolt, A. U., & Wolff, M. J. 2003, ApJ, 594, 279

Gordon, K. D., Engelbracht, C. W., Rieke, G. H., et al. 2008, ApJ, 682, 336

Gordon, K. D., Galliano, F., Hony, S., et al. 2010, A&A, 518, L89+

Gordon, K. D., Meixner, M., Meade, M. R., et al. 2011, AJ, 142, 102

Gordon, K. D., Misselt, K. A., Bouwman, J., et al. 2021, ApJ, 916, 33

Gordon, K. D., Misselt, K. A., Witt, A. N., & Clayton, G. C. 2001, ApJ, 551, 269

Gordon, K. D., Roman-Duval, J., Bot, C., et al. 2014, ApJ, 797, 85

Gould, R. J. & Salpeter, E. E. 1963, ApJ, 138, 393

Grange, J. 2002, Bulletin de la Sabix, 30, 11

Greenberg, J. M. 1968, in Nebulae and Interstellar Matter, ed. B. M. Middlehurst & L. H. Aller, 221

Greenberg, J. M. 1974, ApJ, 189, L81

Greenberg, J. M., Gillette, J. S., Muñoz Caro, G. M., et al. 2000, ApJ, 531, L71

Greenstein, J. L. 1938, ApJ, 87, 151

Grenier, I. A., Casandjian, J.-M., & Terrier, R. 2005, Science, 307, 1292

Griffin, M. J., Abergel, A., Abreu, A., et al. 2010, A&A, 518, L3

Guertler, J., Henning, T., Koempe, C., et al. 1996, A&A, 315, L189

Guhathakurta, P. & Draine, B. T. 1989, ApJ, 345, 230

Guillet, V., Fanciullo, L., Verstraete, L., et al. 2018, A&A, 610, A16

Haas, M., Lemke, D., Stickel, M., et al. 1998, A&A, 338, L33

Habart, E., Walmsley, M., Verstraete, L., et al. 2005, Space Sci. Rev., 119, 71

Hacking, I. 2006, The Emergence of probability (Cambridge University Press)

Hahn, R. 2005, Pierre Simon Laplace, 1749-1827: A Determined Scientist (Harvard University Press)

Hall, J. S. 1937, ApJ, 85, 145

Hall, J. S. 1949, Science, 109, 166

Hao, C.-N., Kennicutt, R. C., Johnson, B. D., et al. 2011, ApJ, 741, 124

Hastings, W. K. 1970, Biometrika, 57, 97

Hauser, M. G., Arendt, R. G., Kelsall, T., et al. 1998, ApJ, 508, 25

Head, M., Holman, L., R., L., A.T., K., & Jennions, M. 2015, PLoS Biol, 13, 3

Hegel, G. 1807, La phénoménologie de l'esprit (GF Flammarion)

Heger, A., Fryer, C. L., Woosley, S. E., Langer, N., & Hartmann, D. H. 2003, ApJ, 591, 288

Heger, M. L. 1922a, Lick Observatory Bulletin, 10, 141

Heger, M. L. 1922b, Lick Observatory Bulletin, 10, 146

Hellmann, J. L., Hopp, T., Burkhardt, C., & Kleine, T. 2020, Earth and Planetary Science Letters, 549, 116508

Hellyer, B. 1970, MNRAS, 148, 383

Helou, G., Malhotra, S., Hollenbach, D. J., Dale, D. A., & Contursi, A. 2001, ApJ, 548, L73

Hempel, C. G. 1945, Mind, 54, 1

Henning, T. 2010, ARA&A, 48, 21

Henning, T. 2010, Laboratory Astrophysics of Cosmic Dust Analogues (Berlin, Heidelberg: Springer Berlin Heidelberg), 313–329

Henry, R. B. C. & Worthey, G. 1999, PASP, 111, 919

Hensley, B., Murphy, E., & Staguhn, J. 2015, MNRAS, 449, 809

Hensley, B. S. & Draine, B. T. 2017, ApJ, 836, 179

Hensley, B. S. & Draine, B. T. 2021, ApJ, 906, 73

Hensley, B. S., Draine, B. T., & Meisner, A. M. 2016, ApJ, 827, 45

Henyey, L. G. & Greenstein, J. L. 1941, ApJ, 93, 70

Herbig, G. H. 1995, ARA&A, 33, 19

Herschel, W. 1785, Phil. Trans. R. Soc., 75, 213–266

Herwig, F. 2003, in Planetary Nebulae: Their Evolution and Role in the Universe, ed. S. Kwok, M. Dopita, & R. Sutherland, Vol. 209, 61

Hildebrand, R. H. 1983, QJRAS, 24, 267

Hiltner, W. A. 1949, Science, 109, 165

Hinz, J. L., Engelbracht, C. W., Skibba, R., et al. 2012, ApJ, 756, 75

Hippelein, H., Haas, M., Tuffs, R. J., et al. 2003, A&A, 407, 137

Hirashita, H. & Kuo, T.-M. 2011, MNRAS, 416, 1340

Hoang, L. 2020, The Equation of Knowledge: From Bayes' Rule to a Unified Philosophy of Science (CRC press)

Hobbs, L. M., York, D. G., Thorburn, J. A., et al. 2009, ApJ, 705, 32

Hobson, M. P. & Padman, R. 1993, MNRAS, 264, 161

Hogg, D. W. 1999, ArXiv Astrophysics e-prints

Hogg, D. W., Bovy, J., & Lang, D. 2010, arXiv e-prints, arXiv:1008.4686

Hollenbach, D. J. & Tielens, A. G. G. M. 1997, ARA&A, 35, 179

Hony, S., Gouliermis, D. A., Galliano, F., et al. 2015, MNRAS, 448, 1847

Hony, S., Kemper, F., Woods, P. M., et al. 2011, A&A, 531, A137

Hony, S., Van Kerckhoven, C., Peeters, E., et al. 2001, A&A, 370, 1030

Hoppe, P. 2010, in Nuclei in the Cosmos, 21

Hoppe, P. & Zinner, E. 2000, J. Geophys. Res., 105, 10371

Hou, K.-C., Hirashita, H., Nagamine, K., Aoyama, S., & Shimizu, I. 2017, MNRAS, 469, 870

Houck, J. R., Roellig, T. L., van Cleve, J., et al. 2004, ApJS, 154, 18

Hoyle, F. & Wickramasinghe, N. C. 1962, MNRAS, 124, 417

Hoyle, F. & Wickramasinghe, N. C. 1970, Nature, 227, 473

Hu, C.-Y., Zhukovska, S., Somerville, R. S., & Naab, T. 2019, MNRAS, 487, 3252

Hu, D., Galliano, F., Onaka, T., et al. 2021a, in prep.

Hu, D., Galliano, F., Onaka, T., et al. 2021b, in prep.

Hubble, E. 1936, The Realm of nebulas (Yale University Press)

Huchtmeier, W. K., Seiradakis, J. H., & Materne, J. 1981, A&A, 102, 134

Huheey, J., Keiter, E., & Keiter, R. 1993, Inorganic chemistry (Harper Collins College Publisher)

Hunt, L. K., Draine, B. T., Bianchi, S., et al. 2015, A&A, 576, A33

Hunt, L. K., Thuan, T. X., Izotov, Y. I., & Sauvage, M. 2010, ApJ, 712, 164

Hunter, D. A., Elmegreen, B. G., & Martin, E. 2006, AJ, 132, 801

Hurwitz, M., Bowyer, S., & Martin, C. 1991, ApJ, 372, 167

Huygens, C. 1657, De Ratiociniis in Ludo Aleae or The Value of all Chances in Games of Fortune (1714 English translation published by Keimer & Woodward)

Hynes, K. M. & Gyngard, F. 2009, in Lunar and Planetary Science Conference, Lunar and Planetary Science Conference, 1198

Indebetouw, R., de Messières, G. E., Madden, S., et al. 2009, ApJ, 694, 84

Indebetouw, R., Mathis, J. S., Babler, B. L., et al. 2005, ApJ, 619, 931

Israel, F. P. 1997, A&A, 328, 471

Israel, F. P., Wall, W. F., Raban, D., et al. 2010, A&A, 519, A67+

Izotov, Y. I., Chaffee, F. H., Foltz, C. B., et al. 1999, ApJ, 527, 757

Izotov, Y. I., Thuan, T. X., & Guseva, N. G. 2007, ApJ, 671, 1297

Jackson, J. 1999, Classical electrocynamics (John Wiley & Sons)

Jansen, F., Lumb, D., Altieri, B., et al. 2001, A&A, 365, L1

Jarrett, T. 2004, PASA, 21, 396

Jaynes, E. T. 1976, Confidence Intervals vs Bayesian Intervals (W. L. Harper and C. A. Hooker), 175

Jaynes, E. T. 2003, Probability Theory: The Logic of Science (Cambridge University Press)

Jeffreys, H. 1939, Theory of Probability (Clarendon Press, Oxford)

Jenkins, E. B. 2009, ApJ, 700, 1299

Jenkins, E. B. & Wallerstein, G. 2017, ApJ, 838, 85

Jenniskens, P. & Desert, F.-X. 1994, A&AS, 106

Joblin, C., Bron, E., Pinto, C., et al. 2018, A&A, 615, A129

Joblin, C., Leger, A., & Martin, P. 1992, ApJ, 393, L79

Joblin, C., Szczerba, R., Berné, O., & Szyszka, C. 2008, A&A, 490, 189

Johnson, J. A. 2019, Science, 363, 474

Johnson, K. E. 2001, PhD thesis, University of Colorado at Boulder

Johnson, K. E., Leitherer, C., Vacca, W. D., & Conti, P. S. 2000, AJ, 120, 1273

Johnson, T. V., Yeates, C. M., & Young, R. 1992, Space Sci. Rev., 60, 3

Jones, A. 2009, in EAS Publications Series, Vol. 35, EAS Publications Series, ed. F. Boulanger, C. Joblin, A. Jones, & S. Madden, 3–14

Jones, A. G., Bendo, G. J., Baes, M., et al. 2015, MNRAS, 448, 168

Jones, A. P. 2004, in ASP Conf. Ser. 309: Astrophysics of Dust, ed. A. N. Witt, G. C. Clayton, & B. T. Draine, 347

Jones, A. P. 2012a, A&A, 540, A1

Jones, A. P. 2012b, A&A, 540, A2

Jones, A. P. 2012c, A&A, 542, A98

Jones, A. P. 2016a, Royal Society Open Science, 3, 160221

Jones, A. P. 2016b, Royal Society Open Science, 3, 160223

Jones, A. P. 2016c, Royal Society Open Science, 3, 160224

Jones, A. P., Fanciullo, L., Köhler, M., et al. 2013, A&A, 558, A62

Jones, A. P., Köhler, M., Ysard, N., Bocchio, M., & Verstraete, L. 2017, A&A, 602, A46 (THEMIS)

Jones, A. P., Tielens, A. G. G. M., & Hollenbach, D. J. 1996, ApJ, 469, 740

Jura, M., Kim, D. W., Knapp, G. R., & Guhathakurta, P. 1987, ApJ, 312, L11

Juvela, M. 2019, A&A, 622, A79

Juvela, M. & Ysard, N. 2012, A&A, 539, A71

Kapala, M. J., Groves, B., Sandstrom, K., et al. 2017, ApJ, 842, 128

Karakas, A. I. & Lattanzio, J. C. 2003a, Publications of the Astronomical Society of Australia, 20, 393

Karakas, A. I. & Lattanzio, J. C. 2003b, Publications of the Astronomical Society of Australia, 20, 279

Karakas, A. I. & Lattanzio, J. C. 2014, PASA, 31, e030

Kaufman, M. J., Wolfire, M. G., & Hollenbach, D. J. 2006, ApJ, 644, 283

Kawada, M., Baba, H., Barthel, P. D., et al. 2007, PASJ, 59, S389

Kebukawa, Y., Koga, M., Sakon, I., et al. 2019, in 82nd Annual Meeting of The Meteoritical Society, Vol. 82, 6160

Keller, L. P. & Messenger, S. 2008, in Lunar and Planetary Science Conference, Lunar and Planetary Science Conference, 2347

Kelly, B. C., Shetty, R., Stutz, A. M., et al. 2012, ApJ, 752, 55

Kemper, F., Vriend, W. J., & Tielens, A. G. G. M. 2004, ApJ, 609, 826

Kennicutt, R. C., Calzetti, D., Aniano, G., et al. 2011, PASP, 123, 1347

Kennicutt, R. C. & Evans, N. J. 2012, ARA&A, 50, 531

Kennicutt, Jr., R. C. 1998a, ARA&A, 36, 189

Kennicutt, Jr., R. C. 1998b, ApJ, 498, 541

Kennicutt, Jr., R. C., Armus, L., Bendo, G., et al. 2003, PASP, 115, 928

Kessler, M. F., Steinz, J. A., Anderegg, M. E., et al. 1996, A&A, 315, L27

Kewley, L. J., Nicholls, D. C., & Sutherland, R. S. 2019, ARA&A, 57, 511

Kimura, H. 2016, MNRAS, 459, 2751

Kirchhoff, G. 1860, The London, Edinburgh, and Dublin Philosophical Magazine and Journal of Science, 20, 1

Kirchschlager, F., Mattsson, L., & Gent, F. A. 2021, arXiv e-prints, arXiv:2109.01175

Kirchschlager, F., Schmidt, F. D., Barlow, M. J., et al. 2019, MNRAS, 489, 4465

Klessen, R. S. & Glover, S. C. O. 2016, Saas-Fee Advanced Course, 43, 85

Kogut, A., Banday, A. J., Bennett, C. L., et al. 1996, ApJ, 464, L5

Köhler, M., Jones, A., & Ysard, N. 2014, A&A, 565, L9

Köhler, M., Ysard, N., & Jones, A. P. 2015, A&A, 579, A15

Kondo, T., Kaneda, H., Oyabu, S., et al. 2012, ApJ, 751, L18

Koornneef, J. 1978, A&A, 64, 179

Kroupa, P. 2001, MNRAS, 322, 231

Krügel, E. 2003, The physics of interstellar dust (IoP)

Krüger, H., Strub, P., Altobelli, N., et al. 2019, A&A, 626, A37

Kunth, D. & Östlin, G. 2000, A&A Rev., 10, 1

Lacy, J. H., Baas, F., Allamandola, L. J., et al. 1984, ApJ, 276, 533

Ladjal, D., Justtanont, K., Groenewegen, M. A. T., et al. 2010, A&A, 513, A53

Lai, T. S. Y., Smith, J. D. T., Baba, S., Spoon, H. W. W., & Imanishi, M. 2020, ApJ, 905, 55

Lai, T. S. Y., Witt, A. N., & Crawford, K. 2017, MNRAS, 469, 4933

Lallement, R., Capitanio, L., Ruiz-Dern, L., et al. 2018, A&A, 616, A132

Lamarre, J. M., Puget, J. L., Ade, P. A. R., et al. 2010, A&A, 520, A9

Lan, T.-W., Ménard, B., & Zhu, G. 2015, MNRAS, 452, 3629

Landau, L. & Lifshtiz, E. 1960, Electrodynamics of continuous media (Pergamon press)

Lanz, T. & Hubeny, I. 2007, ApJS, 169, 83

Laor, A. & Draine, B. T. 1993, ApJ, 402, 441

Laplace, P.-S. 1774, Mémoires de l'Académie royale des sciences de Paris, 4, 27

Laplace, P.-S. 1812, Théorie analytique des probabilités (Académie des sciences)

Laporte, N., Ellis, R. S., Boone, F., et al. 2017, ApJ, 837, L21

Lara-López, M. A., Hopkins, A. M., López-Sánchez, A. R., et al. 2013, Monthly Notices of the Royal Astronomical Society: Letters, 433, L35

Laurent, O., Mirabel, I. F., Charmandaris, V., et al. 2000, A&A, 359, 887

Lęcznar, F. J. 1977, Florida Scientist, 40, 42

Le Bourlot, J., Le Petit, F., Pinto, C., Roueff, E., & Roy, F. 2012, A&A, 541, A76

Le Floc'h, E., Mirabel, I. F., Laurent, O., et al. 2001, A&A, 367, 487

Le Petit, F., Nehmé, C., Le Bourlot, J., & Roueff, E. 2006, ApJS, 164, 506

Lebouteiller, V., Cormier, D., Madden, S. C., et al. 2012, A&A, 548, A91

Lebouteiller, V., Kunth, D., Roman-Duval, J., et al. 2019, BAAS, 51, 157

Lebouteiller, V., Péquignot, D., Cormier, D., et al. 2017, A&A, 602, A45

Lee, J. C., Kennicutt, R. C., José G. Funes, S. J., Sakai, S., & Akiyama, S. 2009a, ApJ, 692, 1305

Lee, J. C., Xiang, J., Ravel, B., Kortright, J., & Flanagan, K. 2009b, ApJ, 702, 970

Lee, J. H., Hwang, H. S., Lee, M. G., Lee, J. C., & Matsuhara, H. 2010, ApJ, 719, 1946

Léger, A. & Puget, J. L. 1984, A&A, 137, L5

Lemke, D., Klaas, U., Abolins, J., et al. 1996, A&A, 315, L64

Lenz, D., Hensley, B. S., & Doré, O. 2017, ApJ, 846, 38

Leroy, A. K., Bolatto, A., Gordon, K., et al. 2011, ApJ, 737, 12

Levi, A. F. J. 2016, Essential Classical Mechanics for Device Physics, 5

Li, A. 2005, in Journal of Physics Conference Series, Vol. 6, Journal of Physics Conference Series, 229–248

Li, A. 2008, in "Small Bodies in Planetary Sciences" (Lecture Notes in Physics vol. 758), ed. I. Mann, A. Nakamura, & T. Mukai, Vol. Chapter 6, 167–188

Li, A. & Draine, B. T. 2001, ApJ, 554, 778

Li, A. & Greenberg, J. M. 2003, in Solid State Astrochemistry, ed. V. Pirronello, J. Krelowski, & G. Manicò, Vol. 120, 37–84

Li, Y., Calzetti, D., Kennicutt, R. C., et al. 2010, ApJ, 725, 677

LIGO collaboration, Abbott, B. P., Abbott, R., et al. 2016, Phys. Rev. Lett., 116, 061102

Lillie, C. F. & Witt, A. N. 1976, ApJ, 208, 64

Lindblad, B. 1935, Nature, 135, 133

Lindley, D. V. 1957, Biometrika, 44, 187

Lindley, D. V. 2001, Journal of the Royal Statistical Society, 49, 293

Lisenfeld, U. & Ferrara, A. 1998, ApJ, 496, 145

Lisenfeld, U., Israel, F. P., Stil, J. M., & Sievers, A. 2002, A&A, 382, 860

Lodders, K. 2003, ApJ, 591, 1220

Loftus, G. 1996, Current directions in psychological science, 5, 161

Loredo, T. J. 1990, in Maximum Entropy and Bayesian Methods, ed. P. F. Fougère (Dordrecht: Springer Netherlands), 81–142

Loredo, T. J. & Lamb, D. Q. 1989, Annals of the New York Academy of Sciences, 571, 601

Lucke, P. B. & Hodge, P. W. 1970, AJ, 75, 171

Lutz, D., Feuchtgruber, H., Genzel, R., et al. 1996, A&A, 315, L269

Lyons, L. 2013, Contemporary Physics, 54, 1

Madau, P. & Dickinson, M. 2014, ARA&A, 52, 415

Madden, S. C., Cormier, D., Hony, S., et al. 2020, A&A, 643, A141

Madden, S. C., Galliano, F., Jones, A. P., & Sauvage, M. 2006, A&A, 446, 877

Madden, S. C., Poglitsch, A., Geis, N., Stacey, G. J., & Townes, C. H. 1997, ApJ, 483, 200

Madden, S. C., Rémy-Ruyer, A., Galametz, M., et al. 2013, PASP, 125, 600

Maddox, L. A., Cowan, J. J., Kilgard, R. E., et al. 2006, AJ, 132, 310

Maíz Apellániz, J., Pantaleoni González, M., Barbá, R. H., García-Lario, P., & Nogueras-Lara, F. 2020, MNRAS, 496, 4951

Malhotra, S., Helou, G., van Buren, D., et al. 1996, A&A, 315, L161

Mandolesi, N., Bersanelli, M., Butler, R. C., et al. 2010, A&A, 520, A3

Marassi, S., Schneider, R., Limongi, M., et al. 2019, MNRAS, 484, 2587

Marcillac, D., Elbaz, D., Chary, R. R., et al. 2006, A&A, 451, 57

Marciniak, A., Joblin, C., Mulas, G., Mundlapati, V. R., & Bonnamy, A. 2021, A&A, 652, A42

Markwardt, C. B. 2009, in Astronomical Society of the Pacific Conference Series, Vol. 411, Astronomical Data Analysis Software and Systems XVIII, ed. D. A. Bohlender, D. Durand, & P. Dowler, 251

Martin, J. D. 2013, PhD thesis, University of Minnesota

Martín-Hernández, N. L., Peeters, E., Morisset, C., et al. 2002, A&A, 381, 606

Martín-Hernández, N. L., Schaerer, D., & Sauvage, M. 2005, A&A, 429, 449

Martínez-González, S., Wünsch, R., Palouš, J., et al. 2018, ApJ, 866, 40

Martins, F., Schaerer, D., & Hillier, D. J. 2002, A&A, 382, 999

Marx, K. 1872, Le Capital. Tome I (BnF)

Mason, R. E., Wright, G. S., Adamson, A., & Pendleton, Y. 2007, ApJ, 656, 798

Mather, J. C., Cheng, E. S., Cottingham, D. A., et al. 1994, ApJ, 420, 439

Mather, J. C., Fixsen, D. J., Shafer, R. A., Mosier, C., & Wilkinson, D. T. 1999, ApJ, 512, 511

Mathewson, D. S. & Ford, V. L. 1970, MmRAS, 74, 139

Mathis, J. S. 1970, ApJ, 159, 263

Mathis, J. S. 1990, ARA&A, 28, 37

Mathis, J. S. 1998, ApJ, 497, 824

Mathis, J. S., Mezger, P. G., & Panagia, N. 1983, A&A, 128, 212

Mathis, J. S., Rumpl, W., & Nordsieck, K. H. 1977, ApJ, 217, 425 (MRN)

Matson, D. L., Spilker, L. J., & Lebreton, J.-P. 2002, Space Sci. Rev., 104, 1

Matsuura, M., Dwek, E., Barlow, M. J., et al. 2015, ApJ, 800, 50

Mattila, K. 1970, A&A, 9, 53

Mattioda, A. L., Hudgins, D. M., Boersma, C., et al. 2020, ApJS, 251, 22

Mattsson, L. 2020, MNRAS, 491, 4334

Mattsson, L. & Andersen, A. C. 2012, MNRAS, 423, 38

Mattsson, L., Andersen, A. C., & Munkhammar, J. D. 2012, MNRAS, 423, 26

McElwain, M. W., Feinberg, L. D., Kimble, R. A., et al. 2020, in Society of Photo-Optical Instrumentation Engineers (SPIE) Conference Series, Vol. 11443, Society of Photo-Optical Instrumentation Engineers (SPIE) Conference Series, 114430T

McGrayne, S. 2011, The Theory That Would Not Die: How Bayes' Rule Cracked the Enigma Code, Hunted Down Russian Submarines, and Emerged Triumphant from Two Centuries of Controversy (Yale University Press)

McKee, C. F. & Ostriker, J. P. 1977, ApJ, 218, 148

McLuhan, M. 1967, The medium is the massage (Bantam)

Meixner, M., Galliano, F., Hony, S., et al. 2010, A&A, 518, L71+

Meixner, M., Gordon, K. D., Indebetouw, R., et al. 2006, AJ, 132, 2268

Meixner, M., Panuzzo, P., Roman-Duval, J., et al. 2013, AJ, 146, 62

Mennella, V., Baratta, G. A., Esposito, A., Ferini, G., & Pendleton, Y. J. 2003, ApJ, 587, 727

Mennella, V., Brucato, J. R., Colangeli, L., et al. 1998, ApJ, 496, 1058

Meny, C., Gromov, V., Boudet, N., et al. 2007, A&A, 468, 171

Merrill, P. W. 1934, PASP, 46, 206

Metropolis, N., Rosenbluth, A. W., Rosenbluth, M. N., Teller, A. H., & Teller, E. 1953, Journal of Chemical Physics, 21, 1087

Meyniel, F. & Dehaene, S. 2017, Proceedings of the National Academy of Sciences, 114, E3859

Mezger, P. G., Duschl, W. J., & Zylka, R. 1996, A&A Rev., 7, 289

Micelotta, E. R., Dwek, E., & Slavin, J. D. 2016, A&A, 590, A65

Micelotta, E. R., Jones, A. P., Cami, J., et al. 2012, ApJ, 761, 35

Micelotta, E. R., Jones, A. P., & Tielens, A. G. G. M. 2010, A&A, 510, A37

Mie, G. 1908, Annalen der Physik, 330, 377

Mill, J. 1843, A system of logic (Félix Alcan)

Minamidani, T., Tanaka, T., Mizuno, Y., et al. 2011, AJ, 141, 73

Misselt, K. A., Gordon, K. D., Clayton, G. C., & Wolff, M. J. 2001, ApJ, 551, 277

Miville-Deschênes, M.-A., Ysard, N., Lavabre, A., et al. 2008, A&A, 490, 1093

Moffat, A. F. J., Shara, M. M., & Potter, M. 1991, AJ, 102, 642

Molster, F. & Kemper, C. 2005, Space Sci. Rev., 119, 3

Moos, H. W., Cash, W. C., Cowie, L. L., et al. 2000, ApJ, 538, L1

Morgan, D. H. 1980, MNRAS, 190, 825

Morgan, D. H., Nandy, K., & Thompson, G. I. 1976, MNRAS, 177, 531

Morgan, H. L. & Edmunds, M. G. 2003, MNRAS, 343, 427

Mori, T. I., Onaka, T., Sakon, I., et al. 2014, ApJ, 784, 53

Mori, T. I., Sakon, I., Onaka, T., et al. 2012, ApJ, 744, 68

Motte, F., Bontemps, S., & Louvet, F. 2018, ARA&A, 56, 41

Muñoz-Mateos, J. C., Gil de Paz, A., Boissier, S., et al. 2009, ApJ, 701, 1965

Murakami, H., Baba, H., Barthel, P., et al. 2007, PASJ, 59, S369

Murphy, E. J., Helou, G., Condon, J. J., et al. 2010, ApJ, 709, L108

Nanni, A., Burgarella, D., Theulé, P., Côté, B., & Hirashita, H. 2020, A&A, 641, A168

Natale, G., Popescu, C. C., Tuffs, R. J., et al. 2015, MNRAS, 449, 243

Nersesian, A., Verstocken, S., Viaene, S., et al. 2020a, A&A, 637, A25

Nersesian, A., Viaene, S., De Looze, I., et al. 2020b, A&A, 643, A90

Nersesian, A., Xilouris, E. M., Bianchi, S., et al. 2019, A&A, 624, A80

Neufeld, D. A. 1991, ApJ, 370, L85

Neugebauer, G., Habing, H. J., van Duinen, R., et al. 1984, ApJ, 278, L1

Neugebauer, G. & Leighton, R. B. 1968, Scientific American, 219, 50

Nisini, B., Kaas, A. A., van Dishoeck, E. F., & Ward-Thompson, D. 2005, Space Sci. Rev., 119, 159

Nittler, L. R., Stroud, R. M., Trigo-Rodríguez, J. M., et al. 2019, Nature Astronomy, 3, 659

Nozawa, T., Kozasa, T., & Habe, A. 2006, ApJ, 648, 435

Öberg, K. I., Fraser, H. J., Boogert, A. C. A., et al. 2007, A&A, 462, 1187

O'Connell, R. W., Gallagher, III, J. S., & Hunter, D. A. 1994, ApJ, 433, 65

Oey, M. S. 1996, ApJ, 467, 666

O'Halloran, B., Galametz, M., Madden, S. C., et al. 2010, A&A, 518, L58+

O'Halloran, B., Satyapal, S., & Dudik, R. P. 2006, ApJ, 641, 795

Okasha, S. 2001, Erkenntnis (1975-), 55, 371

Onaka, T., Matsuhara, H., Wada, T., et al. 2007, PASJ, 59, S401

Oort, J. H. & van de Hulst, H. C. 1946, Bull. Astron. Inst. Netherlands, 10, 187

Ortega, A. & Navarrete, G. 2017, Bayesian Hypothesis Testing: An Alternative to Null Hypothesis Significance Testing (NHST) in Psychology and Social Sciences (IntechOpen), 235

Osterbrock, D. E. 1989, Astrophysics of gaseous nebulae and active galactic nuclei (Research supported by the University of California, John Simon Guggenheim Memorial Foundation, University of Minnesota, et al. Mill Valley, CA, University Science Books, 1989, 422 p.)

Overbeck, J. W. 1965, ApJ, 141, 864

Paerels, F., Brinkman, A. C., van der Meer, R. L. J., et al. 2001, ApJ, 546, 338

Pagel, B. E. J. 1997, Nucleosynthesis and Chemical Evolution of Galaxies (Nucleosynthesis and Chemical Evolution of Galaxies, by Bernard E. J. Pagel, pp. 392. ISBN 0521550610. Cambridge, UK: Cambridge University Press, October 1997.)

Pagel, B. E. J. 2003, in Astronomical Society of the Pacific Conference Series, Vol. 304, Astronomical Society of the Pacific Conference Series, ed. C. Charbonnel, D. Schaerer, & G. Meynet, 187–+

Paladini, R., Montier, L., Giard, M., et al. 2007, A&A, 465, 839

Papoular, R. J. & Papoular, R. 2009, MNRAS, 394, 2175

Paradis, D., Paladini, R., Noriega-Crespo, A., et al. 2012, A&A, 537, A113

Paradis, D., Reach, W. T., Bernard, J., et al. 2009, AJ, 138, 196

Pascal, B. 1670, Pensées (Guillaume Desprez)

Pascale, E., Ade, P. A. R., Bock, J. J., et al. 2008, ApJ, 681, 400

Pearson, K. 1892, The Grammar of Science (A. and C. Black)

Peel, M. W., Dickinson, C., Davies, R. D., Clements, D. L., & Beswick, R. J. 2011, MNRAS, 416, L99

Peeters, E., Hony, S., Van Kerckhoven, C., et al. 2002a, A&A, 390, 1089

Peeters, E., Martín-Hernández, N. L., Damour, F., et al. 2002b, A&A, 381, 571

Peeters, E., Martín-Hernández, N. L., Rodríguez-Fernández, N. J., & Tielens, X. 2005, Space Sci. Rev., 119, 273

Peeters, E., Spoon, H. W. W., & Tielens, A. G. G. M. 2004, ApJ, 613, 986

Perrin, J. M. & Lamy, P. L. 1990, ApJ, 364, 146

Perry, G. W., Frissell, N. A., Miller, E. S., et al. 2018, Radio Science, 53, 933

Pilbratt, G. L., Riedinger, J. R., Passvogel, T., et al. 2010, A&A, 518, L1

Pilleri, P., Montillaud, J., Berné, O., & Joblin, C. 2012, A&A, 542, A69

Pilyugin, L. S. & Grebel, E. K. 2016, MNRAS, 457, 3678

Planck, M. 1900, Verhandlungen der Deutschen Physikalischen Gesellschaft, 2, 202

Planck Collaboration, Abergel, A., Ade, P. A. R., et al. 2014a, A&A, 571, A11

Planck Collaboration, Abergel, A., Ade, P. A. R., et al. 2014b, A&A, 566, A55

Planck Collaboration, Adam, R., Ade, P. A. R., et al. 2016a, A&A, 594, A10

Planck Collaboration, Adam, R., Ade, P. A. R., et al. 2016b, A&A, 596, A103

Planck Collaboration, Ade, P. A. R., Aghanim, N., et al. 2016c, A&A, 586, A132

Planck Collaboration, Ade, P. A. R., Aghanim, N., et al. 2014c, A&A, 571, A8

Planck Collaboration, Ade, P. A. R., Aghanim, N., et al. 2011a, A&A, 536, A17

Planck Collaboration, Ade, P. A. R., Aghanim, N., et al. 2011b, A&A, 536, A20

Planck Collaboration, Ade, P. A. R., Aghanim, N., et al. 2015a, A&A, 582, A28

Planck Collaboration, Ade, P. A. R., Alves, M. I. R., et al. 2015b, A&A, 576, A107

Planck Collaboration, Aghanim, N., Akrami, Y., et al. 2020a, A&A, 641, A12

Planck Collaboration, Aghanim, N., Alves, M. I. R., et al. 2016d, A&A, 596, A105

Planck Collaboration, Akrami, Y., Andersen, K. J., et al. 2020b, A&A, 643, A42

Platt, J. R. 1956, ApJ, 123, 486

Poglitsch, A., Krabbe, A., Madden, S. C., et al. 1995, ApJ, 454, 293

Poglitsch, A., Waelkens, C., Geis, N., et al. 2010, A&A, 518, L2

Popper, K. 1959, The logic of scientific discovery (Hutchinson & Co)

Press, W. H., Teukolsky, S. A., Vetterling, W. T., & Flannery, B. P. 2007, Numerical Recipes 3rd Edition: The Art of Scientific Computing (Cambridge University Press)

Price, S. D. 1968, AJ, 73, 431

Priestley, F. D., Barlow, M. J., & De Looze, I. 2019, MNRAS, 485, 440

Priestley, F. D., De Looze, I., & Barlow, M. J. 2021, MNRAS, 502, 2438

Purcell, E. M. & Pennypacker, C. R. 1973, ApJ, 186, 705

Reach, W. T., Boulanger, F., Contursi, A., & Lequeux, J. 2000, A&A, 361, 895

Reach, W. T., Dwek, E., Fixsen, D. J., et al. 1995, ApJ, 451, 188

Reach, W. T., Morris, P., Boulanger, F., & Okumura, K. 2003, Icarus, 164, 384

Reach, W. T., Rho, J., Jarrett, T. H., & Lagage, P.-O. 2002, ApJ, 564, 302

Rémy-Ruyer, A., Madden, S. C., Galliano, F., et al. 2014, A&A, 563, A31

Rémy-Ruyer, A., Madden, S. C., Galliano, F., et al. 2013, A&A, 557, A95

Rémy-Ruyer, A., Madden, S. C., Galliano, F., et al. 2015, A&A, 582, A121

Rieke, G. H., Wright, G. S., Böker, T., et al. 2015, PASP, 127, 584

Rieke, G. H., Young, E. T., Engelbracht, C. W., et al. 2004, ApJS, 154, 25

Rigopoulou, D., Barale, M., Clary, D. C., et al. 2021, MNRAS, 504, 5287

Robert, C. 2014, Philosophy of science, 216

Robitaille, P.-M. 2009, Progress in Physics, 4

Rocca-Volmerange, B., Prevot, L., Prevot-Burnichon, M. L., Ferlet, R., & Lequeux, J. 1981, A&A, 99, L5

Roche, P. F. & Aitken, D. K. 1984, MNRAS, 208, 481

Rogalski, A. 2012, Opto-Electronics Review, 20

Rogantini, D., Costantini, E., Zeegers, S. T., et al. 2019, A&A, 630, A143

Rogantini, D., Costantini, E., Zeegers, S. T., et al. 2020, A&A, 641, A149

Rojas, J., Duprat, J., Engrand, C., et al. 2021, Earth and Planetary Science Letters, 560, 116794

Roman-Duval, J., Bot, C., Chastenet, J., & Gordon, K. 2017, ApJ, 841, 72

Roman-Duval, J., Gordon, K. D., Meixner, M., et al. 2014, ApJ, 797, 86

Rouleau, F. & Martin, P. G. 1991, ApJ, 377, 526

Roussel, H., Wilson, C. D., Vigroux, L., et al. 2010, A&A, 518, L66

Rowan-Robinson, M. & May, B. 2013, MNRAS, 429, 2894

Rowlands, K., Gomez, H. L., Dunne, L., et al. 2014, MNRAS, 441, 1040

Roy, A., Martin, P. G., Polychroni, D., et al. 2013, ApJ, 763, 55

Rubin, D., Hony, S., Madden, S. C., et al. 2009, A&A, 494, 647

Rudnick, J. 1936, ApJ, 83, 394

Russell, H. N. 1922, Proceedings of the National Academy of Science, 8, 115

Rybicky, G. B. & Lightman, A. P. 1979, Radiative processes in astrophysics (Wiley)

Sadler, E. M. & Gerhard, O. E. 1985, in Lecture Notes in Physics, Berlin Springer Verlag, Vol. 232, New Aspects of Galaxy Photometry, ed. J.-L. Nieto, 269–273

Sales, D. A., Pastoriza, M. G., & Riffel, R. 2010, ApJ, 725, 605

Salpeter, E. E. 1955, ApJ, 121, 161

Sandstrom, K. M., Bolatto, A. D., Bot, C., et al. 2012, ApJ, 744, 20

Sandstrom, K. M., Bolatto, A. D., Draine, B. T., Bot, C., & Stanimirović, S. 2010, ApJ, 715, 701

Sauvage, M., Blommaert, J., Boulanger, F., et al. 1996, A&A, 315, L89

Sauvage, M., Sacchi, N., Bendo, G. J., et al. 2010, A&A, 518, L64

Sauvage, M., Tuffs, R. J., & Popescu, C. C. 2005, Space Science Reviews, 119, 313

Savage, B. D. & Bohlin, R. C. 1979, ApJ, 229, 136

Scaife, A. M. M., Nikolic, B., Green, D. A., et al. 2010, MNRAS, 406, L45

Schalén, C. 1929, Astronomische Nachrichten, 236, 249

Schalén, C. 1931, in Publications of the American Astronomical Society, Vol. 6, Publications of the American Astronomical Society, 376

Schalén, C., medd. Upsala, Astron. Obs., 64, 1936

Schaller, G., Schaerer, D., Meynet, G., & Maeder, A. 1992, A&AS, 96, 269

Schmidt, G. D., Cohen, M., & Margon, B. 1980, ApJ, 239, L133

Schmidt, M. 1959, ApJ, 129, 243

Schoenberg, E. & Jung, B. 1937, Astronomische Mitteilungen der Koeniglichen Universitaets-Sternwarte zu Breslau, 4, 61

Schruba, A., Leroy, A. K., Walter, F., et al. 2012, AJ, 143, 138

Schure, K. M., Kosenko, D., Kaastra, J. S., Keppens, R., & Vink, J. 2009, A&A, 508, 751

Sellgren, K., Werner, M. W., & Dinerstein, H. L. 1983, ApJ, 271, L13

Seok, J. Y., Hirashita, H., & Asano, R. S. 2014, MNRAS, 439, 2186

Serkowski, K. 1973, in IAU Symposium, Vol. 52, Interstellar Dust and Related Topics, ed. J. M. Greenberg & H. C. van de Hulst, 145

Serra, G., Giard, M., Bouchou, F., et al. 2002, Advances in Space Research, 30, 1297

Shetty, R., Kauffmann, J., Schnee, S., & Goodman, A. A. 2009, ApJ, 696, 676

Shipley, H. V., Papovich, C., Rieke, G. H., Brown, M. J. I., & Moustakas, J. 2016, ApJ, 818, 60

Siebenmorgen, R., Heymann, F., & Efstathiou, A. 2015, A&A, 583, A120

Siebenmorgen, R., Voshchinnikov, N. V., & Bagnulo, S. 2014, A&A, 561, A82

Silva, L., Granato, G. L., Bressan, A., & Danese, L. 1998, ApJ, 509, 103

Silva Aguirre, V. 2018, in Asteroseismology and Exoplanets: Listening to the Stars and Searching for New Worlds, ed. T. L. Campante, N. C. Santos, & M. J. P. F. G. Monteiro, Vol. 49, 3

Simmons, J. P., Nelson, L. D., & Simonsohn, U. 2011, Psychological Science, 22, 1359, pMID: 22006061

Skibba, R. A., Engelbracht, C. W., Aniano, G., et al. 2012, ApJ, 761, 42

Slavin, J. D., Dwek, E., & Jones, A. P. 2015, ApJ, 803, 7

Smith, G. D. & Ebrahim, S. 2002, BMJ, 325, 1437

Smith, J. D. T., Croxall, K., Draine, B., et al. 2017, ApJ, 834, 5

Smith, J. D. T., Draine, B. T., Dale, D. A., et al. 2007, ApJ, 656, 770

Smith, M. W. L., Gomez, H. L., Eales, S. A., et al. 2012, ApJ, 748, 123

Smith, R. K. 2008, ApJ, 681, 343

Smith, R. K. & Dwek, E. 1998, ApJ, 503, 831

Smoot, G. F., Tenorio, L., Banday, A. J., et al. 1994, ApJ, 437, 1

Sodroski, T. J., Bennett, C., Boggess, N., et al. 1994, ApJ, 428, 638

Sodroski, T. J., Odegard, N., Arendt, R. G., et al. 1997, ApJ, 480, 173

Soifer, B. T., Neugebauer, G., & Houck, J. R. 1987, ARA&A, 25, 187

Sokal, A. 1996, in Lectures at the Cargèse Summer School on "Functional Integration: Basics and Applications"

Solomon, P. M., Rivolo, A. R., Barrett, J., & Yahil, A. 1987, ApJ, 319, 730

Spitzer, L. 1946, Astronomical advantages of an extra-terrestrial observatory, Tech. rep., report to the RAND corporation

Spitzer, L. 1978, Physical processes in the interstellar medium (New York Wiley-Interscience, 1978. 333 p.)

Spoon, H. W. W., Keane, J. V., Tielens, A. G. G. M., et al. 2002, A&A, 385, 1022

Spoon, H. W. W., Marshall, J. A., Houck, J. R., et al. 2007, ApJ, 654, L49

Spoon, H. W. W., Tielens, A. G. G. M., Armus, L., et al. 2006, ApJ, 638, 759

Stebbins, J., Huffer, C. M., & Whitford, A. E. 1939, ApJ, 90, 209

Stebbins, J. & Whitford, A. E. 1943, ApJ, 98, 20

Stecher, T. P. 1965, ApJ, 142, 1683

Stecher, T. P. & Donn, B. 1965, ApJ, 142, 1681

Stein, C. 1956, in Proceedings of the Third Berkeley Symposium on Mathematical Statistics and Probability, Volume 1: Contributions to the Theory of Statistics (Berkeley, Calif.: University of California Press), 197–206

Stein, W. 1966, ApJ, 144, 318

Steinacker, J., Bacmann, A., & Henning, T. 2002, J. Quant. Spec. Radiat. Transf., 75, 765

Steinacker, J., Bacmann, A., & Henning, T. 2006, ApJ, 645, 920

Steinacker, J., Baes, M., & Gordon, K. D. 2013, ARA&A, 51, 63

Steinicke, W. 2016, Journal of Astronomical History and Heritage, 19, 305

Stephan, T., Bose, M., Boujibar, A., et al. 2020, in Lunar and Planetary Science Conference, Lunar and Planetary Science Conference, 2140

Stepnik, B., Abergel, A., Bernard, J., et al. 2003, A&A, 398, 551

Stevens, J. A., Amure, M., & Gear, W. K. 2005, MNRAS, 357, 361

Strömgren, B. 1939, ApJ, 89, 526

Struve, F. G. W. 1847, Etudes d'Astronomie Stellaire: Sur la voie lactee et sur la distance des etoiles fixes (Imprimerie impériale de l'académie des sciences de St. Pétersbourg)

Sugerman, B. E. K., Ercolano, B., Barlow, M. J., et al. 2006, Science, 313, 196

Tabatabaei, F. S., Braine, J., Xilouris, E. M., et al. 2014, A&A, 561, A95

Tauber, J. A., Mandolesi, N., Puget, J. L., et al. 2010, A&A, 520, A1

Tchernyshyov, K., Meixner, M., Seale, J., et al. 2015, ApJ, 811, 78

Temim, T. & Dwek, E. 2013, ApJ, 774, 8

Temim, T., Dwek, E., Arendt, R. G., et al. 2017, ApJ, 836, 129

The Geodetic Congress. 1883, Nature, 28, 616

Thomson, W. 1889, Popular Lectures and Addresses: Constitution of matter (Macmillan and Company)

Thorburn, J. A., Hobbs, L. M., McCall, B. J., et al. 2003, ApJ, 584, 339

Tielens, A. G. G. M. 1998, ApJ, 499, 267

Tielens, A. G. G. M. 2005, The Physics and Chemistry of the Interstellar Medium (Cambridge University Press)

Tielens, A. G. G. M. 2008, ARA&A, 46, 289

Tielens, A. G. G. M., McKee, C. F., Seab, C. G., & Hollenbach, D. J. 1994, ApJ, 431, 321

Todini, P. & Ferrara, A. 2001, MNRAS, 325, 726

Trewhella, M., Davies, J. I., Alton, P. B., Bianchi, S., & Madore, B. F. 2000, ApJ, 543, 153

Trumpler, R. J. 1930, PASP, 42, 214

Trčka, A., Baes, M., Camps, P., et al. 2020, MNRAS, 494, 2823

Tuffs, R. J., Lemke, D., Xu, C., et al. 1996, A&A, 315, L149

Turcotte, S. & Wimmer-Schweingruber, R. F. 2002, Journal of Geophysical Research (Space Physics), 107, 1442

Turing, A. M. 1937, Proceedings of the London Mathematical Society, s2-42, 230

Useli-Bacchitta, F., Bonnamy, A., Mulas, G., et al. 2010, Chemical Physics, 371, 16

Valencic, L. A. & Smith, R. K. 2015, ApJ, 809, 66

Valiante, R., Schneider, R., Bianchi, S., & Andersen, A. C. 2009, MNRAS, 397, 1661

van de Hulst, H. C. 1949, The solid particles in interstellar space. (Drukkerij Schotanus & Jens)

van de Hulst, H. C. 1986, in Light on Dark Matter, ed. F. P. Israel, Vol. 124, 161–170

van der Tak, F. F. S., Madden, S. C., Roelfsema, P., et al. 2018a, PASA, 35, e002

van der Tak, F. F. S., Madden, S. C., Roelfsema, P., et al. 2018b, PASA, 35, e002

van Winckel, H. 2003, ARA&A, 41, 391

VanderPlas, J. 2014, in Proceedings of the 13th Python in Science Conference, ed. Stéfan van der Walt & James Bergstra, 85 – 93

Városi, F. & Dwek, E. 1999, ApJ, 523, 265 (VD99)

Veneziani, M., Piacentini, F., Noriega-Crespo, A., et al. 2013, ApJ, 772, 56

Venghaus, H. 1977, Physica Status Solidi B Basic Research, 81, 221

Ventura, P., di Criscienzo, M., Schneider, R., et al. 2012, MNRAS, 424, 2345

Verma, A., Charmandaris, V., Klaas, U., Lutz, D., & Haas, M. 2005, Space Science Reviews, 119, 355

Vermeij, R., Peeters, E., Tielens, A. G. G. M., & van der Hulst, J. M. 2002, A&A, 382, 1042

Verstraete, L., Pech, C., Moutou, C., et al. 2001, A&A, 372, 981

Verstraete, L., Puget, J. L., Falgarone, E., et al. 1996, A&A, 315, L337

Viaene, S., Baes, M., Tamm, A., et al. 2017, A&A, 599, A64

Viaene, S., Nersesian, A., Fritz, J., et al. 2020, A&A, 638, A150

Vogler, A., Madden, S. C., Beck, R., et al. 2005, A&A, 441, 491

Voshchinnikov, N. V. 2004, Astrophys. Space Phys. Res., 12, 1

Wagenmakers, E.-J., Lee, M., Lodewyckx, T., & Iverson, G. J. 2008, Bayesian Versus Frequentist Inference (New York, NY: Springer New York), 181–207

Walker, G. A. H., Bohlender, D. A., Maier, J. P., & Campbell, E. K. 2015, ApJ, 812, L8

Walker, H. J. 2000, Astronomy and Geophysics, 41, 10

Walsh, W., Beck, R., Thuma, G., et al. 2002, A&A, 388, 7

Walter, F., Cannon, J. M., Roussel, H., et al. 2007, ApJ, 661, 102

Wasserstein, R. & Lazar, N. 2016, Am. Stat., 33, 70

Weaver, H. & Weaver, P. 1957, PASP, 69, 304

Weil, S. 1947, La pesanteur et la grâce (Plon)

Weingartner, J. C. & Draine, B. T. 2001a, ApJ, 548, 296

Weingartner, J. C. & Draine, B. T. 2001b, ApJS, 134, 263

Weisskopf, M. C., Brinkman, B., Canizares, C., et al. 2002, PASP, 114, 1

Werner, M. W., Roellig, T. L., Low, F. J., et al. 2004, ApJS, 154, 1

Westphal, A. J., Butterworth, A. L., Tomsick, J. A., & Gainsforth, Z. 2019, ApJ, 872, 66

Westphal, A. J., Stroud, R. M., Bechtel, H. A., et al. 2014, Science, 345, 786

Whaley, C. H., Irwin, J. A., Madden, S. C., Galliano, F., & Bendo, G. J. 2009, MNRAS, 395, 97

Whelan, D. G., Lebouteiller, V., Galliano, F., et al. 2013, ApJ, 771, 16

White, D. W., Gerakines, P. A., Cook, A. M., & Whittet, D. C. B. 2009, ApJS, 180, 182

Whitney, B. A. & Hartmann, L. 1992, ApJ, 395, 529

Whittet, D. C. B. 2003, Dust in the galactic environment (IoP)

Willner, S. P., Russell, R. W., Puetter, R. C., Soifer, B. T., & Harvey, P. M. 1979, ApJ, 229, L65

Wilms, J., Brand, T., Barret, D., et al. 2014, in Society of Photo-Optical Instrumentation Engineers (SPIE) Conference Series, Vol. 9144, Space Telescopes and Instrumentation 2014: Ultraviolet to Gamma Ray, ed. T. Takahashi, J.-W. A. den Herder, & M. Bautz, 91445X

Wilson, R. N. 2007, Reflecting Telescope Optics I: Basic Design Theory and its Historical Development (Springer)

Witt, A. N. 1977a, ApJS, 35, 1

Witt, A. N. 1977b, ApJS, 35, 7

Witt, A. N. 1977c, ApJS, 35, 21

Witt, A. N., Friedmann, B. C., & Sasseen, T. P. 1997, ApJ, 481, 809

Witt, A. N. & Oshel, E. R. 1977, ApJS, 35, 31

Witt, A. N. & Vijh, U. P. 2004, in Astronomical Society of the Pacific Conference Series, Vol. 309, Astrophysics of Dust, ed. A. N. Witt, G. C. Clayton, & B. T. Draine, 115

Wolfire, M. G., Hollenbach, D., McKee, C. F., Tielens, A. G. G. M., & Bakes, E. L. O. 1995, ApJ, 443, 152

Wood, K. 1997, ApJ, 477, L25

Wood, K. & Jones, T. J. 1997, AJ, 114, 1405

Wood, K., Whitney, B. A., Robitaille, T., & Draine, B. T. 2008, ApJ, 688, 1118

Woolf, N. J. & Ney, E. P. 1969, ApJ, 155, L181

Woosley, S. E. & Weaver, T. A. 1995, ApJS, 101, 181

Wright, E. L., Eisenhardt, P. R. M., Mainzer, A. K., et al. 2010, AJ, 140, 1868

Wu, R., Bron, E., Onaka, T., et al. 2018a, A&A, 618, A53

Wu, R., Galliano, F., & Onaka, T. 2018b, in The Cosmic Wheel and the Legacy of the AKARI Archive: From Galaxies and Stars to Planets and Life, ed. T. Ootsubo, I. Yamamura, K. Murata, & T. Onaka, 133–136

Wu, R., Hogg, D. W., & Moustakas, J. 2011, ApJ, 730, 111

Wu, R., Madden, S. C., Galliano, F., et al. 2015, A&A, 575, A88

Wu, Y., Charmandaris, V., Hao, L., et al. 2006, ApJ, 639, 157

Xilouris, E. M., Byun, Y. I., Kylafis, N. D., Paleologou, E. V., & Papamastorakis, J. 1999, A&A, 344, 868

Xue, M., Jiang, B. W., Gao, J., et al. 2016, ApJS, 224, 23

Yamagishi, M., Kaneda, H., Ishihara, D., et al. 2012, A&A, 541, A10

Yamagishi, M., Kaneda, H., Ishihara, D., et al. 2015, ApJ, 807, 29

York, D. G., Drake, J. F., Jenkins, E. B., et al. 1973, ApJ, 182, L1

Young, E. T., Becklin, E. E., Marcum, P. M., et al. 2012, ApJ, 749, L17

Ysard, N., Jones, A. P., Demyk, K., Boutéraon, T., & Koehler, M. 2018, A&A, 617, A124

Ysard, N., Köhler, M., Jones, A., et al. 2015, A&A, 577, A110

Ysard, N. & Verstraete, L. 2010, A&A, 509, A12+

Yusef-Zadeh, F., Morris, M., & White, R. L. 1984, ApJ, 278, 186

Zeegers, S. T., Costantini, E., de Vries, C. P., et al. 2017, A&A, 599, A117

Zhu, M., Papadopoulos, P. P., Xilouris, E. M., Kuno, N., & Lisenfeld, U. 2009, ApJ, 706, 941

Zhukovska, S. 2014, A&A, 562, A76

Zhukovska, S., Dobbs, C., Jenkins, E. B., & Klessen, R. S. 2016, ApJ, 831, 147

Zhukovska, S., Gail, H.-P., & Trieloff, M. 2008, A&A, 479, 453

Zubko, V., Dwek, E., & Arendt, R. G. 2004, ApJS, 152, 211 (ZDA04)

Zubko, V. G., Mennella, V., Colangeli, L., & Bussoletti, E. 1996, MNRAS, 282, 1321

Titre : Propriétés et évolution de la poussière interstellaire. Le point de vue des galaxies proches.

Mots clés : Milieu interstellaire – Poussière – Astronomie infrarouge – Évolution des galaxies – Science des données.

Résumé : La poussière interstellaire est un ingrédient physique clef des galaxies, responsable de l'obscurcissement de la formation stellaire, de la régulation du chauffage et du refroidissement du gaz, et de la croissance de la complexité chimique. Dans ce manuscrit, je donne une large revue des propriétés de la poussière interstellaire et des techniques modernes utilisées pour l'étudier. Je commence avec une introduction générale, présentant les principaux concepts, en physique moléculaire et physique du solide, requis pour comprendre la littérature contemporaine sur le sujet. Je passe ensuite en revue les évidences empiriques que nous utilisons de nos jours pour contraindre les modèles à l'état de l'art. S'ensuit une longue discussion sur notre compréhension actuelle des propriétés des grains dans les galaxies proches, avec un accent sur la modélisation des distributions spectrales d'énergie. Le chapitre suivant présente l'évolution des grains, à toutes les échelles. Je passe en revue les différents processus microphysiques d'évolution et la manière dont ils sont pris en compte dans les modèles d'évolution cosmique des grains. Je donne mon opinion sur l'origine de la poussière interstellaire dans les galaxies en fonction de la métallicité. Le dernier chapitre traite de méthodologie. J'y donne une introduction sur la méthode bayésienne et la compare aux techniques fréquentistes. J'y discute les conséquences épistémologiques des deux approches, et montre pourquoi le champ d'étude de la poussière interstellaire requiert un point de vue probabiliste. Je finis le manuscrit par un résumé des avancées majeures obtenues au cours de la dernière décennie et je fais une prospective pour la prochaine.

Title: A Nearby Galaxy Perspective on Interstellar Dust Properties and their Evolution.

Keywords: Interstellar medium – Dust – Infrared astronomy – Galaxy evolution – Data science.

Abstract: Interstellar dust is a key physical ingredient of galaxies, obscuring star formation, regulating the heating and cooling of the gas, and building-up chemical complexity. In this manuscript, I give a wide review of interstellar dust properties and some of the modern techniques used to study it. I start with a general introduction presenting the main concepts, in molecular and solid-state physics, required to understand the contemporary literature on the subject. I then review the empirical evidence we currently use to constrain state-of-the-art dust models. Follows a long discussion about our current understanding of the grain properties of nearby galaxies, with an emphasis on the results from spectral energy distribution modeling. The following chapter presents dust evolution at all scales. I review the different microphysical evolution processes, and the way they are accounted for in cosmic dust evolution models. I give my take on the origin of interstellar dust in galaxies of different metallicities. The last chapter focusses on methodology. I give an introduction to the Bayesian method and compare it to frequentist techniques. I discuss the epistemological consequences of the two approaches, and show why the field of interstellar dust requires a probabilistic viewpoint. I end the manuscript with a summary of the major breakthroughs achieved in the past decade, and delineate a few prospectives for the next decade.

Université Paris-Saclay, France